Ana Luísa Gonçalves Ramos

Assessment of the Long Term Dynamic Behaviour of Innovative Railway Track Solutions

August, 2021

Universidade do Minho
Escola de Engenharia

Ana Luísa Gonçalves Ramos

Assessment of the Long Term Dynamic Behaviour of Innovative Railway Track Solutions

PhD Thesis
Civil Engineering

Work performed under the supervision of:
Professor Doutor António Gomes Correia
Professor Doutor Rui Calçada

August, 2021

Direitos de Autor e Condições de Utilização do Trabalho por Terceiros

Este é um trabalho académico que pode ser utilizado por terceiros desde que respeitadas as regras e boas práticas internacionalmente aceites, no que concerne aos direitos de autor e direitos conexos.

Assim, o presente trabalho pode ser utilizado nos termos previstos na licença abaixo indicada.

Caso o utilizador necessite de permissão para poder fazer um uso do trabalho em condições não previstas no licenciamento indicado, deverá contactar o autor, através do RepositóriUM da Universidade do Minho.

Licença concedida aos utilizadores deste trabalho

Acknowledgments and financial support

Statement of integrity

I hereby declare having conducted this academic work with integrity. I confirm that I have not used plagiarism or any form of undue use of information or falsification of results along the process leading to its elaboration.

I further declare that I have fully acknowledged the Code of Ethical Conduct of the University of Minho.

Avaliação do comportamento dinâmico a longo prazo de soluções ferroviárias inovadoras

Resumo

A investigação apresentada nesta Tese visa aprofundar o conhecimento sobre o comportamento dinâmico a curto e longo prazo da via em laje, da via balastrada e das zonas de transição (com base em estudos numéricos e experimentais), utilizando uma abordagem inovadora e integrada para analisar o problema, contribuindo para uma gestão mais eficiente da via-férrea. Primeiramente, são apresentadas as principais diferenças e semelhanças da via em laje e balastrada. Posteriormente, com o objetivo de contextualizar o estudo das zonas de transição, apresentam-se as principais causas e problemas identificados nestas áreas, as medidas de mitigação usualmente implementadas e as ferramentas numéricas utilizadas. Tendo em vista a compreensão do comportamento a curto e longo prazo das vias férreas, são apresentados os principais modelos que permitem caracterizar o módulo resiliente e a deformação permanente induzidos pelo carregamento cíclico, com principal enfoque nas abordagens empíricas. A partir deste estudo, foi selecionado o modelo capaz de prever a deformação permanente e que será utilizado nos diversos estudos apresentados. Após a compreensão acerca destas metodologias, apresenta-se uma comparação da performance da via em laje e da via balastrada a curto e longo-prazo considerando os mecanismos quasi-estático e dinâmico utilizando a abordagem 2.5D FEM-PML. As tensões do leito são comparadas e avaliadas através do *SAF* e a deformação permanente através do *PDAF*. Após este estudo numérico, foram medidos experimentalmente em laboratório, os deslocamentos da via em laje e da via balastrada ao longo de mais de três milhões de ciclos a partir da simulação da passagem do comboio em apenas alguns dias de teste usando o equipamento GRAFT-2. Foram definidos dois modelos 3D correspondentes à via em laje e balastrada com o intuito de reproduzir numericamente o ensaio laboratorial. Com base nos resultados, foram calibradas numericamente as propriedades geo-mecânicas e o modelo empírico de deformação permanente através do ajuste das duas curvas: numérica e experimental. A partir da calibração realizada, é apresentada a análise relativa à avaliação da performance a curto e longo-prazo de uma zona de transição entre um aterro e um túnel considerando a via em laje como sistema de via. Assim, foi desenvolvido um modelo 3D desta zona de transição de forma a simular o comportamento dinâmico da mesma, incluindo o comportamento a longo prazo da via e os seus principais efeitos na zona de transição, sendo implementada uma metodologia que simula numericamente a evolução do perfil deformado da via resultante do tráfego ferroviário.

Palavras chave: carregamento cíclico, comportamento a longo-prazo, modelação numérica, via balastrada e via em laje, zonas de transição

Assessment of the long term dynamic behaviour of innovative railway track solutions

Abstract

The investigation presented in this Thesis aims at providing insight into the understanding of the short and long term dynamic behaviour of the ballastless track, the ballasted track and the transition zones (based on numerical but also experimental studies) using an innovator and integrated approach to analyse the problem, contributing to a more efficient management of railway track. Firstly, the main differences and similarities of the ballasted and ballastless tracks are presented. Posteriorly, in order to contextualize the study of the transition zones, the main causes and the problems identified in these areas are presented, the main mitigation measures usually implemented, and the numerical tools used. In order to understand the short and long-term behaviour of the railway tracks, the main models that allow characterising the resilient modulus and the permanent deformation induced by cyclic loading are presented, with the main focus on empirical approaches. From this study, the model capable of predicting the permanent deformation was selected and will be used in the various studies presented. After understanding these methodologies, a comparison between the short and long-term performance of the ballasted and ballastless tracks considering the quasi-static and dynamic mechanisms using the 2.5D FEM-PML approach is presented. The subgrade stresses are compared and evaluated through the *SAF* and the permanent deformation through the *PDAF*. After this numerical study, the slab and ballasted tracks' displacements were measured experimentally in the laboratory over more than three million cycles from the simulation of the train passage in just a few test days using the GRAFT-2 facility. Two 3D models corresponding to the ballastless track and ballasted track were defined in order to reproduce numerically the laboratory test. Based on the results, the geo-mechanical properties of the materials were numerically calibrated, as well as, the selected empirical model of permanent deformation by adjusting the two curves: numerical and experimental. From the performed calibration, the analysis of the short and long term performance of a transition zone between an embankment and a tunnel is presented, considering the ballastless track as the railway track system. Thus, a 3D model of this transition zone was developed in order to simulate its dynamic behaviour, including the long term behaviour of the track and its main effects in the transition zone, being implemented a methodology that numerically simulates the evolution of the deformed track profile resulting from the rail traffic.

Keywords: ballasted and ballastless tracks, cyclic loading, long-term behaviour, numerical modelling, transition zones

Summary

List of Abbreviations

AREA	American Railway Engineering Association
BEM	Boundary Element Method
CBGM	cement-bound granular mixtures
CBR	California Bearing Ratio
DEM	Discrete Element Method
FE	Finite Element
FEM	Finite Element Method
FKN	Normal penalty stiffness factor
FPL	Frost Protection Layer
FRA	Federal Railroad Administration
HBL	Hydraulically Bonded layer
HSL	High Speed lines
HMA	Hot Mixed Asphalt
LFWD	Light Falling Weight Deflectometer
LVDT	Linear variable differential transformer
PDAF	Permanent deformation amplification factor
PLT	Plate load test
PML	Perfectly Matching Layers
SAF	Stress amplification factor
SERA	Single European Railway Area
SNCF	National Society of French Railways
SPT	Standard penetration test
TD	Technical Demonstrators
UGM	Unbound granular material
UIC	International Union of Railways
USP	Under sleeper pads

List of Figures

xxvii

List of Symbols

The symbols specifically related to the resilient modulus and empirical permanent deformation models (Chapter 4) are explained in detail in the Annex. The consideration of those symbols in the glossary would just double the information. In the Annex, the explanation of the symbols is accompanied by the context and scope of its definition and nature.

<u>General symbols</u>

(x, y, z)	Cartesian Coordinates
λ	Wavelength
t	Time
x	Space
T	Period
k_I	Wavenumber

<u>Elastodynamics</u>

f	Frequency
ω	Angular frequency
EI	Bending stiffness
k_{eq}	Equivalent stiffness
m	Mass of the track per unit length
$v\ or\ c$	Train speed
M	Mass matrix
M^*	Mass matrix in the PML domain
K	Stiffness matrix
K^*	Stiffness matrix in the PML domain
C	Damping matrix/ Viscous damping/ *Rayleigh* damping matrix
$C_{weighted}$	Weighted damping matrix
$\delta\varepsilon$	Virtual strain field
σ	Stress field
δu	Virtual displacement field
u	Displacement field
$u_{c,i}$	Vertical displacements of the contact point i of the vehicle

u_r	Rail displacement
Δu	Rail unevenness
a_i	Location of the contact point i at t=0s
P_i	Dynamic interaction load developed at the connection point i. wheel-rail contact is simulated by a linearized *Hertzian* stiffness
P_z	Amplitude of the harmonic
$p(\Omega)$	Vector that contains the interaction forces for each connection points
$[F]$	Train compliance at the contact points with the track
$[F^a]$	Diagonal matrix where the terms are equal to $1/k_H$,
$[A]$	Compliance matrix of the track
Ω	Driven frequency
u_c^G	Vertical displacement of the rail in the transformed domain due to a half-unit load applied in the head of each rail
p	Applied loads
N	Shape function matrix
B	Matrix with the derivative of the shape functions
D	Strain-stress matrix
u_n	Nodal displacements (in the transformed domain)
L	Differential operator matrix $[L]$ (on the transformed domain)
λ_y	Stretching function in the y-direction
λ_z	Stretching function in the z-direction
F	Exterior loads
$M\ddot{u}$	Inertia forces
$C\dot{u}$	Damping forces
Ku	Elastic forces
u_n	Displacements at the instant calculus time n
u_{n+1}	Displacements at the instant calculus time $n+1$
β and γ	Constants of the Newmark's method
Δt	Increment time
N_{mat}	Total number of the materials

α	Parameter of the damping Rayleigh matrix that multiplies the mass' matrix of the system
β_i	Parameter of the damping Rayleigh matrix that corresponds to the material i that multiplies the global stiffness's matrix (K)
C_p or v_p	Primary wave speed
C_s or v_s	Shear wave speed
C_1 and C_2	Dimensionless relaxation coefficients or viscosity coefficients
s	Ratio between the propagation speeds of the S and P waves

Contact theory

a	Radius of the circular contact area
P	Total load (compression of the bodies in contact)
R	Radius of curvature equivalent
E_1	Deformability modulus of one of the two bodies in contact
E_2	Deformability modulus of one of the two bodies in contact
v_1	Poisson's ratio of one of the two bodies in contact
v_2	Poisson's ratio of one of the two bodies in contact
δ	Distance between the two points of the solids in contact
p_0	Maximum contact pressure
C_H	Hertzian constant
k_H	Contact stiffness
X^a	Coordinate of the body C^a
u^a	Displacement vector
Γ^1	Boundary of the body 1
Γ^2	Boundary of the body 2
ξ	Local referential
D	Minimum distance
$\bar{x}^1$	Orthogonal projection of x^2 of the contact surface Γ^2 in the contact surface Γ^1
g_N	Condition of non-penetration between the bodies
$\bar{g}_n$	Function of penetration between the bodies
t^1	Normal component of the stress vector

$\Pi(u)$	Potential energy between two bodies in contact
b	Vector of the volumetric forces
t	Vector of the forces of the surface applied in the body α
σ	Vector that characterises the stress state at a certain point
ε^{α}	Vector that characterises the deformation at a certain point
Πc	Additional/contact parcel (considered in the determination of the equilibrium equation of the bodies)
δu^{α}	Infinitesimal variation of the displacement u
$\delta\varepsilon^{\alpha}$	Infinitesimal deformation correspondent to δu^{α}
e_N	Penalty parameter
Π_{int}	Intern energy of the two bodies in contact,
u	Displacements vector and contains the nodal displacements of the bodies
P	Matrix that stores all the forces applied into the bodies' surface volumetric forces
$G(u)$	Vector that depends on the field of displacements u of the nodes possibly involved in the contact.

Geotechnical Symbols

E	Deformability modulus or *Young* modulus
E_{v2}	Second deformation modulus
M_r	Resilient modulus
ν	Poisson's ratio
c	Cohesion
ϕ	Friction angle
γ	Dry density
ε_p or ε_N	Permanent deformation (or plastic strain)
K_0	Coefficient of horizontal earth pressure at rest
δ	Cumulative permanent displacement
ρ	Mass density
ξ	Hysteretic damping
σ_s or q	Soil deviator stress

q_{ini}	Initial soil deviator stress
q_{am}	Deviator stress induced by the passage of the vehicle
$d_{q;max}$	Maximum increment of the deviator stress
p	Isotropic or mean stress
p'	Effective mean stress
p_{ini}	Initial isotropic stress
p_{am}	Mean stress induced by the passage of the vehicle
$d_{p;max}$	Maximum increment of the mean stress
q_o	Ordinate of the line of the critical state in the referential p-q when p is null
M	Slope of the line of the critical state in the referential p-q
k	Stiffness
θ	Invariant stress
J_2 and J_3	Invariants of the stress state
I_1, I_2 and I_3	invariants of the stress state
σ_1, σ_2 and σ_3	Principal stresses
Sx, Sz, Sy, Sxy, Sxz, Syz or σx, σz, σy, σxy, σxz, σyz	Horizontal, vertical and shear stresses, respectively
$\sigma_{rupture}$	Stress of rupture
N	Number of load cycles
$N_{i,eq}$ or N_i^{eq}	Equivalent load cycle
N_{i-1}	Total number of load cycles at the end of the previous $(i\text{-}1)_{th}$ stress path
ΔN	Set of cycles
P_i	Required resistance capacity
QS_i	Soil's classification
n	Porosity
μ	Friction coefficient
$|\delta_{cum;max}|_{stat}$	Maximum value of the cumulative permanent deformation (static conditions)
$|\delta_{cum;max}|_{dyn}$	Maximum value of the cumulative permanent deformation (dynamic conditions)

G	Shear modulus
N_{SPT}	Number of blows during the SPT test
P	Pre-load coefficient
P_0	Reference of the pre-load
x	Factor that takes into account the influence of the pre-load

Track properties

k_c	Continuous vertical stiffness
k	Discrete stiffness of the support
$k_{railpad}$	Stiffness of the railpad
$k_{sleeper}$	Stiffness of the sleeper
$k_{ballast}$	Stiffness of the ballast
$k_{foundation}$ or k_f	Stiffness of the foundation
$k_{ballast+foundation}$	Combined stiffness of the ballast and foundation
e or D	Spacing between the supports (normally corresponds to the sleepers)
k_{rp}	Discrete stiffness of the railpad
c_{rp}	Damping of the railpad
k_b	Discrete stiffness of the ballast
c_b	Damping of the ballast
k_{sb}	Discrete stiffness of the sub-ballast
k_{sb}	Stiffness of the sub-ballast
c_{sb}	Damping of the sub-ballast
k_f	Discrete stiffness of the foundation
c_f	Damping of the foundation
M_{bal}	Punctual mass of the ballast block
k'_b	Stiffness of the ballast in the longitudinal direction
c'_b	Damping of the ballast in the longitudinal direction
k'_{sb}	Stiffness of the sub-ballast in the longitudinal direction
c'_{sb}	Damping of the sub-ballast in the longitudinal direction
H_b or h_b	Thickness of the ballast
H_{sb}	Thickness of the sub-ballast

h_1	Thickness of the slab
h_2	Thickness of the support layer
x_p	Displacement of the railpad
K_1 and K_2	Stiffness of the railpads (independent of the frequency),
C_2	Damping (dependent on the frequency)
E_b	Deformability modulus of the ballast
E_{sb}	Deformability modulus of the sub-ballast
E_f	Deformability modulus of the foundation
l_e	Effective support of half sleeper
l_b	Width of the sleeper's base
α	Angle of degradation of the stresses in the layer
M_b	Vibrant mass of the ballast layer
M_{sb}	Vibrant mass of the sub-ballast layer
ρ_b	Density of the ballast
θ_b	Friction angle of the ballast
θ_{sb}	Friction angle of the sub-ballast
L_s	Length of the support area that corresponds to the sleeper
B_s	Width of the support area
R	Curvature of a profile with a sinusoidal shape
L	Length of a profile with a sinusoidal shape

Generation of irregularity profiles

N	Total number of harmonics considered in the generation of the irregularity profile
δ_{u_j}	Complex entity that reflects the amplitude of the correspondent harmonic considered in the generation of the irregularity profile
A_j	Amplitude of the correspondent harmonic considered in the generation of the irregularity profile
θ_j	Random phase angle
φ	Phase angle (in radians)
Δk_1	Increment of the wave-number

S_{rzz}	Parameter used to define the amplitude of the artificial irregularity profile
A	Parameter dependent on the geometric quality of the railway
k_1	Wavenumber
k_2 and k_3	Constants
$D1$ and $D2$	Classes related to the geometric quality of the railway defined in the standard EN13848-5 (2008)

Train properties

K_p	Stiffness of the primary suspension
C_p	Damping od the primary suspension
M_e	Concentrated mass of the wheelset
K_s	Stiffness of the secondary suspension
C_s	Damping od the secondary suspension
M_b or m_2	Mass of the bogie
M_c	Mass of the car body
m_1	Mass of the axle
m_3	Mass of the box of the vehicle

Optimization

lb	Lower bound
ub	Upper bound
$x0$	Initial values
x	Values to be determined

Other

k	Ratio of dynamic to static wheel load
D	Wheel diameter
α	Factor that multiplies the loads (dynamic loads), also known as a dynamic factor; the loads from the LM71 can be multiplied by the factor α
ψ_i	Combination factors
P	Load
y_m	Maximum displacement measured

A_e	Average axle load
L	Tamping lift
Δt	Time lag between neighbouring actuators
Δs	Distance between the two adjacent actuators

List of Tables

1 Introduction

1.1 Background and motivation

The high-speed railway in Europe had its genesis in France, in the 80s of the 20th century with the construction of the *Paris-Lyon* railway line. Since that time, new high-speed lines have already been built (some are in operation and some are in construction) and significant growth is expected in the next years.

Historically, the first high-speed train service occurred in Japan in 1964 from Tokyo to Osaka (with a speed equal to 210 km/h). However, some significant speeds in Europe before that date were also recorded, mainly in Germany, Italy, UK and especially in France, in 1955, with a record speed equal to 331 km/h. The maximum operating speed and speed record are presented in Figure 1.1. This figure shows the continuum search for higher speeds in order to increase the connectivity between cities and even countries. For example, nowadays, the maximum operating speed is close to 500 km/h but this speed can increase until 700 km/h, which corresponds to the maximum record speed. In the past, the above-mentioned Japanese line was built to support and follow the impressive growth of the Japanese economy. Indeed, the "new" high-speed lines defined a new transport system that was later extended to other Japanese areas to serve future generations. Considering the success in Japan, new technologies and innovative tools to build the "railway of the future" were developed in Europe. Indeed, Europe presented important advantages since the "new European railway network" was compatible with the existing railway lines, in contrast with the Japanese railway network (UIC, 2015). Thus, the growth of high-speed lines wasn't just a European or even Japanese phenomenon but also occurs worldwide. In fact, the continued exponential growth of the high-speed railways is expected considering that, currently, there are 29792 km of high-speed lines in the world. The high-speed system and its distribution in the world (recorded on 1st April of 2015) are presented in Figure 1.2, with the main focus on Asia and Europe. The distribution of 1600 million passengers per year and per country is shown in Figure 1.3 based on the data presented by UIC (2015). Thus, from Figure 1.2 and Figure 1.3, it is possible to understand that the railway market is more prominent and promising in Asia, especially in China. This is due, obviously, to the number of passengers but also due to the area of the country and the necessity to increase the connectivity between the major cities by the railway lines.
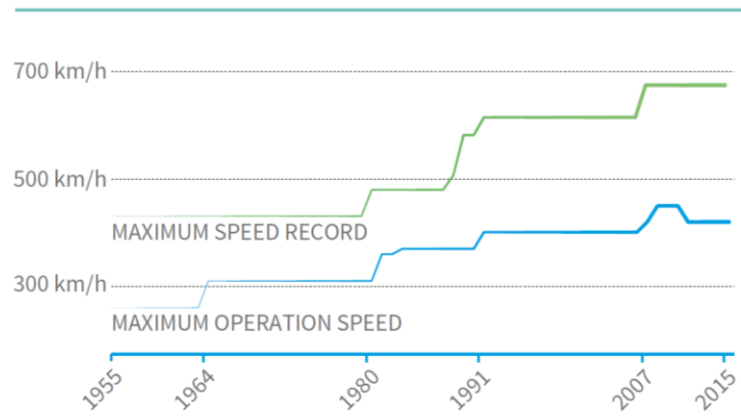
Figure 1.1 - Maximum operation speed and speed record (UIC, 2015)

a)

b)

Figure 1.2 – High-speed system in the world: a) European area; b): Asia area (UIC, 2015)
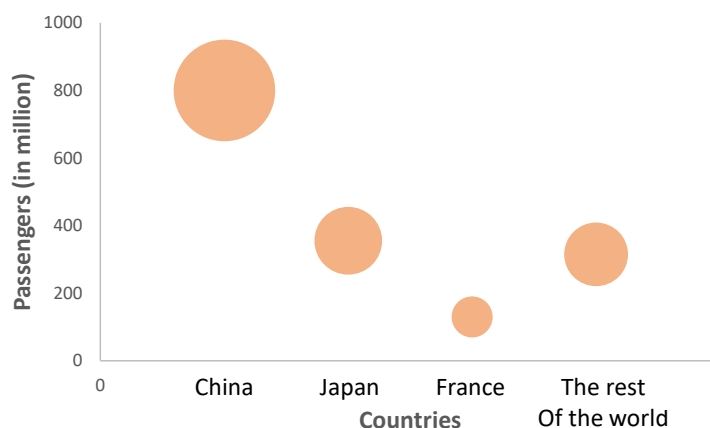
Figure 1.3 - Distribution of the passengers by the main countries where the high-speed have a significant presence

The growth and the necessity to build new railway tracks are justified by the growth of the world population and urgency regarding the decrease of the intensive use of the vehicles that lead, as is well-known, to the increase of the traffic congestion and environmental problems allied to climate change (Paixão, 2014). The European Union faces, nowadays, these problems, and requires that the railway sector (which includes, above all, enterprises and also universities) assumes significant importance in the demand for this type of transport in the next decades. The necessity of increasing urgently the offer of the railway network is also justified by the fact that, in 2025, it is expected exist more than 40000 km of high-speed railway tracks in the world, as depicted in Figure 1.4, and Europe needs to keep up with this exponential growth.
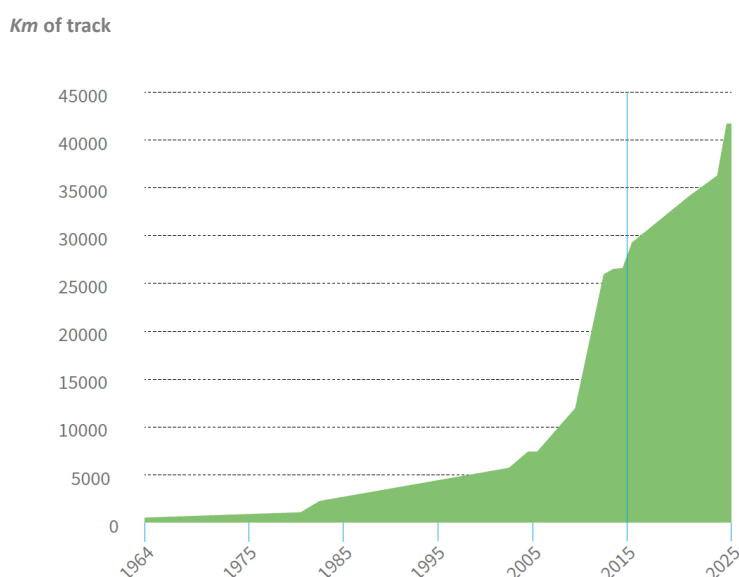
Figure 1.4 – Prediction of the temporal evolution of high-speed railway tracks in the world (UIC, 2015)

The European Commission, aligned with the political positions of the European Union, under the *SHIFT2RAIL* project, aims to create a *Single European Railway Area* (SERA), considering that is imperative to have, over the next few years, a modal shift from road transportation towards rail freight and passenger transport, increasing the competitiveness and economic growth. Furthermore, the urgent need for a modal shift is also supported by the greener and sustainable characteristics of the railway system, as shows Figure 1.5.

Considering the results presented in Figure 1.4 and also Figure 1.6, the current results remain unsatisfactory, which means that is necessary to introduce better trains in the market (more quiet, comfortable and dependable) that will circulate in an innovator rail network with a lower life cycle cost. The *SHIFT2RAIL* project wants to contribute and introduce innovation in the railway sector and sustain the European rail industry as the leadership of the global market. This work will be developed by European companies to increase and help to gain a stronger global market position. In fact, these changes present several advantages to the future EU passengers that will have more travel options and more comfort. In the case of the freight trains, this innovator project offers a more cost-effective and also punctuality. The *SHIFT2RAIL* project purposes a reduction of the life-cost of the railway transportation (that includes construction, exploration, maintenance and renovation costs of the existing railway lines, as well as the rolling stock) up to 50%, duplication of the railway capacity and increase of the reliability and punctuality up to 50%. Thus, the *SHIFT2RAIL* project commits itself to make some changes in all the segments of the railway market which includes the high-speed lines, regional, urban/subway, suburban and freight service.
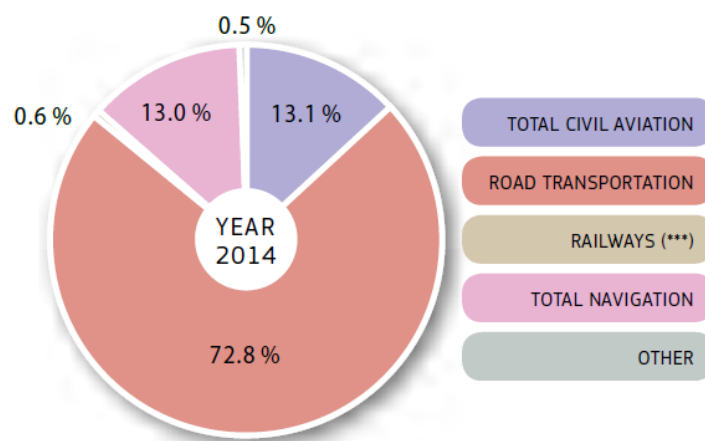
(***) Excluding indirect emissions from electricity consumption.

Figure 1.5 - CO2 emissions of the transports considering the EU (European Union) – 28 (EC, 2016)
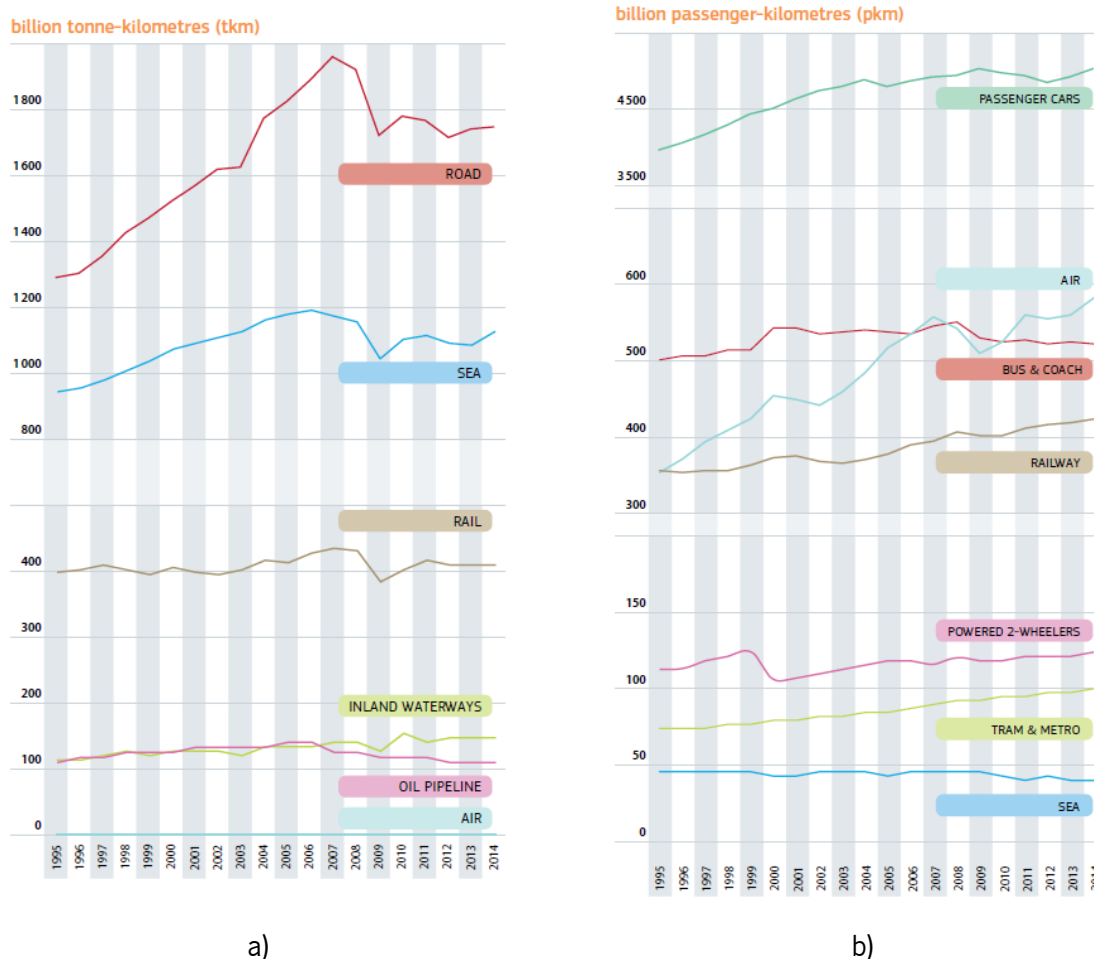
Figure 1.6 - Evolution and comparison between the performance by mode for (**1995–2014**): a) freight transport; b) passenger transport (EC, 2016)

In order to have an interoperable and a *Single European Railway Area* (SERA), it is important to analyse the design, construction, operation and maintenance of the railway network since it needs to be sustainable, cost-effective, reliable, safe and supportive of the customer needs. Therefore, it is imperative to have a gradual elimination of the differences and diversity observed in the railway network.

The main costs of the railway network operations are related to the infrastructure (one-third), mostly related to the maintenance (usually preventive). This is one of the focuses of the *SHIFT2RAIL*, which expects to define measures and strategies to reduce the maintenance costs and replaced them with simplified procedures and efficiently deployed. Another problem to be solved by the *SHIFT2RAIL* project is related to the nearing maximum capacity of the existing railway infrastructure (lines, stations and terminals) since it is extremely important to offer to the customers a service quality that they demand, using practices that help to improve the reliability, the capacity and the economy of railway transportation.

The Innovation Programme 3 (*IP3*) has several Technical Demonstrators (*TDs*) that cover the main areas of the *SHIFT2RAIL*. This work is included in the *TD3.3* and *TD3.4* that are related to the *optimized track*

5

system and the look for new, innovative solutions (products, processes and procedures) and the next-generation track system, recognising the long-term needs and potential solutions to the railway problems. Indeed, the *IN2TRACK* project intends to set the foundations for a resilient, consistent, cost-efficient, high capacity European network by delivering important building blocks that unlock the innovation potential that has been identified as part of the *Shift2Rail* Innovation Programme 3. Moreover, the *IN2TRACK2* project (which is a continuation of the *IN2TRACK* project) proposal addresses the topic of "Research into optimised and future railway infrastructure". This project aims to reduce lifecycle costs, improve reliability and punctuality, whilst increasing capacity, enhancing interoperability and improving the customer experience.

Thus, this PhD thesis is included in the *IN2TRACK* and *IN2TRACK* 2 projects and is aligned with the *SHIFT2RAIL* objectives regarding the assessment of the ballasted but mostly, the ballastless (or slab) high-speed tracks, considering the followed research areas: IP3 - *Cost Efficient and Reliable High Capacity Infrastructure - TD3.3&TD3.4 Innovative track design and materials*. The *IN2TRACK* project aims to improve and optimize the switch & crossing and track system, look and analyse ways of extending the life of bridges and tunnels assets (through the maintenance and repairing actions) and development of a holistic, whole system-approach. The *IN2TRACK2 Track* activities aim at both exploring new track construction to optimise the today track system and improving the track system substantially to provide a step-change in performance. The *IN2TRACK2 Bridges and Tunnels* activities aim at improving methods and repair techniques to reduce costs, improve quality and extend the service life of structures. Thus, it is possible to state that the objectives of all these projects are complementary and in some points are overlapping.

Indeed, these objectives are also aligned with the projects developed by *UIC*, which highlights the importance of the subject. For example, in the past years (2017 and 2018), UIC (2018) developed a project that aimed at drawing up a harmonised methodology for formulating the ageing laws of track components, to come to a common understanding of the physical factors which determine these laws and to allow a more accurate prediction of maintenance needs. This project was important since contributed to the "technical-economical asset management", theme of the *Rail System Forum Strategy*, and fitted with the maintenance optimisation objective of the *Rail Technical Strategy Europe*. This type of study is helpful to fully understand the factors that governed the deterioration of the track components and the life-cost of a railway structure. Furthermore, provides the maintainer with essential tools to

accurately predict the maintenance needs and costs and to optimize the maintenance policies accordingly to UIC (2018).

Considering the information above and the projects developed and under developing, it is possible to understand the interest and importance of the main topics of this thesis since it seeks to understand better the degradation mechanisms of the components/materials of the railway structures (ballasted and ballastless tracks), which have a direct influence on its global performance, with main focus on the ballastless track and its performance on specific areas such as transition zones.

The high-speed ballastless railway lines are, currently, a very popular alternative when compared with the ballasted ones, presenting several advantages, namely, related to the reduced maintenance costs, the longer effective life of the track, smaller risk of derailment, etc. In fact, the increase of this type of structure has been observed in Asia (Japan, China, South Korea), but also all over Europe (Germany, France and Spain). Over time, some modifications on the structures and implemented solutions were verified. Initially, the ballast was replaced by a concrete slab and the sleepers were maintained. In some solutions, the sleepers disappeared and the rails were embedded in the slab (Gautier, 2015). In Figure 1.7 is possible to observe a small part of the evolution of the ballastless tracks. The *Rheda* system was firstly implemented in 1972 on the line from *Bielefeld to Hamm*. The *Öbb Porr* system is relatively recent and has been built in Germany since 2001. The main difference between both structures is related to the concrete slab execution mode: *in situ* or concrete pre-casted.

a)   b)

Figure 1.7 - Evolution/modifications of the ballastless tracks: a) *Rheda* system classic; b) *Öbb Porr* - prefabricated system

The ballastless tracks have also been optimized over the years and the *Rheda* system is one of the examples of this optimization process. In fact, numerous modifications of *Rheda*-type structures have been developed and its implementation has been used not only in Germany but also in the Netherlands, Taiwan and China. However, the pre-casted slabs are the "new" innovation in the ballastless tracks (Leykauf et al., 2006). Yet, it is important to note that, besides the implementation of this type of structure, particularly in tunnels, the study of its dynamic behaviour, mostly in transition zones, is still little explored, when compared with the existing bibliography for ballasted tracks (Zhang et al., 2008, Zhu et al., 2011,

Luomala and Nurmikolu, 2012, Shi et al., 2013b). Furthermore, the current requirements to increase the speed lead to new challenges in order to improve the rail track performance due to the significant amplification effects of the track-ground vibrations induced by the high-speed trains, especially at the critical speeds (Alves Costa et al., 2015, Sayeed and Shahin, 2016a).

Considering the importance of the ballastless tracks nowadays, especially, in high-speed lines, one of the positive contributions of this work is related to the study of the performance of the ballasted and ballastless tracks in order to understand its main similarities but also the differences, with special focus on the long-term performance. Firstly, it is important to identify the elements of each structure and understand their main functions, and the structural and material models techniques normally used to simulate the behaviour of these structures. The analysis of the long-term response is based on the implementation of a mechanistic-empirical permanent deformation model, which is grounded on an extensive study about this topic and explored in this thesis through numerical simulations and comparison of several models and materials. Thus, the accumulation of the permanent deformation is described, in this work, by empirical models developed through the results obtained in the laboratory tests (mainly triaxial tests). The tests allow purposing "new" laws for different types of geomaterials. The mathematical expressions associated with different types of geomaterials are usually defined in function of the stress level or stress ratio, number of load cycles and initial stress, among other parameters, which include the strength parameters (cohesion and friction angle). This means that the models are developed considering the properties of a certain material, which includes its stress state, physical state, etc. Thus, these properties can have a significant influence on the behaviour of the materials. Furthermore, the failure also varies according to the type of geomaterial and its properties. For example, the failure of the fine-grained subgrade soils is one of the typical problems of track degradations. In the particular case of the concrete slabs, they may also exhibit failure models similar to concrete pavements as faulting (in case of jointed slabs), cracking and pumping due to poor subgrade conditions.

In order to understand the track degradation of a ballastless track, the comparison with the ballasted track is necessary, since the accumulated knowledge in this area is more significant because it has been studied over the last years. Understanding well the phenomenon in the ballasted track, the results obtained for the ballastless track will be more reliable and much more robust. Thus, a sensitivity analysis is presented in this thesis where the long-term response of the ballasted and concrete slab (or ballastless) tracks is analysed considering the quasi-static and dynamic mechanism, in this case, induced by the

8

presence of irregularities on the track. This work aims to evaluate and quantify the influence of the degradation process on the response of the two types of tracks.

Furthermore, from the evaluation of these different types of structures, a particular solution of the railway lines is analysed: transition zones. The transition zones (examples depicted in Figure 1.8) usually present a poor long-term performance due to the problems related to the differential settlements induced by the passage of the trains or due to problems related to consolidation or compaction conditions. Indeed, the long-term performance of a railway track is an important aspect of its assessment, which means that the prediction and control of the permanent deformation of the structures in these areas are key factors in its analysis and design, with repercussion in the maintenance operations (frequency) and respective costs.

a)   b)
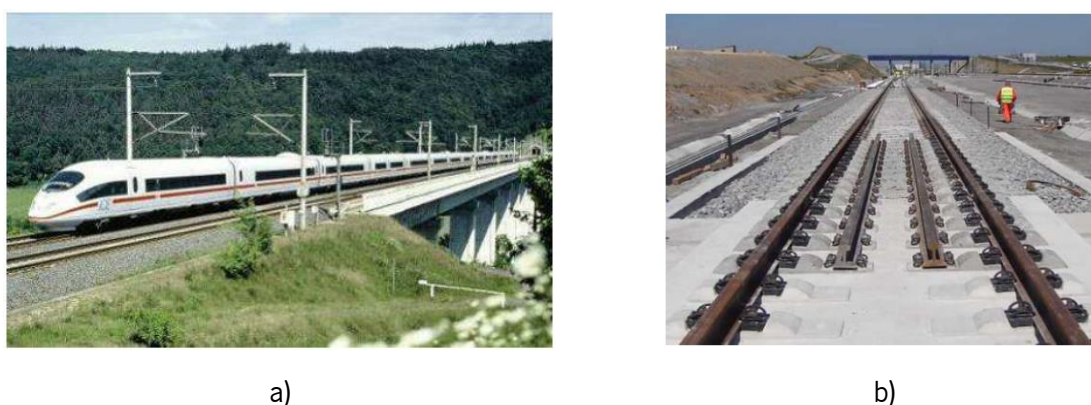
Figure 1.8 – Example of real transition zones: a) embankment-bridge transition (Paixão, 2014); b) transition between different track configurations (Ochoa de Olza Galé, 2007)

In detail, the importance of the transition zones is related to its accelerated degradation process (due to the abrupt differences in the stiffness between the structures), occurring problems related to the differential settlements. Thus, this is one of the focuses of this work, since it is mandatory to understand this phenomenon to try to minimize its effects. Despite the several studies over the decades, its complex behaviour led to few meaningful conclusions, probably because of the empirical approaches that did not take into account the influence of some factors: dynamic train-track interactions (due to geometric defects of the track and/or abrupt variation of the stiffness), characteristics of the materials (superstructure and substructure) and environmental factors (Paixão, 2014).

Thus, in the study of permanent deformation induced in the substructure layers (including the subgrade) by the trains is important to understand the degradation process and the phenomenon itself, which will allow to analyse and define significant mitigation measures, especially in transition zones. The accumulated settlements due to the repeated loading induce larger differential settlements that can be

responsible for the track degradation, accelerating the dynamic effects. In the case of the ballastless track, the erosion of the superstructure is a relevant subject but, will not be studied in this work.

This thesis congregates several complex analyses and concepts and different numerical modelling techniques. The 2.5D FEM-PML approach and respective models are used to understand the individual behaviour of ballasted and ballastless tracks and compare them considering the quasi-static and dynamic mechanism. The 3D models are used to validate the 3D numerical models of the ballasted and ballastless tracks (the calibration process is based on the obtained laboratory results from physical modelling) and also to evaluate the behaviour of these structures in the specific case of a transition zone. The results of the tridimensional modelling allow evaluating the long-term performance of the railway structures, which includes the analysis of the influence of differential settlements, stresses and permanent deformation developed at the geomaterials' levels. The 3D models, despite the significant computational effort and calculus time, are more consistent with the real behaviour of these structures.

The numerical results are a contribution to a better understanding of the potential of a given rail track system under given a certain loading that can lead to the design of a more cost-effective track solution.

1.2   Aim of the research and expected contributions

The developed work includes two important areas of the railway's engineering: structural and geotechnical behaviour. The proposed study comprehends two knowledge areas that complement each other, namely, in the scope of the long-term behaviour where the geotechnical behaviour of the geomaterials due to cyclic loads induced by the trains assumes an important role in the global behaviour of the structure. In order to correctly understand the behaviour of a railway structure, it is necessary to use advanced numerical model techniques and understand the behaviour of the elements that constitute the ballasted and ballastless tracks: rail, raipad, fastening system, sleeper, concrete slab, hydraulically bonded layer, ballast, sub-ballast, subgrade, resilient elements and foundation soil. Thus, the evaluation of the dynamic behaviour of the geomaterials, for example, depends on several aspects such as the modelling of the vehicle (and speed), the inclusion of contact models and other complex numerical methodologies.

From the extensive bibliography about the ballasted tracks, this work also aims to analyse the long-term performance of the ballastless tracks, comparing the results between the ballasted and concrete slab tracks.

The main objective of the research presented in this thesis is to contribute to a deeper understanding of the long-term performance of the railway tracks, especially in specific areas of the railway lines that often

evidence higher degradation rates and are associated with abrupt changes in the track support conditions: transition zones. The presented analyses aim at proving an insight into the long-term behaviour of railway tracks considering the dynamic train-track interaction and, thus improving the design of infrastructures and contributing to the efficient management of the railway assets, within the scope of the life-cycle cost reduction paradigm. Therefore, the developed work includes the following tasks and goals to accomplish:

- Study about the phenomenon of permanent deformation in the geomaterials, identification of the main variables and factors that can influence this behaviour. This study is complemented by the analysis of the several approaches, models and laboratory tests also used to determine the resilient modulus;

- Development of a parametric study about the resilient modulus and permanent deformation, which allows comparing the several models and materials tested and also defining a ranking of the materials. The comparison of the models is very helpful to understand which are the variables that most influence the phenomena of permanent deformation and also the resilient modulus. The purposed rankings are important tools to obtain a novel geomechanical classification of the geomaterials, which is based on numerical simulations. The purposed geomechanical classification was developed in the scope of the pavements and railways;

- Comparison of the long-term behaviour of the ballasted and ballastless tracks due to the quasi-static and dynamic mechanisms through an extensive parametric study;

- Assess the influence of the dynamic mechanism in the response of the subgrade of the ballasted and ballastless tracks. This influence is evaluated through the stress amplification factor (short-term analysis) and permanent deformation amplification factor (long-term analysis). The analysed factors comprise the range of wavelength, the train's speed (including the critical speed), mechanical characteristics of the subgrade (which includes the influence of the friction angle) and the spatial variability of the unevenness profile;

- Numerical calibration of 3D numerical models of two railway structures (ballasted and ballastless tracks). The calibration is based on the cyclic tests performed on the physical models of the ballasted and ballastless tracks sections in a laboratory. The calibration comprises the adjustment of the properties of the materials (short-term calibration) and the parameters of the empirical permanent deformation model of the ballast and ballastless tracks (long-term calibration). This study is complemented by assessing the influence of strength properties such as cohesion in the development of the permanent deformation;

11

- Give more insights about the long-term performance of the ballastless track inserted in a transition zone (embankment-tunnel). This study contemplates the analysis of the displacements and stresses induced on the main elements of the track (rail, concrete slab, HBL, FPL and subgrade) as well as the permanent deformation induced in the substructure (FPL and subgrade) through the implementation of a calibrated empirical permanent deformation model. This analysis is performed through a hybrid method between the software ANSYS and MATLAB.

Thus, according to the main goals defined previously, the author intends, at the end of the proposed work, to understand the whole system of the ballasted and ballastless tracks, namely, its long-term dynamic behaviour. Furthermore, a model that includes a transition zone with the same structural system (ballastless track) is analysed and evaluated. This study can be used as a base analysis of further optimization processes that will lead to innovative solutions with an impact on the system that can reduce the maintenance operations and also reduce the life-cycle cost of the railway transport, increasing the attractiveness and competitiveness of the system. The expected results are following the vision of European transport that bases its strategy on smart and sustainable growth.

1.3   Thesis outline

The thesis consists of eight Chapters.

Chapter 2 presents a brief overview of the main concepts that characterise the railway track structures: ballasted and concrete slab tracks. This Chapter evaluates the existent types of railway structures, as well as the differences and similarities. The structural models used to model the railway systems are listed. This Chapter also includes topics related to the load types and to the comparison between the structural models and the numerical tools used to model a railway structure. The different techniques used to model each element of the railway structures are also presented, from 2D until 3D.

Chapter 3 provides a review of railway transition zones, which includes the study and framing of this problematic. After understanding the differences and similarities between the ballasted and ballastless tracks and the main techniques used to model the railway structures and their materials, this Chapter is focused on the study of specific zones of the railway lines (transition zones) that can include these two structures. The review is focused on the causes of deterioration and its consequence, the methods used to mitigate the problems on transition zones, the numerical models developed within this scope (based on the numerical models described in Chapter 2), the experimental measurements and the main obtained conclusions. At the end of this Chapter, it is possible to understand the importance of this topic and the necessary work yet to be developed.

Chapter 4 addresses in more detail the mechanistic-empirical resilient and permanent deformation models used to simulate the behaviour of the geomaterials. The modelling of the materials of the railway structures is exploited in Chapter 2. However, the geomaterials exhibit a very particular behaviour when submitted to cyclic loads induced by the passage of the vehicles and have a significant influence on the long-term performance of a railway system. This analysis is the base of this thesis since allows understanding the development of permanent deformation and the variables that have more impact on this phenomenon. The analysis includes the factors that most influence these types of behaviour (resilient and permanent deformations), the laboratory testing and the mechanistic-empirical approaches themselves. Furthermore, to understand better which are the factors or variables more important used to characterize this type of behaviour, a parametric study was developed to compare the several models of the resilient modulus and the permanent deformation models. In the end, a novel geomechanical classification of the geomaterials is proposed based on the numerical simulation. This can be a helpful tool in the modelling of a substructure of a railway and/or pavement structures since gathers information about the UIC classification and permanent and resilient deformations.

Chapter 5 evaluates the short and long-term behaviour of the ballasted and ballastless tracks under quasi-static and dynamic mechanisms (considering several factors such as the range of the wavelength of the unevenness profile, influence of the train's speed and the characteristics of the subgrade) with focus on the permanent deformation. This Chapter can be summarised as a parametric sensitivity study. From the work developed in Chapter 4, after understanding the phenomenon of the permanent deformation, the main variables and the factors that can influence the long-term behaviour of the geomaterials, the performance of the subgrade (in terms of stress and permanent deformation) of the ballasted and ballastless tracks is compared, introducing a new concept related with stress amplification factor and permanent deformation amplification factor. This methodology allows simulating the degradation and assessment of the permanent deformation of the geomaterials based on the stress levels and number of load cycles induced in the railway track.

Chapter 6 is focused on the calibration of the numerical models (ballasted and ballastless tracks) from the results of laboratory physical tests. The structures were submitted to cyclic tests (more than 3 million cycles) at the laboratory, where the accumulated deformations of the structure were measured during the tests. This analysis is important to understand the influence of the foundation on the long-term performance of the ballasted and ballastless tracks under cyclic loading and to confirm the previous conclusions (obtained in Chapter 5) about the degradation process of the subgrade of the ballasted and

ballastless tracks since this study is based on physical modelling. The results of the slab and ballasted tracks were compared to each other and allowed understand which are the layer that most contributes to the long-term behaviour. Furthermore, the properties of the materials, as well as the parameters of the permanent deformation model, were calibrated for each geomaterial of each structure. Instead of the 2.5D FEM-PML approach used in the previous studies, 3D numerical models of the sections of the railway structures were developed. These 3D models were posteriorly used in Chapter 7 in the scope of the modelling of transition zones (considering the necessary adaptations in terms of geometry and modelling optimization).

Chapter 7 presents the application of the knowledge acquired in the previous Chapters in a particular problem of the railway lines: transition zones. After evaluating different types of existing railway systems, and after the calibration of the models, a particular solution of the railway lines is analysed. Indeed, from the 3D model developed in the previous Chapter and the calibrated parameters of the permanent deformation model, a transition zone between a ballastless track over an embankment and tunnel was studied to understand the particular degradation process that is observed in these areas. The transition is simulated considering two structures with different stiffnesses (the tunnel presents a much higher stiffness when compared to the embankment), which induces differential settlements and leads to a more accelerated degradation process. The displacements and stresses were analysed in the main elements of the ballastless track: rails, concrete slab, HBL, FPL and subgrade. Furthermore, the stresses along the concrete slab and HBL were analysed in detail since these are the elements that ensure the continuity of the track. The long term behaviour was analysed through an implemented methodology that simulates numerically the evolution of the deformed track profile resulting from the rail traffic and stiffness difference between the two structures.

Lastly, in Chapter 8, major conclusions and recommendations for future work are summarised.

2 Ballasted and ballastless tracks solutions – description, comparison and numerical modelling

2.1 Introduction

The rail track presents a complex behaviour, despite its simple structural concept. The system is complex because of the large development of the structure in a certain direction, the behaviour of the materials and a significant number of contacts between the elements, which includes the vehicle-track interaction that has a significant influence on the behaviour of the structure (Vale, 2010).

The railway structures can be divided into ballasted tracks and ballastless tracks. Despite the differences, both structures share the same function: support the train's loads. However, it is important to identify the main advantages and disadvantages of each one regarding its short and long-term behaviour. Thus, to fully understand both behaviours, it is important to comprehend the main function of each one of the components of the ballasted and ballastless tracks (as well as its influence on the short and long term behaviour). Thus, a description of the elements of both railway systems is presented in this Chapter. The research presented in this Thesis can be an important step in the future analysis regarding the long-term performance of the ballasted and ballastless tracks and their comparison and it is based on the existing knowledge presented in this Chapter.

The ballasted track is older and more traditional (more than 150 years of existence) and the evaluation of its behaviour is, in several times, based on empirical methodologies. In the case of the ballastless tracks, this solution is more recent and the analysis is performed considering a mechanistic approach, closer to the structural engineering (Alves Costa, 2011). During the last decades, some of the theories applied on the pavements were extended to railway behaviour, since both structures are designed to allow strain propagation considering the control of the deformation in service ensuring a certain level of performance.

The ballasted and ballastless tracks present some similarities but also important differences. Both systems share some of the materials (such as the rails or fastening system). However, its properties can be different according to the type of structure. Furthermore, the track life-cost, maintenance aspects and generated noise are some of the factors that also vary with the railway system.

This Chapter aims to identify the differences between the ballasted and ballastless tracks but also to describe, list and compare the several structural models and their particularities used to characterize the performance of the railway structures. This research will allow relating the structural models to the

15

material models in order to obtain a full perception of the modelling process of the railway track. The theories and the methodologies used in the design of the railway tracks are also presented in this Chapter. Furthermore, the main techniques/approaches used to solve the dynamic equilibrium are explained, as well as the treatment of the boundaries. Moreover, the modelling of the vehicle and the techniques applied to simulate the interaction between the vehicle and the track are explained. The main concepts of the contact theory are presented, including the *Hertzian* theory. Thus, the complex concepts regarding the kinematic of contact and the imposition of the contact between two bodies are explored and described. In this analysis, more emphasis is given to the penalty method used to solve the contact problem. Previous studies showed the greater simplicity of calculation associated with the penalty method when compared to the *Lagrange* method. The penalty method does not assume the consideration of additional unknowns (Alves Ribeiro, 2012). It is important to understand that the main concepts of the contact algorithms and contact conditions are defined to apply in a continuum medium. However, these conditions are adapted to situations where the surfaces of the bodies in contact are discretized by, for example, finite elements.

2.2   Ballasted and ballastless tracks – description of the structure, materials and comparison

2.2.1   Ballasted track

The conventional ballasted track (depicted in Figure 2.1) is characterized by the superstructure (rail, fastening system and the sleepers) and substructure (ballast, sub-ballast and subgrade).

The ballasted track allows correcting (with automatic mechanical equipment) the changes in the geometry that occur on the ballast layer and also on elements of the superstructure due to its degradation. The sub-ballast and subgrade have, normally, a higher duration (between 50 and 100 years), providing that good maintenance of the superstructure, substructure and drainage is ensured (Fortunato, 2005).

Due to this assumption, during the past years, the main concern of the rail track design was related to the superstructure (Indraratna and Nimbalkar, 2016). However, there is an important group of researchers working on the performance of the subgrade when submitted to cyclic loads. Indeed, this increase of concern regarding the subgrade is related to its influence on the cost of track maintenance (Selig and Waters, 1994).

a)

b)
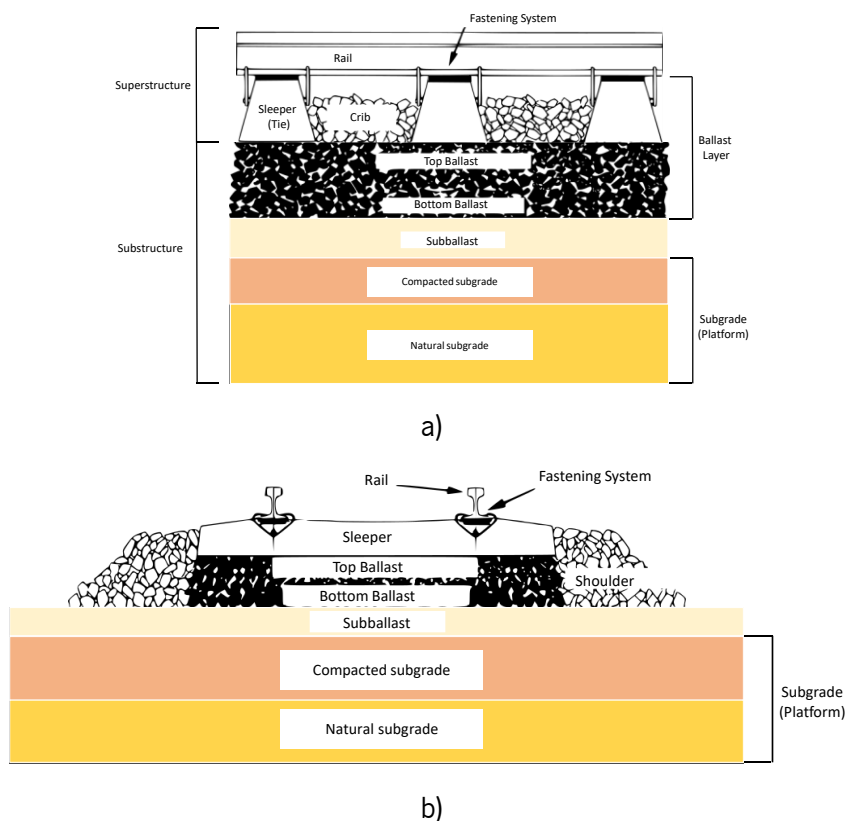
Figure 2.1 – Structural scheme of the ballasted track: a) longitudinal profile; b) cross-section - adapted from Selig and Waters (1994)

2.2.2   Ballastless track

The term "ballastless track" or "slab track" refers to systems with the replacement of ballast with another element as asphalt layer or reinforced concrete. The concept of the ballastless track appeared when the ballast was replaced by a concrete slab, keeping the sleepers. Posteriorly, the sleepers disappeared and the rails were embedded in the slab (Gautier, 2015). A schematic representation of the evolution of the ballastless track's concept is depicted in Figure 2.2. By simplification, the fastening system is not indicated in the scheme of Figure 2.2.
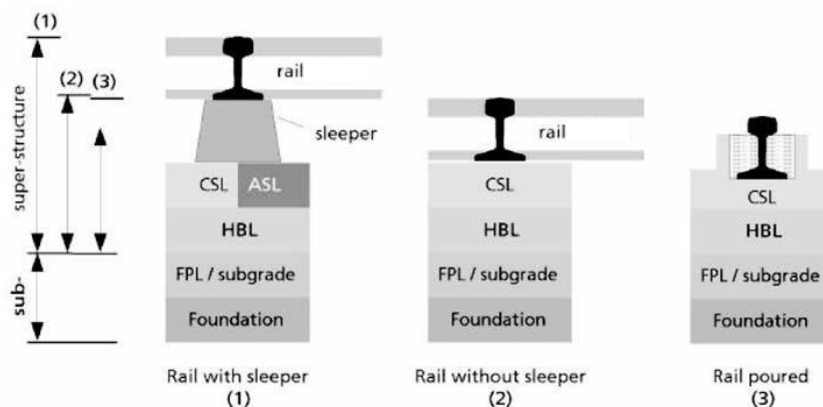
CSL – Concrete Supportive Layer; ASL – Asphalt Supportive Layer; HBL – Hydraulically-Bonded layer; FPL – Frost Protection Layer

Figure 2.2 – Evolution of the ballastless track system: 1) rails supported by sleepers placed on concrete or asphalt layer; 2) rails directly fixed on the concrete slab; 3) rail embedded in a concrete slab (adapted from Quante (2001))

17

The ballastless track is a system that has been used, mostly in Japan, but currently also in Europe and the rest of Asia (China and South Korea), especially because of the necessity to build high-speed lines and increase the connectivity between the cities. In fact, due to the Japanese economic expansion and the growing mobility demands, the ballasted track was being replaced by the ballastless track since there wasn't time and space to carry out the intensive maintenance and to solve the reduced durability. In the 80s, most of the railway Japanese network was built with the ballastless track system because of the need for high-speed lines. Currently, China is probably the country with the greatest expansion in high-speed lines, which is already about 37900 km long at the end of 2020. Furthermore, China also intends to increase up to 400 km/h the train speed in the next future (Paixão et al., 2009, Abadi et al., 2016, Sayeed and Shahin, 2016a).

The ballastless track system allows the optimization of track costs and significant improvements in terms of environmental aspects, safety, service quality, passengers' comfort and durability. However, the choice between each structure depends on several aspects such as the characteristics of the project, design construction, operation costs, experience, track-life cost, environmental factors (noise, vibrations, etc), maintenance (frequency and costs), time of construction, etc.

Thus, the gradual change of ballasted to ballastless track can be justified by the non-linear growth of ballast wear due to the increase of speed and also intensification of the interest in mixed passenger-freight lines, which means that the stresses on the ballast would be higher (Robertson et al., 2015).

The ballastless or slab track is different from the ballasted track mainly because of its configuration. The ballastless track is composed of rails, railpads, fastening systems, sleepers and concrete slab. The substructure is characterized by a support layer (normally is a poor concrete element) and subgrade or foundation. Figure 2.3 shows an example of a ballastless track system.
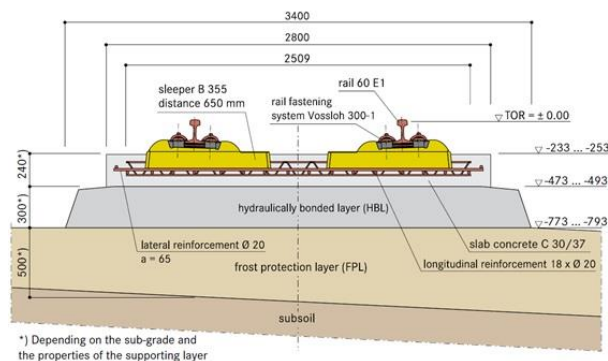
Figure 2.3 - Example of a ballastless track system: a) *Rheda* system

However, there are different ballastless track structures. The ballastless track can be defined according to the type of the rail's fastening (punctual or continuous), execution of the concrete slab (*in situ* or precast), the number of the resilient levels (one or several) and nature and type of the foundation: lean concrete or bituminous material (Vale, 2010). The UIC (2002) distinguishes the ballastless track into seven distinct systems: railway track with continuous fastening of the rail; railway track with punctual fastening of the rail, over the slab or over independent blocks (track without sleepers); railway track with punctual fastening of the rail over sleepers incorporated in the concrete slab; after filling the slab, track with punctual fastening of the rail over sleepers incorporated in the concrete slab by vibration; track with punctual fastening of the rail over sleepers anchored in the concrete slab; track with punctual fastening of the rail over sleepers separated of the concrete slab by a resilient element; track with punctual fastening of the rail over precast slabs.

The placement and incorporation of the sleeper and rail into the ballastless track varies according to the track system:

- Sleeper on slab system – in this case, the sleeper is laid on a concrete or asphalt layer; the sleeper also can be elastically laid over or bound into a continuous slab (*Sonneville-SNCF* (Sonneville, 2009) and *STEDEF* systems (Vale, 2010));
- Embedded sleeper – the sleeper is embedded in a continuous concrete slab to ensure the track geometry (*Rheda* and *Rheda 2000* systems (Rheda-System, 2011) and precast ballastless tracks: *öBB-Porr* (Porr, 2012) and *Bögl* (Tarmac, 2015));
- Direct systems – the rail is set directly on the slab through a baseplate. This system was firstly used in tunnels because of the restraints of the space; the baseplate replaces the fastening;
- Embedded systems – the rail is embedded into an elastomeric layer, suppressing the fastening sleeper (*EDILON* system (Edilon, 2015) implemented in the Netherlands on concrete bridges).

2.2.3   *Description of the elements of the railway structures*

The ballasted and ballastless tracks share some of the railway track elements. However, other elements are quite different. Table 2.1 summarises the mains function of the elements of both railway track systems. This summary is based on the work developed by Selig and Waters (1994), Fortunato (2005) and Vale (2010).

Table 2.1 - Main function of the railway track elements

	Elements	Main Function	Ballasted Track	Ballastless Track
Superstructure	**Rails**	Support and transfer the wheel loads to the sleepers (without causing excessive deflection) Impose direction to the wheels of the vehicle Distribute the braking and traction forces by adherence	✓	✓
	Railpads	Proper support of the rails Damp the vibrations generated by the wheels Reduce the friction between the rail and the sleeper Proper electrical isolation Protect the sleepers: wear and impact damage In the ballastless track, the railpads provide a longer effective life of the fastening systems when compared with the ballasted track	✓	✓
	Fastening System	Promote appropriate support of the rails Resist the efforts due to vertical, lateral, longitudinal and torsion and the efforts related to the temperature variation of the rails Reduce the stresses and vibrations caused by dynamic loads Transmit the applied forces over the rails to the sleepers Guarantee the gauge track and the inclination of the rail In the ballastless track, these elements should provide the proper vertical stiffness	✓	✓
	Sleepers	Proper distribution of the static and dynamic solicitation of the rail to the ballast Support the fastening system of the rails Prevent/restrain the lateral, longitudinal and vertical movements of the rails by anchorage of the superstructure Guarantee/prevent the gauge track and the inclination of the rail Guarantee the electrical isolation between the two rails In the case of the ballastless tracks, the sleepers can be incorporated, anchored, or separated from the structure by resilient elements (it depends on the type of ballastless track)	✓	✓(*)
	Slab	Homogenize, distribute and reduce the stresses in the support layer Reduce vertical displacements		✓
Substructure	**Ballast**	Support for the sleepers Support/resist to the lateral, longitudinal and vertical loads applied on the sleepers Maintain the track in the correct position Mitigate the vibrations Provide resiliency and allows the energy absorptions for the track Facilitate the corrections of operations of the tracks' levelling (maintenance operations) Drain the pluvial water Mitigate the negative impact of the water and the frost in the subjacent layers Reduce and uniform the stresses (induced by the traffic) by the sleepers to the subjacent layers	✓	
	Sub-ballast	Protect the platform Reduce the stress level in the subgrade	✓	

	Separate the ballast and the subgrade layers (preventing the interpenetration and migration of the fine particles and the wear of the foundation by the mechanical action of the ballast) Drain and filter element of the platform (intercept the water from the ballast that moves directly to the subgrade) Allow drainage of water that can flow upward from the subgrade		
Support layer: HBL – Hydraulically- Bonded Layer	The element should be homogeneous to avoid differential settlements, damaging the concrete slab Distribute the load to the underlying layers		✔
FPL - Frost Protection layer	Support the HBL and distributes the loads to the foundation High resistance to frost-defrost cycles Provide good drainage conditions to the track		✔
Resilient elements	Connect the concrete slab to the subjacent layer Contribute to the vertical stiffness of the system Reduce the friction between the concrete slab and the support layer		✔
Subgrade	Support the superior layers; Provide uniform and adequate support; the performance of the track depends on its quality, being the *Young* modulus the most important parameter of this layer; resistant to repeated loads; should be designed to avoid the development of excessive permanent deformations.	✔	✔

(*) In some systems, the sleeper is embedded in the concrete slab or may even be suppressed in some.

From Table 2.1, some particularities of the elements will be explored in more detail below.

Rail

The behaviour of a railway structure can be influenced by some of the steel characteristics of the rail and how actions are imposed on this element. Furthermore, the type and material of the rail, the bending stiffness and some aspects related to the joints (or its absence in the case of continuous welded rail) are important factors, mostly because of the high dynamic loads applied in the substructure that are amplified when there are geometric irregularities in the rail or in the wheels (Fortunato, 2005).

The reduced rail stiffness at the joints can increase the stresses on the ballast and subgrade (Selig and Waters, 1994). These phenomena can lead to the development of permanent settlements, unevenness profiles and deterioration of the rails and sleepers. Thus, the continuous welded rail (CWR) presents some advantages when compared with the rail with joints and this approach is preferred on high-speed lines. The advantages include reduced deterioration of the track elements (longer time interval between the operations of maintenance and conservation and extended life-cycle of the rail), lower generation of noise and vibrations and lower oscillation of the trains, conducting to a better comfort of the passengers. The main disadvantages are related to the significant internal forces that occur due to temperature variations, difficulty to replace the elements of the superstructure and higher initial investment (Fortunato, 2005).

Moreover, the increase of the height of the rails conducts to a higher bending stiffness, which means that it is possible to distribute the load by a higher number of sleepers, reducing its settlement as well as the settlement of the support layers (substructure).

Fastening system

The fastening system is composed of a set of elements that allows, as mentioned previously, the connection between the rails and the sleepers, promoting appropriate support of the rails.

The choice of the fastening system is dependent on the type of sleeper and the possibility to replace its elements easily and faster. In the case of a wooden sleeper, it is necessary to use steel plates between the rails and the sleepers that protect the wood against mechanical wear. Besides that, these elements assist the fasteners in restraining lateral rail movement and provide a sloping surface to help develop proper wheel/rail contact (Selig and Waters, 1994). The size of the sleeper's plate is an important factor because of the pressure induced in the wood that can cause accelerated cutting and premature deterioration of the sleeper.

In the case of concrete sleepers, resilient elements are placed to damp the vibrations caused by the wheels in order to reduce the friction between the rail and the sleeper, providing, also, the resiliency of the rail/sleeper system, electrical insulation for the track signal circuits and preventing the rail/sleeper contact attrition. The type of the fastening system also depends on the type of support: direct (when the rail and the railpad are fixed directly on the sleeper by a single fastening system) or indirect (when there is a fastening to connect the rail to the railpad and another in the connection of the railpad-sleeper) (Vale, 2010).

Sleepers

The sleepers are important elements placed between the rails and the ballast.

There are several types of sleepers, but this section gives more details about the wood (timber) sleepers and prestressed/reinforced concrete sleepers (depicted in Figure 2.4). For a long time and in many countries, wooden sleepers were used extensively. However, environmental and financial problems led to an increase in the use of concrete sleepers, which presents superior technical behaviour. Yet, the durability of the concrete depends on the control of the chemical composition and concrete curing.

On the other hand, the wooden sleepers have a higher cost, short life and less lateral resistance (due to their low weight). The effective life of this type of sleeper (that varies between 25 to 35 years), depends

on the type of timber, type of conservation, climate, axle load, speed and track quality (Kozak, 1992). At the end of the XIX century, metallic sleepers were installed in several places. However, they presented disadvantages: it was difficult to place the sleepers in the correct position because of their shape, the noise generation was significant, they required special electric isolation, the conservation of the element was extremely difficult and they were quite sensitive to the chemical problems.

The concrete sleepers were introduced at the end of the Second World War. These sleepers are heavier, durable and present a better secure fastening system when compared with wooden sleepers. Despite its better rail restraint, the concrete sleeper requires pads to provide proper resiliency.

Comparing the two types of sleepers, despite the wooden sleepers present superior resilience and less fragility, the concrete sleeper remains the first choice since it presents significant advantages (FIB, 2006):

- Long-term durability;
- Low cost of maintenance;
- Better lateral resistance;
- Better solution for high-speed and heavy freight lines;
- Better elasticity of track;
- Minimum life-cycle cost and low first cost;
- Environmentally friendly (there isn't any kind of chemical treatment and can be recycled and applied in road construction).

a)   b)

Figure 2.4 – Wooden (a) and concrete sleepers (b)

Regarding the concrete blocks, there are three types, as indicated in Figure 2.5: mono-block (pre-stressed concrete), bi-block (reinforced concrete) and portico-sleepers. The main advantage of the bi-block (when compared with the mono-block) is its weight and higher lateral resistance of the ballast (because there are more contact surfaces between the ballast and the sleeper). However, the probability of cracking is higher since the mono-block is pre-stressed. Regarding the mono-block, its geometry guarantees better drainage than the bi-block. The mono-block is used extensively throughout the world and can be used in

23

all line types, including high-speed lines and heavy haul lines with axle loads up to 35 t (FIB, 2006). The portico-sleepers present significant lateral resistance regarding the ballast's movement and guarantee greater durability of the initial geometry of the track (Esveld, 2001).
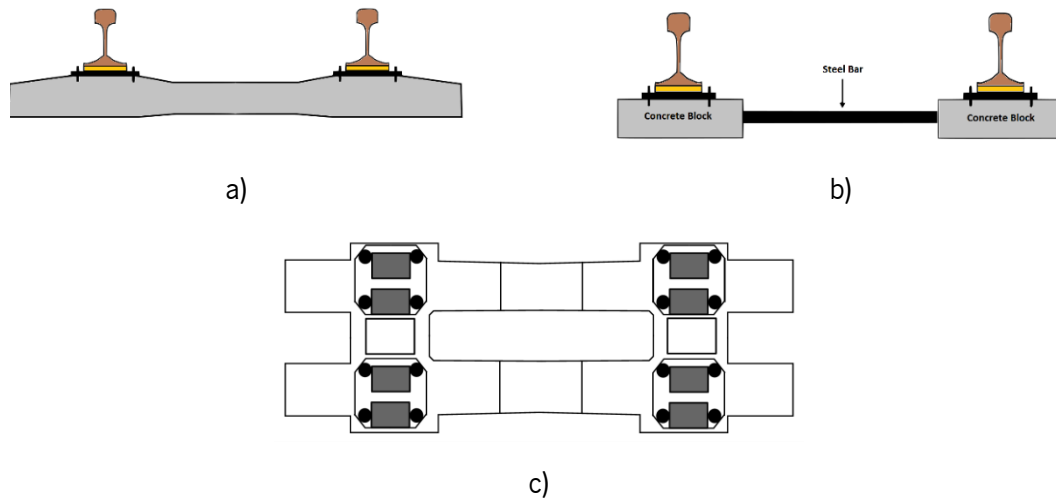
Figure 2.5 - Type of concrete sleepers: a) mono-block, b) bi-block and c) portico - adapted from Vale (2010)

In the case of a static load, the sleeper immediately under the loading alignment, receives 30% of the applied load and the adjacent, about 20%. The values described are dependent on the flexibility of the track.

Regarding the spacing between the sleepers, in the ballasted track, the adopted value in Portugal is 0.60 m. In the ballastless tracks, the spacing value is usually 0.65 m and should not vary more than 20 mm regarding the value defined in the design project, considering the EN13231-1 (2006).

Furthermore, the characteristics of the ballast and subgrade layers can influence the sleeper's behaviour since the increase of the foundation's quality will reduce the amplitude of the bending vibration modes of the sleepers (Vale, 2010).

Over time, the dimensions of the sleepers have increased because of the need to decrease the stress applied in the ballast and increase the lateral stability of the track. In fact, the lateral resistance of the track depends more on the type of sleeper and the type of connections than its dimensions (Fortunato, 2005).

Railpads

The railpads are characterized by their damping and flexibility (stiffness) and depend on the type of load (static or dynamic), type of sleepers and geometry of the track (curve or straight). In the case of a concrete sleeper, the vertical static stiffness varies between 40 and 450 kN/mm (FIB, 2006). In curves, the stiffness of the railpads shouldn't be reduced because of the generated noise and wear of the fastening system. The dynamic vertical stiffness should be less than 600 kN/mm. The NP-EN134581-2 (2009) defined the railpad through its dynamic vertical stiffness: flexible ($k_v <$ 100 kN/mm), medium ($100 \leq k_v <$ 200 kN/mm) and rigid ($k_v \geq$ 200 kN/mm).

Ballast

The ballast layer supports the superstructure of the track and allows resisting the vertical, transverse and longitudinal forces from the trains, distributing the high stresses to protect the sublayers and providing resiliency to absorb shock from dynamic loading. However, the value of the ballast's deformation is higher than the sub-ballast and subgrade layer and depends on the cyclic loading and frequency (train speed). The complex behaviour of the ballast depends on the effects of angularity, particle degradation, *in situ* confining pressure, the frequency of the applied cyclic load and impact loads (Nimbalkar and Indraratna, 2015). Furthermore, this layer influences the vertical, lateral and longitudinal stability of the track, through the friction between the ballast's particles and the contact surfaces (Fortunato, 2005).

The ballast is classified according to its grain size, the shape of the particles, resistance to fragmentation, wear's resistance by friction (Micro-Deval) and durability (NP-EN13450, 2005). The thickness of the ballast is an important factor and its definition and respective methodology have been studied by Esveld (2001) and UIC (2008). The thickness is usually used as a design parameter in several railway design methodologies. However, most of these methodologies are empirical and based on simplified theoretical methods including the work described in the manual of the American Railway Engineering Association (AREA, 1996), the Canadian modified method suggested by Raymond (1978), Japanese National Railways method developed by Okabe (1961), British Railways method proposed by Heath et al. (1972), and the method developed by UIC (1994).

The characteristics of the ballast are defined in the UIC (2008), namely, the deformability modulus (*E*), *Poisson's* ratio (*v*), cohesion (*c*), friction angle (*ϕ*) and specific weight (*γ*). The typical values are described in Table 2.2 and can be found in UIC (2008). Indeed, in this scope, if more accurate data are not available, UIC (2008) purposes the following reference values for the ballast.

Table 2.2: Ballast properties (UIC, 2008)

E (MPa)	ν	c (MPa)	ϕ (º)	γ (kN/m³)
130	0.2	0	45	15

More details about the characteristics of the ballast layer are described in the work developed by Fortunato (2005).

Sub-ballast

The sub-ballast is the layer placed between the ballast and the subgrade and it is defined as a transition between the quality of the two materials. Some important functions of this element can be performed by the ballast: reduction of the traffic-induced stress at the bottom of the ballast layer to a proper level for the top of the subgrade and frost protection of the subgrade. The sub-ballast is less expensive than the ballast since it is a material with less quality.

The presence of the sub-ballast is essential to have a satisfactory track performance and decrease the level of maintenance when compared with a substructure only compose of the ballast and subgrade layers (Selig and Waters, 1994).

The number of the layers (and thickness) that compose the sub-ballast, as well as its characteristics, depend on (Fortunato, 2005):

- Materials used in the construction;
- Climatic and hydrogeological conditions of the local;
- Traffic, which includes the level of the load, speed and frequency;
- Superstructure of the track (type of rail and type and spacing between the sleepers)
- Type of the subgrade material (properties, mechanical characteristics, compactness and water susceptibility).

The sub-ballast should be composed of a well-graded natural material or processed sand-gravel mixtures or well-graded crushed natural aggregates or slags. The sub-ballast should also present low deformability and permeability and its particles should resist the wear. The granulometry is an important characteristic since this element works as a filter and separates the ballast and the subgrade.

Some materials/mixtures/layers can replace the function of the sub-ballast: cement, lime, or asphalt, stabilized local soils, asphalt concrete layers, or geosynthetic materials like membranes, grids and filter fabrics (geotextiles) (Selig and Waters, 1994). In the case of a layer composed of lean concrete, this

material ensures the protection of the subgrade and proper and better distribution of the loads to the platform. However, this solution also presents some disadvantages such as the cracking of the concrete layer, possible pumping of fine particles and the fact that it is an uneconomical solution (UIC, 2008).

Thus, it is possible to conclude that this layer is important since the behaviour of the ballast, which includes the phenomenon of the accumulation of vertical permanent deformation, is influenced by the deformability of the supported layers.

Subgrade

The subgrade is the platform on which the track structure from the sub-ballast is built. This layer can be part of an embankment that is built with filling materials or can be natural ground. The subgrade should be designed in order to resist failure and excessive deformation due to wheel loads, the weight of the track and the substructure. A stable platform should not be affected by environmental conditions and should be maintained over time. In the case of the ballasted track, an overstressed subgrade can present cumulative permanent deformation (formation of ballast pocket) or progressive shear failure (subgrade squeezing) under repeated loads. Indeed, these are common failure modes of typical subgrades composed of fine-grained cohesive soils (Li and Selig, 1998, Sayeed and Shahin, 2017). This type of problems can lead to an increase in dynamic loads and accelerate deterioration. Besides the soft subgrade failures, there are also problems on a hard subgrade that are related to the abrasion by coarse ballast particles in the presence of water that can cause the abraded subgrade fines to infiltrate and foul the ballast. The track stability is not affected but this phenomenon reduces the permeability, affecting the track life-cycle and its performance and maintenance requirements (Li et al., 2016).

According to UIC (2008), in order to guarantee a deformability modulus superior to 80 MPa, the subgrade should be the type P, considering the classes $P1$, $P2$ and $P3$ that correspond to weak, medium and good quality, respectively. The class depends on the materials used in the subgrade and the characteristics of the materials. The UIC (2008) presents a methodology to define the thickness of the subgrade, according to the soil's classification (QS) and the required resistance capacity (P).

The drainage is another important aspect to consider in the performance of the subgrade.

The design of this layer (design period corresponds to 100 years) is defined according to the type of traffic, bearing capacity, configuration of the track, climatic and hydro-geological conditions.

Concrete slab

The concrete slab is used in the ballastless track and can be concreted *in situ* or pre-casted. Regarding the reinforcement, it can be placed on the neutral axis in order to control the cracking by retraction. On the other hand, it is possible to place the reinforcement in the top and bottom of the neutral axis, to support the axial and bending stresses. This solution is applied in soils that present a tendency to settle. In the first solution, the concrete slab has a small thickness and does not support the bending stresses that occur due to the settlements of the foundation's soil. The percentage of ordinary reinforcement varies between 0.8% and 0.9%.

The main function of this element is to homogenize and reduce the stresses in the support layer since the elasticity of the system is concentrated in the railpads. In fact, the concrete slab presents reduced vertical displacements when compared with the total displacement of the track. The ballasted track and the granular layers present higher vertical displacements when compared with the total displacements of the ballastless track, which means that is possible to conclude that the elasticity of the system does not depend only on the railpads but also on the ballast and/or bituminous layer.

Support layer (poor concrete)

The hydraulically bonded layer (HBL) is composed of poor concrete or bituminous material and should present a deformability modulus superior to 120 MPa. In the case of bituminous material, the modulus is superior to 5000 MPa.

In fact, this layer is a mix of aggregates (as sandstone, crushed sand and stone chips) with a bonding agent as the Portland cement. The typical thickness should be 300 mm and the edges of the HBL should be constructed with an outward inclination ≥ 4% to prevent water infiltration between the HBL and concrete or asphalt bearing layer.

This layer should be as homogeneous as possible in order to avoid differential settlements and bending stresses in the concrete slab.

The frost protection layer is usually placed under the support layer and consists of fine gravel to prevent water rising from the subsoil. This layer should present a permeability close to 1×10^{-5} or 1×10^{-4} m/s. The modulus of deformation should be, in the upper part of this layer, at least $E_{v2} \geq 120$ MPa.

2.2.4 Comparison of the ballasted and ballastless tracks

The ballasted and ballastless tracks present some similarities but also important differences, as mentioned previously. One of the most significant differences is related to maintenance works and the frequency associated. In terms of performance, the conventional ballasted railway track requires periodic tamping due to uneven settlements of the ballast. Furthermore, the maintenance work increases for high-speed lines. Besides that, the ballast contamination and the instability under vibrations produced by vehicles are some of the problems that emerge on the ballasted track. Moreover, the ballasted track also presents reduced lateral track resistance since the lateral movement is not fully restrained, mostly, in the direction parallel to sleepers (Indraratna and Nimbalkar, 2016).

Indeed, in the case of high-speed lines, the ballasted track presents some negative characteristics (Riessberger, 2008):

- Higher track deterioration of the ballasted track because of the high contact between the sleepers and ballast particles;
- Significant permanent deformations, mostly because of the ballast;
- Reduced uniformity of track elasticity leading to irregular elastic deformations and increase of dynamic loads;
- Decrease of track geometric quality after tamping operations;
- Reduced lateral track resistance - the track is susceptible to buckling phenomenon when rails are subject to important variations of temperature or when braking systems are applied using frictional or Eddy-current systems.

The problems listed previously can be overcome by reducing the speed in some critical sections of the track, increasing the frequency of maintenance and applying some measures such as the inclusion of base plate pads under the fastenings or under the sleepers in order to increase the vertical track resiliency and reduce the projection of ballast particles.

The ballastless track is an alternative solution because of the significant reduction of the maintenance work allied to a longer life-cycle with constant serviceability conditions (Audley and Andrews, 2013, Esveld and Markine, 2006, Shahraki et al., 2015).

Table 2.3 allows understanding the advantages and disadvantages of each system according to certain selected factors. The table is based on and supported by the work developed by Paixão et al. (2009). Some updates and changes were added to this work.

Table 2.3 – Comparison between ballast and ballastless track (based on Paixão et al. (2009)

Factors	Ballasted track	Ballastless track
Construction costs	Lower investment cost but higher life cycle cost	Significant investment cost (if no mechanized processes are implemented during the construction) but lower life-cycle cost
Effective life	Poor life expectation (15-20 years). It depends on the amount of traffic (may need renewal after 30 years)	Good life expectation (50-60 years). There is low experience with some implemented systems
Cross-section	The depth of the ballasted track is high. Larger area in plan view.	Reduced structural height (more proper to tunnels). Lower dead loads on bridges
Maintenance and rehabilitation costs	Frequency of maintenance work is higher (some elements with shorter life need to be replaced)	Reduce maintenance work (when compared with the ballasted track) Maintenance operations are more complex
Track availability	Conditioned by maintenance works	Nearly full availability
Layout	Track alignment can be corrected	Corrections are difficult
Vertical Stiffness	The unevenness of vertical stiffness. Variation of track parameters in longitudinal development – irregular vertical stiffness	Higher control of stiffness (special care on the transition zones)
Elasticity	High elasticity (due to ballast)	Elasticity obtained due to the use of other elements as rubber pads
Track stability	Limited lateral stability (due to the ballast mechanical properties – the material presents non-linear, irreversible behaviour	Increased stability – allows smaller radii in curves and greater adaptation to field High lateral resistance, which allows the increase of speed
Ballast projection	Projection at very high speeds	-
Eddy-current brakes	Limited use (track instability)	For high-speed vehicles, it is allowed to use the Eddy-current brakes
Permeability	Reduced permeability	High impermeability
Availability of material	Limited	No problem
Noise	Good noise absorption	High noise levels. Can be necessary to adopt elements to reduce the noise
Safety	No access for road vehicles	Most ballastless tracks systems allow access to emergency vehicles

According to the information listed in Table 2.3, in the case of high-speed lines, noise emerges as one of the most important variables. In the case of ballasted tracks, the fastening system and the ballast allow a proper noise absorption, unlike the ballastless system because of its lower fastening system properties and its characteristics as a noise reflector (if it is not properly treated). Indeed, some studies show that the increase of the noise due to the ballastless track structure is about 3 dB(A) (Gautier, 2015).

Regarding the construction, for example, the costs of the ballastless track laid for the *Sanyo Shinkansen* line (in Japan) were 1.3 to 1.5 times those for the ballasted track (Ando et al., 2001). In this particular case, the choice between the two structures was based on some important factors: economy, durability, environment and construction workability.

Comparing the two structures, the construction of ballastless tracks, despite being more expensive, presents lower maintenance operations. However, it is necessary to take special care with the values defined for the parameters of the supporting layer because of its high bending stiffness. Furthermore, in the ballastless track, the differential settlements need to be avoided since geometric adjustments are limited, unlike the ballasted track where is possible to correct the differential settlements. And this is an important aspect, mainly, in the transition zones, where there are significant differential settlements, as explored and referred to in Chapter 3.

Hence, in order to ensure proper foundation conditions, there are some recommendations for the supporting layers in the case of ballastless but also ballasted tracks. According to UIC (2008), the quality of an earthwork is highly dependent on compaction. Thus, the compaction should achieve a minimum deformation modulus with an homogeneous distribution. The deformation modulus can be measured using the plate load bearing test or by dynamic devices. UIC (2008) defines a degree of compaction and minimum deformation modulus, which are specified for each layer:

- Ballasted track: E_{v2} on the upper surface of the embankment equal to 45 MPa in case of fine soils and 60 MPa in case of sands and gravel; E_{v2} on the upper surface of the sub-ballast equal to 120 MPa (minimum value); For the capping layer is required a value equal to 80 MPa for the E_{v2} parameter;
- Ballastless track: E_{v2} equal to 60 MPa at the top of the embankment and 120 MPa at the top of the frost protection layer (FPL) (Esveld, 2001).

2.3   Railway Design Methodologies

2.3.1   Ballasted track

The design of railway tracks depends on concepts such as safety and comfort. The design is often performed under the orientations defined in the standards such as UIC and British Standards and based on some catalogues (in case of more expeditious designs). Firstly, it is necessary to quantify the loads. The initial scenario is composed of static vertical loads. The dynamic part of the analysis depends on the dynamic component related to the speed of the train. In the past, in some analyses, the dynamic load part was added to the static load part.

The main goal of the design of the railway track is to prevent the rupture of the subgrade through the definition, for example, of a proper ballast and sub-ballast thickness (in the case of ballasted tracks). However, it is imperative to determine the stress distributions from empirical equations. In fact, the

evolution of the railway track design was slower because of the complexity of the stress calculations and the inclusion of the dynamic load part.

A methodology was defined to obtain stresses below the sleepers. The Multilayer Elastic model was defined to calculate the stresses and compare them with the allowable values. However, besides the stresses, the analysis of the track stiffness during the design process is also important. So, during the 70s, catalogues were introduced in order to simplify and standardise the design processes. Posteriorly and with the technological advances, the software became an important tool and more robust analyses were performed. Nowadays, numerical methods and tools are often used in railway track design and three-dimensional analyses are required in some situations (as the study of the performance of transition zones). For example, the finite element method (*FEM*) is a numerical approach that allows simulating the materials' behaviour (linear and non-linear analysis) and allows analysing structures with complex geometry, composed of multiple materials and applying different types of loads. The discrete element method (DEM) is also an alternative numerical tool that simulates the discontinuous behaviour of some materials, namely the ballast. However, this methodology is quite demanding at the computational level.

The railway design methodologies depend on the selected procedures and, in the case of the ballasted tracks, the approaches are focused on the determination of the thickness of the trackbed layers. During the design process of ballasted tracks, the subgrade failure (that occurs mainly due to cyclic loading) is the major phenomenon to consider. The traffic induces stresses that can cause (Burrow et al., 2006, Selig and Waters, 1994):

- Subgrade erosion due to the attrition by the ballast;
- Progressive shear failure;
- Excess rate of settlements through the accumulation of permanent deformation that can cause ballast pockets (Figure 2.6);
- Massive shear failure.

The phenomena described previously are characteristic of fine-grained soils such as clays. The process design should prevent progressive shear failure and excessive permanent deformations.
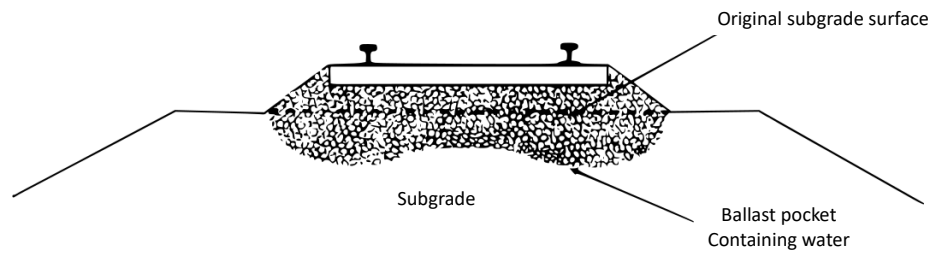
Figure 2.6 – Ballast pockets – adapted from Burrow et al. (2006)

In order to avoid the failures modes, some solutions can be adopted (besides the proper thickness of the trackbed layers):

- Non-ballasted track forms as asphalt layers;
- Increase of the bending stiffness of the rail;
- Soil stabilizations that allow having higher stresses.

The method proposed by Li and Selig (1998) prevents progressive shear failure and also excessive permanent deformations. This method limits the stresses in order to reduce the plastic stresses at an admissible level. According to this procedure, the subgrade stresses are determined using an analytical model of the track system and the allowable stresses are determined from an equation that relates the permanent deformation to the number of loading cycles. For design purposes, the substructure can be modelled as a single trackbed layer overlying a homogeneous subgrade (Burrow et al., 2006). According to Li and Selig (1998), in this method, the dynamic loads are considered by the use of an empirical equation suggested by the AREA (*American Railway Engineering Association*):

$$k = 1 + \frac{0.0052 \times V}{D}$$
(2.1)

where k is the ratio of dynamic to static wheel load, V is the train speed (km/h) and D is the wheel diameter (m). The cyclic load triaxial tests were conducted on various fine-grained soils in order to obtain the allowable permanent deformations under repeated loading. The results of the tests show that the permanent deformation of the subgrade (ε_p) is related to the soil deviator stress (σ_s) and the number of repeated stress applications (N). The cumulative permanent displacement can be determined by the following expression:

$$\delta = \sum \varepsilon_{p_i} H_{si}$$
(2.2)

where H_{si} is the thickness of each sublayer of the subgrade (in m), ε_p is the permanent deformation at the centre of each subdivided layer and δ is the cumulative permanent displacement of the track subgrade

(in m). According to Li and Selig (1998), the permanent deformation (ε_p) and the cumulative displacement should be limited to 2% and 25 mm, respectively. The authors developed two charts to prevent progressive shear failure and excessive permanent deformation that depends on the traffic loading, soil type, trackbed layer, subgrade resilient moduli and subgrade depth.

The UIC, as mentioned previously, also presents a set of references for the design and maintenance of track substructure. However, the recommendations only regard a single thickness of the ballast and sub-ballast and for the prepared subgrade (Figure 2.7). The thickness is determined according to the following factors: type of the foundation soil, traffic characteristics, track configuration and quality and thickness of the prepared subgrade (Burrow et al., 2006). However, this procedure does not determine the thickness of the individual layers of the trackbed: ballast and sub-ballast. The inclusion of the prepared subgrade and geotextile is optional and depends on the quality and characteristics of the foundation. This quality is evaluated primarily considering the percentage of fines. According to UIC (2008), there are four soil classes:

- QS0: is absolutely mandatory the improvement of the soil;
- QS1: is classified as "poor" soil and can be used in its natural condition when subjected to adequate drainage and maintenance; should be considered the possibility to improve the soil's conditions;
- QS2: soils with average quality;
- QS3: is classified as "good" soils.

The traffic is characterized by a line that depends on the tonnage hauled, the tonnage of tractive units, line speed, traffic mix and wear effects of vehicles (Burrow et al., 2006). In the end, the soils classified as "poor" and lines with faster and heavier traffic require thicker trackbed layers.
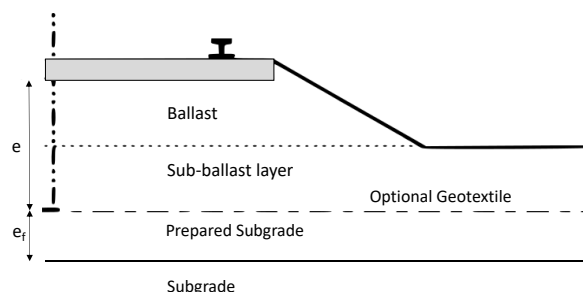
Figure 2.7 – Typical cross-section of a ballasted track – adapted from (UIC, 1994, Burrow et al., 2006)

The *British Rail* also developed a method to prevent the failure of the subgrade by excessive elastic deformation through the design of several charts that relate the required thickness of the trackbed layers

to the threshold stress of the subgrade. This procedure considers the ballast, sub-ballast and subgrade as a homogenous layer in order to determine the stress distribution in the subgrade depending on the sleeper spacing and contact pressure. To define the threshold stress, cyclic triaxial tests were performed, and the permanent deformations were also analysed. Values under the threshold stress lead to an increase of the permanent deformation until reaches a stable condition.

The *Network Rail Code* is an independent regulator that also defined a set of recommendations related to the thickness of the trackbed layers, suggesting that the subgrade should have proper strength and stiffness. The thickness is determined according to design charts described in the standard (defined based on empirical data and multilayer elastic theory) that depend on the undrained subgrade modulus and dynamic sleeper support stiffness (30, 60 and 100 kN/mm that correspond to the minimum requirements for existing lines with or without geogrid and new lines, respectively).

The *West Japan Railways* is a company that also suggests some recommendations about the construction and maintenance of the railway tracks in some lines of Japan (Shinkansen and commuter lines). For both lines, a limit value for bearing capacity was assumed (288 kPa) and below this value, the improvement of the foundations was required. Note that a bearing capacity of 288 kPa equates to a compressive strength, σ_s of approximately 112 kPa assuming a cohesion model plastic solution to a simple strip footing where $\sigma_b = 2.57 \, \sigma_s$ (Burrow et al., 2006).

2.3.2   Ballastless track

The design theories of the ballastless track vary across the world according to the experience and background of each country (Liu et al., 2011). A revision of the calculation methods is presented in Table 2.4, as well as the structural design procedures.

Table 2.4 – Ballastless track theories

Japan	Germany	China
- the train load effect is a primary concern	- temperature load and concrete contraction are the main effects	- design theory based on the allowable stress method considering the train load, temperature and foundation deformation effect
- based on the elastic design method, the safety during manufacturing, hoisting and construction of the slab is maximized	- the reinforcement is located near the neutral axis (for the crack control due to thermal effects and lateral bending) and does not bear the train load	
- the subgrade's uneven settlement and the influence of the weather conditions are considered in the design, as well as the concrete constraints and construction	- the train load and temperature gradient are resisted by the rupture strength of the concrete	
	- railway design based on pavement engineering	

Regarding the loads, the Eurocode (that considers the vertical loads – LM71 and SW2 and SW/0 models –, longitudinal loads and centrifugal forces for curves) is used in Europe and different combinations are considered such as the ultimate limit states, service limit states, or frequent service loads with different multiplicative coefficients for each group loads.

In the case of Japan, the accounting for the wheel tread damage tolerates three times the static load. In the case of fatigue damage, 1.45 times the static load is used. The lateral loads are introduced as allowable lateral force considering the allowable value of the derailment coefficient. The fatigue is analysed by applying half the design value for lateral forces (Gautier, 2015).

The Chinese designs are based on measurements and simulations and the design wheel loads are considered as three times the static wheel load. According to Liu et al. (2011), a coefficient equal to 3 is used for calculations that consider only the train load. The value of 1.5 is used for combinations that include the train load but also other variables as temperature and foundation deformation.

The methods present the same principles but the coefficients that multiply the unitary loads are different. The same conclusions are applied in the case of dynamic analysis since there is still no standardization for this analysis (Gautier, 2015).

2.4 Structural models and modelling of the elements

2.4.1 Load types

The high-speed railway lines are defined as a combination of several elements of a complex system, which includes the infrastructure, rolling stock, equipment and operating conditions. The high-speed network is characterized by the speed of trains: in the new lines the speed is superior to 250 km/h (category I - UIC) and in the updated existing lines the speed of the train is between 200 up to 220 km/h (category II - UIC). Indeed, there is a third category that corresponds to the case of conventional lines upgraded for high-speed trains, however below 200 km/h to allow for topographical particularities, such as in mountainous or urban areas.

The European standard (ISO14837-1, 2005) defines ten types of excitation mechanisms:

1. Quasi-static excitation: the excitation is generated by the loads of the train (axle load) due to the movement of the train with constant speed;
2. Excitation-induced by the geometric imperfections and materials inherent to the fabric process of the rails and the wheels;

3. Parametric excitation due to the stiffness' variation motivated by the discrete support of the rails (in solutions with continuous support, this type of mechanism is irrelevant – railway tracks with the rail embedded);

4. Excitation due to geometric irregularities of the track and wheels of the rolling stock;

5. Excitation due to discontinuities of the track (for example, switches and crossings);

6. Excitation-induced by the poor functioning of the rolling stock's suspension;

7. Excitation due to the spatial variation of the mechanic properties on the surface of the wheel-rail contact;

8. Excitation due to the lateral loads induced by the rolling stock;

9. Excitation to the changes in circulation conditions as the braking and traction;

10. Extreme environmental conditions that can lead to changes in the dynamic properties of the elements.

It is common to found in the bibliography the grouping of the excitation mechanisms in three major groups (Alves Costa, 2011):

- Quasi-static excitation – induced by the movement of the loads that correspond to the static weight of the vehicle per axle; the dynamic character is due to the temporal change of the stress and deformation states of the track at any point of the domain, caused by the mobile character of the solicitation; the vertical displacement of the train's masses is constant and are not developed inertia forces in the vehicle; this excitation is associated with low frequencies that depend on the speed of the train and geometry of the vehicle;

- Dynamic excitation – induced by the vehicle-track dynamic interaction that implies the generation of accelerations on the vehicle and inertia forces; the main factors that cause these phenomena are:
  - Geometric irregularities of the wheel and track – mechanism 4;
  - Discontinuities of the track – mechanism 5
  - Stiffness's variation in the longitudinal direction – mechanism 3.

  The frequencies and magnitude of the vehicle-track interaction loads depend on the speed of the train and the dynamic properties of the vehicle and the railway infrastructure.

- Parametric excitation – is due to the deformability difference of the track depending on whether the solicitation is applied on the rail supports or between them, generating a harmonic excitation that depends on the distance between the sleepers, hence designated as parametric, since it

37

depends on a geometric parameter of the track; some studies show that the dynamic force due to the geometric parametrization of the track tends to increase with the train's speed but remains constant when the excitation's frequency induced by the parametrization of the track overcomes the resonance frequency of the vehicle-track system; the vertical displacement of the rail throughout the movement of the moving load over a perfect track presents a sinusoidal evolution which wavelength is equal to the double spacing between the sleepers; as mentioned, this excitation depends on the spacing between the sleepers and the train's speed.

The loads under consideration are composed of the train loads, temperature effects and subgrade settlements (it is usually considered as an imposed displacement), as mentioned by Gautier (2015).

Throughout this work, the nomenclature referred to by Alves Costa (2011) will be adopted.

Train Loads

According to the Eurocode (EN1991-2, 2003), the static design of the railway tracks must include:

- **Vertical loads** – The LM71 model characterizes the usual traffic and it is represented by four 250 kN axles spaced 1.6 m from each other and 80 kN/m, which corresponds to a distributed load. The loads are multiplied by a factor α. The SW/0 model and SW2 model can also be used for heavy traffic;
- **Horizontal loads**:
  - Centrifugal loads for curves, lateral effects due to the wind and lateral forces corresponding to the lateral component of wheel-rail interaction;
  - Longitudinal forces for accelerations-braking.

The combination factors (ψ) for groups of loads and non-traffic loads (which includes temperature, seismic action, wind, etc.) are indicated in the Annex A2 of the standard EN1990 (EN1990, 2005).

Temperature Effects

The influence of the temperature as the thermal dilatation or contraction (mostly for continuous slabs) can be extremely dangerous for the ballastless tracks.

Subgrade settlements

The settlement is commonly considered as an imposed displacement, which induces bending or warping in the ballastless track (Liu et al., 2011, Gautier, 2015). The settlement effects in the design phase vary depending on the country and its standards.

Throughout this work, the passage of real trains (as the *Alfa Pendular* train) will be simulated and only the vertical loads will be considered. The longitudinal and centrifugal forces are out of the scope of this work.

The structural models used to model the railway structures will be presented below from the simplest to the most complex concepts.

2.4.2 *Modelling of railway track structures*

Throughout the years, different approaches and methods have been used to model the railway tracks: from the simplest modelling until the most recent models that include, for example, a detailed characterization of the railway track through the inclusion of tridimensional elements. The evolution of technology led to an advance in numerical modelling to increase the level of detail.

The complexity and detail of the model depend on the analysed problem and the range of frequencies selected. For example, a model used to study the vehicle-track interaction cannot be the same model used to study the waves' propagation in the foundation soil.

The analysis can be performed in the frequency or time domain. The frequency-domain implies the use of linear or equivalent linear systems. Thus, the modelling of singularities of the track as rail's joints, hanging sleepers, variations of the global stiffness is only possible adopting the time-domain analysis (Alves Ribeiro, 2012).

Despite the several advantages of the numerical models, the analytical and semi-analytical models are still commonly used because of their required reduced computational effort. The models presented in the following sections can be used in the study of the dynamic behaviour of railway tracks.

2.4.2.1 *Analytical models*

The Winkler model (1867) is commonly used because of its simplicity (the rail is modelled as beam elastically supported). Indeed, this model has been used as a basis for other models, through the improvement of its complexity (by the inclusion, for example, of the discretization of each element).

The model presents some problems in the analysis of low and medium frequencies since the dynamic phenomena in the foundation are not properly considered. The Winkler model presupposes that the foundation can be simulated through springs and dampers (Kelvin model).

Posteriorly, this problem was solved through the introduction of the equivalent stiffness concept. Thus, the value of the stiffness is dependent on the angular frequency and wavenumber and it is determined by the dynamic response of the layer subjacent to the track considering the imposed solicitation.

In Figure 2.8, the rail and the springs that simulate the equivalent stiffness of all elements under the rail (continuous model) are represented.
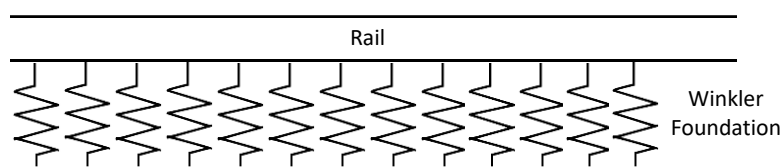
Figure 2.8 - Winkler Model

Besides the complexity of this analytical model, the continuum support of the rail is an approximation since its real support is discrete and depends on the spacing of the sleepers. Knothe and Wu (1998) evidence that the consideration of discrete support is only important in the case of vibrations higher than 600 Hz. Furthermore, the simulation of the variation of tracks' characteristics in the longitudinal direction is possible but limited.

The solution of the analytical models is obtained through a total analytical integration, without using any numerical processes. However, whenever it is not possible, semi-analytical methods are used. These methods allow using the advantages of analytical methods and overcome some of these limitations. More details about these models can be found in the work developed by Alves Costa (2011).

Knothe and Wu (1998) also show the limitations of the analytical models in the case of frequencies inferior to 200 Hz through the comparison between the experimental and numerical results. The authors purpose a model based on the coupling between the tracks' model (where the rail is discretely supported) and the foundation's model, which consists of the half-space ground. Three different scenarios (two stratified soils with different characteristics and homogeneous soil) were considered. The receptance results of the track showed that the receptance until 200 Hz varies with the properties of the foundation's soil. In the case of higher frequencies, it is possible to adopt simpler models since the response of the tracks depends, mostly, on the properties of the railpads.

2.4.2.2 *Semi-analytical methods*

The semi-analytical methods present some problems related to the geometric and mechanical constraints but allow the consideration of the main elements of the tracks including the foundation soil and efforts induced by the traffic (Alves Costa, 2011).

The semi-analytical models allow obtaining the dynamic response of the track and the general aspects of the wave's propagation in the foundation soil. These models are based on the concept of equivalent stiffness considering the coupling of the railway track model with the dynamic response of the ground.

The coupling between the track and the geotechnical ground is defined taking into account the equilibrium of the stresses and compatibility of the displacements in the contact points between the two models. However, it is important to understand that this coupling is established considering only the vertical direction.

The simplest model corresponds to an Euler-Bernoulli beam with infinite length supported by the foundation soil that can be replaced by an elastic foundation, which behaviour depends on the excitation frequency. Considering that the track is solicited by a moving load (speed c), with a harmonic magnitude over time (amplitude P_z), and defined by an angular frequency (Ω), the equilibrium of the system in the stationary regime is traduced by the following expression:

$$EI\frac{d^4w(x,t)}{dx^4} + m\ddot{u}(x,t) + k_{eq}u(x,t) = P_z\delta(x - ct)e^{i\Omega t} \qquad (2.3)$$

where *EI* is the bending stiffness of the track, k_{eq} is the equivalent stiffness of the foundation and *m* is the mass of the track per unit of length.

The solving of the system is easier considering the transformation of the space-time domain into the wavenumber-frequency domain. Applying a *Fourier* transformation into the variable space and using the derivation's properties in the wavenumber domain, the equilibrium is defined according to the following expression:

$$EIK_1^4u(k_1,t) + m\ddot{u}(k_1,t) + k_{eq}u(k_1,t) = P_ze^{i(\Omega-k_1c)t} \qquad (2.4)$$

The solicitation presents harmonic characteristics over time, which is defined by the angular frequency, $\omega=\Omega-k_1c$, being possible to manipulate the previous mathematical expression into:

$$EIK_1^4\tilde{u}(k_1,\omega) - m\omega^2\tilde{u}(k_1,\omega) + k_{eq}\tilde{u}(k_1,\omega) = \tilde{P}_z(k_1,\omega) \qquad (2.5)$$

and,

$$\tilde{u}(k_1, \omega) = \frac{\tilde{P}_z}{EIK_1^4 - m\omega^2 + k_{eq}} \tag{2.6}$$

The model can be improved considering the damping of the track. The results obtained with the previous expression are in the transformed domain, being necessary to apply an inverse *Fourier* transformation regarding the variable wavenumber. Although simple, the calibration of the model and the definition of some parameters as the bending stiffness of the track can complicate the performance of the model and respective obtained results.

Other complex semi-analytical models can be used to model the railway structures. These models are described in more detail in the work developed by Alves Costa (2011).

2.4.2.3 Numerical models

The necessity to overcome the limitations of the analytical models led to the development of numerical models (Cunha, 2013). The numerical models present some advantages when compared to the analytical since allow considering complex geometries and non-linear laws to represent better the behaviour of the materials. The *FEM* (Finite element method) is the most used method and it is implemented in several commercial *software*. The models presented below are different because of their complexity, which depends on the type of problem analysed.

2.4.2.3.1 Bi-dimensional models

The bi-dimensional models are one of the simplest used in the study of the behaviour of the railway track. These models consider the rail supported in springs and dampers (similar to the analytical models) and the different components of the track are also modelled. It is also possible to introduce discrete supports of the rail, which corresponds to the sleepers. The main advantage of the 2D models is the reduced time of the calculus. However, as in the case of analytical models, the foundation is not properly modelled.

The several types of bi-dimensional models are described in more detail below.

Discrete Support model

The bi-dimensional model of the rail discretely supported can present several degrees of complexity, depending on the type of analysis and the information about the elements of the track. The supports can be modelled by discrete spring-damper systems or spring-mass-spring systems. Figure 2.9 presents the simplest model that considers the rail discreetly supported over the springs and considering a certain space (*e*).
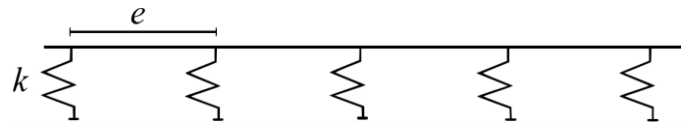
Figure 2.9 - Track model with discrete support (Vale, 2010)

In this case:

$$k = k_c \times e \tag{2.7}$$

where k_c is the continuous vertical stiffness of the Winkler model and k is the discrete stiffness of the support; the rail is an infinite beam. The parameter k represents the stiffness of all the elements underlying the rail.

Considering the k value as the discrete stiffness that corresponds to the vertical stiffness of the several elements that constitute the railway track, the equivalent stiffness of a ballasted track, for example, can be obtained using the following expression:

$$\frac{1}{k_{equivalent}} = \frac{1}{k_{railpad}} + \frac{1}{k_{sleeper}} + \frac{1}{k_{ballast}} + \frac{1}{k_{foundation}} \tag{2.8}$$

Since the sleepers present a lower influence on the global stiffness of the support (because of its stiffness), the equivalent stiffness can be obtained by the following expression:

$$\frac{1}{k_{eq}} = \frac{1}{k_{railpad}} + \frac{1}{k_{ballast+foundation}} \tag{2.9}$$

In the case of the ballastless track, the discrete support model is inadequate, and the continuous support model based on the Winkler model is suggested. Figure 2.10 presents an example of a discrete support model that considers several elements of the track.
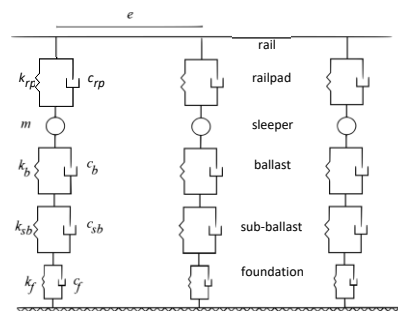
Figure 2.10 - Ballasted model with discrete supports – adapted from (Vale, 2010)

Analysing Figure 2.10, k_{rp} and c_{rp} are the discrete stiffness and damping of the railpad, respectively, m is the mass of the sleeper, k_b and c_b are the discrete stiffness and damping of the ballast, respectively, k_{sb}

and c_{sb} are the discrete stiffness and damping of the sub-ballast, respectively; k_f and c_f are the discrete stiffness and damping of the foundation and e corresponds to the spacing of the supports.

Continuous support model

The previous models do not take into account the longitudinal continuity of the elements underlying the sleepers. In order to consider the longitudinal continuity of the granular layers of the ballasted and ballastless tracks, the models represented in Figure 2.11 can be used.
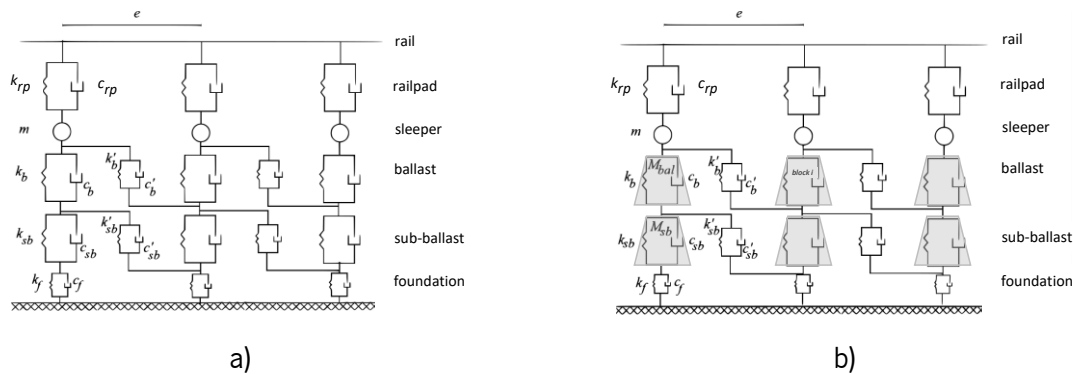
Figure 2.11 – a) Bar elements used to model the ballasted track with longitudinal continuity; b) Bar elements and punctual mass used to model the ballasted track with longitudinal continuity – adapted from Vale (2010)

These models present additional parameters when compared to the models described in Figure 2.9 and Figure 2.10: M_{bal} corresponds to the punctual mass of the ballast block; k'_b and c'_b are, respectively, the stiffness and damping of the ballast in the longitudinal direction; k'_{sb} and c'_{sb} are the stiffness and damping of the sub-ballast in the longitudinal directions, respectively. The models described in Figure 2.11 are different because of the punctual masses of the ballast and sub-ballast.

The longitudinal continuity of the granular layers (in the case of the ballasted track) and concrete slab of the ballastless track can be considered through plane stress state finite elements, as depicted in Figure 2.12.
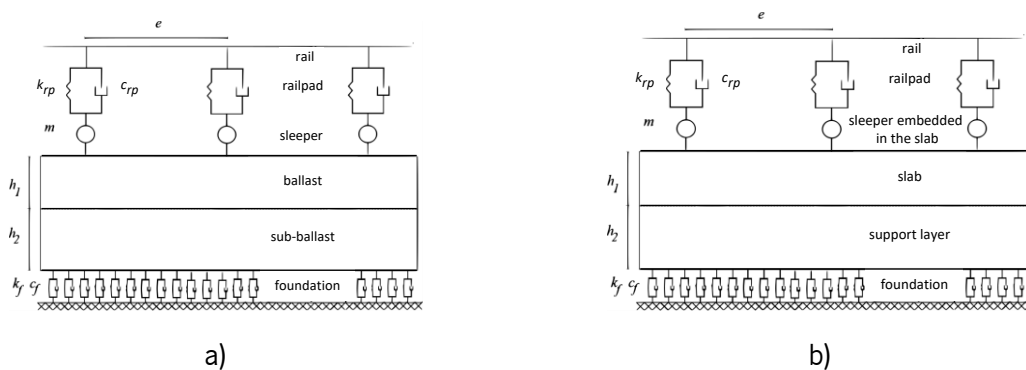
Figure 2.12 – a) Continuous models in longitudinal direction considering plane stress state elements (ballasted track); b) Continuous models in longitudinal direction considering plane stress state elements (ballastless track) – adapted from Vale (2010)

In the case of Figure 2.12, the variables H_b and H_{sb} correspond to the thickness of the ballast and sub-ballast layer respectively and the variables h_1 and h_2 represent the thickness of the slab and support layer, respectively.

2.4.2.3.2 3D Models

The tridimensional model, despite its complexity and computational effort, is an important numerical tool in the modelling of railway tracks. In Figure 2.13, an example of a three-dimensional model of a ballastless track and its cross-section is presented.

a)   b)
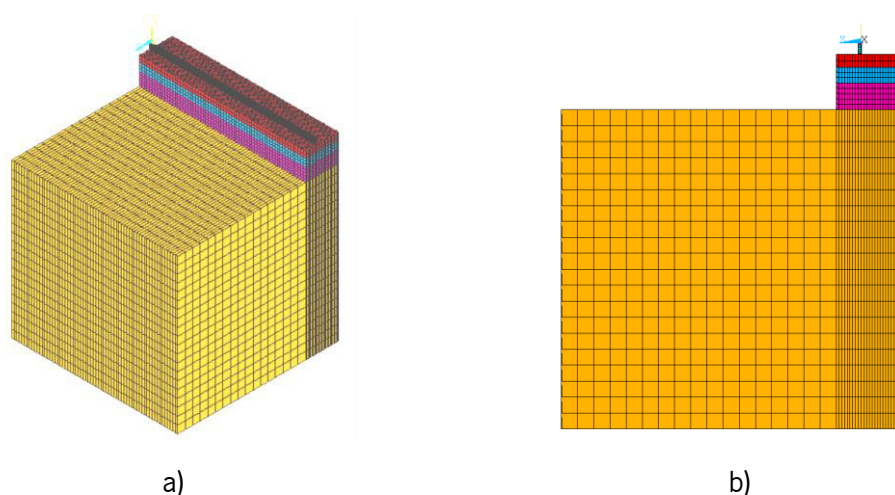
Figure 2.13 – a) 3D ballastless track model developed in ANSYS; b) cross-section of the 3D model developed in ANSYS

The 3D models allow simulating properly the different elements of the railway track, considering complex geometries and providing a more rigorous analysis of the static and dynamic behaviour of the track.

The 3D models are often used when global analysis of the structure's behaviour is required. This analysis includes the study of the structural response of the track and the foundation in the three spatial directions, the influence of the heterogeneity of the track in the transversal and longitudinal directions, the behaviour of the track in a curve, the dynamic behaviour near the joints, etc.

The *FEM* is widely used in this context. However, the ideal application of the *FEM* occurs in models with well-defined boundaries, which does not happen in railway tracks. One way to deal with this problem includes the application of non-reflector boundaries also known as silent boundaries. According to the bibliography, Lundqvist et al. (2006) developed tridimensional models in the LS-DYNA software (based on *FEM*) adopting the boundary conditions previously described. Lane et al. (2007a) also presented a total tridimensional finite element model involved in viscous-elastic layers that allow absorbing the radiations.

Another approach used to reduce the required memory to perform a dynamic analysis is the articulation between the *FEM* and *BEM* (*Boundary Element Method*). Thus, all the elements are modelled as finite elements that are coupled to the boundary elements. In the scope of the 2.5D formulation, the BEM can be implemented using the 2.5D Green's function of the soil as a fundamental solution, which is more efficiently evaluated in the frequency-wavenumber domain than in the space-time domain (Cunha, 2013). This alternative allows simulating the ground considering the radiation conditions in the infinite. The method was tested and validated with experimental results. As mentioned previously, the models can be developed in the time and/or frequency domain (Galvín and Domínguez, 2009, Santos, 2013).

Indeed, the numerical models and tridimensional models, in particular, require FEM meshes with a high number of degrees of freedom. An alternative consists of the use of frequency-domain models, which allow a considerable reduction of computational effort but limits analyses to linear elastic cases (Araújo, 2010). One of these approaches is described below.

2.4.2.3.3 2.5D Models

The 2.5D models are used to study the vibration's propagation in the surrounding areas of the railway tracks. The methodology includes some particularities such as the consideration of an invariant section (geometrically and mechanically). This method allows obtaining a 3D response of the structure in a reduced calculus' time. This formulation is similar to the 2D models, but, each node of the finite element presents 3 degrees of freedom. The analysis is performed in the frequency-wavenumber domain and the response of the structure is linear. The simulation of the discrete support of the rail is not possible since it is assumed that the cross-section of the railway track repeats itself indefinitely.

In the 2.5D models, the response of the structural system is obtained through the application of the *Fourier* transform. However, this method also presents some disadvantages, as mentioned previously (Alves Costa, 2011):

- Not considers non-linear effects;
- Implies restrictions regarding the geometry of the soil mass – the stratification needs to be horizontal and parallel to the surface of the ground;
- Not possible to consider local heterogeneities;
- Imposition of some initial conditions is very difficult or even impossible.

For example, this method does not allow analysing the transition zones, which is one of the main goals of this work since this numerical approach only allows modelling an invariant section of the railway track.

The practical application of the 2.5D modelling and the detailed mathematical description of the formulation of this methodology is presented in Chapter 5, as well as the analysis and comparison of the short- and long-term performance of the subgrade in the ballasted and ballastless tracks.

The periodic models are also an important approach used to simulate the train-track problem. In this case, a 3D section that repeats periodically is selected. This approach can solve some limitations of the 2.5D models, namely, the spacing between the sleepers (Ferreira and López-Pita, 2013).

2.4.3   Comparison between the structural models

The previous sections explore and explain the main differences between the several structural models. Thus, it is important to resume the acquired knowledge to fully understand the available models that can be used to simulate the behaviour of a railway track. Some of the particularities and main advantages of these models are presented in Table 2.5.

Table 2.5 – Comparison between the structural models

	Models	Description	Ballasted Track	Ballastless Track	References
	Analytical model	The Winkler model is an example of this approach that is commonly used but presents some limitations in the case of frequencies below 200 Hz.	✓	✓	Esveld (2001)
	Semi-analytical models	This approach presents geometric and mechanical constraints. It is based on the Winkler model and allows us to obtain the dynamic response of the track but also the general aspects of the vibration's propagation.	✓	✓	Alves Costa (2011)
Numerical	Discrete support model	This approach is not adequate to model the ballastless track.	✓		Vale (2010)
Numerical	Continuous support	The continuous support allows simulating the longitudinal continuity of the track.	✓		Vale (2010)
Numerical	Continuous support with plane stress state elements	The longitudinal continuity is assured by the finite elements.	✓	✓	Vale (2010)
Numerical	2.5D	The main advantage of this model is the reduced calculus time and computational effort when compared with the 3D models.	✓	✓	Alves Costa (2011)
Numerical	3D	Despite the calculus time and computational effort, 3D models are an important tool to model complex geometries, representing better real track conditions.	✓	✓	Lane et al. (2007a)

47

2.4.4 Numerical tools/software used to model the railway structure

The modelling of the railway track is a very complex process since, as mentioned previously, the track is composed of different materials that present a complex behaviour (such as the railpads and the ballast), there are significant contact surfaces between the different elements of the track and some components present almost unlimited longitudinal development, as the rail and foundation soil (Popp et al., 1999).

The railway structures were firstly modelled on commercial software such as ILLITRACK, GEOTRACK and KENTRACK (Correia et al., 2007). Posteriorly, advanced rail track models were developed, using *FEM* and hybrid methods. The hybrid methods couple *FEM* and multi-layer systems: the track-embankment system is modelled by *FEM* and the layered ground through Green's function (using the software *VibTrain* - the models are developed using frequency domain analysis and the materials needed to be modelled with linear behaviour). Correia et al. (2007) also modelled the railway track applying a 2D approach, to compare different commercial *FEM* codes (DIANA, PLAXIS and ANSYS) and to test the dynamic performance of a high-speed train track. In fact, ABAQUS, ANSYS, DIANA, GEOTRACK, KENTRACK, LS-DYNA, FLAC, COSMOS, DARTS, GENSYS, SIMPACK and PLAXIS (that is specialized in geotechnical problems) are some of the commercial software based on *FEM* used to model the railway track and allow simulating the vehicle, the complete track structure, the ground and transition zones. The use of discrete elements depends on the time of calculation, the required analytical precision, etc. The main goal of the work developed by Correia et al. (2007) was to compare the obtained results with experimental data. Thus, although the 2D models allowed understanding the problem, the authors agree that the 3D models are essential to reach accurate results.

Posteriorly, Nimbalkar and Indraratna (2015) simulated the behaviour of the ballast using the 2D PLAXIS (permanent deformation) since the 3D analysis in PLAXIS could not accommodate cyclic behaviour.

The DIANA software (among others similar), for example, allows the user to develop subroutines written in the FORTRAN and combine them with the standard codes. Thus, it is possible to create subroutines to model nonlinear elastic stress-strain relations. Cunha (2013) developed a FORTRAN routine that updates the vector σ, considering the implementation of a non-linear model. This method allows to study the track-soil response due to the passage of a train and to obtain the difference between the equivalent linear model and cyclic non-linear model.

In the case of ANSYS, to model the granular layers, the Drucker-Prager and extended Drucker-Prager models are available in the software. Furthermore, sub-routines can also be developed by the user and implemented in the model.

48

In the case of the 3D *FEM* approach, the computational time is the main concern because of the significant degrees of freedom. During this work, the ANSYS software will be used to calibrate the numerical 3D models and to study the performance of the railway structures in a transition zone.

2.4.5   Modelling of the elements of the railway structures

The modelling approaches of the different elements of the railway structures are described in more detail in this section.

Rail

The behaviour of the rail is similar to a beam and can be characterized through the bending parameters, stiffness and equivalent mass. The rail can be modelled as a 2D or a 3D finite element considering the Euler-Bernoulli beam theory or Rayleigh-Timoshenko beam theory. The first formulation is simpler and more frequently used than the Rayleigh-Timoshenko, which includes the influence of the beam bending, the shear deformation and rotational inertia.

According to several studies (De Man, 2000, Andersson, 2003, Dahlberg, 2006), in the case of low range frequencies (until 500 Hz), the Euler-Bernoulli beam presents good results regarding the vertical vibrations of the rails, since only the bending waves are important. However, in the case of higher frequencies, the Rayleigh-Timoshenko is more appropriate (Dahlberg, 2006, Vale, 2010).

In the case of a 3D element, the rail can be modelled as a finite solid element that allows obtaining the stresses and strains in the three orthogonal directions and also to obtain the deformations of the rail. In some cases, the rail is modelled as a rectangular section (Figure 2.14). The dimensions are defined to maintain the properties of the original rail. This modification reduces the computation effort, time and errors on the mesh due to complex geometry (Shahraki et al., 2015). However, this approach does not allow us to obtain the deformation of the rail.

The deformation at high frequencies can be obtained using beam elements, considering two Timoshenko beams (one simulates the head and the web and the other simulates the foot of the rail) that are connected by a set of springs that allows the movement between both. In the case of low frequencies, the model behaves as one Timoshenko beam. In the case of high frequencies, relative movement between the two beams can occur, which represents the deformation of the web's rail.
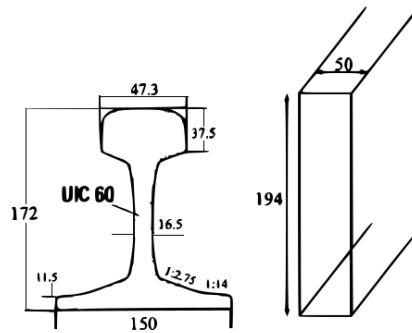
Figure 2.14 - 3D finite element used to model the rail – adopted from (Shahraki et al., 2015)

Despite that, some studies showed concordant results comparing the two models (Euler-Bernoulli and Rayleigh-Timoshenko) considering a static and dynamic analysis until 300 Hz. The choice of the model depends on the direction and range of excitation frequencies. Andersson (2003) states that between 0 and 1000 Hz and considering a vertical excitation, it is possible to adopt the following beam theory:

- Euler-Bernoulli beam in static and dynamic analysis for frequencies between 0 and 500 Hz (the deformation is discarded);
- Rayleigh-Timoshenko beam in a dynamic analysis for frequencies between 500 and 100 Hz.

In the case of lateral excitation, the rail is subjected to bending and torsion even at low frequencies. In this case, for frequencies equal to 500Hz, the Rayleigh-Timoshenko beam theory or solid elements should be applied to model the rail (Vale, 2010).

Fastening system

The stiffness of the fastening, usually, is less than the stiffness of the railpad. Thus, in the case of dynamic analysis, the role of the fastening system is normally neglected.

Sleepers

The modelling of the sleepers depends on the type of the model: 3D or 2D. In the case of a tri-dimensional model, it is possible to use the Euler-Bernoulli beam, Rayleigh-Timoshenko beam and also finite solid elements.

In the case of a bi-dimensional model, the sleepers can be modelled as:

- Rigid bodies;
- Beam elements (Euler-Bernoulli beam or Rayleigh-Timoshenko beam, depending on the frequencies);
- Discrete elements (spring, damper and punctual mass).

The rigid bodies or punctual masses can be used in the dynamic calculus of a certain track considering frequencies until 1000Hz (Vale, 2010). In the case of beam elements, it is possible to choose the Euler-Bernoulli beam or the Rayleigh-Timoshenko beam. In the case of the Rayleigh-Timoshenko beam, the shear deformation can be considered, and the modelling is more accurate.

Railpads

The railpad is a very complex element of the ballasted and ballastless structures because its behaviour depends on the magnitude and type of the applied load, load frequency, pre-load (when installed, the railpads are pre-loaded, since the fastening systems apply a load in each railpad when connecting the rail and the sleepers) and temperature (Popp et al., 1999, Wu and Thompson, 1999b, Vale, 2010, Alves Ribeiro, 2012). Furthermore, linearity is null in the relation between the applied load and deformation by compression.
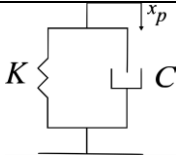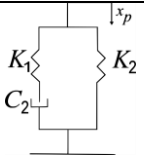
The characteristics of the railpads have a significant influence on the dynamic behaviour of the railway track, mostly in the vertical vibrations with frequencies between 200 and 700 Hz. Regarding the pre-load factor, when a load is applied over the rail on a rigid foundation, the stiffness of the railpad is superior to the stiffness of the railpad without the pre-load effect.

In order to reproduce the railpad's behavior, it is common to use rheological models. In Table 2.6, two models are presented: *Kelvin* and *Poynting-Thomson* models.

Analysing the expressions depicted in Table 2.6, x_p is the displacement of the railpad (in compression), K_1 and K_2 are the stiffness of the railpads (independent of the frequency), C_2 is the damping (dependent on the frequency) and f is the frequency.

The *Kelvin* method is simpler and, because of that, it is usually adopted in the simulation of the railpad's behaviour. As presented in Table 2.6, the model is represented by a spring and damper in parallel. In comparison, the Poynting-Thomson model is more complex because depends on the excitation's frequency that influences the damping and the stiffness through the n parameter. The definition of the parameters K_1, K_2 and C_2 are also complex and this is one of the main reasons that justify the use of the *Kelvin* model.

Table 2.6 – Kelvin and Poynting-Thomson models

Kelvin model	*Poynting-Thomson*

	Viscous damping$\rightarrow C = \alpha C_2 \frac{\bar{z}^2}{n^2}($	(2.10)
	Stiffness $\rightarrow K = k_1 + \alpha k_2$	(2.11)
Viscous damping$\rightarrow$C	$\alpha = \dfrac{n^2}{n^2 + \bar{z}^2}$	(2.12)
Stiffness$\rightarrow$K	$n = 2\pi f$	(2.13)
	$\bar{z} = \dfrac{K_2}{C_2}$	(2.14)

The *Poynting-Thomson* model is characterized by two spring models in parallel and a damper in series. Considering this model, De Man (2000) presents an improved alternative to taking into account the influence of the pre-load in the non-linear behaviour of the railpads:

$$K = K_1 \beta_1 + \alpha K_2 \beta_2 \qquad (2.15)$$

$$C = \alpha C_2 \frac{\bar{z}^2}{n^2} \beta_3 \qquad (2.16)$$

$$\beta_{1,2,3} \in \left\{ \left(1 + \frac{P}{P_0}\right)^2, 1 \right\} \qquad (2.17)$$

where *P* is the pre-load coefficient, P_0 is the reference of the pre-load and *x* is a factor to take into account the influence of the pre-load. If the β coefficients are equal to one, the pre-load is not considered and the previous expressions become equal to the expressions 2.10 and 2.11.

In the spring-damper system, the behaviour of the spring can be assumed as linear and the damping is assumed as proportional to the deformation rate of the railpad.

The consideration of the non-linear behaviour of the railpads in a numerical model is a complex process, since increases the calculus time but, at the same time, can be important to obtain rigorous results.

52

Ballast

The modelling of the ballast layer is particularly difficult. This layer can be modelled as continuous or discrete support, by finite elements and by the discrete element method. The complex behaviour is related to the granular properties and the interactions between the particles. Without any train loadings, internal forces in the ballast are low. However, during the train passages, the friction between the particles increases and the ballast is compressed.

In the case of 2D models, the continuity of the ballast layer is defined by bar elements in the longitudinal direction or by plane stress state elements. In the case of 3D models, the longitudinal continuity is ensured through solid elements. The plane stress state elements are characterized, in the case of linear models, by the deformability modulus, damping coefficients, *Poisson's* ratio and density. In the case of the bar elements, the vertical stiffness of the springs is defined considering the geometric and mechanical properties of the material: friction angle of the ballast, length of the support layer (sleeper), width of the support layer, and thickness of the layer.

The ballast presents several deformation mechanisms when submitted to repeated loads that lead to an increase in the permanent deformation of the track structure. Selig and Waters (1994) present two modes in which granular material deformed: particle breakdown and frictional slip. Several researchers defined empirical models to determine the permanent deformation of the ballast under cyclic loading. The response of the ballast due to cyclic loading is measured by a permanent deformation and a recoverable resilient deformation that is characterized by a resilient modulus. The resilient and permanent deformation models used to characterised the geomaterials will be further explored in Chapter 4. However, a brief resume of the empirical permanent deformation models of the ballast is presented in this section (see Table 2.8).

According to Dahlberg (2001), the permanent deformation of the ballast comprises two phases that include the fast reduction of the gaps between the ballast particles and ballast consolidation after tamping and a slower settlement characterized by an almost linear relationship between settlement and time (or load). According to this author, the second phase of this settlement is caused by several factors divided into two important phenomena, as described in Table 2.7.

53

Table 2.7 – Mechanisms of ballast that cause the second phase of settlement defined by Dahlberg (2001)

Volume Reduction➔Densification of the ballast	Inelastic behaviour
Densification due to the particle rearrangement caused by the repeated train loading	Inelastic recovery on unloading since all the deformation will not be fully recovered upon loading
Sub-ballast and/or subgrade penetration into voids ballast	Movement of ballast and subgrade particles away from sleepers. The sleepers sink into the ballast/subgrade
Particle breakdown due to the train passage or environmental factors	The lateral (and also possible longitudinal) movement of sleepers causes the ballast beneath the sleepers to be pushed away. The sleepers sink deeper into the ballast
Abrasive wear (the original cornered stones become rounded, occupying less space)	

The significant and irrecoverable lateral deformations of the ballast layer occur due to the very low track confinement, particle breakage when subjected to high amplitude of the cyclic loads and instantaneous impact of the loads. The breakage of the ballast is due to the non-uniform stress concentrations that occur in the corners of the sharp angular particles under cyclic loading. Thus, the ballast breakage is greater at the top layer because of the higher inter-particle contact stress at the top, being followed, by the middle and bottom layers (Indraratna and Nimbalkar, 2016).

The permanent deformation of the ballast can be determined by applying some models that depend on the magnitude of the loading, the number of cycles (N) and the permanent deformation at the first cycle (ε_N). The models also depend on other variables as porosity (n), principal stresses (σ_1 and σ_3), average axle load (A_e), tamping lift (L), force (F), vertical pressure (σ) and subgrade stiffness (k_s). In this type of models, the main variable is the number of cycles (N) but the models can be also dependent on some empirical constants. However, the long-term behaviour is strongly influenced by loading, namely the loading amplitude (Varandas et al., 2010). Some authors state that the settlement is proportional to the power of the loading amplitude. In fact, the settlement of the ballast progresses non-linearly with the number of load cycles, since the ballast starts to settle rapidly when first loaded by traffic loads. The rate of the settlement decreases with the decreasing of the gap between the ballast particles until reaching an almost linear relationship between settlement and loading. The non-linear settlement path depends on the loading amplitude range since higher stresses lead to different degradation mechanisms like particle wear or breakage (Varandas et al., 2010).

Table 2.8 is a summary of the models used to characterize the long-term behaviour of the ballast layer. Despite the veracity of the models, the majority does not depend on the stress levels or the failure line. In fact, some of the models have the number of cycles as the only variable. The difficulty of the development of these models is related to the large dimensions of the samples and the conditions and

representative selected stress for the experimental laboratory tests. Besides, other important factors are not included such as the frequency. According to some experimental results, the deformation increases with the frequency (train speed) and increase rapidly in the first cycles, reaching a stable value at large N. Developed studies by Ionescu (2004) and referred by Lackenby (2006) indicate that the initial period corresponds to 1×10^5 load cycles (this period corresponds to the stabilization of the ballast layer that occurs after the execution of the track). In fact, with the increase of the frequency, larger values of N are required to stabilize the permanent deformation. This behaviour is related to the rearrangements and breakage of asperities where high stresses are accumulated (Nimbalkar and Indraratna, 2015). Furthermore, in the work developed by Abadi et al. (2016), the author identifies the importance of other factors as sleeper spacing, sleeper properties, ballast depth, ballast type and shoulder dimensions of the track. Varandas et al. (2010) developed a non-elastic constitutive model for ballast that represents the plastic behaviour of ballast actuated by forces with variable loading amplitude.

Table 2.8 – Models used to determine the permanent deformation of the ballast

Model	Reference	Empirical constants
$\varepsilon_N = 0.082(100n - 38.2)(\sigma_1 - \sigma_3)^2 \times (1 + 0.2 \log N)$	ORE (1970)	-
$\varepsilon_N = a + b\ln(N)$	Barksdale (1972)	a, b
$S_N = S_1(1 + a \log N)$	Raymond et al. (1975)	a
$\varepsilon_N = \varepsilon_1(1 + 0.2 \, log_{10}N)$	Shenton (1978)	-
$S = k_s \frac{A_e}{20}((0.69 + 0.028L)N^{0.2} + (2.7 \times 10^{-6})N$	Shenton (1984)	k_s
$S_N = r(F)^{1.6}(1 + C \ln(N))$	Hettler (1984)	C, r
$\varepsilon_N = (0.85 + 0.38 \log N)\varepsilon_1 + (\varepsilon_1)^2 \times (0.05 - 0.09 \log N)$	Alva-Hurtado and Selig (1981)	-
$\varepsilon_N = \varepsilon_1(1 + C \, log_{10}N)$	Stewart and Selig (1984)	C
$d_N = d_1(1 + C_b \, logN)$		C_b
$\varepsilon_N = \varepsilon_1(1 + C \, logN)$	Selig and Waters (1994)	C
$S_N = 4.318N^{0.17}$		-
$\varepsilon_N = 0.0035N^{0.21}$		-
$y_1 = a(p - b)^2$, p>b	Sato (1997)	a, b
$y_2 = ap^n$		-
$S_N = S_1 + \frac{e \log N}{1 + f \log N}$	Neidhart (2001)	e, f
$S = [log_{10}(N) - 2.4]^2$	Thom and Oakley (2006)	-
$S = [log_{10}(N) - 2.4]^2 \left(\frac{\sigma}{160}\right)\left(\frac{47}{k}\right)$		-
$S_N = S_1(N^y)$	Indraratna et al. (2007)	y
$S_N = c + d(\ln N)$	Indraratna et al. (2011)	c, d
$S_N = 0.07N^{0.1625}$	Cuellar et al. (2011)	-
$S_N = S_1(a \, logN + 1)$	Indraratna et al. (2013)	a
$S_N = S_1(1 + a \, lnN + 0.5 \, b \, ln \, N^2)$	Indraratna and Nimbalkar (2013)	a, b

The mechanical behaviour of ballast material can also be analysed by using the *discrete element method (DEM)*. This method allows a more detailed advanced simulation but is much more time-consuming when compared with the *finite element method (FEM)*. The main concern in *FEM* modelling is related to the correct selection of the material model that should be capable to represent accurately the mechanical behaviour of the ballast. The *FEM* analysis in granular materials allows taking into account the non-linear stress-strain relationship.

The *DEM* (Figure 2.15) is an alternative since allows us to simulate the discontinuous behaviour of this material. In fact, this method is the most suitable approach to simulate the mechanical behaviour of granular materials under large strain, since it is possible to capture the stone angularity (Mahmoud et al., 2016). According to Mahmoud et al. (2016), it is possible to model the ballast and determine the effect of aggregates particles' shape on the overall performance of the railroad ballast, measuring the permanent deformation and degradation of this material. In this case, it is necessary to define the contact between the elements using three models: slip, stiffness and bonding. In the case of the slip model, the input parameter is the friction coefficient (μ). The stiffness model relates relative displacements in the normal and shear directions and contact forces. In this case, the parameters are the normal and shear stiffnesses. The bonding model is related to the strength parameter above which a bond breaks. In this case, the parameters used are the normal contact bond strength and shear contact bond strength. The density is also an important parameter.
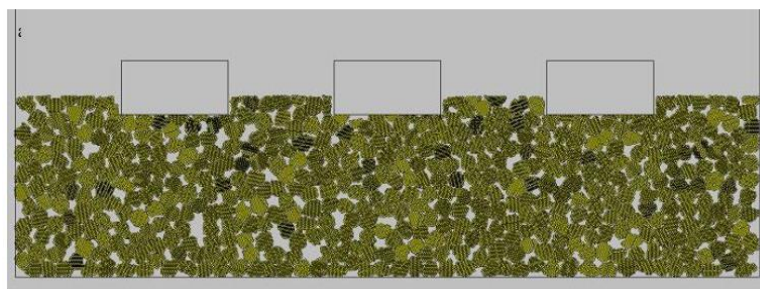
Figure 2.15 - Application of the DEM in the ballast layer (Mahmoud et al., 2016)

The first models appeared during the 80s, using discrete elements to understand and to reproduce rigorously the complex behaviour of this material. The use of discrete elements leads to a significant computational effort because of the existence of several contact points between the particles. In the beginning, the particles presented a circular shape (because of the computational resources) and the dependence of the contact forces between the particles and the friction coefficient or distribution of the stresses under the sleeper were evaluated. Currently, it is possible to model the ballast considering the

angularities of the particles, simulating the short and long term behaviour (Popp et al., 2005, Alves Ribeiro, 2012).

In the studies related to the evaluation of the global dynamic behaviour of the railway track, it is common to use simpler models, considering the ballast as a continuous layer through finite elements.

Besides the finite elements, it is also possible to model the ballast layer as a set of discrete supports under the sleepers considering a spring and damper system, as mentioned in section 2.4.2.3.1. The major difficulty is to find and use the proper parameters to characterise the stiffness and damping. Its determination, normally, is based on the experimental validation of the numerical models. A mathematical expression was developed to determine the stiffness of the ballast layer and it is based on the trapezoidal degradation of the forces and the *Young* modulus (Zhai et al., 2004):

$$K_b = \frac{2(l_e - l_b) \cdot \tan(\alpha)}{\ln\left[(l_e/l_b) \cdot (l_b + 2h_b \tan(\alpha))/(l_e + 2h_b \tan(\alpha))\right]} \cdot E_b \tag{2.18}$$

where E_b is the deformability modulus of the ballast and the remaining variables are geometric parameters represented in Figure 2.16. Analysing Figure 2.16:

- h_b is the height of the layer;
- l_e is the effective support of half sleeper;
- l_b is the width of the sleeper's base;
- α is the angle of degradation of the stresses in the layer.
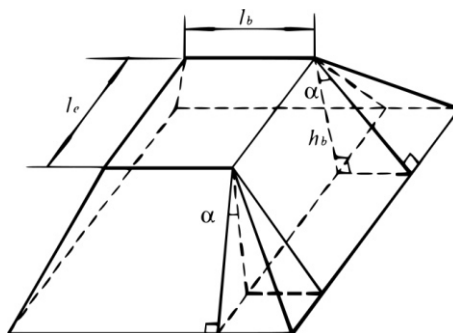
Figure 2.16 – Schematic representation of the model used to define the stiffness of the ballast layer (Zhai et al., 2004)

The same authors suggest a mathematical expression to estimate the vibrant mass of the ballast layer:

$$M_b = \rho_b h_b \left[l_e l_b + (l_e + l_b) h_b \tan(\alpha) + \frac{4}{3} h_b{}^2 \tan^2(\alpha) \right] \tag{2.19}$$

where ρ_b is the density of the ballast layer material.

Sub-ballast

As in the case of the ballast layer, the sub-ballast can be modelled continuously or discreetly. In the case of 2D analysis, the longitudinal continuity is assured by bar elements in the longitudinal direction or by plane stress state elements (section 2.4.2.3.1). In the case of 3D models, the longitudinal continuity is ensured through solid elements. The assumptions adopted in the ballast can be also considered in the sub-ballast layer.

In the case of the bar elements, the granular materials that composed this layer can be modelled through the vertical stiffness of the springs that are defined considering the geometric and mechanical characteristics (Figure 2.17): friction angle of the ballast and sub-ballast (θ_b and θ_{sb}, respectively), length of the support area that corresponds to the sleeper (L_s), width of the support area (B_s), thickness of the ballast and sub-ballast layer (H_b and H_{sb}, respectively). The stiffness of the sub-ballast can be defined through the following expression (Sun and Dahnasekar, 2002):

$$k_{sb} = \frac{2\tan\theta_{sb}(L_s - B_s)E_{sb}}{ln\left[\frac{(2\tan\theta_b H_b + L_s)(2\tan\theta_{sb}H_{sb} + 2\tan\theta_b H_b + B_s)}{(2\tan\theta_b H_b + B_s)(2\tan\theta_{sb}H_{sb} + 2\tan\theta_b H_b + L_s)}\right]} \qquad (2.20)$$

where E_{sb} is the elasticity modulus of the sub-ballast in Pa. Regarding the stiffness and damping of the bar elements in the longitudinal direction (referred to in Figure 2.11), the author states that the value of the parameters k'_b, k'_{sb}, c'_b, c'_{sb} do not influence the dynamic response in the vehicle-track interaction, suggesting values equal to 30% of the vertical stiffness and damping. As in the case of the ballast layer, it is also possible, to associate a vibrating mass to the bar elements that represent the sub-ballast:

$$M_{sb} = \rho_{sb}[(L_s + 2\tan\theta_b)(B_s \\ + 2\tan\theta_b) \\ + H_{sb}\tan\theta_{sb}(L_s + B_s \\ + 4\tan\theta_b) + 4/3H_{sb}^2\tan^2\theta_{sb}] \qquad (2.21)$$
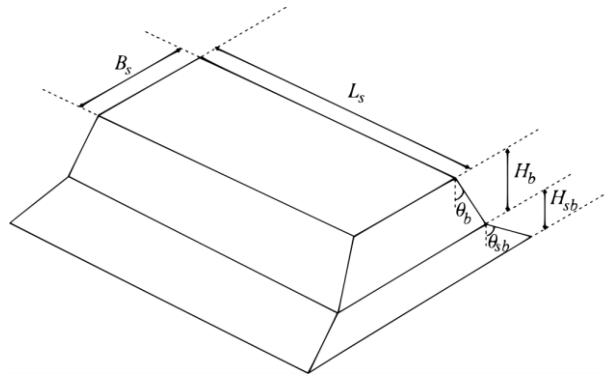
Figure 2.17 – Schematic representation of the ballast and sub-ballast layer (Sun and Dahnasekar, 2002)

Regarding the finite elements, it is possible to model the behaviour of this material when submitted to repeated loads considering the recoverable and permanent deformations. In the case of granular soils, the resilient modulus can be determined according to the models described in Chapter 4. In fact, the growth rate of the newly placed sub-ballast was found to accumulate according to a "power" form of equations. However, in the case of a track built many years ago, it is possible to assume a linear rate for the accumulation of permanent deformations, as suggested by the following expression (Li et al., 2016):

$$\varepsilon_{N\,(\%)} = 1.7 \times 10^{-7} N \tag{2.22}$$

where N corresponds to the number of load cycles and ε_N to the permanent deformation.

Subgrade and foundation soil

The subgrade and foundation can be modelled through springs that reflect its vertical stiffness in the analytical, semi-analytical and numerical models, represented in Figure 2.10, Figure 2.11 and Figure 2.12. Considering Figure 2.17, the foundation can be described by its vertical stiffness considering the following expression:

$$\begin{aligned} k_f = E_f(2\tan\theta_{sb}H_{sb} \\ + 2\tan\theta_b H_b \\ + L_s)(2\tan\theta_{sb}H_{sb} + 2\tan\theta_b H_b + B_s) \end{aligned} \tag{2.23}$$

In the case of finite elements (2D and 3D), the behaviour of the foundation soil is represented by the *Young* modulus, *Poisson's* ratio as well as density, in the case of linear models.

The behaviour of these materials, when submitted to cyclic loads, can also be represented by the resilient modulus and permanent deformation models. The models are described in more detail in Chapter 4.

Concrete slab

The concrete slab can be used in the ballastless track. This element can be modelled using a 2D or 3D formulation. In the case of bi-dimensional models, the concrete slab is modelled through beam elements or plane stress state elements. In the case of tri-dimensional models, it is usual to adopt solid elements (8 or 20 nodes for example) to model this structural layer.

The cyclic loading related to the passage of the trains may lead to cracks in the concrete slab. Thus, some numerical models allow studying the mechanical behaviour of cracked reinforcement concrete to cyclic axial and bending forces with variable amplitude (Sousa, 2012). The numerical models used for

the analysis of cracked RC members subjected to cyclic loading are out of the scope of this work and it is described in detail in the work developed by Sousa (2012).

2.5 Dynamic numerical modelling: analysis of the vehicle-track-ground system in the time domain

The modelling of the dynamic behaviour of a railway track, vehicle and the interaction between both is complex and it is necessary to use specific methodologies that allow simulating the problem properly. This section presents the main concepts and tools used to perform dynamic numerical analysis from the modelling of the track, modelling of the vehicle and the interaction between both using the contact elements and the *Hertzian* theory.

The finite elements method associated with the numerical direct integration method in the time domain allows simplifying the dynamic analysis of a continuum system, and also allow including the contact between the bodies (e.g. the vehicle and the track). These methodologies are already implemented in several *software*.

In order to implement the available methodologies in the software, it is necessary, firstly, to understand them. Thus, the theoretical fundamentals associated with the integration methods are presented in the following section.

2.5.1 *Dynamic analysis: main concepts and general background*

The railway track and the vehicle can be modelled considering two sub-models, which include the track and the vehicle. Thus, it is necessary to assure compatibility regarding the displacements and equilibrium of forces in the contact points of the two domains.

The dynamic interaction between vehicle and track can be described reasonably well in the vertical direction using specific mathematical models (Esveld, 2001). The dynamic calculation is extremely complex, and its behaviour occurs in a range of low frequencies (0.5-1Hz) for lateral and vertical car body accelerations, to 2000 Hz because of geometric irregularities in rails and wheel treads. The interaction of the systems is implemented through the contact between the wheel of the vehicle and the rail of the track. The vehicle can be modelled considering the car body, primary suspension (a combination of a spring/damper that reduces the vibrations generated by the wheel/rail interaction), secondary suspension (reduces the vibrations of lower frequencies), wheelset and the *Hertzian* spring (Figure 2.18). This topic will be analysed in more detail further.
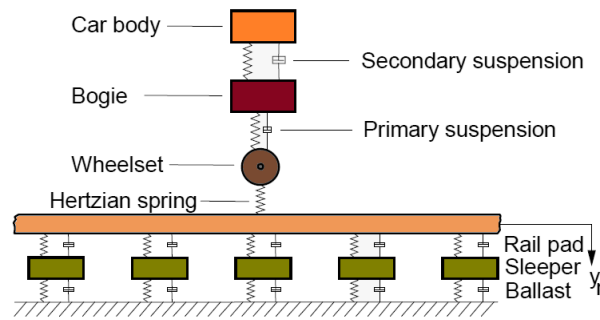
Figure 2.18 - Dynamic model of vehicle-track interaction, adapted from (Esveld, 2001)

Throughout this work, the main goal is to analyse the behaviour of a railway track, and, therefore, the detail of the numerical modelling is focused on the track instead of the vehicle. The inclusion of the interaction between the two systems implies using the *Hertzian* theory and concepts related to the contact models. Besides the interaction between these two systems, it is also possible to impose contact elements between the remaining elements of the track: the support layer and FPL (in the case of a ballastless track). In the case of the wheel-rail, the interaction is simulated considering the contact type point-line, allowing the sliding and loss of contact between the two elements. This phenomenon can be modelled using different methods: *penalty* method, *Lagrange* multiplier method and augmented *Lagrange* methodology (which is a combination of the previous methods). This type of modelling implies a non-linear analysis since the surfaces can or cannot be in contact, which fact is unknown until the beginning of the analysis. The possible friction between the elements also implies a nonlinear analysis. The concepts and the methodologies related to the interaction of the vehicle and the track and the contact models, in particular, will be analysed further in the following sections.

Thus, in a general problem, the *Newmark* method can be used to solve the dynamic equilibrium equation:

$$M\ddot{u}(t) + C\dot{u}(t) + Ku(t) = F(t) \tag{2.24}$$

where *F* corresponds to the exteriors loads and is balanced by *Mü* (inertia forces), *Cù* (damping forces), and *Ku* (elastic forces). The *Newmark* method is an implicit method of direct integration of the systems of differential equations of dynamic equilibrium. The displacements regarding the instant calculus time *n+1* obtained by u_{n+1} are determined considering the information of that instant and the previous ones. The expression is given by:

$$u_{n+1} = f(\dot{u}_{n+1}, \ddot{u}_{n+1}, u_n, \dot{u}_n, \ddot{u}_n \dots) \tag{2.25}$$

One way to solve the equation of the dynamic equilibrium consists to assume constant acceleration in each interval of time, which, using the *Newmark* method, allows to write the following equation (Cook et al., 2002):

$$K_{eff}u_{n+1} = R_{n+1}^{ext} + M\left(\frac{1}{\beta\Delta t^2}u_n + \frac{1}{\beta\Delta t}\dot{u}_n + \left(\frac{1}{2\beta} - 1\right)\ddot{u}_n\right)$$
$$+ C\left(\frac{\gamma}{\beta\Delta t^2}u_n + \left(\frac{\gamma}{\beta} - 1\right)\dot{u}_n + \Delta t\left(\frac{\gamma}{2\beta} - 1\right)\ddot{u}_n\right) \tag{2.26}$$

where β and γ are constants of the Newmark's method and K_{eff} is given by:

$$K_{eff} = \frac{1}{\beta\Delta t^2}M + \frac{\gamma}{\beta\Delta t}C + K \tag{2.27}$$

The implicit methods are unconditionally stable, obeying the following condition:

$$2\beta \geq \gamma \geq \frac{1}{2} \tag{2.28}$$

At this stage, to have a correct analysis of the problem, it is important to set the value of the increment time (Δt), which depends on the maximum frequency to evaluate.

The *HHT* is another time integration method and is an extension of the *Newmark* time integration. However, it will not be applied in this work.

2.5.2   Damping

The results from a dynamic analysis are dependent on the damping matrix. The theoretical background about the definition of the damping matrix performed by the software ANSYS (that will be used posteriorly) is presented below. In the case of this software, the damping matrix is defined based on the *Rayleigh* damping matrix (Chopra, 1995) with some modifications:

$$[C] = \alpha[M] + \beta[K] \tag{2.29}$$

where [C] is the damping matrix, [M] is the mass matrix and [K] is the stiffness matrix. The parameters α and β are the mass and stiffness proportional damping coefficients, respectively.

2.5.3   Treatment of the boundaries

Regarding the boundaries, it is necessary to incorporate in the finite elements, boundary elements (for example, viscous dampers) that simulate the real conditions of the track. Indeed, the imposition of zero or free displacements on the boundaries of the model creates non-real conditions of wave propagation leading to the reflection of the waves in the boundaries, contaminating the results. Indeed, the main limitations of the models formulated in the time/space domain are the high computational effort, added to the fact that the train cannot be considered from infinite to infinite, which means that is necessary to truncate the model.

The absorbing condition purposed by Lysmer and Kuhlemeyer (1969), also designated as viscous, corresponds to the oldest proposal for the treatment of artificial boundaries in the scope of the finite element method. Indeed, this is still, nowadays, one of the most popular approaches due to several aspects:

- Simplicity of the implementation in code (based on finite elements method);
- Compatibility with geometries fewer regulars;
- Possibility of application in harmonic and transient solicitations.

The mathematical formulation of this type of approach is simple and can be deduced through a one-directional equation (Alves Costa, 2011). The main objective of the introduction of an absorbing boundary consists of eliminating the spurious reflection of the wave when it reaches the limit of the interest domain. Considering the constitutive linear elastic law of the material, it is possible to find the dependency between the normal stress induced in any point of a bar and the velocity of that same point, given by the expression:

$$\sigma_{xx} = \rho C_p \dot{u}_x \tag{2.30}$$

In the case where it is assumed the probation of the shear wave, the relationship is almost identical but now considering the speed of the propagation of the S waves. More details about this formulation can be found in Lysmer and Kuhlemeyer (1969).

The generalization of the expression 2.30 for three-dimensional spaces is relatively simple since it is possible to assume that the propagation of the waves P and S can occur in a decoupled way in homogenous and isotropic spaces. Furthermore, considering the concept of plane waves, it is easy to conclude that, in an invariant three-dimensional space (as depicted in Figure 2.19 where the normal is given by the direction y), the absorption condition is guaranteed since, along the artificial boundary, the collected stresses in the vector q are imposed and determined with the following expression:

$$\{q\} = -[C]\{\dot{u}\} \tag{2.31}$$

where the damping matrix is given by:

$$[C] = \begin{bmatrix} \rho C_s & 0 & 0 \\ 0 & \rho C_p & 0 \\ 0 & 0 & \rho C_s \end{bmatrix} \tag{2.32}$$

and,

$$\{q\} = \{\sigma_{xy}, \sigma_{yy}, \sigma_{zy}\} \tag{2.33}$$

$$\{\dot{u}\} = \{\dot{u}_x, \dot{u}_y, \dot{u}_z\}^T \tag{2.34}$$
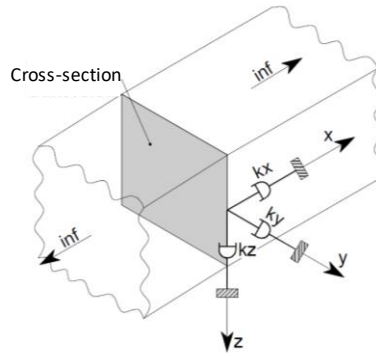
Figure 2.19 - Perfect absorption condition in the artificial boundary of a 2.5D invariant model in direction *x* (Alves Costa, 2011)

However, it is important to highlight that *Lysmer's* formulation has been corrected in the work developed by Kouroussis et al. (2011) since a small mistake was made in its development. According to this formulation, the relationship between stresses in the boundaries and velocities are imposed along the artificial boundary through the following expression:

$$\sigma_n = -C_1 \rho V_p \dot{u}_n \tag{2.35}$$

$$\sigma_n = -C_2 \rho V_s \dot{u}_t \tag{2.36}$$

where ρ is the density of the materials, V_s and V_p are the dilatational and shear wave velocity, respectively; C_1 and C_2 are dimensionless relaxation coefficients or viscosity coefficients that have been introduced to improve the effect of absorption. The studies developed by Lysmer and Kuhlemeyer (1969) suggest that C_1 and C_2 equal to one implies a perfect absorption when the boundary is achieved by perpendicular impinging waves. As a result, these values are exact only for one-dimensional propagation of body waves. For the 3D modelling or even 2D modelling, the perfect absorption depends on the angles of incidence (Fernández Ruiz et al., 2017). However, Cohen (1980) has shown that the viscous boundary is not very sensitive to the viscosity coefficients C_1 and C_2.

White et al. (1977) proposed an alternative formulation to the unified viscous damping. The main goal of this formulation consists of improving the aborting properties of the artificial boundaries when the wave that impinges the boundary presents an arbitrary angle. The authors deduced an absorbing condition of volumetric waves in homogeneous and isotropic ground through the introduction of a damping constitutive matrix dependent on the incident angle of the wave compared to the normal to the plane defined by the artificial boundary. However, this formulation presents an important disadvantage: the orientation of the front of the wave is not an unknown parameter *a priori* (Faria, 1994, Alves Costa, 2011).

In practical terms, the only difference regarding the approach developed by Lysmer and Kuhlemeyer (1969) is related to the constitutive damping matrix that is given by:

$$[C_{weighted}] = \frac{8\rho V_s}{15\pi} \begin{bmatrix} 4+s & 0 & 0 \\ 0 & \frac{5}{2} - 2s + 2 & 0 \\ 0 & 0 & 4+s \end{bmatrix} \tag{2.37}$$

where s is the ratio between the propagation speeds of the S and P waves. The $C_{weighted}$ corresponds to a weighted damping matrix. The deduction of this matrix was developed and presented by White et al. (1977) and explored by Faria (1994).

2.5.4 Modelling of the vehicle

In the dynamic modelling of railway tracks, there are two systems that are characterized by a set of own vibration frequencies: the vehicle and the track. These two systems can interact through the contact between the wheels of the vehicle and the rail of the track.

This section presents a review of the main aspects related to the modelling of the vehicle itself. The concepts related to the modelling of the interaction vehicle-track will be discussed further.

The high-speed trains present some differences according to their configuration and geometry, as depicted in Figure 2.20:

- Conventional – car body has two bogies and each one has two axles. This means that each vehicle is constituted by two independent bogies. The trains ICE2, ETR-Y and VIRGIN are examples of this type of train;
- Articulated – car body has one bogie and two axles in each extremity, sharing with the adjacent car bodies. This means that all the adjacent vehicles (with exception of the locomotive) share the bogies; The trains THALYS, EUROSTAR and TGV are examples of this type of train;
- Regular – car bodies are equally articulated, but the articulation does not support itself in one bogie but on a single axle between the two-car bodies; the adjacent vehicles shared the bogies, but the bogies are constituted only by one axle. TALGO is an example of this type of train.

The train vehicles are composed of the car body, bogies, primary suspension, secondary suspension, wheels, axles and all the equipment that connects the elements. The way of modelling the vehicle (more or less complete) depends on the main goal of the study and the range of frequencies. The easiest way to model the vehicle consists of considering only the vertical load that is transmitted to the track through the wheels, by a set of moving loads, no considering the interaction between the wheel-rail. In this case, it is possible to study the effect of the excitation frequencies induced by the passage of the train's axles in the structure.
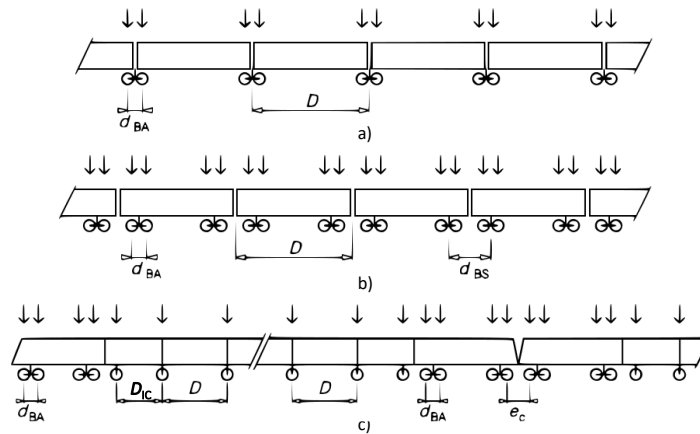
Figure 2.20 - Types of trains of the European network high-speed railway: a) articulated, b) conventional, c) regular (adapted from (EN1991-2, 2003)

The complete modelling of the vehicle is imperative when it is important to evaluate aspects related to the comfort of the passengers during the passage of the train in a specific zone of the track. Or even, when the study aims to consider the dynamic characteristics of the train in the design of the structures (for example in the case of bridges).

According to Nielsen et al. (2003), for excitation frequencies superior to 20 Hz, the dynamic behaviour of the box of the vehicle is decoupled of the bogies due to the secondary suspension. The same phenomenon can also occur to the bogies due to the primary suspension. In this context, the consideration of the bogies and the box of the vehicle can be carried out through more simplified models. This means that, in a dynamic analysis, where the excitation frequencies are framed in the mean range of frequencies, the simplified modelling of the vehicle is normally enough. In this case, is still relevant to consider the deformability and mass of the wheels/axles in contact with the rail.

Figure 2.21 presents several available models that can be adopted to model the vehicle:

- Consideration of only an axle of the vehicle;
- One axle, half bogie and the primary suspension;
- One axle, half bogie, a quarter of the box and the suspensions primary and secondary;
- Two axles, primary suspension, one complete bogie.

Analysing Figure 2.21, m_1 corresponds to the mass of the axle, m_2 corresponds to the mass of the bogie and m_3 corresponds to the mass of half of the box of the vehicle.
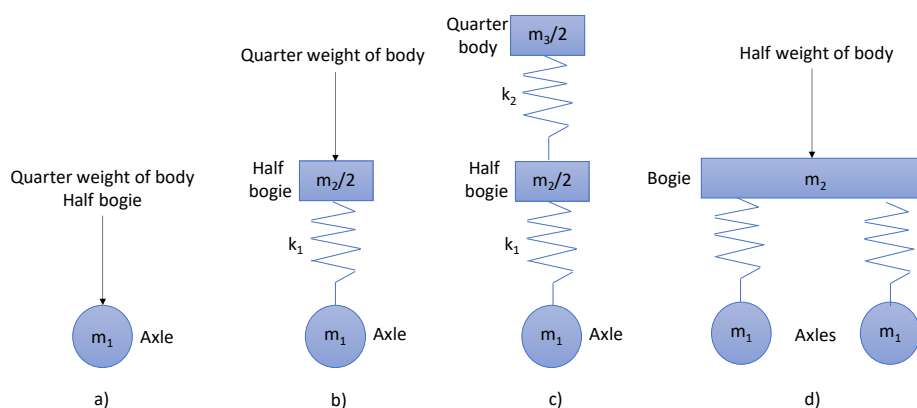
Figure 2.21 - Models of the vehicle (adapted from Hunt (1996)): a) one axle of the vehicle; b) one axle, primary suspension and half bogie; c) one axle, primary suspension, half bogie, secondary suspension and a quarter of the box; d) two axles, primary suspension and one bogie

Hunt (1996) used these models in a study of the dynamic effects induced by the passage of the vehicle by a joint and by a variation of the vertical alignment of the track in a zone of stiffness's transition. From this study, Hunt (1996) concluded that there aren't significant differences between the obtained results with the four models, namely in terms of interaction forces (wheel-rail). The author also concluded that the dynamic effects are derived from the vertical acceleration of the unsprung masses of the vehicle and, in the case analysed, the interaction between axles of a bogie was not relevant.

Furthermore, in a study related to the validation of the contact forces between wheel-rail, Nielsen (2008) compared the dynamic response of the different models of the wheel of the vehicle composed by:

- Only the mass of the wheel (Figure 2.21a);
- Two masses and a set of spring-damper between them, simulating the flexibility of the wheel;
- A tridimensional model of solid elements (the wheel is modelled using solid elements - Figure 2.22).
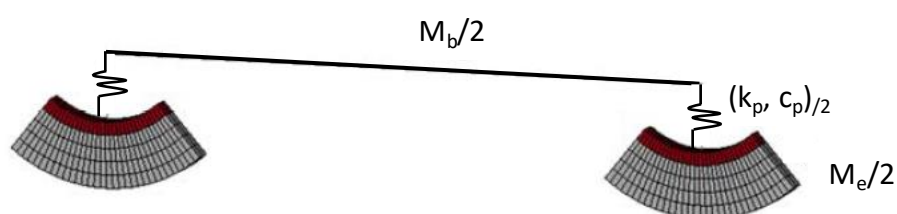
Figure 2.22 – 3D finite elements model of the train (adapted from (Alves Ribeiro, 2012)

With this work, Nielsen (2008) concluded that the model of the wheel can influence the contact forces wheel-rail in the range of high frequencies that are induced, for example, by smooth on the wheels of the vehicle or roughness of the rail. In this particular case, the obtained results using the first model (only the

mass of the wheel) lead to an overestimation in the contact forces since, for high frequencies, the dynamic stiffness of the model is too high. The dynamic stiffness of the second model is closer to the dynamic stiffness of the finite element model.

In the scope of ground vibrations, Alves Costa et al. (2012), later referred to by Colaço et al. (2016) concluded that a structural model of the train comprising the unsprung masses (wheelsets), the semi-sprung masses (bogies) and respective connections (primary suspension) is sufficient for the study of vibrations induced by railway traffic. The study also states that the most influential component of a train model is the unsprung mass and, for that reason, it is reasonable to model only this component (Figure 2.23).
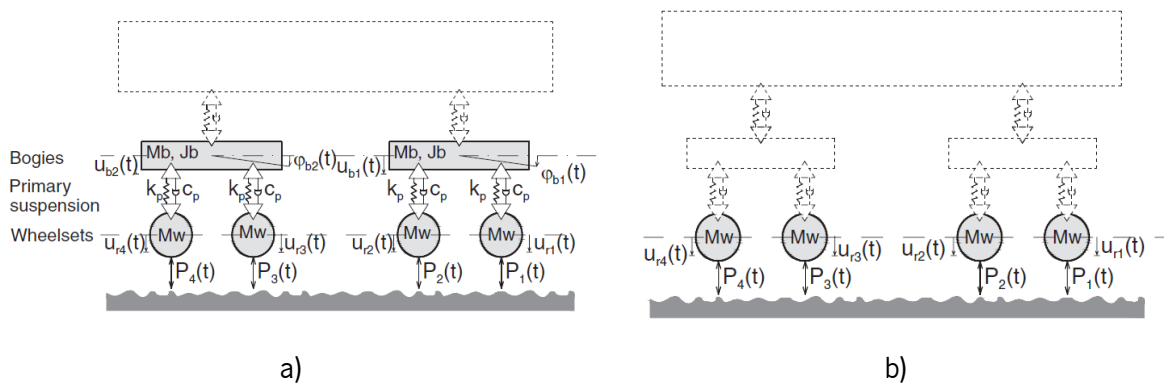
Figure 2.23 - Train models: a) model with unsprung and semi-unsprung masses; b) model with unsprung masses (Colaço et al., 2016)

2.5.5   Vehicle-track-interaction – Hertzian theory

The interaction between the vehicle-track is a very complex subject.

Complex models of detailed detection of contact and the forces generated in the interface are necessary to study some problems such as the derailment of the vehicle or the evolution of stresses in the wheel and rail. However, the consideration of these models in most of the analyses carried out in the scope of the dynamic of railway structure is not viable.

In a case where the analysis is focused on the dynamic behaviour, assuming that the contact occurs mostly along the loading plan in the vertical direction is perfectly acceptable. However, the simplifications in the determination of the contact forces should be performed with some care, not forgetting that the contact depends on the geometric characteristics and mechanisms of the two bodies.

The mechanics of the contact is usually performed through the application of the *Hertz* theory, developed in 1882. This theory considers some assumptions (Johnson, 1985, Neves, 2016):

- Its validity is limited to non-conform contact cases. This means that the initial contact between the bodies only occurs at a point or along a line. When the bodies are loaded, arises between them a contact area that presents an elliptical shape. The dimensions of this area are dependent on the applied force (normal do the contact area);

- The bodies are considered as semi-indefinite to determine the local deformations induced by the contact. So, the contact area should be small when compared to the size of the bodies and curvature of the surfaces. These conditions assure that in the contact zone, the stress field is not influenced by the boundaries of the bodies and also that the deformations are small enough to allow applying the linear elastic theory;

- The *Hertz* theory assumes that there is no friction between the bodies, which implies that, in the contact, only normal stresses occur.

In Figure 2.24, a scheme of contact between two bodies that obeys the assumptions of the *Hertz* theory presented previously is depicted. Analysing Figure 2.24, the A_1 and B_1 are the radius of the curvature of body 1 and A_2 and B_2 are the radius of curvature of body 2. The surface of contact between the bodies presents an elliptical shape.
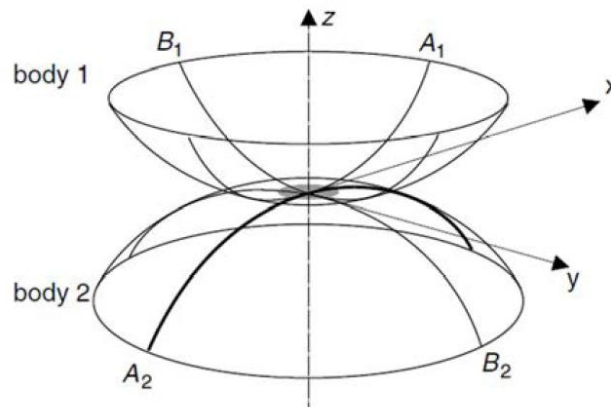
Figure 2.24 – Schematic representation of the contact between two bodies according to the *Hertz* theory (Alves Ribeiro (2012) adapted from Ayasse and Chollet (2006))

For the particular case of contact between two solids of revolution:

$$A_1 = B_1 = R_1 \tag{2.38}$$

$$A_2 = B_2 = R_2 \tag{2.39}$$

where the circular contact area with radius *a* is given by:

$$a = \sqrt[3]{\frac{3PR}{4E^*}} \tag{2.40}$$

where P corresponds to the total load to the compression of the bodies, R is the radius of curvature equivalent given by:

$$R = \sqrt{R_1 R_2} \tag{2.41}$$

and E^* is equal to:

$$\frac{1}{E^*} = \frac{1 - v_1^2}{E_1} + \frac{1 - v_2^2}{E_2} \tag{2.42}$$

where E_1, E_2, v_1 and v_2 correspond to the deformability modulus and Poisson's ratio of the two bodies in contact. The distance between the two points of the solids can be determined through:

$$\delta = \frac{a^2}{R} = \sqrt[3]{\frac{9P^2}{16RE^{*2}}} \tag{2.43}$$

where the maximum contact pressure p_0 is given by:

$$p_0 = \frac{3P}{2\pi a^2} = \sqrt[3]{\frac{6PE^{*2}}{\pi^3 R^2}} \tag{2.44}$$

In the case of contact between two generic soils, the use of these formulas deduced to the contact between two solids of revolution, leads to an overestimation of the contact deformation of only 5% and an underestimation of p_0 of about 8% (Johnson, 1985). These small differences in the results justify the simplification often adopted to consider the contact area between the two generic circular bodies.

Based on the expression 2.43, it is possible to re-write the expression 2.45 that relates the applied load with the deformation in the case where there is contact between the bodies:

$$P = \sqrt{\frac{16RE^{*2}}{9}} \delta^{3/2} \tag{2.45}$$

Thus, it is usual to consider, in this context, that:

$$C_H = \sqrt{\frac{16RE^{*2}}{9}} \tag{2.46}$$

where C_H is designated as *Hertzian* constant and depends on the curvature radius and the mechanical properties of the bodies.

The determination of the contact stiffness, k_H, is obtained through the derivative of P in function of δ.

$$k_H = \frac{dP}{d\delta} \tag{2.47}$$

From this expression, it is possible to obtain:

$$k_H = \frac{3}{2} C_H{}^{2/3} p^{1/3} \tag{2.48}$$

Replacing the variable C_H in the previous expression and considering the expression 2.42, admitting that the materials of the two bodies are equal:

$$k_H = \sqrt[3]{\frac{3RPE^2}{2(1 - v^2)^2}} \tag{2.49}$$

As it is possible to verify from the analysis of the expression 2.49, the relationship between the stiffness (k_H) and the total compression load of the bodies (P) is non-linear.

In the particular case of the contact wheel-rail, the load P varies as a result of the presence of defects, singularities on the track, or roughness of the rail. When these variations are small, it is usual to linearize the stiffness k_H to the value of the static load, reducing the analysis to the resolution of a linear elastic problem. Indeed, some studies developed by Wu and Thompson (2001), highlighted the cases where the dynamic contact between the rail and the wheel can be approximated to a value of linear contact stiffness with satisfying results.

Vale (2010) and Montenegro (2015) also study the use of the linear models in the scope of the contact between the wheel-rail and verified that, in the presence of defects of the track that provoke variations on the dynamic load (higher than the value of the static load used to obtain the linearization of the contact stiffness), it is necessary to use non-linear contact models. In these cases, the linear models lead to an underestimation of the peak values of the dynamic contact forces.

In the contact wheel-rail, it is acceptable that the properties of the materials of the bodies in contact are the same and, in this case, equal to the steel. Regarding the geometric properties, it is usual to consider that the radius of the rail is constant and equal to the value that is verified in the head's rail. Furthermore, it is also assumed that the wheel only presents curvature in the longitudinal direction.

2.5.6 Contact algorithms

The contact algorithms are considered in this study whenever it is necessary to consider the interaction between the different components of the system.

In an analysis that includes contact between the bodies, the equilibrium equation of the system is very identical to the equation presented previously in section 2.5.1. However, it is necessary to introduce the kinetic and kinematic conditions in the interfaces of the contact. The impenetrability is the base condition to consider the contact between the bodies. This condition is imposed numerically, which involves some approximations.

2.5.6.1 Kinematic of the contact

The contact process is divided into two phases (Bathe and Bouzinov, 1997, Wriggers, 2002):

- Identification of the surfaces that become in contact;
- Definition of the kinematic relationships necessary to impose contact restriction between the bodies.

In Figure 2.25 two elastic bodies (C^a where *a* assumes the values 1 and/or 2) are presented, who approach and become in contact. After the contact, the coordinates X^a have the same values. Indeed, X^a corresponds to the coordinate of the body C^a and it is given by:

$$X^a = X^a + u^a \tag{2.50}$$

where u^a is the displacement vector.

The boundary of the body 1 (designated by Γ^1) is parametrized in a local referential (ξ), which is connected to the body, following its deformation.
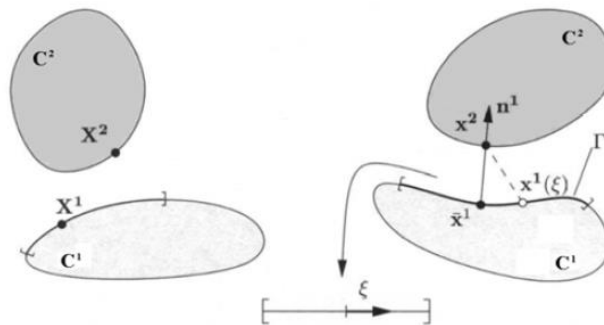
Figure 2.25 - Schematic representation of the bodies C_1 and C_2 in the initial configuration and in the contact configuration (Alves Ribeiro (2012) adapted from Wriggers (2002))

Assuming that the boundary contact is a convex region, at least locally, it is possible to find to any point with coordinate x^2 in the boundary Γ^2, a correspondent point with coordinate $\bar{x}^1 = x^1(\xi)$ in boundary Γ^1 based on the resolution of a problem of determination of the minimum distance, *d*, through:

$$d = \|x^2 - \bar{x}^1\| = \min_{x^1 \subseteq \Gamma^1} \|x^2 - x^1(\xi)\| \tag{2.51}$$

where $\bar{x}^1$ is the orthogonal projection of x^2 of the contact surface Γ^2 in the contact surface Γ^1. As a matter of fact, knowing $\bar{x}^1$ allows defining the condition of non-penetration between the bodies:

$$g_N = (x^2 - \bar{x}^1).\bar{n}^1 \geq 0 \tag{2.52}$$

and the function of penetration between the bodies:

$$\bar{g}_n = \begin{cases} (x^2 - \bar{x}^1).\bar{n}^1 \; where \; (x^2 - \bar{x}^1).\bar{n}^1 < 0 \\ 0 \qquad\qquad where \; (x^2 - \bar{x}^1).\bar{n}^1 \geq 0 \end{cases} \tag{2.53}$$

Analysing the previous expression, when g_N=0, the contact occurs and, consequently, some stresses are developed between the bodies. Assuming that there is no friction in the contact surface, the normal component of the stress vector is given by:

$$t^1 = p_N^1 \bar{n}^1 \tag{2.54}$$

where p_N^1 assume values inferiors to 0 in the case of the normal compression stresses. According to the principle action-reaction, the stress vector actuates in both bodies, verifying the following condition in the contact point $\bar{x}^1$:

$$t^1 = -t^2 \tag{2.55}$$

In a brief resume, whenever there is contact between bodies, and in the absence of friction, the conditions g_N=0 and p_N<0 are verified. When there is a loss of contact, then g_N>0 and p_N=0. Thus the condition $g_N.p_N$=0 is always verified. So, the fundamental conditions of the contact are:

$$g_N \geq 0 \tag{2.56}$$

$$p_N \leq 0 \tag{2.57}$$

$$g_N \cdot p_N = 0 \tag{2.58}$$

2.5.6.2 *Imposition of the contact conditions*

In this section, the formulation of the contact conditions adopted to incorporate the contact between the bodies in the equilibrium equation for the cases where the friction is null is presented.

Within the scope of the finite element method, it is adequate to formulate the equilibrium equation through the minimization of a functional (Delgado, 1990). In the case of an elastic conservative system, the principal of the minimum potential energy defines that, between all the displacements configurations that satisfy the internal compatibility and the kinematic conditions of the boundary, the ones that also satisfy the equilibrium equations make stationary the potential energy. If this value is minimum, then the equilibrium is stable (Alves Ribeiro, 2012).

The generic expression of the potential energy between two bodies in contact is given by:

$$\Pi(u) = \sum_{a=1}^{2} \left\{ \int_{C\alpha} \frac{1}{2} \sigma \varepsilon^{\alpha} dV - \int_{C\alpha} b u^{\alpha} dV - \int_{\Gamma\alpha} t u^{\alpha} dS \right\} + \Pi_C \qquad (2.59)$$

where b is the vector of the volumetric forces and t is the vector of the forces of the surface applied in the body α. σ and ε^{α} are the vectors that characterize, the stress state and the deformation in a certain point, respectively (Bathe and Bouzinov, 1997).

The consideration of the contact conditions implies the incorporation of an additional parcel, *Πc* in the equilibrium equation of the bodies. The solution of a continuum problem is the function u that makes *Π(u)* stationary for small variations of *δu*:

$$\delta\Pi(u) = \sum_{a=1}^{2} \left\{ \int_{C\alpha} \sigma \delta\varepsilon^{\alpha} dV - \int_{C\alpha} b \delta u^{\alpha} dV - \int_{\Gamma\alpha} t \delta u^{\alpha} dS \right\} + \delta\Pi_C \qquad (2.60)$$

where δu^{α} is the infinitesimal variation of the displacement u and $\delta\varepsilon^{\alpha}$ is the infinitesimal deformation correspondent.

Thus, there are several approaches to incorporate the contact parcel (*Πc*). The most commons formulations are the consideration of the contact stress as additional incognitos (*Lagrange* multipliers) or using the *penalty* methods. In this work, the *penalty* method will be used. In this method, the parcel *Πc* is formulated based on the exposed penetration given by:

$$\Pi_C = \frac{1}{2} \int_{\Gamma_C} \left(e_N \bar{g}_N{}^2 \right) dS \text{ with } e_N > 0 \qquad (2.61)$$

where e_N is the penalty parameter. This term of contact is only considered for the cases defined by the penetration function $\bar{g}_N$, otherwise is null.

The parcel of the potential energy in the normal direction, in the *penalty* method, corresponds to the potential energy of a spring with stiffness e_N. Ideally, this stiffness should be infinite to assure the inexistence of penetration between the bodies, but this condition would lead to a significant numerical instability in the calculus. The parameter e_N is then estimated based on the geometric conditions and deformability of the bodies in contact.

From equation 2.61,

$$\delta\Pi_C = \int_{\Gamma_C} (e_N \bar{g}_N \delta \bar{g}_N) dS \text{ with } e_N > 0 \qquad (2.62)$$

The calculus using the *penalty* method is simpler than the *Lagrange* method since additional incognitos are not assumed. The expression $\delta \Pi c$ is then incorporated in the expression 2.60.

2.5.6.3 Spatial discretization and solution

In the previous section, the imposition of the contact conditions in a continuum medium is presented. In the present section, the previous conditions are adapted assuming that the surfaces of the bodies in contact are discretized. In this case, the algorithm needs to find the contact restrictions $\mathcal{J}_A \in \mathcal{J}_C$ where is verified the condition $g_N = 0$, where $\mathcal{J}_C$ includes all the nodes of the surface of the bodies that can experiment contact, as depicted in Figure 2.26.
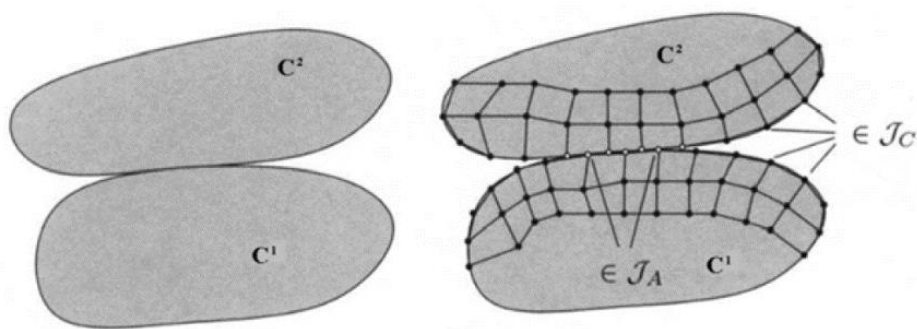
Figure 2.26 - Discretization of two bodies in contact (Wriggers, 2002)

In order to simplify, the following considerations only contemplate the application of the *penalty* method in the formulation of the equilibrium equation, not considering the friction between the bodies.

In the contact between two discretized surfaces, two different scenarios can occur:

- If the contact is stabilised directly between the nodes, occurring only small deformations between the bodies, the determination of the distance function is simple, and the contact conditions can be incorporated directly in the nodes;

- In a generic case, during the contact process, there is the possibility of a certain node or element of a body contact with diverse elements of another body. In this case, it is necessary to use iterative methods (usually the *Newton-Raphson* method) to solve the problem of the determination of the minimum distance (Wriggers, 2002).

The matrix formulation of the expression 2.59 with the parcel of contact (expression 2.61) relative to the application of the penalty method is given by:

$$\Pi(\mathrm{u}) = \Pi_{int} - u^T P + \frac{e_N}{2} G^c(u)^T G^c(u) \tag{2.63}$$

where $\mathit{\Pi}_{int}$ corresponds to the intern energy of the two bodies in contact, u is the displacements vector and contains the nodal displacements of the bodies. The matrix P stores all the forces applied into the bodies' surface volumetric forces and the vector $G^c(u)$ depends on the field of displacements u of the nodes possibly involved in the contact.

By varying this expression, a non-linear equilibrium equation is obtained, since the parcel related to the contact forces is function of the distance or penetration between the bodies, which depends on the displacement field.

In the cases where the inertia and damping forces are not negligible, they should also be considered in the equilibrium equation.

As mentioned previously, the integration of the equilibrium equation can be carried out through implicit or explicit integration methods. Since the problem is non-linear, the use of implicit methods implies the linearization of the expression according to the displacements and the use of iterative methods, such as the *Newton-Raphson* method in each calculation of the time interval. The use of explicit methods simplifies the resolution since the parcel of the contact force is directly added to the parcel related to the internal system forces. This means that it is not necessary to use iterative methods for the resolution of the problem (Belytschko et al., 2000, Wriggers, 2002).

2.6 Final considerations

In this Chapter, the main concepts related to the ballasted and ballastless tracks are described, as well as the materials included in these structures. The ballasted and ballastless tracks present some similarities, but the materials used in each structure are different and their properties influence its short and long performance. The constitution of each structure, the properties, and the function of the main materials and elements are important to establish a comparison between the ballasted and ballastless tracks.

In summary, the ballastless track is more expensive during the construction stage but, at the same time, requires fewer maintenance operations. However, the differential settlements should be avoided since the geometric adjustments are hard to perform. These structures are particularly suitable for high-speed lines. One of the main disadvantages is related to the generated noise due to the lack of resilient and absorbent materials, besides the railpads.

Despite the several advantages of the ballastless track, some countries, leaders in the high-speed industry, continue to prefer and build ballasted tracks, showing that the choice does not only depends on the life-cost and maintenance aspects but there are also other important factors such as design parameters, resources availability, experience gained, particular specifications for constructions (bridges, tunnels, earthworks), constructions methods, restrictions to noise and vibrations, system's capability for geometrical corrections (due to differential settlements on the foundation), etc. (Paixão, 2014). Currently, more efforts are made in order to increase the track durability and reduce the noise, maintenance, optimizing the design, construction and operations.

Furthermore, in this Chapter, several structural models are presented, as well as their advantages and disadvantages. This reflection allows understanding which is the type of model that is more suitable for the analysis that will be performed in the next Chapters. The first models, which include the Winkler model, are not often used currently but are important to understand the main concepts and the evolution of the railway track models in terms of complexity and time of calculus. This complexity is related to the number of elements included in the models as well as the correct representation of the real response of the structure during the passage of the trains (which depends on the accurate modelling of the wave propagation on the ground). Despite the historical importance of the analytical or even semi-analytical models, the numerical models are a powerful tool in the determination and evaluation of the dynamic performance of railway tracks. Currently, the 2D models have been replaced by the tridimensional or even the more sophisticated models such as the 2.5D models or periodic models that use the particularities of the railway tracks such as its periodicity and long development in the longitudinal direction to obtain the same results as a 3D model in a faster way. However, there are particular situations where it is not possible to use the 2.5D or even the periodic models. The transition zones are included in these situations. The modelling of these areas implies the use of a non-invariant cross-section and it is not possible to select a periodic section that will be repeated indefinitely.

Indeed, the constant growth of the use of the 2.5D and 3D models is following the evolution of the technology in terms of *software* and hard skills of the computers.

In this work, two different structural models will be used to evaluate the performance of the ballasted and ballastless tracks. The 2.5D models will be used to compare the behaviour of the ballasted and ballastless tracks, including their long-term performance, through the determination of the induced stresses (short-term behaviour) and the implementation of the permanent deformation models. The 3D models will be used in the numerical model calibration and in the analysis of the performance of transition zones.

Along with the structural models, the numerical tools used to describe the behaviour of each element of the railway track are also analysed in this Chapter. However, the specific models used to represent the behaviour of the geomaterials when submitted to repeated or cyclic loads will be described in Chapter 4.

This Chapter also reviews the main concepts and the theoretical background related to the dynamic numerical modelling of the vehicle-track-ground. Firstly, a general overview about the modelling of the track is presented, followed by the presentation of the main topics related to the damping parameters and treatment of the boundaries. The modelling of the vehicle and *Hertzian* theory are also analysed. The review ends with a detailed presentation about the contact algorithms, that are very explored in this work. These concepts will be applied in the case study developed in Chapter 7.

3 Transition zones

3.1 Introduction

The designation of "transition zone" is usually used to identify zones of the track where there are variations more or less abrupt in terms of support conditions. These variations include:

- Transition of the track from an embankment or excavation to the track over a structure such as a bridge, tunnel, or a box culvert; the transition to a bridge is one of the most studied transition zones since occurs often along the railway lines;

- Transition from an embankment area to an excavation area;

- Transition from a ballasted track to a ballastless track (slab track);

- Transition due to a variation of the characteristics of the foundation soil such as the appearance of rocky areas or alluvial ground areas;

- Transition provided by the presence of switches and crossings in the track.

The variation of the support conditions is traduced by variations of the vertical stiffness and differential settlements of the track experimented by the vehicles. An example of the transition zones described previously is depicted in Figure 3.1. In this case, there is a transition from an excavation zone to a track over a tunnel.

Figure 3.1 – Example of a transition to a tunnel

From the concepts presented in the previous Chapter regarding the comparison of the ballasted and ballastless tracks (in terms of performance, materials, maintenance, costs, generated noise, etc.) and the numerical approaches used to model these structures, in the present Chapter, these concepts are applied to specific areas of the railway lines: transition zones. This Chapter aims to, firstly, present the main problems related to the presence of a transition zone, which includes the theories about the variation of

the vertical stiffness of the track, variation on the wheel-rail dynamic interaction forces and the appearance of differential settlements or hanging sleepers (in the case of the ballasted tracks). Thus, a brief framing of the transition zones' problems is presented as well as the causes of the deterioration and its consequences. This reflection is essential to understand the global interest of the railway Infrastructure Managers in these specific areas of the railway lines.

After understanding the problematic of the transition zones, the mitigation measures usually applied to these areas (solutions implemented on both railway structures: ballasted and ballastless tracks) are presented. This study helps understand the strengths and weaknesses of each solution since there is still no global consensus about the most appropriate one. Each solution should be selected according to the type of transition.

Since part of this thesis is focused on the numerical modelling techniques and their practical applications, some of the numerical modelling techniques used to study the transition zones are described in this Chapter. Each numerical model presents some advantages and also disadvantages, depending on the problem analysed.

Lastly, some aspects related to the monitoring are presented. Indeed, these techniques are still little explored in the study of the transition zones of the railway tracks. However, they can be an important tool to understand most of the problems and can also be used to improve the solutions.

3.2   Railway Transition zones – definitions and main concepts

3.2.1   Framing the problem of transition zones

The transition zones are characterized by an abrupt change in the track stiffness and development of the differential settlements (Figure 3.2 a) leading to the growth of bumps and dips near the junctions of tracks at transition zones. These phenomena are the source of passenger discomfort, lack of circulation security and an important cause of the increasing maintenance costs (Fröhling et al., 1996, Hunt, 1997, Nicks, 2009). Thus, it is possible to state that these phenomena are the main causes of the track's degradation in the railway network (Shahraki and Witt, 2015).

The abrupt changes in support stiffness (Figure 3.2) increase the dynamic wheel load, increasing the rate at which the track geometry degrades (Dahlberg, 2004, Zhang et al., 2007, Ferreira and López-Pita, 2013). This is due to the amplification of the dynamic response of the train-track system at the transition zones. This degradation is the cause of the generation of noise, vibration, poor ride comfort, and higher risks of derailment (Paixão et al., 2016). Indeed, these problems lead to the appearance of the hanging

sleepers phenomenon, permanent rail deformations, ballast penetration into the subgrade, cracking of the concrete sleepers and/or concrete slab, and loss of gauge (Banimahd et al., 2012).
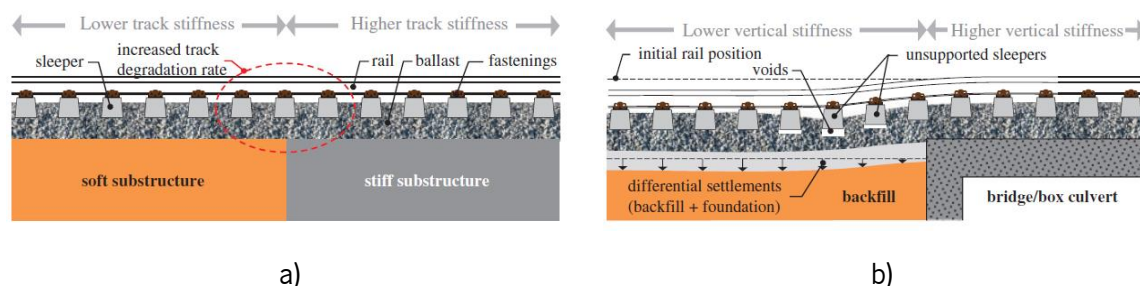
Figure 3.2 – a) Schematic representation of the abrupt variation in track stiffness - Shahraki et al. (2015) based on Paixão et al. (2013); b) differential settlement of the backfill and its foundation (Paixão et al., 2013)

The differential settlements (the result of uneven deformation on both sides of track transitions where the maximum deformation includes the elastic but also the plastic/permanent deformation that continues to accumulate during the loading cyclic - Figure 3.2 b) enhances dynamic loads and accelerates track deterioration (Indraratna et al., 2019). This change in the displacements will excite the train components (namely the wheels, bogies and car body of the vehicles), which will have an impact on the dynamic amplification of the vertical train-track interaction forces. The level of excitation of the train and subsequent increase of the dynamic forces depends on several factors such as the deflection change, train speed, and the masses and suspension characteristics of the train. Moreover, the settlement in the vicinity of a transition zone can be accelerated due to poor drainage or even a soft subgrade.

Indeed, it is possible to state that there is an inter-dependency of enhanced dynamic loads and differential settlement and their relationship to track degradation (Indraratna et al., 2019, Paixão, 2014). This degradation process is a cycle and can be designated as a self-perpetuating mechanism since the settlements can lead to the amplification of the dynamic loads, which conducts to an increase in the differential settlement and so on (Banimahd et al., 2012).

The transitions can occur in several situations: ballasted track underlain by a natural ground and the track underlain by a hard structure such as a bridge, tunnel, or culvert (Hunt, 1997, Fröhling et al., 1996, AREMA, 2005, Lundqvist et al., 2006, Coelho et al., 2011) or even in the case of a conventional track that changes to ballastless track to cross a roadway, a waterway (canal, river, etc.) or valleys through bridges or level crossings (Indraratna et al., 2019), as depicted in Figure 3.3.

<p style="text-align: center;">a)   b)</p>
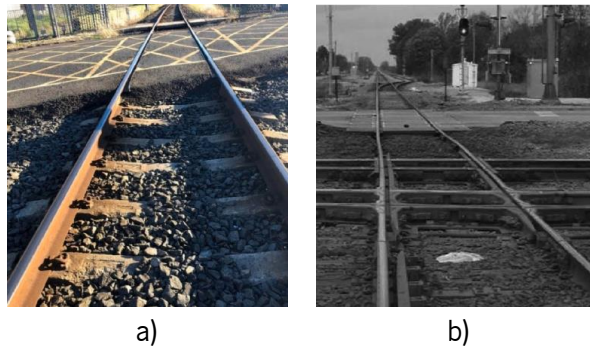
Figure 3.3 – Rail track transitions due to the change of superstructural components (Indraratna et al., 2019): a) Level crossing on a conventional track at Unanderra, NSW, Australia; b) Two crossing diamond (from Indraratna et al. (2019) and adopted from Li et al. (2016))

Due to the increase in the popularity of the ballastless track, probably, it is possible that the number of areas where there is a transition between the ballasted and ballastless tracks also increases. The main purpose is to design a gradual adjustment between the subgrade modulus of the ballastless track and the ballasted track. This is also called a connection area. A good transition zone softens the impact of the dynamic loads of a moving train by minimising the abrupt variations in track stiffness and ensuring a smooth and gradual change from a less stiff (ballasted track) to a more stiff (ballastless track) structure (Indraratna et al., 2019). Some examples of transition zones are depicted in Figure 3.4 and Figure 3.5.

<p style="text-align: center;">a)   b)</p>

<p style="text-align: center;">c)   d)</p>
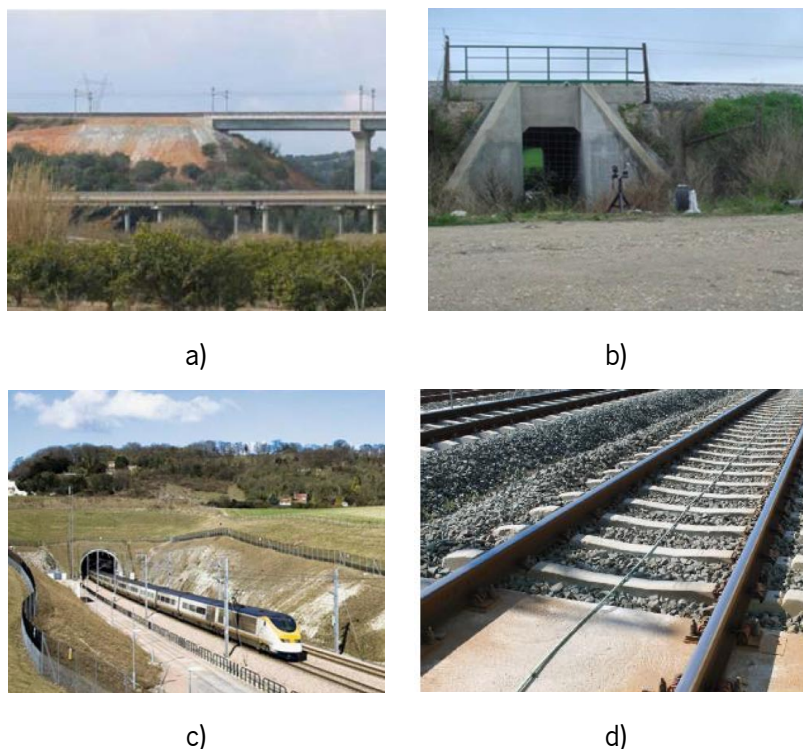
Figure 3.4 – Examples of transition zones (Alves Ribeiro, 2012): a) transition between an embankment and a bridge; b) inferior crossing to the track; c) transition between an excavation and a tunnel; d) transition between a ballasted and ballastless tracks on the high-speed line Cordoba- Malaga (Spain) (Sañudo et al., 2016a)

<p style="text-align: center;">82</p>

Figure 3.5 – Examples of transition zones to bridges (Wang et al., 2017a)

Thus, the transition zones in railway tracks are built to mitigate the impact caused by the structural discontinuities existing along the track (Varandas et al., 2013). The main goal consists of choosing an efficient approach and the most suitable construction method (Shahraki and Witt, 2015). On the ballasted track side, there is also another problem related to the hanging sleepers or unsupported sleepers caused by the uneven settlement in the vicinity of the track with higher stiffness. In some cases, some drastic solutions are adopted such as establishing temporary speed limits along the track to maintain an acceptable level of safety. Despite the hanging sleeper phenomenon is well-known in the ballasted tracks, the appearance of gaps can also occur in the ballastless tracks.

3.2.2 Vertical stiffness of the track

After understanding the main problems of the transition zones and their influence on the performance of the railway tracks, it is important to understand the particular concept of the vertical stiffness of the track.

The vertical stiffness (k) is a parameter that relates the applied load (P) with the maximum displacement (y_m) measured at the load application point:

$$k = \frac{P}{y_m}$$

(3.1)

The determination of the value of the vertical stiffness allows making some conclusions about the bearing capacity of the track and taking some considerations about the performance of the track, conservation state and its quality. Indeed, studies developed by Sussmann et al. (2001) highlighted the significant utility of the evaluation of the vertical stiffness of the track in the maintenance strategies. Thus, the authors proposed a relationship between the vertical stiffness with the maintenance operation, as shows Table 3.1.

Thus, the evaluation of the vertical stiffness is difficult and there isn't an accurate and consensual method. However, several methods have been proposed, from the determination of parameters that allow static and dynamic evaluation in discrete points of the track to the continuous and dynamic determination that is currently possible in some countries.

In the scope of this topic, different studies allow identifying several accelerated degradation points on the track where there are sudden variations in the stiffness (Berggren, 2009, ERRI, 1999a, ERRI, 1999b, ERRI, 1999c, ERRI, 1999d, FRA, 2007, Li and Davis, 2005, Sussmann et al., 2001). In this context, the continuum evaluation may be an important tool, with special interest for the railway Infrastructure Managers since allows detecting variations in the performance of the track. This information is important to define and plan maintenance operations.

Table 3.1 – Relation between the vertical stiffness and the possible maintenance operations (Sussmann et al., 2001, Alves Ribeiro, 2012)

Parameters	Problem	Maintenance
Low stiffness	Foundation's track with poor strength characteristics or ballast's degradation	Re-design of the substructure, stabilization of the foundation of the track
Variable stiffness	Variations of the characteristics of the track's foundation	Placement of the railpads under the rails with proper characteristics, re-design of the substructure, placement of the mats under the ballast
Voids	Degradation of the ballast, localized settlement, or bad rail's conditions fixing	Inspection of the fixing systems, tamping operations

3.2.2.1   *Methods used to perform the continuum stiffness evaluation*

Since the vertical stiffness is not constant throughout the track, it is important to evaluate its variation. Thus, systems that allow evaluating continuously the vertical stiffness of the track were developed.

The general principle of these systems consists of the controlled application of a mobile load and the measurement of the displacement that results from the weight of the vehicle and the deformability of the track. The passage of the vehicle at a certain speed excites the track with frequencies induced by the distance between the axles of the vehicle, by the irregularities on the track and wheels of the vehicle and by the spacing between the sleepers. Furthermore, the system also allows the application of a solicitation with a certain frequency.

This means that the obtained value of the stiffness depends on several factors such as the train's speed and the presence of irregularities since the measured displacement depends not only on the deformability of the track but also on the displacement due to the presence of irregularities. Furthermore, the choice of the spatial resolution of the measurement is also important to assure the proper prospection since along the track can occur significant stiffness's variations in short distances (Berggren, 2009).

The University of Nebraska, working together with the *Federal Railroad Administration* (*FRA*) developed a system without contact (Norman, 2004). The measuring system (depicted in Figure 3.6 a and b) is

composed of two lasers and a camera that are fixed in a beam rigidly connected to the axle of the wheel of the vehicle. Thus, it is possible to assume that the distance between the system and the contact point wheel-rail (H) is constant. The system performs the measuring of the distance between the camera and the surface of the rail (h). From the distances H and h, it is possible to determine the displacement of the surface rail regarding the contact plane wheel-rail (y). This displacement is related to the absolute displacement of the rail under the camera section (y_{camera}) and with the absolute displacement of the rail at the wheel-rail contact (y_{wheel}), which are obtained based on the Winkler beam model. The distance between the camera and the surface of the rail (h) is geometrically determined from the distance between the laser beams (d) registered by the camera, as depicted in Figure 3.6 b). This system was tested for very low speeds, without considering the dynamic effects.

a)   b)
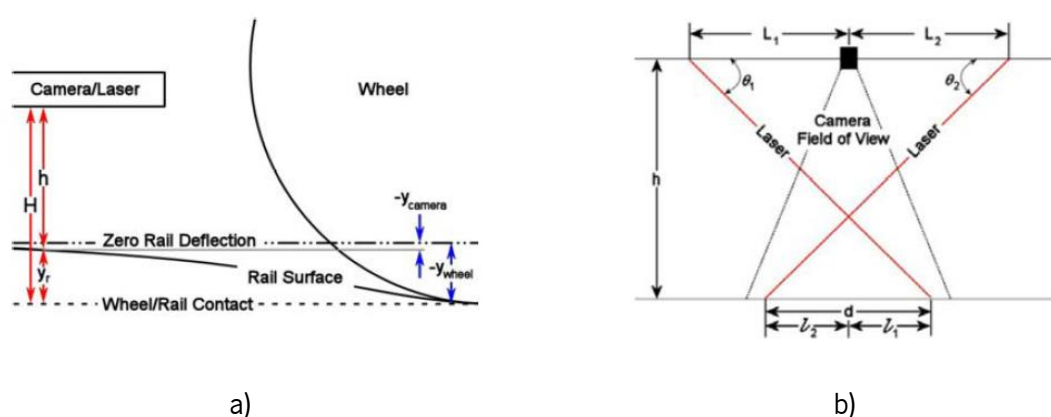
Figure 3.6 – Measuring system (Norman, 2004): a) schematic representation; b) geometric parameters considered in the measuring with laser sensors

The *Delft University*, working together with the *Greenwood Engineering*, developed a measurement system without contact called *High Speed Deflectogram*. The basic principle is based on laser technology and the *Doppler* principle. Using the *Doppler* laser sensors, the speed of the rail's deformation is measured as a result of the load applied. More details about this method can be found in Esveld (2001). The variations of the deformation's speed of the rail indicate discontinuities of the track due to changes at the foundation level or on the support of the rail or sleepers. This system allows performing measurements at a maximum speed of 130 km/h. As shown in Figure 3.7, the laser *Doppler* sensors are installed on a beam positioned in front of a vehicle's wheel axle. These sensors analyse the surface of the rail recording the deformation speed of the rail when loaded. In order to perform the measuring, two lasers are necessary (at least), one aligned with the deformed zone (A1 and A2) and the other, of reference, aligned with the zone where no deformation occurs (B).
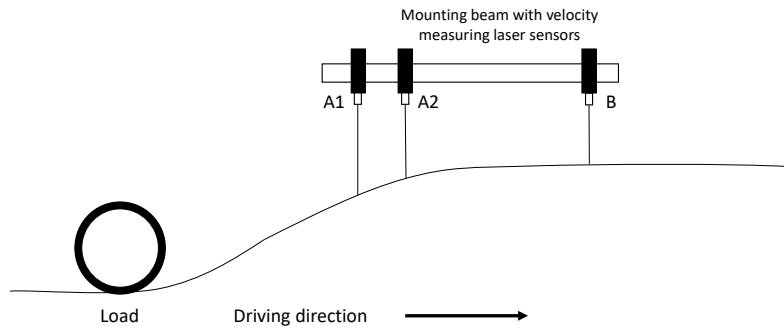
Figure 3.7 – Schematic representation of the measuring principle of the High Speed Deflectometer (adapted from Esveld (2001))

3.2.2.2   *Stiffness's variations in transition zones*

The continuum measurement of the stiffness and its relationship with the longitudinal profile allows associate the variations of the stiffness to the existence of transition zones. For example, Figure 3.8 shows the results obtained in a continuum measurement system of the track, developed by *Banverket*, throughout 3 km (Dahlberg, 2004). Analysing Figure 3.8, it is possible to observe that the presence of a stiff structure (in this case corresponds to a bridge) causes a stiffness's increase that is visible between kilometres 11.4 and 11.65. Similar results can also be found in the work developed by Berggren (2009). In this case, a simple variation in depth of the clay layer in the foundation can induce important stiffness variations.
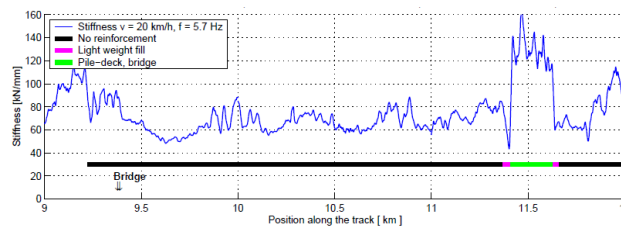
Figure 3.8 – Continuous stiffness measurements - West coast line in Sweden (Dahlberg, 2004)

Li and Davis (2005), using the system developed by *FRA*, also identify significant variations of the stiffness in several transition zones in railway lines in the USA, as depicted in Figure 3.9.

a)

b)
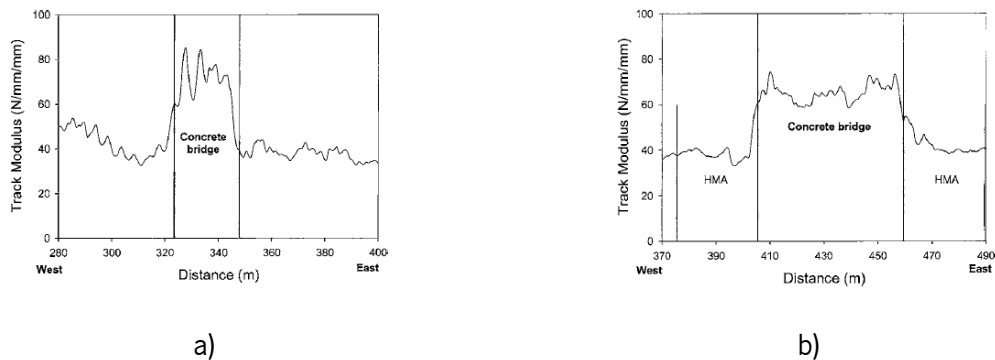
Figure 3.9 – Track modulus result: a) bridge with control approach; bridge with HMA stabilized approach (Li and Davis, 2005)

Analysing Figure 3.9 a), for example, the modulus of the track on the concrete bridge is almost twice the value verified in the embankment zone. Figure 3.9 b) shows the positive impact of the HMA stabilized approach on the track modulus.

3.2.3   Causes of track's deterioration and its consequence in transition zones

As mentioned previously, several causes lead to track degradation, mostly because of the cyclic character of the loading.

Gallage et al. (2013) divided the problems of the transition zones into two main causes: the first one related to the stiffness and damping, geotechnical issues, subgrade failure, excessive permanent deformation, progressive shear failure, soil water response and wetting and shrinking cycles. The secondary causes are related to the train loads and speed, traffic conditions, embankments heights and types of bridge abutments.

This means that the reasons that cause the problems in transition zones are diverse. Wang and Markine (2018b) also divide the major factors into the following categories:

- Differential (relative) settlement between the ballasted track and the engineering structure. The differential settlement can also be considered as a geometrical irregularity, which plays a major role in the degradation process of transition zones (Zhai and True, 2000, Lei and Mao, 2004, Banimahd et al., 2012);

- Abrupt change in the vertical stiffness of tracks (Hunt, 1997, Lundqvist et al., 2006, Lei and Zhang, 2010): the vertical track stiffness determines the rail deflection during the train passages. The stiffness variation leads to changes in the vertical acceleration of the moving trains. This results in changes in vertical wheel forces (about 9% increase calculated in Li and Wu (2008)), rail vertical acceleration (Lei and Zhang, 2010), and ballast stress (Wang et al., 2015). The influence becomes larger with the increase in train velocity (Lei and Zhang, 2010).

- Geotechnical, construction and maintenance issues, such as the poor quality of used materials, inadequate compaction and consolidation of the fill and embankment, poor drainage conditions (Li and Davis, 2005, Nicks, 2009). In Wang et al. (2017b), the authors studied the effect of the moisture condition in transition zones and the results show that the high moisture leads to an increase of dynamic wheel forces in the studied transition zone.

Due to these causes, based on field observations and literature review, the problems that can often be found in a transition zone include (Wang and Markine, 2018b):

- Damage of the track components: rail surface defects, broken fasteners, cracks in concrete sleepers, breakage of ballast particles, and voids between sleepers and ballast (also known as hanging sleepers) (Li and Davis, 2005, Hölscher and Meijers, 2007, Paixão et al., 2013, Alves Ribeiro et al., 2015, Coelho et al., 2011, Lei and Zhang, 2010, Nicks, 2009, Gallage et al., 2013, Read and Li, 2006)

- Deterioration of the track geometry, i.e. extra settlement that appears on tracks and forms a "dip" (European_Rail_Research_Institute, 1999) due to, for example, the breakage of the track component, the ballast pollution, the ballast penetration into subgrade, and the poor drainage. This deterioration can lead to extra maintenance and repair costs;

- Loss of the passenger's comfort (Banimahd et al., 2012).

These problems can increase maintenance costs or even accelerate the frequency between maintenance operations.

3.2.4   The importance of the differential settlements

The settlements on the track are extremely important, mainly when they are differential. In transition zones, the degradation of the geometry due to the appearance of the differential settlements has been identified as the main problem.

Thus, the settlement of the track can have several sources that, actuating, separately or together, can lead to the appearance of differential settlements:

- Settlement induced by the rail traffic;

- Settlement of the foundation soils and embankments;

- Settlements induced by the structure;

- Dynamic effects.

It should be noted that, although the settlement due to rail traffic occurs exclusively during the operation phase of the track, the rest may occur after construction due to consolidation or creep phenomena.

Settlement induced by the rail traffic

The settlement induced by rail traffic is one of the sources of differential settlements. As mentioned previously, the stiffness's variations, in transition zones, induce variations in the vehicle-track dynamic interaction forces that are traduced as an overload localized in the track.

In order to prevent this type of settlement and its effects, some efforts have been made to estimate, sometimes qualitatively, the level of settlement expected in a transition zone. The predicted studies are performed founded on deformation laws based on the results obtained during laboratory tests using cyclic equipment, in reduced physical models, or results obtained based on field measurements on the railway track. The deformation laws will be studied in more detail in Chapter 4. For example, Bruni et al. (2002) study the evolution of the permanent deformation of the track in a transition zone bridge-viaduct with the number of loads (Figure 3.10 a), as well as Wang and Markine (2019). As is known, the settlement evolves with the number of load cycles and, after a certain number of load cycles, the permanent deformation tends to stabilize, and the increment of settlement is reduced until becomes zero. Furthermore, Bruni et al. (2002) also conclude that the variation of the interaction force wheel-rail after a certain number of load cycles varies (Figure 3.10 b). Indeed, after the passage of the first axle, there is a variation of the force by about 3% regarding the static force. After the passage of 345600 axles (which corresponds, approximately, to about a year of operation of the rail track), this variation is about 7%.

a)   b)
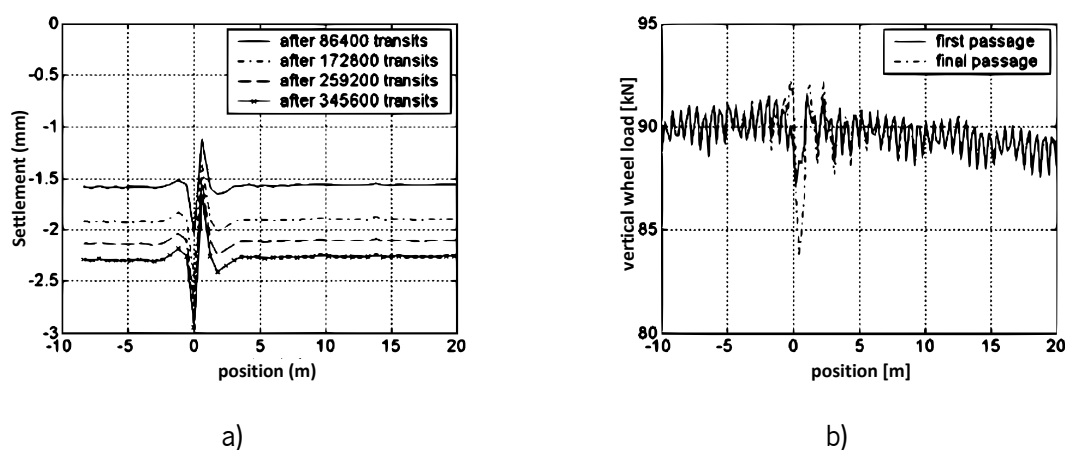
Figure 3.10 – Effects of the permanent displacement of the track in a transition zone: a) evolution of the permanent settlements; b) evolution of the variation of the vertical dynamic load (Bruni et al., 2002)

Details related to the modelling of the vehicle-track system, the permanent settlement of the track due to the cyclical loading induced by rail traffic and the exploration of the different laws used to simulate the degradation of the track are explored in detail in Chapter 7 and Chapter 4, respectively.

Settlements of the foundation soils and embankments

The settlements can also occur due to the settlement of the foundation soils or even due to the settlement of the embankment. Figure 3.11 shows the different sources of settlements in embankments (UIC 2008).
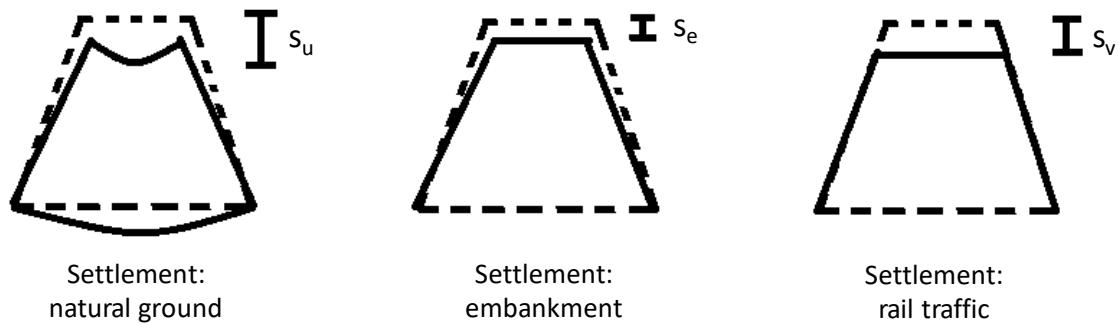
Figure 3.11 – Different sources of settlements in embankments - adapted from (UIC, 2008)

The settlement of the embankments may be due to errors during the compaction or drying. Therefore, the control of the materials used in the construction and its compaction constitutes the basic requirements of various specifications for embankment construction, namely in the vicinity to structures, as in the case of embankment-bridge transition zones or underpasses. For example, UIC (2008) has a section dedicated to the design and construction of embankments.

Furthermore, the presence of water has a significant impact on the performance of the embankments, which means that is necessary to incorporate effective drainage systems, especially in embankments close to structures such as bridges and underpasses. In this case, it is quite normal the inclusion of geosynthetic materials or granular materials close to the concrete structures to have proper water conduction. In the case of clayed or even muddy materials, some acceleration consolidation processes are used such as the application of pre-loads or drainpipes.

This type of settlement, if properly controlled in the construction phase, is not very important during the lifecycle of the structure. However, if they occur during the exploration phase, they can lead to a difficult and costly problem to solve.

Settlements induced by the structure

In the transition zones such as embankment-bridge, beyond the settlements due to the cyclic loading induced by the passage of the trains and the settlements of the foundation soils and embankments, there may also be problems related to the interaction track-bridge in the abutments of the bridge. This interaction is dependent on the characteristics of the bridge and the process of the construction of the embankment (Smekal, 1997). The factors that influence the long-term performance of the transition embankment-bridge are:

- Type of bridge and embankment;
- Type of transition structure;

- Compaction near the abutment;

- Type of drainage system.

Indeed, in general, the deformation that can occur in these transition zones is due to the settlements of the embankment because of inadequate compaction conditions and movements of the bridge or track induced by loading or temperature variations.

When the train is over the bridge, the track bends along the bridge deck, imposing the lifting of the track near the abutment (about 1 to 3 m). Under the sleepers in this zone, the ballast is unloaded and loaded cyclically, leading to the development of higher stresses and the appearance of the ballast's deformations and in the underlying layers (Hess, 2007). The lifting forces are controlled by the design criterion of the railway bridges, through the definition of the rotation limits of the bridge deck, in the transition of consecutive decks, or in the transition between a deck and abutment (Figure 3.12). In Europe, these limits are defined in the standards EN1991-2 (2003) and EN1990 (2005). Furthermore, in bridges with large spans, the forces necessary for fixing the rail can even exceed the limits of conventional fastening systems (Hess, 2007).
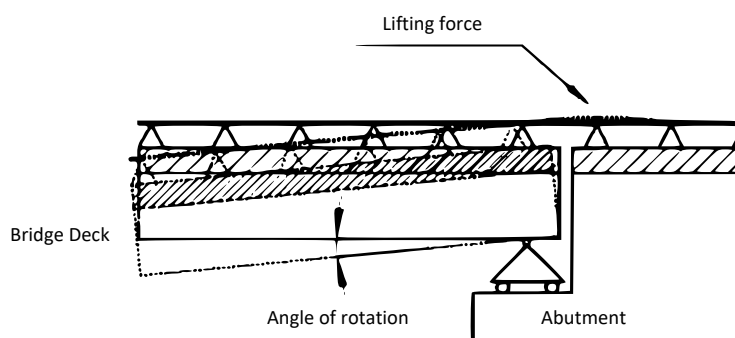
Figure 3.12 – Schematic representation of the rotation effect of the deck of the bridge (Hess, 2007)

Another typical problem of the transitions is the appearance of gaps near the abutments caused by the longitudinal movements of the bridge structure induced by the horizontal forces or thermal effects, whose repetition causes the gradual compaction of the ballast and foundation layers (Smekal, 1997). This is a very common phenomenon in integral bridges where there are no expansion joints neither in the spans nor near the abutments, being the thermal expansion of the bridge responsible for compacting the track layers.

The type of foundation of the embankment is also dependent on the bearing and deformability characteristics of the foundation soil and the type of bridge. The adoption of solutions that directly support the embankment, i.e. direct foundation, have shown good performance namely in reducing the

appearance of differential settlements since they make the abutment more flexible (ERRI, 1999a, ERRI, 1999b, ERRI, 1999c, ERRI, 1999d).

The geometry of the abutment influences the compaction of the embankment, which means that it is necessary, in each case, to study, carefully, the execution process to guarantee a correct compaction in all points (Goicoechea, 2007).

Dynamic effects

Some theoretical studies were developed to evaluate the dynamic effects induced by the changes in the track's geometry due to differential settlements. For example, in the Delft University (Schooleman, 1996), a study was developed, in which the main goal consisted of defining limits for the variation of the geometry of the track in a transition zone, based on the effects that this variation causes in the passenger comfort. Lei and Mao (2004) and Nicks (2009) also developed studies about the dynamic behaviour of the transition induced by the change in the profile of the track, assuming a very simple geometric irregularity. These studies, although currently outdated, were the first analyses in the scope of the evaluation of the dynamic effects on transition zones. These studies allow concluding that the changes in the track's geometry in the transition zone induce significant dynamic effects in the wheel-rail system, which means that the definition of the admissible limits is very important. However, it is important to highlight that most of the settlements of the track presented by the different authors occur in transition zones of the track´s stiffness. Moreover, the changes in geometry are purely theoretical since each transition zone has its own degradation profile and the track would adopt a certain geometry.

3.2.5 *Problematic of the hanging sleepers*

The hanging sleepers are defined as the sleepers whose contact with the ballast layer is reduced or even inexistent due to the existence of voids between the bottom of the sleeper and the surface of the ballast layer. The appearance of these voids is normally associated with the degradation phenomenon of the ballast layer under the sleepers, which occurs, usually, in zones of the track where the ballast layer is subjected to higher stresses. However, the poor compaction in the installation phase or during the maintenance, or the bad quality of the material used in the ballast layer are also important factors in the analysis of this degradation phenomenon. Thus, since the sleepers are connected to the rail, whose bending stiffness is significantly high, the sleeper recovers its position after the loading, not following the deformation of the support layers of the track.

The appearance of the hanging sleepers is very frequent in transition zones since the amplification of the dynamic wheel-rail interaction forces causes the concentration of stresses in the ballast layer. The continuum loading leads to the degradation of the track under the sleepers, which may result in the loss of contact between the base of these elements and the ballast layer. When a sleeper is hanging, it can't perform correctly its function (normally transmits the load of the vehicles to the ballast layer) and induces an important irregularity, which leads to higher efforts on the neighbour's sleepers (Lundqvist and Dahlberg, 2005, Nielsen and Igeland, 1995). When the track is dynamically loaded, the neighbour's sleepers transmit to the track superior forces when compared to the normally applied. In this scope, Lundqvist and Dahlberg (2005) developed a numerical study where the effects induced by the existence of a gap between a sleeper and a ballast layer were analysed. Sussmann et al. (2001) performed some measurements in two sections of the track and detect the presence of voids under the sleepers, which indicates the existence of hanging sleepers. Indeed, some studies state that after the appearance of hanging sleepers, the degradation process accelerates significantly and can lead to the existence of other phenomena such as the fracture of the ballast particles of the broken sleepers.

Thus, it is possible to conclude that the hanging sleepers are a product of the track's settlements, but they are also responsible for the increase of those settlements since they enhance the growth of the dynamic forces (Figure 3.13). In a track where the sleepers are perfectly supported, the loading of the ballast is cyclic. However, in the presence of hanging sleepers, there is a new loading scenario on the ballast layer with the application of forces with singular characteristics: reduced forces on the hanging sleepers and higher forces on the neighbour's sleepers.
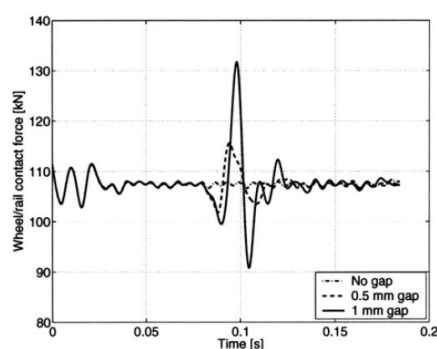
Figure 3.13 – Variation of the wheel-rail interaction forces in the presence of voids under the sleepers (Lundqvist and Dahlberg, 2005)

More recently, the effect of hanging sleepers was studied by Alves Ribeiro (2012). The author defined a methodology to simulate the long-term behaviour in a transition zone with an abrupt stiffness change in order to understand the genesis of some characteristics problems of the transition zones, such as the appearance of differential settlements and hanging sleepers (Figure 3.14). This methodology included

the simulation of the passage of a train in a 2D calibrated model and the implementation of an empirical permanent deformation model to simulate the long-term behaviour (where the stresses obtained in the numerical model are the main inputs). The calculated permanent deformations were incorporated in the finite element model. This is an iterative process and this methodology will be analysed in more detail in Chapter 7.
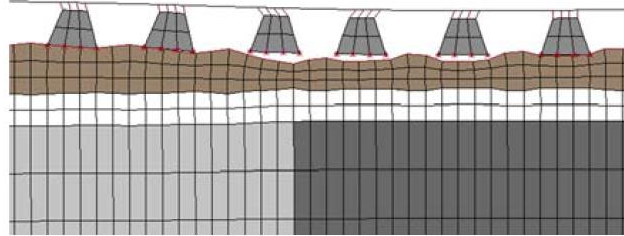
Figure 3.14 – Hanging sleepers: deformed track after 500000 load cycles

Paixão (2014) used a different strategy to study the effects of hanging sleepers. Thus, the author defined different hypothetical bump profiles on the levelling of the track to assess the dynamic response of the train-track system and evaluate its influence. The bump profiles are depicted in Figure 3.15:

- Shape U – uniform settlement of the track substructure;
- Shape W – settlement profile that results from a wedge-shaped backfill using materials with improved mechanical properties (unbound granular material and cement-bound mixture);
- Shape S – sharp settlement variation when approaching the bridge;
- Shape G – gradual settlement variation when approaching the bridge.

Thus, for each shape (U, W, S and G), four bump profiles were analysed considering different maximum amplitudes of settlement: δ_{max} = 1 mm; δ_{max} = 4 mm; δ_{max} = 10 mm and δ_{max} = 15 mm. These bump profiles were applied to the top nodes of the ballast layer.

With the inclusion of these bump profiles, due to the bending stiffness of the rails, after activating the gravity in the track frame, some sleepers were hanging from the rails with gaps under them. The number of hanging sleepers increases with the value of δ_{max}. The profiles U and G yielded the highest number of hanging sleepers and the largest gaps for each value of δ_{max}. The author also concludes that in each tested case, the highest peak loads occurred at the sleepers that were not hanging but were adjacent to the hanging sleepers that had the largest gaps. The author explained this phenomenon by the fact that the static weight of the rail and the hanging sleeper, plus part of the axle load, was directly transferred to those sleepers that were not hanging. Similar conclusions were obtained by Lundqvist and Dahlberg (2005), Alves Ribeiro (2012) and Varandas et al. (2013).
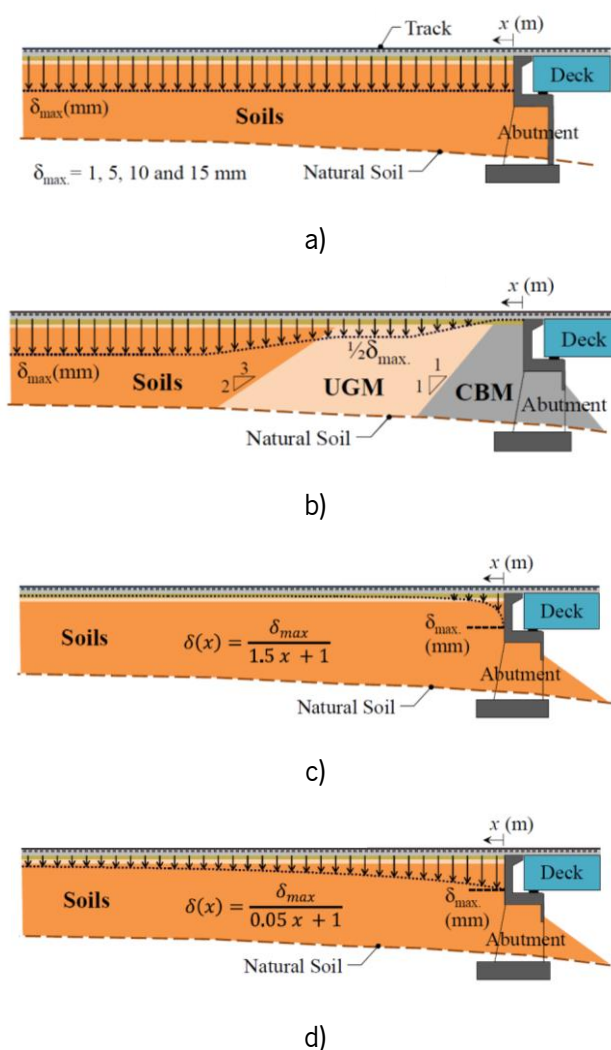
Figure 3.15 – Schematic representation of the bump profiles: a) shape U – uniform settlement profiles; b) shape W – wedge-shaped settlement profiles; c) shape S – sharp settlement profiles; d) shape G – gradual settlement profiles (Paixão, 2014)

3.2.6 Secondary factors that can affect the performance of the railway structures in transition zones

Besides the causes listed in the previous section, there are also secondary factors that can also affect the performance of the transition zones. For example, the degradation process is also dependent on the direction of the train (Sañudo et al., 2016b). Thus, if the train travels from a lower-stiffness track onto a high-stiffness substructure, the wheel is lifted very quickly. This leads to large dynamic loads applied to the rails and the stiff substructure, causing impact damage to both. On the contrary, when the train travels from the high-stiff to the lower stiff, the wheel in effect "falls off" the stiff support, causing large dynamic loads on the track (Coelho et al., 2011).

Another factor that can influence the performance of the transition zones is the position of the supports. Sañudo et al. (2017) tried to find the optimal distance between the supports to achieve a good track performance considering a transition between a ballasted track and a ballastless track. The analysis was performed through numerical simulations using the FE method in the time domain. Usually, the spacing

95

between the supports is defined by the Railway Infrastructure Managers and can differ. In fact, a reduction in the distance between the sleepers can lead to an increase in track stiffness.

3.2.7   Economic aspects related to the transition zones

In the past years, the railway Infrastructure Managers have been increasing their concerns regarding the transition zones due to often additional maintenance required in these areas. This extra maintenance increases the exploitation costs, and eventually causes delays in the operation of the railway track (Shahraki et al., 2015).

In the literature, the track problems at transition zones on European lines date from the 1970s (Paixão et al., 2013). Studies developed in Europe highlight that the maintenance frequency in specific locations (where there is a vertical stiffness discontinuity) may be five times higher and the unit costs twice as high (European_Rail_Research_Institute, 1999). Indeed, the first studies about track degradation were generally focused on tracks over embankments rather than on transition zones, which means that there wasn't a detailed understanding of the mechanisms of track geometry degradation at transition zones. This situation leads to the difficulty to predict the extra required maintenance (Coelho et al., 2011).

In the late 1990s, the European Rail Research Institute carried out a study focused on several aspects of transition zones from different points of view: railway, bridge and geotechnical engineering (Paixão et al., 2013). Indeed, historically, a large proportion of railway operating costs are spent on track maintenance. More recent studies estimate that a track can account for 40-75% of the total maintenance expenditure (Zhai et al., 2004). As expected, the reduction in the track maintenance requirements could lead to a significant reduction in the whole-life costs, which, of course, brings benefits to the railway systems owners, operators and also users. In the Netherlands, for example, the frequency of the interventions is up 2-4 times those in the free embankment (Hölscher and Meijers, 2007). However, some studies state that, in this country, the maintenance activities on the tracks in transition zones are performed up to four-eight times more often than those on "normal/open" tracks (Hölscher and Meijers, 2007, Varandas et al., 2011). Furthermore, in the US, $200 million are spent annually to maintain the transition zones, while in Europe about 97 million are spent on similar maintenance activities (Wang et al., 2017a). Some studies show that in the USA, more than 50% of all bridge transitions face dip/bump problems, with average bumps being 33 mm high and 5.2 m long (Nicks, 2009). In Spain, for example, based on the analysis of track geometry measurements of the Madrid-Seville high-speed railway line, the results evidenced that maintenance works at transitions to bridges or to box culverts can be up to three or six times higher, respectively, than in "normal/open" track (López-Pita et al., 2006).

According to Nicks (2009), the US is spent $26 million per year just repairing bridge related transitions, while in Spain a major portion of their overall investment goes to track maintenance and infrastructure materials (Sañudo et al., 2016a).

3.2.8 Methods used to mitigate the problems in transition zones

Many railway engineers have suggested different recommendations and designs to solve the problems regarding the transition zones. However, it seems none of the available designs is the ultimate solution for the mitigation of track degradation. This means that it is important to understand the efficiency of each approach and choose the most suitable construction method for a track under the passage of high-speed trains (Shahraki et al., 2015).

Several methods can be used to mitigate the sudden change of the stiffness in transition areas and different solutions have been proposed to solve or to mitigate this problem over recent years. These mitigation measures can be divided according to their positions in the track structure: solutions acting on infrastructure, acting on the superstructure, and acting on both (Sañudo et al., 2017). Some solutions improve geotechnical factors and are aimed at preventing the formation of vertical settlements. Others include the replacement of the materials of the underlying layers or act on the sleepers, support rails, or ballast layer using new materials and geocomposites (Woodward et al., 2012, Paixão et al., 2013), as depicted in Figure 3.16.
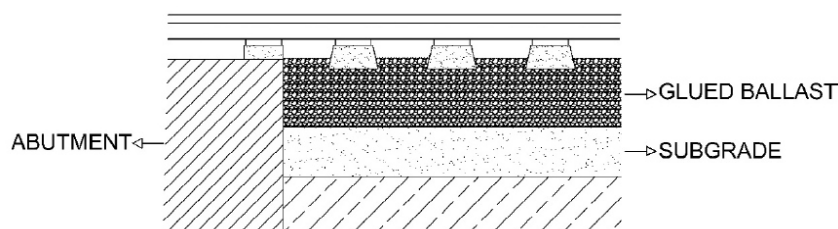
Figure 3.16 - Glued ballast/ polyurethane GeoComposites for ballast stabilization (Sañudo et al., 2016a)

The solutions that include the incorporation of bituminous material, geotextiles, or reinforcement of the foundation through the injection of cement grouts intend to improve the flexible zone of the track introducing a gradual variation in the transition zone. The incorporation of resilient elements such as railpads under the rails or sleepers and resilient mats under the ballast layer (Figure 3.17) are examples of solutions used to flexible the stiff zones of the track. Indeed, the methods of improvement/reinforcement of the more flexible zones of the track prove to be adequate to control the variation in stiffness when it is relatively low. When it is high, the measures are less effective, and it is necessary to incorporate resilient elements in rigid areas to obtain the desired effects (Read and Li, 2006).
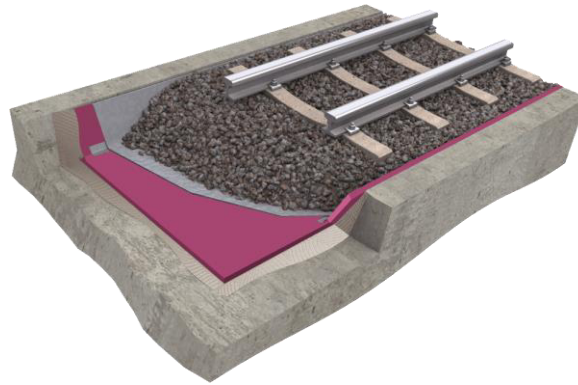
Figure 3.17 – Example of an under ballast mat

Geotextiles are, nowadays, widely used in geotechnical engineering, particularly in the reinforcement of the soil layers. This technique is usually applied in the rehabilitation of tracks with problems, but this technique can also be used in the construction of new tracks, namely in transition zones (Figure 3.18 a). Studies developed in the scope of loading cycles revealed that the reinforcement soils with geosynthetics present higher resistance (and consequently less susceptibility to the development of permanent deformations) than the non-reinforcement soils. For example, Shin et al. (2002) studied the long-term deformation of several solutions with geogrids (the model test is depicted in Figure 3.18 b) and proposed their application in the high-speed line between Seoul and Pusan in South Korea. The authors concluded that the decrease of the permanent settlement of the soil due to the installation of the geosynthetic is due to the stiffness increase and more effective stress distribution. Brown et al. (2007) also conclude that the selection of the geogrid should be dependent on the type of material that is intended to be reinforced to allow the optimal functioning of the set.

a)

b)
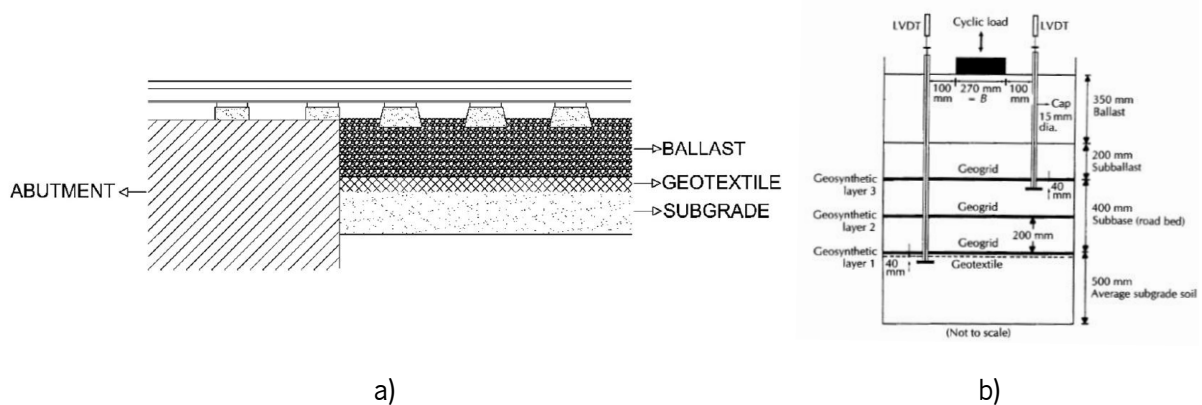
Figure 3.18 – Solutions applied on transition zones: a) geotextile reinforcement under the ballast layer in transition zones (Sañudo et al., 2016a); b) model test arrangement (Shin et al., 2002)

Another main method used to smooth the transition is the installation of the auxiliary rails (this method allows increasing bending stiffness of the rail and it was developed by the *German Federal Railway*) along the ballasted and ballastless tracks (transition) - Figure 3.19. This method is very efficient since the

increase of the bending stiffness allows uniformize the vertical displacements of the track. Indeed, Shahraki and Witt (2015) developed a 3D model to analyse the dynamic effect of a transition, which included the evaluation of the impact of some mitigation measures in the transition zones (installation of auxiliary rails, a gradual increase of longer sleepers, evaluating the displacements, acceleration and stress distribution results). The authors found out that the auxiliary rails showed better results.
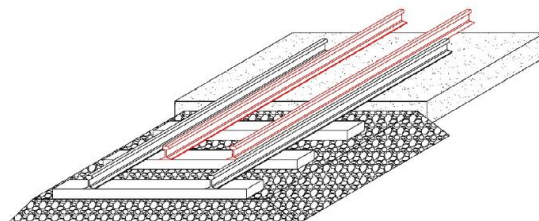
Figure 3.19 – Solutions applied on transition zones: additional inner rails (Sañudo et al., 2016a)

An alternative popular method is the increase of the length of the sleepers in the ballasted area (Figure 3.20) and also the variation of the spacing between them (Figure 3.21). In this approach, the length, width, and height of the sleeper can gradually be increased while the spacing between them gradually decreases when track structures proceed from being less stiff to stiffer (Indraratna et al., 2019). In fact, larger sleepers can be an option to mitigate the ballast settlement but this approach is not very good at reducing the dynamic load factor (Nicks, 2009). According to Nicks (2009), this approach does not help to increase track stiffness. However, it may reduce vertical displacement and induced stresses by distributing train loads over a wider area (Sañudo et al., 2016a).
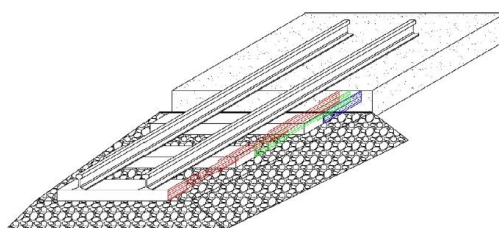
Figure 3.20 - Variable sleeper length solution (Sañudo et al., 2016a)

Indeed, the change in the sleeper's dimension is used to control the global stiffness of the transition zones. The increase of the sleeper's dimensions allows increasing the contact area with the ballast layer, distributing the applied force over a greater surface area, avoiding the concentration of stresses and, consequently, the increase of settlements.

The variation of the spacing between the sleepers (Figure 3.21) is another strategy used to increase the tracks' stiffness in the transition zone.

99
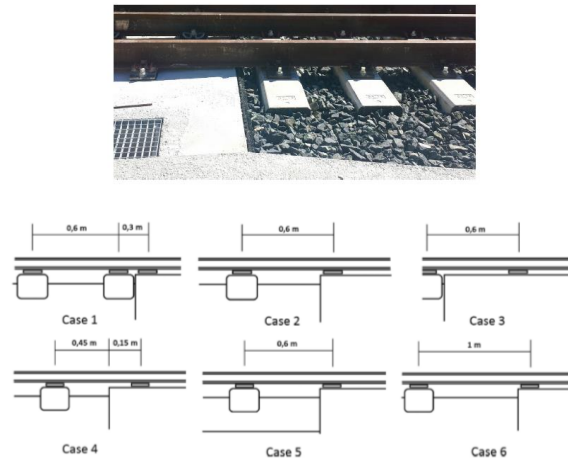
Figure 3.21 - Influence of the support configurations (Sañudo et al., 2017)

Another method used to mitigate the effects of the abrupt change stiffness corresponds to the incorporation of a layer of bituminous material commonly referred to in the bibliography as HMA (Hot Mixed Asphalt). Indeed, this is a common practice in the United States. Furthermore, in Europe, this reinforcement technique has also been used and studied, namely in France, when the SNCF analysed the applicability of the technique through the construction and monitoring of an experimental section of 3 km (Gautier, 2006). The hot-mixed asphalt (HMA) is typically placed between the ballast and subgrade layer to create a smooth change in the transition zone, as depicted in Figure 3.22. This layer is usually replacing the sub-ballast layer. However, there is also the possibility of replacing both ballast and sub-ballast layers with an HMA layer. Nevertheless, this solution does not allow performed conventional track maintenance operations. An alternative to this solution is the use of geocell and the use of a mixture soil-cement. The latter is also a solution of foundation stabilisation, whose stiffness obtained depends on the dosage of cement to be used (Seara and Gomes Correia, 2008).

In the installation of the HMA layer, it is important to assure that this layer is completely protected from the oxidation and temperature variation that can affect the properties of the material (Selig and Waters, 1994). Regarding the dimensions, normally, the values adopted depend on the traffic level and the stiffness of the foundation layers. In the USA, it is usually to have layers with a thickness between 10 to 20 cm with a ballast high of 12.5 to 25 cm from the base of the sleeper until the top of the reinforcement layer. This solution does not constitute such a recurring solution and it is used more in the context of reinforcement of existing structures that present problems.
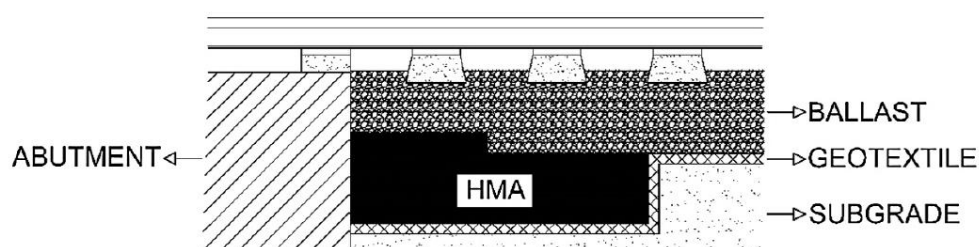
Figure 3.22 - HMA (hot mix asphalt) method used on a transition zone (Sañudo et al., 2016a)

Another strategy is the installation of an approach slab, as depicted in Figure 3.23. This approach has been used, especially in the UK, mostly to improve the performance of a transition in the bridge approach. This solution is usually applied in a transition embankment-bridge or embankment-tunnel. However, as reported by ERRI (1999) (ERRI, 1999a, ERRI, 1999b, ERRI, 1999c, ERRI, 1999d), this solution is not the first option of the management entities of the railway European infrastructures with exception of the UK, Switzerland and Holland. These are reinforced concrete structures buried in the transition zones and have, normally, a length between 3 and 8 meters and a thickness between 20 and 30 cm. In the case of a transition zone embankment-bridge, a slab end supports over the abutment of the bridge and other directly on the embankment, over columns, or even a foundation built for this effect. The mains functions of this structure consist of eliminating the space that can be developed between the structure and the embankment, avoiding the degradation of the ballast layer, and also accommodates the differential settlements that can develop between the structure and embankment. This solution can also contribute to the proper drainage of the water (ERRI,1999). As expected, proper compaction of the embankment before the installation of the transition slab is very important to avoid settlements under the slab (taking special care with the drainage) and consequently the voids that can appear that would compromise the correct functioning of this solution (ERRI, 1999a, ERRI, 1999b, ERRI, 1999c, ERRI, 1999d). According to Sharpe (2002), over the concrete slab and between this and the embankment zone, a wedge of granular material must be built, reinforced with geogrids next to the slab support at the embankment to reduce the effect of discontinuity in this area. Moreover, the application of flexible railpads placed over the transition concrete slab and the embankment of the bridge can be also purposed. Furthermore, it is also important to ensure that the effects of variation of temperature do not introduce additional effort into the slab.

a)

b)
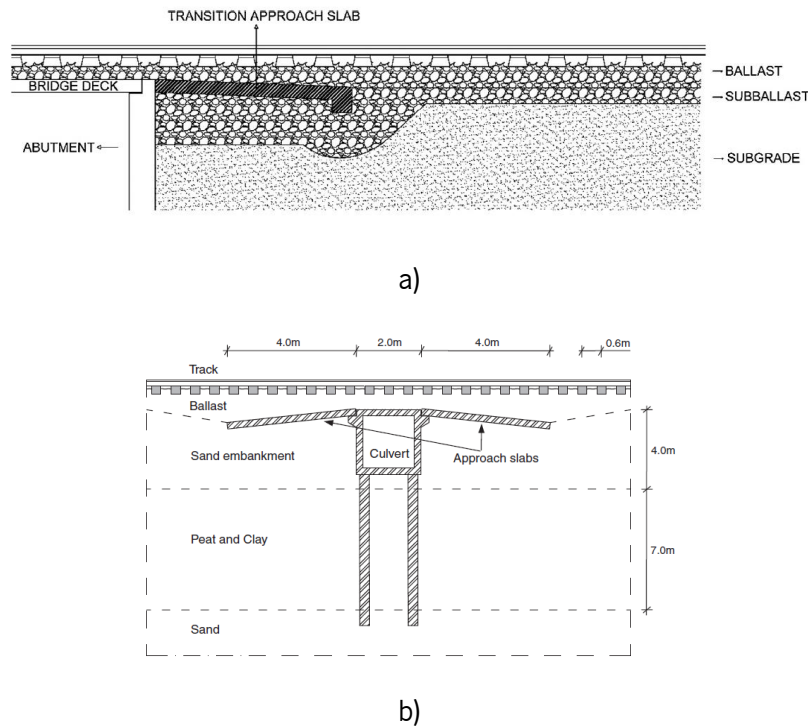
Figure 3.23 – Examples of the installation of an approach slab: a) combination of superstructure solutions for track transitions (Sañudo et al., 2016a); b) approach slab (Coelho et al., 2011)

On the other hand, to soften the stiff side, elastic pads can also be used between the sleepers and the rail to reduce the dynamic load applied on the track in the stiff area (Banimahd et al., 2012). The variation of the stiffness of the elastomers and the use of resilient components as resilient mats are also methods used to mitigate the abrupt change in stiffness (Real et al., 2016). Indeed, the under sleeper pads (USP's) can also be applied to mitigate the problems associated with transition zones because they can reduce the ballast degradation, enabling that the stiffness on the stiffer side (concrete deck) to match the softer (ballasted track) side, minimizing the dynamic load impact (Figure 3.24). However, the placement of the USPs on the ballasted track at bridge approaches may not be that effective in reducing the stiffness variation. Indeed, it makes the softer side of the bridge transition even softer (Nicks, 2009). However, this technique can reduce the ballast stresses significantly due to the increase in the sleeper-ballast contacts, which leads to a reduction in ballast degradation (Navaratnarajah et al., 2018).
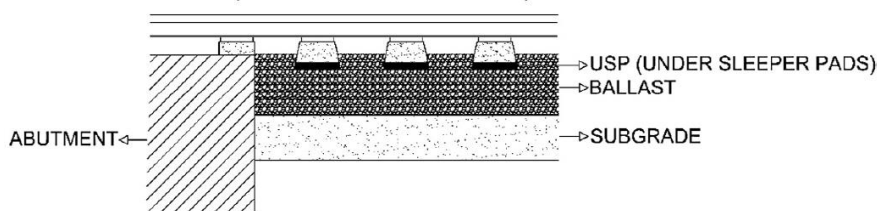
Figure 3.24 –USPs – under sleeper pads (Sañudo et al., 2016a)

Another approach used to smooth the stiffness is the use of wedge-shaped backfills (Figure 3.25). Indeed, this option is often used close to bridges, tunnels, or inferior crossings. The *Japanese Railways* was one of the first to incorporate the wedge-shaped transition zones in the backfills of bridge abutments for HSLs. Furthermore, in the 1970s, the SNCF also recommended wedges built with cement-bound granular mixtures. This technique is highly dependent on the materials selected (due to the high variety of materials' characteristics, which includes the resilient modulus or cementation, etc.) used in the transition wedge and its geometry (in terms of thickness, slope, layer distribution). Regarding this technique, there are two types of wedge-shaped backfills: technical blocks type 1 usually applied at the approach to larger structures (bridges, viaducts and underpasses) and technical blocks type 2 (culverts) (Paixão et al., 2016). The wedge-shaped backfills (also called transition wedges and/or technical blocks) are defined as well-compacted layers of selected granular materials. Thus, with this approach, it is possible to have a gradual transition from soft to stiff material in the transition zones (Indraratna et al., 2019) since creates a gradual transition in the vertical stiffness value between the embankment (built with common/traditional geomaterials) and the stiff structure such as a bridge. The materials used in the wedge usually show higher deformability moduli and are less sensitive to permanent deformation than the traditional geomaterials. For that reason, layers of unbound granular material (UGM) and cement-bound granular mixtures (CBGM) are frequently used in backfills. The technical blocks are, in general, composed of two parts, a wedge of granular material treated with cement and another wedge of the same non-treated materials. The treated material is placed between the abutment of the bridge and the wedge of the non-treated material. Besides the reinforcement introduced on the material of the technical block, it is also usual to reinforce the layers of the track in the transition zone (Alves Ribeiro, 2012).

However, generally, the transition shows poor performance. This can be justified by the faulty execution of the backfill (mostly due to the use of less suitable materials), inadequate compaction layers and poor drainage conditions. This poor performance can occur in both old and new railway lines (Paixão et al., 2013). In fact, currently, there is no universal standard for the design of a transition wedge, which means that different countries choose their own set of parameters (Indraratna et al., 2019). The solutions proposed by different entities in Europe are different between them such as the case of Germany, France, Italy and Spain.

a)

b)

c)   d)
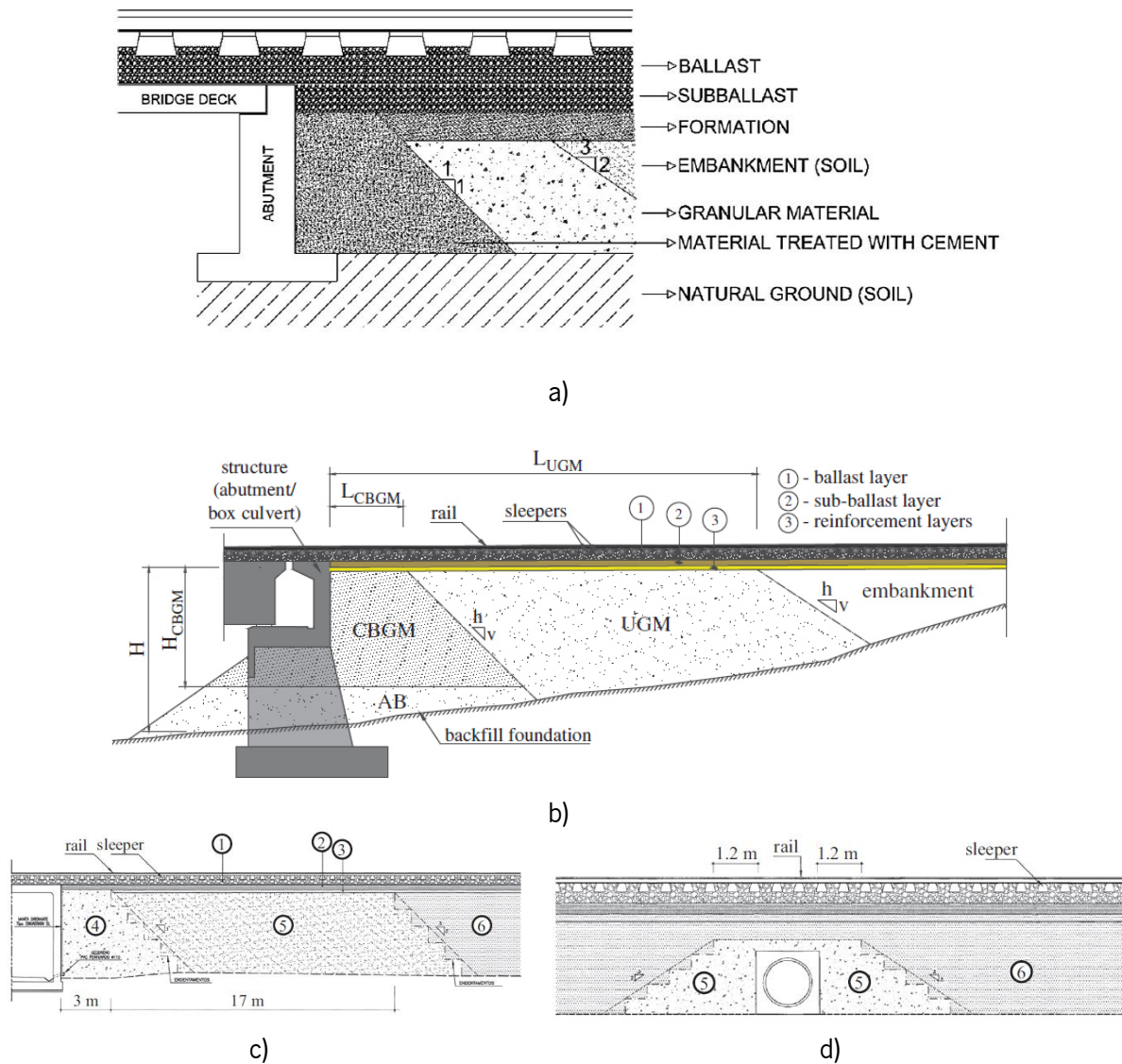
Figure 3.25 - Track transition wedge design: a) track transition wedge design for high-speed lines (based on ADIF standards) (Sañudo et al., 2016a); b) schematic design of a wedge-shaped transition zone (Paixão et al., 2013); c) technical block type 1 (BT1); d) technical block type 2 (BT2) where: 1- ballast; 2- sub-ballast; 3- capping; 4 – cement bond mixture (CBM) with binder content (BC) of 5%; 5 – unbound granular material (UGM); 6 – embankment with soils (Paixão et al., 2016)

Other mitigation measures can be found in Namura et al. (2004), Namura and Suzuki (2007) and Read and Li (2006) and include the concept of piles and stone columns that can also be used in transition zones, as is depicted in Figure 3.26. Furthermore, the injection of cement grouts allows for improving the mechanical properties of the soils. This solution is generally applied as a corrective measure in cases where there are significant deformations in transition zones. Thus, the definition of the local, dimension of the hole size and the pressure of the injection are some of the aspects to be considered to obtain the strength and deformability intended. Moreover, it is also important to control the deformation in the intervention zone, which includes the monitoring of the displacements before, during and after the injection.
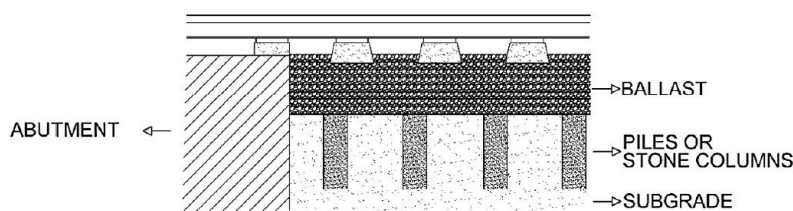
Figure 3.26 - The concept of piles and stone columns used on transition zones (Sañudo et al., 2016a)

Thus, from the list presented above about the several mitigation measures, it is important to highlight that most of the approaches used to improve the performance of transition zones are mainly focused on either increasing the stiffness of the track, increase the stiffness within the transition zone, or reducing the support stiffness on the substructure. In fact, all the approaches intend to create a smooth variation in support stiffness between the free/normal track and the substructure (Coelho et al., 2011). However, the design of transition zones should be based primarily on minimizing potential track fouls and permanent deformation of the substructure (Banimahd et al., 2012).

3.2.9   Numerical models developed to study the transition zones

In recent years, Infrastructure Managers and researchers have been dedicating their efforts to understanding the dynamic behaviour of the train-track interaction system at track transition zones through the development of simulation studies based on analytical or numerical models (Dahlberg, 2010).

The type of model and the modelling software/program influence how reliable and accurate is the dynamic response of transition zones. Indeed, there are several variables/parameters to be selected, which includes: (i) the type of analysis required (static or dynamic), (ii) the inclusion of non-linearity and plasticity of the material, (iii) the calculation time, and (iv) the expected outcomes (Indraratna et al., 2019). Likewise, the modelling of the vehicle is also complex and can or not include the various masses (unsprung and semi-unsprung). The type of modelling can also help to obtain a true dynamic response of track structure. Thus, Shan et al. (2017) state that to comprehensively investigate the dynamic response of the completed system, fully vehicle track-subgrade coupled models should be developed. Furthermore, some of the models developed throughout the years were only focused on the dynamic response of the track components and the subgrade on transition zones. This is the main reason for the development of models based on the track-subgrade systems (Sheng et al., 1999, Dahlberg, 2003, Andersen et al., 2007, Gallego Giner and López Pita, 2009, Bian et al., 2011, van Dalen et al., 2015) implemented to investigate the influence of the material parameters and configuration of the transition zones on the dynamic response of the track-subgrade system. In this case, the track components and the subgrade are treated as a continuous medium and the wave propagation in the track and the subgrade

can be well simulated. In this case, the vehicle-track interaction cannot be simulated (Dimitrovová and Varandas, 2009, Dahlberg, 2010, Shan et al., 2013, Coelho and Hicks, 2015) and the vehicle is modelled as moving loads.

Thus, the choice of models depends on the complexity of the analysis and the required precision. 2D models are incapable of modelling the train load distribution in a transversal direction but are faster. A 3D model can overcome the limitations of the 2D models but the time of analysis is higher.

As described below, there are several computational studies about transition zones (Lundqvist et al., 2006, Dimitrovová and Varandas, 2009, van Dalen and Metrikine, 2008). In the first years of research about transitions and its modelling, Tayabji and Thompson (1977) conclude that the use of finite-element enabled to include proper material characterization, which is an essential property to reproduce the transient response of the railway track. Due to the complexity of the 3D models, the authors divided the analytical calculation into two stages: longitudinal analysis stage and transverse analysis stage. Later, in the 1990s, Hunt (1996) presented different models to simulate the track in transition zones: 1) infinite track on Winkler foundation with properties varying with time; 2) series of track segments, each on a Winkler subgrade and each with different values of subgrade stiffness; 3) finite-element model of the track, enabling continuous variation of the properties of the track and the subgrade. The extremities of the model are contiguous with semi-infinite beams on a Winkler-subgrade.

The first most recent studies in the scope of the transition zones were developed by Lei and Mao (2004), Lundqvist et al. (2006) and Seara and Gomes Correia (2010). They differ in terms of vehicle modelling (whole locomotive, moving wheelset that simulates the load of the axle, etc.), track modelling (3D solid elements, rail modelled as a beam with finite length, etc.), consideration or not of the train-track interaction and type of transition. More recently, other types of models were developed considering the track modelled as a beam supported by a foundation with sudden stiffness change (Dimitrovová and Varandas, 2009). Thus, these models evolved, as well as its complexity such as the model developed by Varandas et al. (2011). The authors developed a numerical model focused on the development of dynamic loads on the ballast due to the passage of the trains in a transition (to and from a culvert founded in piles and on switches) also considering the long-term deformation. The model was validated against field measurements and included the determination of the initial state of the track based on its vertical level (first stage). In this model, the train moves with constant speed, symmetry along the longitudinal axis of the track was assumed, the sleepers were equidistant and the stiffness of the support of the sleeper was non-linear. Moreover, the author assumed that the sleepers could be hanging, the contact

between the sleeper and the ballast could be lost, the ballast around sleeper generated friction damping and the vibration of the sleeper contacting the underlying ballast generated radiation damping and the influence of the motion of the hanging sleeper on the friction damping was neglected. The modelling corresponded to one-dimensional model of a beam on Winkler foundation and presented some limitations: the subgrade and the foundation of the track were simplified as layers of mass, springs and dampers; the support stiffness of the track cannot be correctly simulated; and the wave propagation in the subgrade cannot be considered. From this knowledge, Varandas et al. (2013) present a methodology to predict the settlement of the track due to train loading in transition zones, estimating the loss of the vertical geometry of the track over time (Figure 3.27 a). The methodology presented is based on (non-linear) train-track interactions and an incremental settlement model. The settlement of the track is decomposed into two parts: due to the ballast and due to the subgrade. The train is modelled as an assembly of rigid bodies connected by spring and dampers (with 10 degree-of-freedom) and the track is modelled with a one-dimensional Winkler type model (the symmetry along the track is assumed in the longitudinal axis), as shows Figure 3.27 b). The two systems are coupled through the interaction forces between the rails and the wheels using the non-linear *Hertzian* contact theory. Regarding the methodology, firstly, the dynamic response of the track is obtained and, after that, the deformation in the ballast and subsoil by separate models is also determined (the permanent deformation is modelled by two different empirical models due to the nature of the materials).

a)   b)
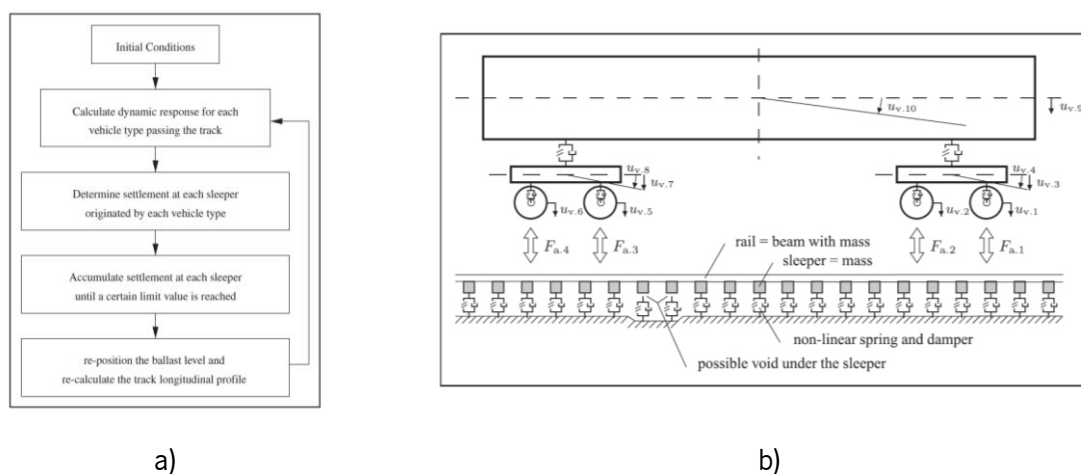
Figure 3.27 – a) Methodology for calculation of track-level degradation; b) Train–track interaction model: $u_{v,i}$ is the *i*th degree of freedom of the vehicle and $F_{a,j}$ is the interaction force between wheel *j* and the rail (Varandas et al., 2013)

More recently, Varandas et al. (2016) developed a numerical model to study a transition of a railway passage over a box-culvert. In the modelling, some options were selected such as the fact that the soil under the approach slabs (close to its support at the box-culvert) would not contribute to the support of

the approach slab. The results show that the long-term motion and slope angle of the approach slabs are important for the increase of the settlements of the ballast over the approach slabs.

Thus, despite the importance of the 3D models, some works developed interesting 2D models to characterize and study the behaviour of a transition zone, as showed previously. In this sense, Paixão et al. (2014) investigated a specific transition to a railway bridge. The work presents a 2D numerical model calibrated and experimental validated with data monitored in the field. The results show that there is an increase in the track stiffness as the train approaches the bridge abutment due to the presence of a backfill constituted of bound and unbound granular geomaterials. Because of the smooth transition, no significant variations were observed on the train-track interaction forces.

In the work developed by Alves Ribeiro et al. (2018) also related to the work developed by Paixão et al. (2014), dynamic analyses were performed through explicitly methods using a 3D model developed in LS-DYNA (Figure 3.28 a) but also implicitly methods using a 2D model developed in ANSYS software. In this work, the authors tried to calibrate and performed experimental validation of a dynamic model of a train-track system at a culvert transition zone (Figure 3.28 b). In both analyses (2D and 3D), contact algorithms were employed to consider the wheel-rail interaction (though the penalty method). The parameters for the 3D model were calibrated based on track receptance tests. In this case, the 3D model was used for the static and dynamic calibration of the 2D model. This method presents obvious advantages regarding the reduction in the calculation time. The results showed that the damping of the 2D models must be amplified to compensate for the radiation damping in the transverse direction of the track since this phenomenon is not reproduced in a plane model.

a)   b)
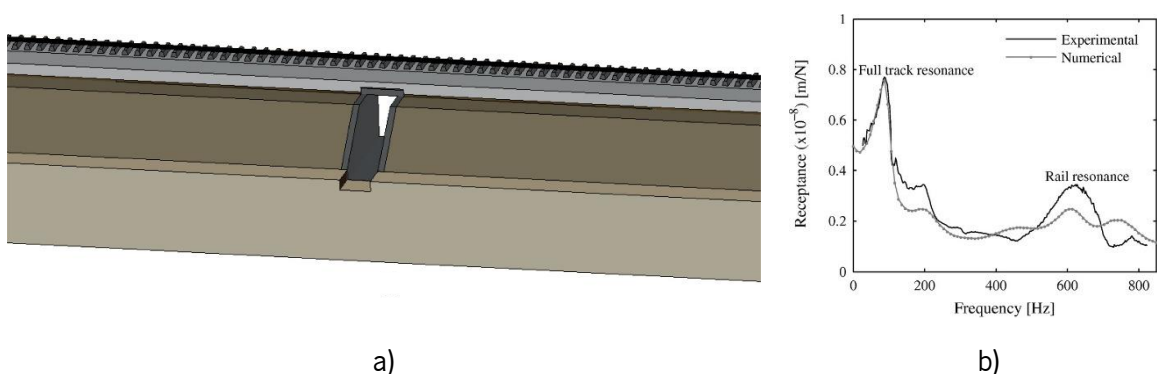
Figure 3.28 – a) 3D model of the transition zone: perspective; b) Comparison of the experimental and numerical receptance functions (Alves Ribeiro et al., 2018)

Shan et al. (2017) developed a plane stress finite-infinite element model of a high-speed railway subgrade-bridge transition zone with high computational efficiency (Figure 3.29). This study analysed the influence of 2 simultaneous varied subgrade material parameters on the dynamic response of the vehicle-track

subgrade system in a railway transition zone with a ballastless track. In this model, the behaviour of the ballastless track with an inverted trapezoid transition zone (which is recommended in code for the design of a high-speed railway in China) is simulated. The results provide the basis for determining the material parameters of the transition zone filler and for optimizing the stiffness matching of the transition zone components. This study can help guide the design and construction of the transition zone. To validate the vehicle-track-subgrade model, data from *in situ* tests from a ballastless track on a transition zone of the high-speed railway line between Beijing and Shanghai were used. The coupling of the vehicle and the track was simulated through the wheel-rail contact force (Shan et al., 2017).
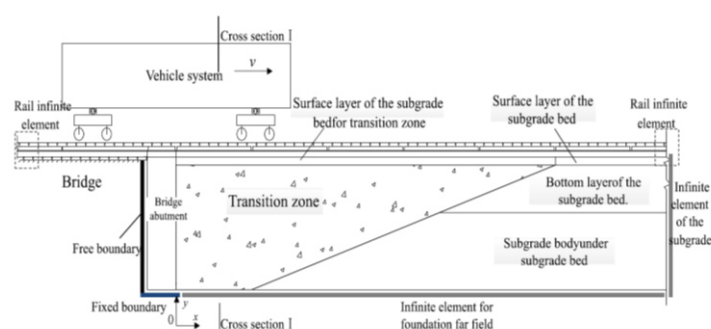
Figure 3.29 – Vehicle-track-subgrade model of the inverted trapezoid transition zone (Shan et al., 2017)

Galvín et al. (2010) used a different approach from the 2D models and developed a fully three-dimensional multi-body-finite element-boundary element model (formulated in the time-domain) to predict the vehicle-track-soil-structure dynamic interaction and the vibrations imposed by the system. The vehicle was modelled as a multi-body system (the quasi-static and dynamic excitation mechanisms were considered), the track components were simulated by finite elements and the boundary element method was used to simulate the foundation soils. This methodology can be used to take into account local soil discontinuities and underground constructions (such as underpasses). The non-linear behaviour was also considered. The numerical model was validated through the experimental records from two HST lines. The transition zones between a ballasted track and ballastless track were also analysed,

Mishra et al. (2014) also implemented a different modelling strategy to investigate an integrated approach that includes the calibration of numerical models using data from track instrumentation performed at the bridge approach. The loading profiles obtained in the numerical model were used as input for a numerical simulation using the concepts of the DEM (discrete element method) to predict individual particle acceleration within the ballast layer.

Regarding the 3D FEM modelling, several authors used this numerical approach to study the behaviour of the structures on transition zones.

Indeed, Banimahd et al. (2012) used different strategies to evaluate the transition zones. The first one includes a train-transition curve model (simulating the response of the train to deflection changes in the vicinity of transition zones). In the second approach, the authors modelled the transition through a three-dimensional finite element model (Figure 3.30). Two train models were considered: quarter coach and full coach. The train models include the primary and secondary suspensions, masses of wheel, bogies, and coach. The transition includes the train movement from a subgrade to a rigid base (representing a tunnel concrete slab track or bridge abutment) of a ballasted track, using Zhai's explicit integration method. In these analyses, the passenger comfort and train-track interaction force were investigated for different train speeds and track properties (softer subgrade soil and higher train speeds can increase the interaction force and after the passenger comfort). As a result of the analysis, the authors concluded that the design of the transition zone should be based on minimizing potential track faults and permanent deformation, rather than simply providing a smoother track stiffness change.
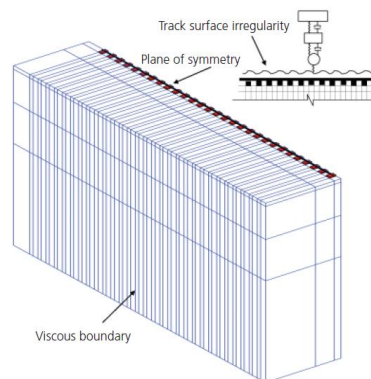
Figure 3.30 - Representation of coupled finite-element train–3D track model; a quarter train in interaction with track model is shown (Banimahd et al., 2012)

Shan et al. (2013) study the dynamic transition properties of two types of transition configurations implemented in HSL's in China through the implementation of a three-dimensional finite element (Figure 3.31). The track-subgrade is simulated by a three-dimensional finite element model. However, the vehicle-track system is not included. Certainly, a moving load cannot capture the vehicle–track interaction behaviour. This is a major limitation of this analysis. However, the simulation of the track components and the subgrade in this model (represented by three-dimensional finite elements) is more realistic than the state-of-the-art simulation of the vehicle–track system (represented by layers of springs and dampers). With this work, the authors conclude that: a) a longer transition length leads to better dynamic performance; b) the most important criterion is the vertical stress of the subgrade; c) the dynamic response of the two-part transition is better than that of the inverted trapezoid transition; d) the dynamic

response of the track-subgrade system changes abruptly in the first 3m of the transition zone; w) auxiliary rails were installed on transitions zones to reduce the dynamic response of the track-subgrade system.

| a) | b) |
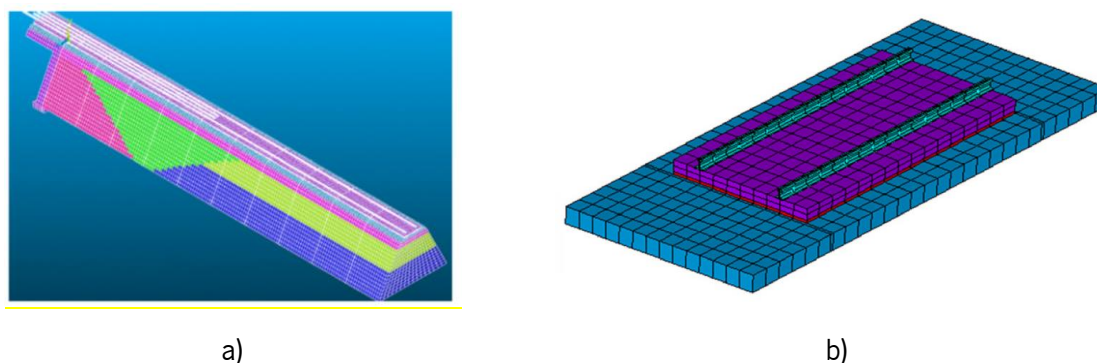
Figure 3.31 – a) Finite element model of the two-part transition section with additional rails; b) ballastless track structure (Shan et al., 2013)

Huang and Brennecke (2013) also developed a three-dimensional sandwich model to study and compare different stiffness transition scenarios properly (Figure 3.32). This model consists of a discrete tie support system and a three-dimensional (3-D) subgrade. This means that the subgrade is discretized by a finite element mesh. The obtained results showed that the transition zone decreased the tie–ballast contact force. An increase in speed will increase the tie–ballast contact force both with and without the transition zone. The study shows that a longer exponentially increasing stiffness transition zone was proved to be better in terms of decreasing the tie–ballast contact force than was the linearly increased transition zone.
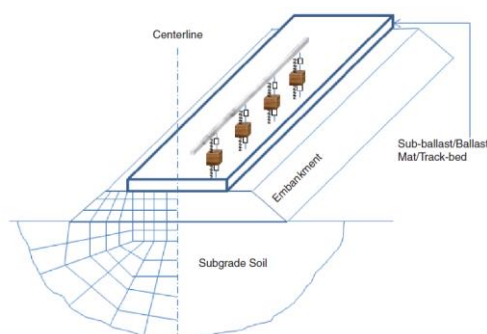
FIGURE 1   Three-dimensional sandwich track model for high-speed rail.

Figure 3.32 - Three-dimensional sandwich track model (Huang and Brennecke, 2013)

In the work developed by Shahraki and Witt (2015) and Shahraki et al. (2015), the FE method was used. A 3D finite element model was developed in software Midas GTS NX to analyse the behaviour of a transition zone under the passage of high-speed trains. The model included a transition between a ballasted track and a ballastless track characterized by the *Rheda* system (Figure 3.33 a). The train load was modelled as a sequence of discrete/stationary pulse loads at rail nodes with a time-dependent modulus. In this analysis, the symmetry of the model (loading is symmetrical, and half of the model was

111

used to decrease the number of elements) was adopted to reduce the calculation time. Regarding the boundaries, the elastic/viscous boundary elements were implemented as ground surface springs for dynamic analysis. At the bottom of the model, fixed conditions were adopted, simulating the bedrock conditions. In this paper, two mitigation measures were studied: auxiliary rails (Figure 3.33 b) and implementation of longer sleepers applied on the ballasted section to increase the track stiffness. The simulation showed better results of the model with the installation of the auxiliary rails (Shahraki and Witt, 2015).

a)   b)
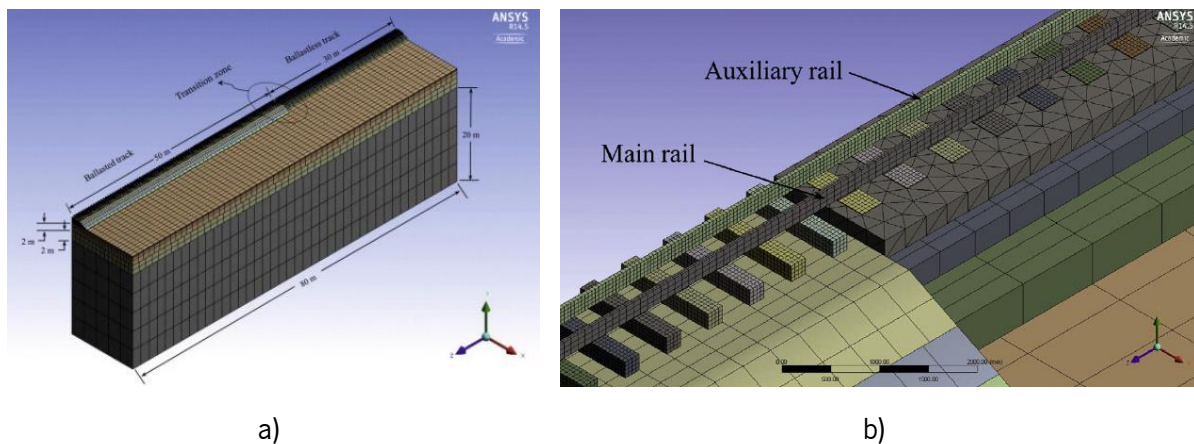
Figure 3.33 – a) Transition zone model without any improvement; b) Modelling of the mitigation measure installation of auxiliary rails (Shahraki et al., 2015)

Real et al. (2016) analysed two different transitions between three different track typologies: ballasted track, concrete slab track and asphalt slab track (Figure 3.34). The transition has already been designed and executed on a real track. The field accelerations registered were used to develop a 3D FEM model to study the first transition (asphalt slab track to concrete slab track) and the second transition (ballasted track to asphalt slab track). The second transition also considered closer sleepers in the ballasted track in the vicinity of the transition zone to obtain an increase of the stiffness (however this can bring some difficulties in the tamping operations). This work also presented three different methods that exist in the literature used to achieve a stiffness transition: implementation of additional/auxiliary rails in the ballasted track, variation of the stiffness of the elastomers and placement of a resilient mat in the infrastructure.

In the work developed by Sañudo et al. (2016a), the author highlighted that comparing the studies on the short-term behaviour of transition zones, to the studies on the long-term behaviour of transition zones, the last ones are relatively lacking.

Figure 3.34 – Detail of the stretch of asphalt slab track (20 m) inserted between the previously existing concrete slab track and ballasted track (Real et al., 2016)

To overcome this problem, in the work developed by Wang and Markine (2018a), a methodology is purposed to simulate and predict the accumulated settlement of the track in transition zones, through an iterative process. The methodology was based on a FE method, which included the vehicle-track and sleeper-ballast interactions. The simulations were performed using a 3-D dynamic FE model (using explicit integration) of a track transition zone. The stress results were after used as input in the empirical permanent deformation model. The iteration scheme is demonstrated by calculating the track settlement in the transition zone for 60,000 loading cycles, or 3.5 MGT (Million Gross Tonnes). Wang and Markine (2018b) also presented a methodology for the analysis of a track transition zone, which comprises experimental analysis, short-term numerical analysis, long-term numerical analysis (Figure 3.35) and design variation analysis. According to the authors, the methodology for the comprehensive analysis of the track in transition zones should include:

1) An advanced measurement technique using DIC (Digital Image Correlation) – a device used to measure the dynamic displacements of rails at multiple points along the track in transition zones. This measurement technique is capable of evaluating the current condition of transition zones.

2) A FE (Finite Element) model of transition zones – considers the stiffness variation and differential settlement at the same time. The model should be capable of simulating the realistic settlement curve of rails, the hanging distance of sleepers, and therefore, it can study the short-term responses of transition zones during passing trains, e.g. ballast stress and vehicle dynamics.

3) An iterative procedure to predict the track settlement in transition zones, combining the FE model of transition zones and an empirical settlement model of ballast. Using this procedure, the long-term behaviour of transition zones can be explored.

113
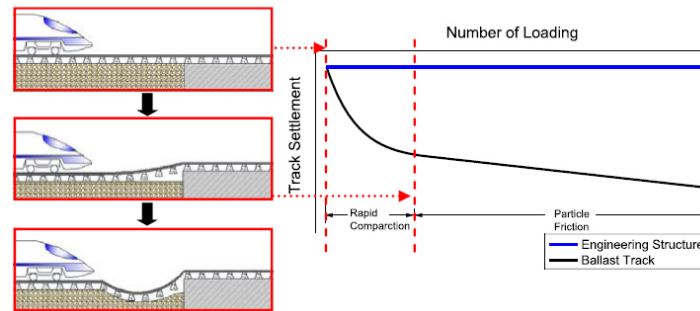
Figure 3.35- Schematic diagram of the track settlement (long-term) in transition zones (Wang and Markine, 2019)

More recently, in the work developed by Wang and Markine (2019), a 3D finite element model (explicit calculus) was developed in LS-DYNA software to study the phenomenon of the hanging sleepers. The modelling presents a particularity regarding the inclusion of the rapid compaction of the ballast after a few months of operation (while the track on engineering structure barely settles), which leads to the appearance of hanging sleepers. This phenomenon is modelled by the inclusion of non-linear contact elements between the sleepers and the ballast. Furthermore, contact elements are also used between the wheel and the rail (through the penalty method). The FE model includes three main parts: two ballasted tracks on the embankment and a ballastless track on a bridge. As a matter of fact, the bridge is symbolic, and it is not analysed (the bridge is simplified to reduce the calculation time). Despite the non-linear behaviour of the ballast, all the materials are modelled with linear elastic models since, in the case of the ballast, it is assumed that this material has been compacted after the rapid compaction stage. The differential settlement on the ballast is modelled by the application of downwards displacements only on the ballast layer. The bridge remains unchanged. The validation of the model includes three important parts: vehicle-track model, transition zone with settlement (using the field measurements) and the car body acceleration.

A summary and comparison (computational modelling) of most of the models developed to study the transition zones are summarized in the work developed by Indraratna et al. (2019), where is included the information about the author, the type of model (2D, 3D, etc.), the numerical method (FEM – finite element method -, DEM – discrete element method), software used, the analysis type (static, dynamic or quasi-static), the beam type (Timoshenko, Euler-Bernoulli, Hughes-Liu, simple-beam or rectangular beam) and also the modelling of foundation layer (linear elastic, non-linear elastic, linear visco-elastic, non-linear visco-elastic and elastoplastic). Furthermore, the work also includes information about the model calibration, model validation, transition type, train speed, axle load, parameters studied, train direction, mitigation measures studied and factors for transition zone design considerations (Figure 3.36).

114
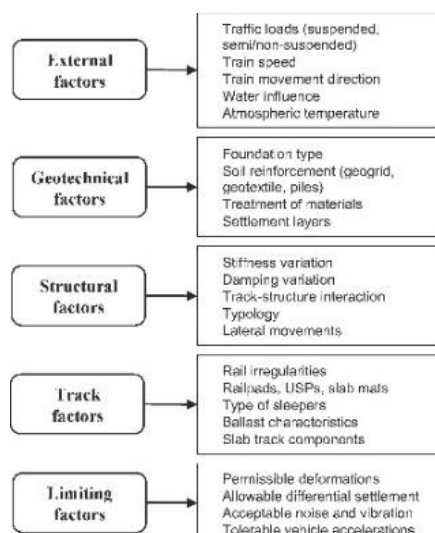
Figure 3.36 - Summarised important factors for transition zone design considerations (Indraratna et al., 2019)

3.2.10 Experimental measurements performed on transition zones

The monitoring can be an extremely useful tool, especially in transition zones where the performance of the railway structures raises significant doubts. Despite the importance of long-term monitoring, little work has been developed in this area and, it is, therefore, a field that is still little explored (Alves Ribeiro, 2012).

According to Indraratna et al. (2019), several instruments can be used to measure or investigate the response of rail track at transition zones in real-time scenarios: multi-depth deflectometers (MDD), uniaxial and triaxial accelerometers, strain gauges, pressure cells, settlement pegs, video gauge systems, position sensitive devices, geophones, inclinometers, linear variable displacement transducers (LVDT's), among others (Indraratna et al., 2014, Zuada Coelho et al., 2017, Boler et al., 2018, Paixão et al., 2018, Wang and Markine, 2018b). Furthermore, the measurement of the variation of the vertical stiffness along the track is probably the most common strategy used to monitor the performance of the transition zones (Li and Davis, 2005, FRA, 2007, Li and Berggren, 2010). This type of study is very useful since allows determine the magnitude of the stiffness's variation in certain zones of the track, identifying the places where more localised monitoring may have higher interest.

The experimental measurements in transition zones are extremely important to understand the phenomenon but also because this type of information is scarce. Indeed, despite the efforts undertaken to minimize the track transition zones problems, these areas continue to exhibit poor performance and a significant amount of maintenance is required (Wang et al., 2017a).

The techniques and procedures used in the monitoring of the transition zones are, in general, the same used in the monitoring of full track. The techniques with more interest are:

- Determination of dynamic displacements of the track due to the train's passage;

- Installation of accelerometers or geophones in the rails and sleepers;

- Determination of the dynamic loads and reactions under the sleepers through the instrumentation of the rail with extensometers;

- Determination/measurement of track displacements using a contactless system named PSD (position sensitive detector). This system was already applied in an embankment/underpass transition zone (Pinto et al., 2015)

- Determination of the stresses in-depth, in the different layers of the track (analysing not only the vertical but also the horizontal stresses);

- Monitoring of the vehicles in movement using accelerometers strategically placed.

Ideally, the proper monitoring of the transition zones should be performed in the field. The performance of these studies in the laboratory always leads to some doubts about the obtained conclusions since the reproduction of the real field conditions is very complicated if not impossible. One interesting option could be the simulation of the transition zones through the use of reduced-physical models. Furthermore, the monitoring of areas already degraded (where the problems are already identified) is even more complex (Coelho et al., 2011). Thus, it is advisable to install the instrumentation during the construction phase.

In the calibration of the numerical models used on the simulation of the short and long-term dynamic behaviour, the results from the monitoring could be very important.

Thus, in the work developed by Coelho et al. (2011), extensive monitoring and investigation program was undertaken in a typical transition zone. This monitoring included the reinforced concrete approach slabs linking the normal track onto a concrete culvert. Furthermore, to complete the plan, the track settlements and pore water pressures were also monitored over a year.

In the work developed by Wang et al. (2017a), the results regarding the experimental analysis performed in three transition zones were presented. The monitoring included the measurement of the dynamic displacements of the rails at multiple points in the approaching zones. These measurements were performed through a digital image correlation technique. The study focused on several aspects such as the length of the approaching zone, the dynamic profiles of the rail displacement in the embankment-bridge and bridge-embankment and the dynamic profiles of the transition zones in several conditions.

Paixão et al. (2016) developed an investigation regarding the geometry data (track geometry quality) to be integrated into the numerical analysis. The data was obtained considering the longitudinal level of the

track of the *Alcácer* bypass located in Portugal (left and right rails). In some studies performed (based on calibrated and validated models with field measurements), the uneven longitudinal profiles were imposed on the top nodes of the ballast layer (on which the track settled due to gravity force after an initial stabilization).

Previously, in the work developed by Paixão et al. (2015), the influence of using USPs at transition zones to underpasses was investigated. As mentioned previously, the USP reduces the sleeper–ballast contact stresses, slow track degradation and can be used to control stiffness variations (Alves Ribeiro et al., 2015). This impact of the USP on transition zones was evaluated by comparing two similar box-culvert transitions: one with the implementation of USPs in 44 sleepers and the other without USPs – standard/reference track. The track characterization was performed through the results of non-destructive tests (LFWD test at the centre of the sleeper and receptance tests). Furthermore, the measurements of the track response due to the passage of trains were also analysed. The results indicated that USPs influence the dynamic behaviour of the track, increasing its vertical flexibility and amplifying both rail displacements and sleeper accelerations. To fill the gap between numerical and field studies, the authors used finite element method models (2D), calibrated and validated with field measurements to study and confirm the advantages of the use of USPs. These models considered the train track interaction and included all relevant track components, substructure layers and backfill geomaterials. According to the authors, the main advantage of these 2D models is that they still provide accurate results, even though they require less computational resources than the 3D models used in other studies of the transition zones. The authors concluded that the stiffness of the USP should be carefully determined for each transition zone before installation (Alves Ribeiro et al., 2015). Indeed, within this scope, Insa et al. (2013) focused their investigation on the combination of transition zones and the implementation of under sleeper pads through the inclusion of the dynamic vehicle-track interaction by synthesising a series of sub-models of individual effects. The analysis performed allowed the consideration of several track configurations and train travelling speeds. The stiffness of the USPs was investigated and the obtained results showed that the use of USPs in transition zones allows a more homogenous vertical stiffness along the track, improving the dynamic behaviour of the vehicle-track system.

In the work developed by Indraratna et al. (2019), the authors present a summary of the main outcomes of field measurements on track transition zones, which includes information about:

- the description of the transition zones: wedge-shaped backfills, auxiliary rails, soil reinforcement with piles, hot mix asphalt wedge/layer, under sleeper pads, rail pads, backfill confinement with

117

walls, concrete wedge/slab, approach slab, soil reinforcement with geogrid, wider sleeper, longer sleeper, resilient sleepers, changing the material of sleepers, sleeper spacing/location, moisture content effect, steel bars and hydraulic sub-base;

- the transition type: ballasted track on the rock, ballasted track on soil, ballasted track on the concrete deck, ballastless track on rock, ballastless track on soil, ballastless track on the concrete deck, ballasted track on the concrete culvert, ballasted track on a concrete viaduct);

- the transition length;

- the train speed;

- the loading;

- the train direction: soft to stiff and stiff to soft;

- The track-type: passenger track, freight track, mixed traffic/track;

- The parameters studied, such as the vertical displacement/deflection, track velocity, track acceleration, ballast/subgrade stresses, wheel load, track modulus, rail deflections, railpad force, contact force, or ballast particles acceleration;

- The instrumentation used: multidepth deflectometers, strain gauges, LASER units, position sensitive devices, accelerometers, linear variable differential transducer, video gauge system, video cameras, geophones, inclinometer tuber, survey equipment, track loading vehicles;

- The main outcomes.

3.2.11 Regulatory limits defined by the standards

In the scope of the transition zones there isn't specific regulation regarding its design, which means that, whenever necessary, it is usual to adopt reference limits using the regulations of different areas: geotechnics, bridges, or track.

The limits defined in the standard EN1990 - Annex A2 (CEN, 2005), regarding passenger comfort can be applied to verify the performance of the transition zones. According to this standard, different levels of passenger comfort are defined based on the acceleration on the interior of the carriages, when the train moves in the approaching zone of the bridge, over the bridge and its exit. Table 3.2 presents the limit values of the acceleration considering different levels of comfort.

Table 3.2 – Limit values of acceleration in the interior of a carriage according to the level of comfort (adapted from CEN (2005)

Comfort level	Vertical acceleration (m/s^2)
Very good	1.0
Good	1.3
Acceptable	2.0

118

Furthermore, López-Pita et al. (2006) present, beyond the acceleration limits on the vehicle body, limits for the vertical accelerations of the axles of the vehicle (Table 3.3). These limits were defined for the high-speed line *Madrid-Sevilla* based on the experience of SNCF (*Société Nationale des Chemins de fer Français*).

Table 3.3 – Vertical acceleration limits of the axle of the vehicle (adapted from López-Pita et al. (2006))

Vertical acceleration of the axle (m/s²)	Recommendation
a < 30	Normal control
30 < a ≤ 50	Careful control
50 < a ≤ 70	Programming correction
a > 70	Immediate correction

The UIC (2005) specifies the admissible limits of the vertical alignment of the track for vehicle testing, by defining three levels of quality: QN1, QN2 and QN3. Table 3.4 shows the maximum isolated defect values in the vertical alignment to be respected, according to the circulation speed and considering wavelengths between 3 m and 25 m.

Analysing Table 3.4, the defect QN1 refers to values that need some care and are integrated into regular maintenance actions, QN2 refers to values that require short-term maintenance and QN3 refers to values which, when exceeded, imply the interruption of that section of the line, being QN3 equal to $1.3 \times$ QN2.

Table 3.4 –Definition of isolated maximum defects in vertical track alignment for different quality levels, depending on circulation speed (adapted from UIC (2005))

Circulation's speed (km/h)	QN1 (mm)	QN2 (mm)
V ≤ 80	12.0	16.0
80 < V ≤ 120	8.0	12.0
120 < V ≤ 160	6.0	10.0
160 < V ≤ 200	5.0	9.0
200 < V ≤ 300	4.0	8.0

3.3   Final considerations

In this Chapter, the main concepts and problems related to the transition zones are presented. These are very specific zones of the railway lines but are one of the main concerns of the railway Infrastructure Managers due to its more accelerated degradation process, which implies higher costs and maintenance operations.

Thus, this Chapter synthesises the work developed in this field, which includes important topics such as the methods used to mitigate the problems on transition zones or even the extensive works developed in

the scope of the numerical modelling applied to study these areas. From this research, it is possible to conclude that there is still no method that generates an absolute consensus between the researchers and railway Administrators. Each mitigation approach presents advantages and disadvantages. Some methods are more popular due to the satisfactory results in some situations and particular conditions. For example, the installation of auxiliary rails is a popular approach but the most popular is the implementation of a transition wedge. However, there is no universal standard for this approach which means that there is a set of different solutions developed by different countries, including within Europe. For example, Germany, France, Italy and Spain propose different solutions for this specific mitigation measure. Furthermore, this method is also very dependent on the errors that may occur during the construction in terms of compaction and drainage, which may decrease its efficiency, increasing the lack of consensus and preventing the definition of a common solution.

Numerical modelling is another important subject in this research field. In this Chapter, several works regarding the modelling of different transition zones with different numerical techniques are listed. However, the difference between the works goes beyond the type of software selected and the obtained results are depending on the type of analysis, domain of analysis, the inclusion of non-linearity and plasticity of the material, calculation time, expected outcomes and other factors. Each option has repercussions in the obtained results. Thus, this analysis allows understanding which are the options that should be made in the development of the numerical modelling and the ones that match with what it is expected to achieve. This analysis is important in order to understand the concepts that are behind the modelling of the transition zones and exposes the choices that should be made in the development of a transition zone modelling. The practical application of these concepts will be presented in Chapter 7, which is related to the modelling of a specific transition zone in a ballastless track from an embankment to a tunnel with higher track stiffness.

Furthermore, despite it is still scarce, the review developed in this Chapter also presents the works developed in the monitoring field. This is still a field to be explored since there are more works about numerical modelling than monitoring. However, they can give important insights into the performance of the transition zones and can be also used as a tool to improve the numerical models in the prediction of the long-term performance of the transition zones.

4 Mechanistic-empirical resilient and permanent deformation models of the subgrade: laboratory testing, modelling and ranking

4.1 Introduction

The understanding and knowledge about the deformation and failure mechanisms of the geomaterials under repeated loading are extremely important for the proper design and maintenance planning in the railway structures (Li and Selig, 1996). Typically, the subgrade layer of railway track is composed of geomaterials (mainly coarse-grained soils due to its better performance when compared to the fine-grained soils) and presents two types of deformation when submitted to cyclic loads: the recoverable (or reversible) and permanent (or plastic) deformations, which have significant importance in the long-term performance of the substructure (Ling et al., 2017).

Regarding the resilient deformation, the concepts were introduced by AASHTO in 1986 (AASHTO, 1994). This property is often used to characterize the materials in several railway layers (Liang et al., 2008). However, due to the complexity of conducting resilient modulus tests, there have been several efforts to develop equations capable to simulate the real behaviour of the materials. However, the performance of the materials is dependent on numerous variables such as the stress state, physical state, and type of material, increasing the complexity of the analysis. In the case of the permanent deformation, an accurate estimation or prediction of the amount of cumulative settlement will help railway structures avoid a mediocre performance (Barksdale, 1972, Monismith et al., 1975, Puppala et al., 1999). This is why the permanent deformation of geomaterials should be included in the design since otherwise, it can lead to higher annual maintenance costs (Puppala et al., 1999). Indeed, over the past decades, researchers have been concerned about permanent deformation and they continually search for the most accurate methods and models that will measure and predict these values (Monismith et al., 1975, Lentz and Baladi, 1980, Ullidtz, 1993, Gidel et al., 2001). To achieve these objectives, laboratory investigations using cyclic triaxial tests, simple and cyclic shear tests, resonant column and hollow cylinder tests, among others have been carried out. These tests are often used to determine shear stress-strain behaviour, resilient modulus (M_r) of subgrade geomaterials considering recoverable and permanent deformations under cyclic loads (Gomes Correia, 2004, Gomes Correia, 2008). The recoverable (elastic) is usually described by non-linear elastic models. However, the permanent deformation is more complex, since it depends on the accumulation of N loading cycles.

One of the main objectives of this work is to review the available resilient and permanent deformation models in the scope of the geomaterials found in the specialized bibliography considering the information about the conditions for its development (properties of the materials tested, compaction tests, degree of compaction, moisture content, etc.) and the mains variables/factors that can influence the response of the material. In the first part of this work, an extensive literature review about the existing methods used to estimate da recoverable and permanent deformations of the geomaterials when submitted to repeated loads is presented. Furthermore, the main causes of permanent deformation on railway structures are exploited as well as the factors that can increase this phenomenon. In fact, the materials should be able to resist permanent deformation, however, this resistance will depend on the number of load cycles and stress levels (Lekarp and Dawson, 1998), the thickness of the layer, and the granulometry of the material. This also includes other external factors such as the physical state of the soil, which is often difficult to control because it depends on other environmental aspects such as the moisture content, degree of saturation, etc. Thus, it is possible to conclude that the recoverable and permanent deformations constitute a particular behaviour of the geomaterials when submitted to cyclic loads. Indeed, the modelling of these materials is away more complex than the material modelling presented in Chapter 2.

The behaviour of geomaterials under cyclic loads can be characterised by either using complex elastoplastic models (recoverable and permanent deformations are both considered) or by shakedown theory and mechanistic-empirical models (Hornych and Abd, 2004). Thus, the elastoplastic models, however, despite their ability to accurately predict permanent deformation (the loading history is considered because the equation is solved based on incremental steps), are difficult to implement, time-consuming, and complex (Ling et al., 2017). Most of these models consider a low number of load cycles, which is not in accordance with the *in situ* conditions where the number of loads is up to million cycles. Indeed, these models are very demanding computationally because they require the simulation of repeated load applications. The development of formulations based on cyclic constitutive laws may be expressed through conventional concepts such as the yield condition, hardening and flow rules. However, numerical implementation can lead to problems related to computational accuracy (Abdelkrim et al., 2003). So, despite the existence of several approaches used to predict resilient and permanent deformation, the focus of this analysis will be on mechanistic-empirical models. These models are based on extensive laboratory testing results, so they can correctly simulate the response of materials; they are easy to implement, and they depend on fewer parameters than conventional elastoplastic models.

This Chapter reviews the existing methods used to estimate the recoverable and permanent deformations of geomaterials (allowing to select the best testing approach and the most suitable model), followed by a parametric study that includes comparisons among some selected models that are based on different materials with different classifications (*UIC* and *ASTM*), properties, granulometry, and physical states. This comparison allows to estimate the resilient modulus and the permanent deformation and to rank the materials according to the predicted modulus and deformation data and soil classification, which is a helpful tool in the design of the railway structures and also pavements. It is also noted that this ranking should be interpreted as a reference value because it depends on several properties and soil conditions.

This Chapter establishes a link between Chapter 2 (about the structural models applied to railway structures and modelling of some of the materials) and the present research that is specifically applied to the performance of the geomaterials when submitted to cyclic loads, which are a type of loading that is characteristic of the railway structures (due to the passage of the vehicles). This study is also important in the scope of the transition zones, as mentioned in Chapter 3, where the development of the permanent deformation and track degradations can have a significant impact on the behaviour of the railway structure.

Despite the importance of resilient modulus, this Chapter presents more emphasis on the permanent deformation since its concept and evaluation are transversal to the whole thesis. Indeed, the studies and analysis presented in the further Chapters are based on the study of the permanent deformation and the model selected in this analysis/parametric study.

The analysis presented in this Chapter is based on the work developed in Ramos et al. (2020).

4.2   Resilient modulus

The resilient modulus is used to characterize the recoverable/reversible behaviour. In the traditional theory of elasticity, the elastic properties (which are material's parameters) are defined, mostly, by the *Poisson*'s ratio (ν) and *Young* modulus (E). In the analysis of the response of the material when submitted to cyclic loads, the modulus of the elasticity is replaced by the resilient modulus to consider the nonlinearity (i.e., dependence on stress level) on the performance of the material. Another important aspect in the formulation of the resilient modulus is related to the consideration of the inelastic properties of the materials, i.e., the loading and unloading of the stress-strain curve aren't totally overlapped due to the dissipation of the energy, as depicted in Figure 4.1.

Indeed, in the case of repeated load tests with constant confining pressure, the resilient modulus and the *Poisson*'s ratio are defined, respectively, by the following expression (Lekarp et al., 2000b):

$$M_r = \frac{\sigma_d}{\varepsilon_{1;r}}; \; \upsilon = -\frac{\varepsilon_{3,r}}{\varepsilon_{1,r}} \tag{4.1}$$

where σ_d is the deviatoric stress, $\varepsilon_{1,r}$ is the recoverable axial deformation and $\varepsilon_{3,r}$ is the recoverable horizontal deformation.
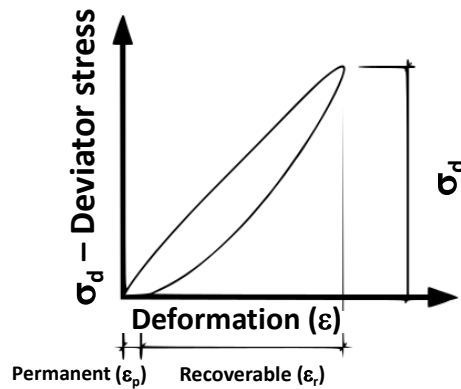
Figure 4.1 - Definition of the recoverable and permanent deformation

The experimental method used to determine the experimental value of the resilient modulus is described on AASHTO (1994) and it is based on the application of deviatoric stress under constant confining stress. The response of the materials varies according to its own nature. The cohesive materials are more sensitive to the deviator stress than the confining pressure since the experimental results show that there is a decrease of the resilient modulus with the increase of the deviatoric stress. On the other hand, the granular materials show a different tendency since the resilient modulus increases with confining stress.

The first developed models were only dependent on the confining stress (this is the main parameter that influences the resilient modulus in the case of the unbound granular materials). Posteriorly, the models start to include the deviator stress. More recently, the models are dependent on important factors regarding environmental aspects such as moisture content.

The computational modelling of resilient behaviour is a very and difficult task due to the necessity of translate complex behaviours into simple mathematical expressions and procedures for routine analysis. In the end, the main purpose of the researchers is to traduce a stress-strain relationship through constitutive laws. However, one of the main challenges is truly understanding the response of the materials at a microscopic level that goes beyond the study at a macroscopic level.

In this analysis, the resilient modulus and its models were divided into two main groups: fine-grained and coarse-grained materials.

4.2.1 Factors influence the resilient modulus

The list of factors that influence the resilient modulus is extensive. However, the importance of each factor is wide range (and not absolutely consensual) and also depends on the type of soil. For example, in the granular materials, its deformation depends on three parameters: attrition, consolidation and distortion (Lekarp et al., 2000b), which may not correspond to the main parameters of the cohesive soils. The resilient behaviour is dependent on several factors such as the stress level, fines content, particle shape, grading, density, maximum grain size, aggregate type, moisture content, stress history, number of load cycles, effect of load duration, frequency and load sequence (Lekarp et al., 2000b). Considering this list, two important factors stand out: the applied stress level and moisture content. Indeed, regarding the remaining factors, despite their importance in some cases, the researchers do not always agree on their impact level and there are some opposite conclusions. The stress (in terms of confining stress, sum of principal stresses and deviator stress) is the most important factor in the analysis of the resilient behaviour since its impact in the response of the material is very significant.

Regarding the granular materials, a curious behaviour is observed. Brown and Hyde (1975), cited by Lekarp et al. (2000b), conclude that the VCP (variable confining pressure) and CCP (constant confining pressure) present the same values of resilient modulus. This fact is justified by the mean value of the pressure used on VCP that is equal to the pressure used on CCP tests. Regarding the resilient *Poisson*'s ratio, there are some differences in the conclusions since the VCP leads to a decrease of the *Poisson*'s ratio with an increase of the deviator stress ratios, while CCP tests show the opposite.

Concerning the density, many researchers conclude that there is an increment of the resilient modulus with the increase of the density. Indeed, there is an increase in the number of contacts between the particles with the increase of density. The deformation in particle contacts decreases and the resilient modulus increases (Kolisoja, 1997). However, these conclusions are not unanimous since some studies show a reduced influence of density in the resilient response of the material (Thom and Brown, 1988, Brown and Selig, 1991). Other researchers show that the density depends on the granulometry of the material and fines content (Hicks and Monismith, 1971).

As mentioned previously, the grading, fines content and maximum grain size influence the resilient behaviour. Some studies show that resilient modulus decreases with the increase in the amount of fines

125

(Thom and Brown, 1988, Kamal et al., 1993). Furthermore, several studies show that resilient modulus increase with the maximum particle shape (Gray, 1962, Thom, 1988, Kolisoja, 1997).

The moisture content and degree of saturation also influence the resilient behaviour of the geomaterials. In the case of the granular materials, the granulometry and the fines content (in a well-graded material) have a significant influence on the response of the material. Indeed, the water cannot drain freely since it is kept held in the pores of the materials (Raad et al., 1992). The resilient response of dry and mostly partially saturated granular materials is very similar but when the saturation is close to the maximum, the resilient behaviour is affected (Vuong, 1992). Previous studies show that in the granular materials submitted to repeated loads, there is an increase in the excess pore-water pressure, which means that the effective stresses decrease. Some authors cited by Lekarp et al. (2000b) state that the decrease of the resilient modulus with the degree of saturation is only obtained when the analysis is performed in the total stresses domain (Seed et al., 1967, Hicks, 1970). Indeed, in the tests performed based on effective stresses, the resilient modulus remains practically unchanged (Pappin, 1979). Regarding the resilient *Poisson*'s ratio, in the granular material, this variable is affected by the moisture content and degree of saturation (ν decreases with the increase of the degree of saturation). Furthermore, the variation is also dependent on the type of analysis: in terms of effective and/or total stresses (Hicks, 1970, Hicks and Monismith, 1971).

4.2.2 Laboratory testing

The resilient modulus is an important property used to measure the stiffness of a material under different conditions such as moisture content, density and stress level.

The resilient modulus is usually determined through laboratory tests (through the repeated load cyclic triaxial test) by measuring the stiffness of a cylinder specimen that is subjected to a cyclic axle load. Its determination requires a fundamental understanding of the test procedures, and a review of the underlying concepts related to these procedures.

In the laboratory, the repeated axial cyclic stress of fixed magnitude, load duration and cycle duration is applied to a cylindrical test specimen. During testing, in a triaxial pressure chamber, the specimen is subjected to dynamic cyclic stress and static stress. The resilient modulus testing is performed at different confining stresses. The deviatoric stress is applied in order to simulate the typical loadings of different vehicles at different depths in the structures (which includes the railway structures and pavements). In more detail, the cylindrical specimens are subjected to different stress states under different constant all-round confining pressures to simulate the lateral stress caused by the overburden pressure. To avoid the

failure of the test samples, at the beginning of the test, it is recommended that the load application should start at the highest confining pressure with the corresponding axial stress at the lowest level. This technique ensures that the stress states at which the material is least likely to fail are chosen first, followed by stress states at which the samples are most likely to fail. This approach is usually adopted for fine-grained soils.

In Figure 4.2, the stress state concepts associated with the resilient modulus testing are presented. The total recoverable axial deformation response of the specimen is measured during the test and is used to estimate the resilient modulus. Analysing Figure 4.2, σ_1 is the total axial stress, σ_d is the dynamic deviator and σ_3 is the static confining stress or confining pressure. The confining pressure is composed of only a static stress component where $\sigma_2 = \sigma_3$ in the horizontal direction. Both stresses (deviator and confining stresses) have a significant influence on the resilient behaviour of geomaterial layers in the railway structures. The shear stress on the plane of the sample is zero during the test.

Despite the importance of resilient modulus, there isn't a unique approach that can be used during testing. Indeed, during the past decades, several research groups and agencies in different countries have proposed different test methods and procedures in the scope of repeated load testing to help establishing appropriate resilient modulus test procedures for, for example, pavement design. This development was very important and contributed to the use of resilient modulus in some pavement design guidelines. In the work developed by Anochie-Boateng et al. (2009), the main differences between the various resilient modulus test procedures are summarised.
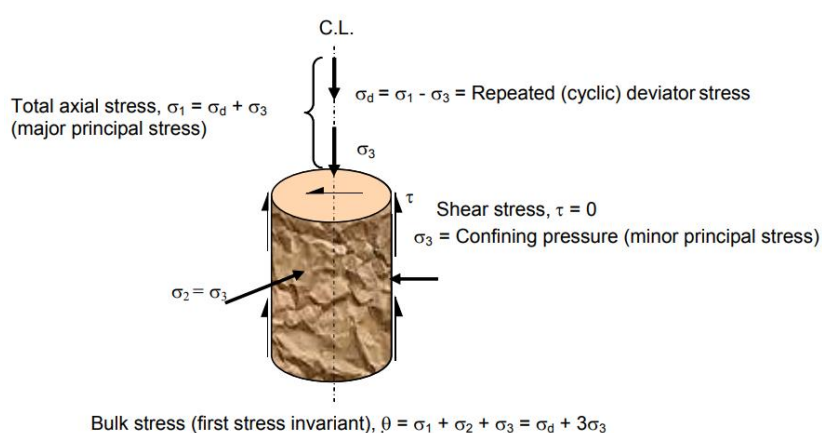
Figure 4.2 – Stress state concept associated with the resilient modulus testing (Anochie-Boateng et al., 2009)

Thus, it is possible to conclude that the resilient modulus test requires special equipment due to, for example, the dimensions of the sample. This is why the correlations of resilient modulus with soil index

127

properties and other simpler tests have been developed by different studies. For example, Yau and Von Quintus (2004) and Titi et al. (2006) developed prediction models of the resilient modulus for fine-grained soils using index properties. Louay et al. (1999) estimated the resilient modulus considering the soil index properties, California Bearing Ratio (CBR), and unconfined compressive strength (q_u). Moreover, the resilient modulus was already correlated with conventional Unconfined Compression (UC) test results by Lee et al. (1997), where the UC test corresponds to a static triaxial compression test without confinement. The resilient modulus test standard (AASHTO, 2003) includes a methodology for performing a UC test directly following a resilient modulus test and it is also known as the quick shear (QS) test (Quick Shear test is a type of static compression test and it is included in the standard AASHTO (2003)). Hossain and Kim (2015) developed prediction models of resilient modulus for fine-grained soils from QS test. Unlike the resilient modulus test, the QS test uses a static loading system, rather than a more complex cyclic loading system, and is quicker, simpler, less expensive, and easier to perform.

However, most of the correlation studies have been focused on fine-grained soils and there is still a lack of available data in the case of coarse grained soils. Rahman et al. (2019) develop models that relate the resilient modulus for coarse grained soils with the results obtained from QS tests and soil index properties (developed for remolded soils). The developed models were validated with test results using undisturbed subgrade soil samples collected from different locations.

4.2.3   *Mechanistic-empirical modelling approach*

The mechanistic-empirical modelling approaches used to determine the resilient modulus are divided according to the type of material tested (granular or cohesive). Furthermore, the more complex models that are dependent on the physical state of the material are also presented. Moreover, in the annex, the state of the art of the resilient models developed based on laboratory tests (mostly cyclic triaxial tests) considering all types of materials (such as clays, silts, sands and gravels) is summarized.

4.2.3.1   *Materials*

Cohesive materials

In cohesive materials, the fine fraction is an important factor in the analysis, which means that the resilient modulus should be dependent on the soil's physical state. Indeed, in the cohesive materials, certain characteristics may have more importance in the value of the resilient modulus, besides the stress state, such as the moisture content, suction and saturation degree. In the work developed by Ooi et al. (2004), the authors state that the new generation models not only provide a better fit than the older models, but they also provide a reasonable fit to the data that can capture the effects of stress state, soil type, soil

structure, and the soil physical state quite effectively. Furthermore, according to Zhang et al. (2019a), there are prediction models that combine the effect of the stress state and matric suction on the resilient modulus. These models not only reflect the relationship between the resilient modulus of subgrade soils and the stresses but also the effects of seasonal variation of moisture content on the resilient modulus. The authors also conclude that the degrees of stress and moisture content have a significant impact on the resilient modulus of compacted cohesive soils. Moreover, the results show that the resilient modulus of the tested cohesive soils increases with the increase in confining pressure, matric suction, and degree of compaction and decreases with the increase in deviator stress and moisture content. Therefore, lower moisture content and a higher degree of compaction are beneficial to the stiffness of the subgrade.

Considering the extensive bibliography about this topic, several models were developed to describe the resilient modulus: bilinear, exponential, semi-log, hyperbolic, octahedral, etc. Table 4.1 is a brief resume of the older resilient models applied in the case of cohesive soils.

Table 4.1 - Resilient moduli for cohesive materials (adapted from Nimbalkar et al. (2020))

Models	Expressions	Parameters	Authors
Bilinear	$M_r = K_1 + K_2\sigma_d$ when $\sigma_d < \sigma_{di}$ $M_r = K_3 + K_4\sigma_d$ when $\sigma_d > \sigma_{di}$	k and n are parameters dependent on the type of soil and physical state	Thompson and Robnett (1976)
Power	$M_r = k\sigma_d^n$	k and n are parameters dependent on the type of soil and physical state; the parameter n usually has a negative value	Moossazadeh and Witczak (1981)
Power (with the influence of the confining stress for overconsolidated saturated soils)	$M_r = k\left(\dfrac{\sigma_d}{\sigma_3'}\right)^n$	σ_3 is the confining stress	Brown et al. (1975)
Semi-log	$M_r = 10^{(k-n\sigma_d)}$	k and n are empirical parameters	Fredlund et al. (1975)
Hyperbolic	$M_r = \dfrac{k + n\sigma_d}{\sigma_d}$	M in ksi and σ_z in psi	Drumm and Pierce (1990)
Octahedral	$M_r = k\dfrac{\sigma_{oct}^n}{\tau_{oct}^m}$	σ_{oct} and τ_{oct} are the shear and normal octahedral stresses	Shackel (1973)

Furthermore, in the scope of the cohesive soils, it is also important to take also into account the type of approach in terms of stresses: total and/or effective. In the work developed by Sas et al. (2017), the developed model can describe the phenomena of modulus development during the cyclic undrained condition and takes into account the actual values of effective stress (p'), excess pore water pressure, the loading characteristic and the position of the effective stress path.

<u>Granular materials</u>

The modelling of the resilient behaviour in the case of granular materials can be performed through two different approaches: simulation of the resilient modulus considering a constant value of the *Poisson's* ratio and the division of the response of the material into the volumetric and shear component, which is more complex and harder to implement.

Resilient behaviour expressed through the resilient modulus and Poisson's ratio

The models expressed by the resilient modulus and constant *Poisson's* ratio are very easy to understand, very simple and easy to implement numerically. In fact, initially, in terms of variables, the models were only dependent on the confining stress and material parameters and/or the sum of the principal stresses (Dunlap, 1963, Brown and Pell, 1967). Due to the necessity to include the influence of the deviator stress, Uzan (1985) modified the well-known *k-θ* model, introducing the influence of the mean and deviatoric stress (*p* and *q*, respectively):

$$E = k_1 \theta^{k_2} q^{k_3}$$ (4.2)

where k_1, k_2 and k_3 are parameters dependent on the state of the soils.

Posteriorly, some models were improved considering, for example, the porosity of the material and the variable confining stress (Kolisoja, 1997, Karasahin, 1993).

However, some of the previous models show some problems regarding the consideration of a constant value of the *Poisson's* ratio: despite the good results regarding the axial deformations, it was difficult to simulate correctly the volumetric and radial deformations. Indeed, some authors also suggested that the use of these models could lead to *Poisson's* ratios superiors to 0.5. However, some of these models are still used and were also improved. This is due to its simplicity and acceptable obtained results (ARA Inc. ERES Division, 2004).

Nevertheless, in order to solve *Poisson's* ratio problem, other models were developed, dividing the recoverable deformation into the volumetric and shear components.

Resilient behaviour expressed through the shear modulus (G) and bulk modulus (K)

The models based on the division of the recoverable deformation present a different formulation. In these models, the recoverable deformation is characterized by the bulk modulus (*K*) and the shear modulus (*G*). This formulation (in terms of *G* and *K*) is more "complete" than the models only characterized by the

resilient modulus and *Poisson's* ratio since it is dependent on more complex laboratory tests and with a more generic interpretation than an axial loading.

 Indeed, Brown et al. (1975) cited by Lekarp et al. (2000a) identify three important conditions in the application and formulation of these models:

- In each increment of calculus, a linear elastic behaviour is adopted;
- The shear and volumetric components of stress and strain are analysed independently;
- Better adjust to the experimental results, mostly when the solicitation presents a 3D character;

Boyce (1980) developed a well-known model dependent on bulk modulus and shear modulus:

$$K = \frac{p}{\varepsilon_v} \tag{4.3}$$

$$G = 3.\frac{q}{\varepsilon_q} \tag{4.4}$$

where ε_v and ε_q are the volumetric and shear resilient strain:

$$\varepsilon_v = \frac{1}{K_1} p^n \left[1 - \beta \left(\frac{q}{p}\right)^2\right] \tag{4.5}$$

$$\varepsilon_q = \frac{1}{3G_1} p^n \left(\frac{q}{p}\right) \tag{4.6}$$

In this model, there is a clear division between the volumetric and shear deformation and the values of K and G are stress-dependent (p and q, respectively). Posteriorly, this model was updated by other authors (Jouve and Elhannani, 1994, Hornych et al., 1998, Fortunato, 2005) in order to consider the anisotropy of the material, which is an important characteristic regarding the deposition and compaction conditions. Indeed, Hornych et al. (1998) purpose an orthotropic version of Boyce's model introducing an anisotropic coefficient (γ): when the parameter is equal to 1 means that the material is isotropic.

4.2.3.2   *Models dependent on the physical state – suction and degree of saturation*

Recently, some studies were developed in order to include the physical state into the resilient models (Yang et al., 2005, Liang et al., 2008, Sawangsuriya et al., 2009, Salour and Erlingsson, 2015b).

In this section, a brief reference is made regarding the models dependent on the suction and degree of saturation. These models were developed based on experimental results and include suction as one of the main parameters. In the case of non-saturated soils, three important variables influence recoverable/reversible behaviour (Erlingsson et al., 2017):

- Net confining stress: σ_3-u_a;
- Deviatoric stress: σ_1-σ_3;
- Suction matrix: ψ_m=u_a-u_w.

where σ_3 is the confining stress, σ_1 is the axial stress, u_a is the air pressure and u_w is the water pressure.

Based on Uzan's model, Cary and Zapata (2011) developed a model that includes the suction in the determination of the resilient modulus:

$$M_r = k_1 p_a \left(\frac{\theta_{net} - 3\Delta u_{w-sat}}{p_a}\right)^{k_2} \left(\frac{\tau_{oct}}{p_a} + 1\right)^{k_3} \left(\frac{\psi_m - \Lambda\psi_m}{p_a} + 1\right)^{k_4} \tag{4.7}$$

where θ_{net}=θ-3u_a (u_a is pore air pressure), $\Delta\psi_m$ is the variation of the suction matrix regarding the initial suction (Δu_{w-sat}=0) and Δu_{w-sat} represents the increase of the pore pressure in saturated conditions (ψ_m=0).

Despite the simplicity of the model's formulation (which is based on the work developed by Uzan (1985)), the characterization of the suction increases the complexity and application of these types of models since this is a parameter that is difficult to characterize.

Recent studies show the influence of the water content (with special attention on the role of the suction in the interpretation of the results) and consider the possibility to apply an effective stress approach to characterize the changes in normalized resilient modulus as a function of a single parameter that includes the total stresses and suction (Coronado et al., 2016). Moreover, some studies are focused on the importance of the degree of saturation (and the controlling in the soil's compaction) and its relationship with the soil structure design. In fact, the degree of saturation and also the *CBR* (*California Bearing Ratio*) are parameters that are easy to obtain and easy to use when compared to the suction. The authors conclude that *CBR* (soaked and unsoaked) and also the elastic shear modulus (representative of the stress-strain behaviour at small strains of the subgrade), unconfined compression strength, cyclic undrained shear strength, among other parameters, of saturated soil are controlled by ρ_d and S_r at the end of compaction (Tatsuoka and Gomes Correia, 2018).

4.2.3.3 *Main differences of the resilient modulus's formulation – analysis and comparison*

Most of the geomaterials (especially the granular materials) show a stress-dependency under repeated loads. To replicate this non-linearity and time-dependency, the resilient response of the materials isn't solved by the traditional elasticity theory but by the definition of the resilient modulus and *Poisson*'s ratio. However, as mentioned previously, there are other formulations to characterize the response of the material such as the replacement of the resilient modulus and *Poisson*'s ratio by the shear and bulk modulus.

To reproduce the stress-strain relationship, some researchers tried to describe this dependency using several stress variables based on simple curve-fitting using the laboratory triaxial tests, which can lead to some errors. This means that the resilient models only fit the laboratory data used for their own development, which means that the mathematical formulation can only be used in a particular situation.

The approach based on the resilient modulus and *Poisson*'s ratio has been widely used and several expressions were purposed with stress components. This formulation is simple and based on a curve-fitting approach. However, the bulk and shear modulus's approach deal better with the non-linear response of the geomaterials (mostly in the case of granular materials) from a theoretical point of view and it is more realistic regarding the physical meaning in a 3D stress regime. But, as presented in the previous section, these models have a more complex formulation and the parametrization is also difficult to obtain through the available test data (Lekarp et al., 2000b).

Despite the several advantages of the empirical models, the main limitation is related to the confidence in the extrapolation of the analysis beyond the conditions in which they were defined (Lekarp et al., 2000b). The tables presented in Annex (Table A.1, Table A.2, Table A.3, Table A.4 and Table A.5) contain information regarding the type of soils (UIC and ASTM classification), source (authors), the mathematical models and respective variables and empirical constants. This information is quite significant in the modelling of the subgrade of the railway tracks since adds information about the materials used to define the model, as well as, its physical conditions such as moisture content and dry density.

A similar analysis is performed for permanent deformation.

4.3   Permanent deformation

4.3.1   Factors and causes of permanent deformation

An important cause of permanent deformation is related to the complex stress conditions since the geomaterials are subjected to vertical, horizontal and shear stresses during the passage of vehicles as well as the effects of moving loads; all of which imply the rotation of principal stresses. Chan (1990) showed an increase in permanent deformation when the rotation of principal stresses was included. These tests took place in a hollow cylindrical apparatus which allows for simulation in the laboratory and similar conditions to be verified *in situ*.

The self-weight of the embankment and traffic loading are other important causes of post-settlement in railway structures. Permanent deformation includes the settlement of the roadbed beneath the track and the subgrade. Several studies show that the main influencing factors are the level of stress and stress

history; in fact, the experimental results and field measurements show that the dynamic and cyclic loads from the train passage make a significant contribution.

Permanent deformation has a significant effect on the performance of structures because it leads to an increase in maintenance operations and costs and reduces ride quality. Despite this is long-term behaviour, it must be predicted during the design stage because although the accumulation is very small during each cycle, it may still lead to the ultimate collapse of the structure (excessive rutting) due to the accumulation of millions of cycles. Figure 4.3 & Figure 4.4 show that the permanent deformation can be defined and characterised by the accumulation of small increments of deformation during N loading cycles. Several studies demonstrate that permanent strains depend directly on the mean and deviator (p and q, respectively) stresses (Lekarp et al., 2000a). The mean stress is dependent on the sum of the principal stresses while the deviator stress is dependent on the sum of squares of the differences of the principal stresses:

$$p = \frac{\sigma_1 + \sigma_2 + \sigma_3}{3} \tag{4.8}$$

$$q = \sqrt{\frac{1}{2}} \times \sqrt{(\sigma_1 - \sigma_2)^2 + (\sigma_2 - \sigma_3)^2 + (\sigma_3 - \sigma_1)^2} \tag{4.9}$$
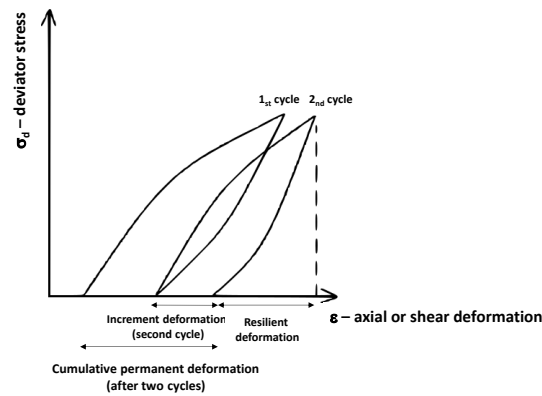
Figure 4.3 - Illustration of the accumulation of permanent deformation under cyclic loads (after two cycles)
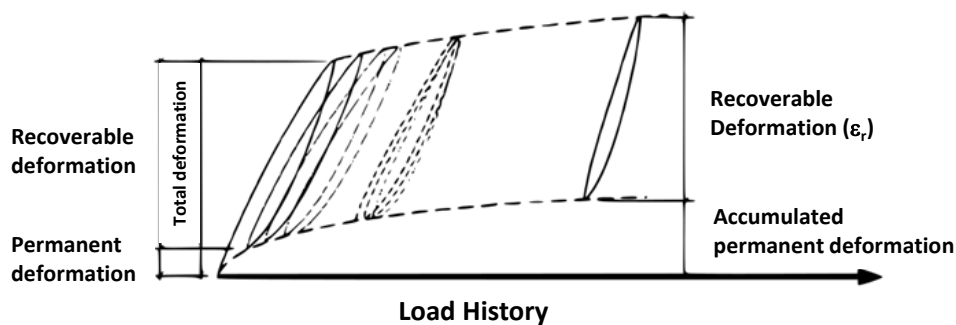
Figure 4.4 - Accumulation of permanent deformation (or plastic strain) (adapted from Erlingsson et al. (2017)

134

Thus, the development of the permanent deformation is a complex process that directly depends on the number of load cycles (N) and stress levels. The factors can be divided into load-related factors and material properties. The load factors will include the applied stress levels, number of load applications, the strength of the material, as well as the loading history and the effect of principal stress rotation. However, other factors can also influence the permanent deformation: moisture content (degree of saturation), matric suction, fines content, density (degree of compaction), aggregate type, particle size distribution (gradation), and the amount and type of fines (plastic or non-plastic) (Lekarp, 1999, Xiao et al., 2015). Gidel et al. (2001) also found that for unbound granular materials, the mineralogical nature of the material (including aggregate mineralogy and particle morphology) also influences permanent deformation (Coronado et al., 2011). This factor has important effects on particle shape, the quality of the fines content, and sensitivity to water and surface roughness. However, the stress level and the number of load cycles emerge as the most important factors. In fact, those models that only consider the value N should not be used to predict permanent deformation because they are too simple and lacks accuracy.

4.3.2 Laboratory testing

There are several laboratory tests currently used to evaluate the permanent deformation of geomaterials; they attempt to reproduce *in situ* stress conditions in railway structures. The cyclic triaxial test is the most widely used to study geomaterials subjected to cyclic loads. However, in these tests, the principal stresses are always horizontal or vertical, which may not always correspond to *in situ* conditions where the materials are subjected to moving loads and rotations of principal stresses. The cyclic vertical stress, designated as σ_1, is applied, and horizontal stress, designated as the confining stress - σ_3 - is also applied. This test begins when deviator stress is applied, and then the applied vertical stress progressively increases until it reaches an allowable displacement of the apparatus.

Another test used to evaluate permanent deformation is a cyclic torsional test, which also includes a hollow cylinder test. This particular test enables the magnitude and the direction of principal stresses to be controlled. In fact, this test device has been developed to study permanent deformation and resilient behaviour by considering the rotation of principal stresses and then applying the laboratory results to *in situ* conditions. In this case, the specimen is cylindrical and hollow. The main limitations of this test are the dimensions of the sample. Furthermore, the stress path can only be simulated on the symmetrical plane of the track. However, the results show that the permanent deformations are often higher in this test than the convention cyclic triaxial tests due to the simulation of the rotation of principal stresses.

Cyclic shear tests can also be used to study the dynamic behaviour of soil. In this test, the sample is cylindrical, and a horizontal shear force is applied to the bases of the samples. This test can also be used to evaluate stability under seismic events, quantify the degradation of shear stresses in cohesive soils under cyclic loads, and evaluate the liquefaction parameters of non-cohesive soils under cyclic loading.

There are also other approaches for studying the permanent deformation of geomaterials; for example, while expensive, physical models (1-to-1 prototype model test) can be used to evaluate the performance of geomaterials and the stability of structures subjected to dynamic and repeated loading. These models will provide actual field data to help understand the behaviour of railways under moving loads and enable the study of permanent deformation and the stresses induced in the soil through proper measurement devices.

While small scale models of railways were introduced in the past (Momoya Y. et al., 2005, Al Shaer A. et al., 2008), several models focusing on the development of permanent deformation of railways under cyclic loadings or moving loads at low speed (Bian et al., 2014) are currently available. The field measurements and numerically calibrated results show that increased train speed has a huge influence on the long-term performance of a structure (i.e., higher dynamic stresses and higher permanent deformation). A test facility should be able to simulate the actual speed of a moving train under a very large number of load cycles. This means that full-scale models are better because the measured results from a test can be considered directly in the track design and maintenance operations as this approach reduces any uncertainties in the measurements (Bian et al., 2014).

4.3.3 Modelling approaches

Permanent deformation can be predicted either by numerical simulations using elastoplastic models applying the shakedown theory or mechanistic-empirical deformation models based on laboratory tests such as cyclic triaxial tests or hollow cylinder apparatus.

Mechanistic-empirical permanent deformation models have become much more complex due to the inclusion of other variables, apart from the number of load cycles and stresses. More recently, a study to correlate the resilient modulus (M_r) with the permanent deformation (ε_p) has been developed in the scope of the pavements. Studies that relate the two parameters (M_r and ε_p) have shown that for subgrade soils, M_r has a significant effect on the ε_p or pavement rutting since soils with a higher M_r present less permanent deformations (Orobio and Zaniewski, 2011, Rahman and Gassman, 2019). However, mixed soils such as silty sand or sandy silts still show significant rutting despite having higher resilient characteristics (Ullidtz, 1993, Puppala et al., 2009).

Existing permanent deformation models can be divided into two main categories: rutting models based purely on mechanics, or mechanistic-empirical models. Rutting models are based on elastoplastic theory (Desai, 1980, Desai and Faruque, 1984, Vermeer, 1982, Uzan, 1999, Chazallon, 2000, Chazallon et al., 2002, Chazallon et al., 2006). While they can consider how the stress levels and stress paths can affect permanent deformation, they are very complex and difficult to use because: (i) the increment of permanent deformation per cycle is very small; and (ii) the response of the track in each cycle is a challenge for cyclic constitutive models (Chazallon et al., 2006) and numerical implementation (Abdelkrim et al., 2003) is hard due to the extensive calculation time and cumulative errors.

Mechanistic-empirical models often describe a relationship between the number of load cycles and the accumulated permanent deformation. They are very simple to use, the numerical results can be obtained very quickly, and they also predict permanent deformations very well. However, one of the particularities of these models is that their derivation from triaxial tests; which means the conventional and well-known heart-shaped stress path (stress rotation) induced by the passage of trains cannot be reproduced in this type of laboratory test.

Mechanistic-empirical models can be divided into single-stage models and multi-stage models. A single-stage implies that the repetitive load tests are carried out at one stress level in one test; in this instance, multiple specimens are tested at different stress levels. Multi-stage models can test multiple levels of stress in one test on one specimen. This approach enables the effects that the stress level and stress history have on permanent deformation to be considered (Grégoire, 2011).

Elastoplastic models

Elastoplastic models enable the cyclic response of a material to be determined by their ability to separate the behaviour of materials into either elastic or plastic phases. The main advantage here relates to the loading history because the equation is solved based on incremental steps, which means the response for any loading history can now be considered. However, most of these models only consider a low number of load cycles, which is not in accordance with the *in situ* conditions where the number of loads is up to million cycles. Furthermore, since the number of parameters needed is much higher than for the empirical models, monotonic and cyclic tests with different stress paths must be additionally carried out to determine those parameters (Hornych and Abd, 2004).

Elastoplastic models, however, despite their ability to accurately predict permanent deformation, are difficult to implement, time-consuming, and complex (Ling et al., 2017). Chazallon (2000) extended

findings by Hujeux (1985) introduced an elastoplastic model that includes kinematic hardening and can be implemented for a large number of load cycles. Here, the elastic part is defined by a non-linear model (Boyce model) and the elastic parameters and the anisotropic parameters are determined from cyclic triaxial tests to obtain resilient behaviour. This model includes 4 non-linear elastic parameters, 7 plastic parameters that describe monotonic loading, and 5 plastic parameters that describe cyclic loading (through cyclic tests). Each group is uncoupled and can be determined separately. The monotonic parameters are determined through triaxial monotonic tests until failure by considering different initial confining stresses, and the cyclic parameters are determined through cyclic triaxial tests by considering a large number of load cycles. This model also assumes the permanent deformations tend to stabilise (Hornych and Abd, 2004). Eventually, the number of variables and properties required are very large and the model is not efficient enough.

Several advanced elastoplastic models have been used to characterise the behaviour of granular materials. These advanced models include recoverable and permanent deformations using complex concepts such as elastoplasticity or even hypoplasticity. For example, the model by Suiker (2002) (it is based on the shakedown concept), named *Densification Cyclic Model*, can be used to characterise the behaviour of ballast aggregates. In this model, permanent deformation is divided into frictional sliding inter-particles and volumetric compression; these two mechanisms have a plastic nature and only occur when a certain stress level is exceeded.

Numerical modelling of permanent deformation should include the influence of plasticity. Elastoplastic models are very efficient in static loading conditions with incremental loading or constant strain rate loading, and they allow permanent deformations to be simulated under monotonic loading based on the strain hardening mechanism. However, these characteristics mean that if a load is not increasing, these models will not consider permanent deformations after the first load repetitions. This is why different models have been introduced to simulate cyclic loading in subgrade soils and include concepts based on isotropic and kinematic hardening. These models are very demanding computationally because they require the simulation of repeated load applications in pavements/railway structures. The development of formulations based on cyclic constitutive laws may be expressed through conventional concepts such as the yield condition, hardening and flow rules. The main problem with the numerical implementation is that the increment of permanent deformation per cycle becomes very small quickly, and this leads to problems with the computational accuracy of the results (Abdelkrim et al., 2003). Yesufa and Hoffa (2015) developed a numerical model that is dependent on isotropic hardening and includes several

138

important factors/parameters such as the load magnitude, confining stress, accumulation of permanent deformation on the first cycle of loading (permanent deformation from the first loading cycle is based on the Drucker-Prager yield criterion), and proximity to plastic failure. Material parameters are obtained from the triaxial tests, while the numerical implementation of the model is based on the decomposition of the total strain into elastic and plastic (or permanent) components; the plastic component is controlled by the yield criterion, the flow rule and hardening rule.

Shakedown theory

Shakedown theory is another approach used to characterise load-deformation responses of geomaterials. This theory was developed initially based on the behaviour of metals subjected to repeated loading. Werkmeister et al. (2002) further developed to apply for unbound granular materials. The cyclic loads may not lead to the instantaneous collapse of the structure since they can induce permanent deformation in the material in every load cyclic. Indeed, if the load level is lower than a critical limit, the material will show permanent deformation in the first load cycles. However, after a certain number of N, the material will respond elastically to the subsequent load cycles. This phenomenon is defined as shakedown and this critical limit is called shakedown limit.

Here, the material is divided into three categories (by considering its stress dependency): range A, range B, and range C, as shown in Figure 4.5.

Werkmeister (2003) defined the shakedown limits based on the repeated load triaxial test (RLT); these values are also defined by EN13286-7 (2004):

- Range A: $\left(\varepsilon_p{}^{5000} - \varepsilon_p{}^{3000}\right) < 0.045 \times 10^{-3}$
- Range B: $0.045 \times 10^{-3} < \left(\varepsilon_p{}^{5000} - \varepsilon_p{}^{3000}\right) < 0.4 \times 10^{-3}$
- Range C: $\left(\varepsilon_p{}^{5000} - \varepsilon_p{}^{3000}\right) > 0.4 \times 10^{-3}$

These limits represent the deformation that accumulates between the 3000th and 5000th number of load cycles.
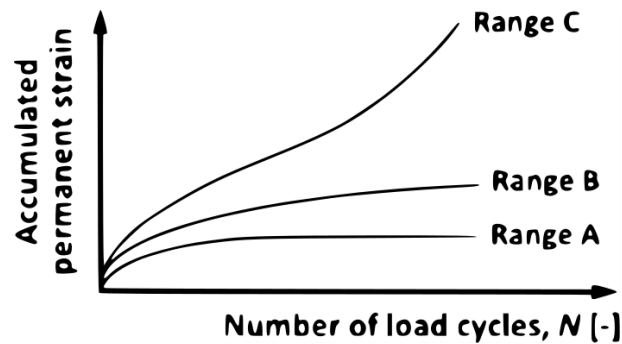
Figure 4.5 - Illustration of shakedown theory (Erlingsson et al., 2017)

Range A (depicted in Figure 4.5) is designated as plastic shakedown where the permanent deformation stabilises after a finite number of load cycles and the material becomes completely resilient. In fact, after a certain point, the cyclic stress does not cause any damage to the structure, which means that the permanent deformation does not increase, and the failure does not occur. *Range B* is designated as the intermediate range where accumulated deformation increases without complete stabilisation. In this case, permanent deformation develops at a very slow rate and is almost linear. *Range B* occurs when the repeated load cycles overcome plastic shakedown and failure can occur after a large number of load cycles. *Range C* is defined as incremental collapse because the permanent deformation accumulated per cycle increases until the failure occurs. This is caused by shear failure associated with the reorientation and rearrangement of particles, breakage, and the slip and loss of friction between the particles Indeed, failure can occur after a low number of loading cycles. This type of behaviour should never be accepted, unlike materials in the range *A* or even range *B*. It is reported in recent works that the shakedown limits were used for the pavement analysis (Qian et al., 2018, Qian et al., 2019b) and in railway structures studies (Alves Costa et al., 2018).

The shakedown analysis is used to find the shakedown limit of the structure under cyclic load. In the case of railway structure, the shakedown is used to predict whether the settlement will keep increasing or reach a stable status. Indeed, there are studies (Werkmeister et al., 2005, Brown et al., 2012) about laboratory studies based on different types of materials (granular and soils) where the possibility of shakedown under traffic loads was evaluated (Liu and Wang, 2019). Indeed, the shakedown approach has becoming very popular in pavement engineering, where some progress had been reported (Collins and Boulbibane, 2000, Chazallon et al., 2009a, Chazallon et al., 2009b, Chazallon et al., 2012, Brown et al., 2012). Keep this phenomenon in mind, in order to prevent excessive permanent deformation in a certain structure, it is important to guarantee that the loading level is below the elastic shakedown limit.

Indeed, the assessment of this limit is not easy since demands a significant computational effort mainly in 3D modelling since the loading time-history needs to be considered.

Considering the classical limit analysis theory, two main theorems were formulated to define the limits of shakedown load: the lower bound theorem (conservative solution) and the upper bound theorem (unconservative solution). The application of the lower bound theorem demands an accurate evaluation of the elastic response of the track's foundation due to the traffic. A numerical model can be used to assess the elastic dynamic response of the system (Alves Costa et al., 2018). During the shakedown phenomenon, the structure is subjected to a load that is lower than this limit but higher than the elastic limit and, after the accumulation of permanent deformation in the beginning (finite number of cycles), the material start to show elastic response and after this point, there is no accumulation of permanent deformation. This behaviour is explained by the total stress field that is given by the sum of the residual stress field with origin in the previous cycles. These conclusions were also obtained by Wang and Yu (2013). The key point of this problem is the assessment of the load that is compatible with the shakedown state. The lower bound theorem states that an elastic perfectly plastic material will shakedown if it is possible to fund a time-independent, self-equilibrated, residual stress field that combined with cyclic elastic stresses gives rise to a stress field that no violates the yielding criterion. The shakedown will occur if the following condition is respected (any time and any location):

$$f(\lambda\sigma_{ij}^e + \sigma_{ij}^o + \sigma_{ij}^r) \leq 0 \qquad (4.10)$$

where f represents the yielding criterion, λ is a load factor of stress field, σ_{ij}^o is the rest stress state, $\lambda\sigma_{ij}^e$ are the elastic stresses induced by the cyclic loads and the residual stress field is given by σ_{ij}^r. The maximum value of λ, corresponds to the lower value of the shakedown multiplier. The kinematic shakedown theorem states that if any kinematic acceptable mechanism of permanent deformation can be found, the shakedown phenomenon can not occur since the structure will fail due to fatigue (Alves Costa et al., 2018).

Having realised the importance of elastoplastic models and shakedown theory as approaches to predict permanent deformation, the mechanistic-empirical models are also an essential approach and will be presented in the next section. These models are simple, and they present an elegant formulation with good results.

141

4.3.4 Mechanistic-empirical permanent deformation models

The mechanistic-empirical model is often derived from laboratory test results such as the triaxial cyclic tests, direct shear tests, or large-scale cubical tests. There have been a number of predictive models used to study permanent deformation range from purely empirical to mechanistic and plasticity theory-based models. However, some of these models are only applicable to specific stress states or testing conditions so they have never been evaluated for a wide range of stress states, or types of materials and their physical conditions (Xiao et al., 2015).

It is noted that most of the developed models considered total stress conditions while ignoring the importance of suction. With regards to the resilient modulus (M_r), there have been several studies about the influence that suction has on the M_r even though this influence is not widely used in the study of permanent deformations (Coronado et al., 2016). Salour and Erlingsson (2016) used a triaxial testing system to control the pore-water pressures of a specimen, so the tests for permanent deformation took place with the control matric suction of the soil samples, and an effective stress approach has been used for modelling.

The mechanistic-empirical permanent deformation models can be divided by considering the materials used in the tests, the approach used during the tests, and the complexity (variables included in the model), as illustrated in Figure 4.6 and described in the following sections.
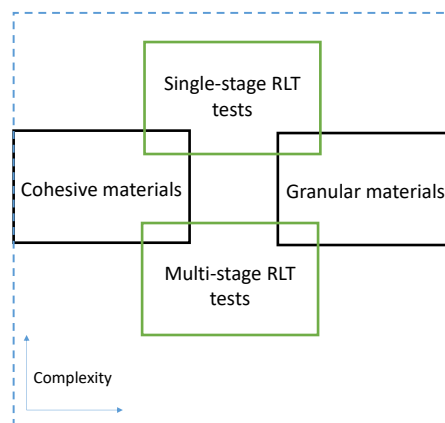
Figure 4.6 - Division of the mechanistic-empirical permanent deformation models

4.3.4.1 Materials

Empirical permanent deformation models can be divided by classifying materials tested as cohesive and granular materials. In the Annex, Table A.6 and Table A.7 summarises the empirical models that can be used to characterise the permanent deformation of cohesive materials: fine-grained soils-clays and fine-grained soils- silts, respectively. Also, Table A.8 and Table A.9 present key features of empirical models

that can be used to obtain the permanent deformation of granular materials classified as sands and sandy gravels, respectively.

4.3.4.1.1 Cohesive materials

The permanent deformation that accumulates in cohesive materials is a result of the permanent deformation of shear strain, the accumulation of deformation due to compaction, consolidation, and associated residual accumulation of excess water pressure. Models for cohesive materials should consider the stress state, the type of soil, and the physical state of the materials, and variables related to the moisture content and dry density. These types of materials are also influenced by environmental conditions and traffic loading, so regardless of the physical state of the material, its influence is considered in most models, and indirectly in the material parameters/constants, as summarised in Table A.6 & Table A.7.

The shakedown behaviour of cohesive soils is characterised by the stress-strain loop, and when the load increases, the progressive transition of material from plastic shakedown through plastic creep to incremental collapse can be identified (Yang and Huang, 2007). Yang et al. (2008) indicated that it is not possible to identify the pattern for the cohesive materials shown in Figure 4.5. Under lower levels of stress, the subgrade will reach an equilibrium deformation state after a certain number of load cycles. In these cases, permanent deformation accumulates very slowly as the number of load cycles increases. As expected, the failure of the subgrade can be prevented by controlling the accumulation of excessive permanent deformation by keeping repetitive load levels below the critical stress. Test results have shown that subgrade soils can easily accumulate excessive permanent deformation at high water content, but this will vary depending on the environmental conditions (Yang and Huang, 2007).

4.3.4.1.2 Granular materials

There have been substantial studies on the use of permanent deformation models for granular materials because of their common use in pavement/railway structures (Indraratna et al., 2013). The study of granular materials subjected to repetitive loads is fostered by the gradual accumulation of multiple increments of permanent deformation (Figure 4.4), which could lead to pavement failure due to excessive rutting (Lekarp et al., 2000a). In order to justify the use of these materials in pavements, some researchers tried to correlate repetitive loading with simple static loading tests (Lentz and Baladi, 1980), but there was no consensus with this approach because granular materials respond differently under static and cyclic loads (Sweere, 1990). Other studies also tried to correlate resilient and permanent deformation through a mathematical expression.

143

About resilient behaviour, researchers choose different approaches. Jouve et al. (1987) proposed decomposing axial and horizontal stresses and strains into volumetric and shear components, even though this expression depends on the permanent volumetric and shear strain (N>100) with the mean and deviatoric stresses. Other studies have expressed permanent deformation as a function of the number of load cycles (Barksdale, 1972, Sweere, 1990, Wolff and Visser, 1994, Khedr, 1985, Paute et al., 1988, Paute et al., 1994), and some researchers related permanent deformation with the stress level and stress ratio (Brown and Hyde, 1975, Barksdale, 1972, Pappin, 1979). Lekarp et al. (2000a) found a dependency between permanent deformation and the maximum stress ratio and length of the stress path in *p-q* space. In fact, the applied stress is one of the primary factors that can influence the permanent deformation of aggregates (Xiao et al., 2015). To simulate the correct response of granular materials subjected to cyclic loads (similar to *in situ* conditions) in a laboratory, variable confining pressure triaxial tests are a practical approach because the effect of horizontal and vertical stresses can be combined.

The behaviour of granular materials under cyclic loads is complex due to the gradual accumulation of permanent deformation with the number of load cycles. When a cyclic load is applied to a material there is a gradual accumulation of permanent deformation, a reduction in the number of voids, and an increase in stiffness (Erlingsson and Rahman, 2013, Ba, 2018). As with cohesive soils, the shakedown theory can be used to classify the response of the material in terms of permanent deformation. Furthermore, physical characteristics such as granulometry (poor or well graded) can also influence the response of granular materials, as well as their physical state (Gomes Correia, 2000). However, in most empirical models these variables are not directly considered.

4.3.4.2 Approach

Based on the approach and procedures for a cyclic load test, mechanistic-empirical models can be categorised as either single-stage (SS) or multi-stage (MS) models. Single-stage models mean that repeated load test (RLT) is performed at one stress level in one test, while multi-stage models mean that RLT tests are performed at multiple stress levels in one test on one specimen. This approach is relatively recent and considers how the stress level and stress history will affect permanent deformation (Erlingsson and Rahman, 2013). Actually, a multi-stage RLT represents better the real conditions of soils in the field that are subjected to cyclic loads. With the MS approach, the influence of different stress paths with different magnitudes (representing the influence of the effects of stress history) can be analysed. This approach is referred to in EN13286-7 (2004) and it allows for the application of a certain number of consecutive stress paths to the same specimen, thus reducing the time spent in the laboratory, but it also

increases the complexity compared to the single-stage RLT. Gidel et al. (2001) introduced this concept into their work, as did Erlingsson and Rahman (2013) noting that their work was based on the time-hardening concept introduced earlier by Lytton et al. (1993) and Gidel et al. (2001). In this method the permanent deformation formulation is modified (Erlingsson and Rahman, 2013):

$$\varepsilon_p = f_1(N) f_2(p, q, \varepsilon_r) \tag{4.11}$$

to

$$\varepsilon_p = f_1(N - N_{i-1} + N_i^{eq}) f_2(p_i, q_i, \varepsilon_{ri}) \tag{4.12}$$

where the subscript *i* refers to the *ith* stress path and N_i^{eq} is determined by considering the following expression:

$$N_i^{eq} = f_3(\hat{\varepsilon}_{pi-1}, p_i, q_i, \varepsilon_{ri}) \tag{4.13}$$

where, $\hat{\varepsilon}_{pi-1}$ is the accumulated permanent deformation at the end of the (*i*-1)th stress path.

Despite the reduction in time, most of the models presented in the bibliography are developed under the single-stage RLT like the Korkiala-Tanttu (2005) model.

4.3.4.3 Complexity

Empirical permanent deformation models have been changing over time with an increase in their complexity (variables included in the model). Most models establish a relationship between permanent deformation with the number of load cycles and the levels of stress. Some initial studies on resilient and permanent deformations only considered the number of load cycles (Barksdale (1972). Despite their simplicity, these models have some historical significance and enable us to understand why stresses are an important factor when determining permanent deformation. In fact, some of these models did consider the stress conditions indirectly in their constants, as presented in Table 4.2.

Some studies showed the importance of the stress state and its influence was considered in the permanent deformation models, as shown in Table 4.3. It is noted that in most of the empirical permanent deformation models, the stress levels are defined through the deviatoric (*q*) and mean (*p*) stresses.

The most recent well-known models are an improvement on the others. Indeed, the first model only depended on the number of load cycles (*N*), whereas later models depended on the stress levels and some included the influence of stress indirectly (through their constants); these models are still simple as those developed by Monismith et al. (1975), Sweere (1990) and Huurman (1997).

Table 4.2 - Empirical models dependent on the number of load cycles

Authors	Permanent deformation	Parameters
Barksdale (1972)	$\varepsilon_1^p = a + b \, log \, (N)$	- a and b are constants
Khedr (1985)	$\dfrac{\varepsilon_1^p}{N} = A \cdot N^{-b}$	- b is a material parameter - A is a material and stress-strain parameter given as a function of shear stress ratio and resilient modulus
Paute (1988)	$\varepsilon_1^p = A_0 \dfrac{\sqrt{N}}{\sqrt{N} + D} + \varepsilon_1^p \, (100)$	- A_o – parameter function of the stress level, - D is a regression parameter - $\varepsilon_1^p \, (100)$ – permanent deformation after the first 100 cycles
(Tseng and Lytton, 1989)	$\varepsilon^p = \varepsilon_0^p e^{-\left(\frac{\rho}{N}\right)}$	- ε_p is the permanent deformation - ε_0^p is the maximum permanent deformation - N is the number of load cycles - ρ is the scale factor - β is the shape factor
Sweere (1990)	$log \left(\varepsilon_1^p(N)\right) = a + b \, log \, (N)$	- a,b – material parameters *for each stress level, separate permanent deformation; parameters a and b need to be determined from the results of cyclic load triaxial test **Sweeres's formula is valid for granular materials (Gidel et al., 2001)
Hornych (1993)	$\varepsilon_1^p(N) = A \left[1 - \left(\dfrac{N}{100}\right)^{-B}\right] + \varepsilon_1^p(100)$	- A and B - $\varepsilon_1^p \, (100)$ - permanent deformation after the first 100 cycles
Vuong (1994)	$\varepsilon_1^p = \varepsilon_1^r \left(\dfrac{a}{b}\right) N^c$	- a,b and c - ε_1^r is the resilient axial deformation
Wolff and Visser (1994)	$\varepsilon_1^p = (cN + a)(1 - e^{-bN})$	- a, b and c are regression parameters
Huurman (1997)	$\varepsilon_1^p(N) = A \left[\left(\dfrac{N}{1000}\right)^{B}\right] + C \cdot (e^{D\frac{N}{1000}} - 1)$	- A, B, C, D are parameters function of stress level

Most models depend directly on the mean (p) and deviatoric (q) stresses and evaluate the length and slope of the stress path through the relationship established between q and p, as does the model developed by Hyde (1974), Lekarp and Dawson (1998) and Rahman and Erlingsson (2015). This last model is dependent on the factor S_f:

$$\varepsilon_p(N) = \alpha N^{bS_f} S_f$$

$$S_f = \frac{\left(\dfrac{q}{p_a}\right)}{\left(\dfrac{p}{p_a}\right)^{\alpha}} \tag{4.14}$$

Table 4.3 - Empirical permanent deformation models dependent on the number of load cycles and stress levels

Authors	Permanent deformations	Parameters
Barksdale (1972)	$$\varepsilon_1^p = \frac{q/a.\sigma_3^b}{1 - \left[\frac{R_f \cdot q \cdot (1 - \sin\emptyset)}{2(C \cdot \cos\emptyset + \sigma_3 \sin\emptyset)}\right]}$$	- $a.\sigma_3^b$ is a relationship defining the initial tangent modulus as a function of confining pressure (σ_3); a and b are constants - R_f is the ratio of the applied deviator stress at failure q_f - ϕ is the friction angle and C is the cohesion
Hyde (1974)	$$\varepsilon_1^p = a\frac{q}{\sigma_3}$$	- a is a constant; - σ_3 is the confining stress; - q is deviator stress.
Shenton (1974)	$$\varepsilon_1^p = K\left(\frac{q_{max}}{\sigma_3}\right)^\alpha$$	- K and α - q_{max} is the maximum deviatoric stress applied
Pappin (1979)	$$\varepsilon_1^p = f_n(N) \cdot L \cdot \left(\frac{q^0}{p^0}\right)^{2.8}$$	- $f_n(N)$ – depends on the number of cycles (shape factor); - q^0 is the modified deviator stress ($\sqrt{2/3} \cdot q$) - p^0 is the modified mean normal stress ($\sqrt{3} \cdot p$) - $L = \sqrt{p^2 + q^2}$ (length of stress path)
Lentz and Baladi (1980)	$$\varepsilon_1^p = \varepsilon_{0.95S} \ln\left(1 - \frac{q}{S}\right)^{-0.15} +$$ $$\left[\frac{n\,(q/S)}{1 - m(q/S)}\right] ln(\text{N})$$	- $\varepsilon_{0.95S}$ is the axial deformation at 95% of the deviatoric stress at failure - m is the slope of the failure line - S is the deviatoric stress at failure
Tseng and Lytton (1989)	$$\varepsilon_1^p = \varepsilon_0^p e^{-(\rho/N)^\beta}$$	- ε^p is the permanent deformation of the granular material; - ε_0^p is the maximum permanent deformation; - N is the number of load cycles; - ρ is the scale factor; - β is the shape factor.
Paute et al. (1994)	$$\varepsilon_1^{p*} = f(N) \cdot A = f(N)$$ $$\cdot \frac{\frac{q}{(p + p^*)}}{b\left(m - \frac{q}{(p + p^*)}\right)}$$	- ε_1^{p*} is the permanent axial deformation after the first 100 cycles - b – regression parameter - p^* is a stress parameter defined by the intersection of the static failure line and *p-axis* in *p-q* space - m is the slope of the failure line in *p-q* space - $f(N)$ function of the number of cycles N
Nishi (1994)	$$\varepsilon_{1,ult}^p = k\frac{q^a}{p^b}$$	- a and b - $\varepsilon_{1,ult}^p$ is the ultimate permanent axial deformation
Lekarp and Dawson (1998)	$$\frac{\varepsilon_1^p(N_{ref})}{(L/p_0)} = a \cdot \left(\frac{q}{p}\right)_{max}^b$$	- a and b - N_{ref} - $L = \sqrt{q^2 + p^2}$, - $p_0 = 100$ kPa (reference mean stress)

Nevertheless, these models have considered the influence of stress dependency by including the stress ratio; for example, Huurman (1997) included the effect of the stress ratio on one of the model constants by considering the failure ratio of the major principal stresses σ_1/σ_{1f}. This formulation means the deformations are larger when the failure ratio is close to failure. The model defines the ratio as the relationship between deviatoric stress and deviatoric stress at failure (q/q_f) because the deviatoric stress is supposed to be the most dominating stress component for permanent deformations (Li and Selig, 1996, Chai and Miura, 2002, Korkiala-Tanttu, 2005, Chow et al., 2014, Xiao et al., 2015, Yesufa and Hoffa, 2015, Gu et al., 2016). The model developed by Gidel et al. (2001) and further extended by Chen

et al. (2014) is more complex because it depends on the failure criterion by including the strength parameters *m* and *s* of the *Mohr-Coulomb* yielding criterion.

Subsequently, there have been several models including the influence of initial stress indirectly and explicitly (Chai and Miura, 2002, Chen et al., 2014, Ling et al., 2017, Wei et al., 2017) that can explain the apparent decrease of permanent deformation as the initial mean stress increases. Put simply, a higher initial stress leads to a greater distance to the failure criterion which then leads to a lower value of permanent deformation.

Some other recent models based on the power-law - $\varepsilon_p = a \cdot N^b$ (where *a* and *b* are constants and *N* is the number of load cycles) - include, among other factors, the octahedral normal and shear stresses (σ_{oct} and τ_{oct}) instead of the *p* and *q* in the formulation of the model (Puppala et al., 1999, Puppala et al., 2009, Cai et al., 2015).

Some more complex models also include the influence of the physical state of the material, as the model by Xiao et al. (2015). However, this model depends on several parameters that can be very difficult to obtain.

To simulate and predict permanent deformation, the most suitable model for each analysis/situation must be chosen and, therefore, the model must be selected according to the material to be tested and its physical condition. The model must then be evaluated according to its complexity in terms of modelling to the number of variables required by the formulation, and to its efficiency and accuracy with regards to expected results. A simpler model can easily represent *in situ* conditions rather than complex models that depend on several variables, which means that can be necessary to carry out certain laboratory tests or extrapolate existing values of the bibliography, leading to errors in the prediction of permanent deformation.

4.4 Resilient modulus: parametric study

Considering the extended information presented in section 4.2 and also the tables presented in the Annex, a first attempt was done to compare the resilient modulus of different materials under a certain stress level. This analysis is also important to comprehend how the models differ from each other in terms of formulation and the importance of certain variables. Section 4.2 presents a chronological evolution of the resilient modulus (through the compilation of the models) and allows understanding the importance of each variable and its influence on the resilient modulus (according to the type of material). The study

presented in this section allows to compare and better understand each selected model as well as the variables involved.

The models were calibrated considering the same stress path for all materials during the calibration process. The stress path described by Chen et al. (2014) was used. This stress path is characterised by a cyclic deviator stress of 24 kPa and a constant confining stress of 60 kPa, which is aligned with some of the field stresses induced by the vehicles. Furthermore, these cyclic tests were performed in the scope of the evaluation of the performance of a full-scale model test on high-speed railway. During the cyclic tests, the stress ratio (σ_d/σ_c) was kept constant at 0.4, which is a representative ratio in the subgrade of a full-scale model test. It is noted that other confining stresses from 60 kPa to 210 kPa were also tested.

In this analysis, four models were applied in order to compare the resilient modulus for the coarse-grained soils, as depicted in Table 4.4.

Table 4.4 - Models considered in the analysis of the coarse-grained soils

Authors	Models
Seed et al. (1967); Brown and Pell (1967); Hicks and Monismith (1971)	$M_r = k_1(\theta)^{k_2}$
Uzan (1985)	$M_r = k_1 p_0 \left(\dfrac{\theta}{p_0}\right)^{k_2} \left(\dfrac{q}{p_0}\right)^{k_3}$
Gomes Correia et al. (2001)	$E_v = C\sigma'_v{}^m$
MEPDG (ARA Inc. ERES Division, 2004)	$M_r = k_1 p_0 \left(\dfrac{\theta}{p_0}\right)^{k_2} \left(\dfrac{\tau_{oct}}{p_0} + 1\right)^{k_3}$

The first part of this work is based on the experimental results presented by Garg and Thompson (1997). The authors studied six granular materials representative of the base and sub-base materials used on flexible pavements. Garg and Thompson (1997) performed rapid shear tests and repeated-load tests in order to determine the shear strength parameters (cohesion and friction angle), resilient modulus, rutting potential and moisture susceptibility. The properties of the materials are presented in Table 4.5.

Table 4.5 - Properties of the materials (coarse-grained soils)

No.	UIC and ASTM Classification	Materials	Properties	Observations
1	QS3 GW	Well-graded gravel	Cu=27; Cc=2 (PI_{min}=NP; PI_{max}=6) $W_{L,max}$=25 W=6.3% W_{OMC}=6.8%	Granular material used as based and sub-base in the flexible pavement sections; The target moisture content and densities were selected based on AASHTO T99 test results and field-measured values (Garg and Thompson, 1997).
2	QS2/QS3 SW/SM-ML	Sand	Cu=20 ; Cc=0.8-1.1 (PI_{min}=NP; PI_{max}=6) $W_{L,max}$=25 W=7.7% W_{OMC} =7.7%	

149

To compare the models, the results from the repeated-load tests (which included the measured resilient modulus and number of load cycles from the work developed by Garg and Thompson (1997)) were used, as well as the selected stress path defined by Chen et al. (2014). The constants of each model were determined by regression analyses. The results of the four models and the two materials are presented in Table 4.6. It is important to refer that for material 2, due to the lack of data, it was not possible to present the regression results for the model developed by Gomes Correia et al. (2001) and *MEPDG* model. Analysing Table 4.6, in general, the models present similar *r*-squared values. Therefore, considering the obtained constants and the stress path selected, the models were compared in terms of the resilient modulus, as depicted in Table 4.7. Analysing Table 4.7, the models present similar results. Material 2 present an inferior resilient modulus when compared to the well-graded gravel, as expected. Regarding the material classified as QS3-GW, it is evident the close values between the Uzan's model, k–θ and *MEPDG's* model.

Table 4.6 - Summary of the values of the regression analysis based on experimental results

Models	Material/ Classification	Parameters	Regression analysis – R^2
$M_r = k_1(\theta)^{k_2}$	Well-graded gravel QS3-GW	k_1=5176 k_2=0.64	0.997
	Sand QS2/QS3 - SW/SM-ML	k_1=36942 k_2=0.32	0.933
$M_r = k_1 p_0 \left(\dfrac{\theta}{p_0}\right)^{k_2} \left(\dfrac{q}{p_0}\right)^{k_3}$	Well-graded gravel QS3-GW	k_1=5306 k_2=0.59 k_3=0.05	0.998
	Sand QS2/QS3 - SW/SM-ML	k_1=34336 k_2=0.45 k_3=-0.15	0.942
$M_r = k_1 p_0 \left(\dfrac{\theta}{p_0}\right)^{k_2} \left(\dfrac{\tau_{oct}}{p_0}+1\right)^{k_3}$	Well-graded gravel QS3-GW	k_1=1.02 k_2=0.62 k_3=-0.01	0.997
	-	-	-
$E_v = C\sigma'^m_v$	Well-graded gravel QS3-GW	C=6768 m=0.65	0.988
	-	-	-

After the analysis of the coarse-grained soils, the fine-grained soils were evaluated. In the case of the fine-grained soils, four models (Table 4.8) and two materials were compared (Table 4.9). The materials were tested through the triaxial test and both materials were compacted at optimum water content and 2% above the optimum. The measured resilient modulus is based on the work developed by Liang et al. (2008).

Table 4.7 - Determination of the resilient modulus for the coarse-grained materials

Models	Materials/Classification	Resilient Modulus
$M_r = k_1(\theta)^{k_2}$	Well-graded gravel QS3-GW	M_r= 156 MPa
	Sand QS2/QS3 - SW/SM-ML	M_r= 109 MPa
$M_r = k_1 p_0 \left(\dfrac{\theta}{p_0}\right)^{k_2} \left(\dfrac{q}{p_0}\right)^{k_3}$	Well-graded gravel QS3-GW	M_r= 143 MPa
	Sand QS2/QS3 - SW/SM-ML	M_r=131 MPa
$M_r = k_1 p_0 \left(\dfrac{\theta}{p_0}\right)^{k_2} \left(\dfrac{\tau_{oct}}{p_0}+1\right)^{k_3}$	Well-graded gravel QS3-GW	M_r= 159 MPa
	-	-
$E_v = C{\sigma'_v}^m$	Well-graded gravel QS3-GW	M_r=118 MPa
	-	-

Table 4.8 - Models selected for the fine-grained soils

Authors	Models
MEPDG ARA Inc. ERES Division (2004)	$M_r = k_1 p_0 \left(\dfrac{\theta}{p_0}\right)^{k_2} \left(\dfrac{\tau_{oct}}{p_0}+1\right)^{k_3}$
Yang et al. (2005)	$M_r = k_1(\sigma_d + \chi\psi_m)^{k_2}$
Liang et al. (2008)	$M_r = k_1 p_a \left(\dfrac{\theta + \chi\psi_m}{p_a}\right)^{k_2} \left(\dfrac{\tau_{oct}}{p_a}+1\right)^{k_3}$
Dawson and Gomes Correia (1993)	$E_r = A + B p'_0 + C q_r$

Table 4.9 - Properties of the fine-grained materials

No.	UIC and ASTM Classification	Materials	Properties	Observations
1	QS1 Low plasticity CL	Lean Clay	- W_L=30.8%; - W_P=18.4%; - IP=12.3%;	- The effect of the matric suction will be included in the effective stress; - The triaxial tests following the AASHTO T307-99 procedure were conducted on both materials
2	QS1 Low plasticity CL-ML	Silt-lean clay	- W_L=27.8%; - W_P=19.8%; - IP=8%;	

Considering the results obtained by Liang et al. (2008) regarding the measured resilient modulus, the constants of the parameters were determined through regression analyses (Table 4.10). However, it is important to refer that the *MEPDG* model is defined in terms of total stresses, which means that the regression analysis is performed for each material on both moisture content (optimum and optimum +2%). The remaining models are dependent on effective stresses, which means that the regression analysis is performed considering the whole set of moisture content (optimum and optimum+2%). This type of information allows analyzing the sensibility of the resilient modulus regarding the moisture content. The models developed by Yang et al. (2005), Liang et al. (2008) and Dawson and Gomes Correia (1993)

are dependent on the ψ_m and χ_m parameters, which means that the results are presented considering M_r^{opt} and $M_r^{opt+2\%}$, although the regression is performed with the whole set (OPT and OPT+2%).

The model developed by Dawson and Gomes Correia (1993) is simpler than the remaining models and does not takes into account directly the influence of the moisture content. Indeed, this factor is included in the suction matrix in the initial mean normal stress (p'_0). From multiple linear regression analyses, the empirical constants were determined, and the values are expressed in Table 4.10.

Table 4.10 - Regression results for the fine-grained materials

Models	Material/ Classification	Parameters	Regression analysis – R^2
$M_r = k_1 p_0 \left(\dfrac{\theta}{p_0}\right)^{k_2}\left(\dfrac{\tau_{oct}}{p_0}+1\right)^{k_3}$	QS1 Low plasticity CL **OPM**	K_1=0.55 K_2=0.15 K_3=-1.82	0.98
	QS1 Low plasticity CL **OPM+2%**	K_1=0.35 K_2=0.14 K_3=-1.61	0.90
	QS1 Low plasticity CL-ML **OPM**	K_1=0.97 K_2=-0.17 K_3=-1.97	0.96
	QS1 Low plasticity CL-ML **OPM+2%**	K_1=0.68 K_2=-0.10 K_3=-1.13	0.87
$M_r = k_1(\sigma_d + \chi\psi_m)^{k_2}$	QS1 Low plasticity CL	K_1=5.45 K_2=0.36	0.09
	QS1 Low plasticity CL-ML	K_1=72.11 K_2=-0.04	0.002
$M_r = k_1 p_a \left(\dfrac{\theta + \chi\psi_m}{p_a}\right)^{k_2}\left(\dfrac{\tau_{oct}}{p_a}+1\right)^{k_3}$	QS1 Low plasticity CL	K_1=0.24 K_2=0.85 K_3=-2.29	0.62
	QS1 Low plasticity CL-ML	K_1=0.78 K_2=0.13 K_3=-2.01	0.61
$E_r = A + Bp'_0 - Cq_r$	QS1 Low plasticity CL	A=3499.51 B=261.25 C=-190.78	0.91
	QS1 Low plasticity CL-ML	A=60443.76 B=-167.96 C=-474.39	0.69

From the constant parameters and the selected stress path, the resilient moduli of the materials were found, as depicted in Table 4.11.

Considering the obtained results for the fine and coarse-grained materials, the *MEPDG* model (ARA Inc. ERES Division, 2004) will be adopted in the following analyses, despite its complexity when compared to the remaining models. The main reason is related to its universal character since the model can be applied in the prediction of the resilient modulus of all types of geomaterials.

Table 4.11 - Resilient modulus of the fine-grained materials

Models	Materials/Classification	Resilient Modulus
$M_r = k_1 p_0 \left(\dfrac{\theta}{p_0}\right)^{k_2} \left(\dfrac{\tau_{oct}}{p_0} + 1\right)^{k_3}$	QS1 Low plasticity CL	M_r= 50 MPa (OPT) M_r= 33 MPa (OPT+2%)
	QS1 Low plasticity CL-ML	M_r= 70 MPa (OPT) M_r= 56 MPa (OPT+2%)
$M_r = k_1 (\sigma_d + \chi \psi_m)^{k_2}$	QS1 Low plasticity CL	The regression coefficient is extremely low
	QS1 Low plasticity CL-ML	The regression coefficient is extremely low
$M_r = k_1 p_a \left(\dfrac{\theta + \chi \psi_m}{p_a}\right)^{k_2} \left(\dfrac{\tau_{oct}}{p_a} + 1\right)^{k_3}$	QS1 Low plasticity CL	M_r= 53 MPa (OPT) M_r= 47 MPa (OPT+2%)
	QS1 Low plasticity CL-ML	M_r= 73 MPa (OPT) M_r= 72 MPa (OPT+2%)
$E_r = A + Bp'_0 - Cq_r$	QS1 Low plasticity CL	M_r= 83 MPa (OPT) M_r= 76 MPa (OPT+2%)
	QS1 Low plasticity CL-ML	M_r= 80 MPa (OPT) M_r= 71 MPa (OPT+2%)

This analysis shows a possible way to rank materials according to the resilient modulus, as depicted in Figure 4.7. In the case of the material classified as QS2/QS3 SW/SM-ML, instead of the *MEPDG* model, Uzan's model was used due to the lack of information (it was not possible to perform a regression analysis). However, as the previous analysis showed, the *MEPDG* and Uzan's model present similar results. All the materials present in Figure 4.7 are at optimum moisture content, except the material classified as QS2/QS3 SW/SM-ML. In this case, the moisture content is close to the optimum conditions.

153
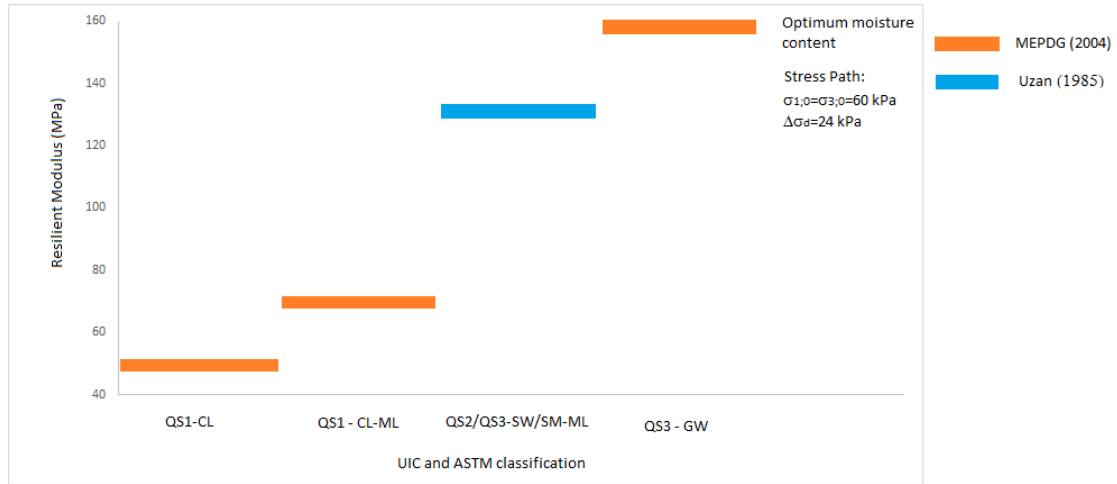
Figure 4.7 - Resilient modulus predicted by *MEPDG* for the different types of soils

4.5   A comparison of permanent deformation models – parametric study

This section attempts to compare different permanent deformation models available for different types of soils considering the model developed by Chen et al. (2014). Whereas this comparison depends on the soil classification, the results go beyond the soil type. Indeed, while two soils can be integrated into the same classification (UIC or ASTM), the laboratory conditions may differ greatly and therefore lead to different results.

It is noted that Chen et al. (2014)'s model considers the stress level (the model includes the amplitude of diagram *p-q*), the number of load cycles, the initial stress state, and it quantifies the proximity of the peak stress point (p_{max}, q_{max}) to the *yielding criterion*. This particular model, therefore, includes several important conditions in its analysis of permanent deformation.

For all the experimental data, calibration was performed to find the best fit for the experimental data through the parameters $\varepsilon_{p;0}$, α and B (correspond to material properties), presented in the following equation:

$$\varepsilon_1^p(N) = \varepsilon_1^{p0}[1 - e^{-BN}]\left(\frac{\sqrt{p_{am}^2 + q_{am}^2}}{p_a}\right)^a$$

$$\cdot \frac{1}{m\left(1 + \dfrac{p_{ini}}{p_{am}}\right) + \dfrac{s}{p_{am}} - \dfrac{(q_{ini} + q_{am})}{p_{am}}}$$

(4.15)

where p_{am} and q_{am} are the amplitude of the mean stress and deviator stress induced by train loadings, *m* and *s* are defined by the yielding criterion *q=s + mp*; and p_{ini} and q_{ini} are the mean and deviator stress in the initial state of the material.

These selected materials are representative of different types of materials (silt and sand), the percentage of fines, and the granulometry (poor and well graded sands), as depicted in Table 4.12.

The models are calibrated considering the same stress paths for all materials during the calibration process. The stress path described by Chen et al. (2014) was used in this analysis and it was described previously (cyclic deviator stress of 24 kPa, a constant confining stress of 60 kPa and stress ratio constant at 0.4). The stress path and the *Mohr-Coulomb yielding criterion* of each material are depicted in Figure 4.8. This figure shows the stress path applied on the cyclic triaxial test (with a stress ratio equal to 0.4) and the failure envelopes of different materials used in the laboratory tests. The failure envelopes are defined through the *Mohr-Coulomb yielding criterion* from the expression $q = s + mp$.
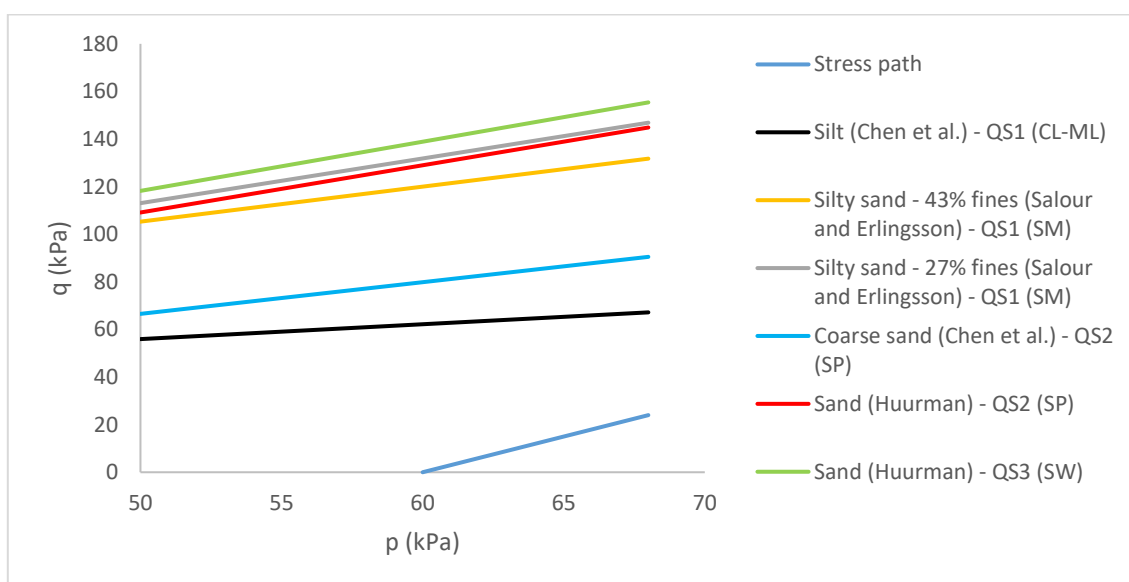
Figure 4.8 - Total stress path selected and failure envelopes of Mohr-Coulomb yielding criteria

It is seen that the distance between the stress path and the failure envelopes influences the development of permanent deformation. In order to understand which main factors influence cumulative settlement, and compare the long term response of the materials selected, three main models were selected and calibrated as introduced by Huurman (1997), Chen et al. (2014) and Rahman and Erlingsson (2015); these models have been formulated and developed under different conditions in terms of materials and applied stress ratios, as described below.

Table 4.12 - Materials selected for the preliminary analysis of the permanent deformation

Author	Soils	ASTM Classification	UIC classification	Observations
Chen et al. (2014)	Sand	SP	QS2	Compacted at field conditions and saturated
	Silt	CL-ML	QS1	Compacted at field conditions and saturated
Salour and Erlingsson (2016) and Erlingsson et al. (2017)	Silty Sand (42.2% fines)	SM	QS1	Compacted at optimum compaction – standard Proctor
	Silty Sand (27.4% fines)	SM	QS1	Compacted at optimum compaction - standard Proctor
Huurman (1997)	Well-graded Sand	SP	QS2	Compacted at optimum compaction - standard Proctor
	Poor-graded Sand	SW	QS3	Compacted at optimum compaction - standard Proctor

With the Huurman (1997) model, the samples are tested according to their optimum moisture content and with a confining pressure equal to 12 kPa, whereas with the Chen et al. model, the specimens are saturated, and the boundary is the drainage condition. With the Rahman and Erlingsson (2015) model, the influence that the moisture content has on permanent deformation, and the degree of saturation, are analysed but this analysis only considers the optimum moisture content for each type of soil. Confining pressure, σ_3, is tested as 27.6, 41.4 and 55.2 kPa, and cyclic deviator stress varies according to the stress path. Thus, the development of these models includes different laboratory conditions such as soils under different state conditions and different stress conditions.

Whereas Huurman (1997) considers seven poorly graded sands and one well-graded sand (designated as crusher), only *C. Bruynweg* and *Crusher* corresponds to the poor and well-graded sands (Table 4.13). Thus, these two sands were selected. In addition, the *C. Bruynweg* was selected as the stress ratio is similar to the one carried out by Chen et al. (2014). The remaining sands were tested for stress conditions close to failure ($\sigma_1/\sigma_{1,f}$ close or equal to one), which is outside the representative stress conditions of this study. In this work, the parameters of Huurman's model are adjusted so that the parameters ε_{p0}, *a* and *B* can be obtained; this adjustment took place through the formulation *lscurvefit* in *Matlab*.

Table 4.13 - Physical properties of the materials - granulometry

Authors	Huurman (1997)		Salour and Erlingsson (2016) and Erlingsson et al. (2017)		Chen et al. (2014)	
Material/ Properties	C. Bruynweg	Crusher	Silty Clay (42.2% fines content)	Silty Clay (27.4% fines content)	Silt	Coarse sand
C_u	2.100	10.50	28.0	33.0	2.51	4.68
C_c	1.050	1.250	0.54	0.75	1.32	0.62
D_{10}	0.148	0.217	-	-	-	-
D_{30}	0.219	0.784	-	-	-	-
D_{50}	0.280	1.722	-	-	-	-
D_{60}	0.310	2.280	-	-	-	-
CBR (%)	22.00	15.70	-	-	-	-

In Rahman and Erlingsson (2015), two silty sands are analyzed and compared with the parameters of Chen's model. The study also shows a correlation between the ε_{p0} and α parameters and the moisture content.

In the work developed by Chen et al. (2014), a coarse sand and a silt are analysed and then the properties of these materials are divided according to their granulometry (Table 4.13), their state conditions (Table 4.14), and their failure parameters (Table 4.15).

Table 4.14 - State conditions of the materials

Authors	Huurman (1997)		Salour and Erlingsson (2016) and Erlingsson et al. (2017)		Chen et al. (2014)	
Material/ Properties	C. Bruynweg	Crusher	Silty Clay (42.2% fines content)	Silty Clay (27.4% fines content)	Silt	Coarse sand
$\rho_{dry,max}$ (kg/m^3)	1723	1755	1998	2070	1620	2110
W_{opt} (%)	12.5	10.5	10.1	7.6	-	-
ρ_{wet} (kg/m^3)	1942	1937	-	-	-	-
Liquid limit (%)	Non-plastic	Non-plastic	Non-plastic	Non-plastic	35	Non-plastic
Plastic limit	Non-plastic	Non-plastic	Non-plastic	Non-plastic	24	Non-plastic

Table 4.15 - Strength properties of the materials

Authors	Huurman (1997)		Salour and Erlingsson (2016) and Erlingsson et al. (2017)		Chen et al. (2014)	
Material/ Properties	C. Bruynweg	Crusher	Silty Clay (42.2% fines content)	Silty Clay (27.4% fines content)	Silt	Coarse sand
φ (°)	48.2	50.20	36.18	45.66	11.7*	0.00*
c (kPa)	5.60	8.680	15.82	10.43	16.4*	33.0*
s (kPa)**	9.90	14.90	31.80	19.10	24.8	0.00
m**	1.98	2.070	1.470	1.880	0.62	1.33

* In this case, the author described the saturated samples (silt and coarse sand) in ϕ' and c'

** s and m are the parameters used to define the failure envelope: $q=s+mp$

It is important to first consider Huurman (1997) work to understand the influence that the granulometry (well and poorly graded soil) has on permanent deformation. The analysis utilises the following stress ratios: 0.695, 0.803, 0.911. Figure 4.9 shows that well-graded sand has larger permanent deformation values for each stress ratio, which means that granulometry has an important influence on permanent deformation.
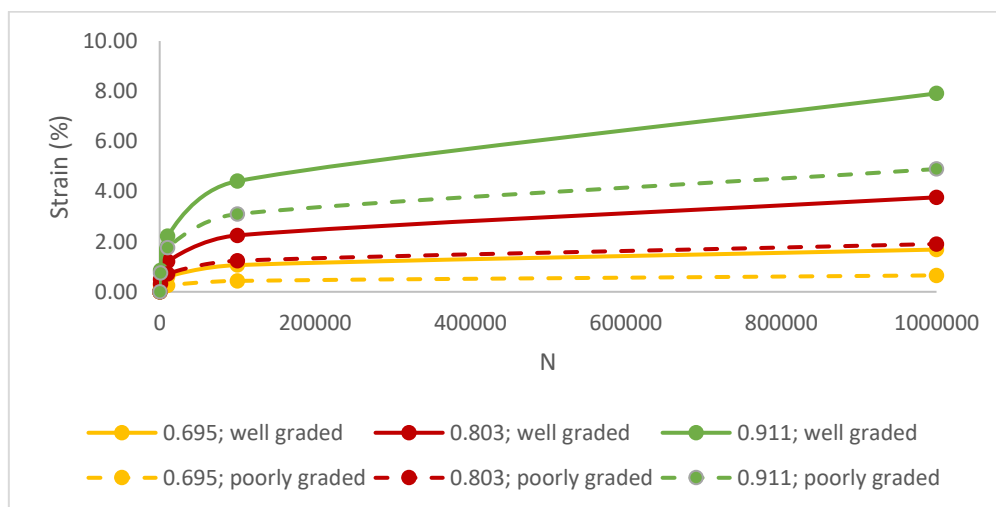
Figure 4.9 - Comparison between the permanent deformation of a poorly graded (*C. Bruynweg*) and well-graded (*crusher*) sand under different stress ratios

Table 4.16 presents the results of the calibration of the models for each selected soil where a regression analysis was performed. It is seen that there is some correlation (exponential and polynomial) between the three constant variables - ε_{p0}, α and β (superior to 0.7) - but the correlation between the constant variables and UIC classification (QS1, QS2, and QS3) is only residual.

Table 4.16 - Parameters of Chen's model and its relationship with the ASTM and UIC classification

	ε_{p0}	α	β	ASTM classification	UIC classification
Silt (Chen et al., 2014)	0.0029	0.2680	0.3390	CL	QS1
Silty sand (43% fines) (Erlingsson and Rahman, 2013)	0.0067	0.6500	0.2000	SM	QS1
Silty sand (27% fines) (Erlingsson and Rahman, 2013)	0.0069	0.6500	0.2000	SM	QS1
Coarse sand (Chen et al., 2014)	0.0018	0.3340	0.3390	SP	QS2
Poor-graded sand (Huurman, 1997)	0.0505	0.0104	0.0018	SP	QS2
Well-graded sand (Huurman, 1997)	0.0486	0.0111	0.0569	SW	QS3

The comparison between the permanent deformation curves is presented in Figure 4.10. It is seen that the results of silty sand and coarse sand (43% and 27% of fines) are very close, whereas the well and poorly-graded sand and silt are at opposite sides (the highest and smallest value of permanent deformation). This result is related to QS3-SW sand because a lower value was expected in comparison to QS2-SP. Another important fact is related to the influence of the stress ratio; in this instance, the permanent deformation results are not 100% aligned with those presented in Figure 4.8 because higher permanent deformation is expected when the stress path is close to the *yielding criterion* that depends on the values *s* and *m* of the *Mohr-Coulomb yielding criterion*. This means that, in addition to the strength properties, the soil physical properties (represented by the constants in the model) are also important in permanent deformation.

The materials and calibration process described in the previous section enable the results to be interpreted. Thus, the materials can be ranked according to their resistance to permanent deformation (Coronado et al., 2011). This information can then be used to predict permanent deformation during the design process. The ranking process provides reference values according to the type of material as well as the moisture content close to optimum conditions. In fact, Figure 4.11 is a re-interpretation of Figure 4.10. This innovative procedure enables that the expected values of permanent deformation can be compared according to the type of material through the UIC and ASTM soil classification; this ranking also includes different types of soils (clays and sands) and different granulometry. Figure 4.11 shows that the materials classified as CL-ML have a higher permanent deformation than the sands (SM, SP, and SW), while the sands with fines have a higher deformation than the SP and SW sands; therefore this parameter influences the permanent deformation and ranking of the geomaterials. During the design process, the long-term behaviour of the materials can be estimated, even though the permanent

deformation will be influenced by their state conditions such as the moisture content; therefore, the influence of this parameter in this analysis must be traduced.
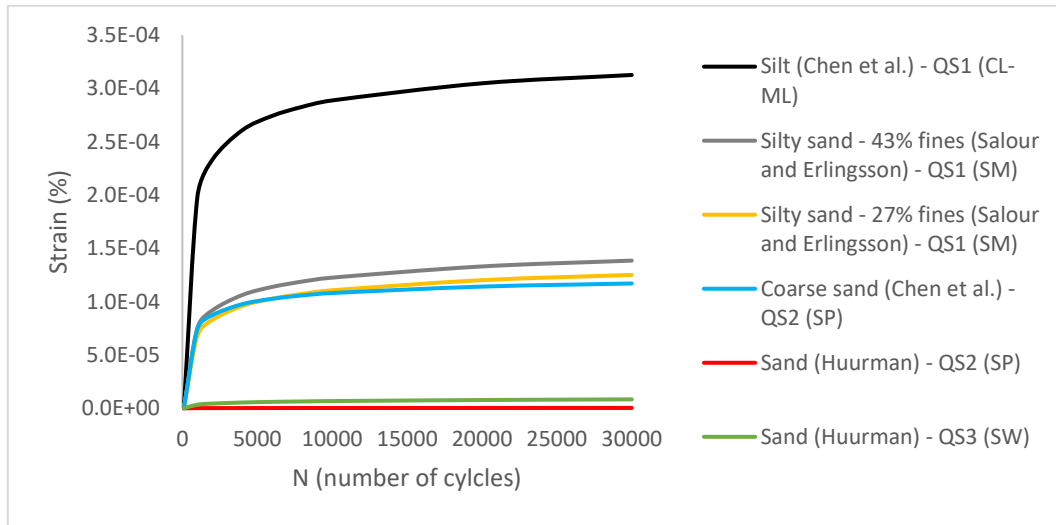
Figure 4.10 - Permanent deformation of the materials applying the Chen et al. (2014) model
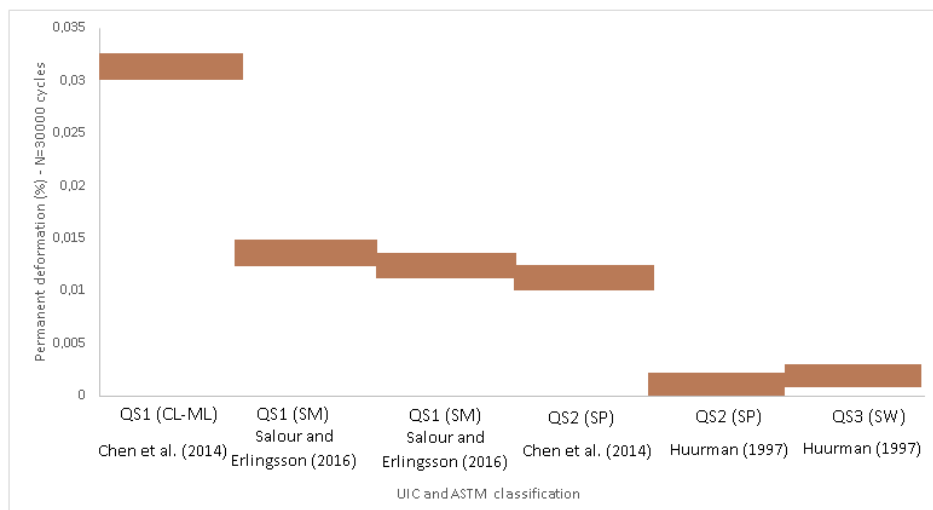
Figure 4.11 - Permanent deformation predicted by Chen et al. (2014)'s model for different soils (N=30,000 cycles) under a stress ratio $\sigma_1/\sigma_{1f} = 0.4$

Among other factors, moisture content also influences permanent deformation. Puppala et al. (2009) developed a model that depends on the octahedral normal and shear stresses (Table A.6 and Table A.8). Different materials, clay, silt, and sand with moisture contents ranging from dry of optimum, optimum and wet of optimum were tested. Three different confining pressures were applied to the clay and silt (0, 21 and 42 kPa), and confining pressures of 21, 48 and 97 kPa were applied to the sand. The deviatoric stress was determined by considering a percentage of the maximum deviatoric stress of each soil sample obtained in the unconsolidated undrained triaxial tests, so the deviatoric stress varies from $0.2\sigma_{d,f}$, $0.4\sigma_{d,f}$ and $0.6\sigma_{d,f}$.

To evaluate the influence that the moisture content has on permanent deformation, the results from Puppala et al. (2009) are used, but this analysis only focuses on the behaviour of clay (QS1 – CL) because it was not contemplated in previous studies. This exercise shows how important this parameter is, and the consequences in terms of permanent deformation when the moisture content moves away from the optimum conditions. Material properties are presented in Table 4.17, and as with the previous models and materials, the curve of permanent deformation has been adjusted to obtain the model parameters.

Figure 4.12 shows that the differences between dry, optimum and wet materials in terms of permanent deformation after 30 000 cycles are significant; the optimum material is 4-8 times higher than the dry material, and the wet material is 1-2 times higher than the optimum conditions. Therefore, when the moisture content is far away from optimum conditions, the variations of permanent deformation in the clays are substantial. In dry conditions, this value decreases significantly and in wet conditions, it increases which means that maximum permanent deformation occurs when the moisture content is beyond optimum (wet) due to an increase in the residual accumulation of excess water pressure.

Table 4.17 - Properties of the clay (in optimum conditions) tested in the Puppala et al. (2009)

Properties and parameters	Clay
ϕ ($^{\circ}$)	18
c (kPa)	60
Liquid limit (%)	28.19
Plasticity index (%)	12.55
Maximum dry unit weight (kN/m^3)	17.10
W_{opt} (%)	17.11
α_1	0.24
α_2	0.31
α_3	-1.77
α_4	2.85

161
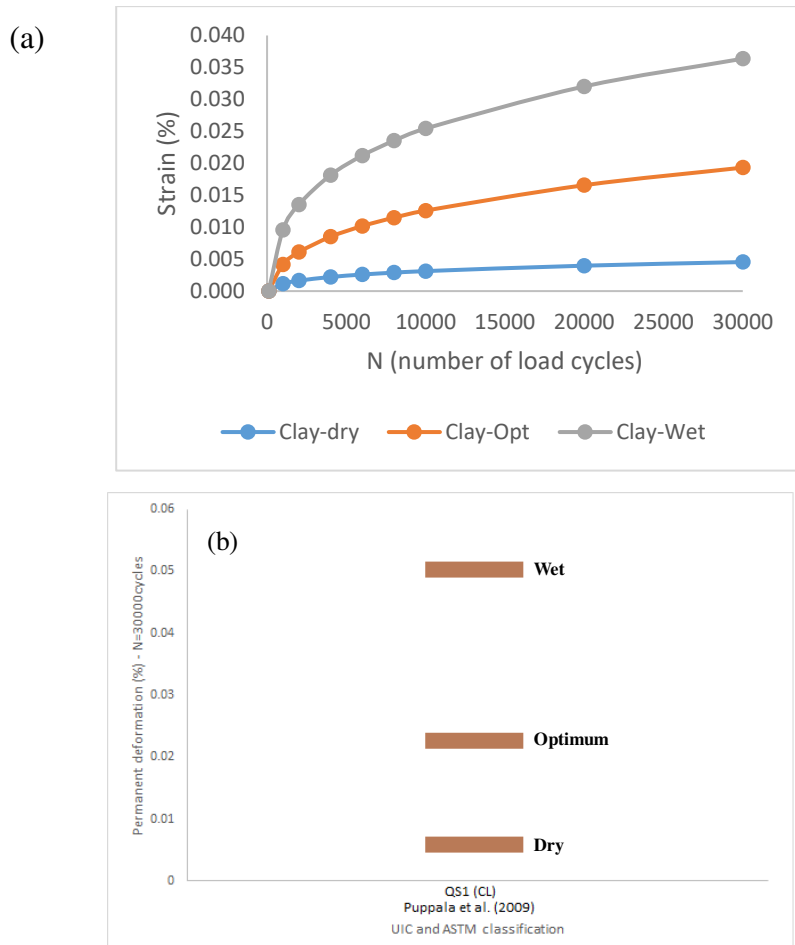
Figure 4.12 - Influence of the moisture content in the permanent deformation of a clay (Puppala's model): a) permanent deformation results applying the Chen et al. (2014) model; b) Ranking of permanent deformation for clay

4.6   Geomechanical classification of the geomaterials

Considering the results presented in previous sections (4.4 and 4.5), two models were selected to characterize the resilient modulus and permanent deformation of the geomaterials. Indeed, this is an attempt to relate the resilient modulus with the permanent deformation under a certain stress level. As in the previous analysis, the selected stress path is characterized by a cyclic deviator stress equal to 24 kPa and a confining constant stress equal to 60 kPa. The permanent deformation was determined considering a number of load cycles equal to 30,000. The selected materials are presented in Table 4.18. Some of the materials are the same used in sections 4.4 and 4.5 and others were added to increase the robustness of the analysis and the ranking. The work developed by Puppala et al. (2009) was included due to the significant information about both types of deformation (resilient and permanent) under different water content conditions. It is important to refer that, for these particular materials, are presented, whenever it is possible, the values of both deformations: resilient/recoverable and permanent deformations. For some materials, this is not possible due to the absence of data. This table also includes information about compaction conditions.

Table 4.18 - Properties of the materials

Information	UIC and ASTM Classification	Materials	Properties	Observations
Section 4.4	QS1 Low plasticity CL	Lean Clay	W_L=30.8%; W_P=18.4%; IP=12.3%;	The effect of the matric suction will be included in the effective stress; The triaxial tests following the AASHTO T307-99 procedure were conducted on both materials
Puppala et al. (2009)	QS1 Lean clay (CL)	Silty clay	W_L=28.19%; I_P=12.55% (low plasticity); G_s=2.63; Passing #200 =80%; Maximum dry unit weight = 17.10 kN/m³; W_{opt}=17.11%; c=60 kPa; ϕ=18°.	Compacted at optimum compaction – standard Proctor
Section 4.5	QS1 CL - ML	Silt	W_L=35 %; W_P =24 %; I_P =11 % (low to medium plasticity); G_s=2.67; C_u=2.51; C_c=1.32; Maximum dry density =15.89 kN/m³; Hydraulic permeability = 5.3×10⁻⁷ m/s; c'=11.7 kPa; ϕ'=16.4°.	Compacted at field conditions and saturated
Section 4.4	QS1 Low plasticity CL-ML	Silt-lean clay	W_L=27.8%; W_P=19.8%; IP=8%;	The effect of the matric suction will be included in the effective stress; The triaxial tests following the AASHTO T307-99 procedure were conducted on both materials
Section 4.5	QS1 SM	Silty Sand (42.2% fines)	C_u≈28; C_c≈0.54; G_s=2.68; Fines content=42.2%; Maximum dry density =19.6 kN/m³; W_{opt} =10.1%.	Compacted at optimum compaction – standard Proctor
Section 4.5	QS1 SM	Silty Sand (27.4% fines)	C_u≈33; C_c≈0.75; G_s=2.67; Fines content=27.4%; Maximum dry density =20.3 kN/m³; W_{opt} =7.6%.	Compacted at optimum compaction – standard Proctor
Puppala et al. (2009)	QS1 Silt (SM)	Silty clayed sand	W_L=16.70%; I_P=7.50% (low plasticity); G_s=2.70; Passing #200=38%; Maximum dry unit weight =16.9 kN/m³; W_{opt}=19.3%; c=103 kPa,; ϕ=35°.	Compacted at optimum compaction – standard Proctor

Section 4.5	QS2 SP	Well-graded Sand	C_u=2.10; C_c=1.05; Maximum dry Density = 16.90 kN/m³; W_{opt}=12.5%; c=5.60 kPa; ϕ=48.2⁰;	Compacted at optimum compaction – standard Proctor
Section 4.5	QS2 SP	Sand	G_s=2.66; C_u=4.8; C_c=0.62; Maximum dry density =20.69 kN/m³; Minimum dry density =15.89 kN/m³; Hydraulic permeability = 3.2×10⁻⁵m/s; c'=0 kPa; ϕ'=33°.	Compacted at field conditions and saturated
Puppala et al. (2009)	QS2 SP	Poorly graded sand	W_L=26.40%; G_s=2.71%; Passing #200=0.70%; C_u= 1.79; C_c=0.89; Maximum dry unit weight =15.70 kN/m³; W_{opt}=13.70%; c=20 kPa; ϕ=42°;	Compacted at optimum compaction – standard Proctor
Section 4.4	QS2/QS3 SW/SM-ML	Sand	Cu=20 Cc=0.8-1.1 (PI_{min}=NP; PI_{max}=6) W_L;máx=25 W=7.7% W_{OMC} =7.7%	Granular material used as based and sub-base in the flexible pavement sections; The target moisture content and densities were selected based on AASHTO T99 test results and field-measured values (Garg and Thompson, 1997).
Section 4.5	QS3 SW	Poor-graded Sand	C_u=10.5; C_c=1.25; Maximum dry Density = 17.21 kN/m³; W_{opt}=10.5%; c=8.68 kPa; ϕ=50.2⁰.	Compacted at optimum compaction – standard Proctor
Section 4.4	QS3 GW	Well-graded gravel	Cu=27 Cc=2 (PI_{min}=NP; PI_{max}=6) W_L;máx=25 W=6.3% W_{OMC}=6.8%	Granular material used as based and sub-base in the flexible pavement sections; The target moisture content and densities were selected based on AASHTO T99 test results and field-measured values (Garg and Thompson, 1997).

The resilient modulus and permanent deformation of the selected materials (Table 4.18) are presented in Table 4.19. The materials with both values of M_r and ε_p allow validating the mechanical classification.

Table 4.19 - Resilient modulus and permanent deformation of the selected materials

Information	Materials/Classification	Resilient Modulus	Permanent Deformation
Section 4.4	QS1 Low plasticity - CL	M_r= 50 MPa	–
Puppala et al. (2009)	QS1-CL	-	ε_p=0.01864 %
Section 4.5	QS1-CL/ML Silt	-	ε_p =0.03126 %
Section 4.4	QS1 Low plasticity - CL-ML	M_r= 70 MPa	–
Section 4.5	Silty Sand (42.2% fines) QS1-SM	M_r= 258 MPa	ε_p=0.01385 %
Section 4.5	Silty Sand (27.4% fines) QS1-SM	M_r= 294 MPa	ε_p=0.01251 %
Puppala et al. (2009)	QS1 - SM	M_r= 511 MPa	ε_p=0.00658 %
Section 4.5	Well-graded sand QS2-SP	M_r= 509 MPa	ε_p=0.00003%
Section 4.5	Sand QS2-SP	-	ε_p=0.01170%
Puppala et al. (2009)	QS2 - SP	M_r= 172 MPa	ε_p=0.01873%
Section 4.4	Sand QS2/QS3 - SW/SM-ML	M_r= 131 MPa	–
Section 4.5	Poor-graded sand QS3-SW	M_r= 178 MPa	ε_p=0.00084%
Section 4.4	Well-graded gravel QS3-GW	M_r= 159 MPa	ε_p=0.00320 %

From the results presented in Table 4.19, it is possible to define guiding/limit values associated with the *UIC* classification: QS1, QS2 and QS3 (UIC, 2008). This work only presents a preliminary geomechanical classification. The lack of information about the models' parameters found in the bibliography (namely the models that include the suction and other complex model coefficients) and the necessity and difficulty to performed back analysis to find important parameters (as the cohesion and friction angle used to define the failure criterion) reduced the number of models and materials that could be used in this geomechanical classification. Besides, some of the models found in the bibliography tested materials classified as QS0, which implies its elimination in the geomechanical classification, since these materials require mechanical improvement. They are considered as non-stabilized materials that need special compaction conditions to optimize the stability in terms of mechanical behaviour.

The geomechanical classification is an attempt to define a novel helpful guide to be used as a support for the modelling and design of the substructure of railways and also pavements. Indeed, this novel geomechanical classification tries to rank soils in a very similar way developed by Coronado et al. (2011) that was inspired by EN13286-7 (2004). This work allows understating which are the acceptable values of the permanent deformation and resilient modulus according to the type of material and its classification. In this particular case, UIC (2008) classification was used. The classification is depicted in Figure 4.13.

Analysing Figure 4.13, a significant range of values was obtained for each classification. This was expected due to the mineralogical nature and physical properties of each material, which can have an influence on several parameters used in the determination of the resilient modulus and permanent deformation. Indeed, in the case of the materials classified as QS1 (fine soils), the type of the material (CL, CH, ML, or MH) associated with its plasticity's characteristics and consistency index (as well as the percentage of fines), can have a significant impact in the permanent deformation and resilient behaviour, as depicted in Figure 4.14. For the materials classified as QS2 and QS3, the type of materials (sand or gravel) as well as its granulometry (well or poor-graded) and the percentage of fines (in the well-graded materials) can also influence the response of the material in terms of recoverable and permanent deformations.

With this work, it was possible to define sub-sets associated with the properties of the soils, despite the need for more information. For example, as shows Figure 4.14, a silty soil (classified as QS1-ML) presents a superior resilient modulus when compared to clayed soils (QS1-CL). Moreover, the difference in terms of permanent deformation can be explained by the plasticity properties of the fines content. Regarding the granular materials, the subsets can be defined by the granulometry of the materials (well or poor-graded). However, it is important to refer that the fines' percentage can also influence the obtained results.

Indeed, despite the importance of the granulometry and plasticity properties, the fines content and the moisture content have also significant importance, mostly in the fine soils. As mentioned previously, the work developed by Puppala et al. (2009) shows the influence of the moisture content in the soils. From these results, an estimation was performed considering the stress path selected (σ_3=60 kPa and σ_d=24 kPa) and the results are presented in Figure 4.15 and Figure 4.16. This property can influence both deformations as depicted in Figure 4.16, which means that can affect severely the track's performance. This influence was also demonstrated by Coronado et al. (2011) in the case of non-standard unbound granular materials for pavements.

166
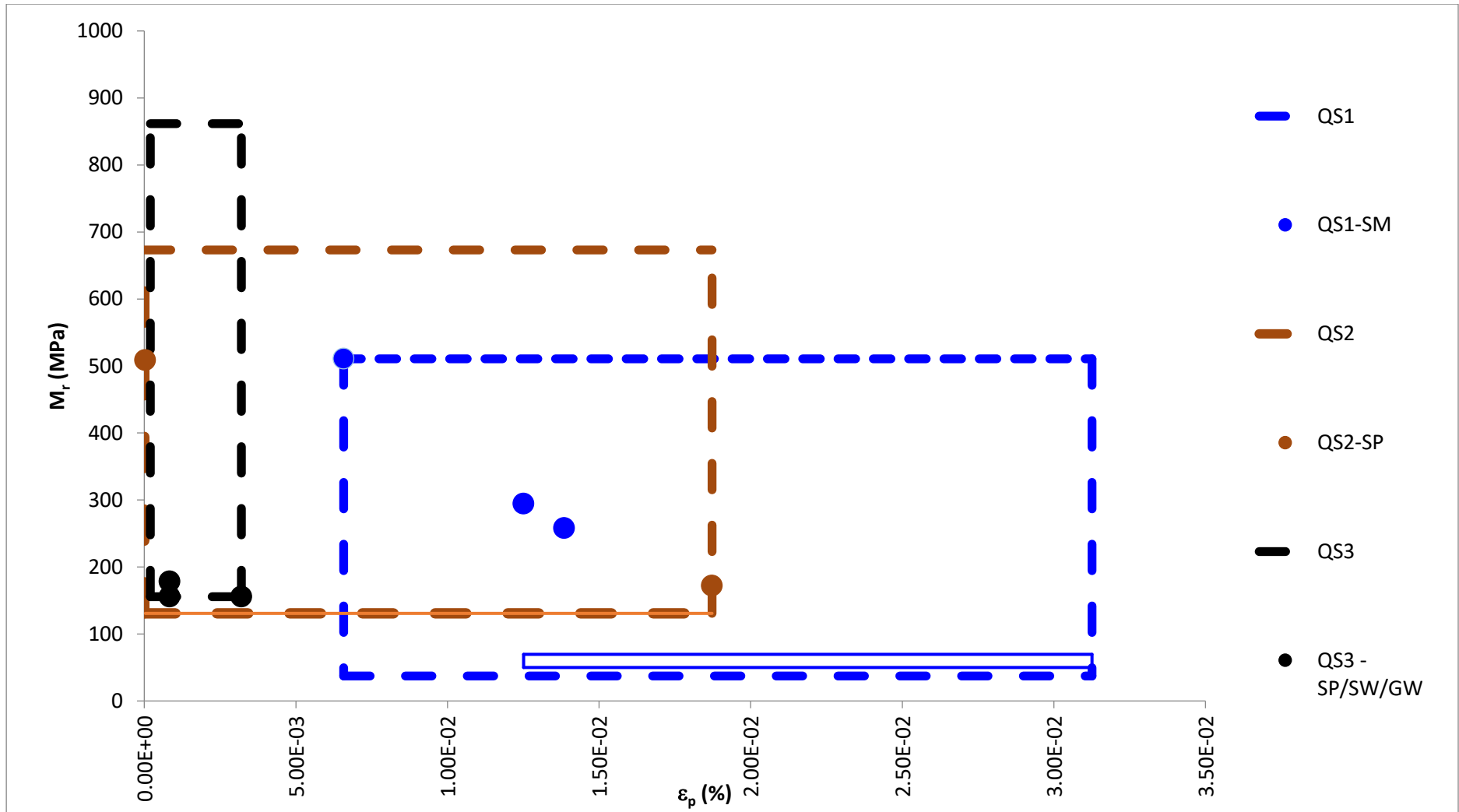
Figure 4.13 - Mechanical classification based on the resilient modulus and permanent deformation
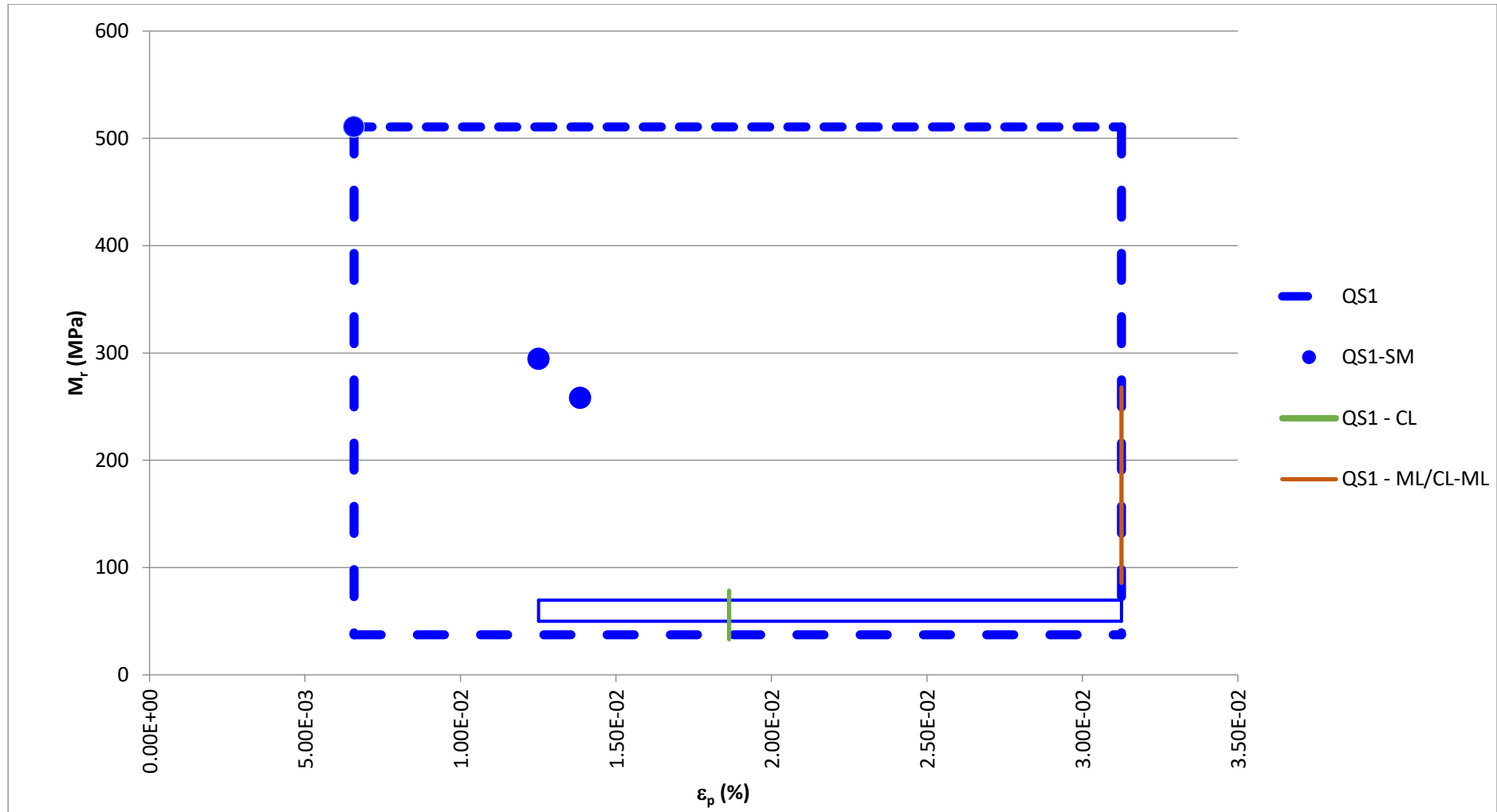
Figure 4.14 - Influence of the type of materials in the classification QS1
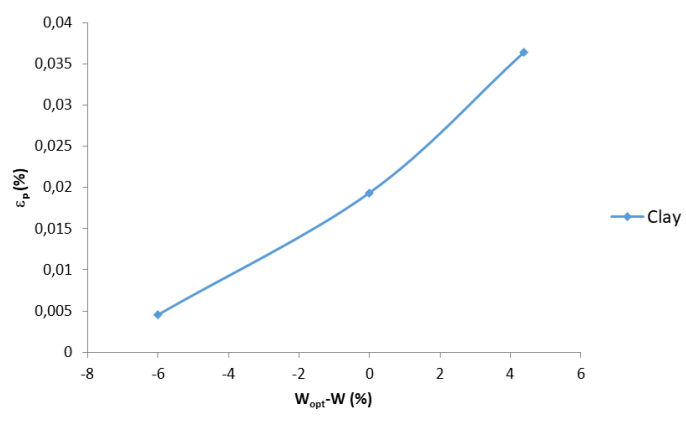
Figure 4.15 - Influence of the moisture content in the permanent deformation (clay)
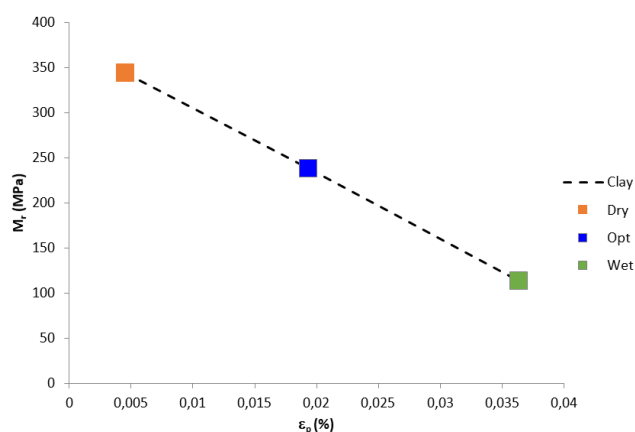
Figure 4.16 - Influence of the moisture content in the clay in the resilient modulus and permanent deformation

4.7 Final considerations

The capability to determine the resilient modulus and permanent deformation of geomaterials is very important in the modelling and evaluation of the performance of railway structures and pavements; it is also a key factor when estimating future maintenance operations and the respective costs. This work explains the main concepts regarding the elastoplastic behaviour of the geomaterials when submitted to cyclic loads and attempts to identify and summarize the main models to estimate the resilient modulus and also the permanent deformation. This work also has aimed to frame the main reasons why permanent deformation models were developed, particularly in pavements and railway structures. However, some issues related to traffic-induced permanent deformation weren't evaluated in this Chapter, such as the estimation of the dynamic stresses and strategies to simulate the effect of rotation of principal stresses. These topics, namely the assessment of the dynamic stresses, will be evaluated in further Chapters where the railway structures (ballasted and ballastless tracks) are modelled, and the short and long-term behaviour is evaluated. The long-term performance of the railway systems is evaluated through the implementation of the permanent deformation model selected in this Chapter, which corresponds to the model developed by Chen et al. (2014).

169

At the beginning of the analysis, the most simplistic models are presented for both types of deformation. In the case of the resilient modulus, the models should include the influence of the deviatoric and confining stresses and the constant parameters should reflect the influence of other factors as the moisture content and physical state of the material. Regarding the permanent deformation models, the same strategy was adopted. In this case, it was found that permanent deformation can be evaluated and predicted through laboratory tests, and most of the mechanistic-empirical models were based on cyclic triaxial tests. Thus, the main concepts of permanent deformation and the laboratory tests used to predict them were reviewed and the approaches used to simulate permanent deformation such as elastoplastic models, shakedown theory, and mechanistic-empirical models were discussed. Shakedown analysis is a very popular approach nowadays since allows to prevent permanent deformation that can be critical after some years of exploration. This method became popular in pavement engineering with the inclusion of 3D modelling and generalisation of the method for non-isotropic materials. However, the application of the shakedown analysis in railway engineering is limited. The shakedown approach demands an accurate assessment of the response of the track foundation due to railway traffic, which also requires powerful numerical modelling. It was found that the mechanistic-empirical model reduces the time needed for calculations, it has simple and elegant formulations, good predictive results, and is easy to implement in a numerical scheme.

In this work, the resilient modulus models were presented according to the type of material and type of formulation which reflects which variables are included in the model (resilient modulus and Poisson's ratio or shear modulus and bulk modulus). Regarding the mechanistic-empirical permanent deformation models, they were defined and categorised according to the materials tested, the approach used in the laboratory (single-stage or multi-stage), the complexity of the formulation, and the variables included in the mathematical expression. It was concluded that the permanent deformation models should include the influence of the main stress variables (p and q), the initial stress state of the materials, the number of load cycles, and the distance to the rupture line; moreover, the constant parameters should also reflect the influence of factors such as the state conditions of the material. Thus, it is possible to state that the model developed by Chen et al. (2014) complies with the requirements mentioned. A similar conclusion is also applied to the resilient modulus since more complex models have been developed to include variables such as suction. However, those complex mechanistic-empirical models that depend on several variables can also imply a need for other tests than a standard triaxial cyclic test, in order to obtain more parameters.

The mechanistic-empirical models (resilient modulus and permanent deformation) summarised in the Annex were divided according to the type of material (clay, silt, sand and gravel) to better understand the model's formulation and the condition of the material tested in terms of its granulometry (Cu and Cc) and plasticity properties (W_L, W_P, and IP). The Tables also include some observations regarding the laboratory tests and classification of the material (UIC and ASTM). This information (including the classification) can be very helpful when modelling the sub-structure and predicting its performance.

From the available mechanistic-empirical models and after understanding the main variables and factors that can affect the long-term response of geomaterials, it was important to evaluate the robustness of the models and their sensitivity to other factors. Thus, some models and materials were selected to perform a parametric study in terms of resilient modulus and permanent deformation. The selection depends on the data available for each material and the diversity and variability of the geomaterials (type of soils) in terms of granulometry, percentage of fines, moisture content, and plasticity properties, etc.

The analysis of the resilient modulus was divided according to the material's type (fine and coarse-grained material) and the constants of each model were determined through regression techniques. The analysis shows better results in the case of the coarse-grained soils (the *r-square* value is higher and the obtained values for resilient modulus are similar). This fact can be explained by the complexity of the nature of fine-grained soils, namely the variation of its properties in terms of plasticity and fines content. At the end of this analysis, one model was chosen to perform the geomechanical classification. The *MEPDG* model shows better results for both materials. Indeed, the choice of this model it is also justified by its universal character, which means that can be applied to all type of materials. As expected, the comparison of the results of the resilient modulus shows that the values increase with the *UIC* classification: higher resilient modulus is related to well-classified materials (QS2 and QS3).

In the comparative analysis of the permanent deformation, the materials silt, silty sand, and sand were divided according to their properties such as the percentage of fines (27% and 43%) and granulometry (poor and well-graded materials). Selected experimental results found in the literature were then adapted to Chen's model. The calibration process was performed to compare the long-term response of these geomaterials, after which they were defined and ranked based on the results of permanent deformation. This ranking tool can be used during the design process for estimating the permanent deformation of a certain type of material after *N* loading cycles while considering the *ASTM* and *UIC* classification. As expected, the comparison showed that the values of permanent deformation decreased according to the *UIC* classification, so well-classified materials showed a reduction in permanent deformation.

171

Furthermore, the deformation behaviour of these materials is also dependent on their granulometry, the percentage of fines, and moisture content. Based on the proposed ranking, a brief analysis has been carried out to understand and quantify the influence of the moisture content. The results showed that for a material classified as QS1 (CL), designated as clay, the moisture content exerts a significant influence on permanent deformation.

These two analyses were extremely important to gain more confidence in the obtained results. Indeed, the final result of the geomechanical classifications is based on the parametric study of the resilient modulus (applying the *MEPDG* model) and the permanent deformation (applying Chen's model). Moreover, other materials were added to this analysis because of the available information about the moisture content. The results show that both resilient modulus and permanent deformation are sensitive to the variation of the moisture content. Indeed, the results show that this variable should be considered and analysed in more detail in future analyses and classifications.

The novel geomechanical classification aims to reflect, not only the relation between the *UIC* classification and both resilient modulus and permanent deformation but also another aspect related to the nature of the material. This classification presents a wide range of results in terms of permanent deformation and resilient modulus. This range is a reflection of the variation of the properties of the materials with the same classification (QS1, QS2 and QS3) that influence both types of deformations. Indeed, this work is the first attempt to obtain a novel geomechanical classification that can be a helpful tool in the modelling of a substructure of the railway and/or pavement structures since gathers information about the *UIC* classification (which is a reference in the pavements and railway works) and permanent and resilient /recoverable deformations. As a suggestion, in future analysis, more information should be added, namely other types of materials and a range of variations of properties such as granulometry and plasticity. Furthermore, the definitive evaluation should include the performance of the materials in the laboratory and *in situ* conditions to obtain a correct characterization.

The extensive study presented in this Chapter is a very complete review and allows understanding the main concepts related to the phenomena of recoverable and permanent deformations of granular materials when submitted to cyclic loading. Despite this is an academic exercise, the influence of the permanent deformation in the long-term response of the railway structures (ballasted and ballastless tracks) is analysed in the following Chapters, with the numerical implementation of an empirical permanent deformation model (Chen's model). This Chapter corresponds to the first step in the evaluation of the long-term analysis of the railway structures.

5 Modelling of quasi-static and dynamic mechanisms of ballast and ballastless tracks

5.1 Introduction

During the past years, structural and geotechnical researchers were worried about the performance of the railway's superstructure and its influence on the rail-track design (Indraratna and Nimbalkar, 2016). However, some works show the importance of the performance of the subgrade, mostly due to its influence in the track maintenance operations and respective costs (Selig and Waters, 1994, Nielsen and Li, 2018). Recent advances in numerical modelling techniques lead to a better understanding of the short and long term behaviour of the system, allowing to explore the impact of proper measures to reduce the maintenance procedures and to increase the reliability of railway infrastructures (Sadri et al., 2018). Despite the several works about the characterization of the subgrade (already presented in Chapter 4) when submitted to cyclic loads (Li and Selig, 1996, Puppala et al., 1999, Rahim and George, 2005, Puppala et al., 2009, Ng et al., 2013, Salour and Erlingsson, 2015a, Ling et al., 2017, Rahman and Gassman, 2019), it is important to fully understand the short-term but also the long-term performance of the subgrade when subjected to the passage of trains. Thus, the short performance of the subgrade is usually characterized by the resilient modulus (M_r) while the long-term performance is described by the permanent deformation (ε_p).

The work presented in this Chapter intends to compare the performance of the conventional ballasted track, ballastless track (*Rheda* system) and a ballastless track only constituted by the concrete slab (the support layers are omitted – FPL and HBL). The *Rheda* system is commonly used in Germany but this system was also implemented in Spain and southeast China. The Two examples of the ballasted and ballastless track (*Rheda* system) are depicted in Figure 5.1. The ballastless track only constituted by the concrete slab is a possible optimisation of the system as it is not represented in this Figure. This ballastless structure allows understanding the importance of the support layer in the response of the railway structure and the conclusions can be used as a guideline for future possible optimizations of the ballastless track structure in certain situations. This work also intends to identify and study the impact of several factors on the response of the subgrade when subjected to cyclic loading, in terms of stresses and permanent deformations, which includes, firstly, the evaluation of the impact of the range of wavelength of the unevenness on the degradation of the railway track geometry. This analysis considers different ranges of wavelengths besides the range studied by Nielsen et al. (2018), who only considers the wavelengths in the interval 1–25 m. Furthermore, other well-known parameters referred to in the

specialised bibliography are analysed such as the train's speed and the resilient or elastic modulus and the strength properties of the subgrade (Balay et al., 1998, Correia and Biarez, 1999, Li et al., 2018b, Sadri et al., 2018, Sadri and Steenbergen, 2018) since these are, most of the times, aspects that play a relevant role on the track performance. The analysis is complemented by a study focused on the influence of the dynamic mechanisms caused by the unevenness profile in terms of spatial variability. Moreover, the effect of the train's speed close or equal to the critical speed of the system is also analysed in detail since strong amplification of the response of the track can occur, increasing the track's maintenance operations and subgrade deterioration's rate (Alves Costa et al., 2015, Mezher et al., 2016, Tang et al., 2019, Hu et al., 2019).

| a) | b) |
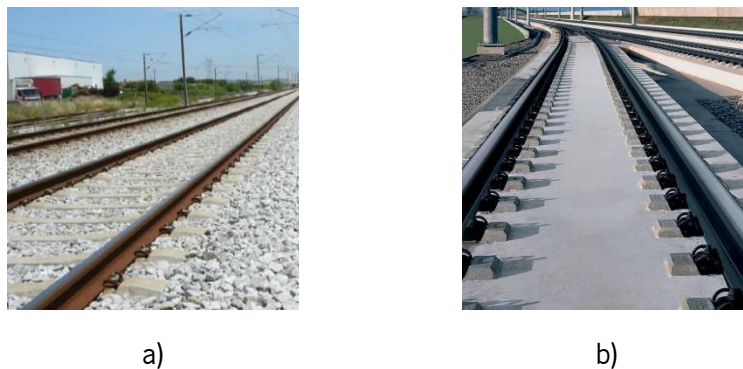
Figure 5.1 – Railway track systems: a) ballasted track (Alves Costa, 2011); ballastless track – *Rheda* system (Rheda-System, 2011)

As mentioned previously, the response of the materials can be divided into recoverable (or elastic) and permanent (or plastic) deformations. This work is focused on the permanent deformation, which is the most influences the long-term performance of the structure (Paixão et al., 2009, Ling et al., 2017). The analyses are focused on the subgrade layer. This layer, in the ballasted track, corresponds to the subgrade while in the ballastless track (*Rheda* system) includes the FPL (frost protection layer) and subgrade (both with the same stiffness). In the case of the ballastless track (*Rheda* system), it is assumed that the FPL is totally integrated into the subgrade. This simplification was very helpful in the performance of the calculus. The calculated dynamic stresses on the subgrade induced by the train vehicle are obtained and used as input of an empirical permanent deformation model to obtain the long-term settlement. Then, the stresses and permanent deformations are compared and quantified through an innovative amplification factor (which is defined by the relationship between the sum of the results of dynamic and quasi-static mechanisms and the dynamic mechanism). The determination of this amplification factor allows evaluating the impact of several important variables on the degradation of the railway tracks such as the moving loads (evaluated through the train's speed), the mechanical properties of the subgrade

(stiffness and strength) and the dynamic mechanisms caused by the unevenness profile (evaluation in terms of wavelength and spatial variability).

This extensive study was performed through a numerical simulation and analysis of 60 case studies using the 2.5D FEM-PML (*Perfectly Matched Layer*) approach which allows obtaining expeditiously the stress levels on the subgrade of each railway structure. The general concepts of the 2.5D modelling were presented in Chapter 2. However, in this Chapter, this approach is presented in more detail and includes mathematical formulation.

5.2   Railway track systems

5.2.1   *Numerical model of the train-track-ground system*

The modelling of the train-track system and its interaction can be performed through sub-structured models to simplify the analysis. This means that both structures are modelled separately, but compatibility and equilibrium restrictions between them are respected.

In the present work, the track-ground system is modelled by a 2.5D formulation. This method presents several advantages when compared to the conventional 2D and 3D FEM methods because combines a reduced computational effort with the consideration of the 3D nature of the problem (Yang and Hung, 2001, Sheng et al., 2006, Muller, 2007, Alves Costa et al., 2010).

5.2.1.1   *Modelling of the track-ground system*

The 2.5D formulation implies two important conditions: the cross-section of the structure needs to be invariant along with the track's development (invariability in terms of geometry and mechanical properties - Figure 5.2) and the response is elastic and linear. These two characteristics are significant in some analysed problems. However, it is important to know when and how to make a compromise between the required results and the time of calculus. Thus, the structure is 2D (since the cross-section remains invariable in the longitudinal direction), but the loading is 3D. This method was first applied by Hwang and Lysmer (1981) in the scope of the study of underground structures under traveling seismic waves. Posteriorly, this method has been applied by a few researchers to study the development and magnitude of vibrations induced by the traffic. In this field, some works should be highlighted such as Yang and Hung (2001), Sheng et al. (2006), Muller (2007) and Alves Costa et al. (2010).

In this method, the usual steps of the finite element procedure are adopted. Firstly, it is necessary to solve the following equilibrium equation that can be derived for any point of the 3D domain:

$$\int_V \delta\varepsilon\sigma dV + \int_V \delta u \rho \frac{\partial^2 u_i(x,t)}{\partial t^2} dV = \int_S \delta u p dS \qquad (5.1)$$

where $\delta\varepsilon$ is the virtual strain field, σ represents the stress field, δu is the virtual displacement field, u is the displacement field, ρ is the mass density and p represents the applied load.
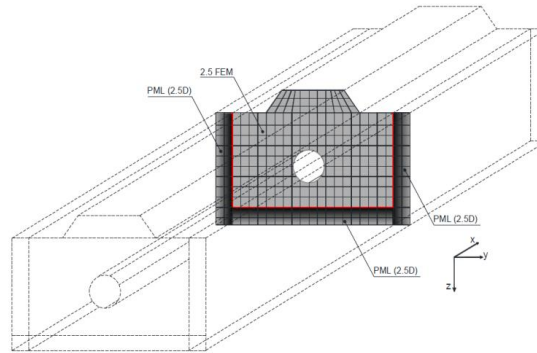
Figure 5.2 - Invariant section considers in the 2.5D formulation (Lopes et al., 2014)

The response of the structure must be linear since the analysis is carried out in the wavenumber-frequency domain, which means that applying the *Fourier* transform in the longitudinal direction, the variables x (space) and t (time) are transformed into the variables wavenumber and frequency, represented by k_1 and ω, respectively (Alves Costa et al., 2010, Lopes et al., 2014). Thus, all the variables, where are included the loads (action) and displacements (response), must be transformed into the wavenumber/frequency domain.

Thus, after the transformation, the cross-section of the domain remains on the untransformed domain and it is discretized by finite elements. This approach allows rewriting equation 5.1 in terms of nodal variables.

To apply the concept of the virtual work on the transformed domain, some considerations should be attended, as the *Parseval's* theorem:

$$\int \delta f(x)p(x)dx = \int \delta f(-k_1)p(k_1)\,dk_1 \qquad (5.2)$$

Equation 5.2 provides the formulation of the principle of virtual works in the transformed domain. Considering equation 5.1 (replacing the equation 5.2 in equation 5.1) it is possible to obtain the virtual works of the internal stresses and inertial forces in the transformed domain, as shows the following equations, respectively:

$$\int_V \delta\varepsilon\sigma dV = \int_{k_1} \delta u_n^T ($$

$$- k_1, w) \iint_{ZY} B^T(-k_1)DB(k_1)dydz\, u_n(k_1, \omega)dk_1 \tag{5.3}$$

$$\int_V \delta u\rho \frac{\partial^2 u(x,t)}{\partial t^2}dV$$

$$= -\omega^2 \int_{k_1} \delta u_n^T (\tag{5.4}$$

$$- k_1, w) \iint_{ZY} N^T \rho N dydz\, u_n(k_1, \omega)dk_1$$

where $[N]$ is the shape function matrix, $[B]$ is the matrix with the derivative of the shape functions, $[D]$ is the strain-stress matrix and u_n is the vector of the nodal displacements (in the transformed domain).

The virtual work performed by the external loads is determined considering as an advantage the fact that the geometry is only discretized on the ZY plane. So, considering a coordinate s, parallel to the edge of the element where traction is applied, the virtual work developed by the load system is given by:

$$\int_S \delta up dS = \int_{k_1} \delta u_n^T(-k_1, \omega)\int_S N^T p(k_1, \omega)\, dsdk_1$$

$$= \int_{k_1} \delta u_n^T(-k_1)p_n(k_1, \omega)dk_1 \tag{5.5}$$

Thus, replacing and rearranging the equations 5.3-5.5 on equation 5.1, the following equation is obtained:

$$\left(\iint_{ZY} B^T(-k_1)DB(k_1)dydz - \omega^2 \iint_{ZY} N^T \rho N dydz\right)u_n(k_1, \omega)$$

$$= p_n(k_1, \omega) \tag{5.6}$$

Following a classic *FEM* formulation, the stiffness matrix $[K]$ and the mass matrix $[M]$ are given by:

$$[K] = \iint_{ZY} B^T(-k_1)DB(k_1)dydz \tag{5.7}$$

$$[M] = \iint_{ZY} N^T \rho N dydz \tag{5.8}$$

177

As described in Alves Costa et al. (2010), the matrix [*B*] is derived from the product of the differential operator matrix [*L*] (on the transformed domain) with the matrix [*N*]. The [*L*] matrix can be obtained by the following expression:

$$[L] = \begin{bmatrix} ik_1 & 0 & 0 & \dfrac{d}{dy} & 0 & \dfrac{d}{dy} \\ 0 & \dfrac{d}{dy} & 0 & ik_1 & \dfrac{d}{dy} & 0 \\ 0 & 0 & \dfrac{d}{dy} & 0 & \dfrac{d}{dy} & ik_1 \end{bmatrix} \tag{5.9}$$

Analysing the previous expression, it is important to highlight that the derivatives in order to k_1 are analytically computed since the direction x (space) is transformed into the wavenumber domain. The damping is introduced by a hysteretic damping model, considering complex stiffness parameters.

The computational efficiency can be improved by dividing matrix [*k*] into sub-matrices (independent of the wavenumber and frequency). This step is carried out considering the matrix [*B*] as the result of the addition of two matrices, where the numerical and analytical derivatives are separated. Thus, equation 5.6 can be replaced by:

$$([K]_1 + ik_1[K]_2 + k_1^2[K]_3 - \omega^2[M])u_n(k_1) = p_n k_1 \tag{5.10}$$

The global system of equations is totally defined after the assembly of the individual matrices of each element and the definition of the *Newman* and *Dirichlet* boundary conditions.

Regarding the finite elements mesh boundaries, they require special treatment to avoid spurious reflections from the arbitrary direction waves that impinge the boundary. Indeed, the limitation of the interest domain, which is implicit in the implementation of finite element formulation, leads to a boundary treatment problem in order to reach the *Sommerfeld* condition. This condition is solved by adding external layers that bound the interest/box domain. To solve this problem, the *Perfectly Matched Layers (PML's)* were applied. In this case, the *Dirichlet* boundary conditions are applied to the external edge of these special layers. This method was implemented by several researchers with satisfactory results and considers the implementation of an external layer to the interest domain that allows the absorption of the energy of the waves that impinge the artificial boundaries, as depicted in Figure 5.3. The methodology is described in more detail in the work developed by Lopes et al. (2014).
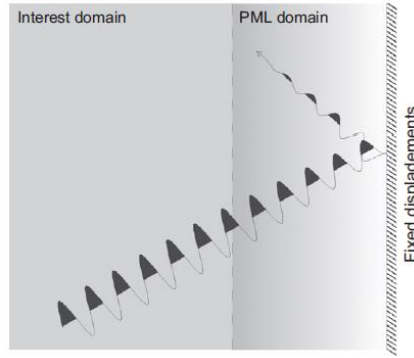
Figure 5.3 - Scheme of the wave attenuation inside the *PML* layer (Lopes et al., 2014)

The absorbing conditions are achieved by stretching the coordinates y and z to a complex domain, which induces an artificial increase in the wave attenuation that propagates along with the *PML* domain. This formulation allows not only to absorb the waves but also considers the non-reflexive properties, which are two important requirements to obtain accurate results (Lopes et al., 2014). The stretching procedure occurs through the application of the following equations:

$$\tilde{y} = \int_0^y \lambda_y(y)dy \tag{5.11}$$

$$\tilde{z} = \int_0^z \lambda_z(z)dz \tag{5.12}$$

where λ_y and λ_z are the stretching functions in the y and z directions. It is important to highlight that the solution analytically continued outside the interest domain satisfies the same differential equations.

Regarding the derivatives, the following equations are applied:

$$\frac{\partial}{\partial \tilde{y}} = \frac{1}{\lambda_y(y)} \frac{\partial}{\partial y} \tag{5.13}$$

$$\frac{\partial}{\partial \tilde{z}} = \frac{1}{\lambda_z(z)} \frac{\partial}{\partial z} \tag{5.14}$$

In the *PML's* layers, the same procedure described in 5.2.1.1 can be followed since the *PML's* elements correspond to 2.5D elements affected by the stretching properties. So, the solution inside the *PML* domain satisfies the same differential equation as in the interest domain. In order to consider the 2.5D approach, the coordinates in equation 5.6 are modified. The *Garlekin* formalism and the equations 5.11 to 5.14 are introduced to obtain the stiffness $[K^*]$ and mass $[M^*]$ matrices in the *PML* domain:

$$[K^*] = \iint_{Z\,Y} B^{*T}(-k_1)DB^*(k_1)dydz \tag{5.15}$$

$$[M^*] = \iint\limits_{Z\,Y} N^T\, \rho N dy dz \qquad\qquad (5.16)$$

The matrix $[B^*]$ is derived from the product of the differential operator $[L^*]$ and $[M]$ matrices.

The *Dirichlet* and *Neummann* boundary conditions in the frequency-wavenumber domain are imposed after the assemblage of the matrices of the interest and *PML* domain. The solution in the space-time domain is obtained by applying a double *Fourier* transformation.

The main advantage of this method when compared to the fully tri-dimensional finite element method is quite evident: instead of solving a system of equations with a high number of degrees of freedom, a smaller system of equations is solved many times, corresponding to a range of wavenumbers. This procedure corresponds to a significant reduction in computational time.

5.2.1.2 *Modelling of train-track-ground system interaction*

The numerical model can be divided into two main moduli: the track-ground structure (modelled by the 2.5D-FEM approach) and the train, which is modelled considering a multi-body formulation. Both models are coupled following a compliance formulation, as depicted in Figure 5.4, which summarizes the procedure to simulate the train-track interaction. Furthermore, the load applied by the train on the track can be decomposed into two components: static load (*i*) and dynamic load (*ii*). The static load is associated with the weight of the vehicle and the dynamic load is due to the dynamic interaction between the train and the track.
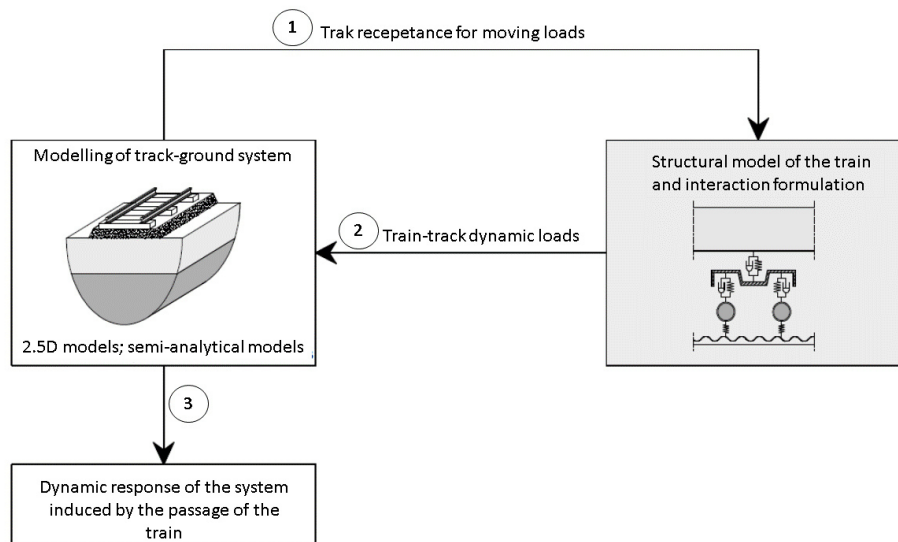
Figure 5.4 - Flowchart representative of the sub-structured models – adapted from Alves Costa et al. (2012)

In this analysis, a 2D model of the train is adopted, which means that only the vertical movement of the train was taken into account (the dynamic loads induced by the movement of the train in any direction other than the vertical are neglected). To obtain the solution, the interaction problem implies compatibility of displacements and load equilibrium at the contact points between the track and the rolling stock.

The compatibility in terms of displacements (for any temporal instant) between the vehicle and the track is determined by the connection i between both structures, applying the following equation (considering that the train moves along the longitudinal direction - x-axle):

$$u_{c,i} = u_r(x = ct + a_i) + \Delta u\left(t + \frac{a_i}{c}\right) + \frac{P_i(t)}{k_H} \tag{5.17}$$

where $u_{c,i}$ is the vertical displacements of the contact point i of the vehicle; u_r is the rail displacement at the same location; Δu is the rail unevenness; t is the time; a_i is the location of the contact point i at t=0s; c is the vehicle speed; k_H is the *Hertzian* stiffness and P_i is the dynamic interaction load developed at the connection point i. Wheel-rail contact is simulated by a linearized *Hertzian* stiffness (taking into account only the dead load transmitted by the wheelset). More details about this methodology can be found in Alves Costa et al. (2012).

To solve the train-track interaction problem, the unevenness profile must be transformed into the wavenumber domain:

$$p(\Omega) = -(F + F^H + A)^{-1}\Delta u_n(\Omega) \tag{5.18}$$

where $p(\Omega)$ is the vector that contains the interaction forces for each connection points, [F] is the train compliance at the contact points with the track (the matrix is computed from the vehicle model), [F^H] is a diagonal matrix where the terms are equal to $1/k_H$, [A] is the compliance matrix of the track ([A] is the dynamic response of the track due to the dynamic force generated by the dynamic mechanism as an unevenness profile) and Ω is the driven frequency (frequency of oscillation of the wheelset due to the unevenness with a wavelength $\lambda = 2\pi c/\Omega$). All matrices of 5.18 are squared with a dimension that is equivalent to the number of wheelsets and the matrix [F] is computed from the vehicle model.

The track-ground model is applied to compute the terms of matrix A, considering the following expression:

$$A_{ij}(\Omega) = \frac{1}{2\pi}\int_{-\infty}^{+\infty} u_c^G(k_1, \omega = \Omega - k_1 c) \cdot e^{i(a_i - a_j)k_1} dk_1 \tag{5.19}$$

where u_c^G corresponds to the vertical displacement of the rail in the transformed domain due to a half-unit load applied in the head of each rail.

181

5.2.2   Case studies and materials properties

This analysis is focused on a parametric study and aims to evaluate the influence of certain factors in the performance of the subgrade of a railway system. To accomplish the proposed challenge, three numerical models (using the 2.5D FEM-PML approach) were defined, as depicted in Figure 5.5: the ballasted track, ballastless track and a ballastless track only constituted by a concrete slab. All elements of the structures were modelled with quadratic finite elements with 8 nodes. The depth of the models was selected based on studies developed in a previous work, which considers the geometric and geomechanical characteristics of a section of the railway *Norte* line in Portugal (Colaço et al., 2015).

As depicted in Figure 5.5, the ballasted track is constituted by the rails, railpads, sleepers, ballast, sub-ballast and subgrade. The ballastless track was modelled as a *Rheda* system and it is composed of the rails, railpads, concrete slab, a support layer designated as hydraulically bounded layer (HBL) and also the frost protection layer (FPL). The further ballastless track is similar to the ballastless track (*Rheda* system), except for the no consideration of the support layers (HBL and FPL).

a)   b)

c)
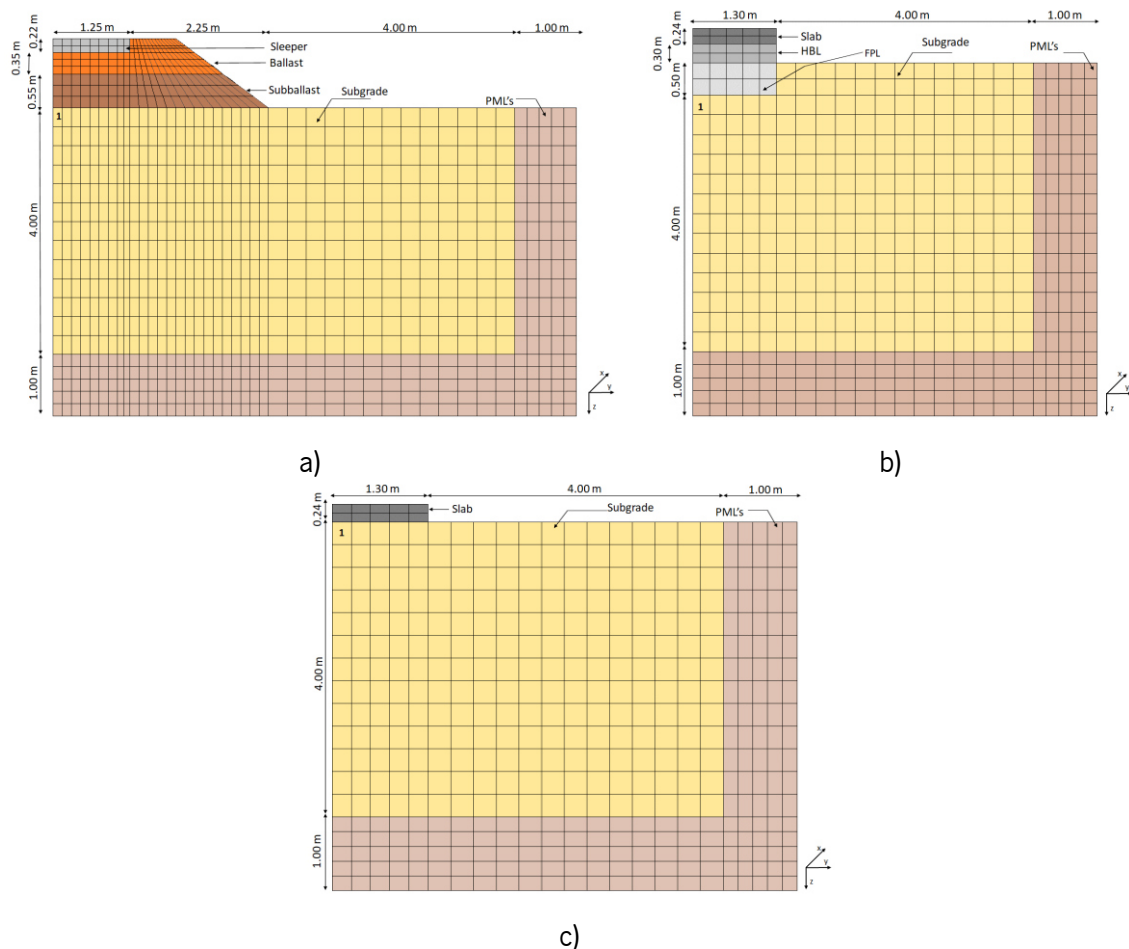
Figure 5.5 - Numerical models: a) ballasted track; b) ballastless track (*Rheda* system); c) ballastless track with only a concrete slab

(Ramos et al., 2018)

The rails (UIC60) were modelled as a beam element. The railpads were modelled applying the *Kelvin* model, which means that its behaviour depends on the value of the stiffness of the spring and also on the damping of the dashpot (in the case of the ballasted track, it was assumed a stiffness of 600 kN/mm and damping of 22.5 kNs/m and, in ballastless tracks, the stiffness is 40 kN/mm and damping is 8 kNs/m). The remaining materials were modelled with linear elastic models. The assumption of a linear elastic model to represent soil behaviour is a simplification to the real constitutive soil behaviour and it is only acceptable when dealing with small-strains (Biarez et al., 1999, Gomes Correia and Cunha, 2014, Alves Costa et al., 2010, Dong et al., 2019). The adopted properties are described in Table 5.1 and Table 5.2 (ballasted and ballastless tracks, respectively). Regarding the sleepers, the constitutive model is based on an anisotropic formulation, which means that this material is modelled as a continuous and orthotropic element (Alves Costa et al., 2010). Thus, in the longitudinal direction (*x*-direction of Figure 5.5), it was assumed the stiffness of the ballast since the sleepers are usually embedded in this material. This solution was tested by Alves Costa et al. (2010) with good results. The damping values (ξ) of the ballast and sub-ballast are based on a calibration and optimization process of these properties considering experimental results from receptance tests (Alves Costa et al., 2012). The remaining damping values were also obtained based on the work developed by Alves Costa et al. (2012) and explored by Colaço et al. (2015). Regarding the subgrade and the FPL, the adopted values are within the acceptable range of these materials (modulus of deformation limits and compaction requirements for the earthwork layers): 120 MPa to 5000 MPa for the FPL and 60 MPa to 500 MPa for the subgrade. The properties of the remaining materials of the ballasted track were obtained from the work developed by Colaço et al. (2015). Regarding the ballastless track, the values of the properties of the concrete slab and HBL are typical of this system.

The initial stresses are obtained assuming an isotropic stress state, i.e., K_0=1. This assumption was adopted to be consistent with the modelling parameters obtained from literature based on cyclic triaxial tests. The model takes into account the symmetric conditions of the problem to reduce the computation effort.

In the ballastless track (*Rheda* system), by simplification, as mentioned previously, from a numerical point of view, the FPL was integrated into the subgrade layer since both materials shared the same stiffness (Table 2). Indeed, they have similar properties and the main difference is related to the density's values (the properties of FPL were adapted from Shahraki et al. (2015)). Thus, in this work, the FPL has not distinguished itself from the subgrade in terms of terminology. This simplification allows to discuss and compare the numerical results of finite elements from the different railway structures at the same depth,

which means that they would have a similar initial stress state. However, because of the density, this comparison is not straightforward but, this is why this is a simplification.

Table 5.1 - Characteristics of the materials - ballasted track

Elements	M_r (MPa)	ν	ξ	ρ (kg/m³)
Sleepers (ballasted track)	30000	0.20	0.010	1833.3
Ballast	97	0.12	0.061	1591.0
Sub-ballast	212	0.30	0.054	1913.0
Subgrade*	120	0.30	0.030	2040.0

M_r= Resilient modulus, ν=Poisson's ratio, ξ=damping and ρ=density

*The subgrade is characterised by a ϕ'=30° and c'=0 kPa

Table 5.2 - Characteristics of the materials - ballastless tracks

Elements	M_r (MPa)	ν	ξ	ρ (kg/m³)
Concrete slab	34000	0.20	0.030	2500
HBL	10000	0.20	0.030	2500
FPL*	120	0.20	0.030	2500
Subgrade*	120	0.30	0.030	2040.0

M_r = Resilient modulus, ν=Poisson's ratio, ξ=damping and ρ=density

*The subgrade and FPL are characterised by a ϕ'=30° and c'=0 kPa

The adopted vehicle throughout this work is the *Alfa Pendular* train. This train is composed of 6 car bodies and presents a symmetry plane, as depicted in Figure 5.6. The average axle load is close to 135 kN. The train was modelled by a simplified model, where only the mass of the wheelsets is taken into account. Studies developed by Alves Costa et al. (2012) and by Colaço et al. (2016) in the scope of ground vibrations concluded that the most influential component of a train model is the unsprung mass and, because of that, it is reasonable to model only this component. Further studies will include the investigation of long wavelengths leading to excitation of low frequency rigid body models of the vehicle (for example, a train's speed of 200 km/h and wavelength of 70 m, leads to an excitation frequency of 0.8 Hz, which is within the range of vehicle resonances). The mechanical properties of the Alfa Pendular train can be found in Alves Costa et al. (2012). The properties of the *Alfa Pendular* train are described in Table 5.3.

a)

b)
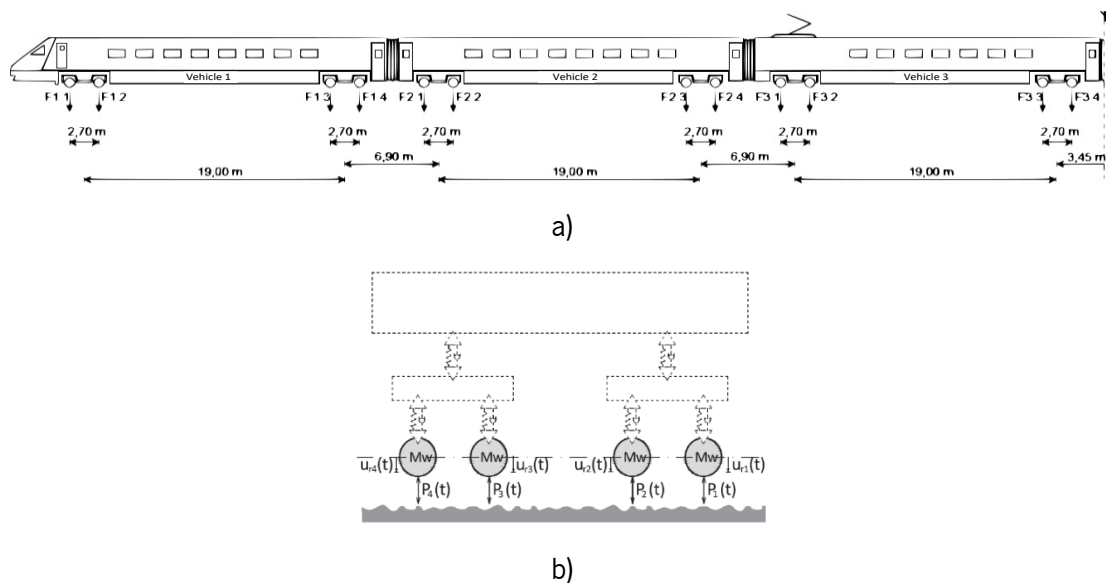
Figure 5.6 - Model of the train: a) geometry of the Alfa Pendular train; simplified train model

Table 5.3 – Mechanical properties of the Alfa-pendular train

			Vehicle 1	Vehicle 2	Vehicle 3	Vehicle 4	Vehicle 5	Vehicle 6
Axles	A_1	F_{i1} (kN)	133.3	135.7	131.5	135.5	135.7	132.7
		M_w (Kg)	1538	1538	1538	1538	1538	1538
		k_h (kN/m)	2.4×10⁹					
	A_2	F_{i2} (kN)	136.8	139.2	131.5	135.5	139.23	136.2
		M_w (Kg)	1884	1884	1538	1538	1884	1884
		k_h (kN/m)	2.4×10⁹					
	A_3	F_{i3} (kN)	136.20	139.2	131.5	135.5	139.23	136.7
		M_w (Kg)	1884	1884	1538	1538	1884	1884
		k_h (kN/m)	2.4×10⁹					
	A_4	F_{i4} (kN)	132.7	135.7	131.5	135.5	135.7	133.3
		M_w (Kg)	1538	1538	1538	1538	1538	1538
		k_h (kN/m)	2.4×10⁹					

5.2.3 Generation of the irregularities' profiles

The irregularities were defined by a sinusoidal function described by a number of harmonics:

$$u(x) = \sum_{j=1}^{N} \delta_{u_j} e^{i\frac{2\pi}{\lambda_j}x} \tag{5.20}$$

where λ_j is the wavelength within the interest interval, N is the total number of harmonics considered and δ_{u_j} is the complex entity that reflects the amplitude of the correspondent harmonic, given by:

185

$$\delta_{u_j} = A_j e^{-i\theta_j} \tag{5.21}$$

where A_j is the amplitude of the correspondent harmonic and θ_j corresponds to a random phase angle (random variable with uniform distribution in the interval]0,2π[). Regarding the parameter A_j, (amplitude of the several harmonics of the artificial profile), it can be evaluated through the following expression:

$$A_j = \sqrt{2 \cdot S_{rzz\cdot}(k_{1j})\Delta k_1} \cdot \tag{5.22}$$

where Δk_i is the increment of the wave-number, $k_{ij}=2\pi/\lambda_i$ and S_{rzz} is obtained by *PSD* (*Power Spectral Density* function) defined by the *FRA (Federal Railroad Administration-*entity responsible for the USA railway lines). The amplitude depends on the spectrum and the sampling step:

$$S_{rzz}(k_1) = \frac{10^{-7} A k_3^2 (k_1^2 + k_2^2)}{k_1^4 (k_1^2 + k_3^2)} \tag{5.23}$$

where A is a parameter that is a function of the geometric quality of the railway track, k_i corresponds to the wavenumber and k_2 and k_3 are constants. *FRA* suggests different expressions for the *PSD*, depending on the type of unevenness (the expression applied in this work is used in the characterization of elevation irregularities) and its definition is based on the statistical treatment regarding *in situ* measurements. More details can be found in Alves Costa (2011).

Parameter A depends on the maximum allowed speed for the track that should be compatible with each track class, as depicted in Table 5.4. To analyse higher speeds (the maximum speed for passenger trains is 176 km/h), the value A of class 6 should be adapted.

Table 5.4 - Power spectral density parameters and allowed train speed proposed by the *FRA* (adapted from Li and Wu (2020))

Class	1	2	3	4	5	6
A (m3/rad)	660.079	376.229	208.841	118.856	65.929	37.505
Max. speed (km/h) (passenger train)	16	48	96	128	144	176

In this work, to analyse higher speeds (≥176 km/h), the value of parameter A was modified taking into account the recommendations and the alert limits defined by EN13848-5 (2008). The standard establishes the limit of the standard deviation of the longitudinal levelling (in mm) for the class *D1* (with wavelengths between 3<λ<25) and the class *D2* (with wavelengths between 25<λ<70) and the maximum peak value regarding the average of the longitudinal levelling, as depicted in Table 5.5. In order to comply with these recommended values for the range of speeds higher than 176 km/h, parameter A was

iteratively modified until the unevenness's profile meets the recommendations of EN13848-5 (2008) in terms of standard deviation and maximum peak value (Table 5.5).

In this case, the generated profile includes 120 frequencies (considering a geometric progression: with a constant equal to 1.036) and the amplitude was defined by applying the *Power Spectral Density*. Furthermore, the unevenness' profile was defined to comply with the recommendations of EN13848-5 (2008), as mentioned previously.

Table 5.5 - Limit of the standard deviation of the longitudinal levelling (in mm) and maximum peak value regarding the average of the longitudinal levelling (in mm) for higher speeds, according to EN13848-5 (2008)

Limits	Speed (km/h)	Alert limit	
		D1	*D2*
Limit of the standard deviation of the longitudinal	160≤v≤220	1.2-1.9	-
levelling (in mm)	220≤v≤300	1.0-1.5	-
Maximum peak value regarding the average of the	160≤v≤220	7-12	14-20
longitudinal levelling (in mm)	220≤v≤300	6-10	12-18

D1 - 3<λ<25; *D2* - 25<λ<70

The unevenness' profile adopted in this work (depicted in Figure 5.7) includes three ranges of wavelengths (each range is composed of approximately 40 frequencies):

- 1<λ<3 (the recommended values of the range *D1* were adopted);
- 3<λ<25 (designated as *D1* in EN13848-5 (2008));
- 25<λ<70 (designated as *D2* in EN13848-5 (2008)).

These ranges allow understanding which are the values of wavelengths (and also frequencies) that most affect the long-term behaviour of the railway structures. All the simulations use the profile depicted in Figure 5.7. In Figure 5.7, the labels A, B, C and D show the different positions (in the longitudinal direction or x-direction) where the stresses and permanent deformations were analysed. Label A corresponds to the maximum amplitude of the unevenness profile and B corresponds to the minimum. The labels C and D correspond to intermediate positions. In the case of the C point, the amplitude is increasing and in the case of the D point, the amplitude is decreasing. The influence of the selected points of the unevenness profile in the stress and permanent deformation results is evaluated further in a specific analysis.
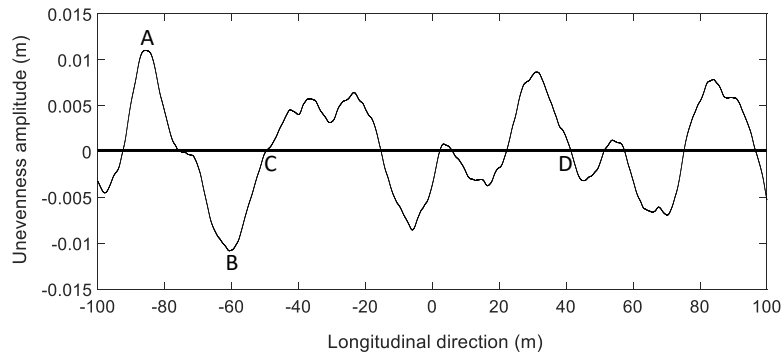
Figure 5.7 – Adopted unevenness profile

5.2.4 Parametric study

The applied methodology considers the application of 2.5D FEM-PML formulation with the implementation of an empirical permanent deformation model. From the numerical model, the principal stresses are determined (σ_1, σ_2 and σ_3), which allows obtaining the mean and deviatoric stresses (p and q, respectively). These two variables are important *inputs* in most of the permanent deformation models, including in the model used in this analysis. The flowchart used in this work is described in Figure 5.8.
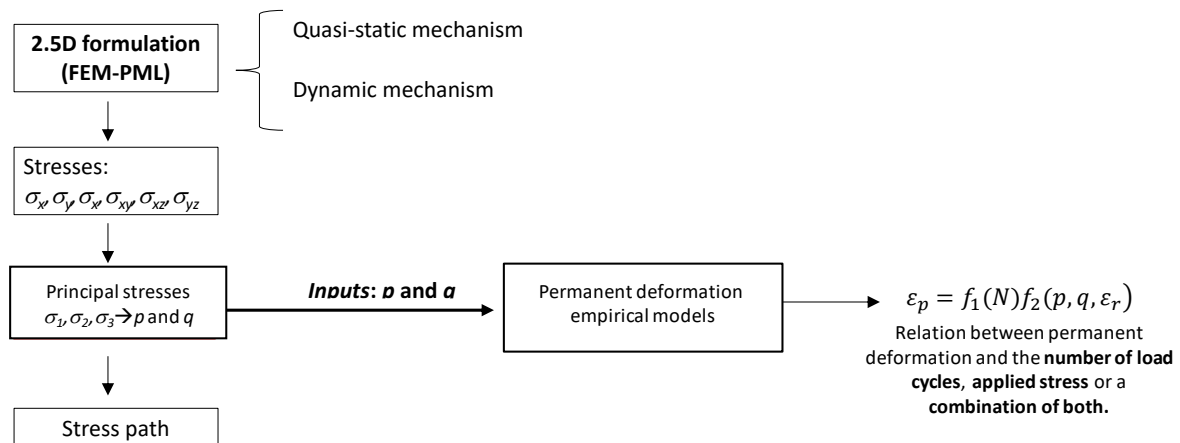
Figure 5.8 – Flowchart with the explanation about the application of the 2.5D formulation (*FEM-PML*) and implementation of an empirical permanent deformation model

The determination of stress paths induced by the train passage is the primary stage of this analysis. The representation of the *yielding criterion* is merely indicative since it allows understand the proximity of the stress path to the failure line, which is an important factor in the determination of the permanent deformations. However, stress paths above the *yielding criterion* are unrealistic and don't have any physical meaning, which means that the results should be analysed carefully. The failure line was defined, considering the *Mohr-Coulomb yielding criterion*, which is characterised by the friction angle and cohesion and it is described in the following expression:

188

$$q = q_0 + M \cdot p \tag{5.24}$$

where M represents the slope of the line of the critical state in the referential p-q and q_o corresponds to the ordinate when p is null. The value of M is given by:

$$M = \frac{3 \sin(\phi')}{\sqrt{3} \cos(\theta) - \sin(\theta) \sin(\phi')} \tag{5.25}$$

The value M depends on the invariant stress θ and the friction angle (ϕ). The invariant stress θ is defined by:

$$\theta = \frac{1}{3} sen^{-1} \left[\frac{-3\sqrt{3}}{2} \frac{J_3}{(J_2)^{\frac{3}{2}}} \right], with \; \frac{\pi}{6} \leq \theta \leq \frac{\pi}{6} \tag{5.26}$$

where J_2 and J_3 are the invariants of the stress state, obtained from the following expressions:

$$J_2 = \frac{1}{2} I_1^2 - I_2 \tag{5.27}$$

and

$$J_3 = \frac{1}{3} I_1^3 - I_1 I_2 + I_3 \tag{5.28}$$

where I_1, I_2 and I_3 represent the invariants of the stress state:

$$I_1 = \sigma_x + \sigma_y + \sigma_z \tag{5.29}$$

$$I_2 = \sigma_x \sigma_y + \sigma_x \sigma_z + \sigma_y \sigma_z - \tau_{xy}^2 - \tau_{xz}^2 - \tau_{yz}^2 \tag{5.30}$$

$$I_3 = \sigma_x \sigma_y \sigma_z + 2 \tau_{xy} \tau_{xz} \tau_{yz} - \sigma_x \tau_{yz}^2 - \sigma_y \tau_{xz}^2 - \sigma_z \tau_{xy}^2 \tag{5.31}$$

In this case, only the compression path is considered. The value of q_o is obtained from the following expression:

$$q_o = \frac{c \cdot 6 \cdot \cos \phi'}{3 - \sin \phi'} \tag{5.32}$$

Since the materials are characterised by an elastic behaviour, the *yielding criterion* is merely indicative and, in this case, it only represents the compression path, as mentioned previously. This means that, regarding the stress, there is no influence of this criterion on the obtained results in terms of stresses. However, this *yielding criterion* is relevant in the determination of the permanent deformations since the empirical model is sensitive to the proximity of the stress path to the failure line, which means that the parameters s and m (that are dependent on the strength properties) are very important.

The performance of the railway structures is compared in terms of stresses and permanent deformations, taking into account the quasi-static and the dynamic excitation mechanism (as depicted in Figure 5.8). The quasi-static excitation is induced by the movement of the loads (static weight of the vehicle per axle) while the dynamic excitations are induced by the vehicle-track interaction that generates accelerations on the vehicle and, consequently, inertia forces.

Throughout this study, the stress results are presented in the *p-q* space. The stresses are analysed in terms of effective stresses considering the initial stresses and the increments. The performed analysis allows establishing a comparison between the total dynamic mechanism and the quasi-static (f=0Hz) in order to define an amplification factor. The analysis is focused on element 1 of each structure (Figure 5.5). Element 1 was selected due to its proximity to the symmetry plane, which simplifies the analysis and interpretation of the results in terms of stresses (*Sx, Sy, Sz, Sxy, Sxz, Syz*). Despite it is expected to have higher stresses and permanent deformations below the rail seats, this work is focused on the comparison of the results and not only on the absolute values of the stresses and permanent deformations.

The results regarding the permanent deformations are presented in terms of cumulative permanent displacement. Regarding the ballastless track (*Rheda* system), the cumulative permanent displacement includes the Frost Protection Layer (FPL) and the subgrade soil, while the ballasted track is only composed of the subgrade soil. This simplification can influence the results since despite both layers share the same stiffness, they present different densities, which can influence the initial stress state, as mentioned previously. In this case, element 1 of each structure is almost at the same depth and this fact is the main reason for the inclusion of the FPL in the long-term analysis since, besides sharing the same stiffness, this material is submitted to a different treatment (granulometry, compaction, etc.) when compared to the subgrade during the construction of the railway line.

In the first analysis, a train speed equal to 200 km/h is considered. Posteriorly, this value is changed to evaluate the influence of the train's speed on the performance of the subgrade.

5.2.4.1 Sensibility analysis – quasi-static mechanism

As mention previously, the quasi-static mechanism is induced by the movement of the loads considering the static weight of the vehicle per axle. Figure 5.9 presents an example of the load-unload process due to the passage of the Alfa Pendular train. In this case, it is possible to observe that, after the passage of the first bogie (blue colour), there is a complete load-unload process. However, after the passage of the second bogie (green colour), and due to the proximity of the third bogie (red colour), the load-unload

process is affected (not fully complete) and leads to the appearance of the well-known shape of the *p-q* diagram depicted in Figure 5.9. This diagram is representative of the quasi-static mechanisms.

After obtaining the stress path diagram, it is possible to define the cumulative permanent displacement. Figure 5.10 presents an illustrative example of the comparison between the quasi-static cumulative permanent displacement between the ballasted and ballastless track (*Rheda* system).
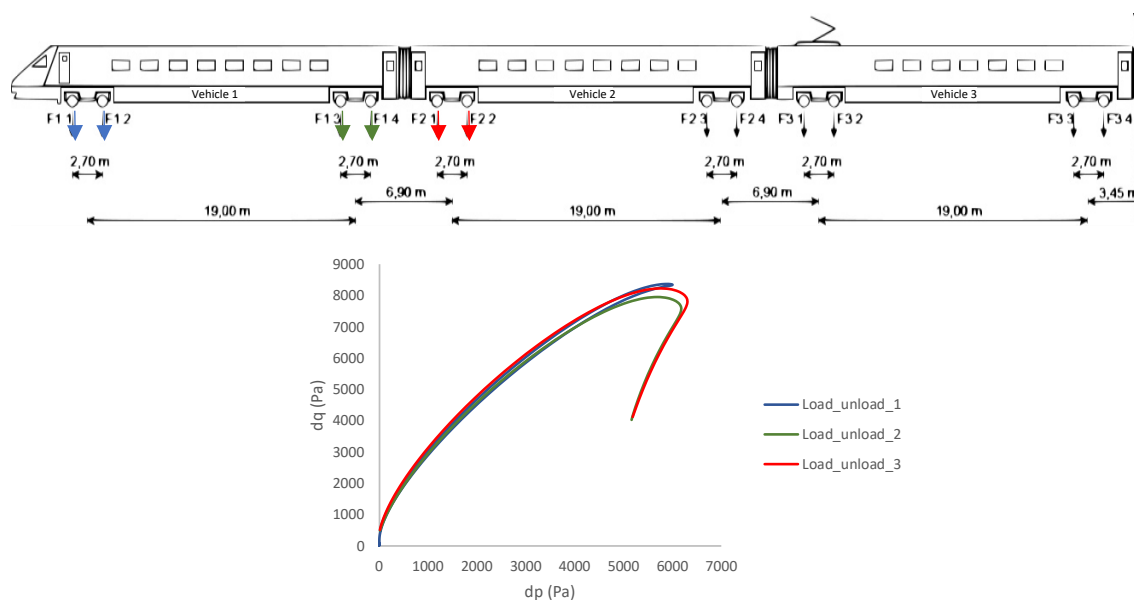
Figure 5.9 - Example of the load-unload process during the passage of the Alfa Pendular train
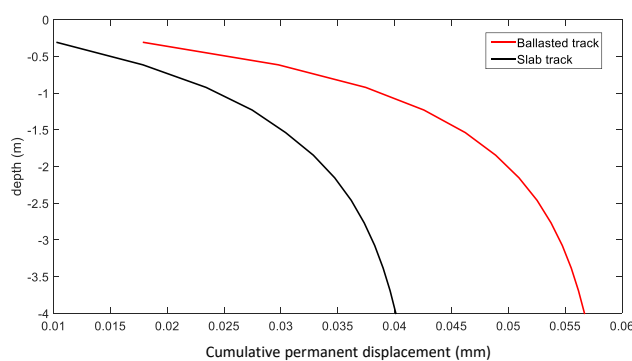
Figure 5.10 – Example of comparison of the quasi-static cumulative permanent displacement between the ballasted and ballastless tracks

In the following sections, the stress and cumulative permanent displacement results are presented considering the dynamic excitation mechanism and the influence of several parameters.

5.2.4.2   *Influence of the wavelength of the unevenness profile on the substructure*

Considering the unevenness profile depicted in Figure 5.7, the influence of the wavelength of the unevenness profile on the subgrade is evaluated considering a train' speed equal to 200 km/h and the material properties described in Table 5.1 and Table 5.2, including the resilient modulus of the subgrade

and FPL equal to 120 MPa. The stress levels were obtained for each wavelength range: $1<\lambda<3$; $3<\lambda<25$; $25<\lambda<70$. Thus, considering the unevenness profile depicted in Figure 5.7, the frequencies were selected based on the train speed and range of wavelength, and the induced dynamic stresses were compared. From the numerical model, the stress paths were determined, as depicted in Figure 5.11. The obtained results show that the three railway structures present different initial mean stresses ($p_{ini:ballasted}$=23 kPa, $p_{ini:ballastless}$=17 kPa and $p_{ini:ballastless;only\ slab}$=9 kPa), which can influence the long-term behaviour in terms of permanent deformations because of the distance between the peak of the stress path and *yielding criterion*. The initial mean stresses (or geostatic stresses) of each railway structure were determined in a separate model (considering the gravity load of the track) and these stresses were added to the empirical permanent deformation model (this is possible because of the linear elastic domain). The gravity load was included considering the density of each material and the thickness of the finite element of each material/layer.

Figure 5.11 - Stress path – v=200 km/h: a) ballasted track; ballastless track (*Rheda* system); c) ballastless track only constituted by the concrete slab

In order to compare the amplitude of the stress levels, the stress paths of the three railway structures were drawn in the same graph (considering 1 m<λ<3 m), as depicted in Figure 5.12. This figure shows that the amplitude of the stress levels (in terms of deviatoric stress, q) when λ varies between 1 m and 3 m are quite similar in this particular element – element 1 (a little higher in the ballasted track, followed by the ballastless tracks). Furthermore, besides the initial mean stress, the shape of the diagrams is also different. This is due to the loading and unloading process and also due to the stress distribution process that depends on the performance and properties of the concrete slab layer (in the ballastless tracks) and the ballast layer (in the ballasted track).
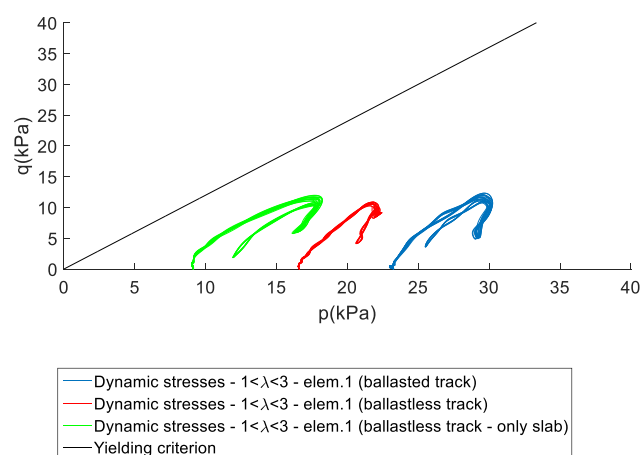
Figure 5.12 - Comparison between the ballasted, ballastless and ballastless only constitute by the concrete slab (element 1)

Analysing the stress results, all the structures present lower amplification of the stress levels for all the defined ranges, including the range associated with lower wavelength: between 1 m and 3 m. Indeed, the stress levels generated by the combined effect of the dynamic and quasi-static mechanisms considering wavelengths between 3 m and 70 m are very similar to the quasi-static mechanism, which means that the amplification is very residual.

In order to evaluate which structure is more sensitive to the presence of irregularities on the track, the maximum increment of the mean stress ($d_{p;max}$) and maximum increment of the deviator stress ($d_{q;max}$) are determined. The maximum increments correspond to the maximum value of the mean stress and deviatoric stress (induced by the passage of the train) of the *p-q* diagram. This analysis is focused on the element 1 of each structure at x=0m of the unevenness profile depicted in Figure 5.7. Indeed, this value was randomly selected and was adopted in this particular analysis and further analyses, but its influence on the performance of the subgrade will be later evaluated. The choice of the same position (x=0m) allows keeping the analyses of the results simpler and comparable.

The results presented in Table 5.6 show the stress amplification factor (*SAF*), which is defined through the ratio between the total stresses induced by both quasi-static and dynamic mechanisms and the stresses only induced by the quasi-static mechanism. The analysis focuses on the range with higher frequencies ($1<\lambda<3$), since present higher stress amplifications when compared to the other ranges (the amplification for the other ranges are very residual and the *SAF* are very much close to one). As matter of fact, this range of wavelengths is not included in the standard EN13848-5 (2008) since the alert limits are only defined for the ranges *D1* and *D2*. However, this range (1 m $<\lambda<$ 3m) is the one that induces higher stresses. The increment of stresses would be more significant if higher train speeds were considered. For this range of wavelengths ($1<\lambda<3$), the frequency varies between 17.40 Hz and 54.4 Hz, which usually corresponds to the wave wear on the rail, periodic defect. This range possibly generates higher dynamic loads probably due to the resonant frequency of the axle over the railway track.

Table 5.6 - Stresses on the railway structures (element 1; v=200 km/h; x=0 m).

		Ballasted track		**Ballastless track** (*Rheda* system)		**Ballastless track (only with concrete slab)**	
		$d_{p;máx}$	$d_{q;máx}$	$d_{p;máx}$	$d_{q;máx}$	$d_{p;máx}$	$d_{q;máx}$
f=0 Hz	Stress (kPa)	6.97	11.85	5.66	10.75	8.99	11.76
$1<\lambda<3$	Stress (kPa)	7.10	12.33	5.83	10.88	9.10	11.98
	SAF	1.02	1.04	1.03	1.01	1.01	1.02

When λ varies between 1 m and 3 m, the *SAF* is higher in the ballasted track, followed by the ballastless track and the ballastless track only constituted by the concrete slab. However, these differences are not significant.

Taking into account the elastic stresses induced by the train passage, the permanent deformation results were determined for each wavelength range, considering a train speed equal to 200 km/h. This analysis is focused on the symmetry plane alignment and contains element 1 (indicated as the first alignment – "alig. 1" - in the caption of the figures).

The empirical permanent deformation model selected in this work to study the long-term performance is based on the work developed by Gidel et al. (2001), where the authors combine the effect of the number of load cycles with the elastic stress state in the soil. As mentioned previously, posteriorly, Chen et al. (2014), based on the work developed by Gidel et al. (2001) updated the model, suggesting some modifications as the introduction of influence of the initial stress state (p_{ini} e q_{ini}). The direct effects of the consideration of the initial stresses on the empirical model are depicted in Figure 5.13. In Figure 5.13,

two stress paths are represented in the *p-q* diagram. The stress path 1 does not consider the initial stresses, which means that the proximity of the peak stress to the failure line is higher and this situation does not correspond to the real behaviour of the geomaterials. That's why the inclusion of the initial stress state is so important and the empirical permanent deformation models should include this variable.
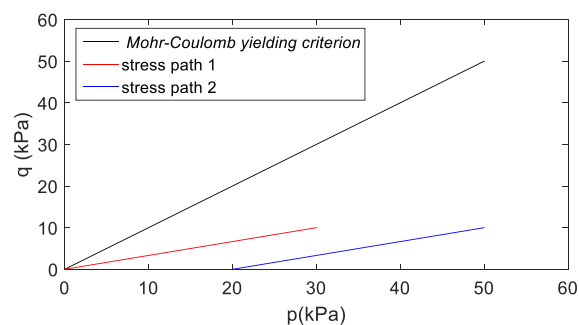
Figure 5.13 - Influence of the initial stresses on the permanent deformation

Chen's model was tested considering the experimental results of a full-scale model on a high-speed railway under varying water levels within the subgrade. The model was applied for the case of the foundation soil (silt) and sub-base layer (coarse sand). Thus, the cumulative settlements of the subgrade were measured under different train speeds. This empirical model is explained in detail in Chapter 4 (section 4.5) and the variables are described considering the expression 4.15. As mentioned previously, this model presents several advantages since it considers the amplitude of the applied load, the proximity of the stress path to the failure line and integrates the influence of the initial stress state. Comparing to other empirical models (Korkiala-Tanttu, 2005, Rahman and Erlingsson, 2015) this model is more complex because it depends on more parameters.

The material parameters were obtained in Salour and Erlingsson (2015) considering ε_1^{p0}=0.00093, *B*=0.2 and *a*=0.65. This material is classified as non-plastic silty sand according to the unified soil classification.

Thus, the model developed by Chen et al. (2014) is the model implemented to study the long-term performance of the railway structures through the determination of the cumulative permanent displacement. The model will be applied to the subgrade material (including the FPL – frost protection layer) and the analysis will not include the ballast.

In Figure 5.14, the cumulative permanent displacement is presented and the long-term performance of the three railway structures is compared. The cumulative permanent displacement (δ) is the sum of the

product of the permanent deformation (applying expression 4.15) of each element of the selected alignment considering *N*=1000000 cycles and the thickness of the element:

$$\delta = \sum_{i=1}^{n} \varepsilon_p^i \times h_i \qquad (5.33)$$

where *i* represent the number of elements of the alignment, *h* is the thickness of the element (in m) and ε_p is the permanent deformation (dimensionless) and it is obtained through expression 4.15. The permanent deformation of each element was determined taking into account the stresses induced by the passage of the train and also considering other variables such as the initial stresses, the influence of the failure criterion, and the constant material parameters. The cumulative permanent displacement is maximum at the bottom of the model since corresponds to the sum of the permanent deformation of all elements. However, the elements that most contribute are close to the surface. The outputs are differentiated by wavelength by filtering the stress results according to the selected frequencies/wavelengths. Each range of wavelength is constituted by 40 frequencies, as mentioned previously.

As expected, when the wavelength varies between 1 m and 3 m, there is an increase in the stress levels, which leads, to an increase in the permanent deformation and cumulative permanent displacements. The results also show that that higher permanent deformation values (and respective cumulative permanent displacements) are induced in the ballastless track constituted only by the concrete slab.

Figure 5.14 also shows that there is a small difference between the ballasted track and the ballastless track in terms of cumulative permanent displacement. Indeed, this value would be higher if the influence of the permanent deformation of the ballast was considered (the influence of the ballast was neglected in this study). Thus, it is important to highlight that this is a comparison at the subgrade level, which justified the similarity of the performance of the subgrade.

The ballastless track with only the concrete slab shows higher cumulative permanent displacement and the difference is significant, which evidences the importance of the support layers (HBL and FPL). Due to the important difference, the scale of the *x-axle* is different. This difference is due to reduced initial mean stress, which leads to higher values of permanent deformation and cumulative permanent displacements since the stress path is closer to the *yielding criterion* (Figure 5.12).

a)

b)

c)
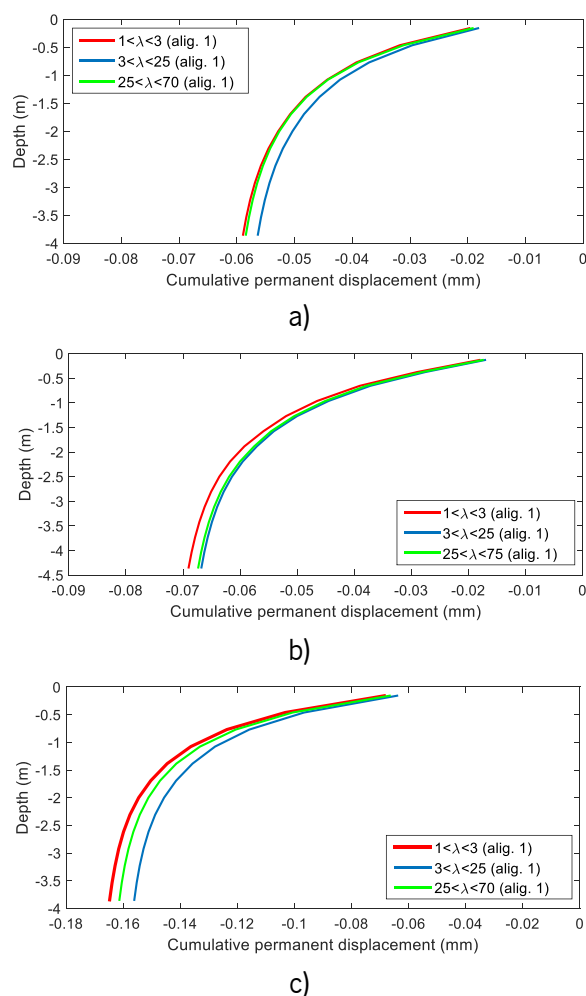
Figure 5.14 - Cumulative permanent displacement: a) ballasted track; b) ballastless track (*Rheda* system); c) ballastless track – only with concrete slab

5.2.4.3 Influence of the train's speed

In this analysis, 6 different train speeds are considered: 80, 144, 200, 300, 360 and 500 km/h. The investigation is focused on element 1 located at x=0 m. In this study, the whole range of wavelengths was included (1 m < λ <70 m) and the properties defined in Table 5.1 and Table 5.2 were maintained, including the resilient modulus of the subgrade and FPL equal to 120 MPa. In order to understand the magnitude of the stresses and permanent deformations for higher speeds, two train speeds closer to the critical speed were also evaluated, which corresponds to values 360 and 500 km/h. In this case, the critical speed of each system was determined expeditiously through the dispersion curves that are an approximated method, but quite effective and efficient (Alves Costa et al., 2020). Alves Costa et al. (2015) show that, when the ground is homogeneous, the characteristics of the track can be neglected since the critical speed is almost the same, regardless of the type of railway structure. In this particular case, the critical speed of the ballasted and ballastless tracks are 515 km/h and 540 km/h, respectively. These values can be obtained through the determination of the intersection's point of the dispersion curve of

the track with the dispersion curve of the ground, which indicates the point where the waves propagate with the same wavelength in the ground and the track, originating the largest amplification of vertical displacements. The critical speed is obtained by the inverse of the slope of the line that joins the origin and the point of intersection of the two curves, as depicted in Figure 5.15. The less inclined that line is, the greater the critical speed of the system. Dispersion curves associated with more rigid tracks are curves associated with lower frequencies than tracks with lower rigidity. It is tempting to think then that higher the stiffness of the track, higher the critical speed of the system. But this may not be true, since the ground dispersion curve will also influence the point of intersection, and it is known that the critical speed of the systems is usually conditioned by the characteristics of the ground. The method based on the dispersion curves is more expeditious than the determination of the critical speed using the 2.5D FEM-PML approach since, in this case, it is necessary to obtain the response of the ground considering the passage of a unit load at different train speeds. In this process, the same point is selected for the different speeds and the absolute maximum displacement is recorded for each train's speed. Thus, with this data, it is possible to obtain a displacement curve versus the train's speed. The critical speed of the system would be the speed at which there is a higher displacement. The results depicted in Figure 5.15 show that, since the ground is homogeneous, to determine the critical speed of the structure, it was only necessary to obtain the slope of the red line since the inverse of the slope is equal to the critical speed.

a)   b)
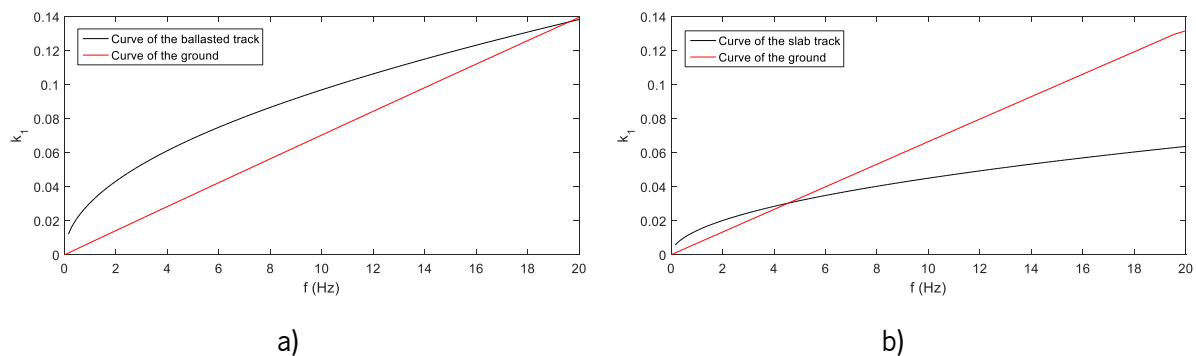
Figure 5.15 - Dispersion curves: a) ballasted track; b) ballastless tracks

From experimental results (mostly in the ballasted track) documented in the bibliography (Sayeed and Shahin (2016b) based on the work developed by Madshus and Kaynia (2000)), it is possible to state that when the train's speed exceeds 75% of the critical speed, the amplitude of the dynamic response of the track increases rapidly. Indeed, 75% of critical speed can be assumed as the practical speed limit of the ballasted railway tracks. This means that the value of 360 km/h is perfectly acceptable as a practical speed limit.

The superior value of the critical speed of the ballastless track can be justified by the stiffness of the track (since both structures share the same subgrade, which means that the dispersion curve of the ground is the same).

Therefore, to assess the influence of the nearing of the critical speed, a higher train's speed than 360 km/h was considered: 500 km/h. This value is higher than 360 km/h and lower than 515 or 540 km/h. Indeed, it is possible to conclude that this speed is unrealistic, but its results are presented to show the ability of the method to capture the behaviour of the structure when submitted to this range of speeds.

In Figure 5.16, Figure 5.17, Figure 5.18, Figure 5.19 and Figure 5.20, the stress paths for the dynamic and static conditions are depicted. The trains' speed equal to 500 km/h is only considered for the ballastless track (*Rheda* system) - Figure 5.21. In the other railway structures, the stress paths go beyond the *yielding criterion*, which is not a realistic situation since it is expected to have stresses' distribution. This means that, for the ballasted track, and considering this particular stiffness of the subgrade and FPL (M_r=120 MPa), the train´s speed of 500 km/h is too much close to the critical speed (515 km/h). This situation does not occur in the ballastless track (500 km/h versus 540 km/h). In the case of the ballastless track only with concrete slab, the results show that the absence of the support layers can influence the stress results when the speeds are close to the critical speed.

a)   b)
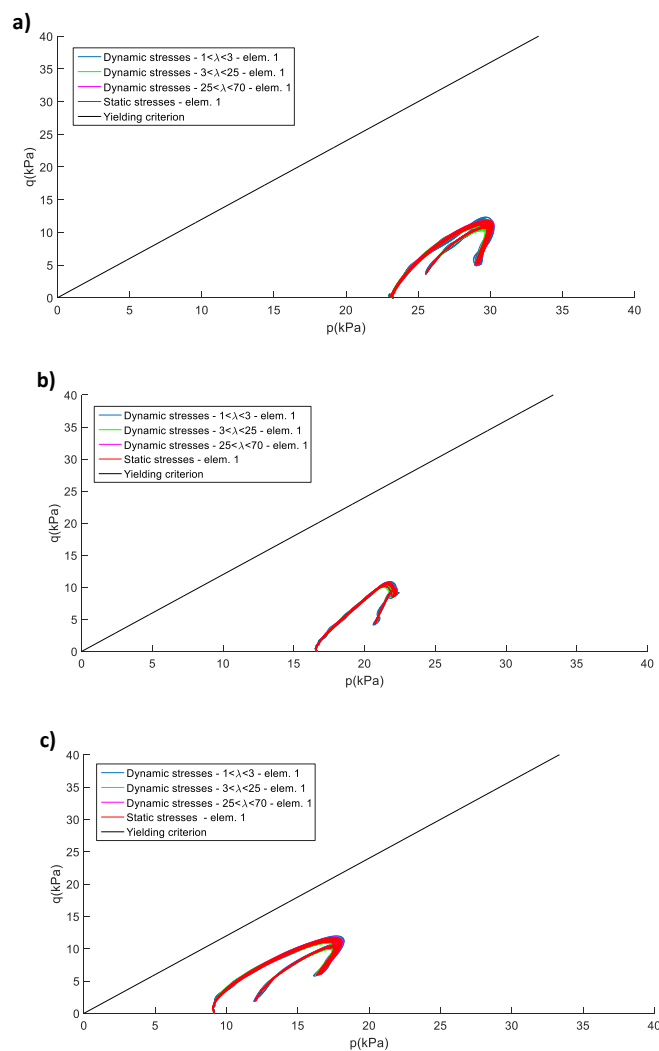

c)
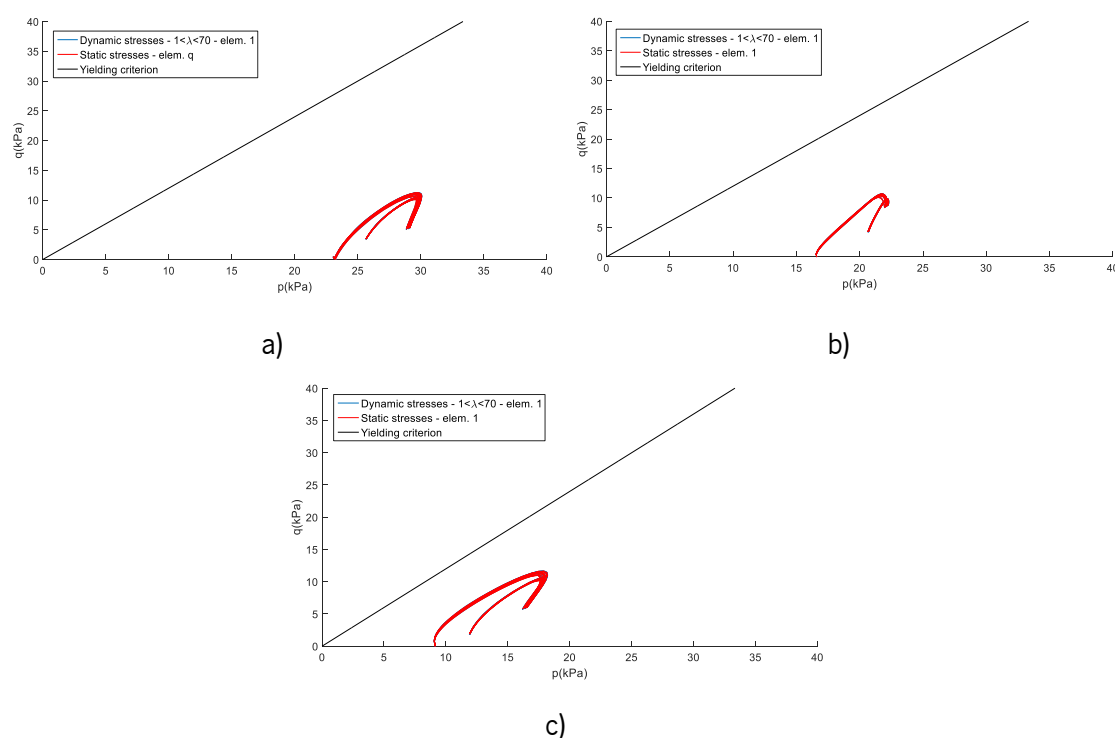
Figure 5.16 - Stress path – v=80 km/h: a) ballasted track; b) ballastless track (*Rheda* system); c) ballastless track only constituted by the concrete slab

a)

b)

c)
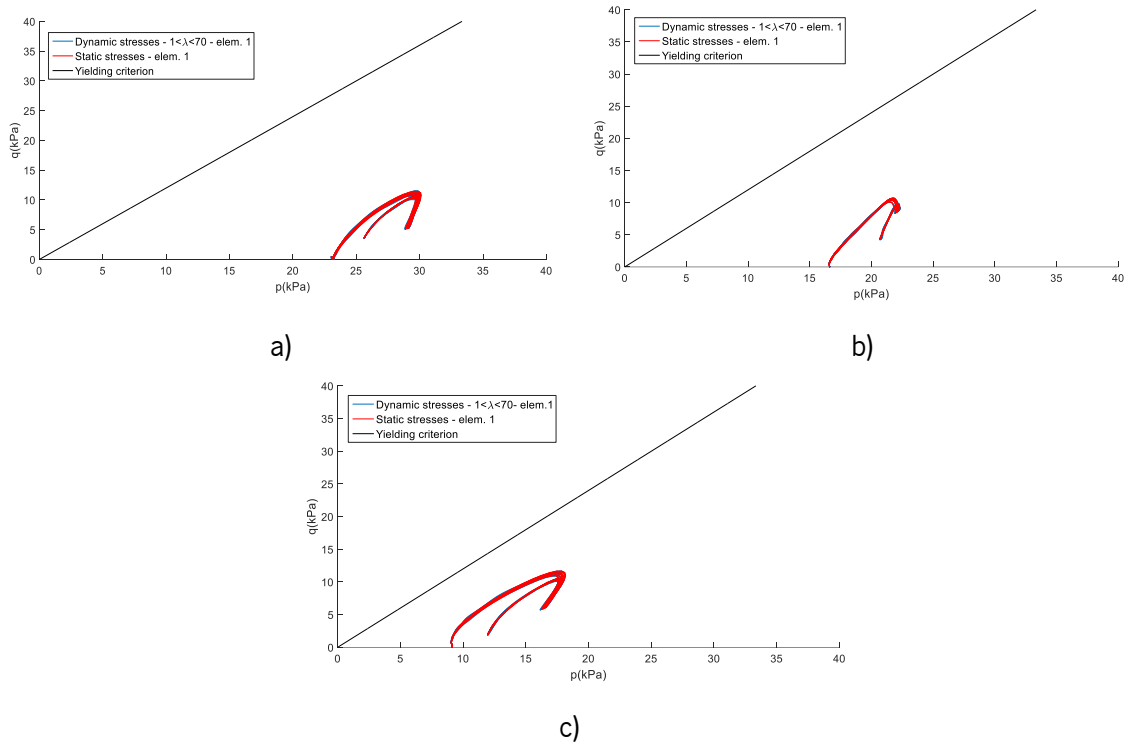
Figure 5.17 - Stress path – *v*=144 km/h: a) ballasted track; b) ballastless track (*Rheda* system); c) ballastless track only constituted by the concrete slab

a)

b)

c)
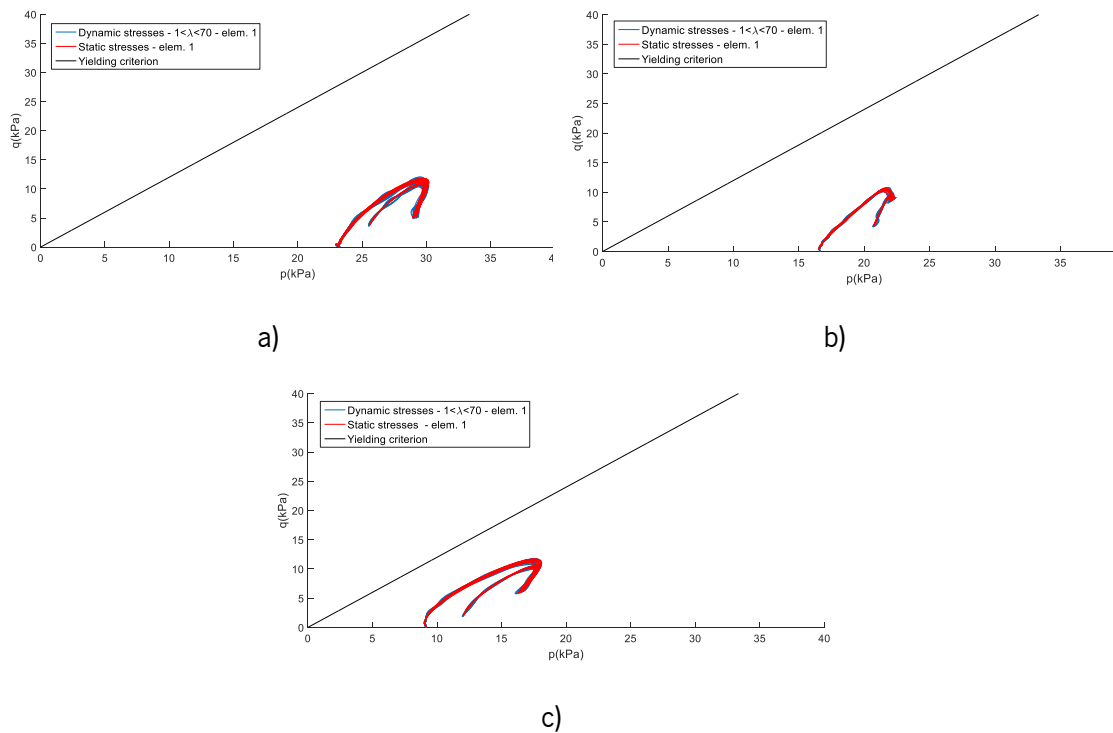
Figure 5.18 - Stress path – *v*=200 km/h: a) ballasted track; b) ballastless track (*Rheda* system); c) ballastless track only constituted by the concrete slab
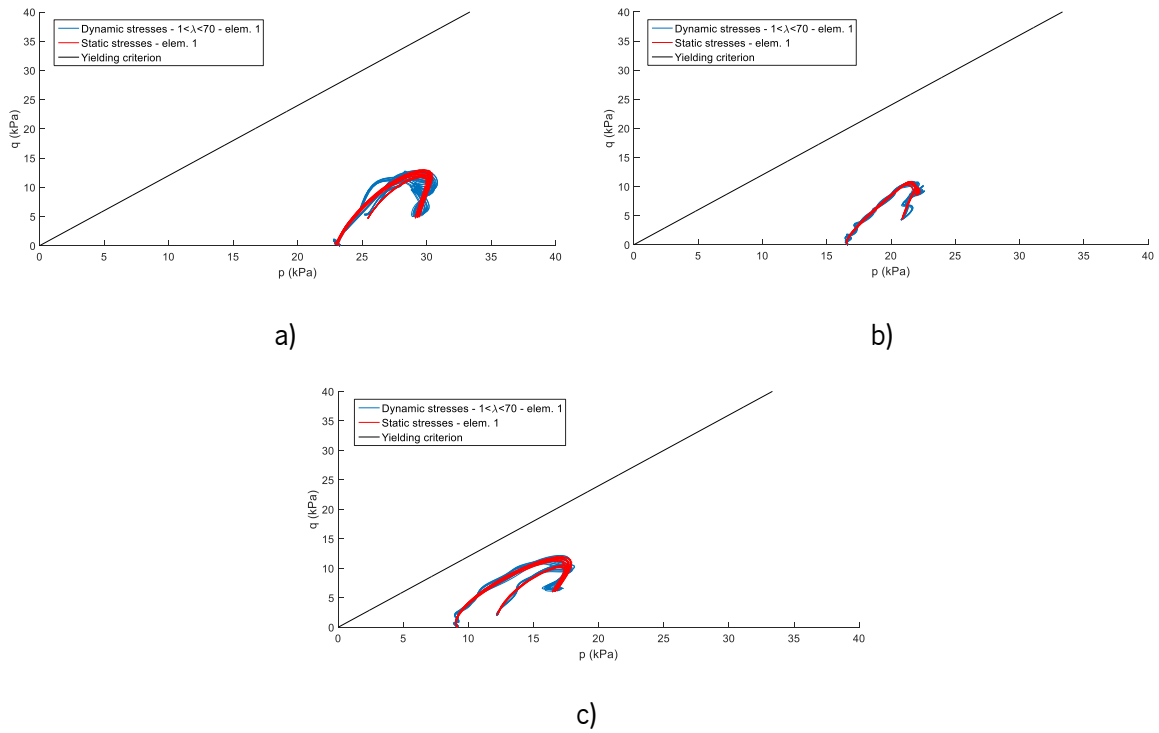
Figure 5.19 - Stress path – v=300 km/h: a) ballasted track; b) ballastless track (*Rheda* system); c) ballastless track only constituted by the concrete slab
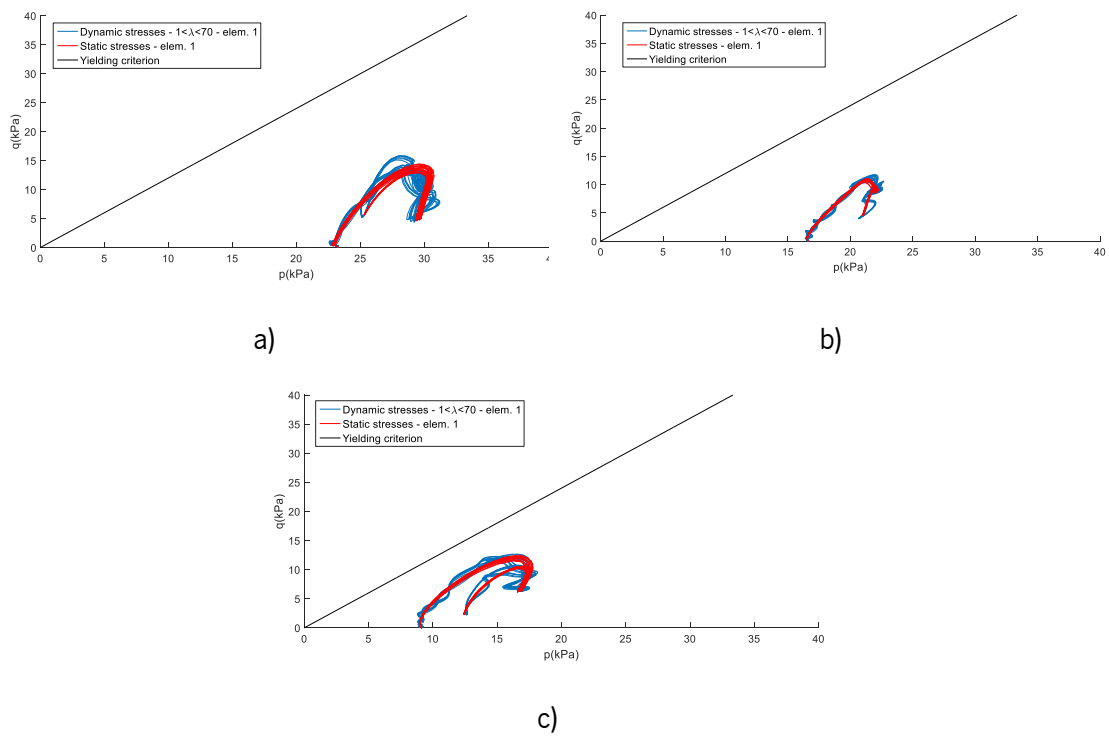
Figure 5.20 - Stress path – v=360 km/h: a) ballasted track; b) ballastless track (*Rheda* system); c) ballastless track only constituted by the concrete slab

201
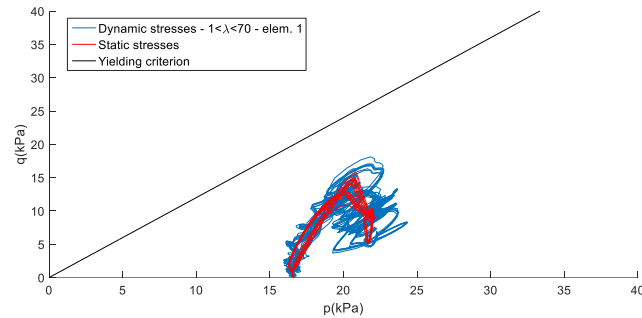
Figure 5.21 - Stress path – ballastless track (*Rheda* system) - *v*=500 km/

Analysing the obtained results, it is possible to conclude:

- The train's speed is one of the factors that most influence the stress levels and stress paths on the subgrade;

- Figure 5.16, Figure 5.17 and Figure 5.18 show that, for reduced train speeds, the dynamic stress results due to the presence of irregularities are almost or even equal to the stress path obtained when only the quasi-static mechanism is taken into account. The stress paths are almost overlaid, and the differences are almost residuals;

- As expected, with the increase of the train's speed, there is an increment in the influence of the presence of irregularities, as show Figure 5.19, Figure 5.20 and Figure 5.21;

- Figure 5.20 and mostly Figure 5.21 show the amplification of the dynamic effects when the train's speed (360 km/h and 500 km/h) is getting closer to the critical speed of the system. In fact, for the ballasted and ballastless track (only with a concrete slab), the stress path of the first element goes beyond the *yielding criterion*. In the case of the ballastless track only with concrete slab, this is due to the amplitude of the stress level and the low value of the initial mean stresses.

In order to understand the scale of the amplification effect, in Figure 5.22 are depicted the stress paths associated with each train's speed for the ballastless track (*Rheda* system) when λ varies between 1 m and 70 m.
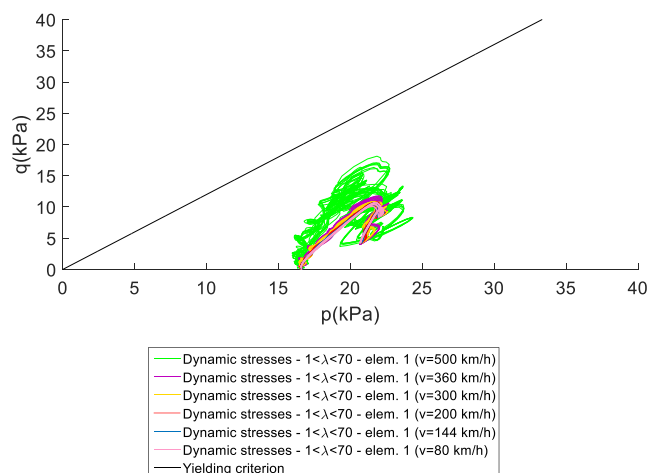
Figure 5.22 - Increment of the dynamic effects considering the increase of the train's speed (ballastless track – *Rheda* system)

In Figure 5.23, the values of the stress amplification factor (*SAF*) for λ between 1 m and 70 m for each structure are depicted. Thus, Figure 5.23 a) shows an increase of the mean stress with the train's speed. This increment is not so clear in Figure 5.23 b) in the case of the deviatoric stress until 300 km/h. For the ballastless track (*Rheda* system), the results show a significant increment of the stresses from 360 km/h, as depicted in Figure 5.23 c) and Figure 5.23 d).
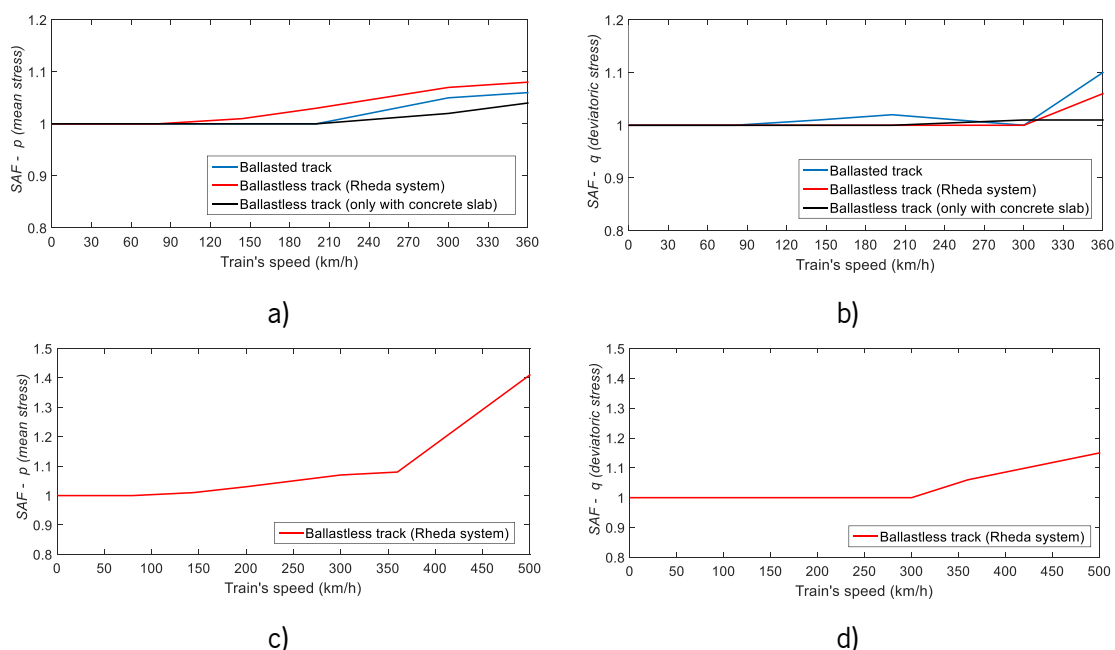
Figure 5.23 - Relationship between the *SAF* and the train's speed; a) mean stress (*p*) – *v* until 360km/h; b) deviatoric stress (*q*) – *v* until 360km/h; c) mean stress (*p*) – *v* until 500km/h (ballastless track – *Rheda* system); deviatoric stress (*q*) – *v* until 500km/h (ballastless track – *Rheda* system)

The mean and deviatoric stresses are important inputs in the determination of the permanent deformation, as described in Chapter 4. However, the mean and deviatoric stresses have an opposite effect on permanent deformation, since the mean stress represents a hardening effect while the deviatoric

stress represents softening effect, which may reflect on the relationship between *SAF* and *PDAF.* The amplitude of the stress path as well as the initial stress conditions are important variables and are used as inputs in the empirical model. This means that the stress results presented in Figure 5.23 can have an impact on the cumulative permanent displacement, *PDAF* (permanent deformation amplification factor), and, consequently, on the degradation of the railway tracks. Analysing the results of Figure 5.23, it is possible to conclude that the significant amplification of the stresses only starts to occur when the train's speed is superior to 360 km/h and is getting close to the critical speed. When the train's speed is close to the critical (from 360 km/h to 500 km/h), the *SAF* of the mean stress increases more than the deviatoric stresses. However, this difference has a low impact on the permanent deformation.

The mean *SAFs* are similar in the ballasted and ballastless track (only with concrete slab) until v=200 km/h. When the train's speed increases, the increments of the mean stresses are higher on the ballastless track (*Rheda* system). On the contrary, regarding the deviatoric stresses, the ballasted track presents superior values when the train's speed increases, which shows higher susceptibility. The lack of consistency prevents defining which structures are more susceptible to the moving loads. However, regarding the ballastless track (only with concrete slab), the values of *SAF* are inferior when compared to the ballasted and ballastless (*Rheda system)* tracks for both mean and deviatoric stresses*,* especially when the train's speed is closer to the critical, which means that this structure is probably less susceptible to the train's speed in terms of stresses (until v=360 km/h).

Furthermore, the results also show the significant impact of the critical speed in the response of the subgrade, which also has an impact on the performance of the railway structures. Indeed, more details about this phenomenon should be included in the standards since, for higher train' speeds, the amplification of the stresses is higher and can lead to a faster track's degradation.

Regarding the permanent displacements, as expected, the ballastless track (only with a concrete slab) shows higher values. The results of the cumulative permanent displacement are depicted in Figure 5.24. In Figure 5.24 b) are depicted the values for the ballastless track (*Rheda system*) but also considering a train's speed of 500 km/h in order to understand the magnitude of these displacements. Although the absolute values of the maximum cumulative permanent displacement are important, it is also necessary to evaluate the permanent deformation amplification factor (represented as *PDAF* in Figure 5.25 and Table 5.7), which is the ratio between the total cumulative permanent displacement induced by both quasi-static and dynamic excitations and the cumulative permanent displacement only induced by quasi-static conditions.

a)

b)

c)

Figure 5.24 - Cumulative permanent displacement: a) ballasted track; b) ballastless track (*Rheda* system); c) ballastless track only with a concrete slab

Table 5.7 - Amplification factor of the permanent deformation with the train's speed

v (km/h)	Ballasted track			Ballastless track (*Rheda* system)			Ballastless track (only with concrete slab)		
	$\|\delta_{cum,max}\|_{stat}$ (mm)	$\|\delta_{cum,max}\|_{dyn}$ (mm)	*PDAF*	$\|\delta_{cum,max}\|_{stat}$ (mm)	$\|\delta_{cum,max}\|_{dyn}$ (mm)	*PDAF*	$\|\delta_{cum,max}\|_{stat}$ (mm)	$\|\delta_{cum,max}\|_{dyn}$ (mm)	*PDAF*
80	0.056	0.056	1.00	0.067	0.067	1.00	0.158	0.159	1.00
144	0.056	0.056	1.00	0.067	0.068	1.01	0.158	0.159	1.00
200	0.058	0.058	1.00	0.067	0.069	1.02	0.160	0.160	1.00
300	0.063	0.065	1.04	0.067	0.070	1.04	0.164	0.166	1.01
360	0.069	0.073	1.06	0.067	0.078	1.15	0.172	0.172	1.00
500	-	-	-	0.093	0.126	1.36	-	-	-

205

The permanent deformation amplification factors for each train's speed are depicted in Figure 5.25 a). Furthermore, in Figure 5.25 b), the increments considering a train's speed equal to 500 km/h are depicted for the ballastless track (*Rheda* system) to understand the magnitude of the increment and its influence on permanent deformation. However, it is important to refer that special attention should be taken in this situation since most of the permanent deformation models are defined for situations where there is a stabilization of the permanent deformation, in which the stress paths are not very close to the rupture. Indeed, for superior stresses (superior to 70% of the $\sigma_{rupture}$), the obtained results could be even higher than those obtained by the empirical permanent deformation models (designated as incremental collapse in the shakedown theory).

a)

b)
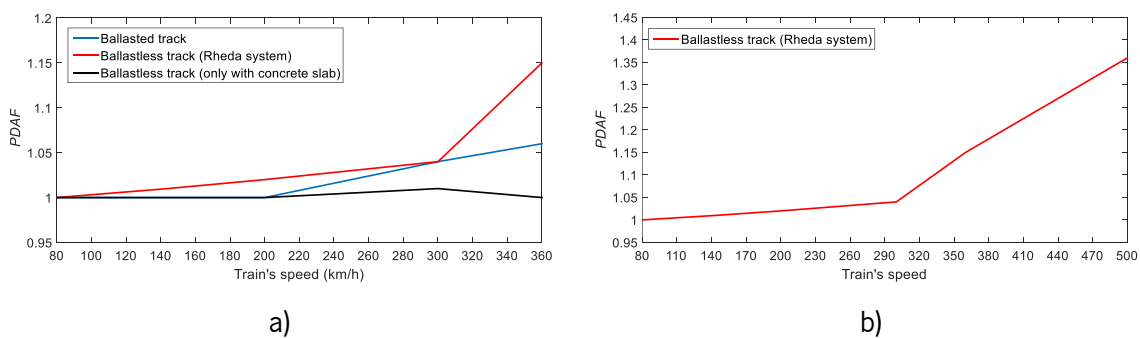
Figure 5.25 - *PDAF* with the train's speed (a); *PDAF* with the train's speed until 500 km/h for the ballastless track (*Rheda* system) (b)

Analysing Figure 5.25 a), it is possible to conclude which is the most susceptible structure to the train's speed in terms of permanent deformation. The conclusions are obtained through innovative *PDAF*. With this approach, it is possible to settle that, considering the results of the subgrade, the ballastless track (*Rheda* system) shows higher susceptibility to the moving loads' factor since shows higher values regarding the *PDAF*. In fact, the increasing tendency is similar in ballasted track and ballastless track (*Rheda* system) but the amplification factor is slightly higher in the ballastless track (*Rheda* system) for each train's speed. Figure 5.25 a) also shows that until 200 km/h, the dynamic mechanisms are neglected, especially in the case of the ballasted and ballastless track only with concrete slab. The results also show a significant increment of the permanent deformation for the train's speed above 360 km/h (in the case of the ballastless track – *Rheda* system), as depicted in Figure 5.25 b). Indeed, the *PDAF* increase significantly when the train's speed became close to the critical speed.

Furthermore, the results show that the ballastless track constituted only by a concrete slab track present constant values and close to 1, which means that is less sensitive to the increment of the train's speed. These conclusions are aligned with the stress results.

5.2.4.4 Influence of the characteristics of the subgrade

The subgrade is modelled by a linear and isotropic model. The *yielding criterion* is dependent on the strength parameters such as the cohesion (c') and friction angle (ϕ'). In this section, the influence of the resilient modulus and strength properties on stress levels and permanent deformation of the subgrade is analysed. The influence of the cohesion will be analysed in Chapter 6 considering a non-zero value. This approach was adopted in order to keep the analysis simple and easy to interpret. This study considers a train's speed equal to 200 km/h, 300 km/h and 500 km/h. The investigation is focused on element 1 located at x=0 m.

In this analysis, the friction angle varies with the resilient modulus, which allows evaluating the influence of both parameters in the permanent deformation results (stiffness and strength properties). The adopted values are:

- M_r= 90 MPa considering c'=0 kPa; ϕ'= 28°;
- M_r= 120 MPa considering c'=0 kPa; ϕ'= 30°;
- M_r= 205 MPa considering c'=0 kPa; ϕ'= 35°;
- M_r= 280 MPa considering c'=0 kPa; ϕ'= 40°.

The remaining material properties were maintained (Table 5.1 and Table 5.2).

The values of the resilient modulus were selected based on the relationship between this variable, the shear velocity (v_s), shear modulus, typical N_{SPT} (Sykora, 1987, Wair et al., 2012) and the friction angles' values, defining a correlation between N_{SPT} and ϕ (Decourt, 1989):

$$\phi' = [15.4(N_1)_{60}]^{0.5} + 20^o \tag{5.34}$$

The obtained results are presented considering the stress amplification factor (*SAF*) for a range of wavelengths range between 1 m<λ<70 m and for each resilient modulus (in terms of mean and deviatoric stress), as depicted in Figure 5.26. In Figure 5.26 a), the curves of the ballasted and ballastless track (only with concrete slab) for v=200 km/h are overlaid. In Figure 5.26 b), the curves of the ballastless tracks (*Rheda* system) are overlaid for a v=200 km/h and v=300 km/h. Furthermore, the curve of the ballastless track (only with concrete slab) for a v=200 km/h is also almost overlaid with the curves of the ballastless track (*Rheda* system). This information allows interpreting the obtained results.

<center>a) b)</center>
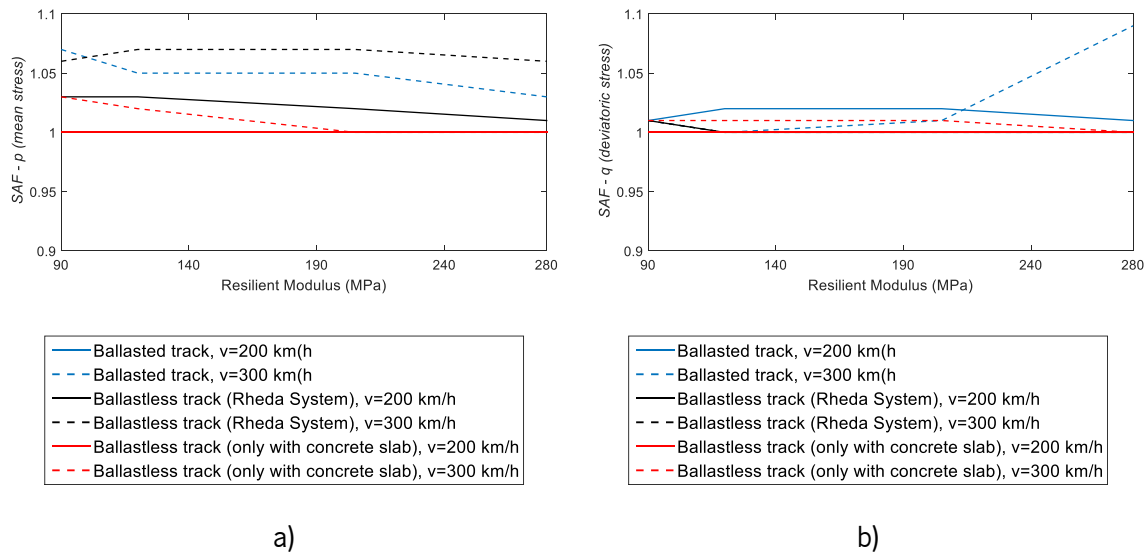
<center>Figure 5.26 - Relationship between *SAF* and the Resilient Modulus: a) mean stress (*p*); b) deviatoric stress (*q*)</center>

For v=200 km/h, the obtained results presented in Figure 5.26 show that all the railway structures present similar behaviour: constant *SAF* values close to 1, which means that the type of subgrade has almost no influence on the stress amplification factor. The ballastless track (*Rheda* system) shows slightly higher values for the mean stress. Regarding the deviatoric stress, the values of *SAF* are constant and very close to 1, and the variation is lower when compared to the mean stress. However, the difference between the mean and deviatoric stresses has a low impact on the permanent deformation since the results are varying between 1.0 and 1.1. Thus, the type of subgrade has no influence on the dynamic amplification of the stresses when the train's speed is lower.

When v=300 km/h, the *SAF* associated with all structures increase in terms of mean stresses when compared to v=200 km/h. Nevertheless, this increment is low. Regarding the mean stress, the ballastless track (*Rheda* system) shows higher susceptibility since the stress amplification is slightly higher when compared to the other structures, followed by the ballasted track. In the case of the deviatoric stress, there is a significant increment of the *SAF* when M_r=280 MPa in the ballasted track from 1 to 1.1, approximately, which is not very significant. However, this may mean that the ballasted track tends to show higher susceptibility to the dynamic effects when the subgrade is stiffer (despite this conclusion is not reflected in the mean stress). As in the previous analysis regarding the train's speed, the lack of consistency between the results of the mean and deviatoric prevents from defining which structure is more susceptible to the moving loads. However, the conclusions may change when the train's speed increases. Indeed, Figure 5.27 shows that the influence of the mechanical properties of the subgrade is more relevant when the train's speed increase (in this case is equal to 500 km/h). However, this speed

<center>208</center>

may not be close to the critical one since the resilient modulus of the subgrade changes in this analysis. Figure 5.28 presents, for each railway structure, the corresponding critical speed for each resilient modulus. The results show that when the resilient modulus is 90 MPa, the critical speed is below 500 km/h (however, despite being inferior, the critical speed is close to 500 km/h and there are also amplifications) and in the opposite, when the resilient modulus is 280 MPa, the critical speed is much higher than 500 km/h.

a)   b)
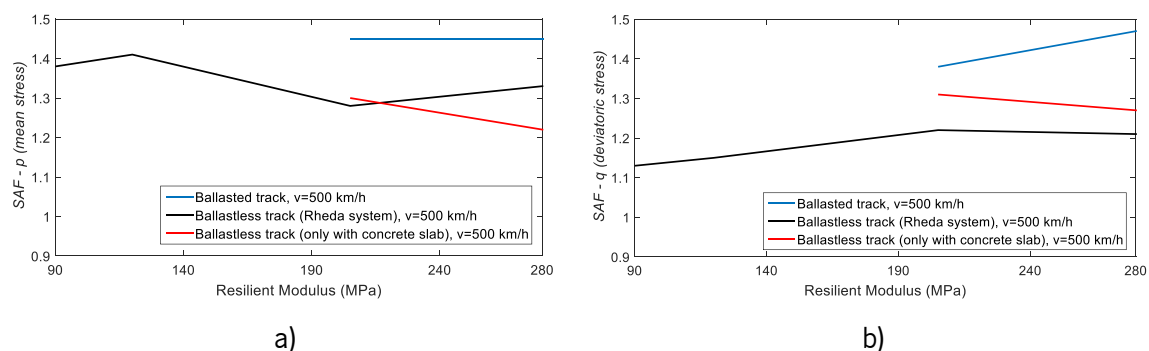
Figure 5.27 - Relationship between *SAF* and the Resilient Modulus (*v*=500 km/h): a) mean stress (*p*); b) deviatoric stress (*q*)
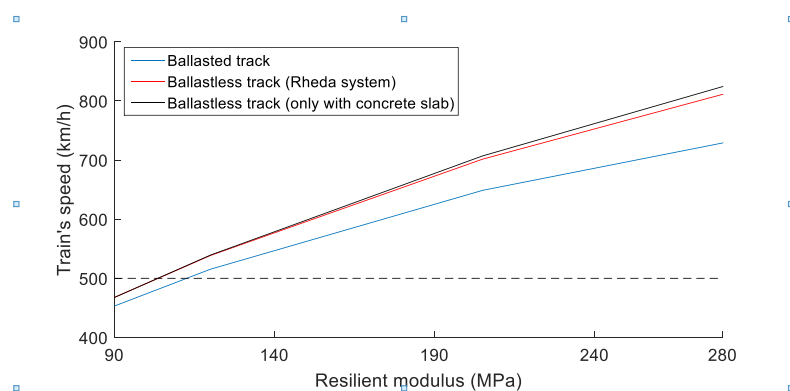
Figure 5.28 - Relationship between the critical speed of the railway structures and the resilient modulus

For the train's speed equal to 500 km/h, the ballasted track and ballastless track (only with concrete slab) show higher amplification stresses when the resilient modulus is lower (M_r=90 MPa and M_r=120 MPa): the stress paths go beyond the *yielding criterion*, which corresponds to a situation where there is a distribution of stresses. For that reason, the obtained results for these particular stiffnesses will not be used in further analysis. The results show significant increments when compared to the train's speed equal to 200 km/h and 300 km/h. This means that these increments would be higher if higher train speeds were considered (close to the correspondent to critical speed).

Analysing the mean stress, the ballastless track (*Rheda* system) shows an increasing tendency between 90 and 120 MPa and between 205 and 280 MPa. Between 120 and 205 MPa, the *SAF* of the mean

209

stress decreases (from 1.4 to 1.3). However, these oscillations may not be significant. For higher stiffness values, the ballasted track shows higher *SAF*. Analysing the deviatoric stresses, the ballasted track also shows higher *SAF* and an increasing tendency. This means that the ballasted track is more susceptible to the variation of the resilient modulus than both ballastless tracks for higher train speeds. This fact is due to the stiffness of the ballast when compared to the concrete slab and may also be related to the inferior values of the critical speed.

The cumulative permanent displacement is also determined for each type of soil. These results are not following the stress results. The main reason is related to the slope of the *Mohr-Coulomb yielding criterion*, which has a significant influence on the permanent deformation, as depicted in Figure 5.29. In the permanent deformation model implemented in this work, the distance between the peak of the stress path and the failure line is one of the parameters that can influence the permanent deformation. Analysing Figure 5.29, the results of the stress paths are close but the distance to each correspondent failure line increases with the increase of the value of friction angle, which will have an impact on the permanent deformation and respective cumulative permanent displacements.

a)

b)
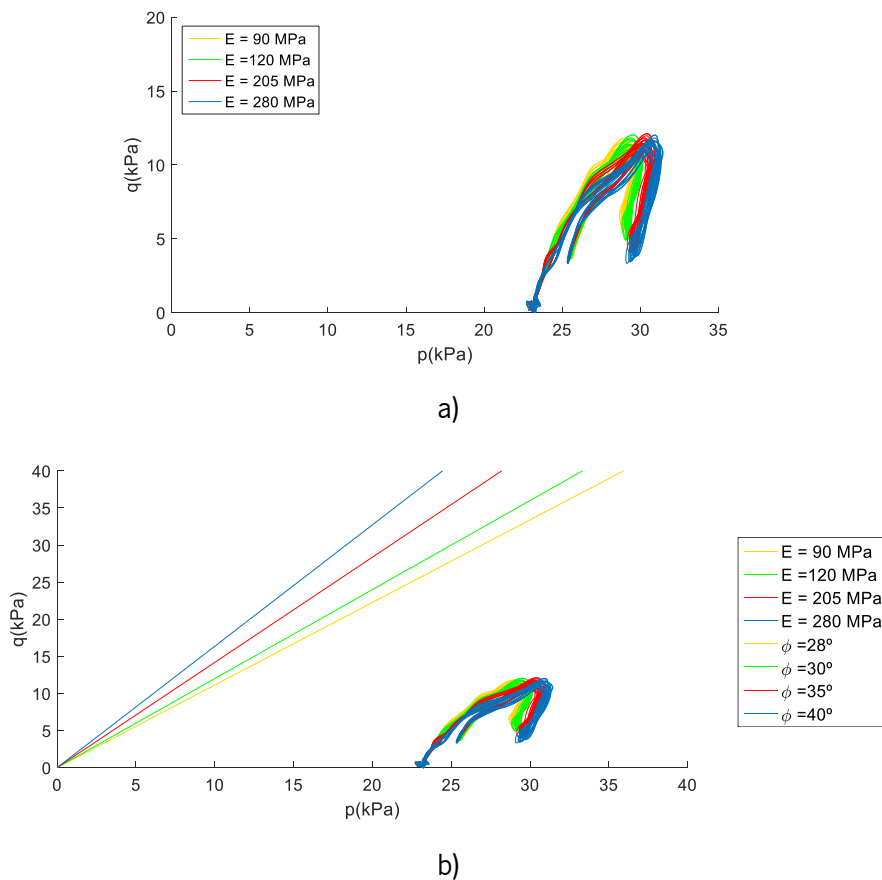
Figure 5.29 - Stress path of element 1 of the ballasted track (v=200 km/h): a) comparison of the amplitude of the stress path; b) stress path and *yielding criterion* associated

Regarding the stress results, the maxima stress amplitude occurs when M_r=280 MPa (Figure 5.29 a). However, the amplitude is not very significant when compared to the stress paths associated with other values of resilient modulus. On the contrary, regarding the cumulative permanent displacements, the value is maximum when M_r=90 MPa and minimum when M_r=280 MPa for most of the cases and considering a train's speed equal to 200 km/h and 300 km/h. However, there are some exceptions, namely the case of the ballasted track when v=300 km/h: the stress paths when M_r=90 MPa and M_r=120 MPa are quite close. The cumulative values of the ballasted track and ballastless track (*Rheda* system) are similar in terms of magnitude for the whole types of subgrade. However, the values are slightly higher in the ballastless track (*Rheda* system).

The obtained cumulative permanent displacements results are depicted in Figure 5.30.

Figure 5.30 allows understanding the magnitude of the cumulative permanent displacements. However, it is also important to evaluate the *PDAF* for each structure, as depicted in Figure 5.31 and presented in Table 5.8. Figure 5.31 a) shows that for lower speeds (200 km/h), the *PDAF* presents values close and close to 1. As expected, the *PDAFs* are higher when v=300 km/h. The ballastless track (*Rheda* system) presents higher values and a decreasing tendency with the increase of the stiffness of the subgrade. The ballasted track also shows a decreasing tendency from M_r=120 MPa. The values of the ballastless track only with concrete slab are almost constant and close to 1, which means that this structure may be less susceptible to the mechanical properties of the subgrade.

This analysis is complemented by the results considering a higher train's speed (500 km/h) - Figure 5.31 b). In the case of the ballasted track and ballastless track only with concrete slab, for soils with stiffness inferior and equal to 120 MPa, there is a significant increment of the stresses and the stress paths go beyond the *yielding criterion*, which could not be real due to the stress distribution (this may also be due to the proximity to the critical speed). This phenomenon occurs when the stress goes beyond the *Mohr-Coulomb* failure envelope, as mentioned previously. With the obtained results, it is possible to conclude that the ballasted track and the ballastless track with only concrete slab show higher susceptibilities for the combination of the factors: lower stiffness of the subgrade and higher speed trains. However, for higher stiffness, the ballastless track (*Rheda* system) presents higher *PDAF* values and a significant increasing tendency from 120 MPa.
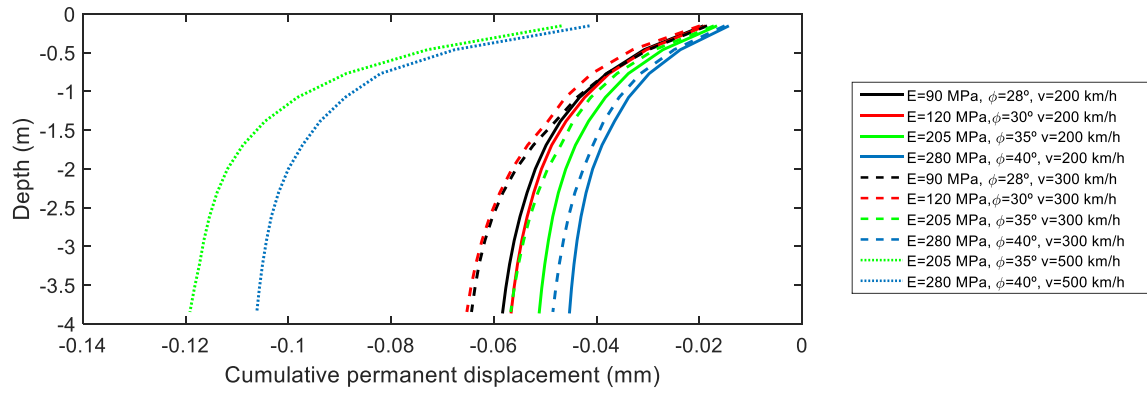
a)
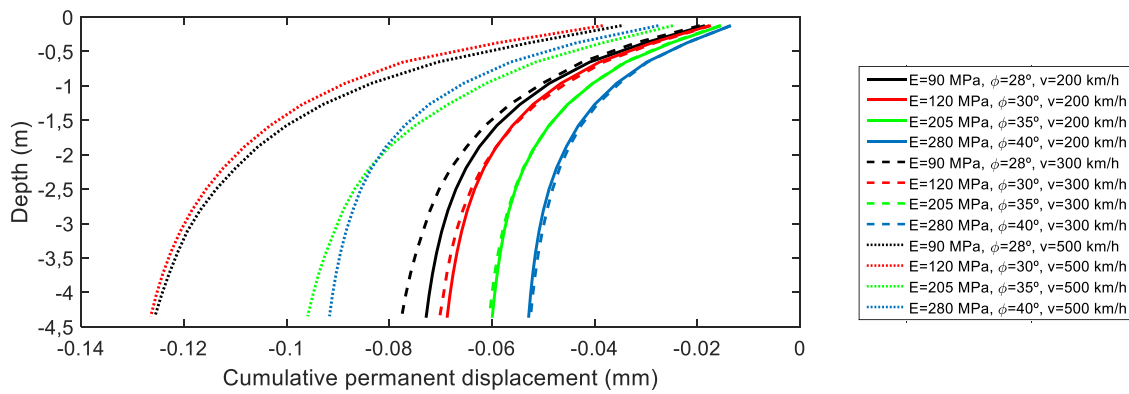
b)
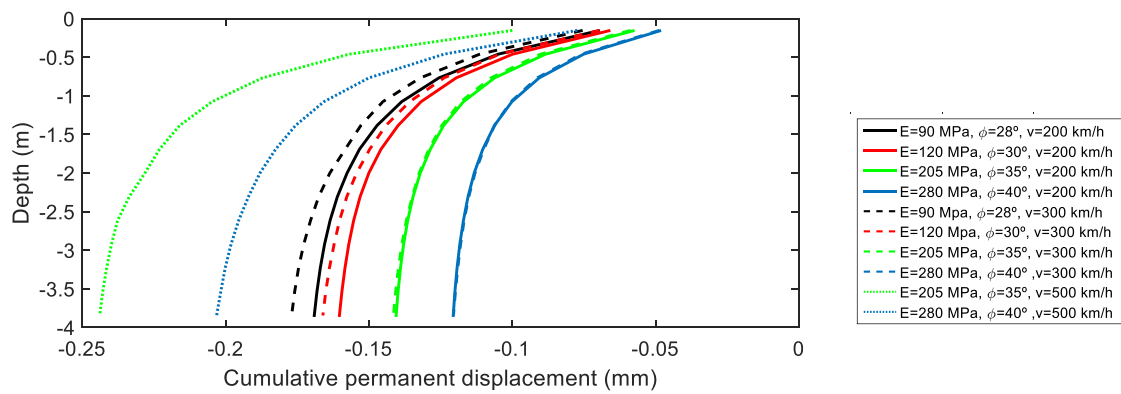
c)

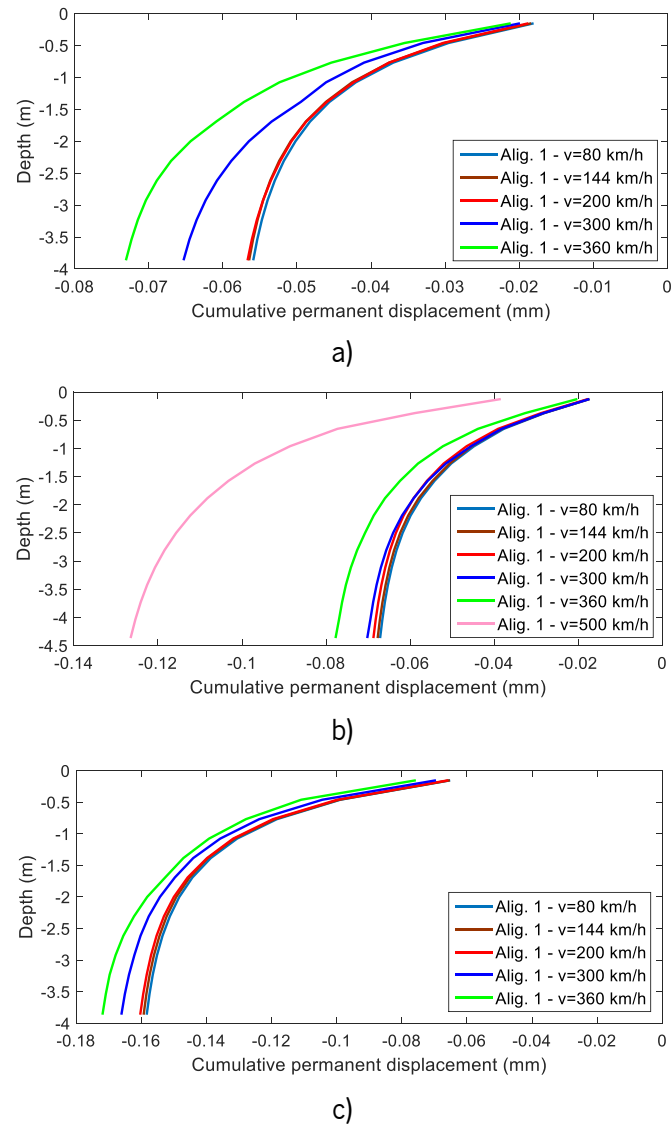Figure 5.30 - Influence of the foundation soil in the cumulative permanent displacement (first alignment): a) ballasted track; b) ballastless track (*Rheda* system); c) ballastless track (only with concrete slab)

a)   b)
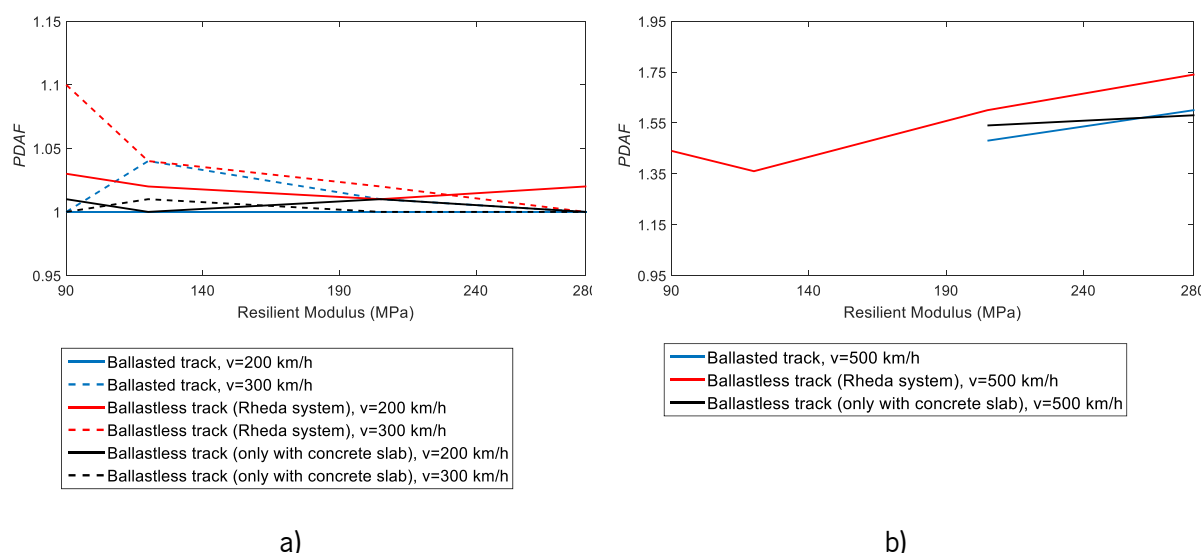
Figure 5.31 - Amplification factor of the permanent deformation with the resilient modulus of the soil (a); Amplification factor of the permanent deformation with the resilient modulus of the soil for train's speed=500 km/h (b)

Table 5.8 - Amplification factor of the permanent deformation with the resilient modulus of the soil

v (km/h)	M_r (MPa)	Ballasted track			Ballastless track (*Rheda* system)			Ballastless track (only with concrete slab)		
		$\left\|\delta_{cum;max}\right\|_{stat}$ (mm)	$\left\|\delta_{cum;max}\right\|_{dyn}$ (mm)	*PDAF*	$\left\|\delta_{cum;max}\right\|_{stat}$ (mm)	$\left\|\delta_{cum;max}\right\|_{dyn}$ (mm)	*PDAF*	$\left\|\delta_{cum;max}\right\|_{stat}$ (mm)	$\left\|\delta_{cum;max}\right\|_{dyn}$ (mm)	*PDAF*
v=200 km/h	90	0.0583	0.0583	1.00	0.0710	0.0728	1.03	0.1680	0.1691	1.01
	120	0.0566	0.0566	1.00	0.0672	0.0687	1.02	0.1596	0.1603	1.00
	205	0.0512	0.0512	1.00	0.0591	0.0599	1.01	0.1396	0.1405	1.01
	280	0.0453	0.0453	1.00	0.0520	0.0528	1.02	0.1206	0.1206	1.00
v=300 km/h	90	0.0644	0.0644	1.00	0.0705	0.0776	1.10	0.1762	0.1770	1.00
	120	0.0629	0.0653	1.04	0.0673	0.0702	1.04	0.1643	0.1661	1.01
	205	0.0561	0.0567	1.01	0.0594	0.0605	1.02	0.1414	0.1414	1.00
	280	0.0485	0.0485	1.00	0.0522	0.0525	1.00	0.1205	0.1205	1.00
v=500 km/h	90	-	-	-	0.0873	0.1256	1.44	-	-	-
	120	-	-	-	0.0930	0.1264	1.36	-	-	-
	205	0.0807	0.1192	1.48	0.0599	0.0959	1.60	0.1581	0.2438	1.54
	280	0.0664	0.1062	1.60	0.0527	0.0916	1.74	0.1283	0.2031	1.58

5.2.4.5   *Influence of the spatial variability of the unevenness profile*

The results presented in previous sections were obtained considering the induced stresses at x=0 m. However, the influence of the spatial variability of the unevenness profile in the stress levels and permanent deformation (and respective cumulative permanent displacements) is also evaluated. Taking into account the profile depicted in Figure 5.7, 4 extra positions were selected to analyse the results: the maximum (relative), the minimum (relative) and 2 intermediate points (y=0 m):

- x=-85.65 m (maximum amplitude value of the unevenness profile) – point A;

- x=-60.60 (minimum amplitude value of the unevenness profile) – point B;

- x=-49.6 (intermediate point: y=0 - amplitude value of the unevenness profile is null but is increasing) - point C;

- x=41.4 (intermediate point: y=0 - amplitude value of the unevenness profile is null but is decreasing) – point D.

It is important to note that these positions changed with a different sample of irregularities. This analysis was performed considering a train's speed equal to 200 km/h and the material properties described in Table 5.1 and Table 5.2, including the resilient modulus equal to 120 MPa. The stress results are described in Table 5.9, Table 5.10, Table 5.11 and Figure 5.32.

Table 5.9 - Influence of the spatial variability (ballasted track)

Ballasted track (1<λ<70 [m])						
x (m)	$d_{p;máx;dyn}$	$d_{q;máx;dyn}$	$d_{p;máx;sta}$	$d_{q;máx;sta}$	SAF_p	SAF_q
-32.13	7.1	12.68			1.02	1.07
-3.77	6.97	11.87			1.00	1.00
28.02	7.02	11.88	6.97	11.87	1.01	1.00
28.73	7.21	12.73			1.03	1.07
0.00	6.97	12.33			1.00	1.04

Table 5.10 - Influence of the spatial variability (ballastless track – *Rheda* system)

Ballastless track – *Rheda* system (1<λ<70 [m])						
x (m)	$d_{p;máx;dyn}$	$d_{q;máx;sta}$	$d_{p;máx;sta}$	$d_{q;máx;sta}$	SAF_p	SAF_q
-32.13	5.79	11.05			1.02	1.03
-3.77	5.87	10.81			1.04	1.00
28.02	5.93	10.76	5.66	10.76	1.05	1.00
28.73	5.77	10.84			1.02	1.01
0.00	5.82	10.89			1.03	1.01

Table 5.11 - Influence of the spatial variability (ballastless track – only with concrete slab)

Ballastless track (only with concrete slab) (1<λ<70 [m])						
x (m)	$d_{p;máx;dyn}$	$d_{q;máx;dyn}$	$d_{p;máx;sta}$	$d_{q;máx;sta}$	SAF_p	SAF_q
-32.13	9.23	12.06			1.03	1.02
-3.77	9.06	11.89			1.01	1.01
28.02	8.98	11.82	8.98	11.77	1.00	1.00
28.73	9.05	12.17			1.01	1.03
0.00	8.99	11.98			1.00	1.02

a)   b)
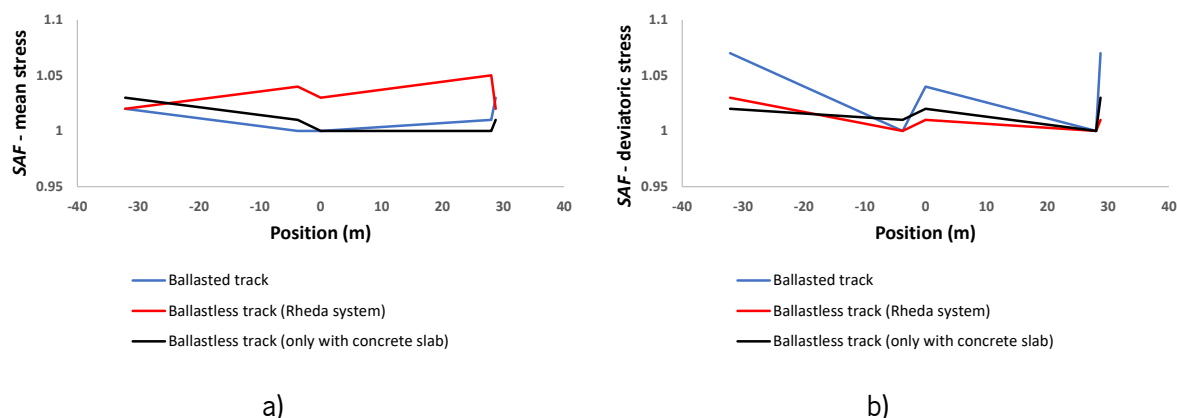
Figure 5.32 - Variation of the stress amplification factor with the position of the selected point of the analysis in the longitudinal direction:
a) mean stress; b) deviatoric stress

The results show that there is almost no variation on the stress levels and stress path (the stress paths are almost overlaid) since the stresses induced by the dynamic mechanism are very small. Nevertheless, the response of the ballasted track varies slightly with the selected position in the unevenness' profile. The ballastless track only constituted by the concrete slab shows a lower influence when compared to the previous structure (lower values of the *SAF* of mean and deviatoric stresses).

Regarding the permanent deformation, Figure 5.33 shows that the spatial variability may influence the permanent deformation and the respective cumulative permanent displacements. However, it is important to highlight that the most severe situation in terms of permanent deformation is not the same for all the structures.

In the ballastless track only with concrete slab, the maximum difference is very residual, as well as in the ballastless track (*Rheda* system), but the curves are closer in the case of the last structure. This analysis was also carried out in terms of increments between the maximum value and the minimum value, as shows Table 5.12. With these results, it is possible to conclude that the ballasted track is more sensitive to this parameter. The results show that the position $x=0$ m is not conservative (quite the opposite in the ballasted track) since the stresses and the permanent deformation are higher in other x-positions.

a)

b)

c)
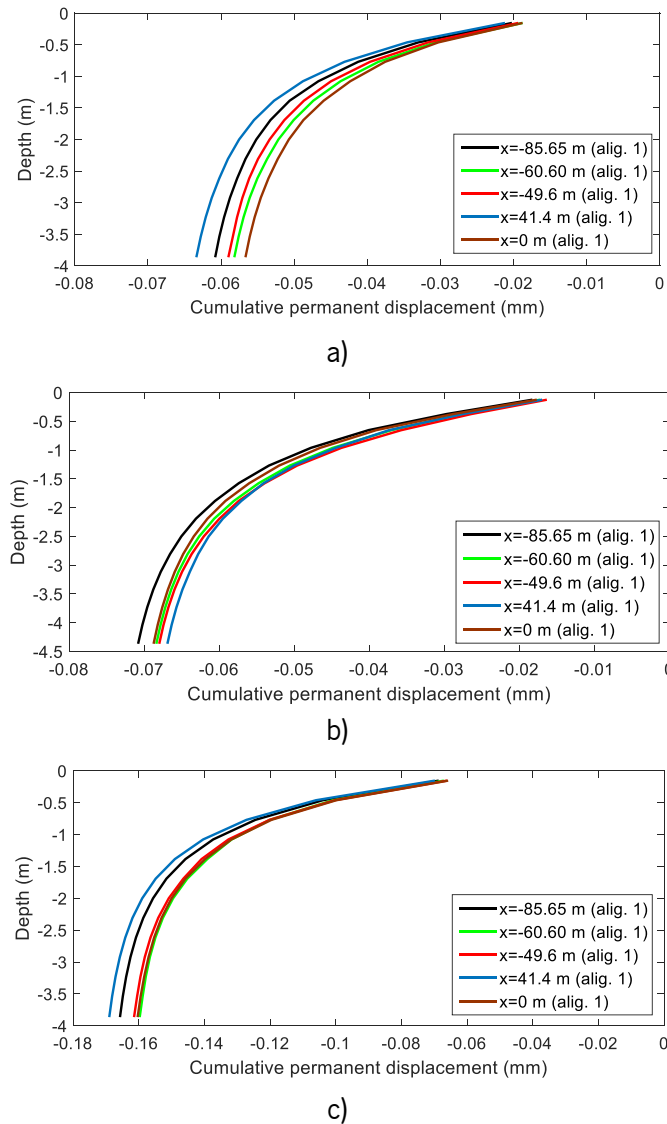
Figure 5.33 - Cumulative permanent displacement – v=200 km/h: a) ballasted track; b) ballastless track (*Rheda* system); c) ballastless track (only with concrete slab)

Table 5.12 - Increments between the maximum and minimum value

Railway structure	|Minimum value| (mm)	|Maximum value| (mm)	Increments (%)
Ballasted track	0.057	0.063	12
Ballastless track (*Rheda* system)	0.067	0.071	6
Ballastless track (only with concrete slab)	0.160	0.169	6

5.3   Final considerations

This work aims to compare the performance of the ballasted and ballastless tracks in terms of stresses and permanent deformations and respective cumulative permanent deformations through an amplification factor that is defined as the ratio between the combination of dynamic and quasi-static and

the quasi-static mechanism. The stress levels are analysed by a numerical tool (2.5D FEM-PML approach), the permanent deformation is evaluated through the implementation of an empirical permanent deformation model and the results are presented in terms of cumulative permanent displacements. The analysis includes a parametric study to identify which are the main factors that may influence the performance of the subgrade of the railway system: wavelength of the unevenness' profile, the train's speed, mechanical properties of the subgrade and the geometric position of the analysis in the track development direction (*x*-axle position). Regarding the ballastless track, the two structures are modelled to evaluate the influence of the support layers in the response of the subgrade. This analysis may be helpful in future optimizations of the ballastless track. The obtained results are a product of a simplification in the ballastless track (*Rheda* system) since for calculation purposes, the FPL was integrated into the subgrade.

About the analysed parameters, the train's speed is the factor that most influences the response of the subgrade, which also includes the influence of the approaching to the critical speed. On the other hand, the range of the wavelengths, characteristics of the subgrade and the spatial variability of the unevenness' profile have less impact.

The conclusions are presented considering each analysed factor:

- The results show that when the wavelength varies between 1 m and 3 m, the stress levels and the cumulative permanent displacements are slightly amplified in the three railway structures under a speed of 200 km/h. However, for ranges superior to 3 m, the dynamic results are equal to the quasi-static mechanism. Indeed, comparing the three railway structures, the stress levels are very similar, and the main differences are related to the initial mean stresses. In fact, the ballasted track is the structure that is more sensitive to the dynamic's effects, despite in practical terms the stress amplification factors being close to 1. For the ballastless tracks, it was concluded that the support layer (HBL+FPL) has no influence on the stress amplification factor of the mean and deviatoric stresses. Regarding the permanent deformation, the ballastless track (only with a concrete slab) presents higher values due to the low initial mean stresses, which means that the induced stress paths are closer to the *yielding* criterion;

- When the train's speed is reduced (i.e. v=80 km/h until v=200 km/h), the quasi-static responses are very similar to the dynamic responses. As expected, when the train's speed increase and it is getting closer to the critical speed (v=360 km/h to v=500 km/h), the amplification effects growth and the amplification factors begin to differ from structure to structure. For instance, the

217

ballastless track (*Rheda* system) for a train speed equal to 500 km/h and considering the whole range of wavelength (1 m < λ < 70 m) has increased by around 17% for the mean stress, 15% for the deviatoric stress and 36% for the permanent deformation. The *SAF* and *PDAF* until 360 km/h (which is defined as the operational speed limit) are slightly higher on the ballastless track (*Rheda* system) for higher speeds;

- The mechanical properties of the subgrade affect the amplification factors, but it depends on the train's speed. Higher speeds (v> 300 km/h) induce higher *SAF and PDAF* in all types of railway structures, independent of the resilient modulus. The ballastless track (*Rheda* system) is the one that seems slightly more influenced by the resilient modulus in the *PDAF*;

- The variability of the unevenness' profile in the track's development direction may have some influence on the amplification factors, mostly in the ballasted track. Indeed, the results show that the position of analysis (*x*-value) should be carefully selected.

With this work, it was possible to conclude that the range 1 m < λ < 3m is the one that induces higher stresses and cumulative permanent displacements. However, the range of wavelengths inferior to 3 m is not included in the standard EN13848-5 (2008) since the alert limits are only defined for the ranges *D1* and *D2*. This study shows that these guidelines should mention the effects of wavelengths for λ < 3 m. Indeed, in the case of isolated effects, the standard confirms that spatial attention should be paid to short wavelengths defects since they can become dangerous when their amplitude is high.

The parametric study shows that both ballasted and ballastless tracks present some advantages and disadvantages depending on the factor analysed. Indeed, this study reveals the significant role of some factors in the design of the railway structures for the importance they can have in the degradation of the railway tracks. Indeed, the presence of irregularities, the moving character of the loads allied to the mechanical properties of the subgrade are crucial parameters in the design and future performance of railway structures. This analysis also shows that the ballastless track with only a concrete slab can be an option instead of the "ordinary" ballastless track - *Rheda* system – (despite the higher absolute values of the permanent deformation) since presents a good overall performance considering all factors analysed. The superior values of the permanent deformation may not be a problem in a free/open track since the track is settling uniformly.

6 Long term performance of ballast and ballastless tracks under cyclic loading: Physical modelling and numerical model calibration

6.1 Introduction

As mentioned in Chapter 2, whether designing ballasted or ballastless railway tracks, short-term and long-term performance must be considered (Chebli et al., 2008, Bezin et al., 2010, Indraratna et al., 2010, Gupta and Degrande, 2010, Lin et al., 2010, Blanco-Lorenzo et al., 2011, Lei and Zhang, 2011, Banimahd et al., 2013, Jiang et al., 2014, Kim and Sung, 2019, Sainz-Aja et al., 2020).

In the selection process between the ballastless and ballasted tracks, there are several important technical and economic issues that need to be addressed, which include construction costs, operability and environmental impact (due to noise and ground vibration). This Chapter is focused on the short and long-term behaviour of both railway structures and aims to compare their performance through the results obtained in a physical modelling. Furthermore, these results are used to calibrate a numerical model.

Indeed, the previous results presented in Chapter 5 are important to understand the main differences in terms of stresses and permanent deformations of the subgrade of the ballasted and ballastless tracks. However, in this part of the work, the results are based on a real-case performance and contain innovative results about the permanent deformation of the railway tracks. Thus, it is possible to contemplate the real influence of the ballast layer in the total permanent deformation of the track.

Thus, in order to better understand and explore the dynamic performance of railway tracks (short and long-term performance), the full-scale laboratory testing of railway tracks is a useful methodology. This approach has been widely used in recent years in studies developed by Bian et al. (2014), Cheng et al. (2014), Tarifa et al. (2015), Bian et al. (2016), Li et al. (2018a), Čebašek et al. (2018), Zhang et al. (2019b), Kim and Sung (2019) and Sainz-Aja et al. (2020). Moreover, full-scale laboratory tests and the related results allow for a better understanding of the role of the subgrade in the global track stiffness, since a low track stiffness can lead to a flexible track with poor load distribution. Further, a high track stiffness can induce greater dynamic loads on the rail, increasing train-track interaction forces (Colaço et al., 2016). In this work, the experimental results are obtained from a full scale laboratory tests of ballast and ballastless tracks performed at Heriot-Watt University.

From the experimental results, two 3D numerical models are developed in commercial software ANSYS. The numerical models aim to capture the behaviour of the full-scale structures when subject to cyclic loads. The 3D FE method is used (since it is the most useful tool to simulate this type of problem) and

the dynamic analysis is performed in the time-domain despite the required high computation cost in dealing with large scale problems (El Kacimi et al., 2013, Sayeed and Shahin, 2017). The short term behaviour is assessed through the comparison of the calculated and measured displacements obtained by the Linear Variable Differential Transformers (LVDTs) placed on both structures (Čebašek et al., 2018). After the calibration of the numerical models, an empirical permanent deformation model (defined based on experimental laboratory testing) for the track foundation is also calibrated through an optimisation procedure. The calibration process includes the evaluation of the model parameters and takes into account the materials' stress history through the inclusion of the time-hardening approach. This analysis is only possible since the structures are submitted to more than 3 million cycles, which allows significant data to be collected related to permanent deformation. The empirical permanent deformation model adopted corresponds to the model developed by Chen presented in Chapter 4 and already implemented in Chapter 5. As mentioned previously, this model is dependent on the number of load cycles (N), initial stress state, amplitude of the stress induced by the cyclic loads and also included the influence of the proximity of the stress path into the yielding criterion (Gidel et al., 2001, Chen et al., 2014). The implemented calibration process can be applied to other conditions and geometries, which means that the extrapolation should be properly contemplated. Furthermore, the calibration regarding the permanent deformation is rare and innovative since there are not many experimental data that allow to carry out this process. Moreover, this calibration is also important to understand in more detail the contribution of each layer to the permanent deformation.

This approach can also be vital in the prediction of the long-term behaviour of track structures, especially in transition zones. In these areas, the phenomenon of the permanent deformation is more complex (due to the differential settlements and differences in terms of stiffness) and the development of numerical studies with the implementation of these calibrated properties can be an important tool in the scope of the study of the long-term performance of the transition zones since increases the confidence in the obtained results. Thus, some parametric studies are developed from the calibrated numerical models. These parametric studies aim to analyse some aspects that go beyond the laboratory conditions such as the increasing of the computation effort (through the consideration of the extension of model and changes in the type of mesh) and efficiency of absorbent boundaries, which is an important topic in the simulation of a real-case railway track and transition zones in particular. These preliminary studies are based on the geometry and materials' properties of the ballastless track and are developed taking into account the cyclic loading applied during the cyclic tests.

The calibrated properties of the materials and parameters of the empirical permanent deformation model as well as the results obtained from the parametric studies will be further used in Chapter 7 in the study of a particular transition zone.

6.2 Laboratory testing

6.2.1 Experimental Setup

The full-scale GRAFT-2 facility (Figure 6.1) was adopted to evaluate the short and long-term performance of the ballasted and ballastless tracks (Yu et al., 2019). The load is applied through six independent hydraulic actuators on full-sized sleepers on both the ballasted and ballastless tracks (in this case, the sleepers were built on the concrete slab). The passage of the trains is simulated using phased loading and each actuator applies a load to each rail segment. The schematic representation of the GRAFT-2 facility and the dimensions are depicted in Figure 6.1b).

| a) | b) |
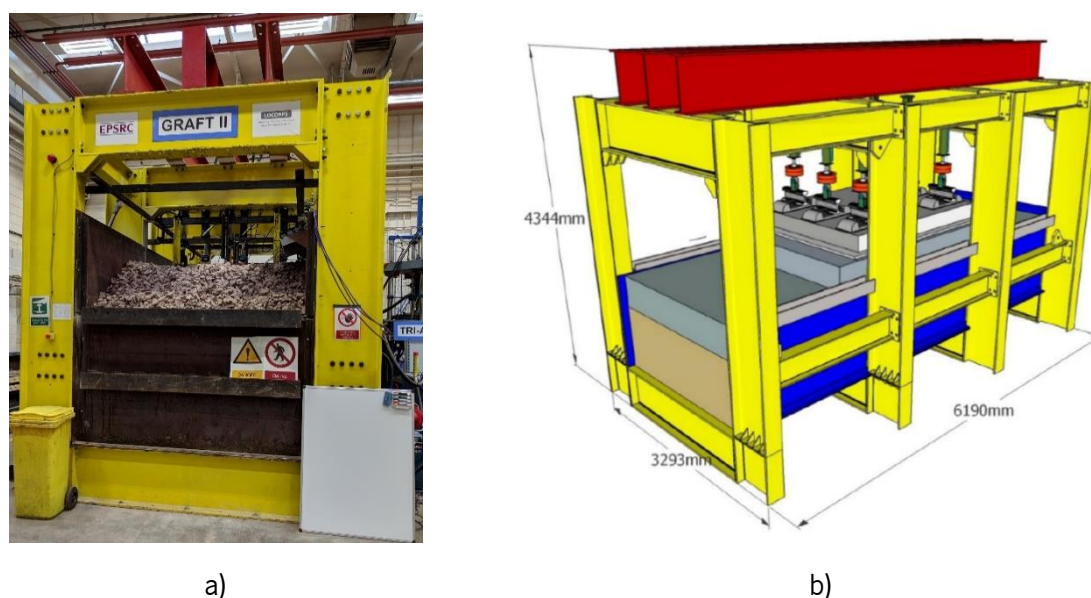
Figure 6.1 - Experimental setup: a) front view; b) diagram of the GRAFT-2 facility and main dimensions (Čebašek et al., 2018)

6.2.2 Ballastless track (Slab track)

The ballastless track is composed of a concrete slab, a thin layer of cement grout, a support layer designated by hydraulically bonded layer (HBL) and a substructure. The substructure is the same as the ballasted track (ASTM-D2487-17, 2017) and consists of the frost protection layer (FPL) and the subgrade (Figure 6.2). The HBL is placed on the top of the FPL. Moreover, between the concrete slab and HBL, there is a gap of 40mm that is filled with a non-shrinking cement grout to bond the two layers. The properties of the HBL are presented in Table 6.1.

221

Table 6.1 - Properties of HBL

Layers	Thickness (mm)	Concrete	E (MN/m²)
HBL	300	C10/12 (with cement intake of 110 kg/m³)	7500
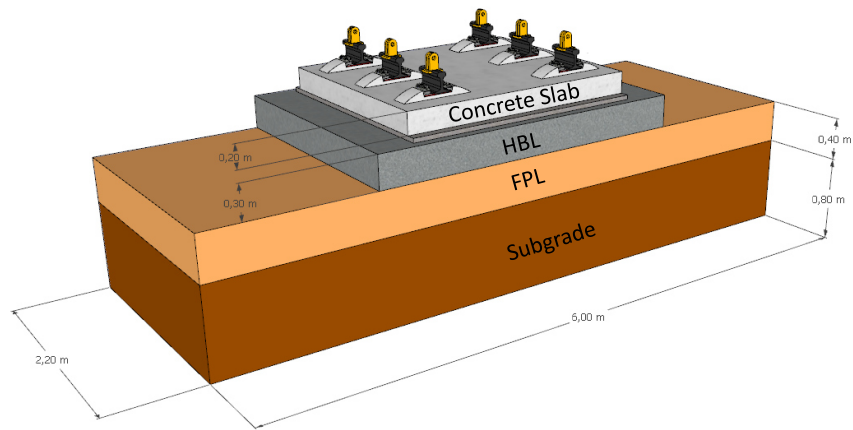
a)
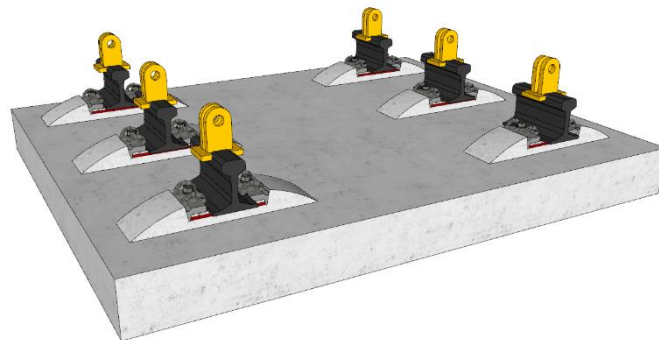
b)

Figure 6.2 - Experimental ballastless track a) full-track; b) superstructure without HBL and grout mass layers

The structure is a pre-cast slab of C45/55 reinforced concrete. The main dimensions of the concrete slab are depicted in Figure 6.3. The track segment has three pairs of sleepers that are integrated into the longitudinal and cross direction uniformly, as depicted in Figure 6.3. The fastening system is a 300-1 (Vossloh Fastening Systems). Regarding the railpad system, the static stiffness of the lower elastic pad is around 22.5 kN/mm and the dynamic stiffness is approximately 40 kN/mm. The upper railpad has a static stiffness between 600-700 kN/mm and a dynamic stiffness of approximately 1600 -1800 kN/mm. In this track, UIC60 rail segments are used (Čebašek et al., 2018).
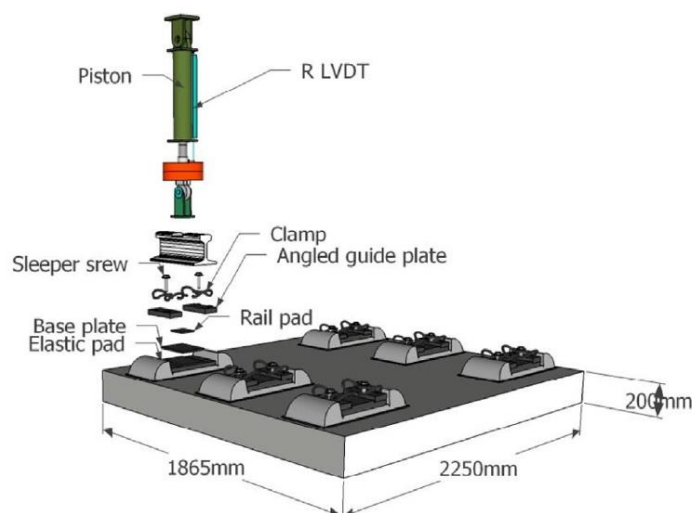
Figure 6.3 - Dimensions of the ballastless track system (Čebašek et al., 2018)

Both ballastless and ballasted tracks are subject to cyclic tests with 3.4 million load cycles (155.4 MGT). This corresponds to 5.2 years of West Coast Main Line (Kennedy et al., 2013) usage, at which the level of loading over the site is 30 MGT per year. The facility used in the performance of the cyclic tests (full-scale GRAFT-2) allows simulating the passage of many trains (years of train passages) in a few days of testing. The number of data generated in terms of displacements obtained throughout the cyclic tests allows study the long-term behaviour and simulate the degradation process of the ballasted and ballastless tracks. In the case of the ballastless track, there is no evidence of concrete cracks during the tests.

6.2.3 Ballasted track

Ballasted track tests are performed after the ballastless track tests. Thus, the ballast is placed after the removal of the concrete slab and HBL. For the ballasted track, the main part of the substructure remains unchanged, and the superstructure is fully replaced, except the railpads. In this case, the same railpads are used for the ballastless and ballasted tracks. This was an option adopted by the Heriot-Watt University research team. The top 50 mm of the FPL are replaced between the tests due to the disturbance caused by the removal of the HBL (Čebašek et al., 2018).

The substructure (with a total thickness of 1.2 m - the subgrade has 0.8 m and the FPL has 0.4 m of thickness) of the ballasted track, as in the ballastless track, is composed of an FPL, subgrade and there is a geogrid placed between the ballast and the FPL (geogrid TX190L) to reduce the penetration of the ballast into the substructure. The substructure is characterised by a well-graded granular limestone according to ASTM (ASTM-D2487-17, 2017). Its Particle Size Distribution is presented in Figure 6.4.

223

Using a modified Proctor compaction test, the optimal moisture content was 4.5 %. The material parameters of the substructure are specified in Table 6.2. In addition to the geotechnical properties presented in Table 6.2, the deformation modulus (E_{v2}) was also estimated via the Plate Load Test (PLT) performed on the subgrade and FPL layer. The plate load tests were carried out according to standards DIN-18134 (1999). The E_{v2} value for the FPL was 133.55 MN/m² and E_{v2}/E_{v1} at 1.42. In the case of the subgrade, E_{v2} was 67.71 MN/m² and E_{v2}/E_{v1} was 1.55.

Table 6.2 - Material properties of the substructure

Properties	Substructure's materials
Effective internal friction angle at OMC - ϕ'(°)	35
Specific gravity - G_s	2.69
Maximum dry density γ_{d-max} (kN/m³)	22.2
Coefficient of permeability – k (m/s)	10^5 (for FPL)
Relative density - D_r (%) (for the FPL and subgrade)	98% - 100%

The ballast consists of micro-granite (medium-grained equivalent of granite; the crystals are slightly smaller than granite indicating that the magma cooled more quickly; this usually occurs in smaller intrusions than granite) with a moisture content of 0.5%. The granulometry of the micro-granite and limestone are depicted in Figure 6.4. As expected, the micro-granite has particles with larger dimensions and no fines content. The limestone (substructure) has a percentage of fines and the particles are smaller when compared to the particles of the micro-granite.
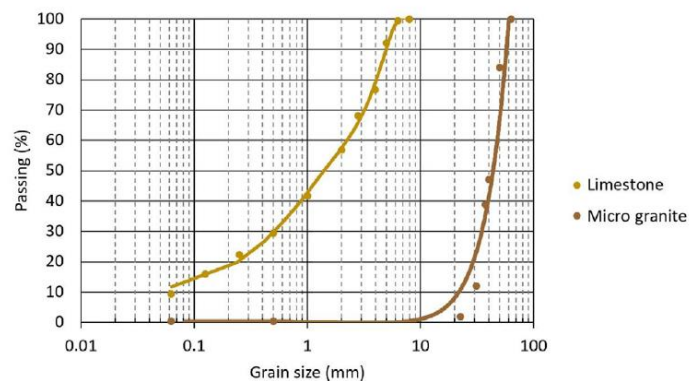
Figure 6.4 - Limestone and microgranite particle size distribution (Čebašek et al., 2018)

In the experimental tests, three segments of BS113A (56E1) are used, as well as G44 sleepers (embedded in the ballast layer) – used by the BS113A rail – that are placed 650 mm apart (Čebašek et al., 2018). The lower elastic pads from the ballastless track test are used as railpads. The Pandrol

fastening system is used to attach the rails to the sleepers. The geometry of the model and the identification of the materials are depicted in Figure 6.5. In this figure, the rail is represented as continuous. However, as mentioned previously, the rails are segmented.
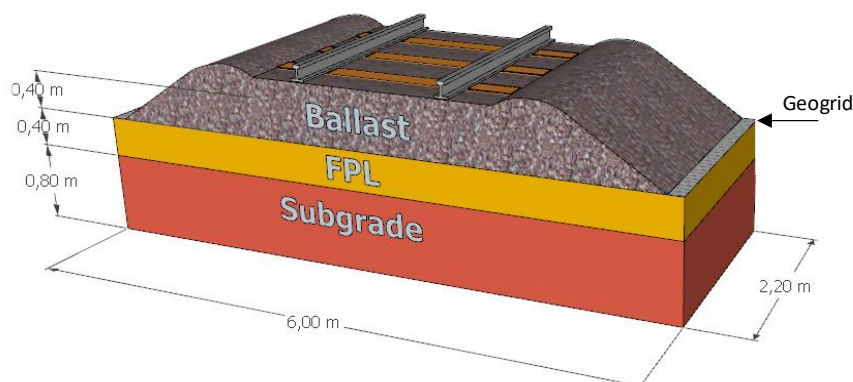
Figure 6.5 - Ballasted track model

6.3 Methodology used for static and cyclic loading testing

The tests are divided into two types: static and cyclic. The appropriate redistribution of the axle load for the initial static tests over the ballastless and ballasted tracks was applied by considering the full axial load. This was simulated by assuming that, approximately, 50% of the load passes directly onto the middle sleeper and a quarter of the load passed to each adjacent sleeper, as depicted in Table 6.3 and Figure 6.6. The effect of wheel-rail irregularities is not considered. For the cyclic tests, this distribution is not adopted. In this case, the full load is used on each sleeper, which represents the worst-case scenario. Table 6.3 presents the loading sequences (2 static and 2 cyclic tests) used for the ballasted track and ballastless track tests. The main differences between the two static tests are related to the duration and the load applied on the sleepers by the actuators. In the cyclic tests, loading is phased (Δt) between adjacent actuators in the track direction, following the expression:

$$\Delta t = \frac{\Delta s}{v} \qquad (6.1)$$

where Δt is the time lag between neighbouring actuators, Δs is the distance between the two adjacent actuators in the track direction in metres, and v is the train's speed adopted in m/s.

The cyclic tests differ in terms of frequency and load magnitude applied by the actuators. The train speed adopted in both dynamic tests is 100 m/s. In the second test (*Dynamic II*), the load is increased, and the frequency decreased when compared to first test (*Dynamic I*). Thus, the frequency of 5.6 Hz (cyclic test 1) was determined based on a given train's speed and distance between two bogies of the same rolling

stock. The frequency of 2.5 Hz was adopted based on the limitations of the facility when simulating higher loads.

Table 6.3 - Loading sequences for the ballasted and ballastless tracks – adapted from Čebašek et al. (2018)

Test	Load on middle sleeper (kN)	Load distribution per actuator (kN)	Load distribution in %	Frequency (Hz)	Time (s) (interval between the sleepers)	Duration
Static I	63.77	15.94;31.88;15.94	25;50;25	-	-	620 s
Static II	83.34	20.84;41.69;20.84	25;50;25	-	-	788 s
Dynamic I	117.72	58.86;58.86;58.86	100;100;100	5.6	0.0065	1.17×10^6 cycles
Dynamic II	166.71	83.34;83.34;83.34	100;100;100	2.5	0.0065	2.20×10^6 cycles
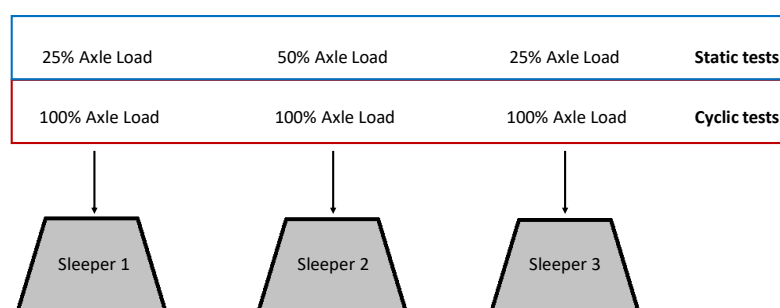
Figure 6.6 - Load distribution scheme for the static and cyclic tests

In the cyclic tests, some situations were not analysed/tested: the effect of the train's speed on the soft subgrade and the effect of critical speed, since the adopted speed is below the critical speed.

6.3.1 Experimental set-up of static and cyclic tests

The acquisition system is composed of 32 channels to acquire data from the sensors during the dynamic/cyclic tests, each with a sampling rate of 200 Hz.

The cyclic/dynamic tests are performed considering the inclusion of several elements to measure stresses and deflections. The control of the deflection of the actuators, the control of the applied loads and the measured settlements are performed using several devices including load cells (6 channels) and LVDTs (6 channels), also designated as CH displacements, as depicted in Figure 6.7. In order to control the total settlements and measure the deflections, four 12 mm high-precision LVDTs and three 75 mm LVDTs were installed on the concrete slab in the ballastless track and on the ballasted track's sleepers. Moreover, three accelerometers were placed on the slab to measure track vibrations. The main elements used in this study are depicted in Figure 6.7.
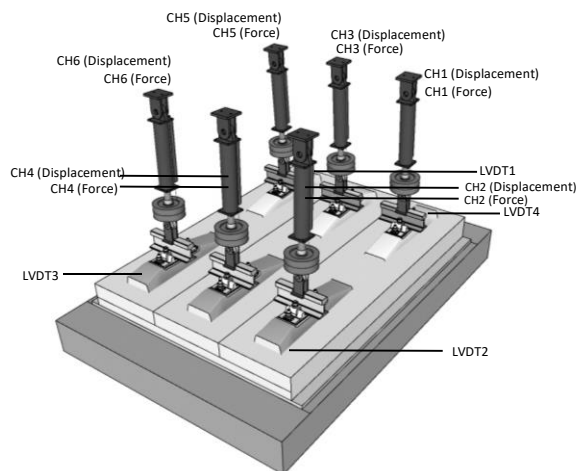
Figure 6.7 - Cyclic test set-up

6.3.2   Static tests – procedure and results

As previously mentioned, the static tests are performed before the cyclic tests. For the adjacent sleepers, firstly a load of approximately 16 kN is applied (*Static I*) for 620 s and after that, a load of 21 kN for 788 s (*Static II*). This procedure is adopted for both tracks. During these tests, the deflections are measured using surface-LVDTs (designated as *S-LVDTs*) placed on the concrete slab surface of the ballastless track and the sleeper surface in the case of the ballasted track. The displacements are also monitored on the surface of the rails using the rail-LVDTs (designated as *R-LVDTs* or $CH_{displacements}$). The results of the *R-LVDTs* and *S-LVDTs* are depicted in Figure 6.8.

The displacement results show that the ballasted track has higher deformation than the ballastless track. This is probably due to the ballast layer stiffness and its unbound nature. It is important to highlight that the same elastic pads (placed under the base plate - Figure 6.3) are used in both the ballastless track and ballasted track tests and this may influence the results of the *R-LVDTS*.

a)   b)
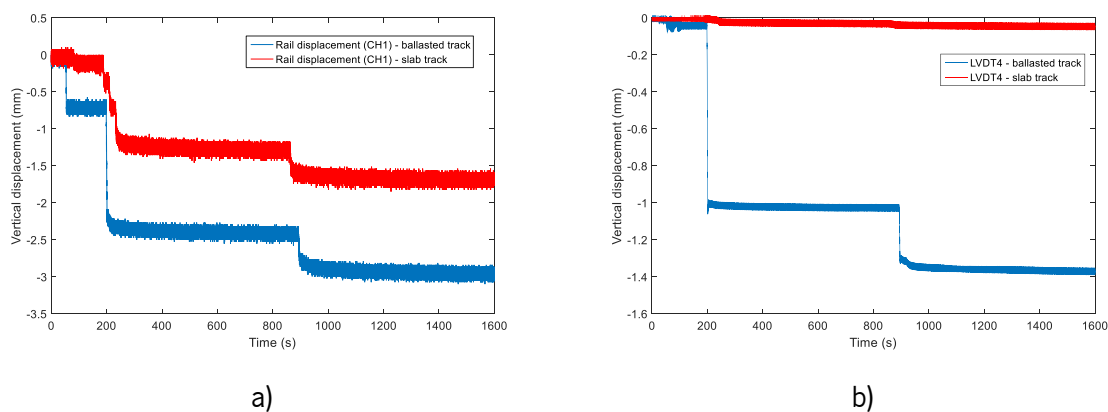
Figure 6.8 - Vertical displacement a) on the top of the rail (*R-LVDTs*) for the ballasted and ballastless tracks; b) on the top of the sleeper for the ballasted track and on the top of the slab for the ballastless track (*S-LVDTs*)

6.3.3   Cyclic tests – procedure and results

Two types of cyclic load are applied to the ballasted and ballastless tracks with different frequencies (5.6Hz and 2.5Hz) and different loads per actuator (58.86kN and 83.34kN).

In order to simulate the rotation of the principal stresses in the experimental tests correctly, phase loading is used. This is an important element in this analysis and it is an important capability of the GRAFT-2 facility. However, the influence and repercussion of the inclusion of the phase loading may be different from one railway track to another due to differences in stiffness. In the ballastless track, its high stiffness will change the stress rotations in the subgrade when compared to the ballasted track (Čebašek et al., 2018).

The rotation of the principal stresses, despite their importance, is not the only important parameter in the analysis of railway settlement. In fact, other parameters influence permanent deformation, such as axle load, number of trains, distance between axles, type and physical state of the materials, stress loading history and previous track condition. The conditions of the track foundation are different for each track structure, despite the same track foundation being shared by both. In fact, after the cyclic tests on the ballastless track, the FPL and subgrade have already been subject to stress cycles. Therefore, the conditions at the beginning of the ballasted track test are not identical to the beginning of the ballastless track cyclic test and this may affect the obtained results. However, this option was assumed from the beginning of the static and cyclic tests.

During the cyclic tests on the ballastless track, the substructure stiffness increased. However, the increase of stiffness on the substructure during the cyclic tests on the ballasted track is small since the soil has already suffered shakedown during the previous tests on the ballastless track. These conclusions are supported by the CBR values obtained using the Dynamic Cone Penetrometer at various times during testing and presented in the work developed by (Čebašek et al., 2018).

The displacement results, depicted in Figure 6.9, show the reduction in amplitude of displacements during cyclic testing, which means that the structure increased its stiffness throughout the cyclic tests. In data processing, all displacements are reset in order to be comparable in terms of amplitude. For the ballastless track and frequency equal to 2.5Hz, the results regarding the final cycles almost overlapped with the initial cycles. This can be explained by the use of the mean of all S-LVDTs (to have a consistent and comparable analysis).
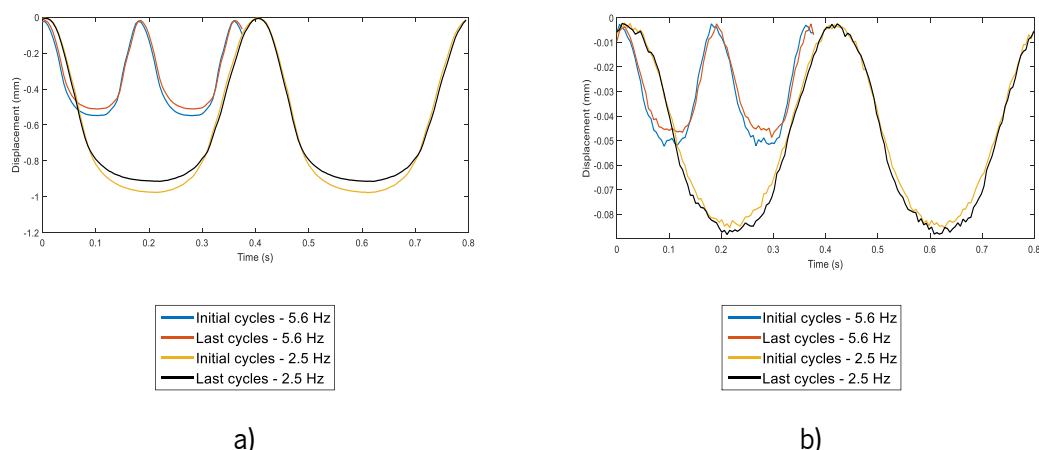
Figure 6.9 - Displacement results from the initial and final cyclic tests (mean of the results obtained for *S-LVDTs*): a) ballasted track; b) ballastless track

6.4 Calibration of ballastless track and ballasted track models

The calibration of the ballasted track and ballastless track models is based on experimental cyclic loading tests. The experimental ballasted and ballastless tracks are depicted in Figure 6.10.
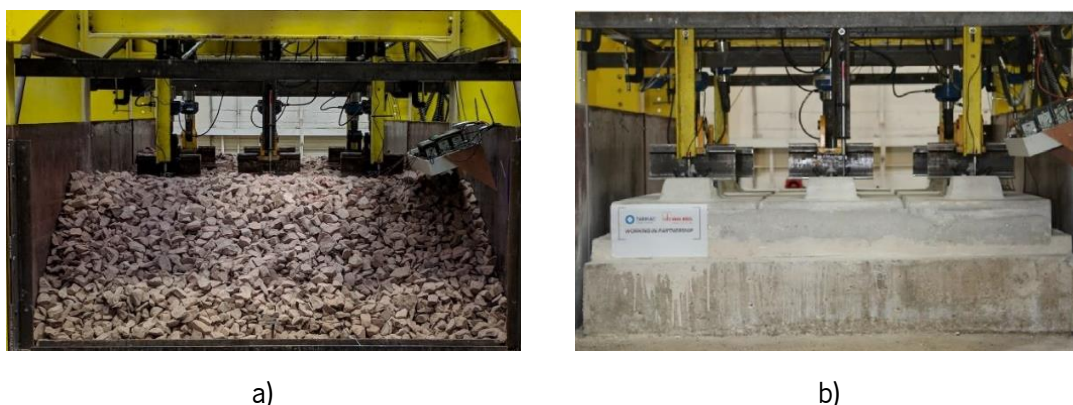
Figure 6.10 - Railway tracks: a) ballasted track; b) ballastless track

6.4.1 Short-term calibration

The 3D finite element models are developed using *ANSYS* 16.2, as depicted in Figure 6.11. The numerical model is used to simulate the short-term behaviour of the ballastless and ballasted track tests explained above. The models, depicted in Figure 6.11, are composed of solid elements with eight nodes, which represent a compromise between the accuracy and efficiency of the numerical model. It is important to mention that the geogrid was not included in the numerical model, since its influence on the numerical results at the displacement level would not be significant.

The load applied by the actuators on the sleepers is presented in Figure 6.12 and Figure 6.13 considering both railway structures and both frequencies: 5.6 Hz and 2.5 Hz.

a)

b)
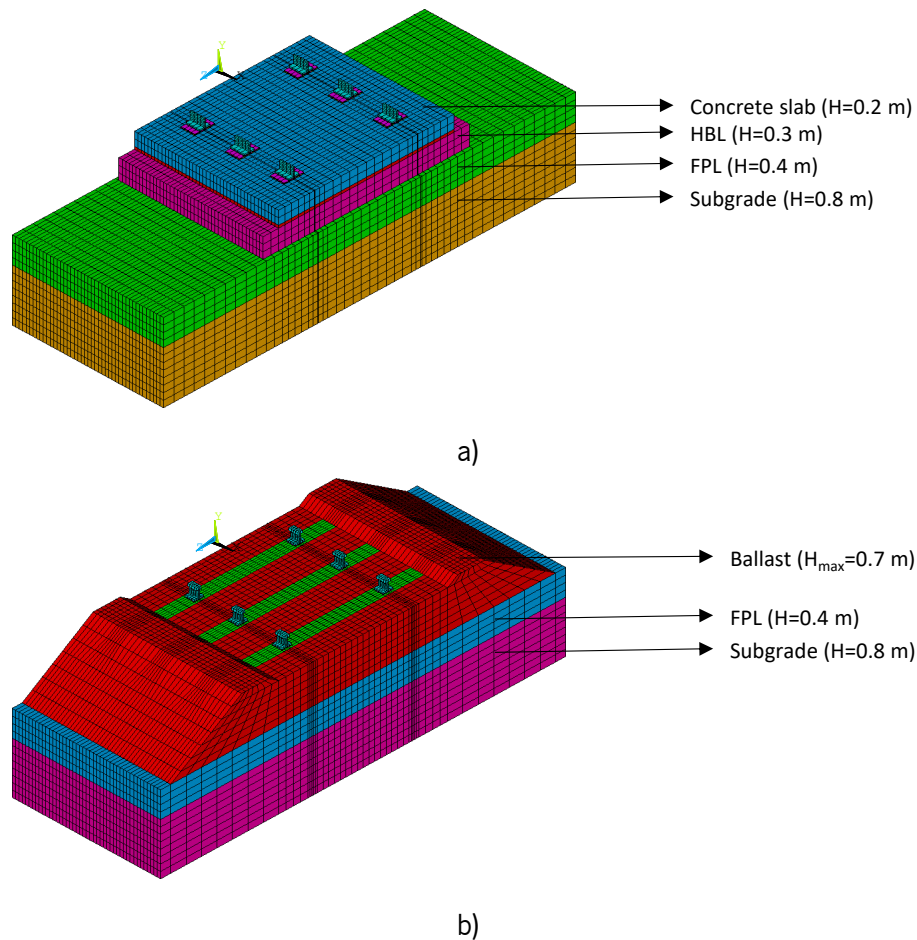
Figure 6.11 - 3D models: a) ballastless track model; b) ballasted track model

From the results of the experimental displacements and its comparison with the numerical displacements, the geotechnical properties of the track foundation materials (subgrade and FPL) in terms of *Young modulus* and *Poisson's* ratio are calibrated. Moreover, the ballast's properties (*Young modulus* and *Poisson's* ratio in the case of the ballasted track), as well as the equivalent properties of the railpads are also calibrated. The experimental displacements are depicted in Figure 6.14 and Figure 6.15. In Figure 6.15, for the case of the ballasted track, the experimental LVDTs results show two different amplitudes. The LVDT frame is not connected to the testing rig and the measuring rod is placed on the sleeper's surface. The reference of the LVDTs is the structure itself. Thus, the tests are performed in force control, meaning the sleeper never loses contact with ballast. The amplitude difference in Figure 6.15 b) and c) is justified by the variation of stiffness along the track.
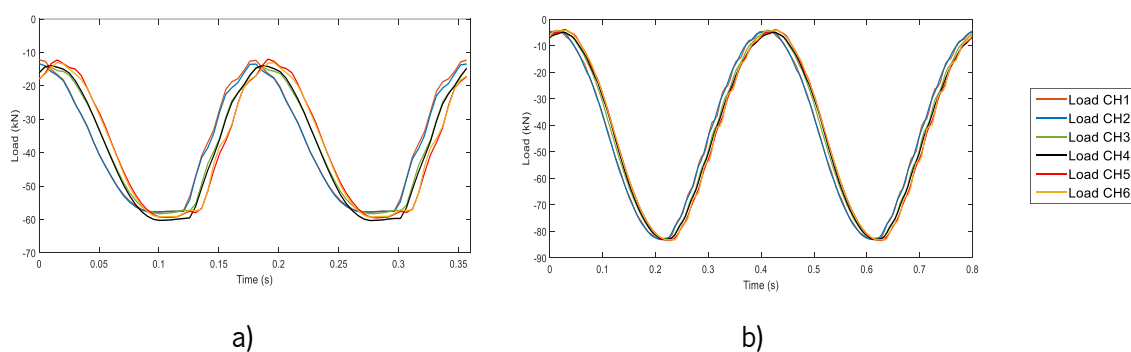
Figure 6.12 - Applied load – ballastless track: a) frequency of 5.6Hz; b) frequency of 2.5Hz
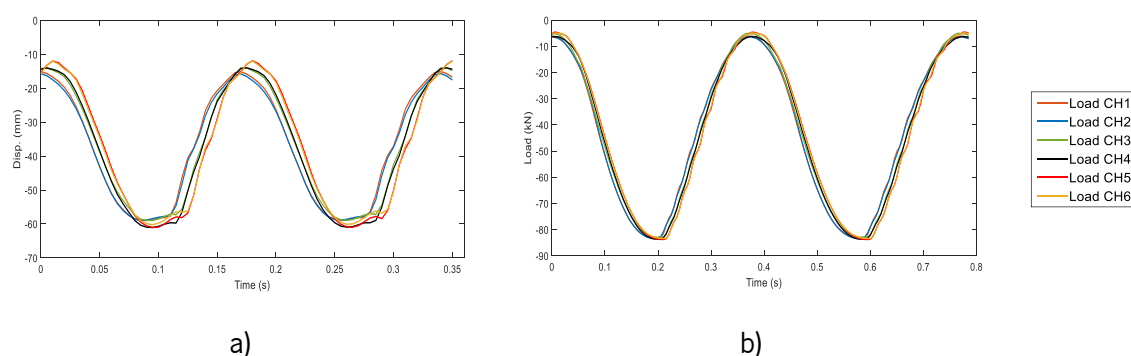
Figure 6.13 - Applied load – ballasted track: a) frequency of 5.6Hz; b) frequency of 2.5Hz

The first step consists of the application of the experimental loads in the numerical model. The load time histories are depicted in Figure 6.12 and Figure 6.13. The comparison between the experimental and numerical results is an iterative process. Firstly, the properties of EPDM are estimated: equivalent *Poisson's* ratio of zero (considering that there is no transverse deformation) and the *Young* modulus is based on dynamic stiffness and geometric properties. In this process, the same EPDM is used in the tests on the ballastless and ballasted tracks. Regarding the ballastless track, the properties of the FPL and subgrade are calibrated. The mass density of the FPL and subgrade are based on the work developed in Čebašek et al. (2018). The *Young's* modulus of the subgrade and FPL is based on the E_{v2} value obtained in the laboratory. In this case, a factor of 3.3 is applied ($E=3.3 \times E_{v2}$). During the calibration process, this parameter is adjusted, as well as the respective *Poisson's* ratio. In fact, the values of *Young* modulus (obtained with this factor) are within the acceptable range of these materials (modulus of deformation limits and compaction requirements for the earthwork layers): 120 MPa to 500 MPa for the FPL and 60 MPa to 500 MPa for the subgrade.

Regarding the ballasted track, the specific weight of the ballast is based on UIC (2008) and the *Young* modulus of the ballast layer is also calibrated in this process. In this case, the value obtained is lower than expected. Therefore, comparing this result with published data, it is possible to conclude that the *Young* modulus is slightly lower than anticipated. The bibliography shows that the value varies between

100 MPa to 150 MPa (Zhai et al., 2004, UIC, 2008). After the calibration, a *Young* modulus equal to 110 MPa was adopted.

The adopted properties of the materials are described in Table 6.4 and Table 6.5 (ballastless track properties and ballasted track properties, respectively).

Figure 6.14 - Ballastless track displacements: a) R-LVDTs considering a frequency of 5.6Hz; b) S-LVDTs considering a frequency of 5.6Hz; c) R-LVDTs considering a frequency of 2.5Hz; d) S-LVDTs considering a frequency of 2.5Hz.

f=5.6 Hz

a)

b)

f=2.5 Hz

c)

d)

Figure 6.15 - Ballasted track displacements: a) R-LVDTs considering a frequency of 5.6Hz; b) S-LVDTs considering a frequency of 5.6Hz; c) R-LVDTs considering a frequency of 2.5Hz; d) S-LVDTs considering a frequency of 2.5Hz.

The experimental results show higher variation when compared to the numerical results (Figure 6.16 and Figure 6.17). This is probably due to a rearrangement of the particles during the cyclic tests, largely in the ballast layer (in the case of the ballasted track) but also in the subgrade and FPL layers. Due to the variability of the experimental results, minimum and maximum values (lower and upper bounds, respectively) are defined. The area defined by these limits is represented by a grey shadow in Figure 6.16 and Figure 6.17. Each curve is a representation of a numerical result for a single R or S-LVDT, considering its exact position in the full-track model. The results show good agreement between the experimental and numerical results. When the frequency is equal to 5.6 Hz, the numerical results are close to the maximum limit (upper bound) of the experimental results. This can be explained by a phenomenon that occurred in the experimental tests related to the movement of the particles since in these numerical results it is not possible to capture this type of behaviour.

f=5.6 Hz

a)

b)

f=2.5 Hz

c)

d)
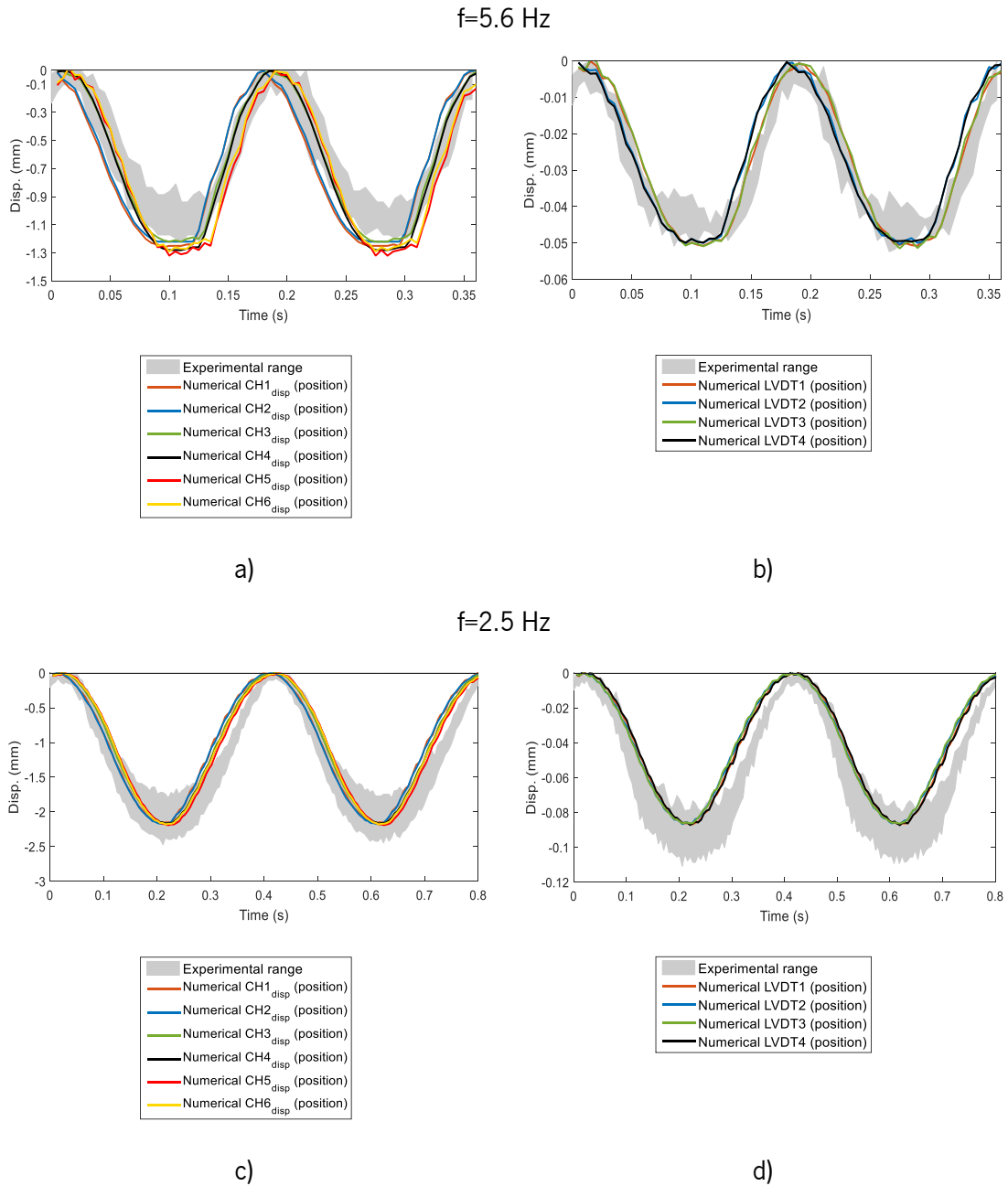
Figure 6.16 - Ballastless track numerical and experimental results: a) R-LVDTs (frequency of 5.6 Hz); b) S-LVDTs (frequency of 5.6 Hz); c) R-LVDTs (frequency of 2.5 Hz); d) S-LVDTs (frequency of 2.5 Hz)

f=5.6 Hz

a)

b)

f=2.5 Hz

c)

d)
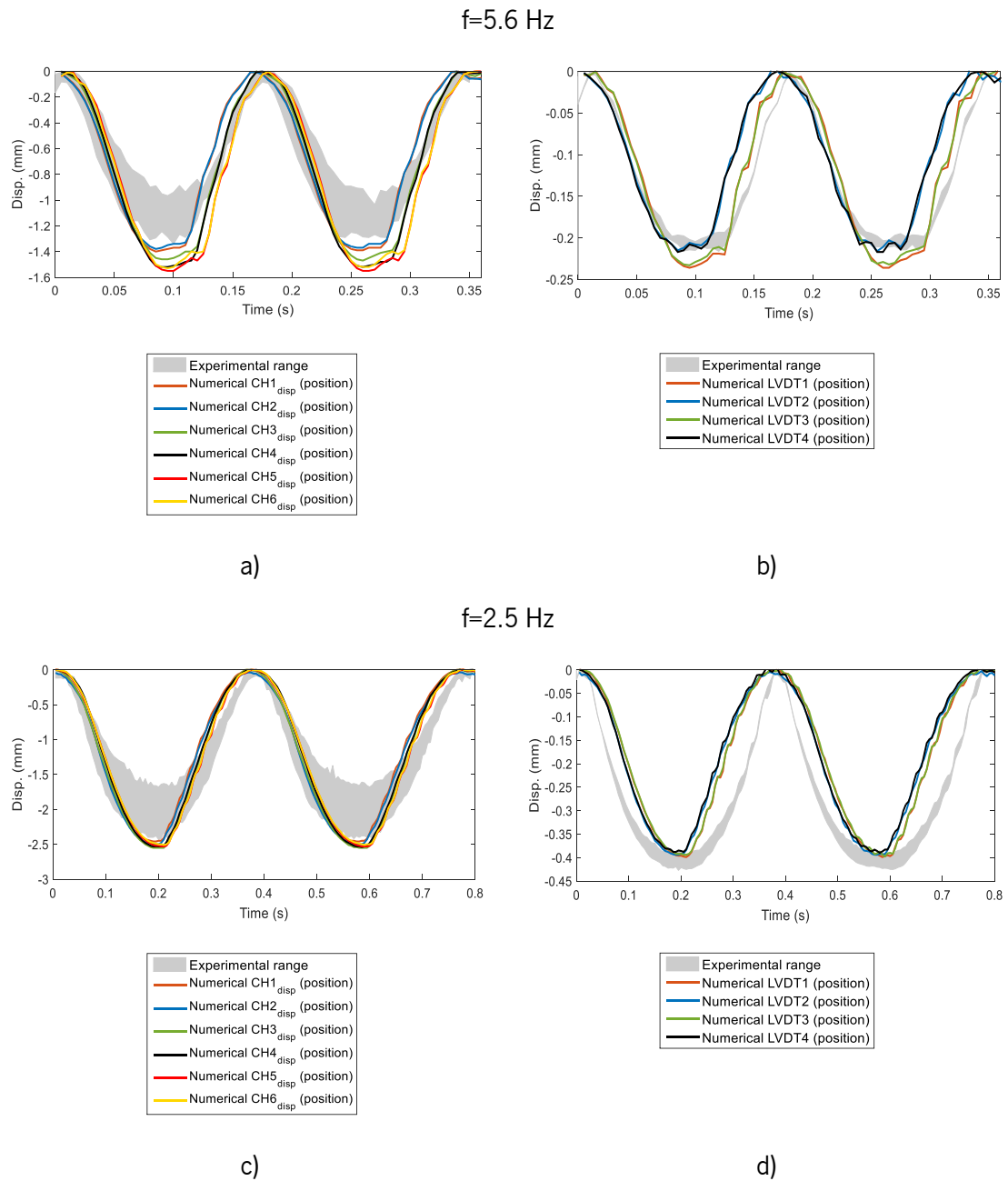
Figure 6.17 - Ballasted track numerical and experimental results: a) *R*-LVDTs (frequency of 5.6 Hz); b) *S*-LVDTs (frequency of 5.6 Hz); c) *R*-LVDTs (frequency of 2.5 Hz); d) *S*-LVDTs (frequency of 2.5 Hz)

Table 6.4 - Adopted properties of the materials – ballastless track

Material	Properties	References
Rail (BS113A)	$E=200\times10^9$ Pa $\rho=7850$ kg/m³ $\nu=0.30$	UIC 60
Railpad	$k=1800\times10^6$ N/m $\rho=1000$ kg/m³ $\nu=0.30$ $E=k\times$thickness/area	Čebašek et al. (2018)
Steel plate	$E=210\times10^9$ Pa $\rho=7850$ kg/m³ $\nu=0.30$	Characteristics of a steel plate –assumed values
EPDM	$k=40\times10^6$ N/m $\rho=1200$ kg/m³ $\nu=0.00$ $E=k\times$thickness/area	Čebašek et al. (2018)
Cement grout mass	$E=25\times10^9$ Pa $\rho=2000$ kg/m³ $\nu=0.25$	-
Concrete slab	$E=40\times10^9$ Pa $\rho=2500$ kg/m³ $\nu=0.25$	-
HBL	$E=15\times10^9$ Pa $\rho=2400$ kg/m³ $\nu=0.25$	Information given by Max-Bőgl
FPL	$E=3.3\times EV_2=3.3\times135\times10^6$ Pa $\rho=2141$ kg/m³ $\nu=0.35$	*E* is based on Ev2 (Čebašek et al., 2018)
Subgrade	$E=3.3\times EV_2=3.3\times65\times10^6$ Pa $\rho=2091$ kg/m³ $\nu=0.35$	*E* is based on Ev2 (Čebašek et al., 2018)

Table 6.5 - Adopted properties of the materials – ballasted track

Material	Properties	References
Rail (BS113A)	E=200×10⁹ Pa ρ=7850 kg/m³ ν=0.30	BS113A (56E1)
EPDM	k=40×10⁶ N/m ρ=1200 kg/m³ ν=0.00 E=k×thickness/area	Čebašek et al. (2018)
Sleepers (G44 - 650mm spacing)	E=38×10⁹Pa ρ=2500 kg/m³ ν=0.15	Sleeper G44
Ballast	E=110×10⁶Pa ρ=1530 kg/m³ ν=0.30	UIC719Rb (2208)
FPL	E=3.3×EV₂=3.3×135×10⁶Pa ρ=2141 kg/m³ ν=0.35	*E* is based on Ev2 (Čebašek et al., 2018)
Subgrade	E=3.3×EV₂=3.3×65×10⁶Pa ρ=2091 kg/m³ ν=0.35	*E* is based on Ev2 (Čebašek et al., 2018)

6.4.2   Long-term calibration

From the short-term calibration, an empirical permanent deformation model (the same used in Chapter 5) is calibrated from the properties described in Table 6.4 and Table 6.5. To do so, a novel approach is used that allows for simulating the long-term behaviour of ballasted and ballastless structures through the calibration of an empirical permanent deformation model.

Again, the yielding criterion is defined based on the *Mohr-Coulomb* yielding criterion that depends on the parameters M (or m) and q_o (or s) which are based on the cohesion (c) and friction angle (ϕ) of each material. The adopted properties of the materials are:

- Ballast: c' = 0 kPa and ϕ'=50°;
- FPL: c' = 0 kPa and ϕ'=48°;
- Subgrade: c' = 5 kPa and ϕ'=35°.

The failure line is obtained from the expression 5.24 from Chapter 5.

These parameters (strength properties and stresses) are defined in terms of effective stresses. In this case, since the pore pressure is zero or null, the effective stresses are equal to the total stresses.

As mentioned previously, the geomaterials usually show elastoplastic behaviour when subject to cyclic loads. In this study, an empirical permanent deformation approach is used instead of an elastoplastic model since, usually, empirical permanent deformation models show good agreement with the observed track behaviour, are less time-consuming and are straightforward to implement. This means that there is a good balance between accuracy and the difficulty to implement. Again, the model used to describe the permanent deformation is based on the work developed by Gidel et al. (2001) and updated by Chen et al. (2014), as described previously in Chapter 4. This model was already implemented in Chapter 5.

Calibration is performed to find the best fit between the experimental and numerical data through the definition of the parameters ε_{p0}, α and B (corresponding to the properties of the materials), applying the permanent deformation model described in expression 4.15 from Chapter 4.

It is important to note that empirical permanent deformation models are developed, in most cases, in situations where there is a stabilisation of the permanent deformation, which can be a disadvantage of these empirical permanent deformation models. In the current analysis, at some locations in the ballast, FPL and subgrade layers, the model is applied to stress paths close to rupture, which means that the permanent deformation could be even higher (this behaviour is called incremental collapse in shakedown theory), as mentioned previously.

After the calibration of the short-term displacements through the material properties, stresses are obtained, including the initial stresses and amplitude of the stress paths for both frequencies. The initial stresses are obtained separately and subsequently added since the domain is considered linear elastic.

The results obtained in terms of p'-q stresses are depicted in Figure 6.19 and Figure 6.20. These results are the main inputs of the permanent deformation model.

Analysing Figure 6.19 and Figure 6.20, each stress path represented in both figures corresponds to one element of each material (ballast, FPL and subgrade). In this case, the ballast and FPL layers are formed from four vertical elements with a length equal to 0.1 m (L_{elem}=0.1 m). The subgrade is constituted of eight elements with a length of 0.1m (L_{elem}=0.1 m). The selected elements (numbered from 1 to 4 from the top to the bottom of the layer in the case of the ballast and FPL and from 1 to 8 from the top to the bottom of the subgrade layer) are located under/in the same alignment of the real position of the LVDTs of both railway tracks. The identification of elements is depicted in Figure 6.18.

Regarding the values obtained, as expected, the frequency of 2.5 Hz generates higher stress levels (justified by the higher load applied by the actuator). Of all the materials, the ballast layer shows the highest stress levels. The FPL of the ballasted track also presents higher stresses when compared to the FPL of the ballastless track. The same conclusion is applied to the subgrade. This is due to the stiffness of each structure since the concrete slab has higher vertical and bending stiffness than the ballast.

a)   b)
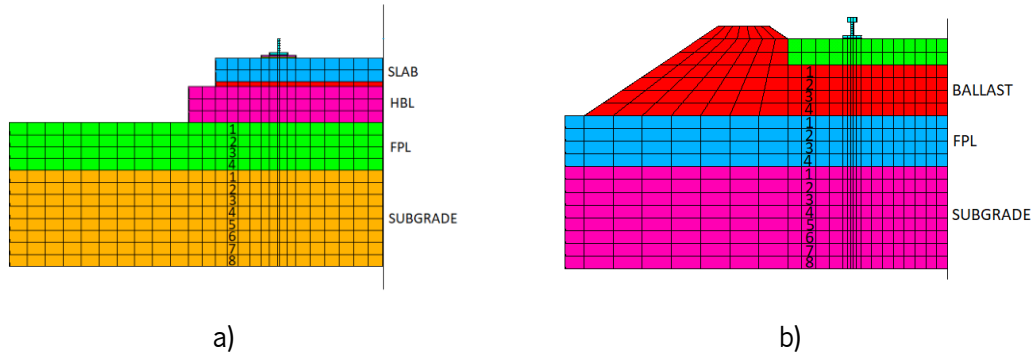
Figure 6.18 - Identification of elements: a) ballastless track; b) ballasted track

f=5.6 Hz

FPL   Subgrade

a)   b)

f=2.5 Hz

FPL   Subgrade

a)   b)
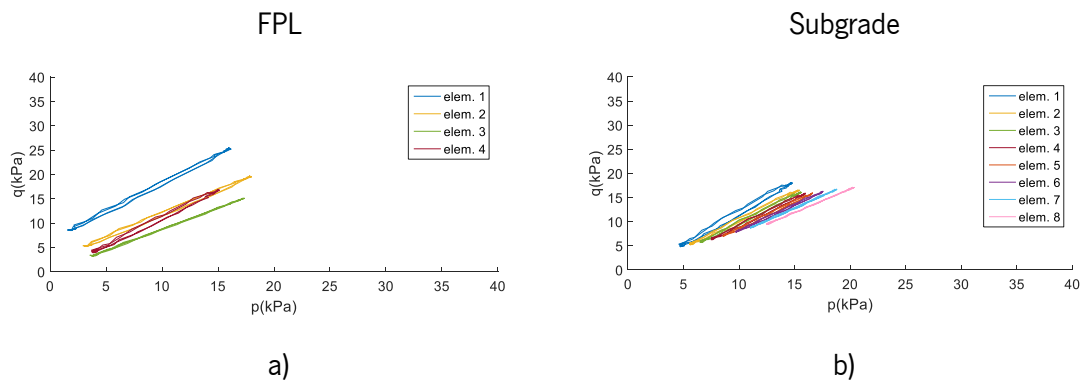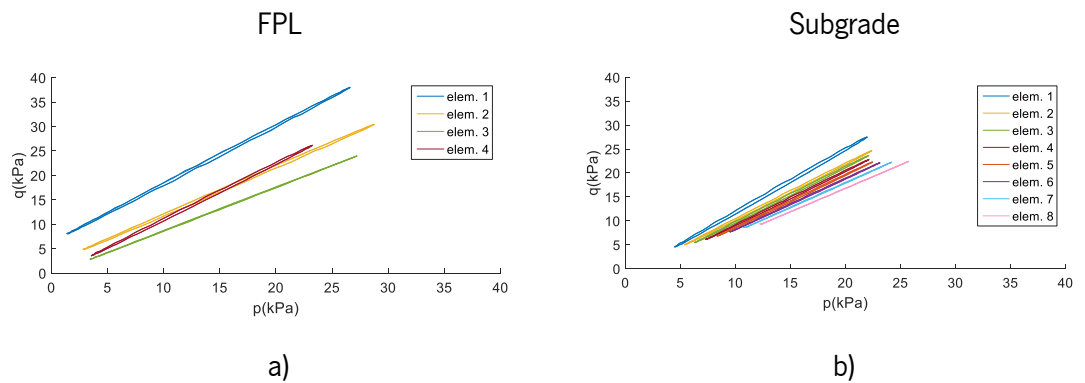
Figure 6.19 - Stress path of the materials of the ballastless track: a) FPL (f = 5.6 Hz); b) subgrade (f = 5.6 Hz); c) FPL (f = 2.5 Hz); d) subgrade (f = 2.5 Hz)

239
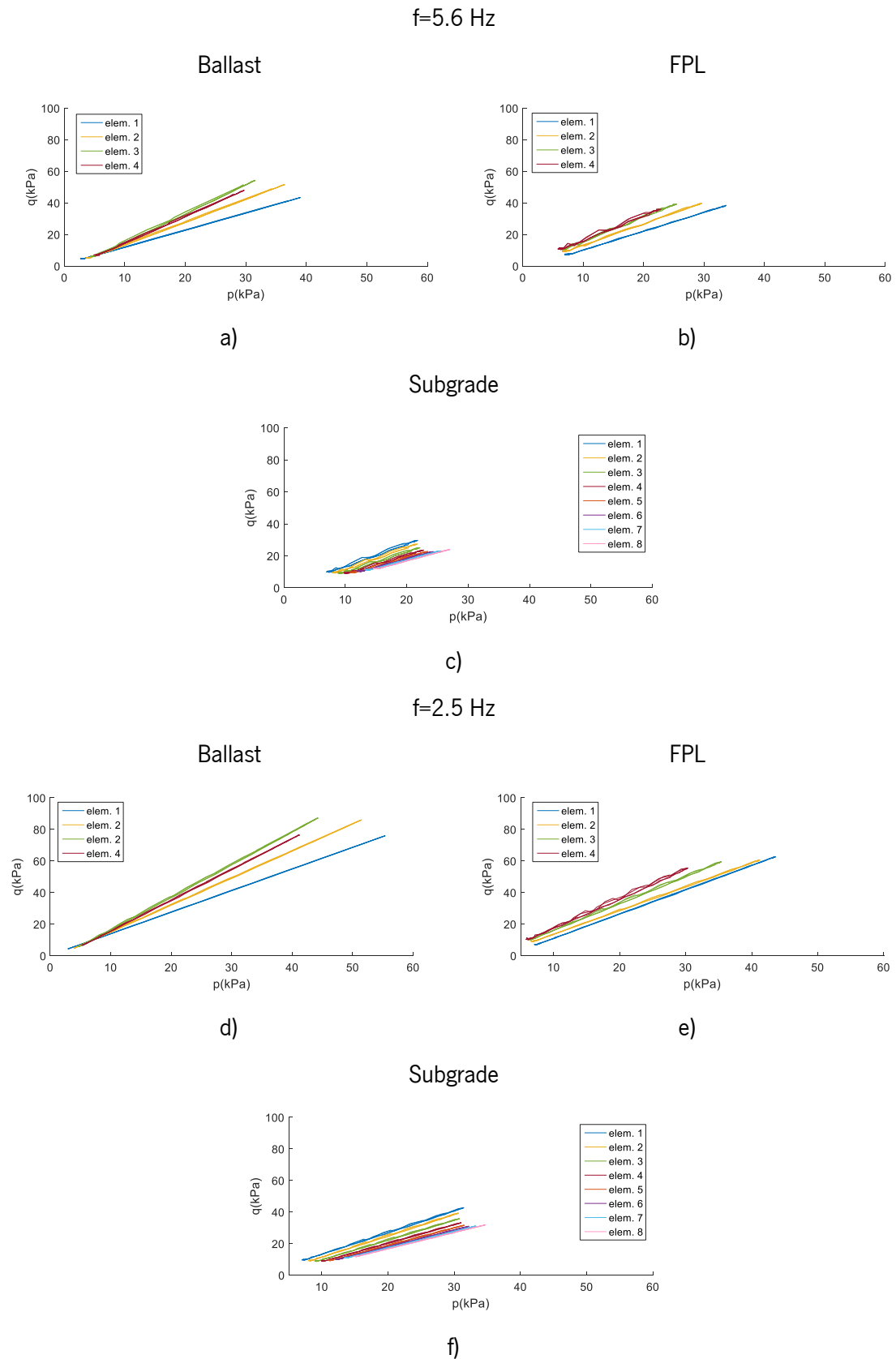
Figure 6.20 - Stress path of the materials of the ballasted track: a) ballast (f = 5.6 Hz); b) FPL (f = 5.6 Hz); c) subgrade (f = 5.6 Hz); d) ballast (f = 2.5 Hz); e) FPL (f = 2.5 Hz); f) subgrade (f = 2.5 Hz)

In the calibration, the time hardening concept is applied. Most empirical models are developed to fit experimental data during a Single Stage (SS) approach to RLT testing. However, in the Multi-Stage (MS) approach, the models can be adapted using the time hardening approach. With this approach, the accumulated permanent deformation from the previous loading stress path is used to calculate the number of load cycles required to achieve the same amount of accumulated permanent deformation in the current stress path (*i*-path). This value is called the equivalent load cycle – $N_{i,eq}$ – and it is used to modify the total number of load cycles N from the beginning of the test to calculate the effective number of load cycles (N -N_{i-1} - $N_{i,eq}$), where N_{i-1} is the total number of load cycles at the end of the previous *(i-1)*ₜₕ stress path. The schematic overview of the time hardening concept is depicted in Figure 6.21. Implementing the time hardening concept into the permanent deformation model, it is possible to obtain an expression based on the model:

$$\varepsilon_p(N) = f_1(N - N_{i-1} + N_i^{eq})f_2(p, q) \qquad (6.2)$$
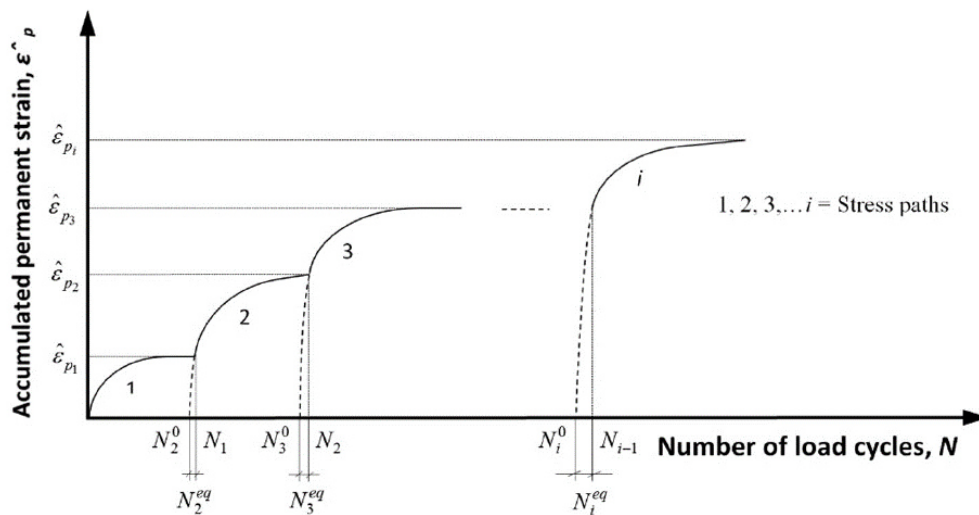
Figure 6.21 - Schematic overview of the time hardening concept (Salour and Erlingsson, 2015a)

In this case, the time-hardening concept is used to simulate the influence of the stresses and permanent deformations induced in the geomaterials during the tests with a frequency of 5.6 Hz in the tests with a frequency of 2.5 Hz, which are performed afterwards (the substructure was the same in both dynamic/cyclic tests).

The calibration process is based on the *least-square fitting* method (available in *Matlab* in the optimisation tool-box) and two approaches are applied: Trust-region-reflective and Levenberg-Marquardt (Mathworks, 2020). The least-squares method is a well-known approach used in regression analysis to approximate the solution of overdetermined systems by minimizing the sum of squares of the residuals made in the

results of every single equation. Indeed, this technique is usually applied in data fitting. The best fit minimizes the sum of squared residuals. The residuals are defined as the difference between the observed and expected values. The *lsqcurvefit* allows solving nonlinear curve-fitting (data-fitting) problems in a least-square sense. The algorithm uses a nonlinear least-squares solver to find the coefficients *x* that solve the problem:

$$min_x = ||F(x, xdata) - ydata||_2^2$$
$$= min_x \sum_i (F(x, xdata_i) - ydata_i)^2 \tag{6.3}$$

where the input data is *xdata* (defined as vector or matrix), the observed/target data is *ydata* (defined as vector or matrix) and *F(x,xdata)* is a matrix-valued or vector-valued function of the same size as *ydata*. The components of *x* can have lower and upper bounds (*lb* and *ub*, respectively). The arguments *x*, *lb* and *ub* can be vectors or matrices. Commonly, the algorithm *lsqcurvefit* starts at *x0* (initial values) and finds coefficients *x* to best fit the nonlinear function to the data *ydata* (in the least-squares sense). In the case where the *lb* and *ub* values are defined, the solution is always in the range *lb* ≤ *x* ≤ *ub*.

The trust-region reflective algorithm is used to solve a constraint optimisation problem. In this case, the non-linear system of equations could not be undetermined, meaning the number of equations is at least as many as the length of *x*. In contrast, the Levenberg-Marquardt algorithm does not deal with bound constraints, which means that it can be used for problems with no bounds, and it is undetermined (fewer equations than dimensions). Based on these properties, the Levenberg-Marquardt approach is mostly used in the first calibration tests to find the approximate parameters. The Trust-region-reflective is used to optimize the values of the parameters.

The calibration process of the ballastless track implies the determination of six unknown parameters (three parameters for each material), while the ballasted track implies the determination of nine unknown parameters. The obtained results (calibrated values of the material parameters ε_{p0}, α and B) are described in Table 6.6. The initial values of the parameters for the ballasted and ballastless tracks were, initially, arbitrarily chosen.

From Table 6.6, it is shown that the parameters of the FPL and subgrade are similar when compared to the ballast. In fact, the permanent deformation of the elements of the ballast is much higher than the elements of FPL and subgrade due to the higher stress levels induced in the material, as depicted in Figure 6.20.

For the ballasted track, a sensitivity analysis is performed for the frequency f = 5.6 Hz. The calibrated parameters and the sensitivity analysis are based on a set of initial values (designated as *x0*), described in Table 6.7.

Table 6.6 - Calibration of the parameters of the materials of the ballastless and ballasted tracks

Type of track	Parameter	f=5.6 Hz	f=2.5 Hz
Ballastless track	**FPL**		
	ε_{p0}	-4.100e-05	0.0155
	B	-0.354	0.0139
	α	0.859	1.15
	Subgrade		
	ε_{p0}	-4.100e-05	0.055
	B	-0.354	0.25
	α	0.648	2.720
Ballasted track	**Ballast**		
	ε_{p0}	0.014	0.008
	B	1.512	0.105
	α	0.995	1.620
	FPL		
	ε_{p0}	0.182	0.007
	B	0.005	0.010
	α	0.969	0.986
	Subgrade		
	ε_{p0}	0.119	0.006
	B	0.004	0.010
	α	0.943	0.954

Table 6.7 - Initial values of the parameters for the ballasted track

Ballast			FPL			Subgrade		
ε_{p0}	B	α	ε_{p0}	B	α	ε_{p0}	B	α
0.019	0.347	0.995	0.014	0.01	0.986	0.016	0.01	0.954

The sensitivity analysis is performed for the FPL and subgrade because their parameters have similar values. This meant that the initial values (*x0*) of the parameters are modified to determine if the results approached the same value. Therefore, the initial values of the parameters ε_{p0}, B and α are modified according to Δ. The adopted value of Δ for each parameter is defined according to the following list:

- ε_{p0}= ±0.01;

- **B** = ±0.01;
- α = ±0.1.

The change in the value of one of the parameters ε_{p0}, B and α has an impact on all parameters of the ballast, FPL and subgrade. The analysis is performed by modifying each parameter individually, as depicted in Table 6.8. The results are depicted in Figure 6.22.

Table 6.8 - Sensitivity analysis - Identification of the cases

	FPL			Subgrade		
Case	ε_{p0}	**B**	α	ε_{p0}	**B**	α
1	Initial-0.01	-	-	–	-	–
2	Initial+0.01					
3	-	Initial-0.01	-	-	-	-
4		Initial+0.01				
5	-	-	-	Initial-0.01	-	-
6				Initial+0.01		
7	-	-	-		Initial-0.01	-
8					Initial+0.01	
9	-	-	Initial-0.1	-	-	-
10			Initial+0.1			
11	-	-	-	-	-	Initial-0.1
12						Initial+0.1
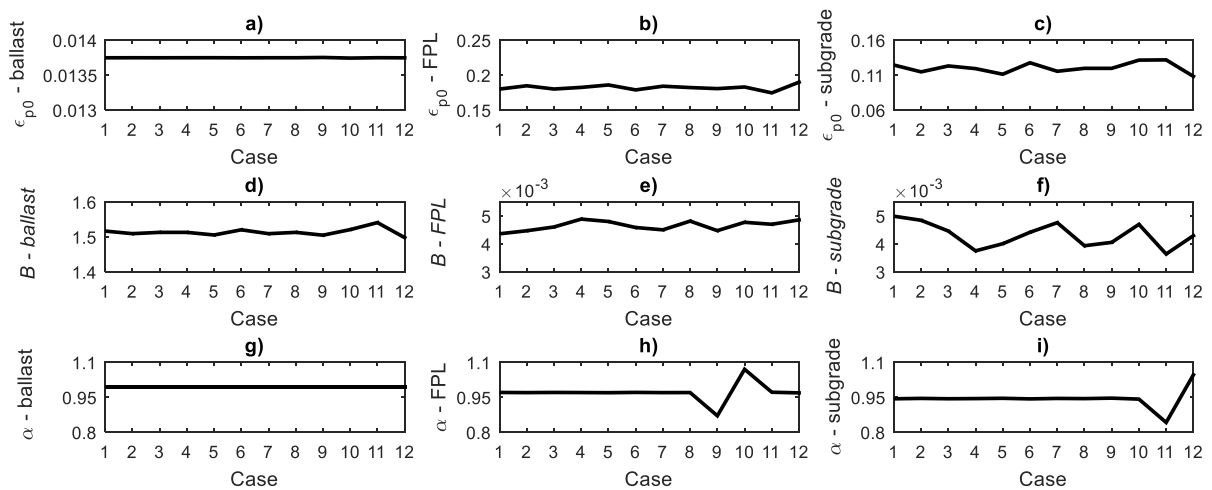
Figure 6.22 - Variation of the parameters according to the Δ defined: a) ε_{p0} of the ballast; b) ε_{p0} of the FPL; c)ε_{p0} of the subgrade; d) B of the ballast; e) B of the FPL; f) B of the subgrade; g) α of the ballast; h) α of the FPL; i) α of the subgrade

Analysing Figure 6.22, it is possible to conclude that the variation of the parameters is not significant. For the parameter α, cases [9-12] have an impact, as expected, because there is a variation of 0.1.

The mean and standard deviation of each parameter is determined, as depicted in Table 6.9. The results show that the standard deviation of each parameter is low and, in some cases, close to zero. However, this analysis is dependent on the scale selected.

Table 6.9 - Mean and standard deviation

Materials	Ballast			FPL			Subgrade		
Parameters	ε_{p0}	B	α	ε_{p0}	B	α	ε_{p0}	B	α
Mean	0.014	1.513	0.995	0.182	0.005	0.9695	0.1202	0.004	0.943
Standard deviation	≈ 0	0.010	≈ 0	0.004	≈ 0	0.041	0.007	≈ 0	0.042

From the results, a normalisation of the data is performed to allow comparison. This meant the values are modified to obtain a common scale, without distorting differences in the ranges of values, since the variables/parameters are measured using different scales. The normalisation is selected instead of the standardisation approach since not all the variables follow a normal distribution considering the Kolmogorov-Smirnov test (the null-hypothesis is rejected since $p_{value}<0.05$) and normal Q-Q plots, which means that standardisation is not a recommended approach) (Douglas Montgomery and Runger, 2003). The normalised data are presented in Figure 6.23.
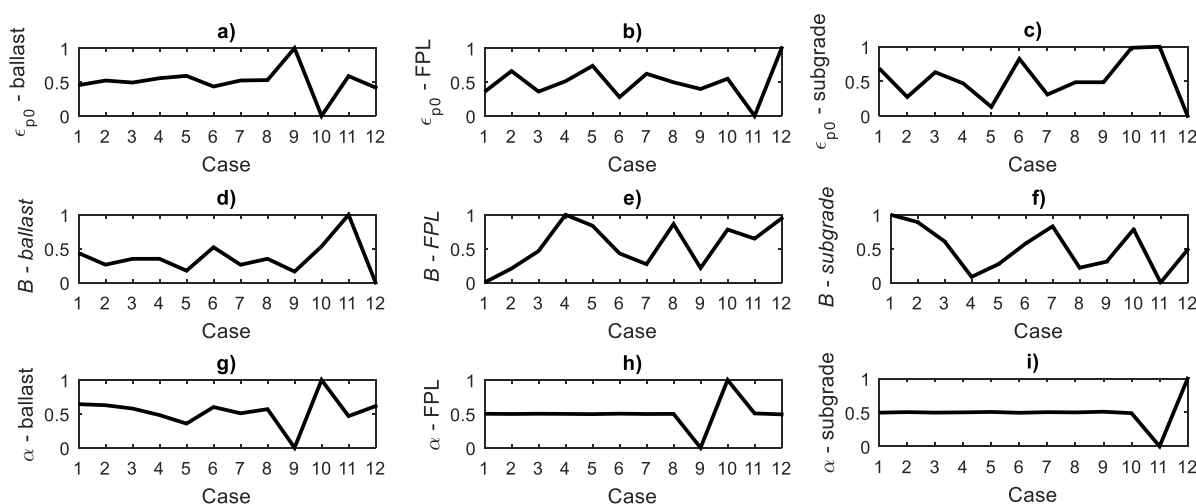
Figure 6.23 - Variation of the parameters according to the Δ defined – normalised data: a) ε_{p0} of the ballast; b) ε_{p0} of the FPL; c) ε_{p0} of the subgrade; d) B of the ballast; e) B of the FPL; f) B of the subgrade; g) α of the ballast; h) α of the FPL; i) α of the subgrade

Analysing Figure 6.23, higher variations occur, usually, in cases [9-12], where there is a variation of parameter α. This was expected since the Δ value associated with this parameter is higher (± 0.1).

245

Furthermore, the variation in the ballast's parameters ε_{p0} and B is smaller compared to the variation of these parameters in the FPL and subgrade. The parameters have a mean close to 0.5 and a standard deviation close to 0.20, as described in Table 6.10.

Table 6.10 - Mean and standard deviation – normalised data

Materials	Ballast			FPL			Subgrade		
Parameters	ε_{p0}	B	α	ε_{p0}	B	α	ε_{p0}	B	α
Mean	0.509	0.367	0.5377	0.497	0.555	0.500	0.524	0.505	0.501
Standard deviation	0.211	0.2407	0.2197	0.242	0.321	0.204	0.305	0.316	0.204

According to these results, it is possible to assume that for cases [1-8], the values of the parameters approach a similar value.

From the p'-q stresses (p_{am}, q_{am}, p_{ini} and q_{ini}), taking into account the strength parameters adopted and the calibrated material parameters, the results obtained for the calibration of the permanent deformation model are depicted in Figure 6.24, for the ballastless track and ballasted track.

The results demonstrate a high level of agreement between the experimental and numerical results for both railway structures, applying the selected permanent deformation model. Furthermore, the cumulative permanent displacements of the ballastless track are significantly lower when compared to the ballasted track (approximately 15-20 times). Indeed, static tests also showed this tendency. Nevertheless, the absolute displacement/settlement of the concrete slab is also justified by the initial good conditions of FPL compaction and subgrade measured by the CBR. The ballasted track displacement/settlement under repeated loading cycles can be explained by the densification and re-arrangement of the ballast particles. Ballast deformation is characterised by different phases (Indraratna and Nimbalkar, 2016), which includes the immediate deformation under initial loading cycles, followed by an unstable zone with the reorientation and re-arrangement of the particles, and breakage (explained in more detail in Chapter 2). The final stage corresponds to a stable shakedown state where the rate of increase is insignificant. Moreover, the degradation and breakage, and abrasive wear of the ballast after a certain number of load cycles could lead to penetration of the finer particles (in a reduced number) into the substructure (in this case into the FPL), despite the presence of the geogrid.

Further, the repeated cyclic loads can also be responsible for the penetration of the sleepers into the ballast layer, due to the volume change of the ballast.
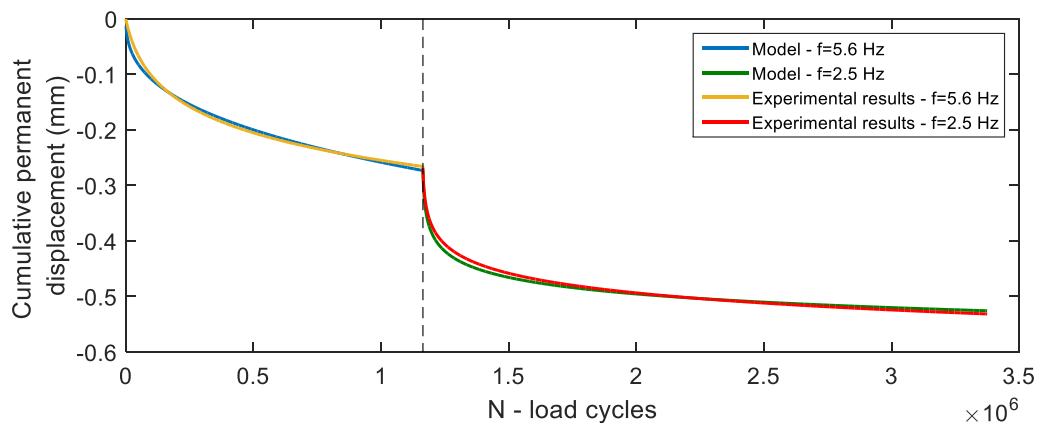
a)
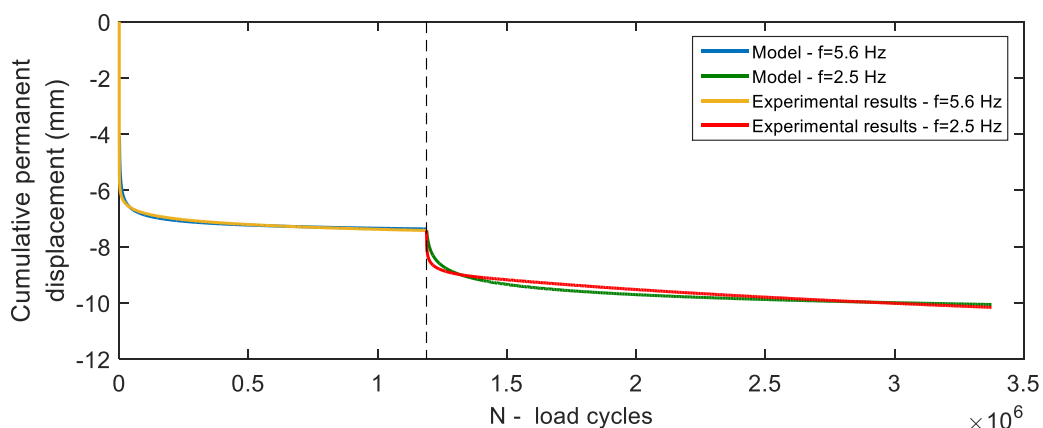
b)

Figure 6.24 - Calibration of permanent deformation model: a) ballastless track; b) ballasted track

Moreover, for the ballastless track, a sensitivity analysis is performed for the cohesion of the subgrade, to understand its influence on the permanent deformation and respective cumulative permanent displacement, since the value adopted is only based on the granulometric curve that showed a significant percentage of fines content. In this analysis, the cohesion varies between 0 kPa and 10 kPa. The results are presented in Figure 6.25.

247

a)

b)
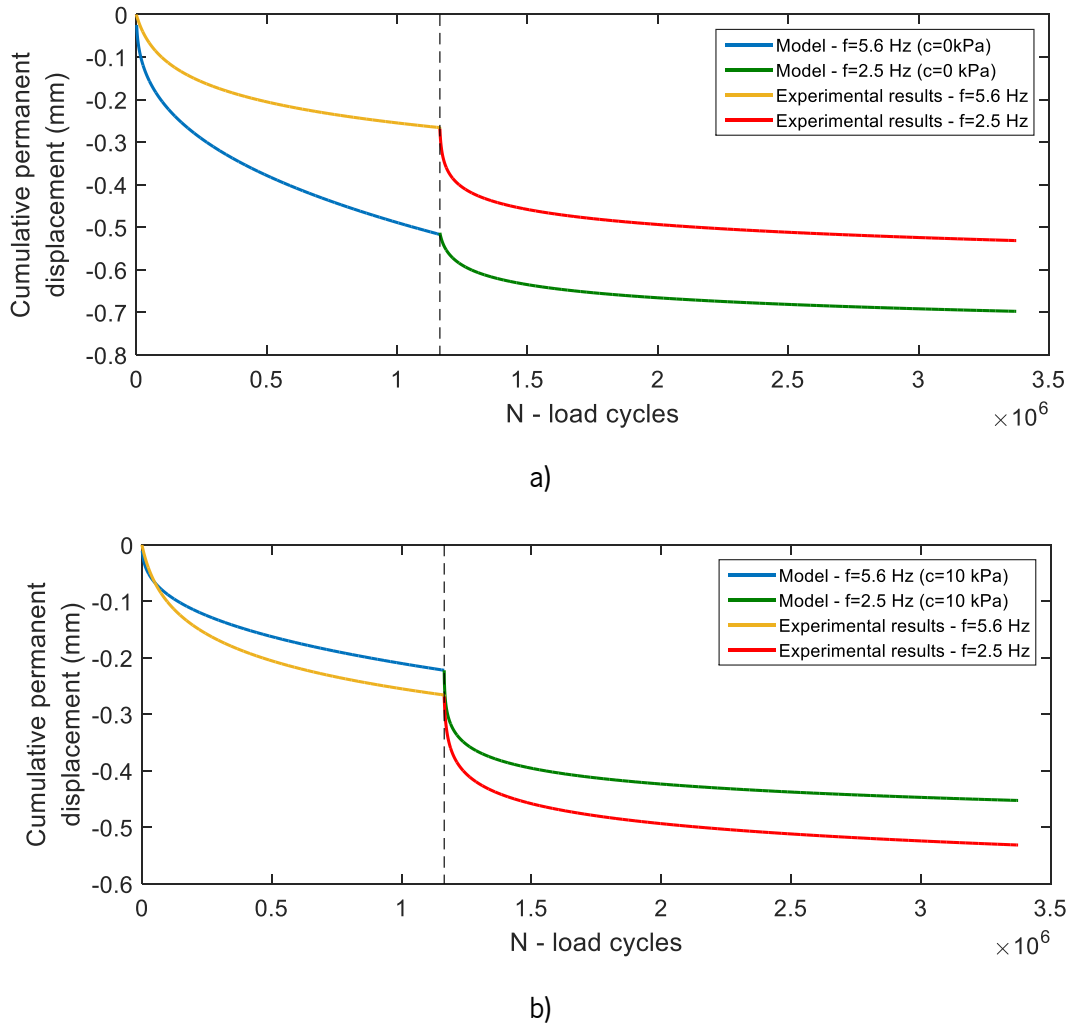
Figure 6.25 - Sensitivity analysis of permanent deformation model – ballastless track: a) c'=0kPa; b) c'=10kPa

Analysing Figure 6.25 a) (c'=0kPa), Figure 6.25 b) (c'=10 kPa) and also Figure 6.24 (c'=5 kPa), it is possible to verify that the cohesion has a significant influence on the permanent deformation (and respective cumulative permanent displacement), meaning that the characterisation of the subgrade material should be performed carefully, although it is difficult to characterize, especially in the field. If necessary, triaxial monotonic tests should be carried out to determine the exact values of cohesion and friction angle. When cohesion is lower, the stress paths are closer to the yielding criterion, resulting in higher permanent deformation. On the contrary, when cohesion is higher, the stress path is further from the yielding criterion and permanent deformation is lower. The cumulative permanent displacement differences between the experimental and numerical results (c' = 0 kPa and c' = 10 kPa) are depicted in Table 6.11.

Table 6.11 - Differences between the experimental results and the numerical results considering $c' = 0$ k Pa and $c' = 10$ kPa for the subgrade

N (number of load cycles)		N= 1.164×10⁶ cycles	N= 3.375×10⁶ cycles
|Cumulative permanent displacement| (mm)	Experimental results ($c'\approx5$ kPa)	0.2657	0.5314
	$c'=0$ kPa	0.5162	0.6977
	Increment rate (%)	94	31
	$c'=10$ kPa	0.2221	0.4525
	Increment rate (%)	-16	-15

Analysing Table 6.11, the largest difference between experimental and numerical results occurs when c' = 0 kPa. When the cohesion starts to increase, the difference between the experimental and numerical results starts to decrease.

These results are complementary to the results considering the variation of the friction angle presented in Chapter 5. In this case, it was proven that the friction angle has also influence on the permanent deformation. This means that the strength properties of the materials should be defined carefully in a long-term analysis.

6.4.3   Comparison of the parameter's values with values available in the bibliography

From the values obtained in the calibration (ε_{po}, B and α), a comparison attempt is performed in order to find a relationship between these values and the others described in the bibliography. However, it is important to highlight that the values of these parameters (ε_{po}, B and α) are hard to find since there is a significant panoply of empirical permanent deformation models, associated with different and several parameters, as presented in Chapter 4. Thus, some empirical permanent deformation models are selected, as well as the materials tested to develop the model (Table 4.12 from Chapter 4). The selection process and this study are based on the work developed in Chapter 4, section 4.5 - A comparison of permanent deformation models – parametric study.

As mentioned previously, the selected models are calibrated according to the empirical model used in this work and the stress path used to develop the model (Chen et al., 2014). However, this calibration is not easy, because the materials were tested at different conditions, which includes differences in terms of stress paths and its confining stress (as depicted in Figure 4.8) and differences in terms of physical state influenced by the moisture content. Furthermore, as evaluated in section 4.5, there are also materials tested in stress conditions close to the rupture. The classification of the materials and the

respective models selected are summarised in Table 6.12. This table is very similar to Table 4.16 from Chapter 4.

Thus, the most important parameters that characterize the materials and have impact on the permanent deformation are the cohesion and friction angle. In order to compare the calibrated parameters of the ballast, FPL and subgrade (ε_{p0}, α and B), it is important to select materials with similar cohesion and friction angle. Therefore, considering the materials presented in Table 6.12, a strategy is defined to find a relationship between the cohesion and friction angle and the parameters calibrated for the selected materials (Figure 6.26).

Table 6.12 - Properties of the materials and parameters calibrated (soils)

Author	Material (ASTM classification)	ε_{p0}	α	B	c' (kPa)	ϕ' (°)
Chen et al. (2014)	Sand (SP)	0.0018	0.3340	0.3390	0.00	33.0
	Silt (ML-CL)	0.0029	0.2680	0.3390	11.7	16.4
Rahman and Erlingsson (2015)	Sand (SM - 42% fines content)	0.0067	0.6500	0.2000	15.8	36.3
	Sand (SM – 27 %fines content)	0.0069	0.6500	0.2000	10.4	45.7
Huurman (1997)	Sand (SP)	0.0509	0.0100	0.0000	5.60	48.2
	Sand (SW)	0.0510	0.0100	0.0005	8.68	50.2
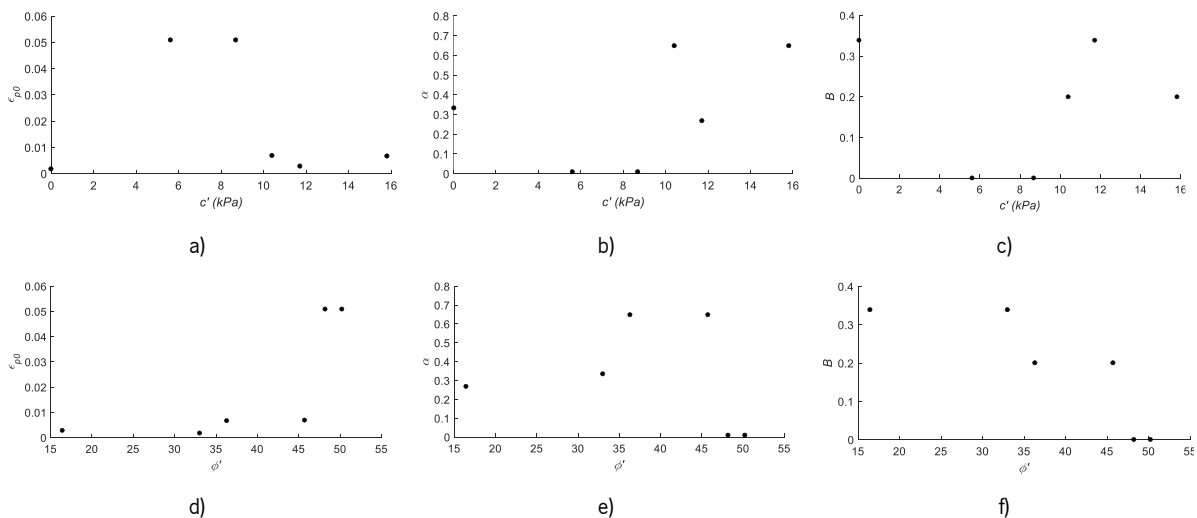
Figure 6.26 - a) relation between cohesion and ε_{p0}; b) relationship between cohesion and α, c) relationship between cohesion and B; d) relation between friction angle and ε_{p0}; e) relationship between friction angle and α; f) relationship between friction angle and B

From Figure 6.26 it is not possible to find a relationship between the parameters of the empirical permanent deformation model (ε_{p0}, α and B) and cohesion and friction angle since it is not possible to identify a pattern. The results seem very random. Thus, it is also possible to conclude that it is not very easy to find a comparison between the calibrated values of ballast, FPL and subgrade (ε_{p0}, α and B) and the values found in the scarce bibliography. Indeed, the first obstacle is related to the match between the properties of these materials and the materials found in the bibliography in terms of cohesion and friction angle, which have a significant impact on the permanent deformation as presented previously. Furthermore, the materials used to develop the empirical permanent deformations are tested at different conditions (stress and state conditions). Thus, it is not possible to find a position of the parameters ε_{p0}, α and B in a certain spectrum.

6.5 From the laboratory to the real conditions of a ballastless track: parametric studies about symmetric conditions, treatment of boundaries and type of mesh

The previous studies were important to calibrate the numerical model considering the short and long-term performance of the railway structures. However, it is important to remind that some of the conditions and the respective responses of the structures were dependent on the laboratory environment. This section aims to analyse some details of the modelling considering three important aspects:

- Requirements in terms of computational effort (symmetric conditions);
- Control of the wave reflection at the boundaries;
- Higher extension of the model and influence of the mesh size.

These preliminary studies allow adapting the numerical model defined considering the laboratory conditions to the real-field conditions of the railway track. These parametric studies are focused on the performance of the ballastless track, which will be the railway system studied in further Chapter.

6.5.1 Influence of the symmetric conditions

Based on the numerical models developed previously regarding the numerical calibration, some tests are performed to understand the viability of considering a half model in further studies in order to reduce the number of nodes and the computational effort. Thus, the same section of the ballastless track was used. In this analysis, the same boundary conditions are also used (except in the symmetry plane), as well as the same loading. In Figure 6.27, the half model and the complete ballastless track model are depicted. In Figure 6.28 and Figure 6.29 the numerical results are presented. In this case, the numerical results from the half and complete model concern the geometric position of the *LVDTs* and *CH_disp*. This

251

nomenclature (*LVDTs* and *CH_disp*) was adopted in order to more easily identify the geometric position of the nodes used to compare the displacements.

a)

b)
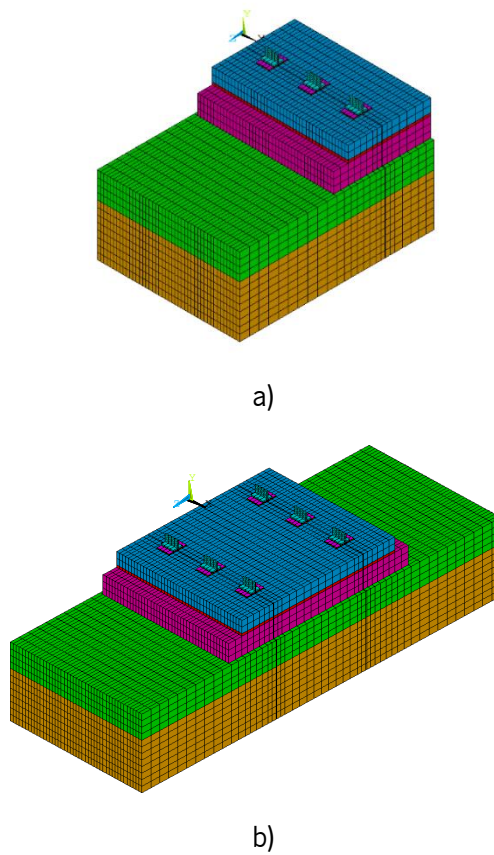
Figure 6.27 - Numerical model (ballastless track): a) half model; b) complete model

a)

b)

c)
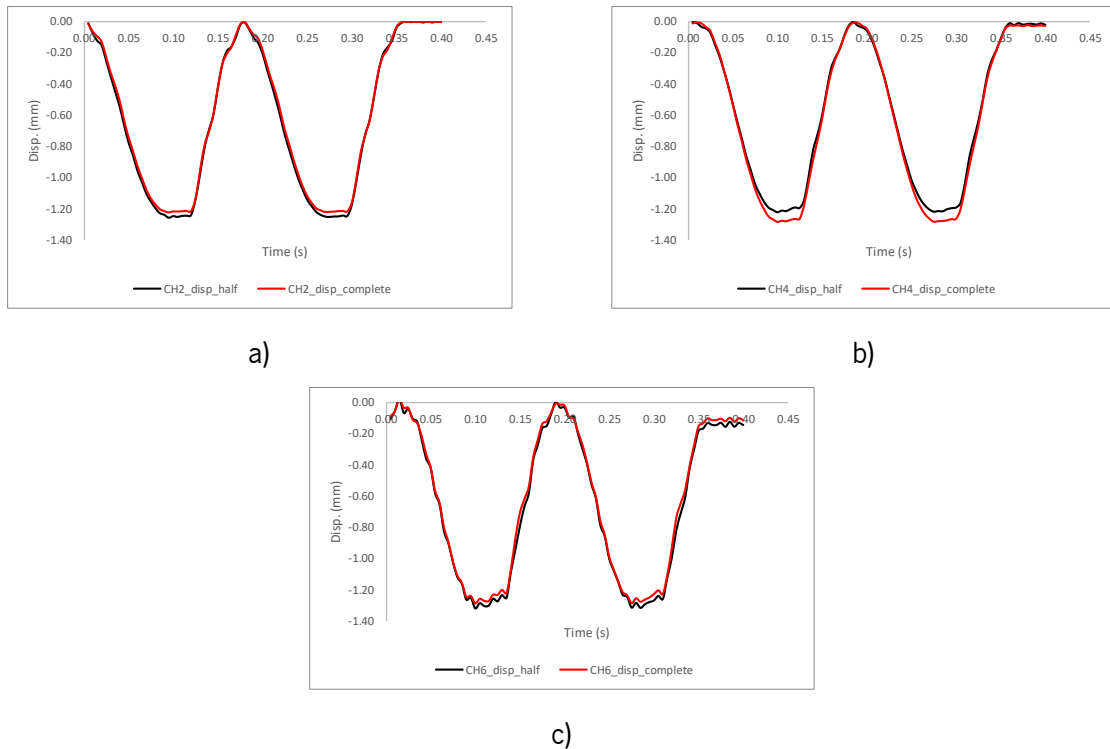
Figure 6.28 - Comparison of the numerical CH$_{disp}$ (half model and complete model): a) CH2_disp; b) CH4_disp; c) CH6_disp

a)   b)
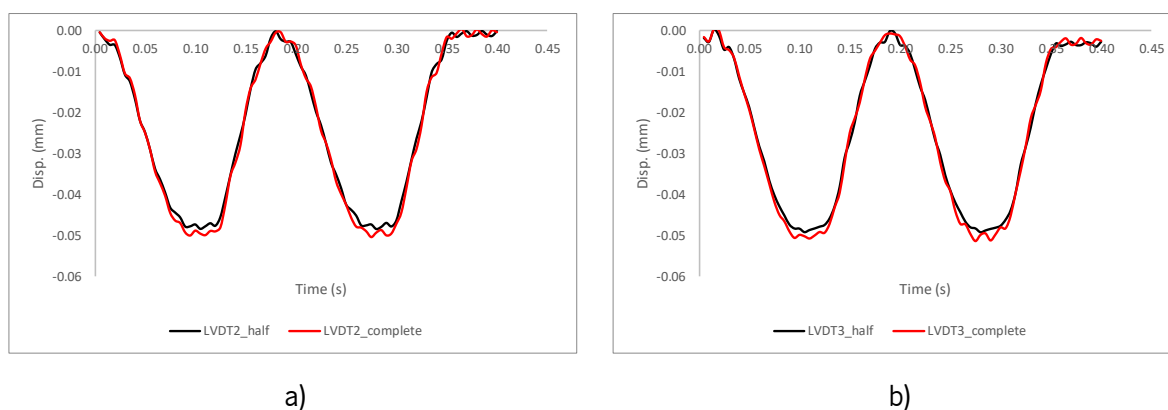
Figure 6.29 - Comparison of the numerical LVDTs (half model and complete model): a) LVDT2; b) LVDT3

Analysing Figure 6.28 and Figure 6.29, it is possible to conclude that the half model is a proper choice to model a more extensive ballastless track model since, in this analysis, the differences in the displacements are very residual.

6.5.2   Treatment of the artificial boundaries – practical application

Some approaches regarding the treatment of the artificial boundaries are tested, namely the Lysmer and Kuhlemeyer (1969) approach and the formulation developed by White et al. (1977). The theoretical background of these formulations is described in Chapter 2.

In order to compare the two different approaches, the dampers are applied in the ballastless track model (without considering the symmetric conditions). In the ANSYS *software*, the boundary conditions are applied manually in 3D models.

In this analysis, the model depicted in Figure 6.27b is stretched (the length of this model is equal to 6.1 m instead of 2.2 m), and the applied loading corresponds to the cyclic loading. Thus, from the sinusoidal function, the cycling loading applied in the laboratory is adapted to perform these preliminary tests:

$$y(t) = A \cdot \sin(\omega t + \varphi) \qquad (7.4)$$

where $y(t)$ is the value of load in kN at any instant t, A corresponds to the amplitude of the load (the peak deviation of the function from zero), ω is the angular frequency (in rad/s), t is the time (in s) and φ is the phase angle (in radians). Thus, the amplitude is equal to 23.43 (which is defined by the approximate half difference between the maximum and minimum value of the loads applied on the laboratory defined in Table 6.3 – 59 kN and 12 kN approximately – Dynamic Test I). The angular frequency is obtained from the ordinary frequency (f), which in this case is equal to 5.6 Hz (this value is based on the distance between two bogies on the same rolling stock). The value φ is adapted until a match is found between the sinusoidal function of the laboratory and the theoretical one, as depicted in Figure 6.30. After the

calibration of the sinusoidal function, this curve is replicated for the remaining sleepers with a shift of 0.0065 s (following the same assumptions presented previously regarding the phase loading used in the laboratory). Thus, the cyclic loading is implemented in the top nodes of the rail with a time interval of 0.065 s. Considering the speed equal to 100 m/s (360 km/h), the load is applied on the first sleeper and after 0.0065 seconds the load is applied on the second sleeper, and so on. The sequence is presented in Figure 6.31.
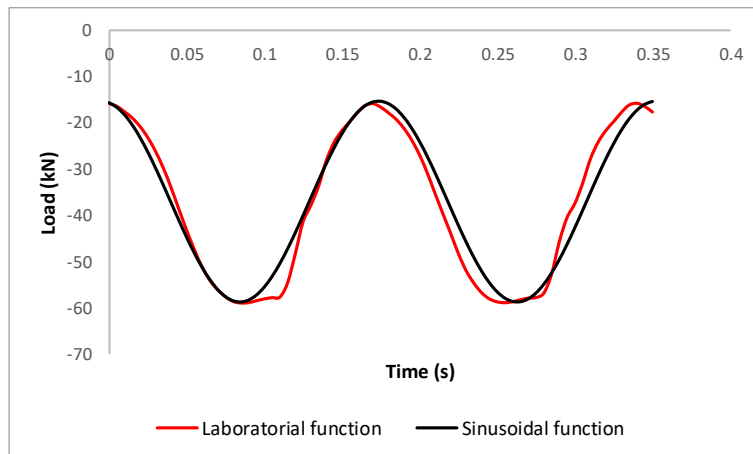
Figure 6.30 - Determination of the wave equation based on the laboratory cyclic tests
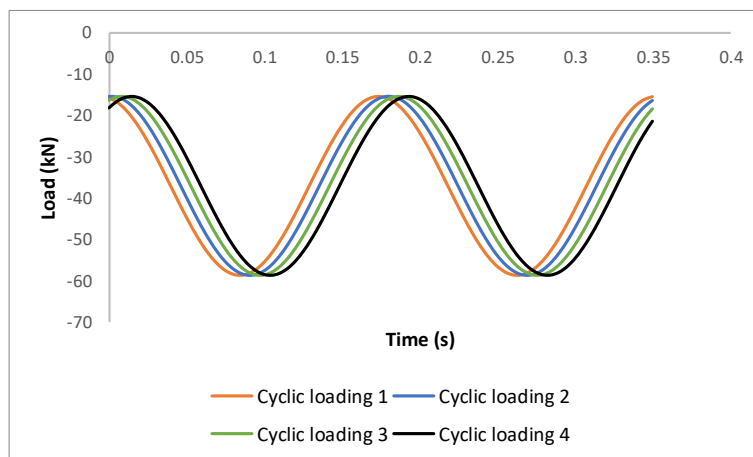
Figure 6.31 - Sequence of the wave equations applied on the top of the rail nodes considering a time interval equal to 0.0065s

The analysis also includes the interaction between the HBL and the FPL through contact elements. The ballastless track model is depicted in Figure 6.32. The obtained displacement results are depicted in Figure 6.33. The maximum displacements are obtained and compared.
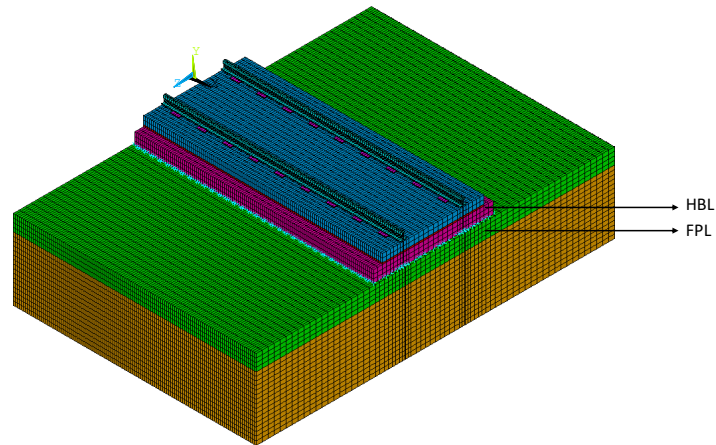
Figure 6.32 – Model of the extended ballastless track
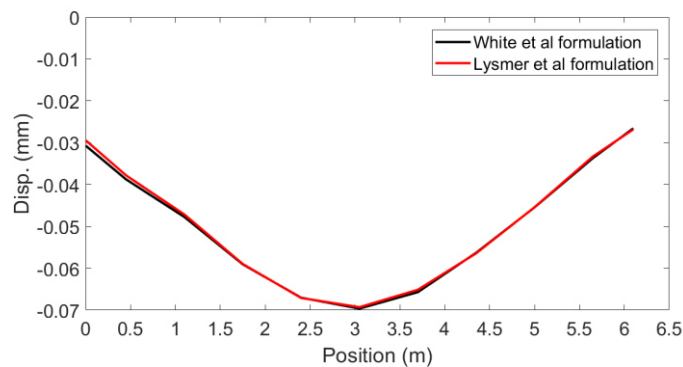
Figure 6.33 - Maximum displacements at the top nodes of the subgrade – comparison between the Lysmer and White formulation

Analysing Figure 6.33, it is possible to conclude that the differences between the results with the two approaches are not very substantial. Indeed, since the differences are not significant, another test is performed taking into account a different loading. In this case, two moving masses (speed equal to 200 km/h) are considered, which represent the load by wheel. The obtained results are depicted in Figure 6.34. These results also include the analysis with fixed supports applied on the boundaries of the model to understand the efficiency of the viscous dampers.

a)

b)
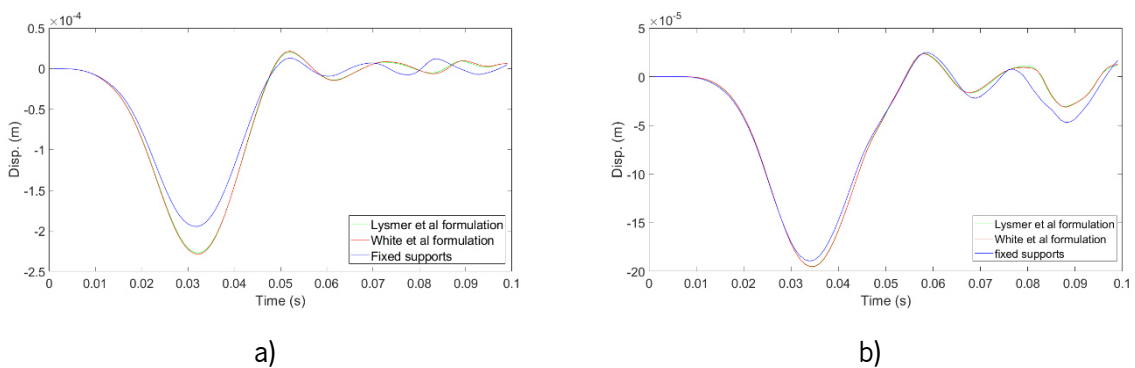
Figure 6.34 - Displacements of the top nodes of the subgrade: a) x=1.75 m; b) x=3.05 m

255

Analysing Figure 6.34, it is possible to conclude that the formulations developed by Lysmer and Kuhlemeyer (1969) and White et al. (1977) present very similar results. Figure 6.34 also shows the efficiency of the viscous dampers when compared to the situation with fixed supports applied on the boundaries. Since the Lysmer and Kuhlemeyer (1969) formulation have been implemented in several developed works (El Kacimi et al., 2013, Kouroussis et al., 2014, Fernández Ruiz et al., 2017, Sayeed and Shahin, 2016b, Sayeed and Shahin, 2017), this type of artificial boundary will be used in the following analyses.

6.5.3 Influence of the size of the mesh

To evaluate the performance of the model, the influence of the mesh is also tested. Thus, two cases are analysed with different meshes. The dimensions of the meshes are defined in accordance with the longitudinal maximum element size. Previous studies performed by Kuhlemeyer and Lysmer (1973) suggested that the maximum element size should be inferior to 1/8 - 1/5 of the minimum shear wave length l_s^{min}.

The first model is represented in Figure 6.32 and the second one is depicted in Figure 6.35. In the model depicted in Figure 6.32, the discretization corresponds to the one used on the numerical model calibration presented in this Chapter (in the longitudinal direction - *x-axis* -, the discretization is constant and equal to 0.05 m). The main differences relate to the "original ballastless track model" (Figure 6.11) is a stretch of the boundaries in all directions (*x*, *y* and *z*). In the model depicted in Figure 6.35, the longitudinal discretization is not constant and it is tighter under the railpads (length of the element equal to 0.1 m) and larger outside the railpads (length of the element equal to 0.225 m).

As in the previous analysis, cyclic loading is applied to the top nodes of the rail. The artificial boundaries are simulated through viscous dampers with C_1 and C_2 equal to one (see Chapter 2, section 2.5.3).

As expected, the number of nodes and elements is very different and there is a significant reduction from the mesh depicted in Figure 6.32 and the mesh depicted in Figure 6.35 (reduction of about 35%). This difference is analysed in Table 6.13 in more detail.

Table 6.13 - Difference in terms of number of nodes and elements considering different meshes

	Number of elements	Number of nodes
Model 1 – discretization of 0.05 m in the *x*-direction	232646	245839
Model 2 - discretization variable in the *x*-direction	81316	86680
Increment - nodes	35%	35%
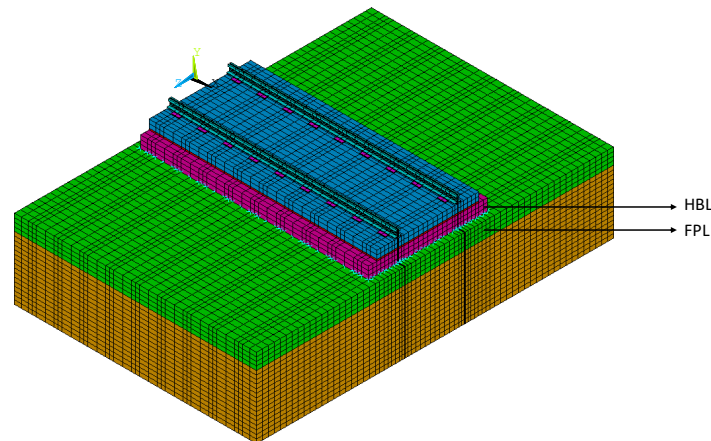
Figure 6.35 - Model considering a new mesh

Thus, the computational performance is analysed (time of analysis) as well as the obtained results in terms of displacements. The time analysis of model 1 (depicted in Figure 6.32) is about 10 h, while in the case of model 2 (depicted in Figure 6.35), the time of calculus is 3 h.

The comparison of both models is performed based on the displacements' results of the subgrade. In this case, the displacements are analysed at the top nodes of the subgrade along the longitudinal direction under the loading area (under the middle position of the railpads). The comparison is depicted in Figure 6.36. The results show a very good agreement between the displacements of the two models. Thus, based on these results, a mesh very similar to model 2 will be used in the modelling of the transition zone presented in further Chapter.
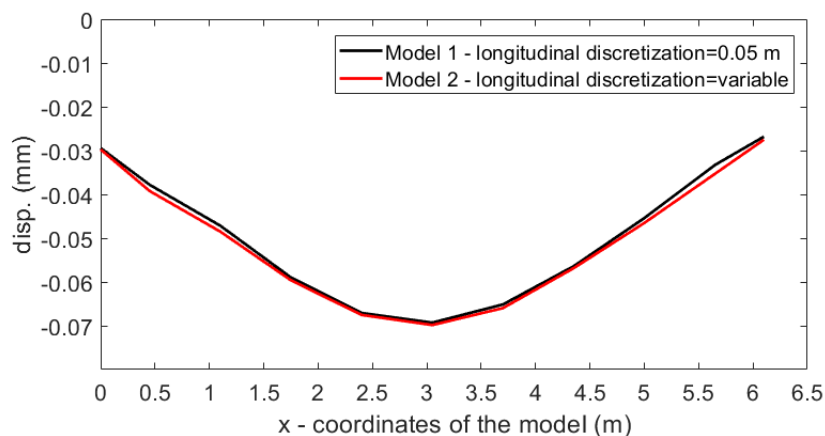
Figure 6.36 - Maximum displacements at the top nodes of the subgrade layer of model 1 (constant discretization=0.05 m) and model 2 (variable discretization)

6.6   Final considerations

Two numerical models were successfully calibrated using experimental results from cyclic loading tests performed on ballastless and ballasted track sections of 2.2 m length. Moreover, the experimental results

confirmed that the ballasted track present higher permanent deformations (and cumulative permanent displacements) than the ballastless track due to the presence of the ballast layer.

The obtained results from the calibration process (short term and long term) showed good agreement between the numerical and experimental results. Regarding the short-term calibration, the *Young* modulus and the *Poisson's* ratio of some of the materials (railpads, ballast, FPL and subgrade) were adjusted.

Furthermore, a novel approach was developed to simulate the long-term behaviour of both structures through the calibration of an empirical permanent deformation model. The material's properties of a mechanistic-empirical permanent deformation model were successfully calibrated. This calibration was performed using the *least-square* fitting method through an optimization tool-box in *MATLAB* and applying the time hardening concept to take into account the stress history of the materials (mostly the FPL and subgrade). The results showed very good agreement between the experimental and numerical results. Furthermore, from a sensitivity analysis, it was identified that the cohesion of the subgrade can have a significant impact on the permanent deformation. The obtained results are aligned with the results from Chapter 5, where it was also demonstrated that the friction angle influences the permanent deformation. The novel approach introduced to predict the permanent deformations on both types of track structures can be a valuable tool in future modelling of the long term degradation of the track structures in transition zones. This will support the development of proactive strategies such as predictive and preventive maintenance.

The calibrated parameters will be used in the analysis of the performance short and long term of a particular transition zone presented in Chapter 7.

Furthermore, parametric tests were performed to analyse the performance of the calibrated model in real-field conditions. Thus, the influence of the symmetric conditions, the elements included in the treatment of the artificial boundaries, or even the size of mesh were studied. These studies also allowed evaluating the impact of computational effort on the results. These numerical tests were performed with cyclic loading, which is less complex than moving loads with train-track interaction associated with the passage of a train. The results showed that an additional study should be performed regarding the inclusion of more cycles in the cyclic loading. The obtained conclusions will be applied to the modelling of the transition zone presented in Chapter 7.

7 Analysis of a transition zone in a ballastless track system: embankment to tunnel

7.1 Introduction

The transition zones are areas where there is a high rate of track degradation due to the stiffness difference between two structures and the generated differential settlements induced by the passage of the trains. These areas usually show poor long-term dynamic performances, which means that it is necessary to fully understand the behaviour of the structures in these zones, in order to find and define strategies to reduce the maintenance operations, respective costs and consequently to optimize the engineering solution. This subject is of great interest from several points of view: structural, geotechnical, economical, etc. Indeed, beyond academic importance, this subject is also a concern for railway infrastructure managers. This work purposes the study of a specific transition zone (and includes the analysis of the short but also the long-term performances), based on the calibration carried out in the previous Chapter in terms of material properties (which also includes the calibrated parameters of the permanent deformation model).

The analysis was performed based on 3D modelling. Indeed, notwithstanding the importance and the advantages of the 2.5D (described in the work developed by Bian et al. (2011), Alves Costa et al. (2012) and/or Lopes et al. (2013)), already exploited in Chapter 5, or even the periodic models (such as the models developed by Chebli et al. (2008) and Gupta and Degrande (2010)), these numerical tools cannot be applied in these conditions since they assume a periodic repetition of the cross-section in the longitudinal direction of the track, which not corresponds to the specific case of the transition zones.

This Chapter is aligned with the *IN2TRACK* projects (1, 2 and 3) of the *SHIFT2RAIL* Joint Undertaking, which purposes to improve and optimize the track system, specially the ballastless track systems at transition zones. Thus, this Chapter aims to demonstrate the performance of the previously developed tools and methodologies by analysing the performance of a specific transition zone in a ballastless track from an embankment to a tunnel with higher track stiffness. This type of transition is still largely unexplored since most of the developed works are based on the transition between ballasted and ballastless tracks (Li and Wu (2008), Shahraki and Witt (2015), Shahraki et al. (2015) and Wang and Markine (2019)), or between ballasted tracks and a stiff structure as a bridge or box culvert (Seara and Gomes Correia (2010), Coelho et al. (2011), Varandas et al. (2011), Varandas et al. (2013), Alves Ribeiro et al. (2015), Paixão et al. (2016), Varandas et al. (2016), Wang and Markine (2018a) and Alves Ribeiro et al. (2018)). However, there are some works settled on transitions with ballastless track such as the

work developed by Shan et al. (2013). In the work developed by Shan et al. (2013), the authors consider a moving load, and, because of that, they cannot capture the vehicle-track interaction, which is a major limitation of the analysis. The load is defined by the product of the static load and a dynamic impact factor. The higher number of works focused on the ballasted track is understandable since the ballasted track is still widely used, mostly in Europe. This is due to the high level of knowledge from the dynamic performance of the materials until the global performance of the structure. Moreover, due to the contribution of the ballast deformation to the global performance of the track, the ballasted track presents, potentially, higher permanent deformations when compared to the ballastless track, which means that is often a study object in the scope of the long-term performance. Furthermore, the ballast layer is the element that assures the continuity of the track and, because of that, presents higher concentration of stresses on the transition. This means that, because of its nature as a geomaterial when submitted to cyclic loads and the higher concentration of stresses, the permanent deformation on the transition would also be very significant. In the ballastless track analysed in this Chapter, the elements that assure the continuity of the track are, essentially, the concrete slab and the HBL (these are the most important in the ballastless track system analysed in this Chapter but there are many others, including track foundation in cement materials and also ground improvement). These elements also present a concentration of stresses on the transition, but they do not contribute to the development of the permanent settlements, when compared to the geomaterials. However, these elements also degrade, crack, loose stiffness, and strength. Thus, it expected that the ballastless track presents a much better long-term performance when compared to the ballasted track implemented in transition zones.

Over the years, the ballastless track has imposed itself as a good option, generally, in the high-speed lines. The concrete slab confers to the track good confidence mostly in terms of long-term performance since the track presents lower permanent deformations, as explained previously. As presented in the previous Chapter, the ballasted track, when compared to the ballastless track, presents superior values of permanent deformation, mainly due to the presence of the ballast, which presents a complex behaviour when submitted to cyclic loading. Indeed, in Chapter 5, it is possible to conclude that the difference in the performance of the subgrade of the ballasted and ballastless track is not that significant, despite the differences in the composition itself of the railway tracks in terms of stiffness and materials used. However, the conclusions would change if the ballast was included in the analysis of the long-term performance of the analysed ballasted track.

Regarding the analysis, firstly, due to the extensive computation time, only the first two bogies were considered to simulate the passage of a train to understand the global behaviour of the structure in a transition zone. Later, more bogies of the *Alfa Pendular* train were included in the dynamic analysis. The viscous dampers were implemented to absorb the waves that impinge the boundaries, and the damping characteristics of the materials were selected. The damping values were determined based on the *Rayleigh* damping matrix. The contact algorithms (using the penalty method) were used to simulate the interaction between the vehicle and the track, but they were also applied to consider the interaction between other different components of the system, such as the support layer (HBL) and the substructure of the track (FPL and subgrade). The modelling took into account the symmetric conditions and the optimized mesh based on the parametric studies presented in Chapter 6 in order to reduce the computation time. The dynamic analysis was performed using implicit methods.

7.2 Description of the case study

This analysis aims to study the amplification dynamic effects generated by the passage of the *Alfa Pendular* train considering that there is a stiffness difference between two structures with different supports: a ballastless track over an embankment and a ballastless track inserted in a tunnel. Figure 7.1 a) shows an overview of this situation. In this problem, the tunnel presents a much higher stiffness when compared to the ballastless track supported by an embankment. The general effects of this stiffness' difference are depicted in Figure 7.1 b) (schematic representation).

a)

b)
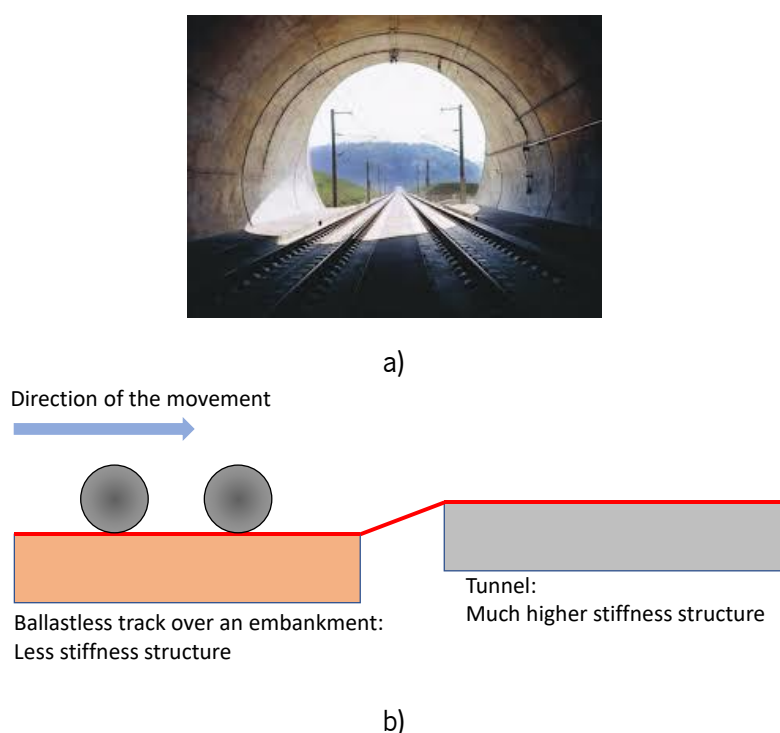
Figure 7.1 - Example of the transition: ballastless track in a tunnel (Rheda-System, 2011) (a) and its effect due to the stiffness's difference (b)

The transition was analysed through 3D modelling. The base model is depicted in Figure 7.2 and presents a total length of 53.1 m (the embankment with 31.65 m and the tunnel zone with 21.45 m). The analysis was performed considering the passage of the *Alfa Pendular* train running at a speed equal to 220 km/h. The train starts its movement and loading 5 meters ahead of the left boundary of the model.

As mentioned previously, viscous dampers (Lysmer and Kuhlemeyer, 1969) were used to attenuate the waves that impinge the vertical boundaries of the FPL and subgrade layers. This approach has been used in the scope of the 3D modelling and transition zones with good results (Banimahd et al., 2012, Varandas et al., 2016, Shahraki and Witt, 2015, Alves Ribeiro et al., 2018). Furthermore, the efficiency of the viscous dampers' elements was already proved in the 3D modelling presented in Chapter 6 (section 6.5.2). The wave propagation is due to the mobile character of the loading that simulates the passage of the *Alfa Pendular* train. Thus, at the bottom of the subgrade layer (horizontal boundary defined by the plane *xz with* y=-11.538 m), fixed supports were implemented. Regarding the part of the ballastless track in the tunnel, fixed supports in the vertical direction were also used at the bottom of the HBL layer. Since this is a very extensive model, symmetric conditions were adopted to reduce the computational effort (the efficiency of the symmetric conditions was tested previously in section 6.5.1 from Chapter 6). The support conditions of the model depicted in Figure 7.2 are explained and described in Table 7.1.

a)

b)

c)

d)

31.65 m   21.45 m

53.10 m

e)

10.4 m

6 m

f)
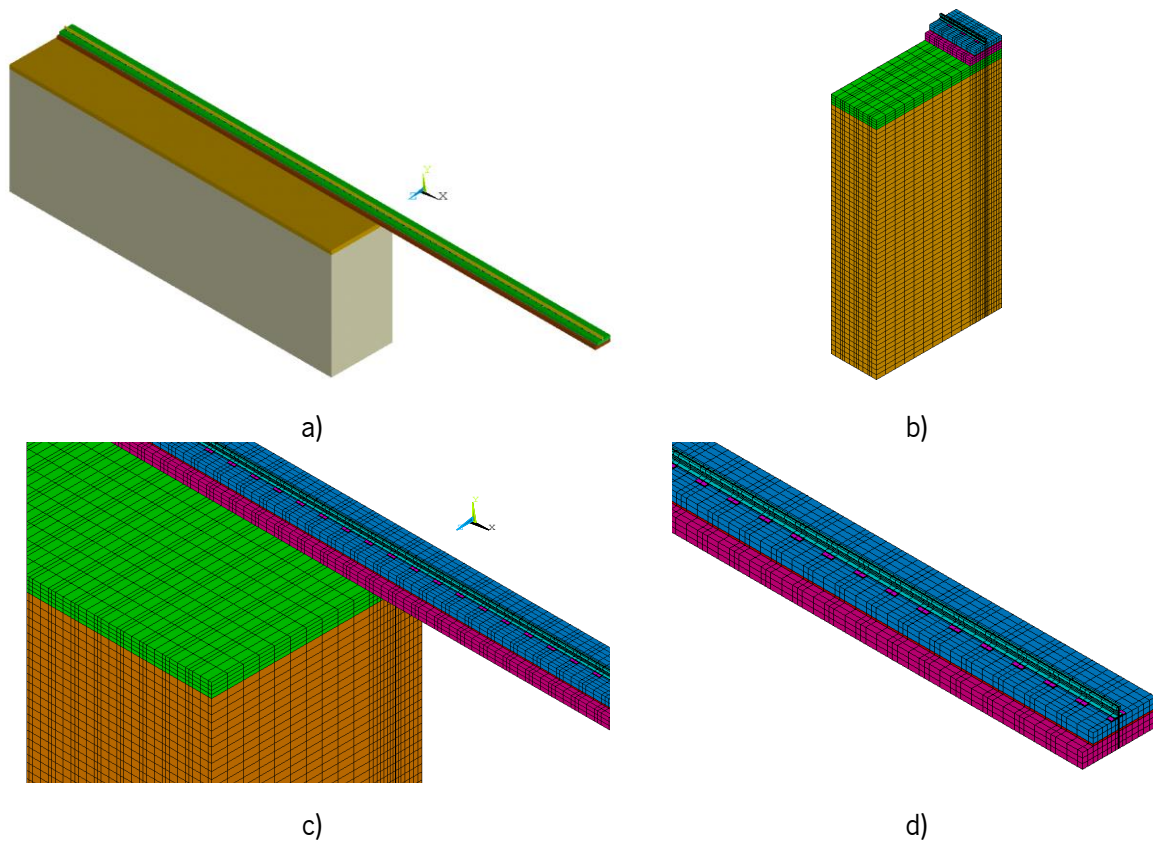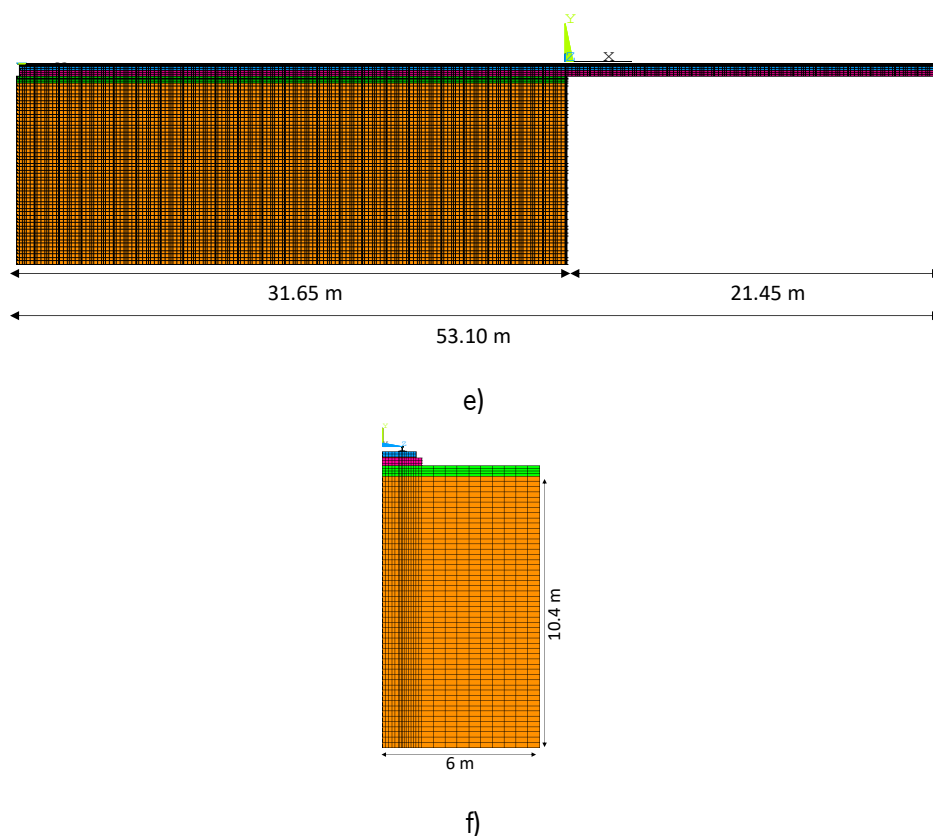
Figure 7.2 - Transition in a ballastless track system: embankment to tunnel: a) complete model; b) slice of the ballastless track; c) detail of the model; d) detail of the ballastless track model in the tunnel; e) longitudinal dimension of the model; f) dimensions of the model (cross-section)

Table 7.1 - Support conditions

<u>Bottom of the model (plane *xz;* y=-11.538 m) – embankment</u>	Fixed supports (all)
<u>Bottom of the model (plane *xz;* y=-0.738) - tunnel</u>	Fixed supports in the y-direction (vertical direction).
<u>Plane *yx* (z=0*)* - plane of symmetry</u>	Fixed supports in the *z*-direction (transversal direction)
<u>Plane *yz* (x=0m) – located in the transition</u>	Fixed supports in the *x*-direction (longitudinal direction) applied on FPL and subgrade
<u>Plane *yz* (x=-31.65 m)</u>	Viscous dampers (all directions) applied on the FPL and subgrade
<u>Plane *yx* (z=6 m)</u>	Viscous dampers (all directions) applied on the FPL and subgrade

The ballastless track is composed of the materials depicted in Figure 7.3. The materials were modelled with solid elements (8 nodes) and contact elements between the HBL and FPL were considered in some modelling exercises. The discussion of this topic will be further explored in the following sections (7.5).

Railpad; steel plate; EPDM
Rail
Concrete slab
HBL
FPL
subgrade
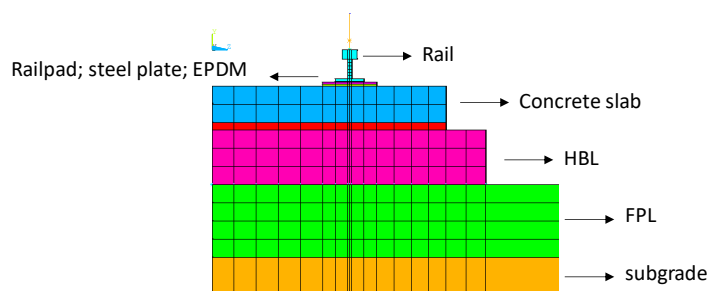
Figure 7.3 - Materials that composes the ballastless track

263

7.3   Damping properties of the materials

The damping of the model was defined through the *Rayleigh* damping matrix (theoretical background presented in Chapter 2). In this case, the damping parameters αi and βi were determined based on some assumptions. The values were estimated based on the receptance curves obtained from the excitation of the rail over the railpad in two sections of the track with different characteristics: over the embankment and over the tunnel. Thus, the Dirac impulse (Figure 7.4) was applied on the top nodes of the rails.

For all the materials, equality $\xi_1 = \xi_2$ was assumed. In the case of the concrete materials and geomaterials, a hysteretic damping of $\xi=0.01$ and $\xi=0.03$ was adopted, respectively. These values are normally used in the scope of the modelling of railway tracks (Fernández Ruiz et al., 2017, Alves Ribeiro et al., 2018). In the ballasted tracks, a $\xi=0.01$ is normally used to model the concrete sleepers. This value was adopted to model the concrete materials of this ballastless track. Regarding the railpads (EPDM) since these elements are modelled by solid finite elements and not by spring-damper elements, as usual, a hysteretic damping was adopted (equal to $\xi=0.05$), instead of the definition of the stiffness (k) and viscous damper (c).

a)   b)
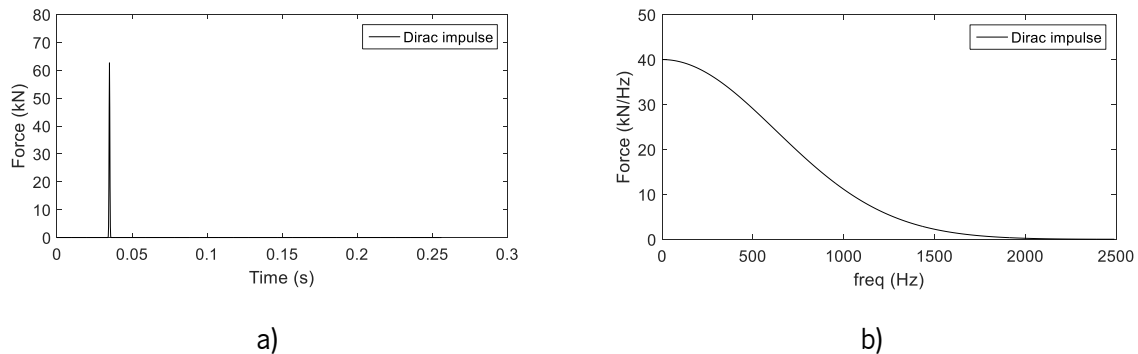
Figure 7.4 - Impulse applied on the track to obtain the receptance curves: a) time-domain; b) frequency-domain

The obtained receptance curves are depicted in Figure 7.5. Analysing Figure 7.5 a), there is a resonant peak at 146.5 Hz. This figure also shows that the receptance curve of the rail in the embankment and the tunnel are almost overlapped. The main difference occurs at the concrete slab level (Figure 7.5 b). The results show that the values of the receptance are lower in the ballastless track over the tunnel as expected due to the higher stiffness given by the fixed supports. Thus, according to these results, a range of frequencies between 5 Hz (f_1) and 200 Hz (f_2) was defined. This range is considered enough to correctly represent the response of the track. More details about the damping formulation can be found in Chopra (1995). From these assumptions, the parameters α and β of each material are presented in Table 7.2

and are represented graphically in Figure 7.6. The α and β parameters were obtained from the following expressions:

$$\alpha = \frac{2 \times \xi \times \omega_1 \times \omega_2}{\omega_1 + \omega_2} \qquad (7.5)$$

$$\beta = \frac{2 \times \xi}{\omega_1 + \omega_2} \qquad (7.6)$$

where ω_1 and ω_2 are the angular frequency defined from f_1 and f_2.

a)   b)
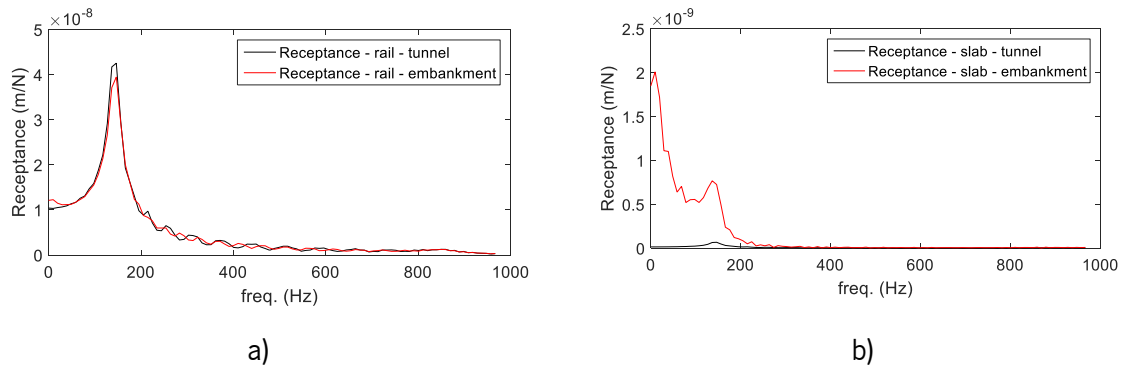
Figure 7.5 - Receptance curves: a) of the rail (top); b) of the concrete slab (top)

Table 7.2 – Damping Rayleigh parameters

Material	ξ	α (s^{-1})	β (s)
Railpad - EPDM	0.05	5.712	0.00014
Concrete slab and HBL	0.01	1.142	2.894×10^{05}
Substructure (FPL and subgrade)	0.03	3.427	8.681×10^{05}

a)   b)

c)
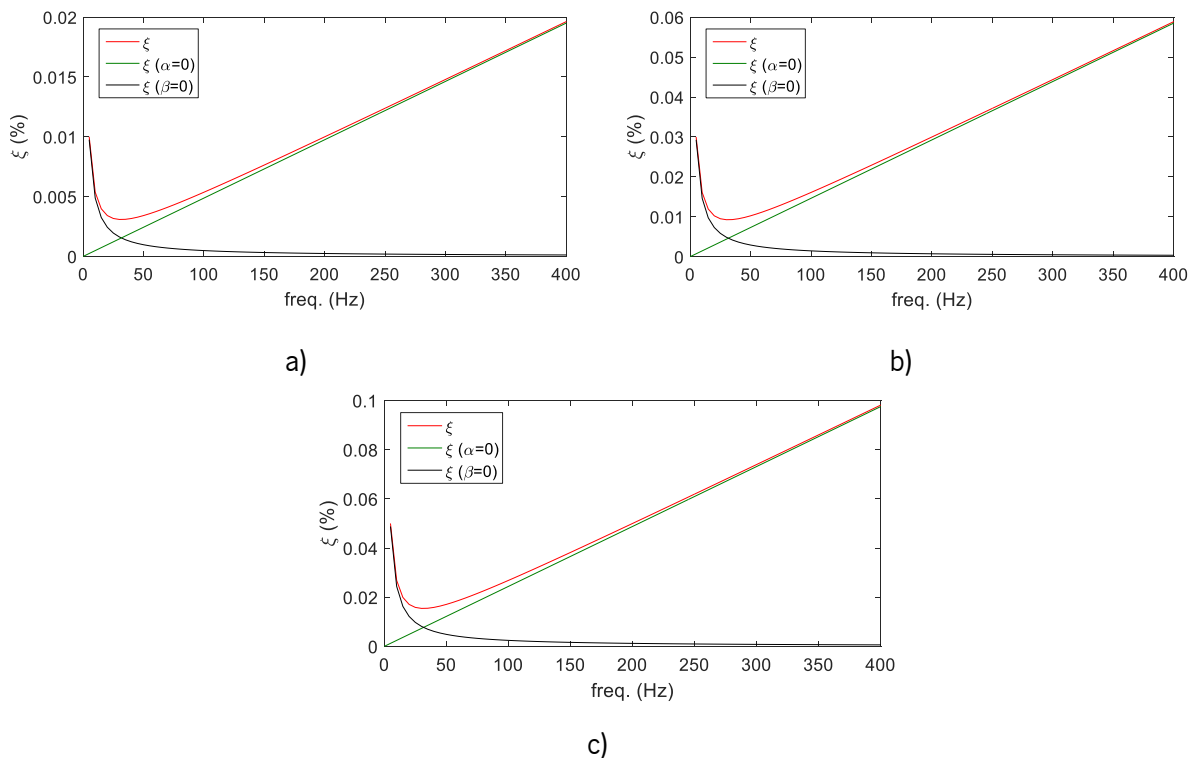
Figure 7.6 - α and β determination: a) $\xi_1 = \xi_2 = 0.01$ - concrete slab and HBL; b) $\xi_1 = \xi_2 = 0.03$ - substructure; c) $\xi_1 = \xi_2 = 0.05$ – railpad (EPDM)

The properties of the materials are presented in Table 6.4 from Chapter 6 and Table 7.2 (damping properties – *Rayleigh* coefficients).

7.4   Optimization

7.4.1   Optimization of the geometry

Before considering the passage of the *Alfa Pendular* (since the calculation time is very significant), an analysis was performed to optimize the geometry of the transition. Thus, the influence of the distance between the centre of the model (symmetry plane) and the vertical boundary defined by plane *yx* was evaluated. In this case, three distances from the centre of the model until the vertical boundary defined by the plane *yx* (Figure 7.7 a) were considered: 6 m, 10.5 m and 15 m. The results (displacements of the top nodes of the rails and concrete slab and the maximum displacements along the longitudinal direction under the loading alignment) showed that the differences between the three options (6 m, 10.5 m and 15 m) were not very significant, mostly in terms of maximum displacements. Thus, the option with 6 m was selected since it allows to reduce significantly the calculation time. Posteriorly, the influence of the distance between the top of the subgrade and bottom boundary defined by the plane *xz* (subgrade thickness) was also analysed (Figure 7.7 b). Thus, the same strategy was adopted, and three different thicknesses of the subgrade were defined: 6.4 m, 10.4 m and 14.4. The results showed that the thickness of the subgrade and the respective position of the fixed supports at the bottom boundary influenced the results of the numerical displacements. This difference is more visible at the concrete slab level than at the rails level since there was a good concordance of the results in this element. The results demonstrated that the adoption of a thickness equal to 6.4m was non-conservative. Furthermore, the shape of the displacements curve was different, which means that the results were contaminated by the reflection of the waves at the bottom of the model. Thus, a thickness of the subgrade equal to 10.4 m was adopted. The influence of the dimension of the model in the longitudinal direction was also analysed. The analysis performed showed that the response of structure was influenced by the proximity of the left boundary (plane *yz* with x=-21.25 m considering the embankment with 21.25 m length and the transition at x=0m). Thus, the length of the embankment has been increased to 31.65 m.
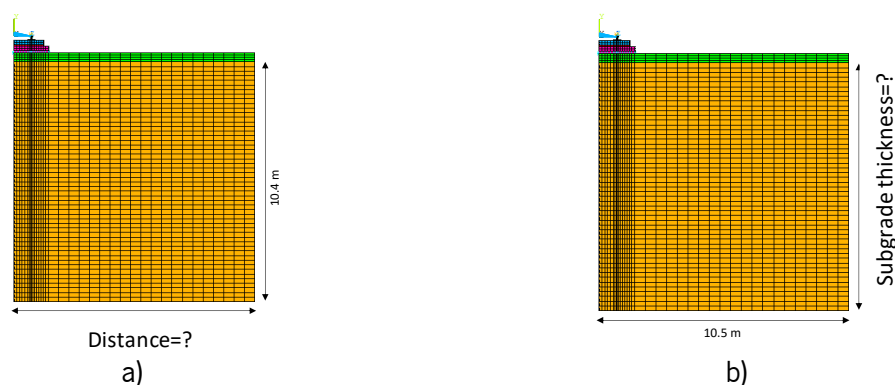
Figure 7.7 - Identification of the distance: a) from the centre of the model until the vertical boundary defined by the plane *yx*; b) between the top of the subgrade and bottom boundary (plane *xz*) - subgrade thickness

7.4.2 Optimization of the number of nodes through the consideration of different type of elements

The optimization of the geometry can also be complemented by the optimization in the scope of the type of elements used in the modelling. Thus, in the previous analyses, solid elements were used to model all elements of the ballastless track. However, to reduce even more the calculation time, several tests were performed with different elements: the rail modelled with a beam element, the railpads (which includes the elements railpad, steel plate and EPDM) modelled with spring-damper elements and the concrete slab, due to its low thickness, modelled as a shell element. Thus, three options were considered:

- Option 1: All materials are modelled with solid elements;
- Option 2: All materials are modelled with solid elements except for the concrete slab – modelled with shell elements;
- Option 3: Rail modelled as a beam element, railpad, EPDM and steel plate modelled with one spring-damper element and concrete slab modelled as shell element.

In the first analysis, the solid elements of the concrete slab were replaced by the shell elements. The results showed that the differences between the results of option 1 (concrete slab with solid elements) and option 2 (concrete slab with shell elements) were not very significant.

The second analysis considered the comparison between option 1 and option 3. In this analysis, the solid elements of the railpad, steel pad and EPDM were replaced by one spring-damper element considering the equivalent stiffness (k_{eq}) of a series of springs. The obtained results showed that the displacements of the concrete slab were similar but there were significant differences in rail's displacements. This is due to a difference in terms of stiffness under the rail. This means that to use this type of modelling (option 3), it would be necessary to calibrate the material's parameters of the elements used to model the railpad, including the stiffness (k) of the spring-damper element but also the damping (c). This type of calibration

267

usually requires the running of several analyses to obtain a satisfactory result. This is not the main focus of this work, which aims the study of the short and also long-term dynamic analysis of the transition zone.

In addition to the numerical results, it was also necessary to analyse whether the differences in terms of time calculation (which reflects the number of nodes) were significant. Thus, the number of nodes and elements were compared: option 1 (solid elements) with option 2 (solid elements for all the material with exception of the concrete slab modelled with shell elements) and with option 3.

Thus, considering option 1 as the reference, the increment of the number of nodes between option 2 and option 1 was only about 1.4%. The increment of the number of nodes between options 3 and 1 was around 3.4%. Therefore, these increments were almost imperceptible in terms of the time of analysis. This is justified by the total number of elements of each material, described in Table 7.3.

Table 7.3 - Comparison of the number of nodes and elements for rail, railpad, EDM, steel plate and concrete slab

Material	Option	Elements	Nodes
Rail	1	5200	9135
	2	5200	9135
	3	260	261
Railpad	1	520	1950
	2	520	1950
	3	258	390
Steel plate	1	780	2730
	2	780	2730
	3	*	*
EPDM	1	780	2730
	2	780	2730
	3	*	*
Concrete slab	1	7800	12428
	2	3900	4176
	3	3900	4176

*This element is omitted and replaced by one spring-damper element (spring in series) composed of railpad, steel plate and EPDM

Table 7.3 shows a reduction of the number of nodes and elements from option 1 to option 2 (in the concrete slab) and from option 1 and option 3. However, this reduction is not significant. Thus, option 1 was maintained, which means that all materials were modelled solid elements (as in Chapter 6 where the ballasted and ballastless tracks were modelled with solid elements to replicate the laboratory results) since this situation represents better the real behaviour of the railway structure. In the work developed by Aggestam and Nielsen (2020), the authors conclude that, for example, in the study of a ballastless track,

the 3D shell model can be used for an accurate calculation of displacements, but the 3D solid model is preferable for calculation of stresses.

7.5   Dynamic behaviour for the passage of the Alfa Pendular train

From the conclusions obtained in the previous sections and Chapters, the passage of the *Alfa Pendular* and its effects on a specific transition zone were analysed. Thus, in this analysis, the *Newmark-Raphson Method* was used. In the present study, the *Hertzian* theory was adopted to model the wheel-rail interaction since several studies presented positive and satisfactory results with this approach. The performed analysis is non-linear due to the simulation of the interaction between the train and the track by the inclusion of contact elements using the *Penalty* method.

7.5.1.1   Modelling of the Alfa Pendular train

The train was simulated by the bogies, primary suspension, mass and axle of the wheelset and *Hertzian* stiffness to simulate the interaction between the vehicle and the track. The bogies were modelled with very stiff beams with distributed mass (M_b) and the primary suspensions were modelled through the set of spring-damper (K_p and c_p) elements. The wheelset was modelled as a concentrated mass (M_e) and a spring with a stiffness determined based on the *Hertzian* theory. Considering the obtained conclusions of the studies presented in Chapter 2 (section 2.5.4) and also the work developed by Alves Ribeiro (2012) and Paixão (2014), a simplified model was adopted where only the bogies, primary suspension, and wheels/axles of the train were considered. This means that the box and the secondary suspensions were not included in the modelling (M_c and K_s and c_s, respectively).

The train was modelled with finite elements. The modelling is depicted in Figure 7.8 and the properties are presented in Table 7.4. Since only half of the track was modelled, the properties were divided by two. It is important to refer that the properties of the *Alfa Pendular* train are not the same along the train (namely the axle load) but, the differences are very small, and a constant value to each property was adopted to simplify the analysis.

269
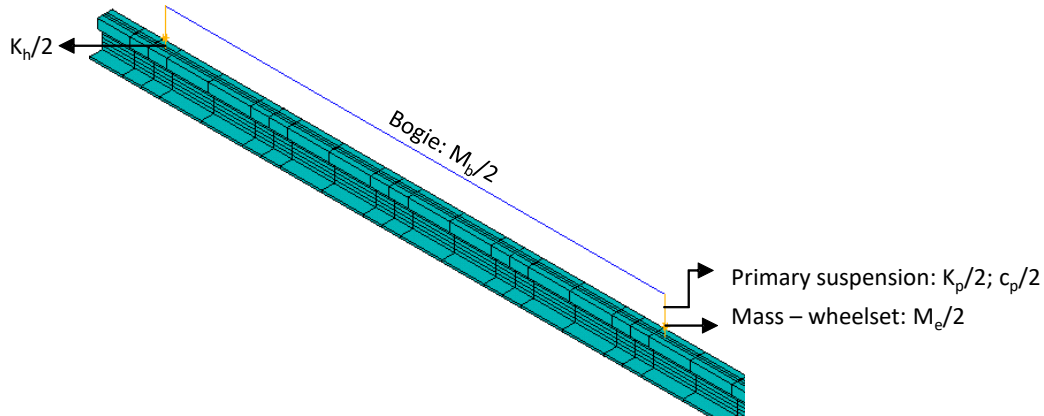
Figure 7.8 - Finite elements model (vehicle and rail)

Table 7.4 - Characteristics of the *Alfa Pendular* train adopted in this study

	Component	Values
	Bogie: $M_b/2$	4932/(2*2.7) [kg]
Primary	$K_p/2$	3420×10³ (/2) [N/m]
suspension:	$c_p/2$	36×10³ (/2) [N.s/m]
	Wheelset Mass: $M_e/2$	1800 (/2) [kg]
	$K_h/2$	2.4×10⁹ (/2) [N/m]

Regarding the loading, a load of 67.5 kN was adopted to simulate the wheel load (axle load/2). Since the interaction between the train and the track was considered and taking into account that this train has a total length of 158.90 m, the simulation of the complete passage of the train would imply the adoption of a model three-four times longer. In the context of this analysis (mostly due to the 3D character of the model using solid elements), this would imply, necessary, a significant increase in the time of analysis. In order to overtake this problem, the simulation of the passage of the bogies was performed considering the following process: at the beginning of the analysis, all the bogies are overlapping in the extremity of the model, being applied to each set of axles of a bogie an evolution law of the load over time and at each bogie an evolution law of the movement (speed) over time. Thus, it is possible to simulate the passage of the different bogies of the train over a more reduced model. Figure 7.9 and Figure 7.10 show the load and speed functions (respectively) related to the passage of the first two bogies considering a train's speed of 220 km/h.
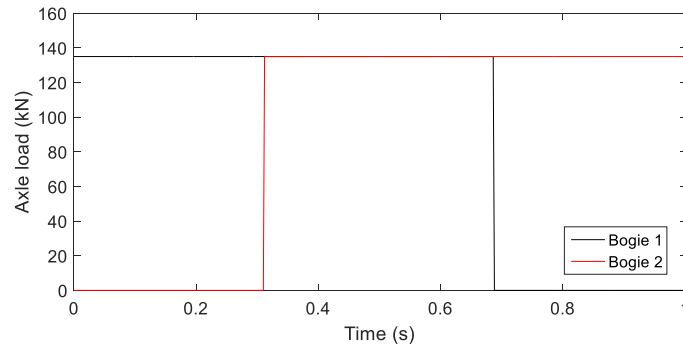
Figure 7.9 - Load function (2 bogies)
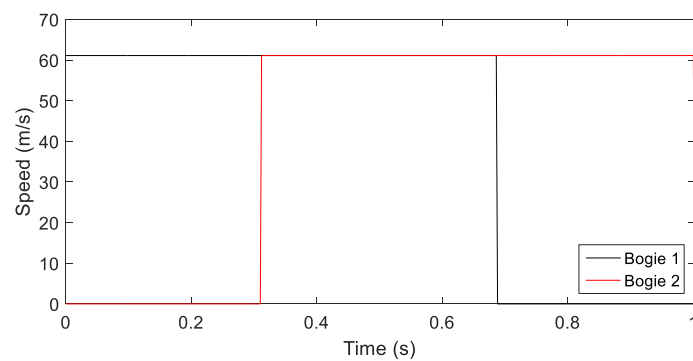
Figure 7.10 - Speed function (2 bogies)

Analysing Figure 7.9 and Figure 7.10, each bogie was loaded and animated with movement during a certain period, which corresponds to the time it takes to travel the entire model. The beginning of the application of the load and the movement is determined according to the geometry and speed of the train. In order to understand this process, Figure 7.11 presents a schematic representation of the position of the first three bogies of the train (B1, B2 and B3) in the model in different instants of the analysis. This representation is valid for the rest of the bogies. The first three were selected only to show how the movement of the *Alfa Pendular* is imposed and the delay between the bogies in the first 0.6 seconds.
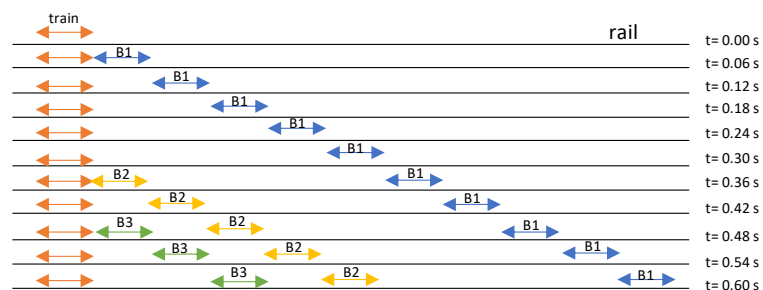
Figure 7.11 - Schematic representation of the modelling of the movement of the train

271

Thus, it is possible to simulate the passage of the whole vehicle (in this case defined only by the bogies and excluding the car body) in a very quick and efficient way. The increase in the calculation time is only function of the time that the train takes to travel the model.

7.5.1.2 Passage of the first 2 bogies

Since the passage of the whole *Alfa Pendular* train is very demanding in terms of the calculation time, a first analysis was performed considering the simulation of the passage of only the first two bogies of the *Alfa Pendular* train, considering its geometric properties and a train's speed of 220 km/h. The important dimensions of the model are depicted in Figure 7.2. The model presented in Figure 7.2 has 404251 nodes and 379861 elements. In this first analysis, a time step equal to 0.002 s was adopted. The influence of this parameter will be further explored.

In order to evaluate the obtained results, some of the top nodes of the rails, concrete slab, FPL, and subgrade were selected (Figure 7.12). The maximum displacement of each node was also obtained, and the results are presented in Figure 7.13. The results were obtained in the alignment under the loading. Furthermore, the stress and strain results of the top nodes of the subgrade were also obtained, as shows Figure 7.14. In this analysis, no contact elements between the HBL and FPL were considered. The only contact elements included were implemented between the train and track. The reference position corresponds to the transition zone at x=0 m. The instant t=0 s corresponds to the time the first bogie takes to reach the transition zone at x=0 m.

Analysing Figure 7.12 and Figure 7.13, it is possible to confirm that the maximum displacements in the rail, concrete slab, FPL and subgrade occur at the beginning of the loading, then stabilize and in the end, the displacements decrease as the train approaching the transition from the embankment to the tunnel. Regarding the displacements of the concrete slab, FPL, and subgrade, the results are similar to each other, and the maximum value is close to 0.25 mm (beginning of the loading). After the maximum, the value stabilised and it is close to 0.2 mm. It is important to highlight that, in the rail displacements (Figure 7.12 a), it is possible to identify the axles of each bogie. However, the displacement of the concrete slab, FPL and subgrade are not sensitive to the 4 axles but to the 2 bogies.

In Figure 7.13, the maximum displacements of the concrete slab, FPL and subgrade along the track are presented, as well as the maximum displacements of the rails. The understanding of this result at this stage is important to comprehend the influence of the railpad on the ballastless track system since it is a very flexible element. Indeed, the displacements of the rails are significantly influenced by the properties and presence of the railpads. The maximum displacement of the concrete slab, FPL and subgrade occur

272

between the position x=-23m and x=-22 m, at the beginning of the application of the loading, which corresponds to the first bogie. These results may be influenced by the left boundary (in the longitudinal direction). Indeed, at the position x=-31.65 m, the displacements are not zero, but they are very close to 0, which indicates a residual influence of the proximity of the left boundary. Furthermore, this residual displacement can also be influenced by the position of the beginning of the loading (at x=-26.65 m). The influence of the boundary on the results should be investigated in more detail in future works with the consideration of an even higher length of the embankment. Indeed, after a certain position, the effect of the boundary is no longer observable.

The stresses and strains of the subgrade show similar conclusions (Figure 7.14). The maximum stress induced in the subgrade occurs at the beginning of the loading and it is close to 25 kPa. After that (x=-18.5 m), the vertical stresses stabilise with a value close to 15 kPa. Close to the transition (x=0 m), there is a sudden decrease in the vertical stresses. Indeed, the value of 15 kPa is close to the calibrated vertical stresses obtained in the numerical analyses presented in Chapter 6 (section 6.4.2). For example, the values of the mean and deviatoric stresses (*p* and *q*, respectively) of element 1 depicted in Figure 6.19 b were determined based on the vertical stress depicted in Figure 7.15, considering the results of the tests with the frequency equal to 5.6 Hz. This element is also located on the top of the subgrade. As is possible to observe, the maximum vertical stress is 17.29 kPa, which is very close to the 15 kPa obtained in the embankment zone of the model.
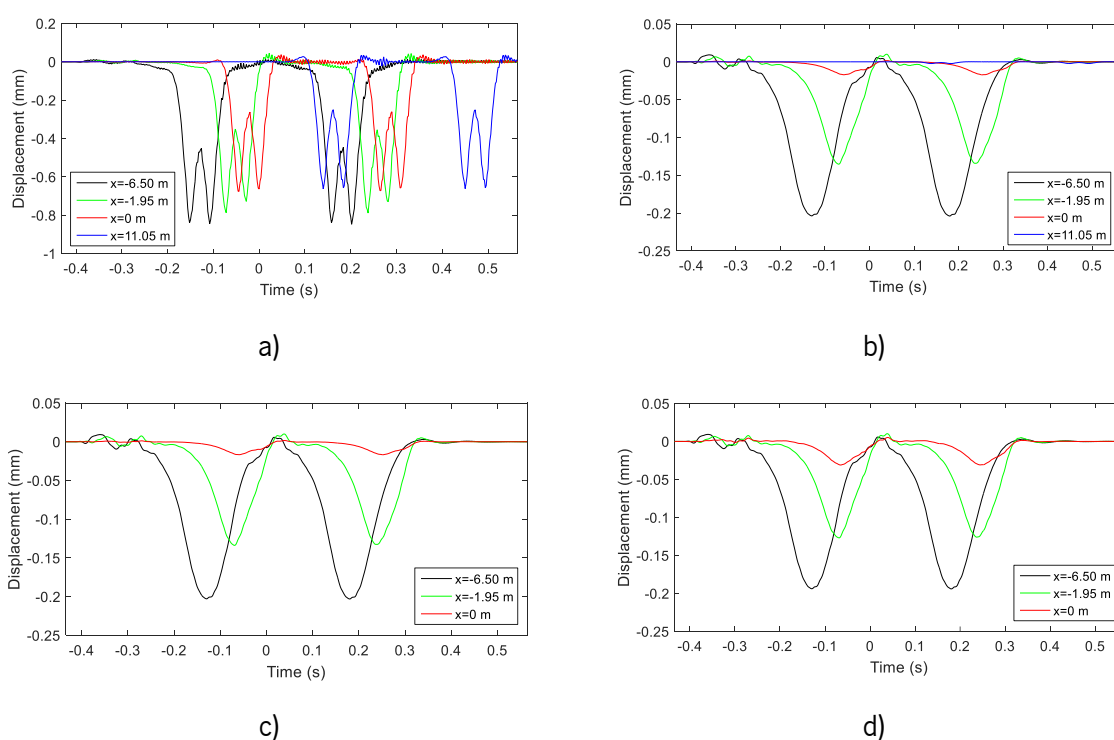
Figure 7.12 - Displacements on the top of the nodes of the: a) rails; b) concrete slab; c) FPL; d) subgrade

273

a)   b)
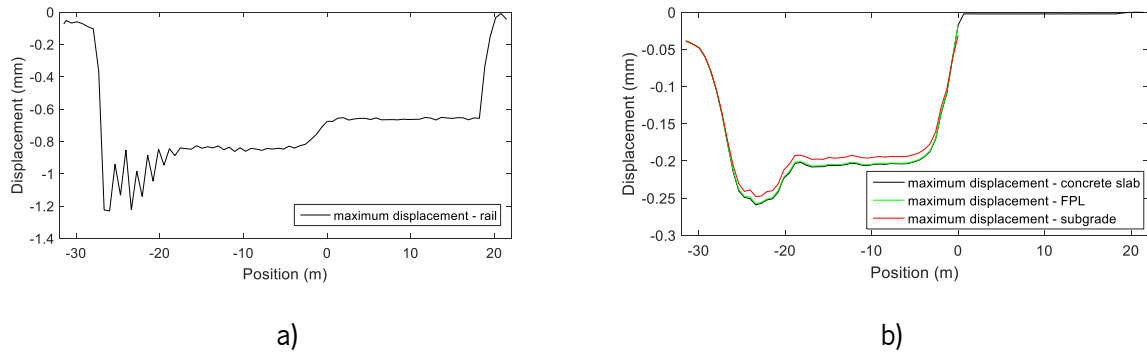
Figure 7.13 - Maximum displacement: a) of the rail along the track; b) of the concrete slab, FPL and subgrade along the track

a)   b)

c)   d)
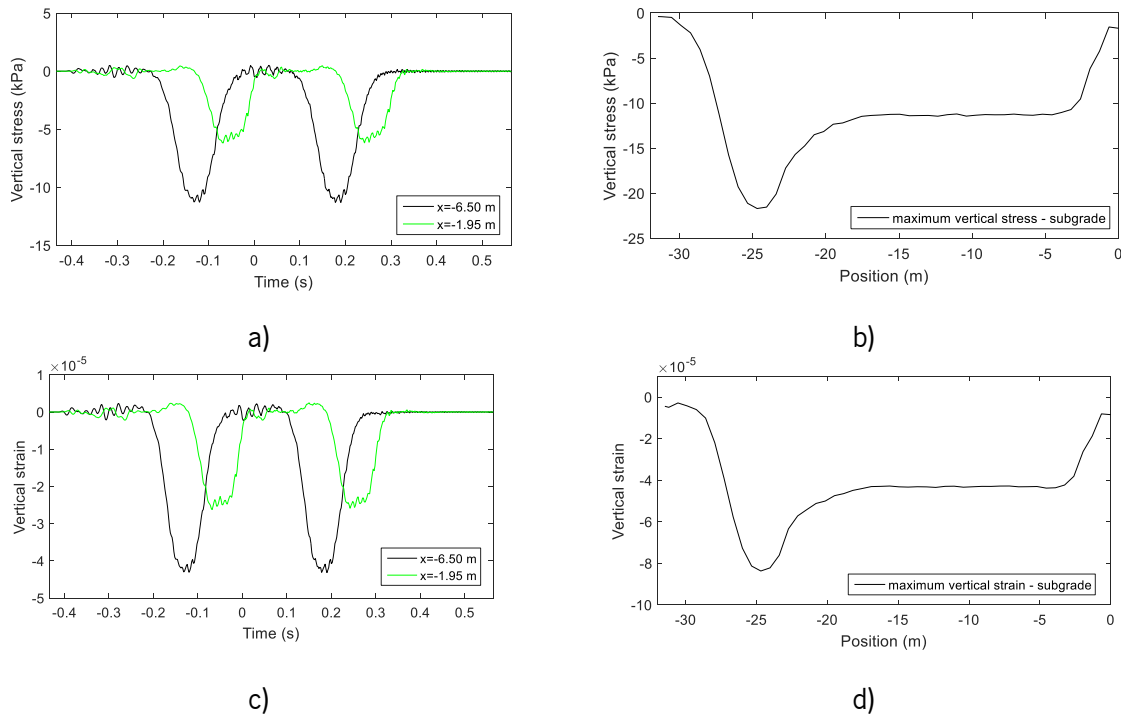
Figure 7.14 - Strain and stresses of the top nodes of the subgrade: a) subgrade – vertical stress; b) maximum subgrade stresses along the track; c) subgrade - vertical strain; d) maximum subgrade strains along the track
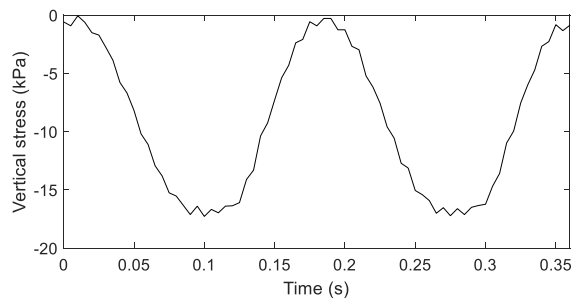
Figure 7.15 – Vertical stress of the calibrated numerical model – element 1

The previous results were obtained considering a time step of 0.002 s. However, in order to try to optimize the time of analysis, a parametric study was performed considering higher time steps. The displacements and stresses were compared in order to evaluate the effectiveness and efficiency of the modelling. The results were analysed in the nodes of the alignment under the loading area (top nodes of the selected layers, as in the previous analysis, in order to keep the consistency and compare the results). The

274

obtained results are depicted in Figure 7.16, Figure 7.17 and Figure 7.18. Figure 7.16, Figure 7.17 and Figure 7.18 show that the results with the time step equal to 0.005 s are not very close to the solutions with smaller time steps (the curves are not totally overlapped). On the contrary, the results with time steps equal to 0.002 s and 0.0025 s are very similar. These conclusions are mostly supported by the maximum displacements and stresses since it is possible to observe that the curves are almost overlaid. Since in the stress results of the subgrade there is a difference between the results with the time step 0.002 s and 0.0025 s, the time step=0.002 s was adopted and will be used in further analyses. The stress results are very important since are the main inputs on the study of long-term performance. The adoption of a smaller time step (for example t=0.001 s) would, on the one hand, significantly increase the calculation time and would not contribute to greater acuity/accuracy in the structure's response. Furthermore, the results with a time step=0.0025 s and time step=0.002 s are extremely close or even equal in some analyses, which means that a lower time step would not influence the response of the structure.

The total computation time considering a time step equal to 0.002 s varies and corresponds to, approximately, 2-5 days in a workstation with a processor INTEL ® Xeon ® platinum8160 CPU (2.10 GHz) and a RAM of 272GB. The computation time also depends on the use of the workstation even considering the option of using shared memory parallel with a number of processors equal to 20/24.

The effects of the contact elements imposed between the superstructure and substructure were also investigated. These contact elements were used to simulate the possible "detachment" between both elements (HBL and FPL) during and after the passage of the train. As expected, this phenomenon is close to the real behaviour of the railway structures in transition zones. Thus, the contact elements were implemented between the HBL (contact element) and FPL (target element). As mentioned previously, a time step equal to 0.002 s was adopted. However, this implementation is not straightforward. Thus, it is necessary to include the gravity effect on the contact elements. Otherwise, there is an uplift of the rail and concrete slab in sections before the transition zone, which does not correspond to the real behaviour of the structure. Some examples of these results are depicted in Figure 7.19. The results correspond to the top nodes of the rail, concrete slab and subgrade and they were obtained in the alignment under the loading. This type of behaviour is more evident in nodes placed in sections further from the transition zones. Furthermore, it is important to highlight that the *Normal penalty stiffness factor* (FKN) must not be so large since it can cause numerical instability. In this case, a *Normal penalty stiffness factor* equal to 1×10^{1} was used. Regarding the vehicle-track interaction, a *Normal penalty stiffness factor* equal to 1×10^{4} was used.

a)

b)

c)
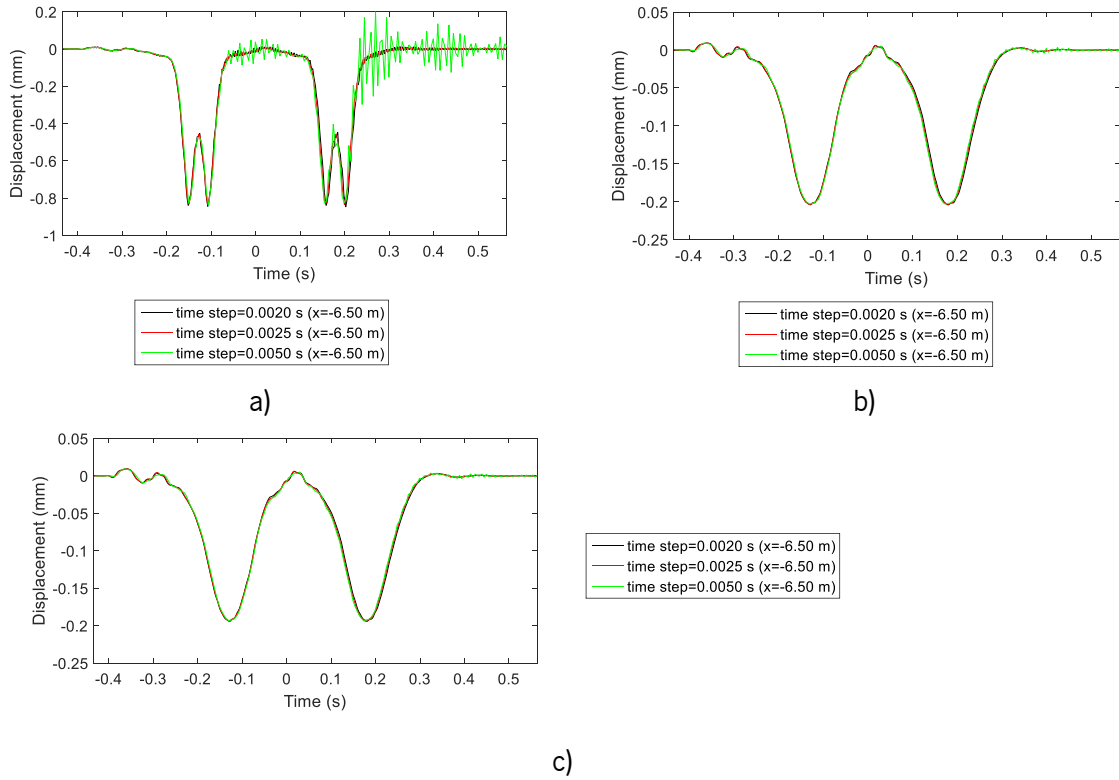
Figure 7.16 - Displacements at x=-6.50 m: a) rail; b) concrete slab; c) subgrade

a)

b)
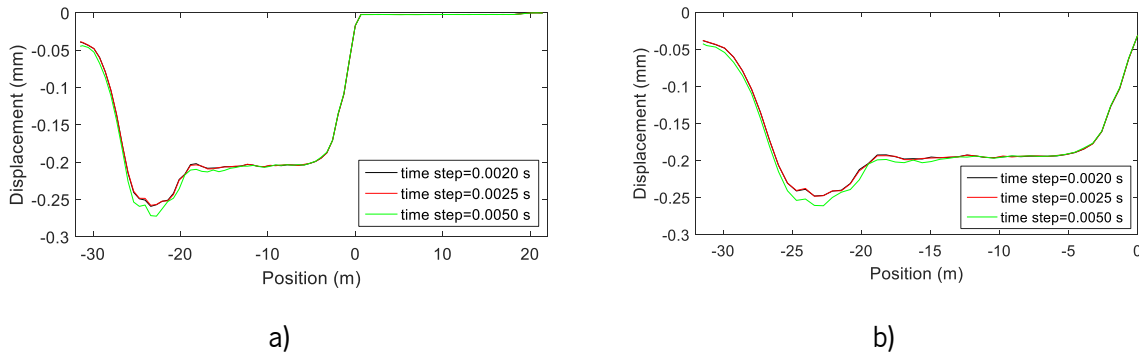
Figure 7.17 - a) Maximum concrete slab displacements of the top nodes along the track; b) maximum subgrade displacements of the top nodes along the track

a)

b)
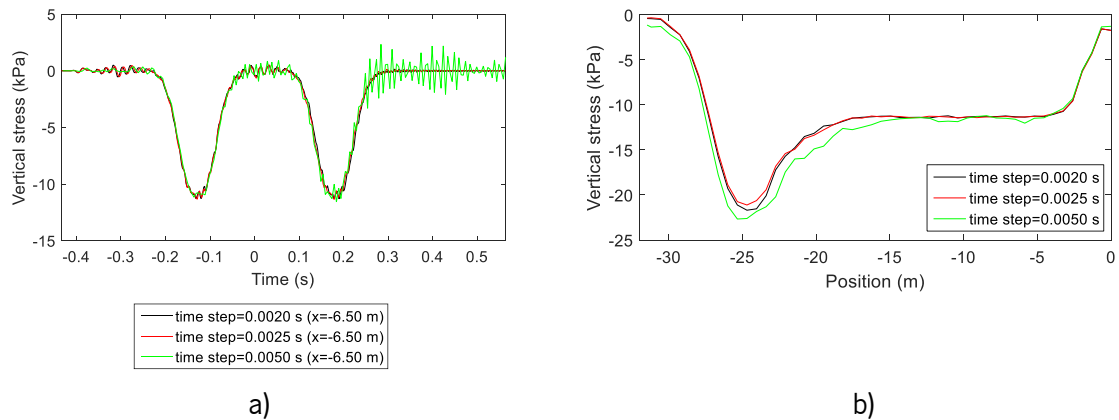
Figure 7.18 - a) Stresses at the top nodes of the subgrade at x=-6.5 m; b) maximum stresses at the top nodes of the subgrade along the track
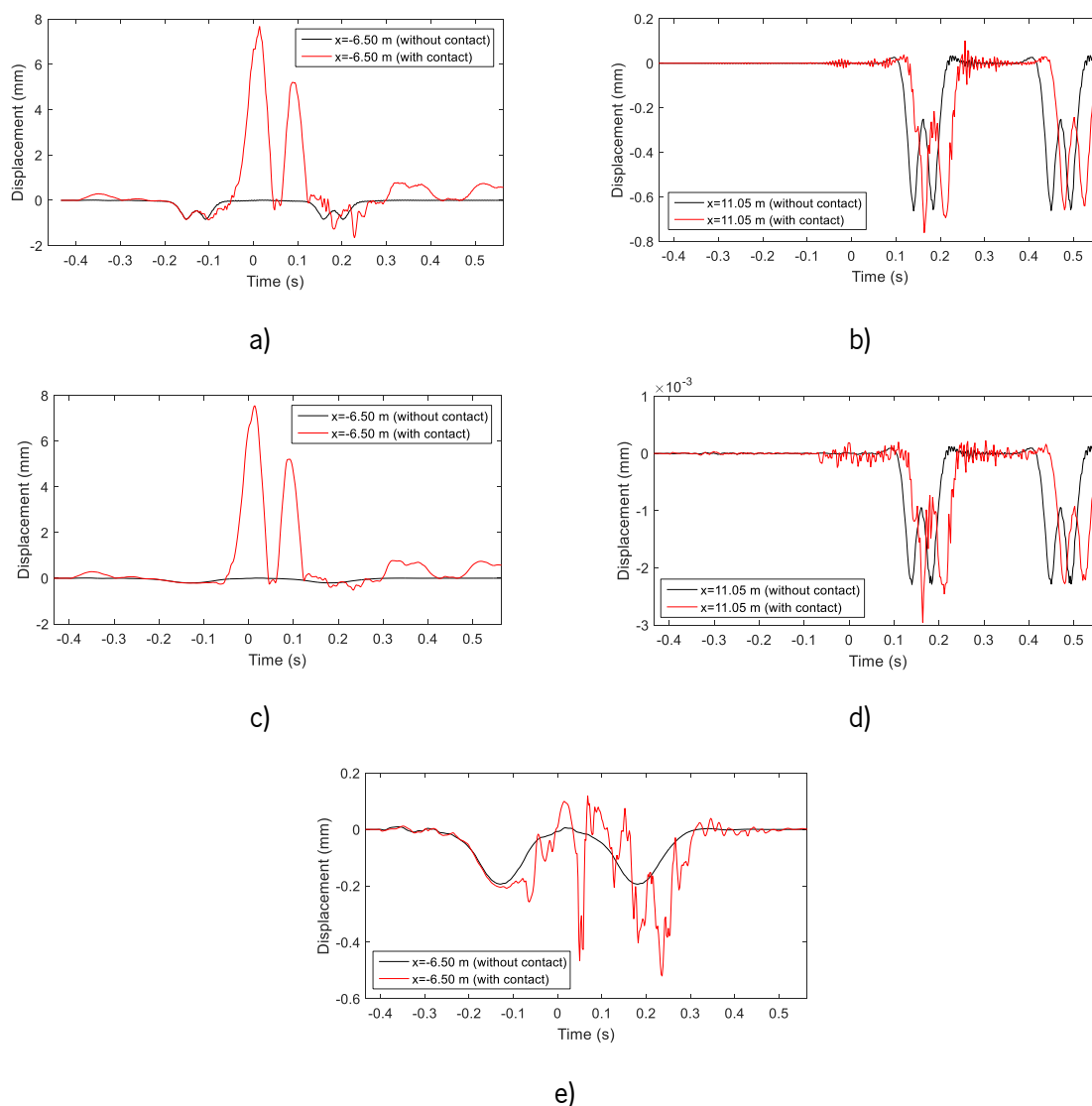
Figure 7.19 - Displacements (considering the contact elements but not considering the gravity effect): a) rail - before transition; b) rail – after transition; c) concrete slab (before transition); d) concrete slab (after transition); e) subgrade

The obtained results considering the gravity effects are depicted in Figure 7.20, Figure 7.21 and Figure 7.22. The comparison of the results with and without contact elements, with the gravity applied, is presented later.

Figure 7.20 a) shows that the rail's displacements reduce along the track, as well as the concrete slab, FPL and subgrade displacements (Figure 7.20 b), c) and d)). Figure 7.21 shows that the maximum displacements occur at the beginning of the loading, as in the previous cases, stabilizes and reduces near the transition zone. The same conclusions were obtained for the strains and stresses of the subgrade (considering the top nodes of the top elements). The maximum subgrade vertical stress is close to 40 kPa and its value varies along the track (Figure 7.22): first stabilize (with a value around 25 kPa) and then reduces in the sections close to the transition. In this case, it is important to highlight that the initial displacement (close to -0.3 mm) at x=-31.65 m depicted in Figure 7.21 is due to the effect of the gravity

load imposed by the superstructure. Otherwise, this value would be close to 0, which means that there would be no significant "residual displacements".

a)

b)

c)

d)
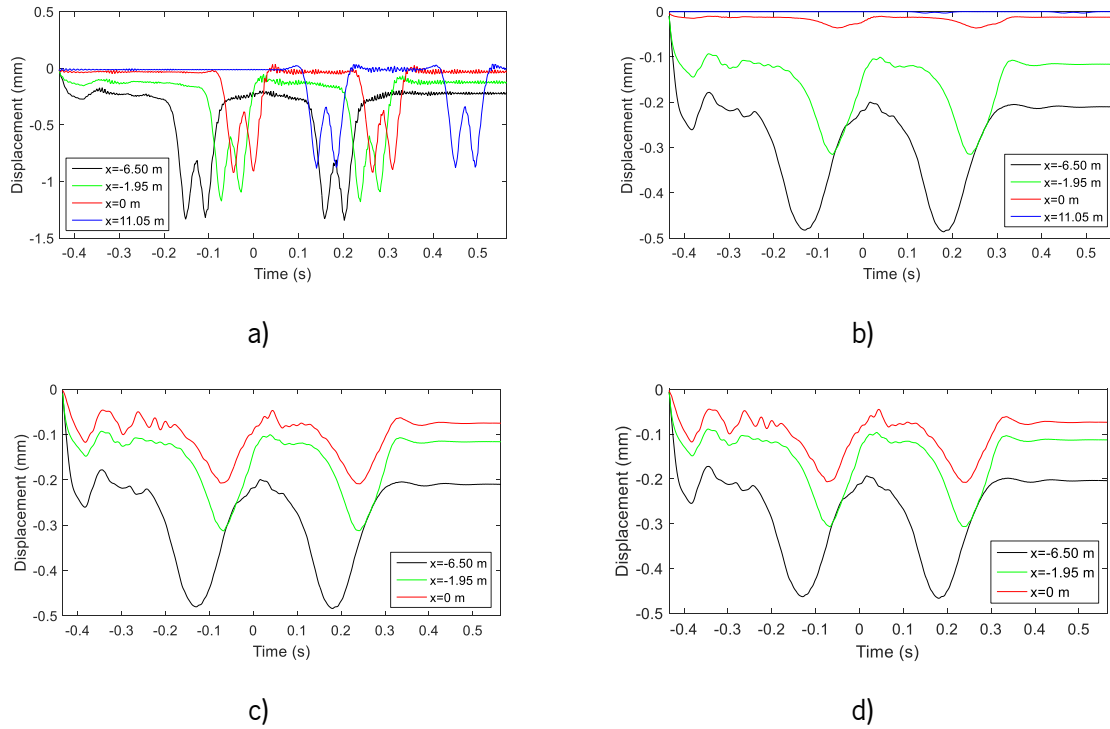
Figure 7.20 - Displacements on the top of the nodes of the (inclusion of contact elements and gravity load): a) rails; b) concrete slab; c) FPL; d) subgrade
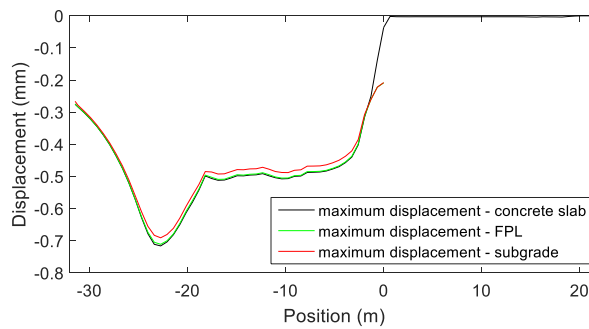
Figure 7.21 - Maximum displacement of concrete slab, FPL and subgrade along the track (inclusion of contact elements and gravity load; top nodes)
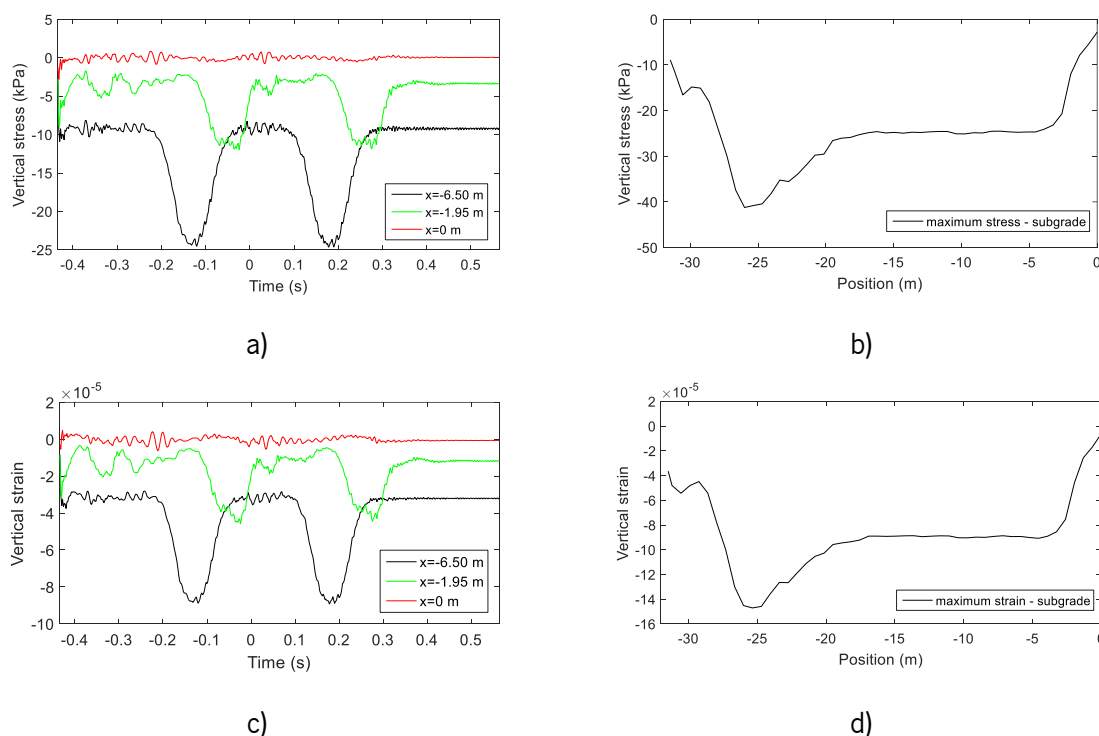
Figure 7.22 - Strain and stresses of the top nodes of the subgrade (inclusion of contact elements and gravity load): a) subgrade's stress; b) maximum subgrade stress along the track; c) subgrade's strains; d) maximum subgrade strain along the track

To comprehend the impact of the contact elements on the displacements and stresses, a comparison between the results with no contact and contact elements between the HBL and FPL materials is presented. The results were analysed in a section close to the transition zone (x=-1.95m), as depicted in Figure 7.23, Figure 7.24 and Figure 7.25. The results correspond to the top nodes of the rail, concrete slab and subgrade located under the loading alignment. As mentioned previously, the penetration value assumed in the contact problem (HBL-FPL) is FKN=1×10^{1}. A simulation with a higher value was considered, but the solution did not converge. Previous studies (Alves Ribeiro, 2012, Paixão, 2014) used a similar value in the simulation of contact problems of the ballasted track (sleeper-ballast contact).

In a comparison between the results with no contact and contact elements between the HBL and FPL materials, the effect of the gravity load was removed to compare the results. This means that the effect of the residual displacement at x=-31.65 m was removed. Nevertheless, there are some differences in the maximum displacement values. This is due to the inclusion of the contact elements on the model and possible detachments. Even so, the results are identical.

279

a)

b)

c)
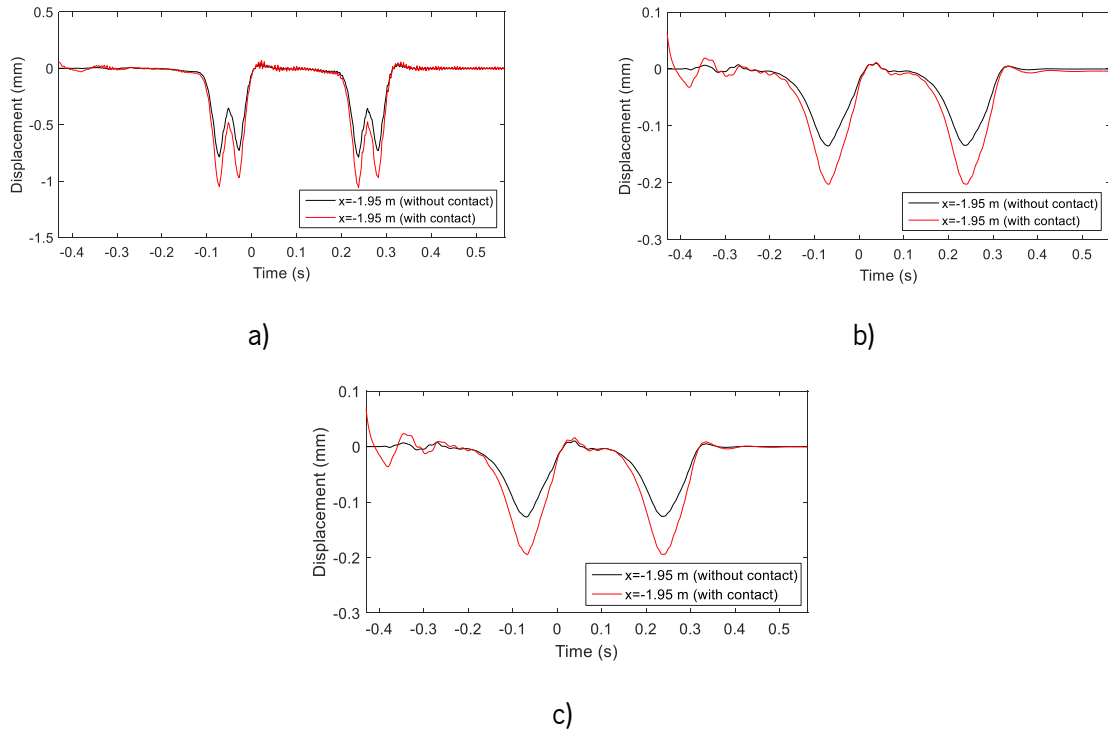
Figure 7.23 - Comparison of the displacements considering the inclusion of the contact and no contact elements: a) top nodes of the rails; b) top nodes of the concrete slab; c) top nodes of the subgrade
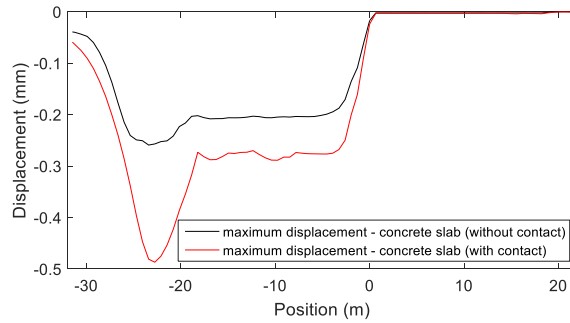
Figure 7.24 - Maximum displacement of the top nodes of the concrete slab along the track (comparison of the models with and without contact elements)

a)

b)
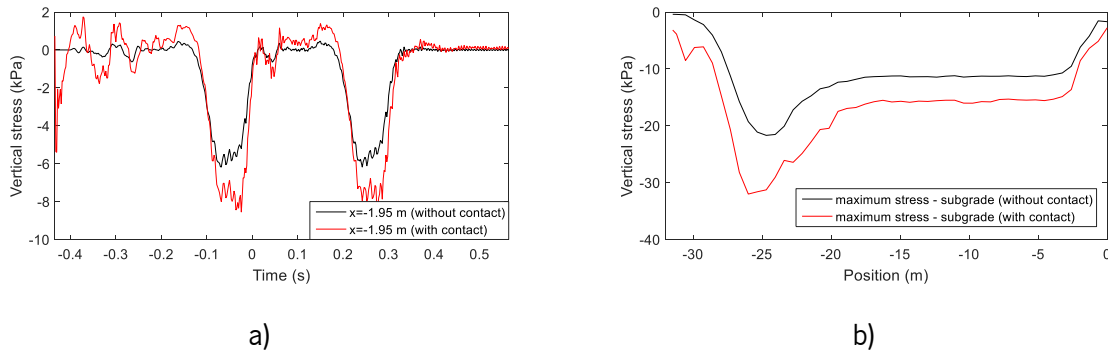
Figure 7.25 - Comparison of the stresses on the top nodes of the subgrade considering the contact and no contact elements: a) x=-1.95 m; b) maximum stresses of subgrade along the track

Analysing Figure 7.23, it is possible to state that there is an increment in terms of displacements equal to 33%, 50%, 53% in the rail, concrete slab and subgrade, respectively. From Figure 7.25 a), similar

conclusions are obtained regarding the stresses (increment equal to 64%). Regarding the maximum displacements and stresses of the subgrade (Figure 7.24 and Figure 7.25 b)) there is a maximum increment of 41% and 36% in the range between -18.5 m<x<0 m, respectively.

7.5.1.3   Passage of the first 4 bogies

In order to simulate the degradation process of the transition zone, the effects of the passage of the first 4 bogies of the *Alfa Pendular* were analysed. This is an interesting analysis since from the 4th bogie, there is a repetition of the geometry of the train. The passage of the 4 bogies allowed including the effect of the load and unload process and its repercussion in the stress path and stress levels, which are important variables in the evolution of the permanent deformation. Between the second and the third bogie, due to the reduced distance between both, the unloading process is incomplete, affecting the response of the structure.

In Figure 7.26 and Figure 7.27, the load and speed functions (respectively) related to the passage of the first four bogies considering a train's speed of 220 km/h are presented. In Figure 7.26 it is possible to verify that the beginning of the loading of bogie 3 is very close to bogie 2.
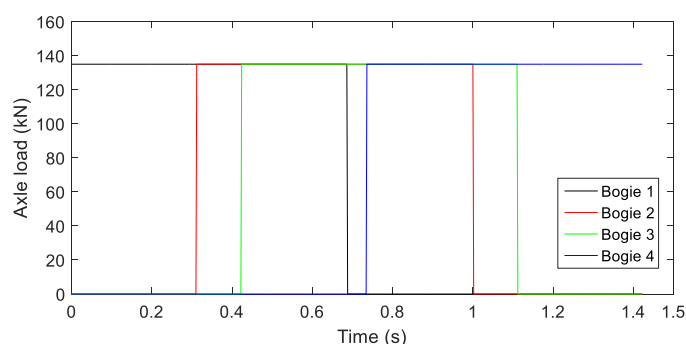
Figure 7.26 - Load function (4 bogies)
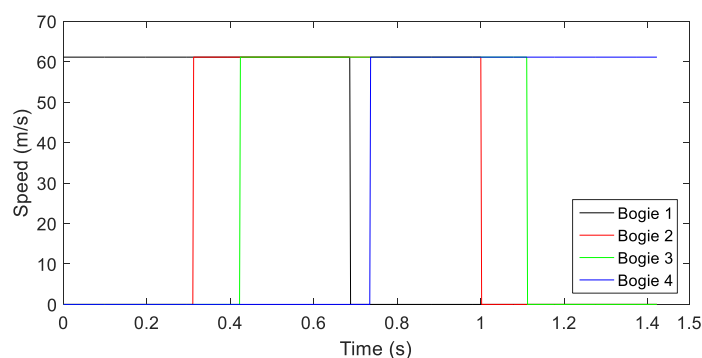
Figure 7.27 - Speed function (4 bogies)

Figure 7.28, Figure 7.29 and Figure 7.30 show the results regarding the displacements of the top nodes of the rail, concrete slab, FPL and subgrade and also the strains and stresses obtained on the top nodes of the subgrade. These results are obtained in the alignment under the loading, as in the previous analyses. After the presentation of the preliminary analyses and understanding of some phenomena on the model, such as the influence of the left boundary and the influence of the loading at the first meters of the model, the results along the track, from now one, will be presented without the consideration of that part of the model.

a)   b)

c)   d)
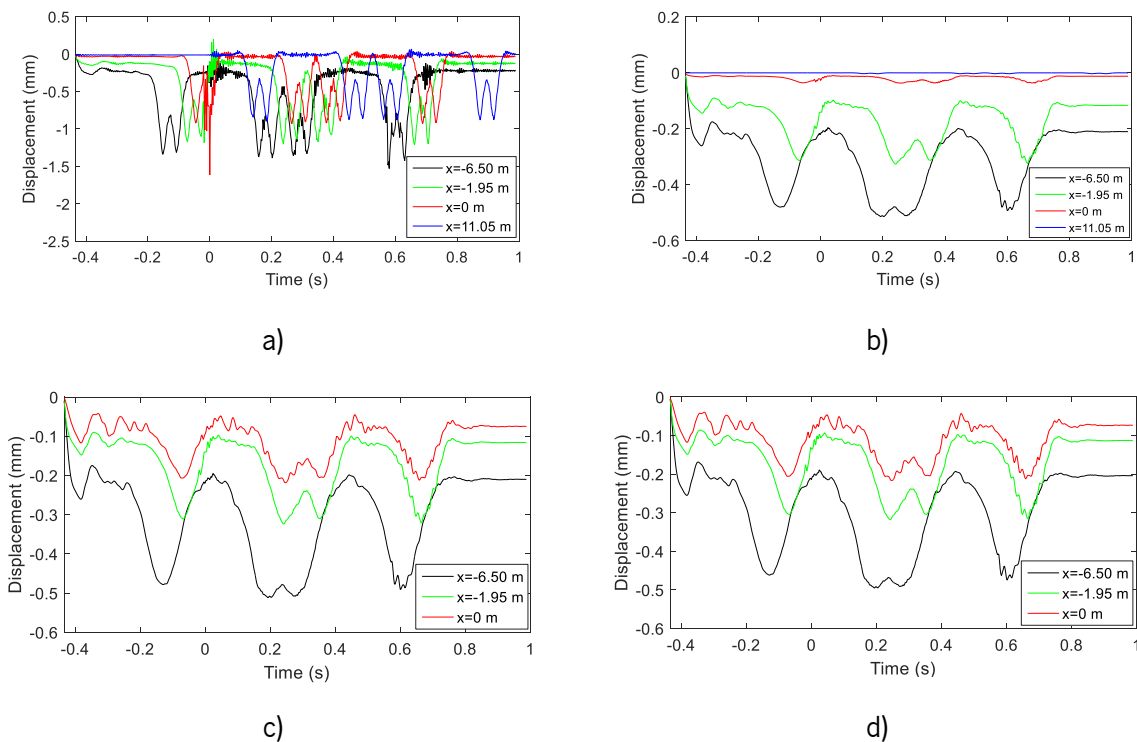
Figure 7.28 - Displacements on the top of the nodes of the (inclusion of contact elements – 4 bogies): a) rails; b) concrete slab; c) FPL; d) subgrade
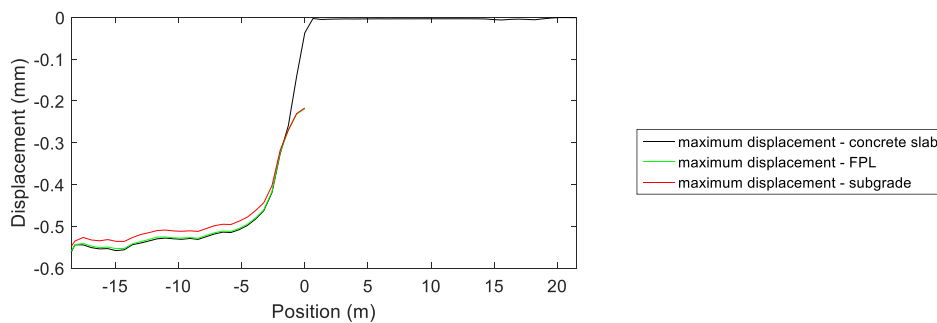
Figure 7.29 - Maximum displacement of the top nodes of the concrete slab, FPL and subgrade (inclusion of contact elements – 4 bogies) along the track
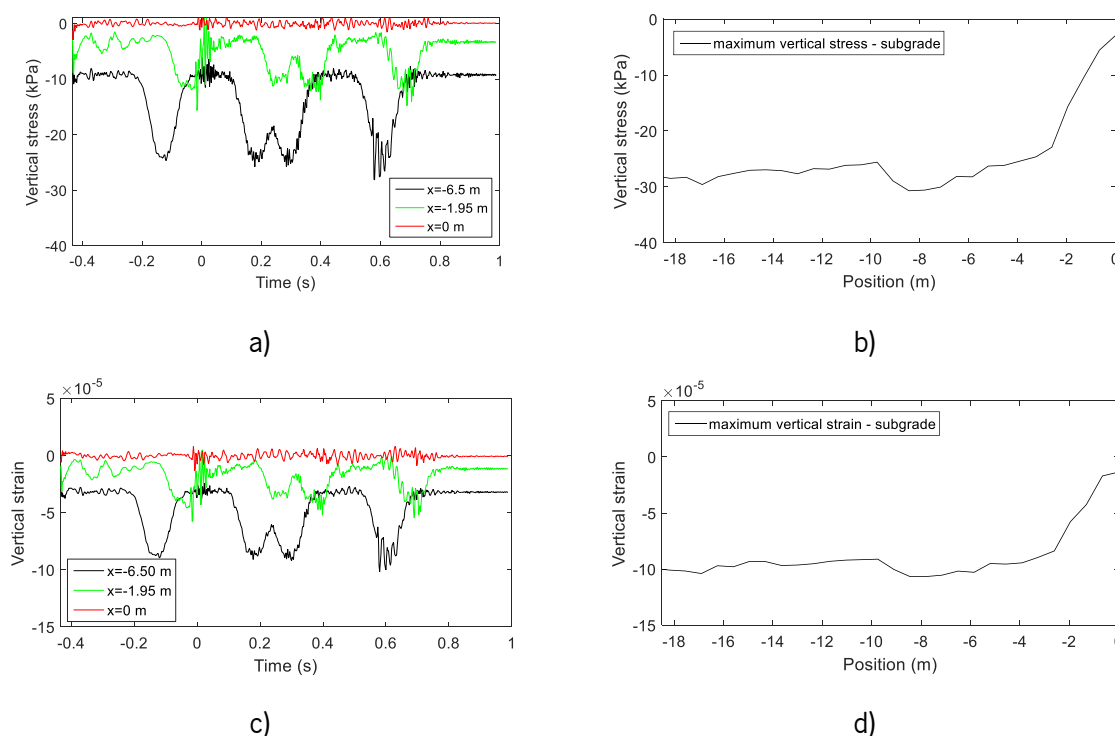
Figure 7.30 - Strain and stresses of the top nodes of the subgrade (inclusion of contact elements – 4 bogies): a) subgrade's stress; b) maximum subgrade stress along the track; c) subgrade's strains; d) maximum subgrade strain along the track

The magnitude of the displacements considering a certain time step (t=-0.086 s and t=1 s) is analysed in some elements of the model (rail, concrete slab, HBL, FPL and subgrade) considering all the nodes of the selected elements. The results are depicted in Figure 7.31 and the colour scale indicates the displacements in meters. This figure allows understanding the distribution of the displacements on the elements and the degradation process in the subgrade. The results show a maximum rail displacement close to 1.72 mm (when the time step is equal to -0.086 s). Regarding the concrete slab, HBL and FPL, the maximum displacement at t=-0.086 s is close to 0.59 mm and at t=1s, the maximum is close to 0.25 mm. Regarding the subgrade, the maximum displacement when t=-0.086 s is close to 0.56mm.

From the previous results, a comparison between the passage of the first 2 bogies and the 4 bogies was carried out to analyse its impact on the displacements and stresses. Figure 7.32 (d, e and f) shows that the main differences occur in sections far from the transition zone. In sections closer to the transition (e.g. x=-1.95 m), the magnitude of the displacements and stresses are very similar. This means that the results may be influenced by the proximity of the left boundary, but also by the incomplete unload and load process described previously since the distance between the second and third bogie is 6.90 m while the distance between the first and second bogies and third and fourth bogies is 19 m.
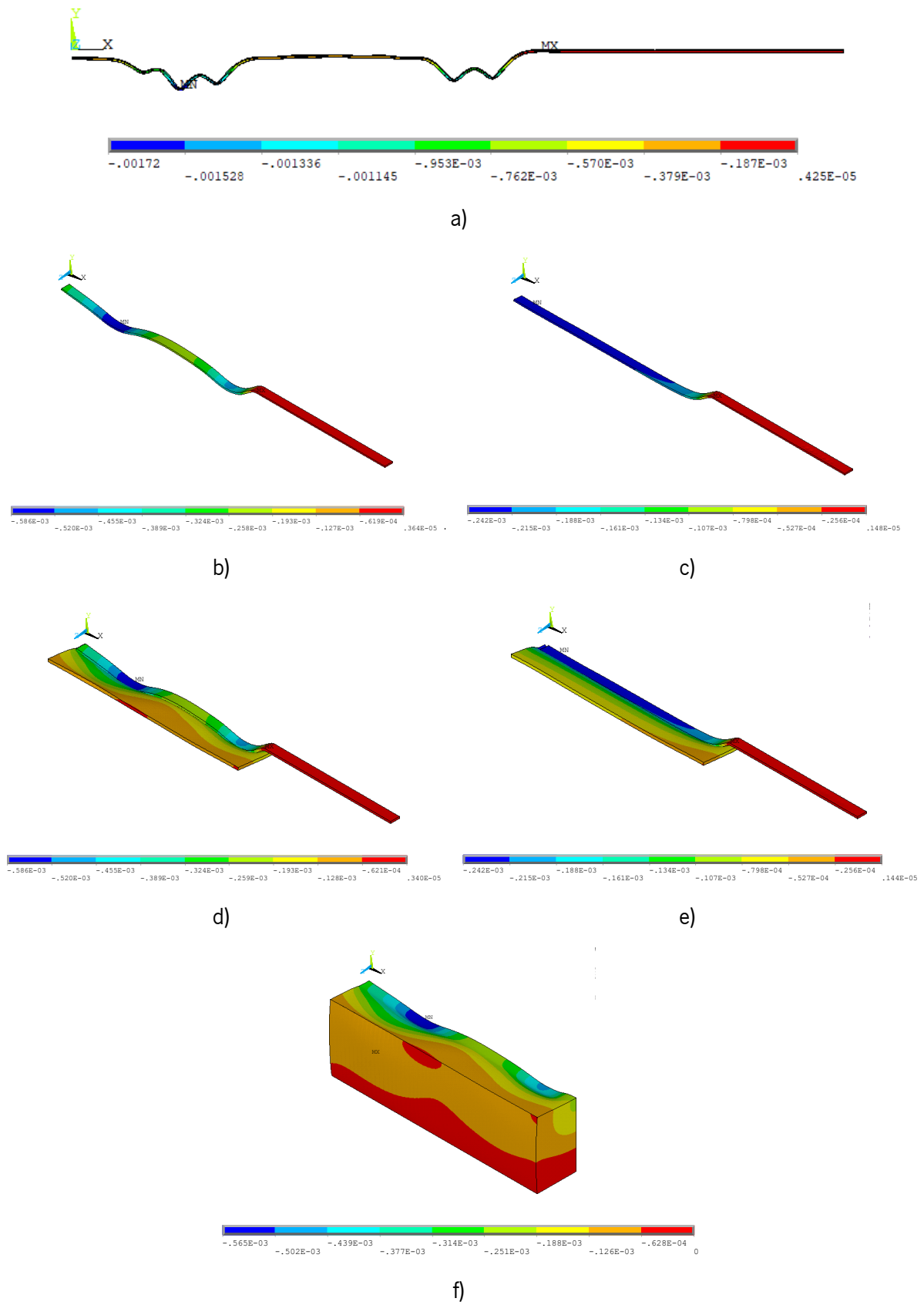
Figure 7.31 - Displacements of the nodes (in meters): a) rail (t=-0.086 s); b) concrete slab (t=-0.086 s); c) concrete slab (t=1 s); d) HBL and FPL (t=-0.086 s); e) HBL and FPL (t=1 s); f) subgrade (t=-0.086 s)

a)

b)

c)

d)

e)

f)
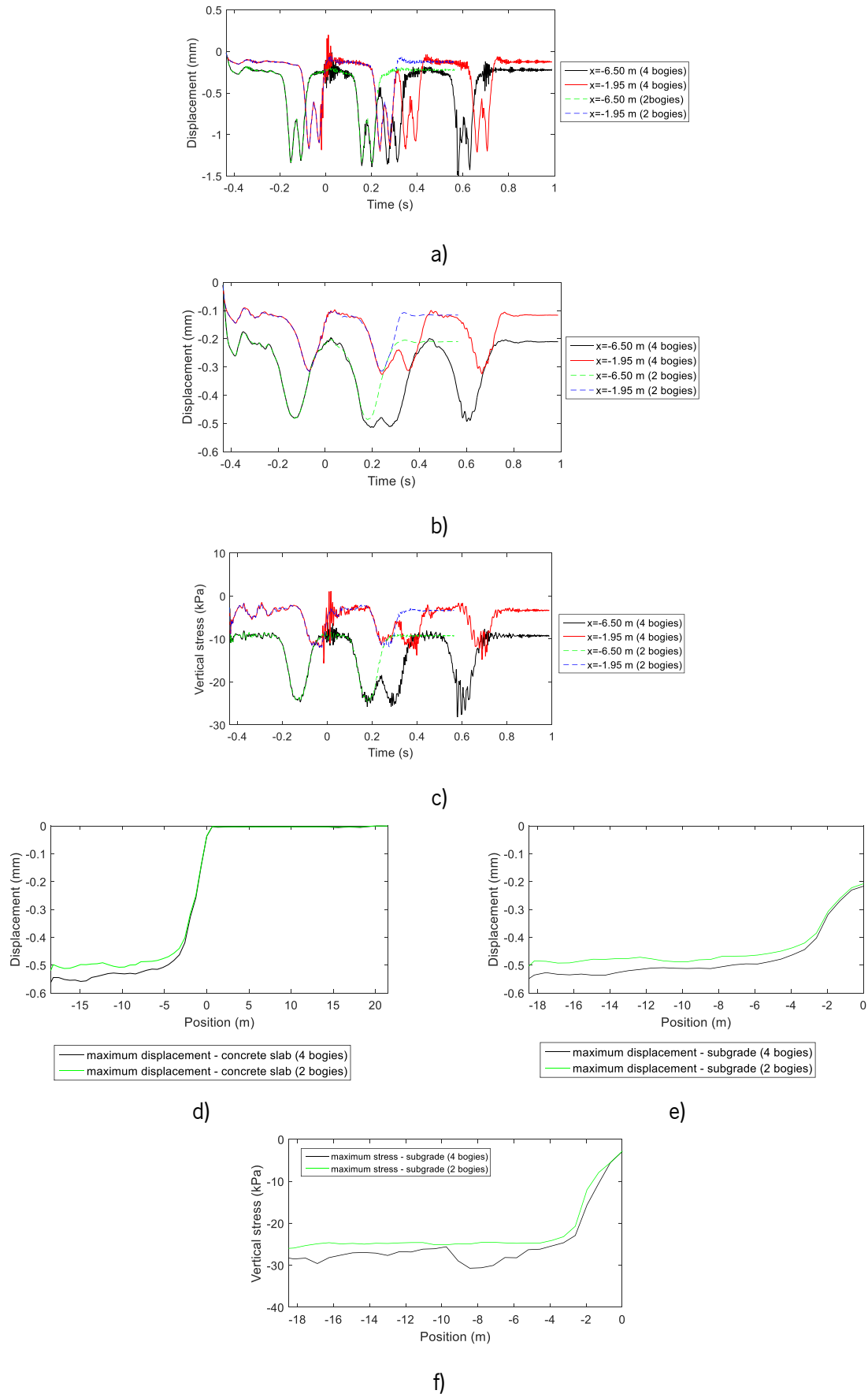
Figure 7.32 – Comparison of the results considering the passage of 4 and 2 bogies (top nodes): a) rail displacements; b) concrete slab displacements; c) subgrade stresses; d) maximum displacements – concrete slab; e) maximum displacements – subgrade; f) maximum stresses – subgrade

The analysis of the results of the modelling considering the passage of the four bogies is presented in more detail in the following sections.

7.5.1.3.1 Displacement of the wheel and interaction force vehicle-rail

The displacements, acceleration and interaction forces of axles of each bogie were determined. Figure 7.33, Figure 7.34 and Figure 7.35 show the results regarding the displacements, accelerations of the axles and interaction forces between the vehicle and rail.

Analysing Figure 7.33, the dynamic displacement experienced by the wheel of the vehicle during the passage of the transition zone constitutes a measure of the variation of the stiffness of the track. As it is possible to observe in Figure 7.33, the vertical displacement varies between 1.4 mm in the flexible zone and 0.85 mm in the stiffer zone, which corresponds to the tunnel. The decrease of the displacements of all the axles corresponds to the passage of the transition zone. The vertical dashed line represented in Figure 7.33 identifies the transition between the embankment and the tunnel (x=0m).
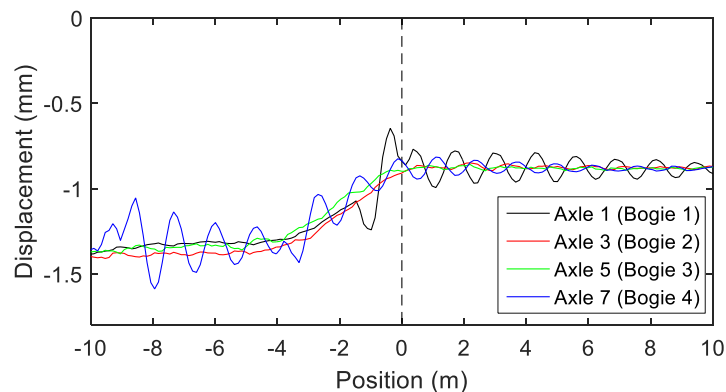
Figure 7.33 - Vertical dynamic displacements of the wheels of the vehicle

The maximum acceleration of the axle of the vehicle is another control parameter in the dynamic response of the vehicle, which can also be adopted to verify the performance of the transition zones. In Figure 7.34 the variation of the vertical acceleration of the first, third, fifth, and seventh axles of the vehicle are represented. As is possible to verify, some of the obtained values (axle 1 and axle 7) are above the alert limit, which is equal to 30 m/s^2, according to the limits established for the high-speed line Madrid-Seville (López-Pita et al., 2006). These limits are described in Table 3.3 from section 3.2.11. Axle 3 and axle 4 are far below the alert limit. The results show that there is an increment of acceleration's values of axle 1 during the passage of the transition zone. In the case of axle 7, this increment occurs slightly before the passage of the transition zone.

286
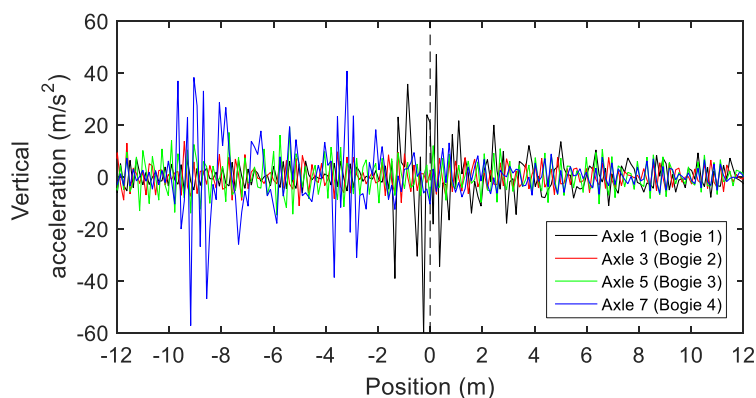
Figure 7.34 - Variation of the vertical acceleration

Figure 7.35 presents the interaction force wheel-rail. Thus, from the vertical acceleration of the axle of the vehicle, it is possible to estimate the variation of the dynamic component of the interaction force wheel-rail, as depicted in Figure 7.35. The dynamic component of the interaction force wheel-rail can be estimated by multiplying the vertical acceleration of the axle by the mass of the axle. Indeed, this is a very interesting approach since allows concluding that the monitoring of the vertical acceleration of the axle of the vehicle can be used to estimate the interaction forces of wheel-rail, which are more difficult to obtain. The results regarding the first and also the seventh axles show an increment of the force during the transition zone, followed by a reduction of the force in the stiffer zone of the track.
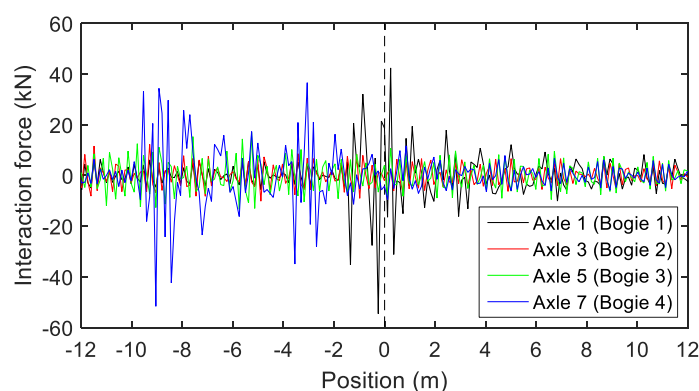
Figure 7.35 - Wheel-rail interaction force

7.5.1.3.2 Interaction forces HBL-FPL

The consideration of contact between the bottom of the HBL and the top of the FPL in the model allows analysing the transmitted forces or stresses to the FPL and identify the "detachment" phenomenon, which is basically similar to the phenomenon of the hanging sleepers in the ballasted track in transition zones. The consideration of the interaction HBL-FPL in a model of finite elements implies, as mentioned previously, the consideration of gravity forces induced by the superstructure of the track to avoid the

287

"uplift" during the dynamic analysis. Thus, gravity is applied at the beginning of the calculus before the passage of the vehicle. Since this is a tri-dimensional model, the type of contact between the FPL and HBL is different from the contact between the wheel and the rail (the type of contact is point-line). In this case, the type of contact is surface-surface (CONTA174 and TARGE170 in ANSYS software). Furthermore, to simulate properly the contact between the HBL (concrete material) and FPL (geomaterial), a friction coefficient of 0.62 was adopted. This value was determined considering ϕ=48° (section 6.4.2 from Chapter 6) and it is based on the following expression:

$$\mu = tan\left(\frac{2}{3}\phi\right)$$
(7.7)

This expression is commonly used to simulate the friction coefficient between the concrete and geomaterials and it is usually applied in the scope of the design of concrete walls to simulate its interface with the soil. Indeed, this value is not far from the reference value, which is 0.5.

In Figure 7.36, the interaction force HBL-FPL (in the alignment under the rail) is represented. Indeed, the nature of this contact is different from the wheel-rail contact and the results should be analysed in terms of contact stresses. However, the forces were extracted along the nodes (nodal forces) under the selected alignment. Thus, the results are presented in terms of forces and not stresses. However, the interaction/contact stresses can be obtained by multiplying the interaction forces by the influence area. Thus, to simplify the analysis and the data processing, the results regarding the interaction between the HBL and FPL are presented in this Chapter by the interaction forces and not by the stresses. The results depicted in Figure 7.36 show the interaction force in the time domain in a section far from the transition zone (x=-6.50 m) and also the variation of the maximum interaction forces along the track.

Analysing Figure 7.36 c), the interaction force varies between 0 kN and -40 kN. Unfortunately, since the FPL is not modelled in the tunnel, it is not possible to analyse the interaction force along the transition zone. As expected, there is a small increase in the computation time when the contact between the HBL-FPL is included.

...

a)

b)

c)
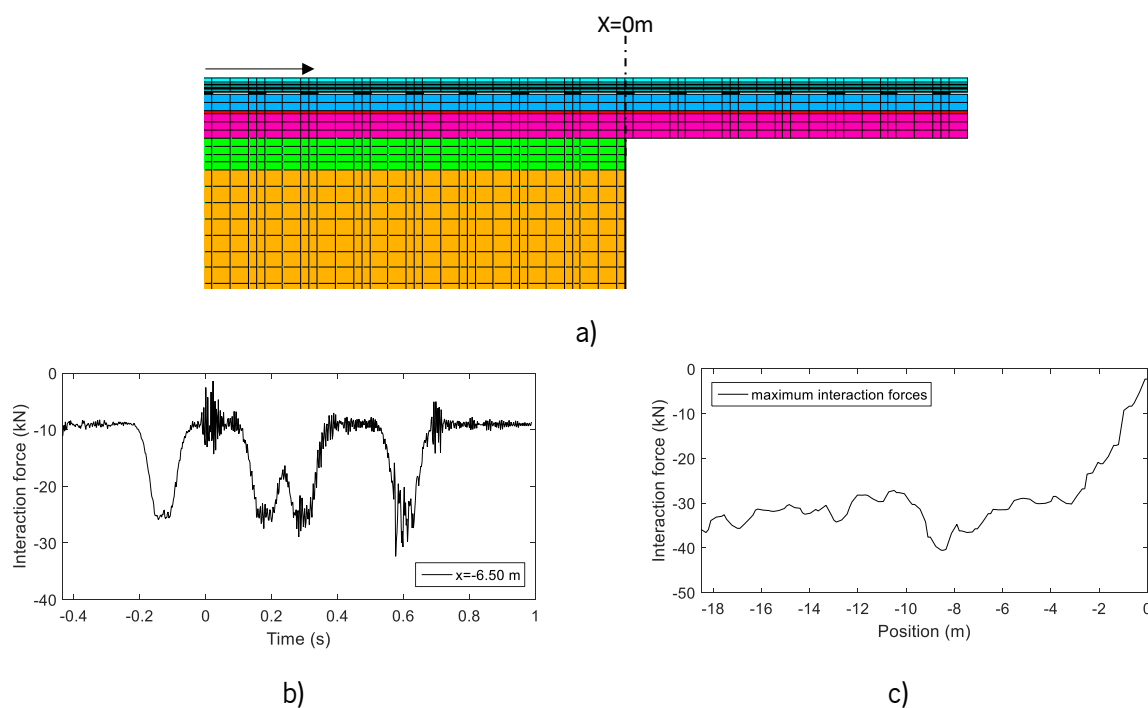
Figure 7.36 - a) Identification of the transition (x=0m) and direction of the movement; b) Interaction force HBL-FPL at x=-6.50 m; c) Maximum Interaction force HBL-FPL along the track

7.5.1.3.3 Track accelerations

In this section, the vertical accelerations of several components of the track are analysed: rail, concrete slab and HBL. This study aims to analyse the variation of this variable along the transition zone. Figure 7.37 shows the maximum and minimum values of the vertical acceleration in the central nodes of the rail over the railpads, along the transition zone. As is possible to observe, there is a slight increase of the vertical acceleration in the rail over the railpads in the transition zone (in the alignment of the loading). After the transition, there is a reduction of the accelerations. The accelerations are higher in the embankment when compared to the tunnel zone.
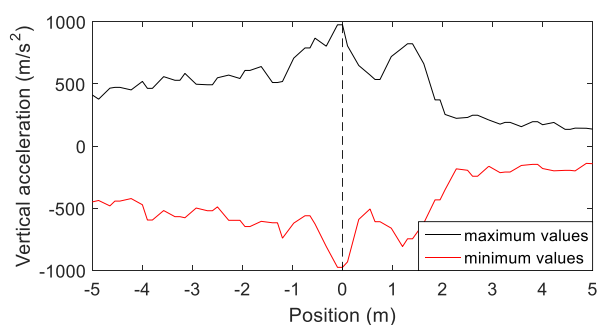
Figure 7.37 - Maximum and minimum values of the vertical acceleration of the rail along the transition zone

In Figure 7.38, the time records of the vertical acceleration on two sections of the concrete slab are presented. One section is located at the flexible zone and the other one is in the stiffer zone. In this

analysis, the bottom nodes of the concrete slab were selected, as depicted in Figure 7.38 a). This analysis was performed considering the cross-direction (*z*-axle).

a)

b)   c)
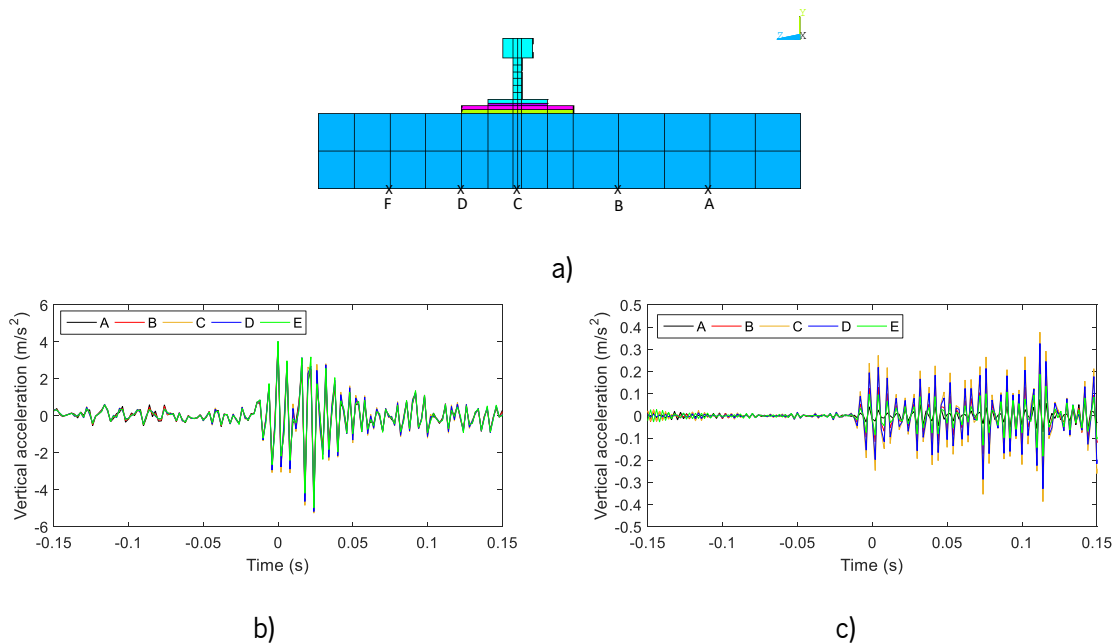
Figure 7.38 - Temporal register of the vertical acceleration of the concrete slab (bottom nodes): a) identification of the alignments; b) flexible zone (x=-6.50 m); c) stiff zone (x=6.50 m)

Analysing Figure 7.38, it is possible to conclude that the variation of the vertical acceleration along the cross-direction in the bottom of the concrete slab is not very relevant. This is due to the high stiffness of the structure. Indeed, the variation of the acceleration along the cross—direction could be relevant in the ballasted track, but not in the ballastless track. As expected, the results allow verifying that the vertical accelerations of the concrete slab are superior in the flexible zone, when compared to the stiffer zone, as also shows Figure 7.39.
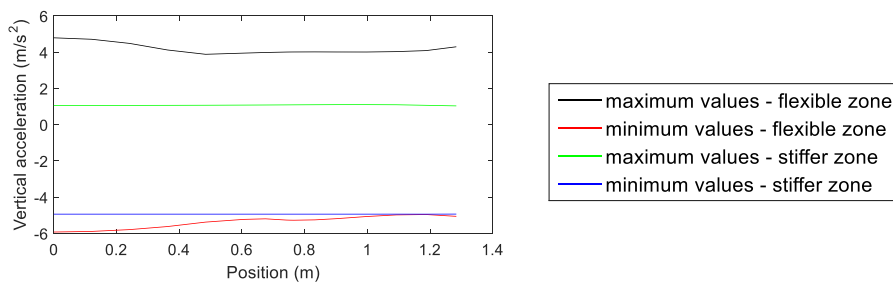
Figure 7.39 - Maximum and minimum values of the vertical acceleration on the bottom of the concrete slab along the cross-direction in the flexible and rigid zones

These results are also supported by the analysis of the vertical acceleration along the transition zone. Thus, in Figure 7.40 the maximum and minimum values of the vertical acceleration in the top and bottom nodes of the concrete slab along the transition zone are compared. This analysis was carried out in the alignment under the loading. Figure 7.41 presents the maximum and minimum values of the vertical

acceleration in the top and bottom nodes of the HBL along the transition zone (also under the loading alignment).
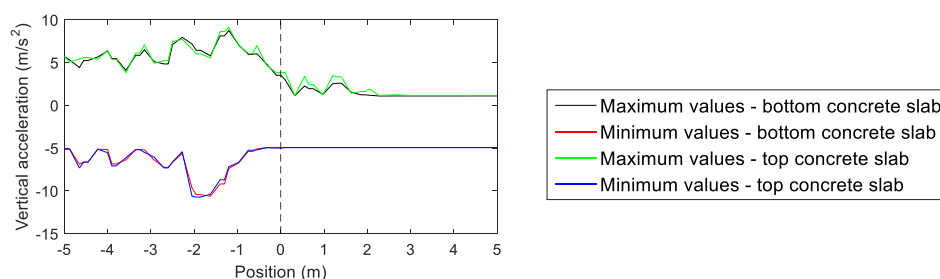
Figure 7.40 - Maximum and minimum values of the vertical acceleration of the concrete slab along the transition zone
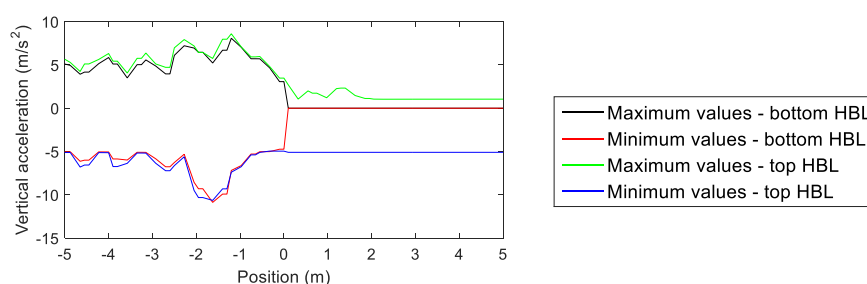
Figure 7.41 - Maximum and minimum values of the vertical acceleration of the HBL along the transition zone

The results show that the maximum values of vertical acceleration at the top nodes of the concrete slab are almost equal to the maximum values of the vertical acceleration at the bottom of the concrete slab. The same conclusions are obtained regarding the minimum vertical accelerations. The results also show a decrease in the vertical acceleration on the transition. Regarding the HBL, the results show that the maximum values of the vertical accelerations at the top nodes of HBL are almost equal to the maximum values of the vertical accelerations at the bottom of this element. The same conclusions are obtained regarding the minimum vertical accelerations. At the transition, there is a decrease in the vertical accelerations. The magnitude of the vertical accelerations on the concrete slab is similar to the vertical accelerations of a ballastless track presented in the work developed by Shan et al. (2013), where two different transition zones between a bridge and an ordinary subgrade are investigated by the finite element method (see section 3.2.9 from Chapter 3). In this work, the vertical accelerations of the concrete slab vary between 3.5 m/s² and 6 m/s².

From these conclusions, it is possible to state that the railway structure is very stiff, which means that the degradation process is less visible when compared to the ballasted track. The vertical accelerations of the concrete slab along the transition zone are higher in the flexible zone when compared to the stiffer zone and there is a slight increase immediately before the transition zone in the flexible zone in the concrete slab and HBL.

7.5.1.3.4 Track stresses

After the analysis of the track accelerations, the stress results are presented and analysed in more detail. Since this is a 3D model, the analysis is performed for the alignments represented in the cross-section of the model (Figure 7.42), where the first alignment (1) corresponds to the plane *xy* where z=0m. These results help to understand the evolution of the stresses along the transition zones. Thus, in Figure 7.43, the maximum values of the vertical stresses on the top nodes of the concrete slab, HBL, FPL and subgrade are presented considering two sections located on flexible and stiffer zones (only for the concrete slab and HBL).
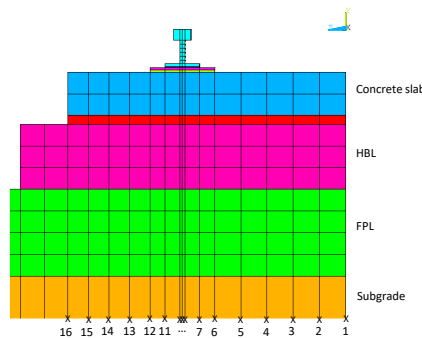
Figure 7.42 - Cross-section of the model (identification of the alignments)

a)

b)

c)
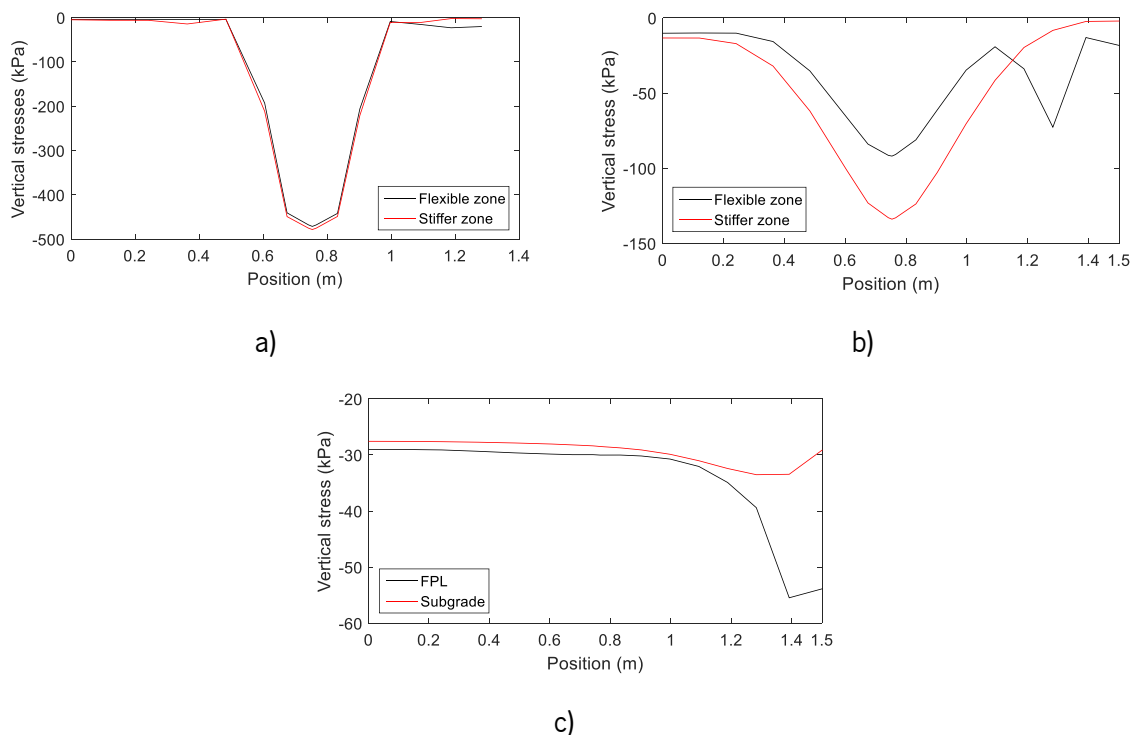
Figure 7.43 - Maximum vertical stress along the cross-sections of a stiffer and flexible zone (top nodes): a) concrete slab; b) HBL; c) FPL and subgrade

292

Thus, based on the previous results, it is possible to conclude that the maximum values of the vertical stresses present variations in the cross-direction of the track. This phenomenon was not so visible in the results of the accelerations on some elements of the track.

Regarding the concrete slab, the stresses are higher under the loading zone and tend to decrease in the extremities (alignments 1 and 16). In the case of the HBL, the stresses are also maximum under the rail and also tend to decrease in the extremities. Furthermore, the results also show that the stresses are higher on the section located in the stiffer zone. In the case of FPL and subgrade, the stresses tend to increase (mostly the FPL) in the direction of one of the extremities (alignment 16), which means that the permanent deformation will be higher in that zone. Both in the rigid and flexible zones, the stresses tend to decrease in-depth, from the concrete slab to the subgrade.

In Figure 7.44, Figure 7.45, Figure 7.46 and Figure 7.47, the maximum and minimum values of the vertical and longitudinal stresses (tensile and compression) obtained along the transition zone at the top and bottom nodes of the concrete slab and HBL are presented, respectively. The points on the graph correspond to the nodal stresses of each finite element. These results are obtained for the nodes under the rail (alignment 9 of Figure 7.42).
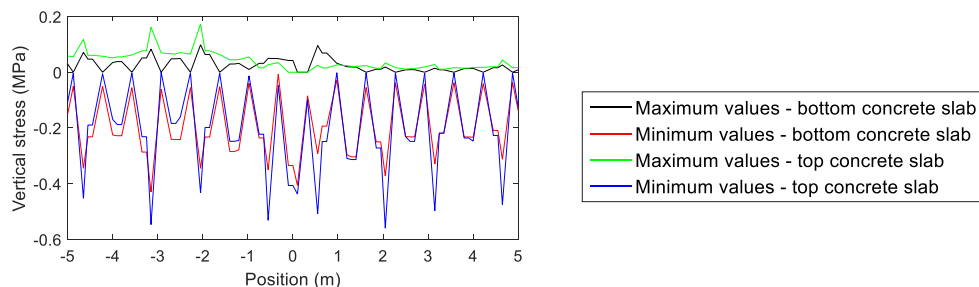
Figure 7.44 - Vertical stress in the top and bottom nodes of the concrete slab along the transition zone
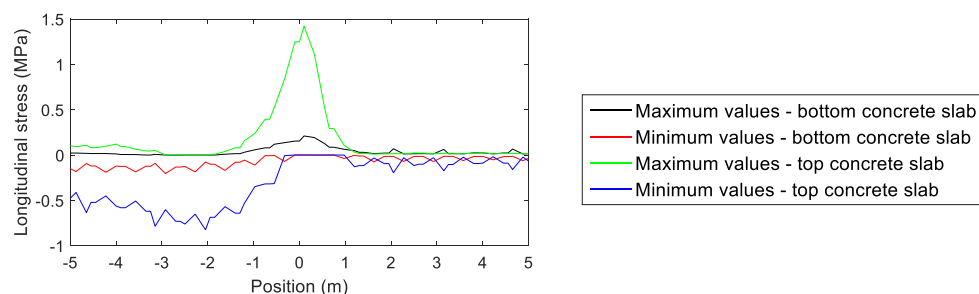
Figure 7.45 - Longitudinal stress in the top and bottom nodes of the concrete slab along the transition zone

293
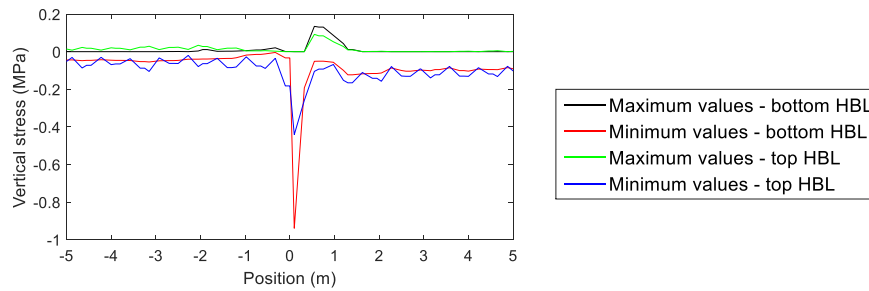
Figure 7.46 - Vertical stress in the top and bottom nodes of the HBL along the transition zone
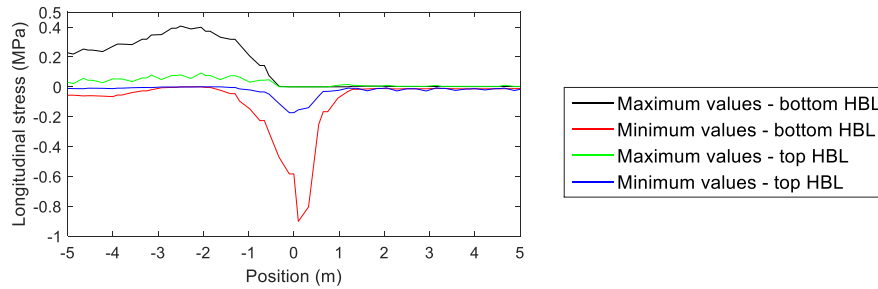
Figure 7.47 - Longitudinal stress in the top and bottom nodes of the HBL along the transition zone

Regarding the concrete slab, it is possible to identify a peak in the transition zone in terms of longitudinal stresses (maximum values at the top of the layer). Analysing the vertical stresses, there is no clear peak in the transition zone, as in the longitudinal stresses. In the HBL, the analysis of results shows that in the transition zone, there is an increase of the vertical stresses (compression). The conclusions are similar regarding the longitudinal stresses. These layers (concrete slab and HBL) allow connecting the embankment and the tunnel, ensuring the continuity of the track and, because of that, are submitted to a complex stress field aggravated due to the variation of the stiffness of the track in the transition. Furthermore, the results also show that in the stiffer zone, the vertical stresses on the top nodes of HBL are slightly higher when compared to the flexible zone.

Despite the importance of the vertical and longitudinal stresses, since the passage of the train causes a multi-directional stress field, the analysis of the mean and deviatoric stresses is interesting because considers the normal and shear stresses.

The mean and deviatoric stresses were obtained considering the following procedure:

1. Determination of the vertical, horizontal and shear stresses of the elements;
2. Based on the previous register, the principal stresses are obtained for each finite element;
3. The mean and deviatoric stresses are determined.

In Table 7.5, the maximum values of the mean and deviatoric stresses induced by the passage of the train (the geostatic stresses are not included) are presented considering distinct sections: one placed at

the flexible zone (x=-16.9 m) and the other one placed immediately after the transition zone (x=-0.325 m). These values were obtained on the top nodes of the FPL and subgrade in the alignment under the loading. The results show that there is a higher concentration of stresses in the flexible zone that tends to decrease in the direction of the transition. Figure 7.48 shows the sum of the incremental and geostatic stresses of the FPL and subgrade elements in the flexible zone as well as its position to the failure line. The results show that the stress paths and respective peaks are far from the yielding criteria.

This type of analysis is interesting since these stresses (mean and deviatoric) are the main inputs in the simulation of the evolution of the permanent deformation of the track.

Table 7.5 – Maximum mean and deviatoric stresses in two sections: flexible and immediately before the transition

Material	Flexible zone (embankment)		Transition*	
	p_{max} (kPa)	q_{max} (kPa)	p_{max} (kPa)	q_{max} (kPa)
Top nodes of the FPL	22.65	20.82	3.137	10.95
Top nodes of the Subgrade	16.8	19.56	2.794	3.674

*In the flexible zone, immediately before the transition to the stiffer zone
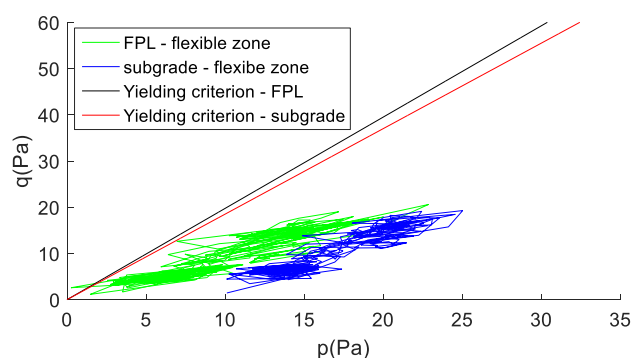
Figure 7.48 – Stress paths of the top elements of the FPL and subgrade at x=-16.9 m (flexible zone)

7.6 Modelling of the permanent settlement

The prediction of the settlement's evolution of the track implies knowledge about the long-term behaviour of the materials and the selection of the models that can traduce properly the dynamic behaviour of the track. Indeed, the long-term behaviour of the different materials when submitted to a cyclic loading (mostly in terms of the axial response) has been extensively explored, as shown in Chapter 4. However, the incorporation of these results and deformation laws in complete models of the track is still a little explored field. For example, Bruni et al. (2002) defined a numerical procedure to simulate the settlement's evolution of the track in a transition zone due to the permanent deformation of the ballast layer. The adopted numerical model allowed considering the vehicle-track interaction and determining the induced forces by the vehicle at the top of the ballast layer, under each sleeper. The forces were used to determine

the settlement of each sleeper at the end of a certain number of loading cycles. Similar procedures were adopted to simulate the permanent deformation as described in the work developed by Hunt (1996), Fröhling (1997), Abdelkrim et al. (2003), Ferreira (2010), Wang and Markine (2018a) and more recently in Grossoni et al. (2021).

According to Alves Ribeiro (2012), the simulation of the permanent deformation of the track based on this procedure is extremely versatile and can be adopted independently of the type of model or laws of permanent deformation.

Thus, one of the goals of this thesis and this Chapter in particular, is the study of the long-term behaviour of a railway structure placed in a transition zone. Therefore, a methodology was developed to simulate numerically the evolution of the permanent deformation of the track. In this study, the evolution of the permanent deformation is only considered on the FPL and subgrade layers, applying the model developed by Chen et al. (2014) used in the previous Chapters and the parameters already calibrated in Chapter 6. This methodology is based on the number of load cycles and also on the stress levels induced by the passage of the train on the geomaterials that constitute the track. In this process, each load cycle corresponds to the passage of one axle train, which means that the passage of the *Alfa Pendular* is equivalent to 24 load cycles. During the simulation of the long-term behaviour of the ballastless track in a transition zone, the evolution of the permanent deformation and the resulting dynamic effects are analysed in detail.

This simulation method is based on the work developed by Alves Ribeiro (2012). However, in this case, a 3D model was considered while in the original work, a 2D model was used to study the behaviour of the transition zones. The simulation method consists of an implemented iterative process through the articulation between the software ANSYS and the software MATLAB, according to the flow chart represented in Figure 7.49. Thus, in the commercial software ANSYS, the numerical modelling of the vehicle and the track is performed, as well as all the processes related to pre and post-processing of the results. In the commercial software MATLAB, the results of the dynamic analysis are imported, and, based on the stress results, the permanent deformation is obtained (through the implementation of the permanent deformation law(s)).

Numerical model of system vehicle-track

Geometry of the track

ANSYS

Dynamic analysis with interaction vehicle-track

Inclusion of contact elements between the super and substructures

Stresses on the subgrade of the track (σ_i)

ANSYS

MATLAB   Permanent deformation laws → $f(N,\sigma)$

Permanent deformation of the substructure

$N=N+\Delta N$

$$\varepsilon = \varepsilon(N) + \varepsilon(\Delta N)$$

MATLAB
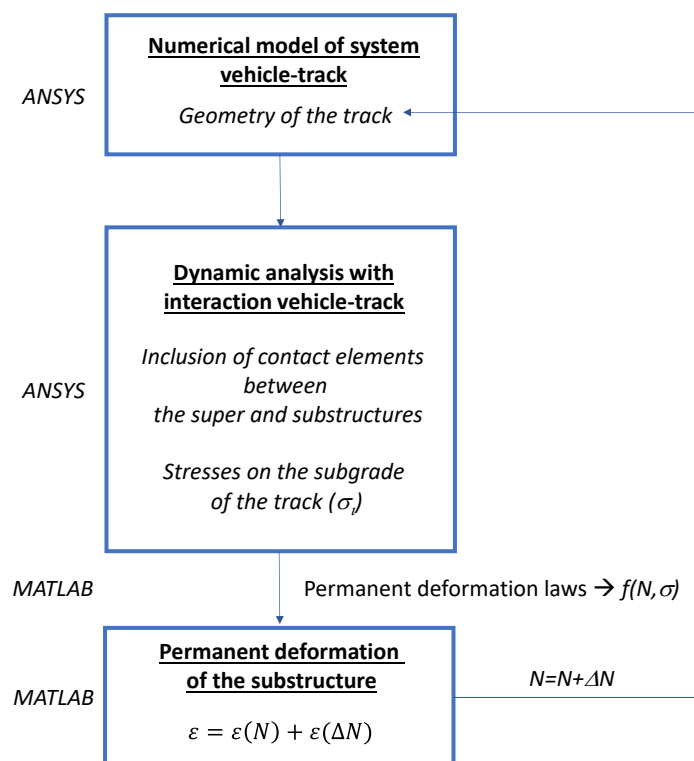
Figure 7.49 - Schematic representation of the simulation process of the permanent deformation of the track (adapted from Alves Ribeiro (2012))

To apply this methodology, all the layers of the track need to be modelled with finite elements that accurately provide information about the state stress verified during the passage of the vehicle. In this case, since the analysis is focused on a ballastless track, this methodology is only applied to the substructure that includes the FPL and subgrade. In the case of a ballasted track, this methodology should be applied to the ballast, sub-ballast and foundation materials.

Thus, after the performance of the dynamic analysis, all the stresses were obtained (vertical, horizontal and shear) in all finite elements of the FPL and subgrade, which are the only materials that significantly contribute to the permanent deformation. The variation of the stresses throughout time in each layer of the track is stored in a matrix, which dimensions depends on the number of time increments (time step) of the analysis and the number of the nodes of the finite elements considered (in this case, all the elements and nodes of the FPL and subgrade were considered). The matrices are 2D [number of time increments ×number of nodes of finite elements in the selected plane] considering a certain longitudinal section of the track in the plane *xy* (Figure 7.50a). The methodology is then replicated to all longitudinal sections of the track, as depicted in Figure 7.50b) (*n* sections). The *n* 2D matrices are obtained for each stress type (σ_x, σ_y, σ_z, σ_{xy}, σ_{xz}, σ_{yz}).

297

a)   b)
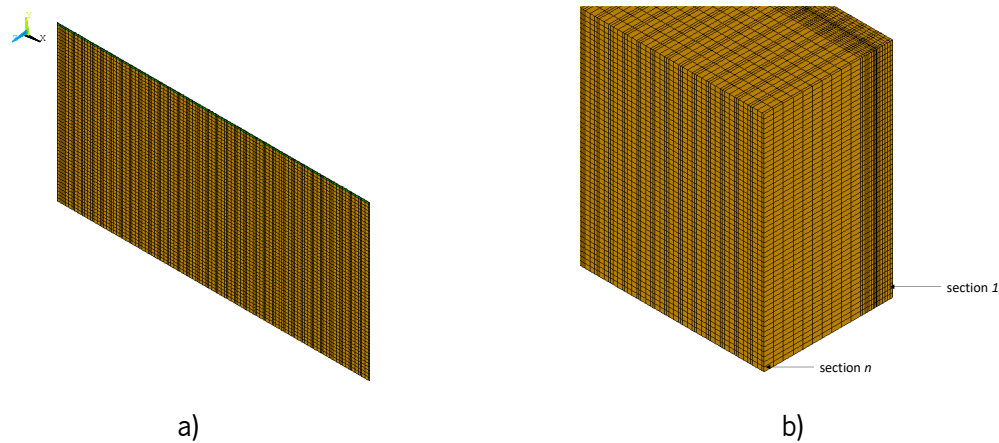
Figure 7.50 - Methodology applied to the 3D modelling: a) cross-section of the subgrade in the plane *xy*; b) *n* planes *xy* of the subgrade

After the determination of the stresses (σ_x, σ_y, σ_z, σ_{xy}, σ_{xz}, σ_{yz}), the principal stresses are determined in MATLAB, as well as the *p'* and *q* stresses, which are the main inputs of the permanent deformation model.

The permanent deformation of the track induced by the passage of only one axle causes a very small deformation. This means that the process is not carried out cycle by cycle but in increments corresponding to a set of cycles (ΔN), assuming that, in this set of cycles, the stress state to which the materials are subjected remains constant. In this case, the selected ΔN corresponds to 1 million cycles.

After the determination of permanent deformation and permanent displacements in MATLAB, the files with these results are written and are read by the software ANSYS. Thus, ANSYS applies the permanent displacement to each node of the finite element, updating the geometry of the track.

After each dynamic analysis, the effects of the new geometry of the track on the dynamic behaviour of the transition zone can be evaluated. This procedure allows analysing the joint effect of the variation of the stiffness and the settlement caused by the passage of the train after the passage of a certain number of axles.

Some considerations and simplifications of the proposed methodology to simulate the permanent deformation of the track are presented:

- In all the dynamic analysis is considered the interaction vehicle-track;
- Contact elements between HBL and FPL are considered to simulate the "detachment" of the substructure from the superstructure;
- To each defined set of number of load cycles, the stress state in the finite elements remain constant;

298

- The determination of the permanent deformation is performed node to node of each element;

- The permanent deformation is function of the adopted permanent deformation law. In this analysis, the meteorological factors, creep conditions or consolidation settlements of the foundation soils were not considered.

7.6.1   Application of the methodology

The methodology explained previously in detail allows obtaining the long-term performance of a transition zone. This methodology was firstly implemented in 2D models (Alves Ribeiro (2012). However, the implementation in 3D modelling is more realistic, even despite the requirement in terms of calculation time, which includes the dynamic analysis and the process to obtain the stresses on all finite elements of the geomaterials (which can be very time demanding).

The evolution of the stress levels in the finite elements considering the passage of the train axles constitutes the basis of the methodology applied in this study. Indeed, as mentioned previously, the deviatoric stress is one of the input elements in the permanent deformation law and allows understanding in an integrating way the evolution of the stress levels on the track. In Figure 7.51, the evolution of the deviatoric stress along the track on the top nodes of the FPL and subgrade are represented. The position x=0 m corresponds to the transition zone and each point of the graph corresponds to a node of the FE model.
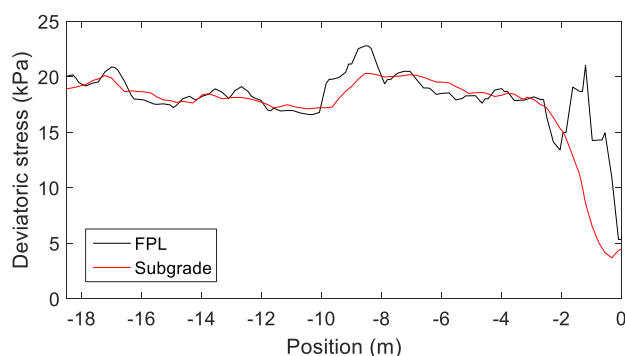
Figure 7.51 - Evolution of the deviatoric stress in the top of the FPL and subgrade along the track

Analysing Figure 7.51, the deviatoric stress is slightly higher in the FPL and tends to reduce in depth. These conclusions are confirmed in Figure 7.52, where are represented the distribution of the maximum values of the deviatoric stress in some of the elements of the subgrade along the track at different depths, from the top at y=-1.338m until y=-7.138m. The results show that the maximum deviatoric stress reduces with the increase of depth. At x=-16m, the stress level at y=-7.138m is almost half of the stress at the top

of the subgrade. This means that, at this depth (and respective stress level), the contribution of these elements in terms of permanent deformation is smaller.
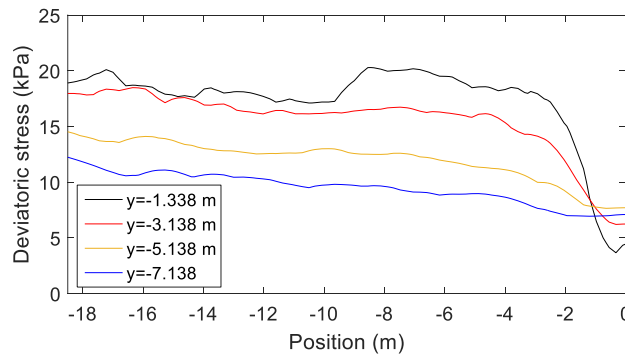
Figure 7.52 - Evolution of the deviatoric stress in the subgrade at different depths along the track

After the performance of the dynamic analysis and the determination of the stresses on the MATLAB, the permanent deformations are obtained. Considering the alignment under the loading (in the cross direction), the results of the variation of the permanent deformation along the track are depicted in Figure 7.53 and Figure 7.54 for the FPL and subgrade, respectively. The results regarding the permanent deformation, from now on, are presented considering the absolute values. The number of cycles associated with each curve is 1 million cycles. In this case, the maximum permanent deformation for each vertical position was obtained, where y=0 m corresponds to the top of the rail. In the case of the FPL, there is an oscillation of the permanent deformation until the maximum (around x=-8m), followed by a decrease, an increase (around x=-4 m), and a sudden decrease until reaches the transition. Regarding the subgrade, there is a stabilization until x=-9 m, an increase (around x=-5 m), and a sudden decrease until reaches the transition. These results are more obvious on the subgrade than the FPL since the permanent deformation and the stresses of the FPL are influenced by the contact elements placed at the top of this layer, which means that the analysis of the results is not as straightforward as in the subgrade. The analysis of Figure 7.54 b) also shows that the elements located from the middle until the bottom of the subgrade layer hardly contribute to the permanent deformation.
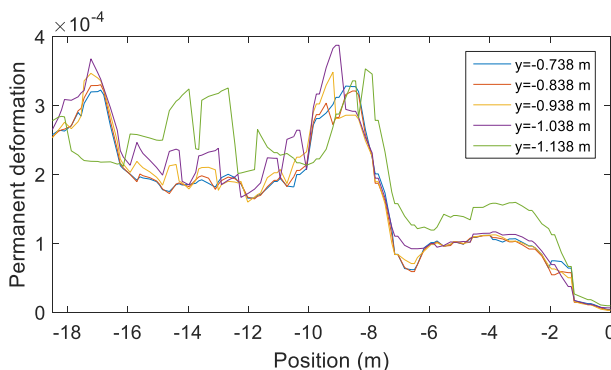
Figure 7.53 - Maximum permanent deformation of the FPL along the track (after 1 million cycles) for each vertical position

a)

b)
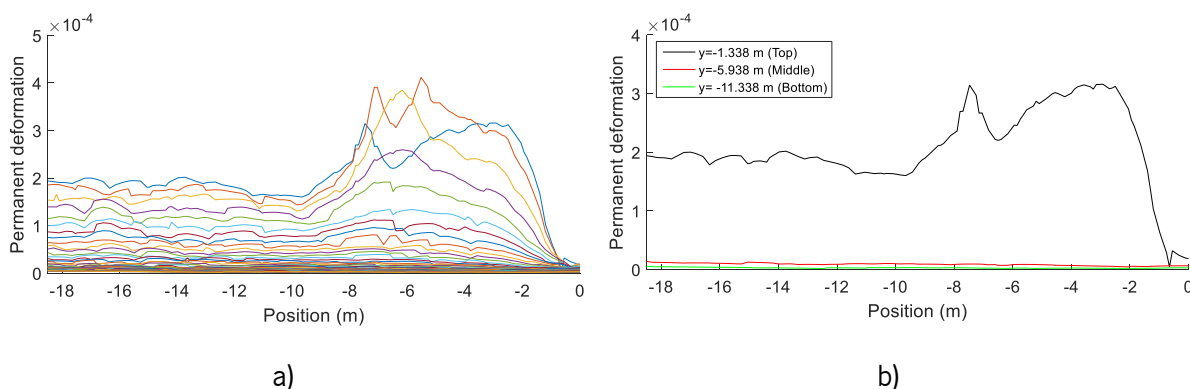
Figure 7.54 - Maximum permanent deformation of the subgrade along the track (after 1 million cycles): a) for each vertical position; b) for the top, middle and bottom nodes of the subgrade

The evolution of the permanent deformation with the number of load cycles should also be evaluated and analysed. Two examples of the development of the permanent deformation in the FPL and subgrade layers with the number of load cycles are depicted in Figure 7.55.

a)

b)
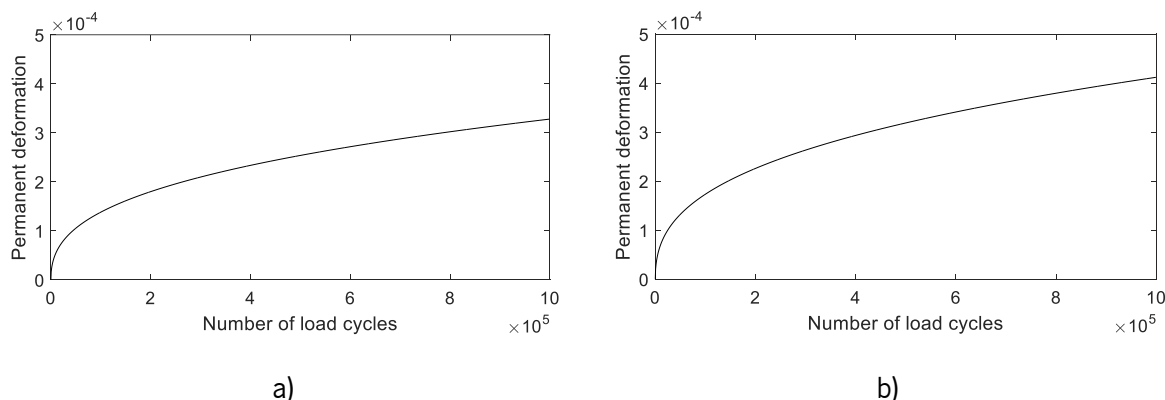
Figure 7.55 - Evolution of permanent deformation: a) on the FPL (x=- -8.7750); b) on the subgrade (x=-5.525)

These results are complemented with the analysis depicted in Figure 7.56. In Figure 7.56 a), the evolution of the permanent deformation in two sections of the subgrade (considering the nodes at the top of the layer) is compared: flexible (or embankment) and immediately before the transition zone. These alignments are identified in Figure 7.56 b) by the letters A (flexible zone) and B (immediately before the

301

transition zone). As is possible to observe, the evolution of the permanent deformation is different in the two zones. In alignment B, close to the transition, the permanent deformation of the element of the subgrade is lower (more than half) than permanent deformation of the alignment A. These results are following the stress results (for example the deviatoric stresses depicted in Figure 7.52).

a)   b)
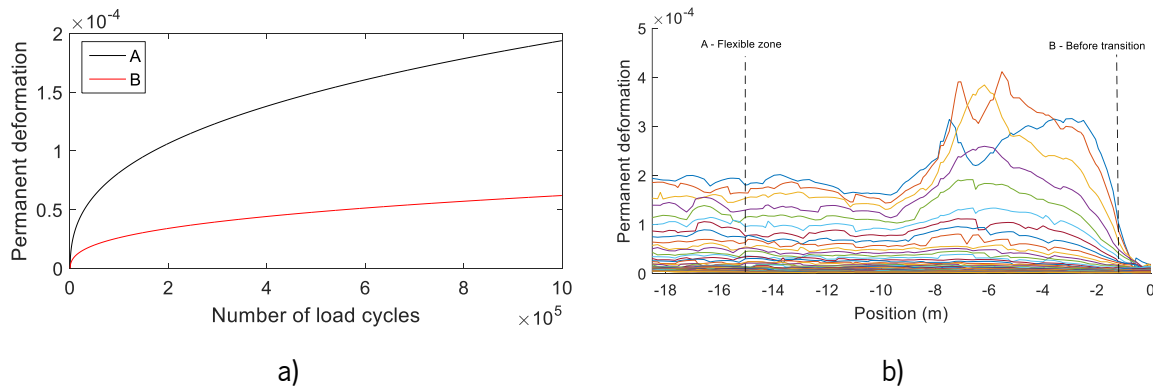
Figure 7.56 - Evolution of the permanent deformation a) with the number of load cycles of the elements in the top of the subgrade in the alignment of a flexible zone (A) and immediately before the transition (B); b) after 1000000 load cycles along the track on the subgrade (maximum values)

The 3D distributions of the permanent deformation on the top of the FPL and subgrade are presented, respectively in Figure 7.57 and Figure 7.58. The peak of the permanent deformation occurs under the HBL area (until z=1.5m – plane *xy*). For z>1.5m, the permanent deformation is almost residual. Furthermore, the maximum permanent deformation occurs at x=-7.25 and x=-3.15m, in the FPL and subgrade, respectively. These figures are also supported by Figure 7.59 (where the values of permanent deformation are depicted along with the adopted mesh), as well as by Figure 7.60 and Figure 7.61, where the distribution of the permanent deformation (absolute values) along the FPL and subgrade are depicted, respectively.
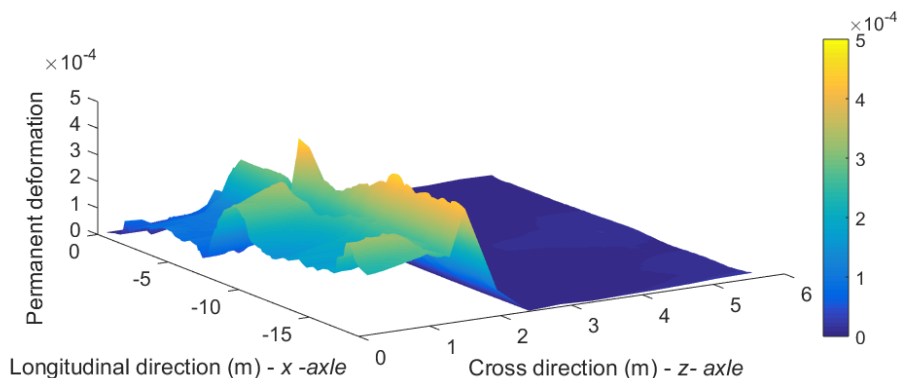
Figure 7.57 - Distribution of the permanent deformation (absolute values) at the top of the FPL

302
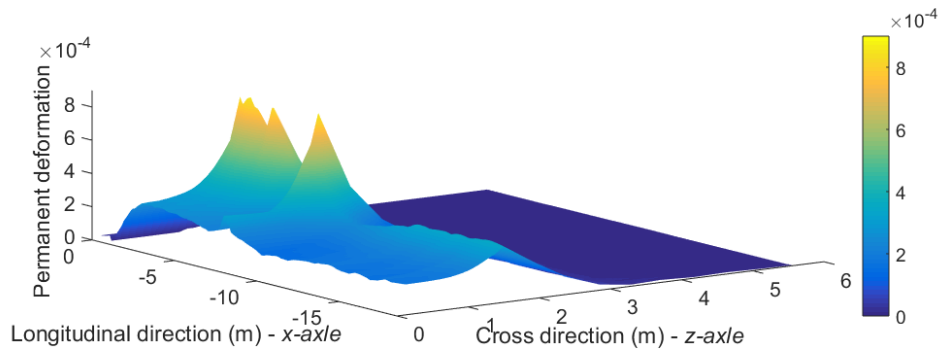
Figure 7.58 - Distribution of the permanent deformation (absolute values) at the top of the subgrade

a)   b)
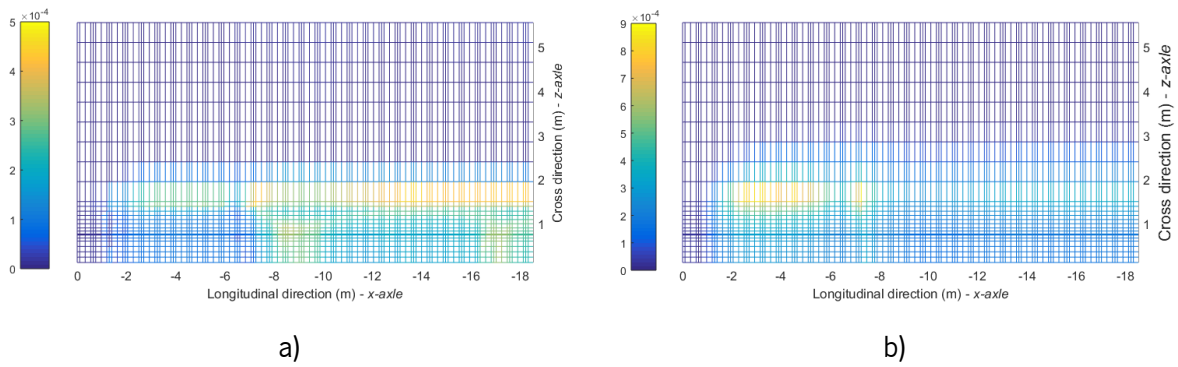
Figure 7.59 - Distribution of the permanent deformation (absolute values) according to the adopted mesh: a)top of the FPL; b) top of the subgrade
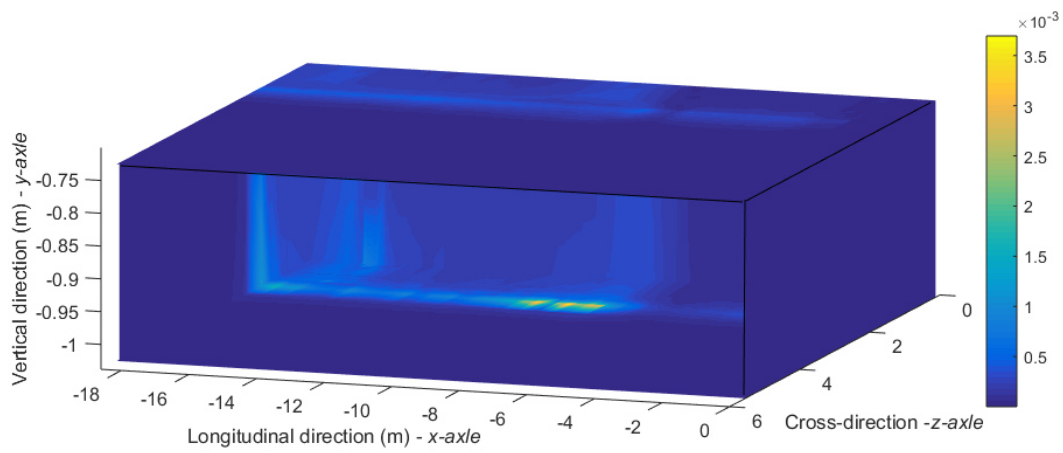
Figure 7.60 - 3D permanent deformation (absolute values) on the FPL

303
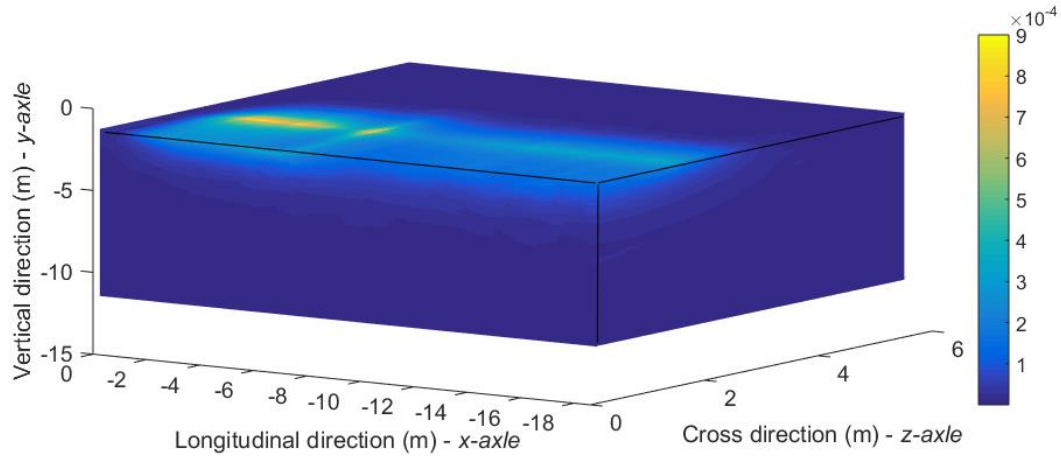
Figure 7.61 - 3D permanent deformation (absolute values) on the subgrade

Despite the importance of the previous results, it is also important to analyse the cumulative permanent displacement. In this case, the same strategy was used, which means that the results were analysed under the loading alignment. In Figure 7.62, the cumulative permanent displacements on the FPL along all the alignments of the track are presented. The maximum cumulative permanent displacement in a range between 18.5 m<x<0 m occurs at x=-8.45 m and corresponds to a value close to 0.1728 mm. This curve is identified in Figure 7.62 b).

a)

b)

c)
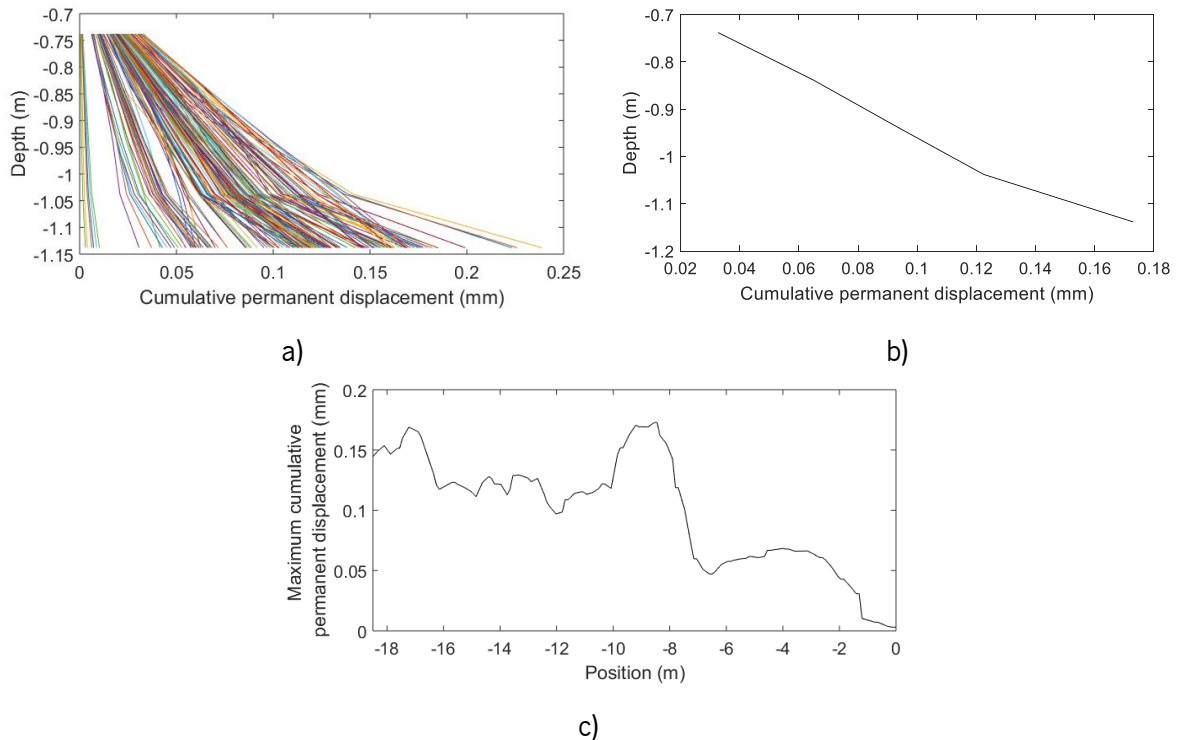
Figure 7.62 - Cumulative permanent displacement on the FPL in mm: a) along the track (considering all the alignments); b) cumulative permanent displacement at x=-8.35 m; c) variation of maximum cumulative permanent displacement along the track

In Figure 7.63, the cumulative permanent displacements on the subgrade along all the alignments of the track are depicted. The maximum cumulative permanent displacement in a range between 18.5 m<x<0 m occurs at x=-7.15 m and corresponds to a value close to 0.46 mm, as depicted in Figure 7.63 b).

a)

b)

c)
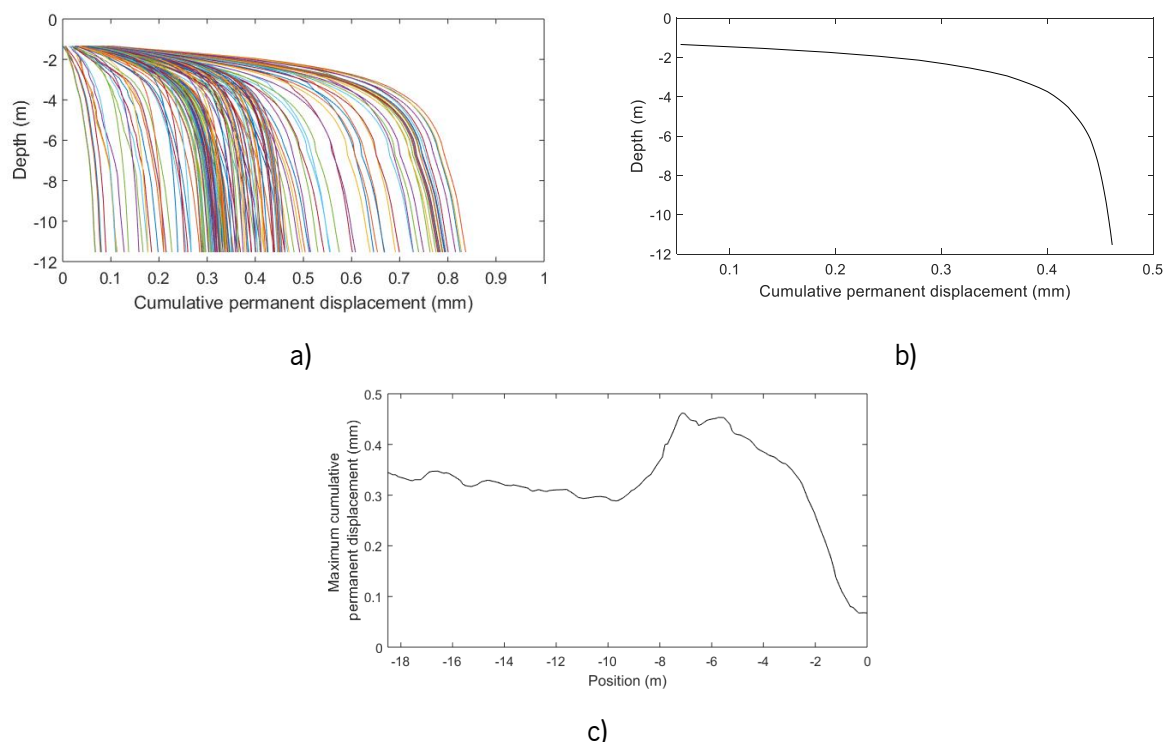
Figure 7.63 - Cumulative permanent displacement on the subgrade in mm: a) along the track (considering all the alignments); b) cumulative permanent displacement at x=-7.05 m; c) maximum cumulative permanent displacement along the track

However, these results are important if analysed together considering the whole substructure with the inclusion of both layers: FPL and subgrade. Figure 7.64 shows the obtained results. The maximum cumulative permanent displacement on the substructure in the alignment under the loading is close to 0.52 mm in the range between -18.5 m <x<0 m and occurs at x=-7.25 m. The results depicted in Figure 7.64 a) also show that the layers that most contribute to the permanent deformation and respective cumulative permanent displacement are located between the top of the FPL (y=-0.738) and y=-4.138m (above half of the thickness of the subgrade). Indeed, all the layers of the FPL contribute to the development of the permanent deformation (and cumulative permanent displacement), as well as about 30% of the subgrade. After the depth y=-4.138m, the cumulative permanent displacement stabilises, which means that about 70% of the subgrade is not contributing to the development of the permanent deformation. This information is helpful since means that in future analysis, there is no need to obtain the stresses in all elements of the subgrade, thus reducing the time of the analysis. Furthermore, this conclusion also shows that, in the design of the structure, special attention should be given to the properties of the subgrade until this thickness (good quality materials should be selected).

Moreover, it is also possible to compare these results with the cumulative permanent displacement obtained in the structures tested in the laboratory (full-scale tests). The results presented in Chapter 6 (Figure 6.24 a) show that the maximum cumulative permanent displacement in the alignment under the loading on the ballastless track was 0.53 mm, which is close to the maximum cumulative permanent displacement obtained in these numerical analyses (0.52 mm). However, it is important to highlight that, the interaction force between the vehicle and the track was considered in this case, as well as the interaction between the super and substructure (FPL and subgrade). Furthermore, the thickness of the subgrade is substantially higher (10.4 m versus 0.8 m), which clearly influences the cumulative permanent displacement of the track. There are also differences in the number of million cycles considered (more reduced in the numerical analysis): 1 million cycles versus 3.4 million cycles.

a)

b)

c)
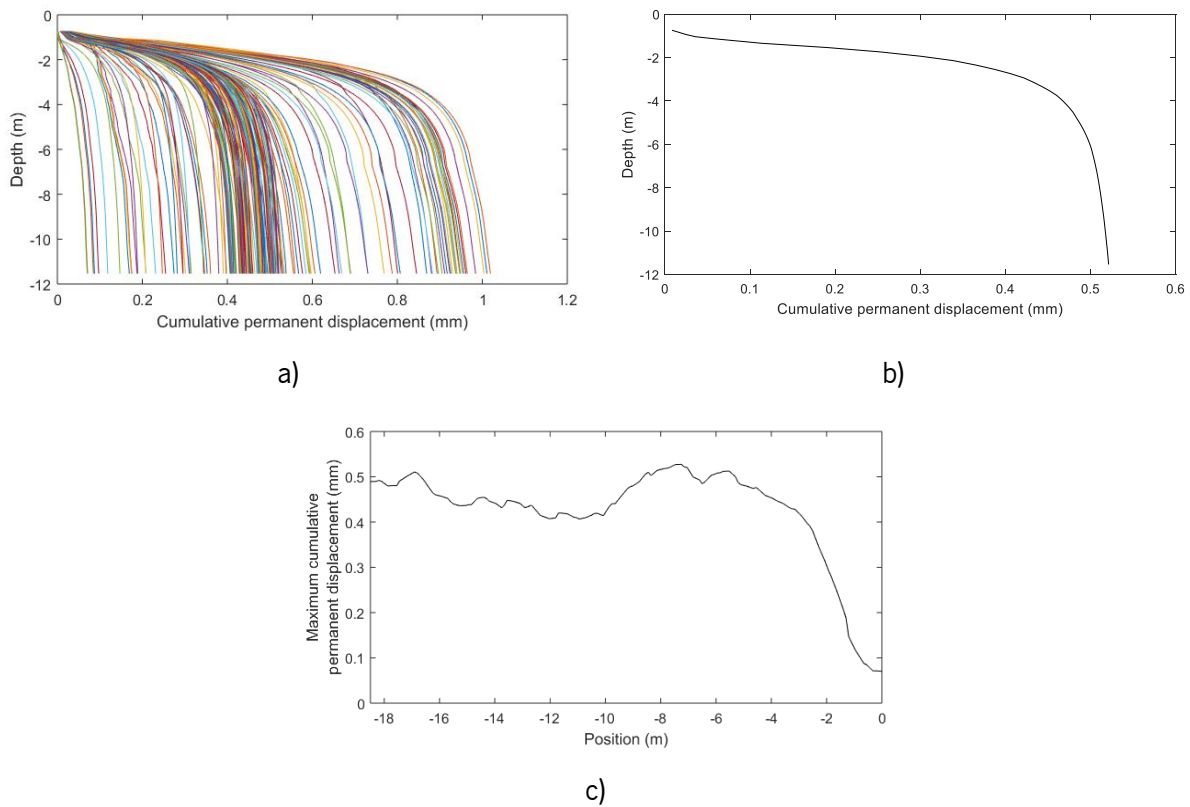
Figure 7.64 - Cumulative permanent displacement on the substructure (FPL+subgrade) in mm: a) along the track (considering all the alignments); b) cumulative permanent displacement at x=-7.05 m; c) maximum cumulative permanent displacement along the track

The maximum cumulative permanent displacement was also determined in the cross-section (z-axle - Figure 7.50). The obtained results are depicted in Figure 7.65. Analysing this figure, it is possible to conclude that the permanent deformation varies in this direction. The maximum cumulative permanent displacement occurs between the alignment under the loading (plane xy - z= 0.7538) and the limit of the HBL (plane xy - z=1.5m). This occurs since the weight of the superstructure influences the initial stress state of the materials and, consequently, the permanent deformation. After the position z=1.5m (limit of

the HBL), the permanent deformation decreases abruptly until reaches a residual value. These results are following the stress results depicted in Figure 7.43.

This conclusion is also supported by Figure 7.66 and Figure 7.67 where the cumulative permanent displacement (in mm) along the three directions in the FPL and subgrade are represented.
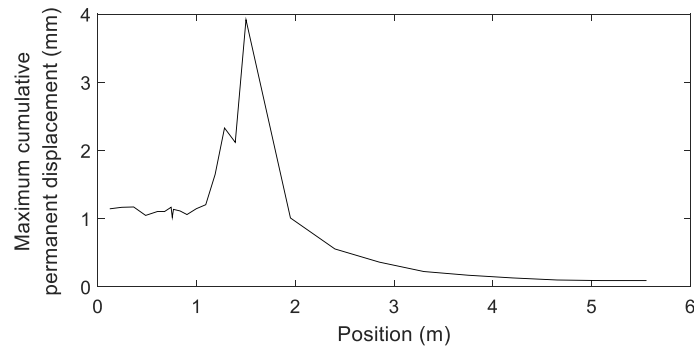
Figure 7.65 - Maximum cumulative permanent displacement in mm along the cross-direction
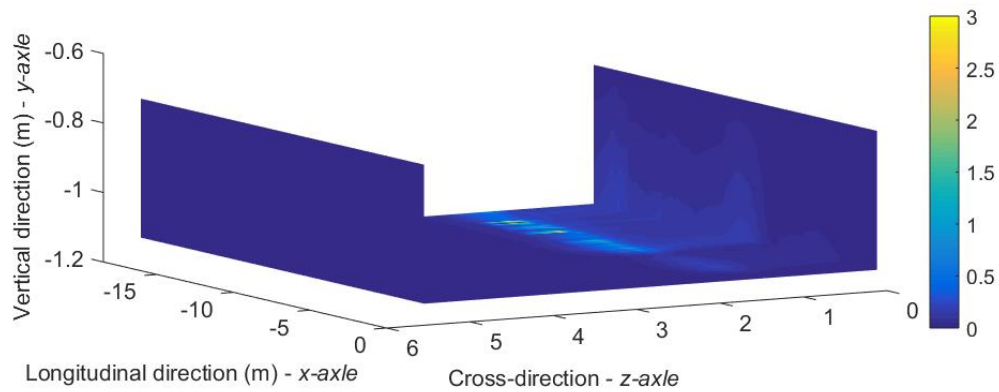
Figure 7.66 - 3D cumulative permanent displacement in mm on the FPL
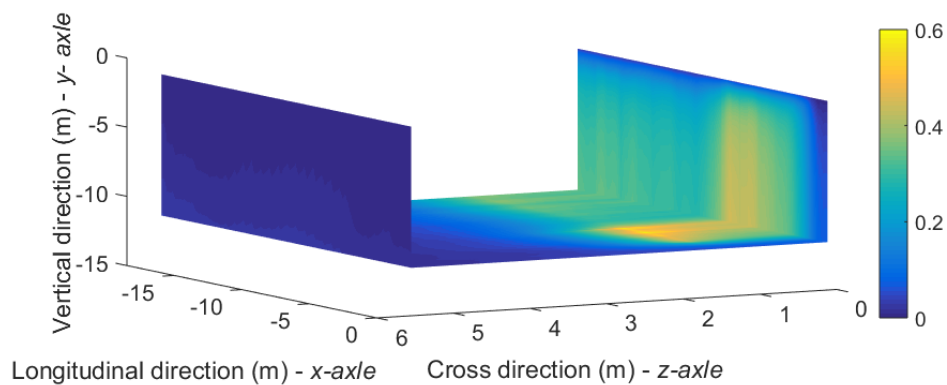
Figure 7.67 - 3D cumulative permanent displacement in mm on the subgrade

307

After the determination of the permanent deformation and permanent displacements (in meters), the obtained results were inputted on the 3D model (ANSYS) in each node of the FPL and subgrade.

7.6.2   Results of the dynamic analysis

The accumulation of permanent deformation with the number of load cycles can lead to a progressive change in the longitudinal profile of the track. In Figure 7.68, the deformed profile along the longitudinal direction (*x*-axle) on the finite elements located at the top of the subgrade after 1 million load cycles is depicted. The profile was scaled 500 hundred times to help to understand the impact that the deformed profile can have on the dynamic results.

a)

b)
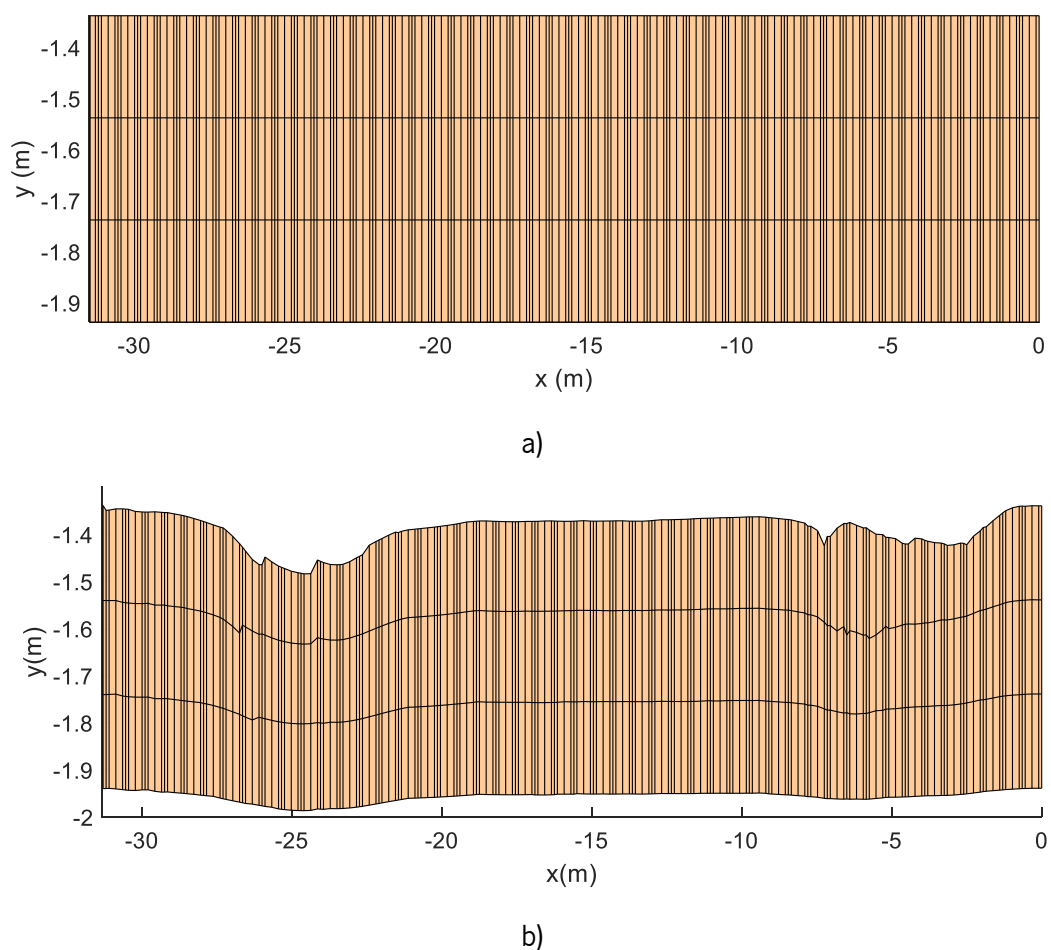
Figure 7.68 - Comparison between the original or non-deformed profile (a) and deformed profile (b) on the top of the subgrade – the deformation was augmented 500 times

Figure 7.69 presents the evolution of the vertical deformation along the track (including the transition zone in the case of the concrete slab and HBL) of the elements located on the top of the concrete slab, bottom of HBL and top of FPL with the number of load cycles.

a)

b)

c)

d)

e)

f)
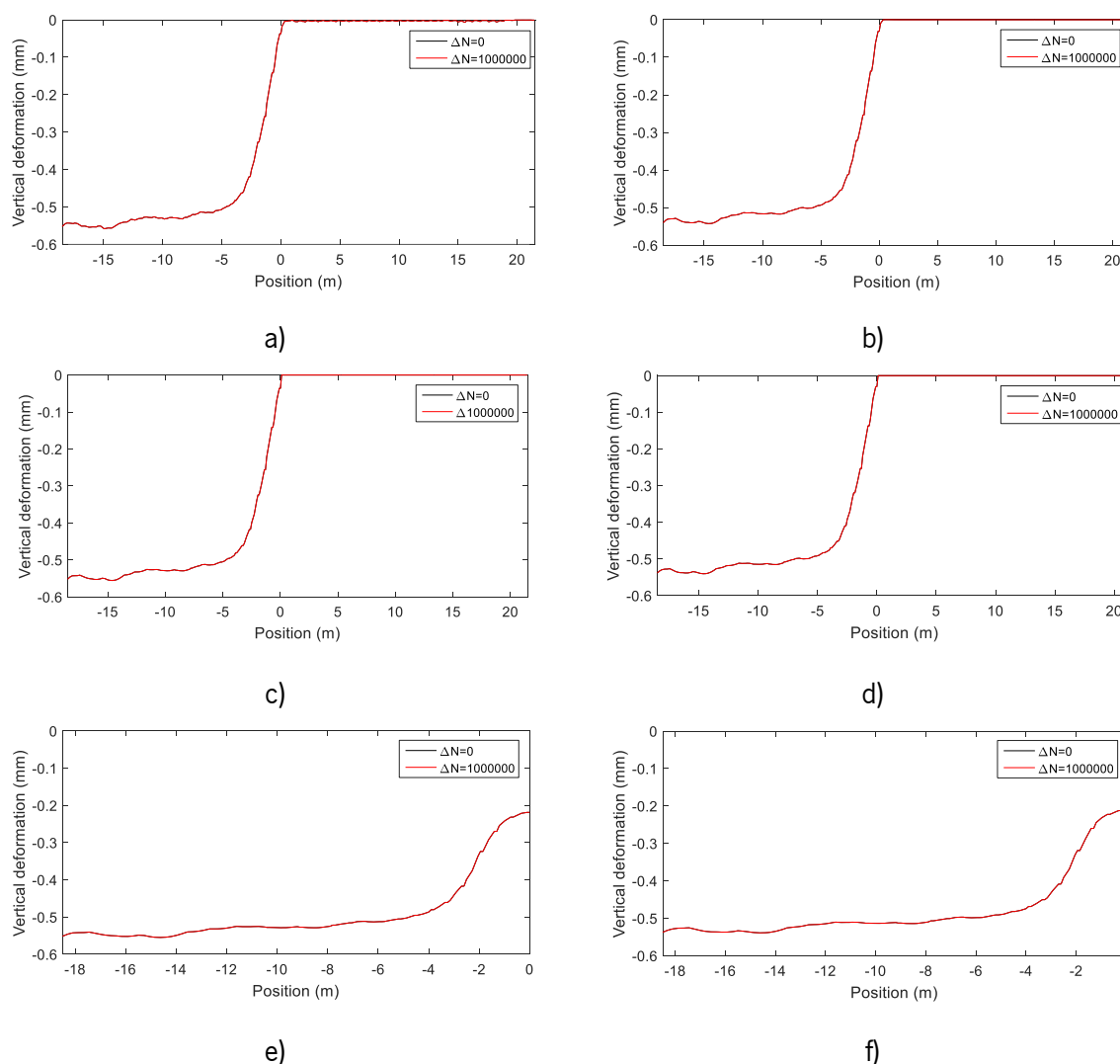
Figure 7.69 - Evolution of the vertical deformation along the track depending on the number of load cycles: a) top of the concrete slab under the loading alignment; b) top of the concrete slab at z= 1.2825 m; c) bottom of HBL under the loading alignment; d) bottom of HBL at z= 1.2825 m; e) top of FPL under the loading alignment; f) e) top of FPL at z= 1.2825 m

Analysing the results, it is possible to draw some conclusions about the evolution of the permanent deformation on the track:

- The vertical deformation at the top of the concrete slab, bottom of HBL and top of FPL are very similar;

- The impact of the evolution of permanent deformation is not significant. After 1 million cycles, the maximum increment in terms of vertical deformation is almost zero. The differences of the displacements between ΔN=0 and ΔN=1 million cycles along the track are almost impossible to identify.

The maximum displacements on the top of the subgrade were also analysed. The obtained results are depicted in Figure 7.70. The results are similar to the vertical deformation obtained at the bottom of the HBL and the top of the FPL. The variation of vertical stresses along the track on the top of the subgrade

309

and FPL are presented in Figure 7.71 and Figure 7.72, respectively. The results show a difference between the initial condition and the condition after 1 million load cycles. However, the differences are not significant. Furthermore, at the position x=-8 m, it is possible to identify a difference between the two conditions ($\Delta N=0$ and $\Delta N=1000000$). However, this difference is due to an inaccuracy of the model.

a)   b)
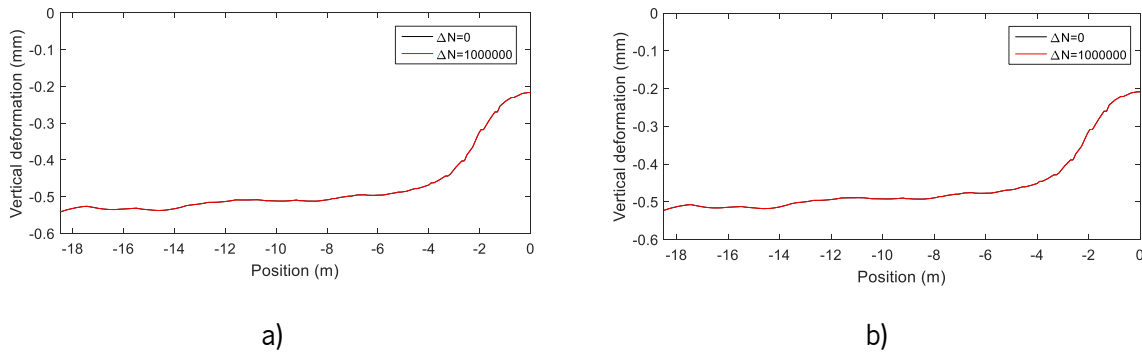
Figure 7.70 - Evolution of the vertical deformation along the track depending on the number of load cycles: a) at the top of the subgrade under the loading alignment; b) at the top of the subgrade at z= 1.2825 m

a)   b)
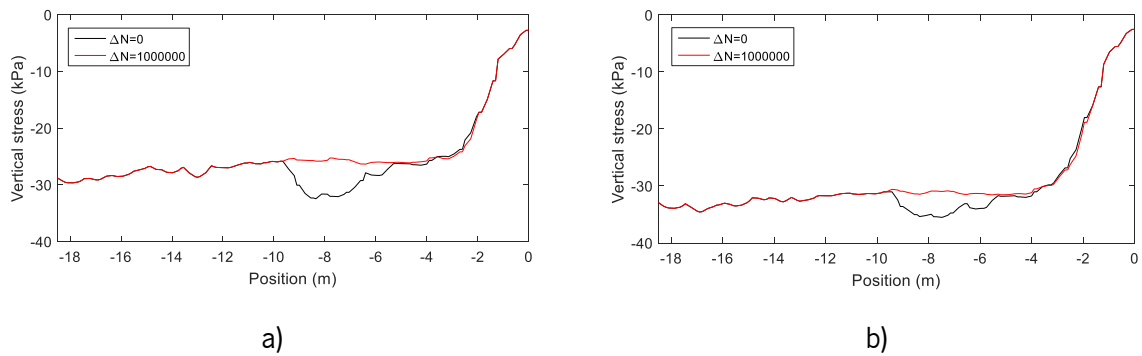
Figure 7.71 - Evolution of the vertical stress along the track depending on the number of load cycles: a) at the top of the subgrade under the loading alignment; b) at the top of the subgrade at z= 1.2825 m

a)   b)
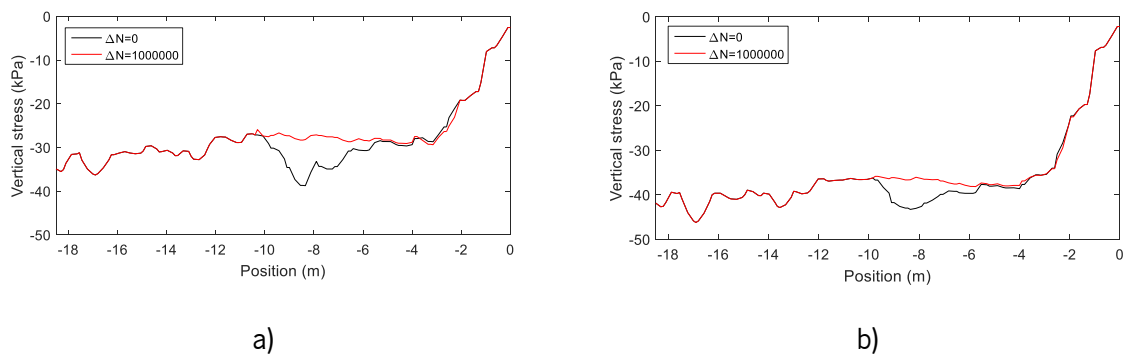
Figure 7.72 - Evolution of the vertical stress along the track depending on the number of load cycles: a) at the top of the FPL under the loading alignment; b) at the top of the FPL at z= 1.2825 m

The vertical displacement of the wheel over the deformed track conjugates the initial curve of the displacement non-deformed with the settlement profile of the substructure, since the voids under the substructure close when the wheel passes, and the vehicle experiences total track deformation. However, as shown in Figure 7.57 and Figure 7.58, the values of the permanent deformation are low due to the

high stiffness of the track, which means that the settlement profile of the substructure is not so different when compared to the non-deformed profile. Indeed, as shown in Figure 7.64, the maximum cumulative permanent displacement of the substructure under the load alignment is lower than 0.52 mm. The variation of the vertical displacement of the wheel along the track with the number of load cycles is presented in Figure 7.73. The results show that there are no significant differences in the area close to the transition zone.
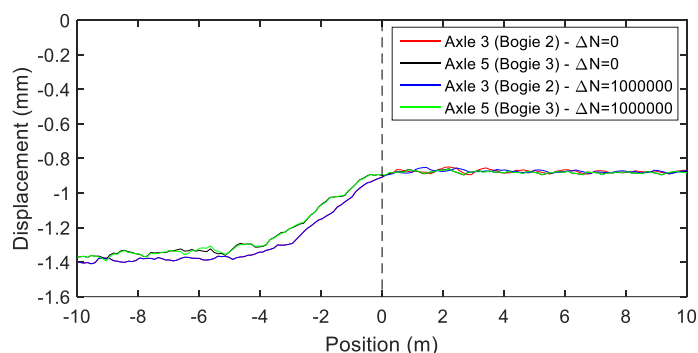
Figure 7.73 - Dynamic vertical deformation of the wheel along the track with the number of load cycles: axle 3 and axle 5

In Figure 7.74 and Figure 7.75, the variation of interaction force wheel-rail and acceleration along the track with the number of load cycles are presented, respectively. However, as in the case of the displacements of the wheel, there are no evident differences in the area close to the transition zone. Thus, the long-term analysis may continue until the maximum value of the acceleration of the axles of the vehicle reaches and exceeds the admissible value (limit between the normal and careful conditions), which is equal to 30 m/s^2 (López-Pita et al., 2006). Above 70 m/s^2, immediate correction is required. In this case, axle 1 shows an increment of acceleration in the transition (maximum peak close to 50 m/s^2). However, for the remaining axles, the results are far from this limit condition (the maximum and minimum peaks are close to -10 m/s^2 and 10 ms/^{2}). This is an indication of the good performance of the structure, which means that the increase in the number of cycles may have no influence on the results regarding the short and long-term behaviour.
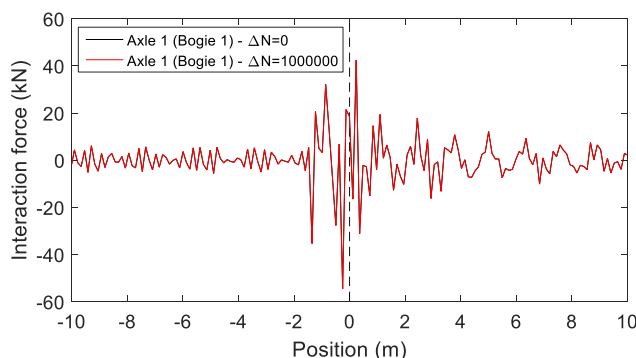
Figure 7.74 - Variation of the interaction force wheel-rail along the track with the number of load cycles: axle 1

311
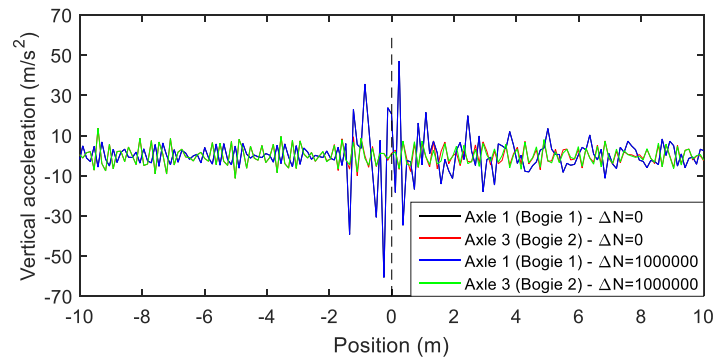
Figure 7.75 - Variation of the acceleration of the axles 1 and 3 along the track with the number of load cycles

Figure 7.76 shows the maximum and minimum values of the vertical acceleration along the track at the bottom nodes of HBL at two cross-sections: in the alignment under the loading and at z=1.2825 m. Figure 7.77 shows the maximum values of the interaction force between the HBL and FPL in the alignment under the loading. In Figure 7.78 and Figure 7.79, the variation of the maximum and minimum vertical and longitudinal stresses obtained along the transition zone at the top nodes of HBL with the number of load cycles at two selected cross-sections are presented, respectively. The results show that the curves associated with the initial conditions (non-deformed track/ΔN=0) and the curve associated with a deformed track (after 1 million load cycles) are overlaid in the transition zone (x=0m). This means that is possible to continue the iterative procedure, incrementing the number of load cycles, to observe the increment of stresses and accelerations in this layer in the transition zone, as well as the interaction forces. Although, due to the good performance of the track, this increment of the number of load cycles may have a residual influence on these results.

a)

b)
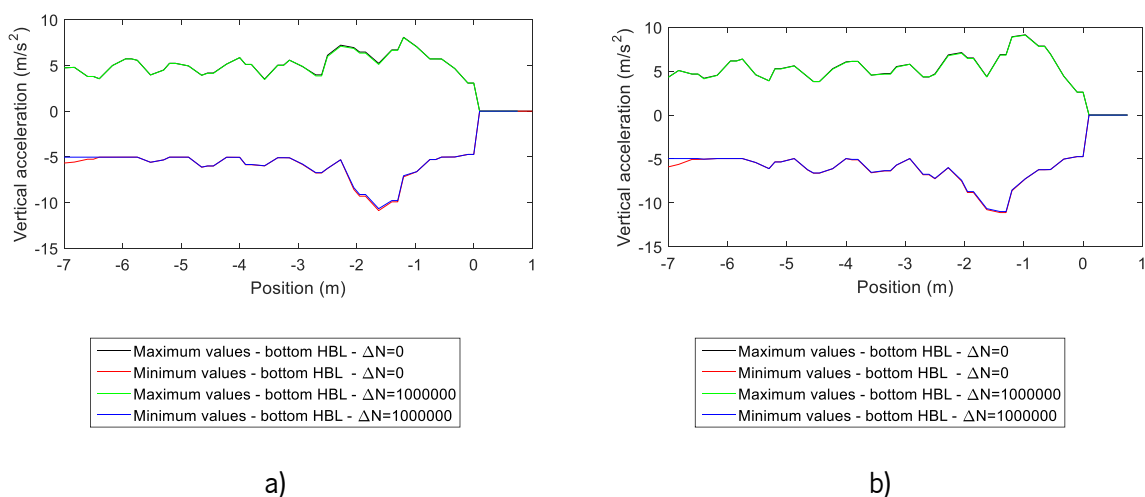
Figure 7.76 - Maximum and minimum values of the vertical acceleration of the HBL along the transition zone: a) bottom of the HBL under the loading alignment; b) bottom of the HBL at z=1.2825 m

312
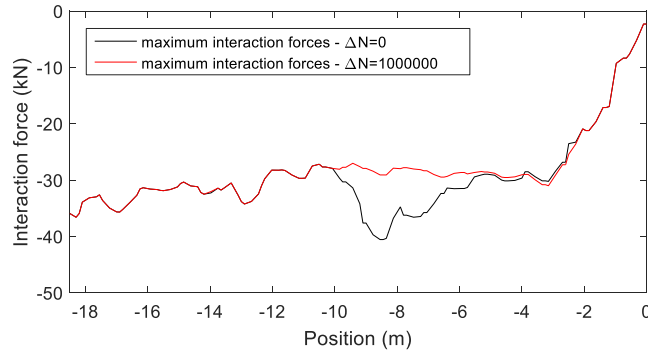
Figure 7.77 - Maximum Interaction force HBL-FPL along the track under the loading alignment
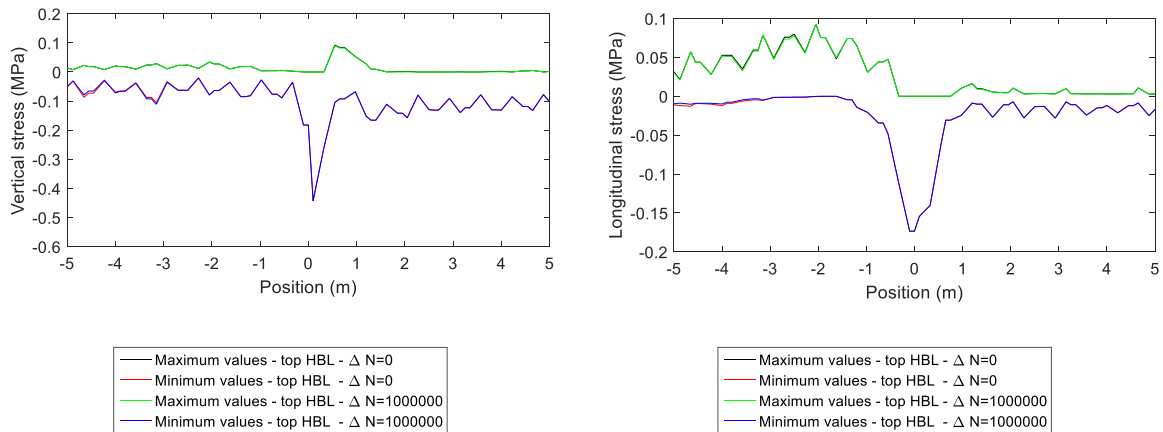
a)

b)

Figure 7.78 - Variation stress in the top nodes of the HBL along the transition zone with the number of load cycles (under the loading alignment): a) vertical stress; b) longitudinal stress
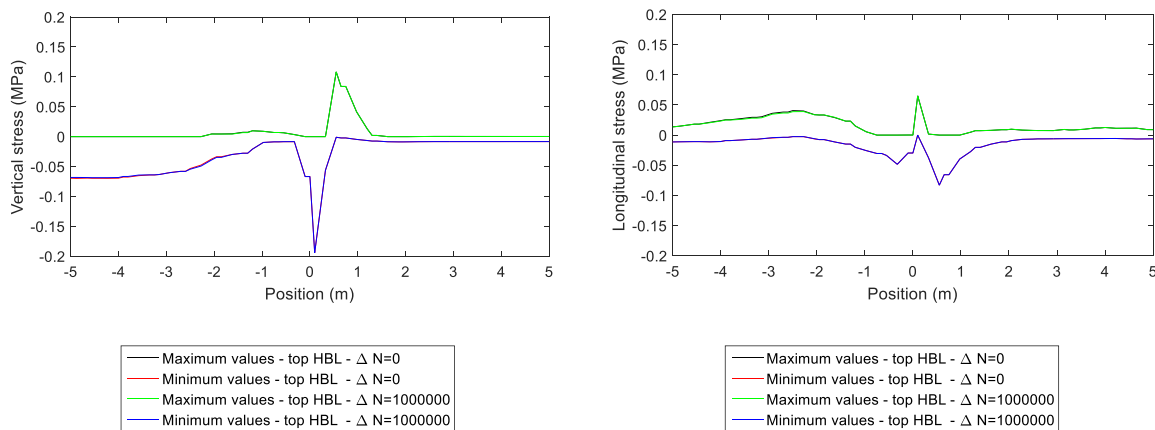
a)

b)

Figure 7.79 - Variation stress in the top nodes of the HBL along the transition zone with the number of load cycles (at z=1.2825 m): a) vertical stress; b) longitudinal stress

From the previous results, it is possible to conclude that this specific transition zone with the ballastless track system shows a satisfactory performance after 1 million load cycles. The results show that the stiffness of the structure given by the concrete slab is significant when compared to the ballast used in

313

the ballasted track. In this case, the long-term performance is only dependent on the subgrade and FPL that usually shows very low values of permanent deformation (see Chapter 5) when compared to the ballast. Furthermore, in the case of the ballasted track, it is the ballast that presents the highest concentration of stresses (since assures the continuity of the track along the transition zone) and shows higher values of permanent deformation due also to its behaviour when subject to cyclic loading. Furthermore, in this study, the materials adopted in the FPL and subgrade present very good properties. However, this may not occur in a similar transition. Thus, to simulate poor subgrade and FPL conditions (also allied to bad compaction conditions), the permanent deformations were scaled 15 times. This means that 3D profiles of the permanent deformation of the FPL and subgrade were maintained (such as the profile depicted in Figure 7.68), and only the deformations were scaled. Thus, from this scaling, a cumulative permanent displacement close to 8 mm was obtained in the alignment under the loading, as depicted in Figure 7.80.

a)   b)
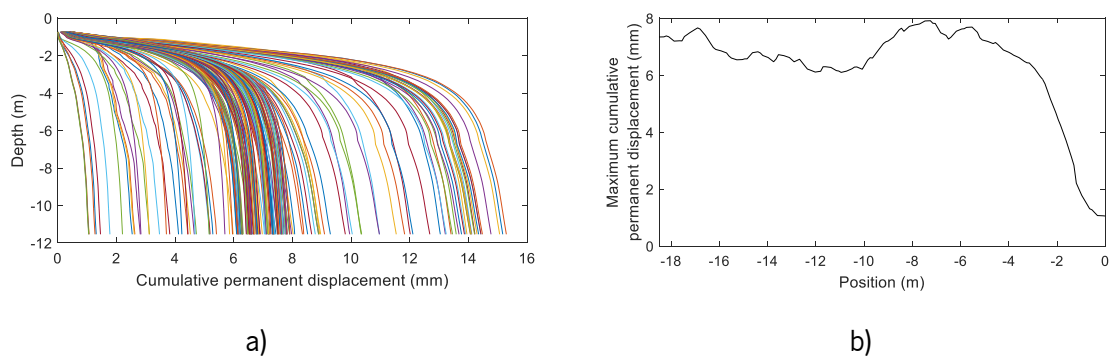
Figure 7.80 - Cumulative permanent displacement on the substructure (FPL+subgrade) in mm scaled 15 times: a) along the track (considering all the alignments); b) maximum cumulative permanent displacement along the track under the loading alignment

The 3D cumulative permanent displacement scaled 15 times on the FPL and subgrade are presented in Figure 7.81 and Figure 7.82. This figure shows the 3D distribution along the several alignments of the track.
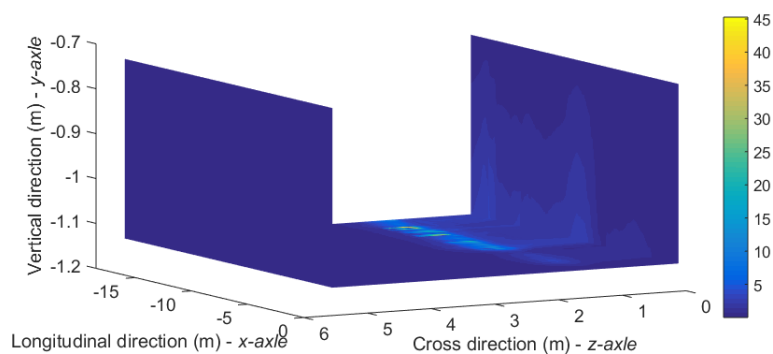
Figure 7.81 - 3D cumulative permanent displacement in mm on the FPL scaled 15 times

314
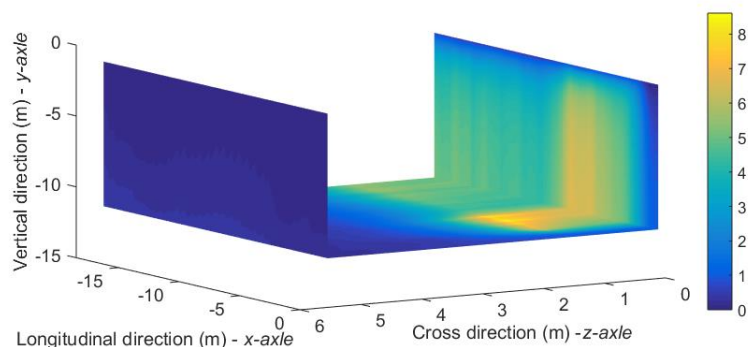
Figure 7.82 - 3D cumulative permanent displacement in mm on the subgrade scaled 15 times

The effects of this scaling are evaluated in the following analysis. Since the scaling is performed considering the same permanent deformation profile, the normalised relative displacement between two consecutive nodes remains the same, as expected. Firstly, the displacements were obtained, as depicted in Figure 7.83. The results show an increment of the displacements in sections far from the transition zone in the concrete slab and HBL. Regarding the FPL and subgrade, the increment of the displacements is significantly lower.
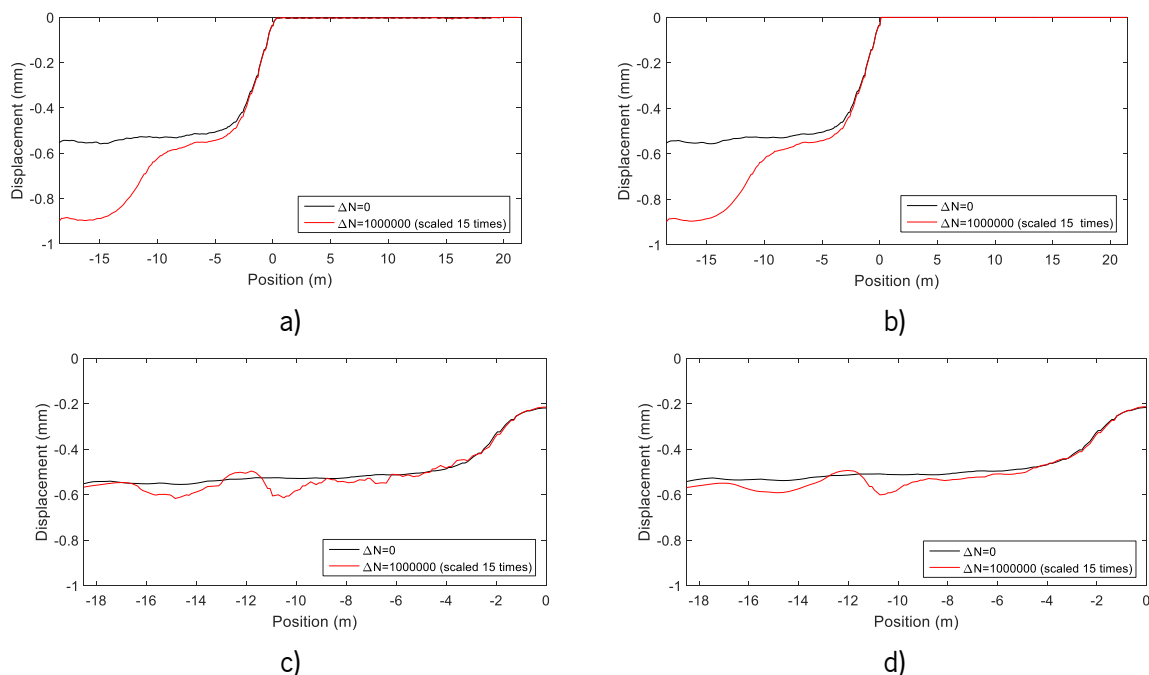
Figure 7.83 - Displacements considering the permanent deformation scaled 15 times: a) top nodes of the concrete slab; b) bottom nodes of HBL; c) top nodes of the FPL; d) top nodes of the subgrade

Posteriorly, the stresses were compared, as shows Figure 7.84. In this analysis, the maximum stresses were obtained along the track in the alignment under the rail. As mentioned previously, the major impact of the scaling of the permanent deformation 3D profile is in the sections far from the transition. In sections close to the transition zone, the stresses are reduced, and, consequently, the permanent deformations are lower. Since the normalised relative displacement between two consecutive nodes is maintained (and

315

the permanent deformation is lower in the sections close to the transition), the scaling of the permanent deformation does not have a significant influence on the stresses of the HBL in the transition. Regarding the FPL and subgrade, there are significant differences in the vertical stress results along the track and this may occur due to the influence of the contact elements and the possible loss of such contact between the HBL and the FPL.
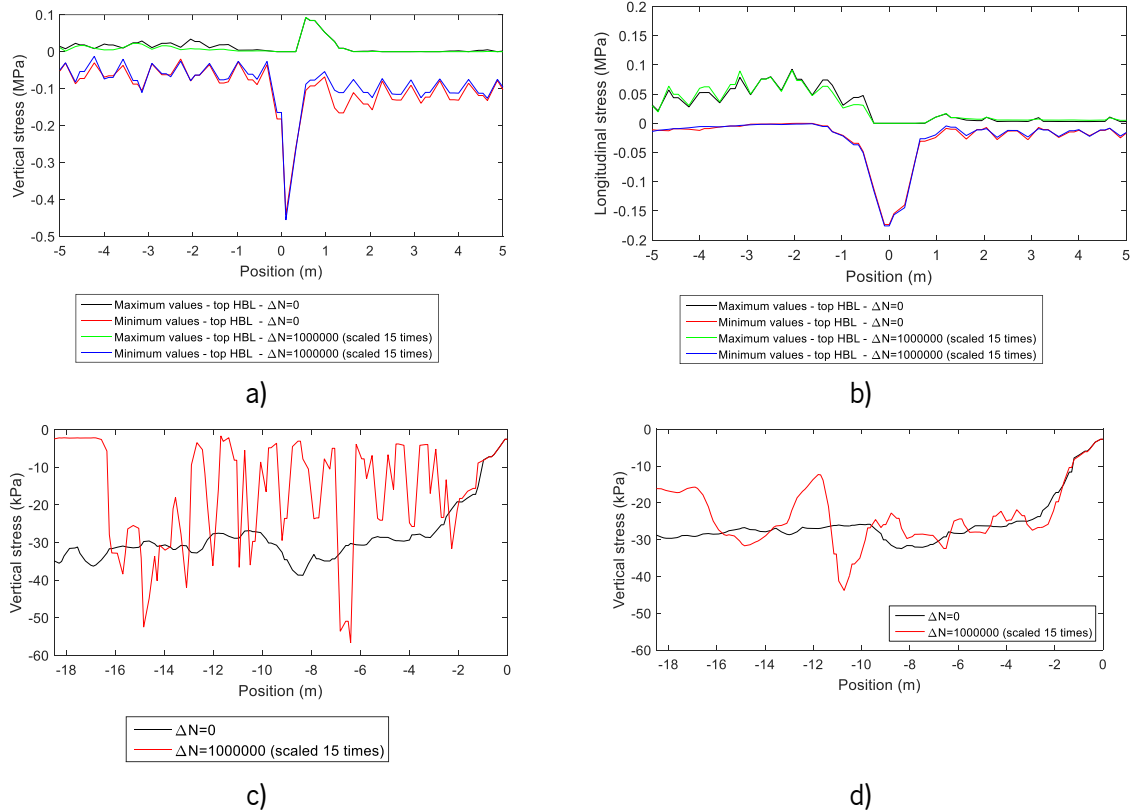
Figure 7.84 - Stresses results considering the permanent deformation scaled 15 times: a) top nodes HBL- vertical stress; b) top nodes HBL- longitudinal stress; c) top nodes of the FPL – vertical stress; d) top nodes of the subgrade – vertical stress

Moreover, the interaction forces between the HBL and FPL were also analysed. The variation of the interaction force along the time is depicted in Figure 7.85 a). Figure 7.85 b) shows the maximum values of the interaction force between the HBL and FPL in the alignment under the rail. The results show that there may be a loss of contact along the track when the value of the interaction force is zero.
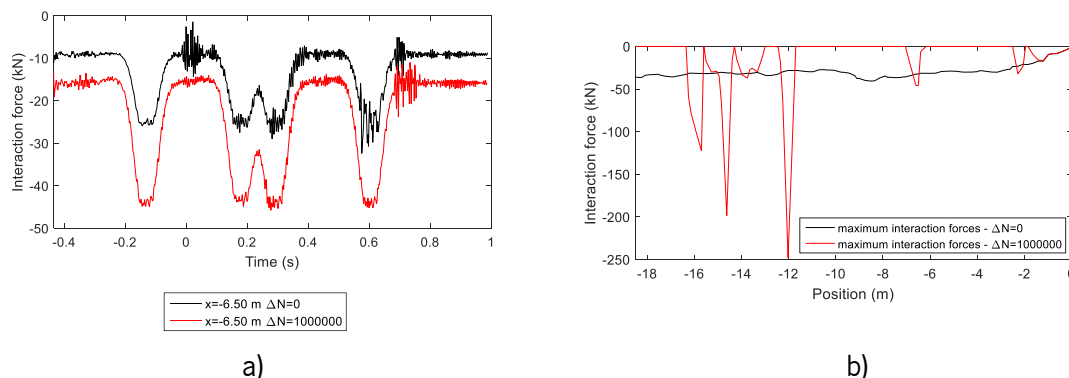
Figure 7.85 – Interaction forces between HBL and FPL considering the permanent deformation scaled 15 times: a) along time at x=-6.50 m; b) along the track (maximum values)

316

The results regarding the displacements, accelerations of the axle and the interaction between the vehicle and the track were also analysed (Figure 7.86). The impact of the scaling of the permanent deformation on these variables was not significant.
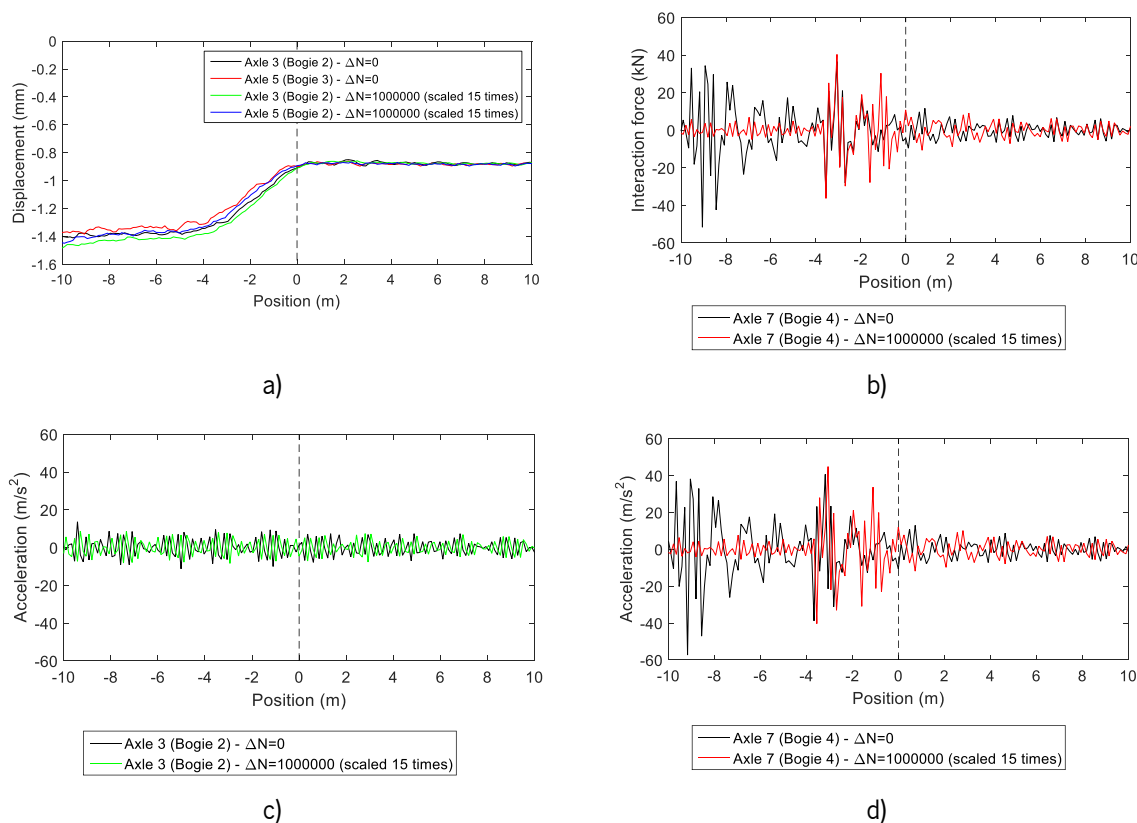
Figure 7.86 –a) Displacements of the axles; b) interaction force (axle 7 from bogie 4); c) accelerations of the axle 3 from bogie 2; d) accelerations of the axle 7 from bogie 4

This study should also be complemented with the increase in the number of load cycles, following the methodology presented below.

7.6.3 Transition between stress states

The results presented previously were obtained considering a ΔN=1 million cycle, where was assumed that during this number of load cycles (ΔN), the stress state remained constant. The methodology presented below, also described by Alves Ribeiro (2012), is purposed to analysed a higher number of load cycles in future developments.

Since this stress state varies after a certain set of ΔN, an evaluation of the stress state of the elements should be performed. With this procedure, different permanent deformation values corresponding to different stress states are obtained for the same moment, which means that it is necessary to make the transition between stress states.

Thus, the transition should follow the work developed by Ford (1995). The scheme of the concept is presented in Figure 7.87.
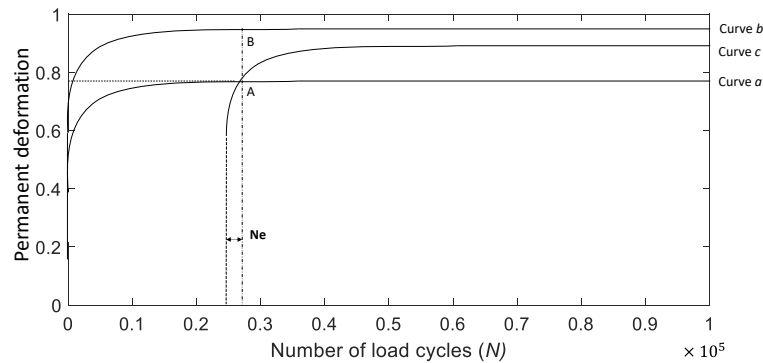
Figure 7.87 - Transition between different stress levels in the evolution of the permanent deformation of the track (adapted from Ford (1995))

Analysing Figure 7.87, Point A (which belongs to the curve of the permanent deformation for the initial situation designated as *a*) corresponds to the permanent deformation obtained at the end of *ΔN* cycles (in the case depicted in the figure it is close to 0.28×10^5). With this permanent deformation installed on the track, a dynamic analysis is carried out, resulting in a new stress state (in this case, higher than the first one), whose evolution of the permanent deformation is reflected by curve *b.* The transition between these two curves should be performed through the determination of a transition curve, curve *c* also represented in Figure 7.87. For trancing of the transition curve, the author suggests the determination of an equivalent number of cycles (N_e), which corresponds to the necessary number of cycles to achieve the permanent deformation corresponding to point *a*, but for the new stress state installed. This new curve results, basically, from the translation of a part of curve *b* to point A.

With this example, it is possible to understand the necessity to re-evaluate the stress state at the end of each set of cycles (*ΔN*). If this evaluation was not considered, the permanent deformation would evolve according to curve *a*, which would lead to an inferior value of permanent deformation. Thus, this procedure allows the conjugation of the successive stress states experienced by the materials, being also valid when the new stress state is lower than the previous one. In this case, the value of N_e will be higher (always >*ΔN),* requiring a greater number of cycles to achieve the permanent deformation corresponding to point A, with the new stress state.

Indeed, this concept is similar to the concept presented and applied in Chapter 6 regarding the time-hardening approach. This methodology will be applied in future works.

7.7   Improvement of the performance of the transition zone: resilient mat

Due to the high concentration of the stresses on the concrete slab and HBL on the transition zone, a resilient mat was included under the concrete slab in the tunnel and the embankment (1 m immediately before the transition) in order to try to mitigate this phenomenon, optimize the ballastless track and soft the transition. This mat is important to give flexibility under the concrete slab and to balance the stiffness between the embankment and the tunnel. Furthermore, this can be an important step in the optimization of this system in transition zones.

Indeed, the implementation of a resilient mat between the concrete slab and the tunnel still is used as an isolation measure, that helps to mitigate the vibrations that are transmitted by the railway to the invert of a tunnel. A schematic representation of this solution is presented in Figure 7.88 a). The implementation of flexible elements under elements with a certain mass will introduce a new natural frequency on the system. Thus, in the scope of the vibrations, for excitation frequencies considered superiors to the resonant frequency induced by the presence of the resilient element, there is an attenuation of the energy that is transmitted by the railway track to its support. The physical interpretation of this problem can be established in parallelism with the dynamic behaviour of the spring-damper system, where k is the stiffness of the resilient element and m is the overlying mass (Figure 7.88 b). Considering this model, it is expectable that, when the excitation frequency leads to an amplification dynamic factor inferior to 1 (when the excitation frequency is superior to the shear frequency of the system), there is an energy reduction that is effetely transmitted to the underlying resilient element. When the excitation frequencies are inferior to the shear frequency, occurs an amplification of the action transmitted to the support of the resilient material. The ideal scenario corresponds to the minimization of the shear frequency value, which can be guarantee by the placement of resilient elements very flexible under elements with a significant mass. It is important to highlight that the elasticity of the elements should have a physical minimum limit, otherwise, static displacements are very high (Lopes, 2015).

a)   b)
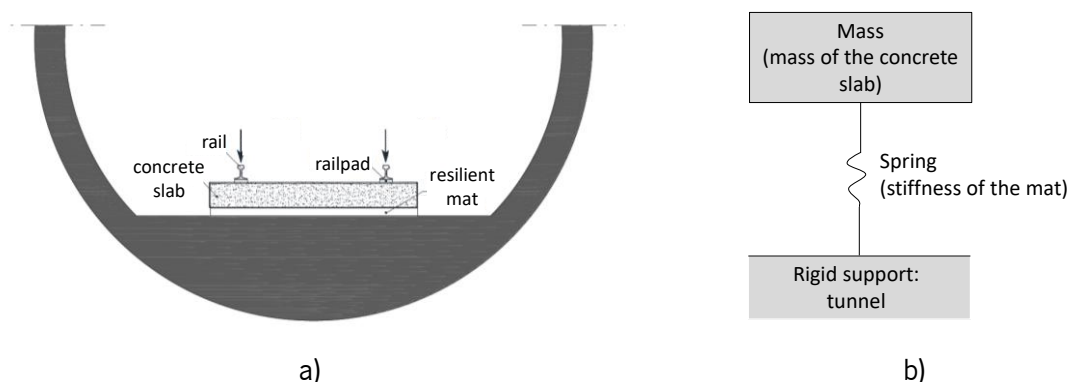
Figure 7.88 - a) Schematic representation of the configuration of the railway track considering the resilient mat (adapted from Lopes (2015)); b) Simplified physical model

Thus, considering the system presented previously, the original cement grout mass was replaced by the resilient mat in the tunnel zone and also in the first meter of the embankment immediately before the transition, as depicted in Figure 7.89 and Figure 7.90.
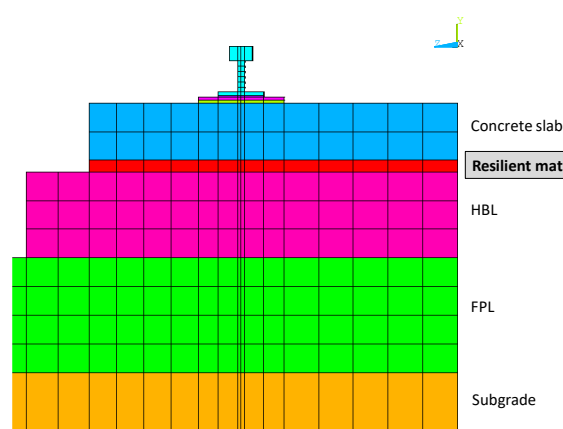
Figure 7.89 - Position of the resilient mat

a)   b)
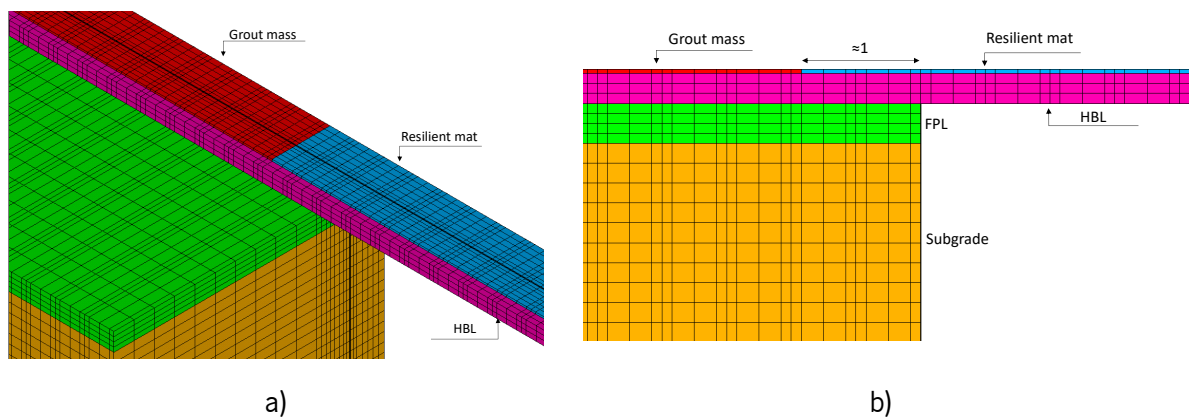
Figure 7.90 –Model with the inclusion of the resilient mat: a) 3D view; b) longitudinal section

Taking into account this geometry, the resilient mat presents a thickness of 40 mm and it was modelled with solid elements. Several values of the stiffness of the resilient mat were tested in an iterative process. The main goal was to balance the stiffness of the ballastless track in the embankment and in the tunnel in order to reduce the concentration of stresses on the concrete slab and HBL in the transition. Thus, static analyses were performed and the displacements were compared in the three sections (Figure 7.91): embankment, tunnel, and tunnel with a resilient mat under the concrete slab. To perform these analyses, the axle loads of a bogie of the Alfa Pendular train were applied statically on the top nodes of the rail. The displacements were measured on the top nodes of the concrete slab in each section (considering the length of the bogie) and were compared.

<center>a)   b)</center>
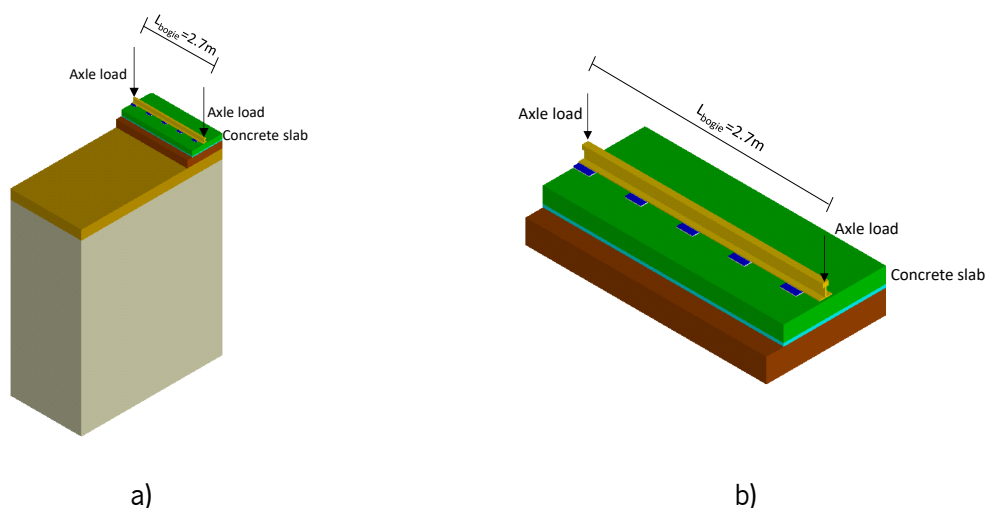
Figure 7.91 - Static analysis on different sections of the model: a) axle load applied on the embankment; b) axle load applied on the tunnel (with and without resilient mat)

The iterative process involves the test of different hypotheses, whose properties are described in Table 7.6. Regarding hypothesis 1, the properties (k – dynamic stiffness - and ρ) were obtained from the catalogue *Trackelast - Slab Track Mats*. Moreover, Sol-Sánchez et al. (2015) categorized the under-ballast mats according to their dynamic bedding modulus (C_{dyn} in N/mm³): hard (>0.22 N/mm³), medium (0.09-0.22 N/mm³), soft (0.05-0.09 N/mm³) and very soft (0.03-0.05 N/mm³). Although this classification has been defined for the under-ballast mats, it was used to categorize the stiffness of the resilient mats tested on the numerical model of the ballastless track system. This means that the first hypothesis considers a very soft mat while in the second hypothesis the mat is classified as medium. Regarding the damping, the values defined in the work developed by Zbiciak et al. (2017) were selected (ξ=2.5%). In this analysis, a *Poisson* ration equal to 0 was adopted since the finite elements that are modelling the resilient mat are confined due to the connection to the concrete slab and HBL. This means that this material can only deform in the vertical direction.

<center>Table 7.6 – Properties of the resilient mat</center>

Hypothesis	Properties	k (kN/mm³)	E (Pa)	ρ (kg/m3)	ν	α (ξ=2.5%)	β (ξ=2.5%)
1	Resilient mat	0.028	1.12×10⁶	450	0	1.5325	3.88183×10⁵
2		0.126	5.04×10⁶	450	0	1.5325	3.88183×10⁵

The obtained results are depicted in Figure 7.92. Figure 7.92 a) compares the vertical displacements obtained on the top nodes of the concrete slab in the longitudinal direction along the length of the bogie in the alignment under the loading. Figure 7.92 b) presents the vertical displacements along the cross-section under the loading. With these results, it is possible to conclude that it is necessary to use a

<center>321</center>

resilient mat with a stiffness equal to or similar to 0.126 N/mm³ with a thickness of 40 mm in order to harmonize the stiffness transition. Otherwise, there is a stiffness difference that can be traduced in the static displacements. Indeed, the results show that, without the resilient mat, the static displacements in the section placed in the tunnel are close to 0 while in the embankment are close to 0.2 mm.

The mean displacements were also compared, and the results are described in Table 7.7. The mean displacement of each section was obtained considering the nodes selected in the longitudinal direction (under the loading of the bogie – L=2.70m) and cross-direction. These results confirmed the graphical results and the necessity to use a resilient mat with stiffness close to 0.126 N/mm³ to balance the stresses and displacements in the transition.

a)   b)
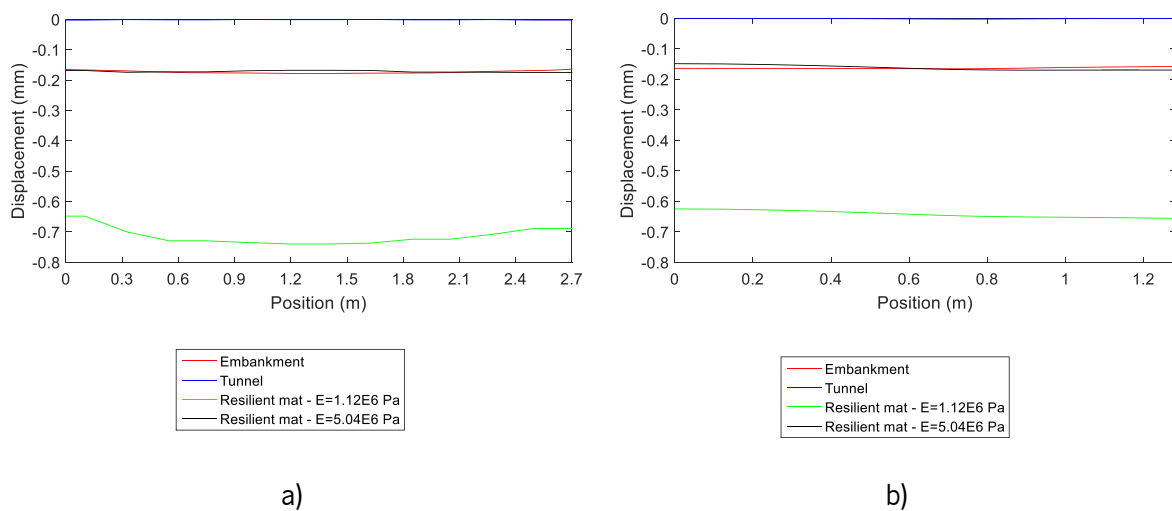
Figure 7.92 - Static vertical displacement at the top nodes of the concrete slab: a) in the longitudinal direction (*x*-axle); b) in the cross-direction (*z*-axle)

Table 7.7 – Mean static displacements

Mean displacement - $\bar{x}$ (m)	Embankment	Tunnel	Resilient mat 1 E=1.12×10⁶ Pa	Resilient mat 2 E=5.04×10⁶ Pa
Longitudinal direction	$\bar{x} = -0.17069$	$\bar{x} = -0.0014$	$\bar{x} = -0.64334$	$\bar{x} = -0.17019$
Cross direction	$\bar{x} = -0.16307$	$\bar{x} = -0.0011$	$\bar{x} = -0.69987$	$\bar{x} = -0.16343$

Considering the geometry and the adopted properties, the displacements on the top nodes of the concrete slab, HBL, FPL and subgrade were obtained. The results are depicted in Figure 7.93. The results show that there are differences in the displacements, mostly in the concrete slab. The differences in the displacements of the HBL, FPL and subgrade are very residual. These results are expected since the placement of the resilient mat has more impact on the displacements of the concrete slab in the tunnel zone.
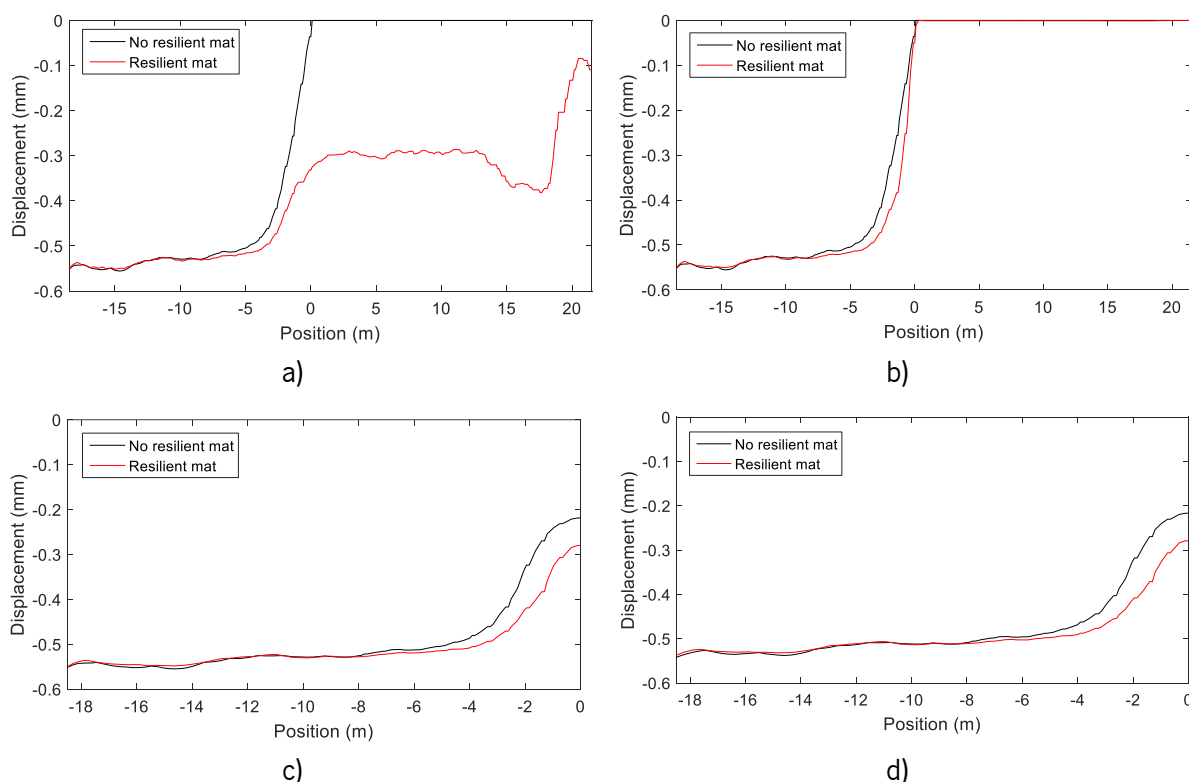
Figure 7.93 - Comparison of the displacements with and without resilient mat along the track: a) maximum displacements on the top nodes of the concrete slab; b) maximum displacements on the top nodes of the HBL; c) maximum displacements on the top nodes of the FPL; d) maximum displacements on the top nodes of the subgrade

Despite the importance of the analysis of the displacements, it is imperative to evaluate the vertical and longitudinal stresses. The results regarding the concrete slab are presented in Figure 7.94. The results regarding the HBL are presented in Figure 7.95.

The results depicted in Figure 7.94 and Figure 7.95 show a reduction of the longitudinal and vertical stresses (σ_x and σ_y) along the track. Regarding the concrete slab, the results present a reduction of the maximum longitudinal stress value at x=0 m. Regarding the vertical stress, there is also a reduction of its value at x=0 m. This attenuation of the stress values is also visible in the HBL in terms of longitudinal and vertical stresses. Thus, despite the differences, the effects of the resilient mat are not extremely significant. A parametric study related to the properties of the resilient mat is purposed in future works to optimize its benefits regarding the stresses at the concrete slab and HBL level.
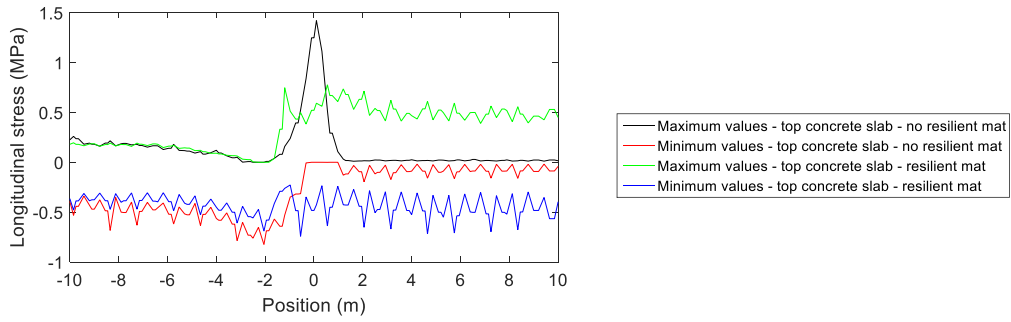
a)
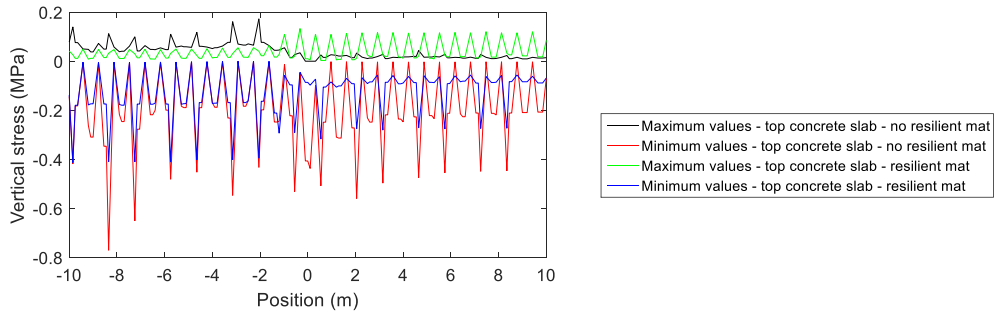
b)

Figure 7.94 - Comparison of the stresses (along the track) with and without resilient mat: a) longitudinal stresses on the top nodes of the concrete slab; b) a) vertical stresses on the top nodes of the concrete slab
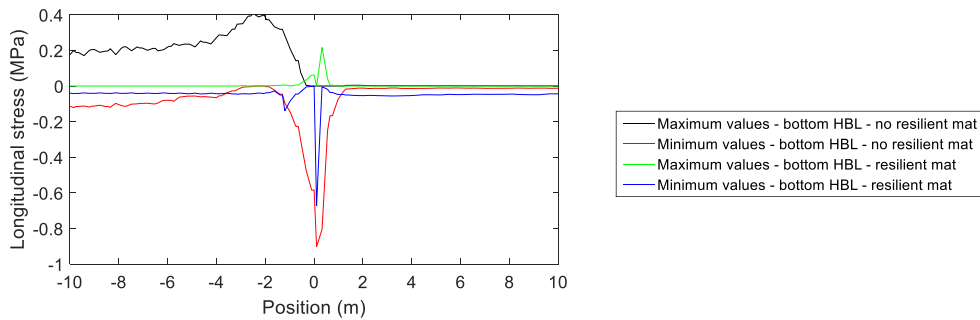
a)
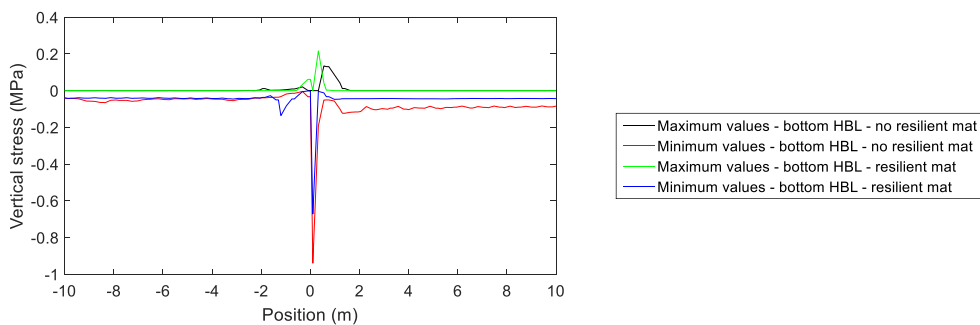
b)

Figure 7.95 - Comparison of the stresses (along the track) with and without resilient mat: a) longitudinal stresses on the bottom nodes of the HBL; b) vertical stresses on the bottom nodes of the HBL

7.8   Final considerations

This Chapter and the obtained results are an important contribution and provide good highlights about the performance of the ballastless track involved in this type of transition zone. The obtained conclusions are based on a powerful 3D modelling which, despite the computation time, is the most suitable tool for this type of numerical analysis.

Several parametric tests were performed before the analysis of the behaviour of this transition zone, which includes the optimization of the geometry, modelling strategies used to model the different materials through different types of elements, selection of the most appropriate time step, inclusion of the contact elements between the super and substructure, analysis of the gravity effects, etc. Each analysed situation had repercussions on the obtained results, which means that some assumptions were adopted throughout these "preliminary" studies. In the end, the results of the modelling of the transition zone considering the passage of the first four bogies were analysed in more detail taking into account the results of the displacements, accelerations, and stresses in some elements of the ballastless track. Indeed, the stresses of the subgrade and FPL were analysed in more detail since these are the main inputs of the selected permanent deformation model. Thus, the stresses of the FPL and subgrade (which include the geostatic stresses and the stresses induced by the vehicle) were used to determine the permanent deformation on these finite elements. These deformations were then implemented on the nodes of the 3D modelling. This methodology allowed simulating the long-term dynamic performance of a transition zone, which was one of the goals of this Thesis. The methodology was implemented with success and allowed to add knowledge within the scope of the study of the ballastless track system in transition zones, which is very different from the performance of the ballasted track. The results show that the maximum cumulative permanent displacement of the ballastless track over the embankment under the loading alignment is close to 0.52 mm. Furthermore, the structure shows satisfactory long-term performance after 1 million cycles. In order to evaluate the impact of higher permanent deformations on the performance of the ballastless track, the permanent deformation results were scaled 15 times. The scaling can be interpreted as a pessimistic scenario when poor FPL and subgrade conditions are observed (in terms of material's properties and compaction). The results have impact, mostly, on the sections far from the transition zones. This impact was evaluated through the displacements, stresses, and interaction force between the HBL and FPL. Indeed, in some sections of the track, loss of contact between these elements was verified. The iterative procedure with a higher number of load cycles should continue in future works.

Due to the high concentration of the stresses on the superstructure (concrete slab and HBL) in the transition zone, a resilient mat was included under the concrete slab in the tunnel and the first meter of the embankment immediately before the transition in order to try to mitigate this phenomenon. This mat gives some flexibility to the system in the tunnel and reduces the higher stresses concentrated on the transition zone. The inclusion of the resilient mat can be an important step in the optimization process of the system among others such as the optimization of the geometry or properties of the materials. The results show a reduction in the stress levels of the concrete slab and HBL. A higher impact was expected with the implementation of this mitigation measure. Thus, a parametric study related to the calibration of the properties of the resilient mat is purposed in future works to optimize its benefits.

8   Conclusions and future developments

This Chapter aims to summarize the main conclusions of this research and highlight the major contributions to the railway field of research. Furthermore, based on the work performed and presented in this document, a direction for future research is also provided.

The research presented in this Thesis aimed at obtaining a more comprehensive understanding of the structural behaviour of transition zones, considering a case study. In order to fully understand the long-term behaviour of the transition zones several steps were accomplished: a) fully understanding of the behaviour of the geomaterials when submitted to cyclic loads induced, for example, by the passage of trains (the behaviour includes the recoverable and irrecoverable deformations); b) comparison between the ballasted and ballastless tracks (identification of the main differences and similarities) including the structural modelling and modelling of the materials; c) short and long-term performance of the ballasted and ballastless tracks through implementation of 2.5D models and the permanent deformation models; d) definition and calibration of 3D models of ballasted and ballastless tracks based on laboratory tests data (obtained through full-scale physical modelling); e) analysis of the short and long term structural performance of a transition zone (ballastless track over an embankment to a tunnel) through a 3D calibrated numerical modelling considering the train-track dynamic interaction.

8.1   Final considerations and achievements

The ballasted and ballastless tracks present some similarities in terms of materials but differences in terms of performance (short-term and long-term), mainly due to the stiffness of each structure. As expected, the ballast layer confers to the ballasted track lower stiffness when compared to the concrete slab of the ballastless track. The work presented in this Thesis is mainly focused on the long-term behaviour of the railway structures with special concern regarding the transition zones. These are areas where the degradation process is more accelerated than the remaining zones of the railway network. As understandable, this is a very complex and sensitive topic that needs a deeper understanding. From this research, it is possible to conclude that there is still no method/mitigation measure that generates an absolute consensus between the researchers and railway Administrators since each mitigation approach presents advantages and disadvantages.

This thesis is about, most of all, the prediction and understanding of the long-term performance of the railway structures. In order to comprehend the phenomenon of the permanent/plastic deformation and also the recoverable deformation, an extensive study was carried out. The presented work summarises

the main models described in the bibliography used to estimate both types of deformations (recoverable and permanent) and identify which are the most complex and simplistic models and approaches and also the variables/factors that most affect the deformation of the geomaterials. Indeed, the mechanistic-empirical models (related to resilient and permanent deformations) are summarised in the Annex according to the type of material. This summary can be very helpful when modelling the sub-structure and predicting its performance. From this analysis (several models are scanned and analysed, including the elastoplastic models and the shakedown theory applied in the scope of the development of permanent deformation), an empirical permanent deformation model was selected to be applied throughout the thesis. The selected permanent deformation model includes the influence of the initial stress state, the yielding criterion and the stress state induced by the traffic. Furthermore, a parametric study was performed to evaluate the robustness of the models and their sensitivity. In this analysis, some models and materials were selected. Based on these results, a novel geomechanical classification was purposed. This tool establishes a relation between the UIC classification and both resilient and permanent deformation. The final product shows a wide range of results/deformations. Indeed, this range is a reflection of the variation of the properties of the materials even with the same UIC classification that influenced both types of deformations. For example, the results show that both resilient modulus and permanent deformation are sensitive to the variation of the moisture content. Indeed, the novel geomechanical classification can be a helpful tool in the modelling of a substructure since gathers several important informations: UIC classification, permanent deformation and resilient modulus.

In order to comprehend the importance of the subgrade in the long-term behaviour of the ballasted and ballastless tracks, a parametric study was performed. The results showed that the performance of the subgrade of the ballasted and ballastless tracks are not so different according to the factors analysed: wavelength of the unevenness' profile, the train's speed, mechanical properties of the subgrade and the geometric position of the analysis in the track development direction (x-axle position). Indeed, the results showed that both ballasted and ballastless tracks present some advantages and disadvantages depending on the factors analysed. Furthermore, this study shows the importance and the influence of some factors in the degradation process of the railway tracks. For example, the train speed and, mostly, its approaching to the critical speed of the structure have a very significant impact on the performance of the railway structures in terms of stresses and permanent deformations. On the other hand, the range of the wavelengths, mechanical properties of the subgrade (cohesion and friction angle) and the spatial variability of the unevenness' profile have less impact. The evaluation of these parameters was performed through the stress amplification factor (*SAF*) and the permanent deformation amplification factor (*PDAF*).

Indeed, a new approach regarding the evaluation of the long term performance (considering the influence of the quasi-static and dynamic mechanisms) was introduced through the *PDAF*. Moreover, regarding the ballastless track, two structures were modelled to evaluate the influence of the support layers in the response of the subgrade: *Rheda* system and a simplification of this structure considering only the concrete slab (the support layers were omitted). Indeed, this analysis can be interpreted as the first step to future optimizations in the ballastless track. The results showed that the ballastless track only with concrete slab can be an option instead of the "ordinary" ballastless track (*Rheda* system) since presents a good overall performance considering all the factors analysed (taking into account the evaluation of the *SAF* and *PDAF*). The only disadvantage is related to the higher absolute values of the permanent deformation.

Thus, the parametric study shows the importance of the ballast layer in the permanent deformation of the ballasted track, since, without the inclusion of this layer in the long-term analysis of the ballasted track, the performance is similar to the ballastless track. This conclusion was confirmed considering the experimental results obtained in physical modelling developed in the laboratory of the Heriot-Watt University. The full-scale GRAFT-2 facility was adopted to evaluate the short and long-term performance of the ballasted and ballastless tracks. The long-term analysis was only possible since both structures were submitted to 3.5 million cycles, which allowed to obtain significant data regarding the permanent deformation. The experimental results showed that the ballastless track displacements were significantly lower when compared to the ballasted track (about 15-20 times), as expected. Thus, the results confirm the significant influence of the ballast layer in the permanent deformation of the ballasted track structure. From the experimental cyclic loading tests, two 3D numerical models were successfully calibrated using experimental results from the cyclic loading tests performed on slab and ballasted tracks sections of 2.2 m length. The calibration process started with the short-term calibration where the experimental and numerical displacements were compared in an iterative process and the geotechnical properties of the track foundation materials (subgrade and FPL) in terms of *Young modulus* and *Poisson's* ratio were calibrated. Furthermore, the ballast's properties (*Young modulus* and *Poisson's* ratio in the case of the ballasted track), as well as the equivalent properties of the railpads were also successfully adjusted. The displacements measured by the LVDT's showed higher discrepancies when compared to the numerical results where the curves corresponding to each LVDT were almost overlaid. It was possible to conclude that this phenomenon occurs due to a rearrangement of the particles during the cyclic tests, especially in the ballasted layer, but also in the subgrade and FPL. After the short-term calibration, a novel approach was introduced to simulate the long-term behaviour of both structures through the calibration of an

empirical permanent deformation model to find the best fit between the experimental and numerical data. This calibration was improved since the time-hardening concept was used to simulate the influence of the stresses and permanent deformations induced in the geomaterials during the tests with a frequency of 5.6 Hz in the tests with a frequency of 2.5 Hz, which are performed afterwards (the substructure was the same in both dynamic/cyclic tests). This calibration was performed using the *least-square* fitting method. Furthermore, from a sensitivity analysis, it was possible to conclude that the cohesion of the subgrade can have a significant impact on the permanent deformation. Indeed, the parametric study performed previously also showed that the friction angle has influence on the permanent deformation. Thus, the obtained results from the calibration process (short term and long term) show good agreement between the numerical and experimental results. Furthermore, this novel approach introduced in this analysis can be a valuable tool in future modelling of long-term degradation of track structures in transition zones and can be used to develop predictive strategies and maintenance, reducing life-cycle costs.

The studies about the long-term performance of a transition zone allow analysing several variables that can affect the numerical results in such complex models. The influence of the adopted time step, the treatment of the artificial boundaries, the influence of a complete or symmetric model, the type of mesh, the geometry, and the distance of the centre of the model to the horizontal and vertical boundaries were analysed in this work. In this case, the *Lysmer* formulation was adopted to absorb the waves and the contact elements between the super and substructure were included after the consideration of the gravity load. The obtained results show that, in the flexible zone (placed on the embankment), the stresses of the elements (namely the HBL) of the superstructure are lower when compared to the stiffer zone, which corresponds to the tunnel. This is due to the stiffness effect. The results also show that the stresses present some variation along the transversal direction. Furthermore, in the analysis of the displacements of the axles, there is a decrease in the value of this variable along the transition between the flexible and the stiffer area. The results also show higher displacements of the rail, concrete slab, HBL, FPL and subgrade when the contact elements are included between the HBL and FPL. These elements allow simulating the detachment of the superstructure after the passage of the vehicle. Regarding the long-term analysis, the maximum cumulative permanent deformation of the substructure under the loading alignment was determined and is equal to 0.52 mm. The permanent deformation results also show that the layers that most contribute to the permanent deformation are located between y=-0.738 m (top of the FPL) and y=-4.138 m (in the subgrade). This means that all the layers of FPL and 30% of the layers of the subgrade contribute significantly to the development of the permanent deformation. After the determination of the permanent deformation considering 1 million load cycles, the results were inputted

on the 3D model. The ballastless track shows a good long-term performance since no significant differences were obtained in the displacements and stress results when the initial conditions were compared to the conditions associated with the deformed track. This is due to the high stiffness of the ballastless track structure given, mostly, by the concrete slab. Indeed, several studies show that the subgrade has a small contribution to the permanent deformation of the track when compared to the ballast in the ballasted track. Indeed, some of these results were presented in Chapter 5 where is shown that, in some situations, the long term performance of ballasted and ballastless tracks structures are similar. To overcome this problem and analyse the impact of higher permanent deformations on the performance of the ballastless track in a transition zone, the permanent deformation was scaled 15 times. The main goal of this analysis is to simulate poor subgrade and FPL conditions (also associated with bad compaction conditions). The results show a significant impact on the displacement and stress results mainly in sections far from the transition zone. In this area (or close), the impact is not significant since the stresses of the geomaterials are lower, which means that the permanent deformations are also reduced, even when scaled. The continuation of the iterative process is purposed, and a higher number of load cycles should be contemplated to analyse its effect on the long-term performance of the ballastless track in transition zones.

Furthermore, an optimization of the system was purposed. The solution includes the placement of a resilient mat under the concrete slab in the tunnel and in the first meter immediately before the transition to reduce the concentration of the stresses on the transition. The mat gives some flexibility to the system in the tunnel and its stiffness was statically calibrated. The results show a reduction in the stress levels of the HBL and concrete slab. Thus, it is possible to conclude that the capacity of the model and the methodologies implemented can be used to study other solutions with a view to their optimising.

8.2 Perspectives for future work

The long-term behaviour of the substructure of a railway track is, nowadays, an important topic in the scope of the evaluation of the performance of the railway lines. Thus, efforts should be put into mitigating problems associated with the poor performance of the substructure, preventing high maintenance costs and operations. Furthermore, this topic assumes special importance in some specific areas of the railway lines: transition zones. In these areas, the degradation rate is meaningfully higher, which causes problems to the Railway network Administrators since this degradation can lead to, for example, a decrease in passenger comfort. In order to prevent this and other problems such as the reduction of the train speed

331

in these areas, a higher number of maintenance operations are required, increasing the track life-cycle costs of the structure.

Throughout this work, the concept of permanent deformation and its consequences were explored from the beginning until the end of this Thesis. Firstly, the main concepts of resilient and permanent/plastic deformations were explained, including the factors that affect these behaviours and the strategies (laboratory tests and mathematical models) used to predict and control them. In the end, a novel geomechanical classification is presented based on two parametric studies about the resilient modulus and empirical permanent deformation models. Indeed, this work is new and should be complemented and improved considering the information about more and different models and, above all, materials. The classification presented in this work is considered as the first step of this type of analysis but is still incomplete. The inclusion of more materials implies the research of even more models and full information about the materials tested (mostly in terms of granulometry and plasticity properties), which is difficult to find. Furthermore, the state condition of the materials during the laboratory tests, representative of field conditions, is also an important information to consider in the geomechanical classification.

After understanding the concept and consequences of the permanent deformation and its influence on the long-term behaviour of the track substructures, a parametric study was carried using the 2.5D FEM-PML approach to evaluate the behaviour (short and long-term) of the ballasted and two types of ballastless tracks (original *Rheda* system and an optimized version without the support layers). Despite the extensive list of analyses (more than 60 case studies), other parameters could be included in this research:

- Train geometry, type of train – passenger or freight train -, track stiffness and layered ground;
- Analysis of the combined effect of the variation of the friction angle and cohesion using the 2.5D FEM-PML and also the results from the 3D modelling (based on the laboratory physical tests);
- Extension of the analysis to other elements and respective alignments in addition to element 1 in order to reduce the uncertainty of the obtained conclusions;
- Analysis of the influence of the ballast layer in the permanent deformation of the ballasted structure and its comparison with the ballastless track. Moreover, it would be interesting to replicate this analysis considering fully 3D models, mostly in the case of the ballasted track since in the 2.5D models, a continuity of the sleepers is assumed, which not corresponds to the reality since the sleepers present a periodic character. The results obtained with the 2.5D FEM-PML

approach can be compared with the results obtained in the 3D calibrated model based on the laboratory physical tests.

The calibrated material properties and permanent deformation parameters were implemented in the study of a specific transition zone (ballastless track over an embankment - tunnel) presented in the last Chapter. Due to the very demanding calculation time, some important variables and effects weren´t included in this study. This work should be complemented through:

- Study/influence of the train's speed. Indeed, higher train speeds should be considered since this is a factor that has a significant influence on the long-term behaviour, even more, when the train's speed is close to the critical speed of the structure. These studies could provide valuable information to the Railway Infrastructure Managers, and thus contributing to a more efficient and sustainable railway transport system;

- Analysis of the influence of the model of the vehicle (the effects of the freight train on the railway track should also be analysed) and the direction of the train's circulation. In this case, only the direction from the flexible to the stiffer zone was considered;

- Study of the effect of the inclusion of resilient elements on the embankment;

- Analysis of the effect of full-passage of the *Alfa Pendular*. The results should be compared with the passage of the first two and four bogies;

- Increase of length of the embankment zone, despite the growth in terms of the calculation time;

- Consideration of a higher number of load cycles in the simulation process of the permanent deformation of the track (application of the iterative methodology presented in Chapter 7). Indeed, the continuation of the long-term analysis (with higher number of load cycles) is purposed until the maximum value of the acceleration of the axle's vehicle (all) reaches the limit value, which is equal to 70 m/s^2, despite the good performance of the structure;

- Adoption of poor subgrade and FPL conditions in order to increase the stiffness difference and analyse its impact on the performance of the track. Furthermore, artificial bump profiles (with different magnitudes) can be added to the top of the FPL and analyse its influence on the response of the ballastless track. This study is similar to the analysis performed with the scaling of the permanent deformation but allows to change the normalised relative displacements between two consecutive nodes. With these artificial bump profiles, it is possible to have higher permanent deformation values in sections close to the transition that may have impact on the concrete slab and HBL stresses;

- Performance of a parametric study related to the properties of the resilient mat to analyse the impact of its benefits with the stiffness adopted;

- Definition and study of other optimization solutions to try to reduce the costs and increase the efficiency of the long-term dynamic performance of the railway track, mostly in transition zones. Study of possible optimisation measures at the structure level in terms of geometry or properties of the materials. Indeed, the suppression of the support layer is purposed as a study case to complement and support the analysis performed in Chapter 5.

9   References

Aashto 1994. Standard test method for determining the resilient modulus of soils and aggregate materials

Aashto 2003. Determining the resilient modulus of soils and aggregate materials. *T307–99, Standard specifications for transportation materials and methods of sampling and testing.* Washington, D.C.

Abadi, T., Pen, L. L., Zervos, A. & Powrie, W. A Review and Evaluation of Ballast Settlement Models using Results from the Southampton Railway Testing Facility (SRTF).   Advances in Transportation Geotechnics. The 3rd International Conference on Transportation Geotechnics (ICTG 2016), 2016 Guimarães, Portugal. 999–1006.

Abdelkrim, M., Bonnet, G. & Buhan, P. D. 2003. A computational procedure for predicting the long term residual settlement of a platform induced by repeated traffic loading. *Computers and Geotechnics,* 30**,** 463–476.

Aggestam, E. & Nielsen, J. C. O. 2020. Simulation of vertical dynamic vehicle–track interaction using a three-dimensional slab track model. *Engineering Structures,* 222**,** 110972.

Al Shaer A., Duhamel D., Sab K., Foret G. & L., S. 2008. Experimental settlement and dynamic behavior of a portion of ballasted railway track under high speed trains. *Journal of Sound and Vibration,* 316**,** 213-233.

Alva-Hurtado, J. E. & Selig, E. T. 1981. Permanent Strain Behavior of Railroad Ballast. *In:* ICSMFE, P. C. O. X. (ed.). 10th International Conference on Soil Mechanics and Foundation Engineering, 15-19th June 1981 Stockholm. A.A Balkema, Rotterdam.

Alves Costa, P. 2011. *Vibrações do Sistema Via-maciço Induzidas por Tráfego Ferroviário. Modelação Numérica e Validação Experimental.* PhD Thesis, Faculdade de Engenharia da Universidade do Porto, Porto, Portugal.

Alves Costa, P., Calçada, R. & Silva Cardoso, A. 2012. Track–ground vibrations induced by railway traffic: In-situ measurements and validation of a 2.5D FEM-BEM model. *Soil Dynamics and Earthquake Engineering,* 32**,** 111-128.

Alves Costa, P., Calçada, R., Silva Cardoso, A. & Bodare, A. 2010. Influence of soil non-linearity on the dynamic response of high-speed railway tracks. *Soil Dynamics and Earthquake Engineering,* 30**,** 221-235.

Alves Costa, P., Colaço, A., Calçada, R. & Silva Cardoso, A. 2015. Critical speed of railway tracks. Detailed and simplified approaches. *Transportation Geotechnics,* 2**,** 30–46.

Alves Costa, P., Lopes, P. & Silva Cardoso, A. 2018. Soil shakedown analysis of slab railway tracks: Numerical approach and parametric study. *Transportation Geotechnics,* 16**,** 85-96.

Alves Costa, P., Soares, P., Colaço, A., Lopes, P. & Connolly, D. 2020. Railway critical speed assessment: A simple experimental-analytical approach. *Soil Dynamics and Earthquake Engineering,* 134.

Alves Ribeiro, C. 2012. *Transições Aterro – Estrutura em Linhas Ferroviárias de Alta Velocidade: Análise Experimental e Numérica.* PhD thesis Faculdade de Engenharia da Universidade do Porto, Porto, Portugal.

Alves Ribeiro, C., Calçada, R. & Delgado, R. 2018. Calibration and experimental validation of a dynamic model of the train-track system at a culvert transition zone. *Structure and Infrastructure Engineering,* 14**,** 604-618.

Alves Ribeiro, C., Paixão, A., Fortunato, E. & Calçada, R. 2015. Under sleeper pads in transition zones at railway underpasses: numerical modelling and experimental validation. *Structure and Infrastructure Engineering,* 11**,** 1432-1449.

Andersen, L., Nielsen, S. R. K. & Krenk, S. 2007. Numerical methods for analysis of structure and ground vibration from moving loads. *Computers & Structures,* 85**,** 43-58.

Andersson, C. 2003. Vertical and lateral track dynamics – measurements, model and calibration. Research Report, Chalmers Applied Mechanics, Gothenburg

Ando, K., Sunaga, M., Aoki, H. & Haga, O. 2001. Development of slab tracks for Hokuriku Shinkansen lines. *Quarterly Report of RTRI,* 42**,** 35-41.

Anochie-Boateng, J. K., Paige-Green, P. & Mgangira, M. 2009. Evaluation of test methods for estimating resilient modulus of modules of pavement geomaterials. *28th Annual Southern African Transport Conference "Sustainable Transport".* CSIR International Convention Centre, Pretoria, South Africa.

Ara Inc. Eres Division 2004. Guide for Mechanistic-Empirical Design of New and Rehabilitated Pavement Structures National Cooperative Highway Research Program Transportation Research Board, National Research Council

Araújo, N. 2010. *High-speed trains on ballasted railway track: Dynamic stress field analysis* PhD Thesis.

Area 1996. Manual for railway engineering. Vol. 1. American Railway Engineering Association (AREA). Washington, D.C.

Arema. Implementing track transition solutions for heavy axle load service. In Proceedings of the AREMA 2005 Annual Conferences, 2005 Chicago, IL, USA, 25–28 September 2005.

Astm-D2487-17 2017. Standard practice for classification of soils for engineering purposes (Unified Soil Classification System). *ed. West Conshohocken.* PA: ASTM International.

Audley, M. & Andrews, J. 2013. The effects of tamping on railway track geometry degradation. *Proceedings of the Institution of Mechanical Engineers, Part F: Journal of Rail and Rapid Transit,* 227**,** 76-391.

Ayasse, J.-B. & Chollet, H. 2006. Wheel-Rail Contact. *Handbook of Railway Vehicle Dynamics.* Taylor & Francis.

Ba, M. 2018. Correlation between resilient modulus and permanent deformation during a large scale model experiment of unbound base course. *Lecture Notes in Civil Engineering.*

Balay, J., Gomes Correia, A., Jouve, P., Hornych, P. & Paute, J. 1998. Étude expérimentale et modélisation du comportement mécanique des graves non traitées et des sols supports de chaussées dernières avancées. *Bulletin Des Laboratoires Des Ponts Et Chaussées,* 216**,** 3-17.

Banimahd, M., Woodward, P., Kennedy, J. & Medero, G. 2013. Three-dimensional modelling of high speed ballasted railway tracks. *Proceedings of the Institution of Civil Engineers: Transport,* 166**,** 113-123.

Banimahd, M., Woodward, P. K., Kennedy, J. & Medero, G. M. 2012. Behaviour of train-track interaction in stiffness transitions. *Proceedings of the Institution of Civil Engineers: Transport,* 165**,** 205-214.

Barksdale, R. D. Laboratory evaluation of rutting in base course materials. Proc. 3rd Int. Conf on the Structural Design of Asphalt Pavements, 1972 London.

Bathe, K. J. & Bouzinov, P. A. 1997. On the constraint function method for contact problems. *Computers & Structures,* 64**,** 1069-1085.

Belytschko, T., Liu, W. K., Moran, B. & Elkhodary, K. 2000. *Nonlinear Finite Elements for Continua and Structures*, Wiley.

Berggren, E. 2009. *Railway Track Stiffness - Dynamic Measurements and Evaluation for Efficient Maintenance.* Ph.D Thesis.

Bezin, Y., Farrington, D., Penny, C., Temple, B. & Iwnicki, S. 2010. The dynamic response of slab track constructions and their benefit with respect to conventional ballasted track. *Vehicle System Dynamics,* 48**,** 175-193.

Bian, X., Chao, C., Jin, W.-F. & Chen, Y.-M. 2011. A 2.5D finite element approach for predicting ground vibrations generated by vertical track irregularities. *Journal of Zhejiang University SCIENCE A,* 12.

Bian, X., Jiang, H., Chen, Y., Jiang, J. & Han, J. 2016. A full-scale physical model test apparatus for investigating the dynamic performance of the slab track system of a high-speed railway.

Proceedings of the Institution of Mechanical Engineers, Part F: Journal of Rail and Rapid Transit, 230**,** 554-571.

Bian, X., Jiang, H., Cheng, C., Chen, Y., Chen, R. & Jiang, J. 2014. Full-scale model testing on a ballastless high-speed railway under simulated train moving loads. *Soil Dynamics and Earthquake Engineering,* 66**,** 368–84.

Biarez, J., Liu, H., A., G. C. & Taibi, S. Stress-strain characteristics of soils interesting the serviceability of geomaterials structures. Proc. II Int. Conf. on Pre-failure Deformation Characteristics of Geomaterials, IS Torino 99, Jamiolkowski, et al.Eds. Balkema, Rotterdam. (1) 617-624, 1999.

Blanco-Lorenzo, J., Santamaria, J., Vadillo, E. G. & Oyarzabal, O. 2011. Dynamic comparison of different types of slab track and ballasted track using a flexible track model. *Proceedings of the Institution of Mechanical Engineers, Part F: Journal of Rail and Rapid Transit,* 225**,** 574-592.

Boler, H., Mishra, D., Tutumluer, E., Chrismer, S. & Hyslip, J. P. 2018. Stone blowing as a remedial measure to mitigate differential movement problems at railroad bridge approaches. *Proceedings of the Institution of Mechanical Engineers, Part F: Journal of Rail and Rapid Transit,* 233**,** 63-72.

Boyce, J. R. 1980. A non-linear model for the elastic behaviour of granular materials under repeated loading. Proc. Int. Symp. Soils under Cyclic & Transient Loading, 1980 Swansea. 285-294.

Brown, S., Yu, H., Juspi, H. & J, W. 2012. Validation experiments for lower-bound shakedown theory applied to layered pavement systems. *Géotechnique* 62**,** 923–932.

Brown, S. F. & Hyde, A. F. L. Significance of cycling confining stress in repeated-load triaxial testing of granular material. Transp. Res. Rec, 1975 Washington D.C.: Transportation Research Board, 49-58.

Brown, S. F., Kwan, J. & Thom, N. H. 2007. Identifying the key parameters that influence geogrid reinforcement of railway ballast. *Geotextiles and Geomembranes,* 25**,** 326-335.

Brown, S. F., Lashine, A. K. F. & Hyde, A. F. L. 1975. Repeated load triaxial testing of a silty clay. *Geotechnique,* 25**,** 95-114.

Brown, S. F. & Pappin, J. W. 1985. Modeling of granular materials in pavements. *Transport Research Record, Transportation Research Board, Washington, D.C.,* 1022**,** 45–51.

Brown, S. F. & Pell, P. S. An experimental investigation of the stresses, strains and deflections in layered pavement structure subjected to dynamic loads. Proceedings of the 2nd International Conference on Structural Design of Asphalt Pavements 1967 Ann Arbor, USA. 487-504.

Brown, S. F. & Selig, E. T. 1991. *The design of pavement and rail track foundations,* Blackie and Son Ltd., Glasgow, Scotland, 249–305.

Bruni, S., Collina, A. & Corradi, R. Numerical Modelling of Railway Runnability and Ballast Settlement in Railroad Bridges. Eurodyn, 2002.

Burrow, M. P. N., Bowness, D. & Ghataora, G. S. 2006. A Comparison of Railway Track Foundation Design Methods. *In:* SCHOOL OF ENGINEERING, U. O. B., EDGBASTON, BIRMINGHAM (ed.).

Cai, Y., Sun, Q., Guo, L., Juang, C. H. & Wang, J. 2015. Permanent deformation characteristics of saturated sand under cyclic loading. *Canadian Geotechnical Journal,* 52**,** 795–807.

Cary, C. E. & Zapata, C. E. 2011. Resilient Modulus for Unsaturated Unbound Materials. *Road Materials and Pavement Design,* 12**,** 615-638.

Čebašek, T. M., A.F. Esen, Woodward, P. K., Laghrouche, O. & Connolly, D. P. 2018. Full scale laboratory testing of ballast and concrete slab tracks under phased cyclic loading. *Transportation Geotechnics,* 17**,** 33-40.

Cen 2005. EN1990 Eurocode: Basis of Structural design. Annex A2: Application for bridges. European Committee for Standardization.

Chai, J.-C. & Miura, N. 2002. Traffic-load-induced permanent deformation of road on soft soil. *Journal of Geotechnical and Geoenvironmental Engineering,* 128**,** 907-916.

Chan, A. H. 1990. *Permanent deformation resistance of granular layers in pavements.* PhD thesis, University of Nottingham, England.

Chazallon, C. 2000. An elastoplastic model with kinematic hardening for unbound aggregates in roads. *UNBAR 5 Conference.* Nottingham.

Chazallon, C., Allou, F., Hornych, P. & Mouhoubi, S. 2009a. Finite elements modelling of the long-term behaviour of a full-scale flexible pavement with the shakedown theory. *Int. J. Numer. Anal. Meth. Geomech,* 33**,** 45-70.

Chazallon, C., Habiballah, T. & Hornych, P. 2002. Elastoplasticity framework for incremental or simplified methods for unbound granular materials for roads. *BCRA workshop on modelling of flexible pavements.* Lisbon.

Chazallon, C., Hornych, P. & Mouhoubi, S. 2006. Elastoplastic model for the long-term behavior modeling of unbound granular materials in flexible pavements. *Int. J. Geomech.***,** 279–289.

Chazallon, C., Koval, G., Hornych, P., Allou, F. & Mouhoubi, S. 2009b. Modelling of rutting of two flexible pavements with the shakedown theory and the finite element method. 36**,** 798-809.

Chazallon, C., Koval, G. & Mouhoubi, S. 2012. A two-mechanism elastoplastic model for shakedown of unbound granular materials and DEM simulations. *Int. J. Numer. Anal. Meth. Geomech,* 36**,** 1847-1868.

Chebli, H., Clouteau, D. & Schmitt, L. 2008. Dynamic response of high-speed ballasted railway tracks: 3D periodic model and in situ measurements. *Soil Dynamics and Earthquake Engineering,* 28**,** 118-131.

Chen, R., Chena, J., Zhaob, X., Bian, X. & Chen, Y. 2014. Cumulative settlement of track subgrade in high-speed railway under varying water levels. *International Journal of Rail Transportation,* 2**,** 205–220.

Cheng, C., Bian, X., Jiang, H. & Jiang, J. Model testing on dynamic behaviors of the slab track of high-speed railway. Proceedings of the International Conference on Structural Dynamic , EURODYN, 2014. 813-818.

Chopra, A. K. 1995. *Dynamics of Structures: Theory and Applications to Earthquake Engineering*, Prentice Hall.

Chow, L. C., Mishra, D. & Tutumluer, E. 2014. Framework for development of an improved unbound aggregate base rutting model for mechanistic-empirical pavement design. *Transportation Research Record: Journal of the Transportation Research Board,* 2401**,** 11–21.

Coelho, B., Hölscher, P., Priest, J., Powrie, W. & Barends, F. 2011. An assessment of transition zone performance. *Proceedings of the Institution of Mechanical Engineers, Part F: Journal of Rail and Rapid Transit,* 225**,** 129-139.

Coelho, B. Z. & Hicks, M. A. 2015. Numerical analysis of railway transition zones in soft soil. *Proceedings of the Institution of Mechanical Engineering, Part F: Journal of Rail and Rapid Transit.*

Cohen, M. 1980. *Silent boundary methods for transient wave analysis.* PhD thesis, California Institute of Technology.

Colaço, A., Alves Costa, P. & Lopes, P. 2015. Análise Numérica da Alteração do Estado de Tensão Geomecânico Induzida pelo Tráfego Ferroviário. *Revista Internacional de Métodos Numéricos para Cálculo y Diseño en Ingeniería,* 31**,** 120-131.

Colaço, A., Costa, P. A. & Connolly, D. P. 2016. The influence of train properties on railway ground vibrations. *Structure and Infrastructure Engineering,* 12**,** 517-534.

Collins, I. & Boulbibane, M. 2000. Geomechanical analysis of unbound pavements based on shakedown theory *J Geotech Geoenviron Eng* 126**,** 50–9.

Cook, R. D., Malkus, D. S., Plesha, M. E. & Witt, R. J. 2002. *Concepts and applications of finite element analysis*, John Wiley & Sons, Inc.

Coronado, O., Caicedo, B., Taibi, S., Correia, A. G. & Fleureau, J.-M. 2011. A macro geomechanical approach to rank non-standard unbound granular materials for pavements. *Engineering Geology,* 119**,** 64-73.

Coronado, O., Caicedo, B., Taibi, S., Correia, A. G., Souli, H. & Fleureau, J.-M. 2016. Effect of water content on the resilient behavior of non standard unbound granular materials. *Transportation Geotechnics, 7***,** 29-39.

Correia, A. G. & Biarez, J. Stiffness properties of materials to use in pavement and rail track design. Geotechnical Engineering for Transportation Infrastructure. Proceedings of the 12th European Conference on Soil Mechanics and Geotechnical Engineering, 1999 Amsterdam, Netherlands., 1245-1250.

Correia, A. G., Cunha, J., Marcelino, J., Caldeira, L., Varandas, J., Dimitrovová, Z., Antão, A. & Silva, M. G. D. 2007. Dynamic analysis of rail track for high speed trains. 2D approach. 5th Intl Worksop on Application of Computational Mechanics on Geotechnical Engineering, Portugal.

Cuellar, V., Navarro, F., Andreu, M. A., Camara, J. L., Gonzalez, F., Rodriguez, M., Gonzalez, P., Diaz, R., Navarro, J. & Rodriguez, R. 2011. Short and Long Term Behaviour of High Speed Lines as Determined in 1:1 Scale Laboratory Tests. *9th World Congress on Railway Research.* Lille.

Culley, R. W. 1971. Effect of freeze-thaw cycling on stress-strain characteristics and volume change of a till subjected to repetitive loading. *Canadian Geotechnical Journal, 8***,** 359-371.

Cunha, J. 2013. *Modelling of ballasted railway tracks for high-speed trains.* PhD Thesis, University of Minho - School of Engineering.

Dahlberg, R. 2010. Railway track stiffness variations- consequences and countermeasures. *International Journal of Civil Engineering, 8*.

Dahlberg, T. 2001. Some Railroad Settlement Models - A Critical Review. *Journal of Rail and Rapid Transit,* 215**,** 289-300.

Dahlberg, T. 2003. Railway track dynamics -a survey.

Dahlberg, T. 2004. Railway track settlements - a literature review. The EU project SUPERTRACK. Linköping, Sweden.

Dahlberg, T. 2006. Chapter 6: Track Issues. *In:* IWNICKI, S. (ed.) *Handbook of Railway Vehicle Dynamics.* CRC Press: Taylor & Francis.

Dawson, A. R. & Gomes Correia, A. 1993. The effects of subgrade clay condition on the structural behaviour of road pavements, Flexible Pavements, Balkema. 113-119.

De Man, A. P. 2000. Pin-pin resonance as a reference in determining ballasted railway track vibration behaviour. *Heron,* 45.

Decourt, L. The standard penetration test. State-of-the-Art Report. *In:* BALKEMA, A. A., ed. Proc. 12th Internation Conference on Soil Mechanics and Foundation Engineering, August 13-18 1989 Rio de Janeiro, Brazil. Taylor & Francis, 2405-2416.

Delgado, R. 1990. Método dos Elementos Finitos, Texto de apoio às aulas. Faculdade de Engenharia da Universidade do Porto.

Desai, C. S. 1980. A general basis for yield, failure and potential function in plasticity. *Int. J. Numer. Anal. Methods Geomech., 4***,** 361–375.

Desai, C. S. & Faruque, M. O. 1984. Constitutive model for geologic materials. *J. Eng. Mech. Div.***,** 1391–1408.

Dimitrovová, Z. & Varandas, J. N. 2009. Critical velocity of a load moving on a beam with a sudden change of foundation stiffness: Applications to high-speed trains. *Computers & Structures, 87***,** 1224-1232.

Din-18134 1999. Determination of deformation and strength characteristics of soil by the plate loading test. *Deutsche Norm.*

Dong, K., Connolly, D. P., Laghrouche, O., Woodward, P. K. & Alves Costa, P. 2019. Non-linear soil behaviour on high speed rail lines. *Computers and Geotechnics,* 112**,** 302-318.

Douglas Montgomery & Runger, G. C. 2003. *Applied statistics and probability for engineers*, John Wiley and Sons INC.

Drumm, E. C. & Pierce, T. J. 1990. Estimation of Subgrade Resilient Modulus from Standard Tests. *Journal of Geotechnical Engineering,* 116

Dunlap, W. S. 1963. A Report on a Mathematical Model Describing the Deformation Characteristics of Granular materials. *Technical Report 1, Project 2-8-62-27.* TTI: Texas A &M University.

Ec. 2016. *EU Transport in figures* [Online]. https://ec.europa.eu/transport/sites/transport/files/pocketbook2016.pdf. [Accessed 2017].

Edil, T. B. & Moran, S. E. 1979. Soil-water potential and resilient behavior of subgrade soils. *Transp. Res. Rec.,* 705**,** 54-63.

Edilon. 2015. *One system crossing the boundaries: embedded rail system for optimum integration into tunnel, station and bridge structures* [Online]. Edilonsedra. Available: https://www.edilonsedra.com/track-system/edilonsedra-ers-for-train-tunnels-2/#tab-id-2 [Accessed].

Edris, E. V. J. & Lytton, R. L. 1976. Dynamic properties of subgrade soils, including environmental effects. *TTI-2-18-74-164-3, Texas Transp. Inst., Texas A&M Univ., College Station, Tex., May.*

El Kacimi, A., Woodward, P. K., Laghrouche, O. & Medero, G. 2013. Time domain 3D finite element modelling of train-induced vibration at high speed. *Computers & Structures,* 118**,** 66-73.

Elfino, M. K. & Davidson, J. L. 1989. Modeling field moisture in resilient moduli testing. *Resilient moduli of soils: laboratory conditions, ASCE Geotech. Special Publication, No. 24, ASCE.* New York, N.Y.

Elhannani, M. 1991. *Modèlisation et simulation numérique des Chaussées Souples.* PhD thesis, University of Nantes, Nantes, France.

Elliot, R. P. & Lourdesnathan, D. 1989. Improved characterization model for granular bases. *Transport Research Record: Transportation Research Board, Washington, D.C.,* 1277**,** 128–133.

En1990 2005. Eurocode : Basis of Structural Design – Annex A2. *ANNEX A2 : Application for bridges (Normative).* European Committee for Standardization (CEN). Brussels.

En1991-2 2003. Eurocode 1: Actions on structures - Part 2: Traffic loads on bridges. *Annex D - Basis for the fatigue assessment of railway structures.* European Committee for Standardization (CEN). Brussels.

En13231-1 2006. Railway applications - Track - Acceptance of works - Part 1: Works on ballasted track - Plain line. *EN13231.* European Committee for Standardization (CEN).

En13286-7 2004. Unbound and hydraulically bound mixtures. *Part 7: Cyclic load triaxial test for unbound mixtures* Brussels.: CEN-European Committee for Standardization.

En13848-5 2008. Railway Applications - Track - Track geometry quality - Part 5: Geometric quality levels. *EN13848.* European Committee for Standardization (CEN), Brussels, Belgium.

Erlingsson, S. & Rahman, M. S. 2013. Evaluation of permanent deformation characteristics of unbound granular materials by means of multistage repeated-load triaxial tests. *Transport Research Record: Journal of the Transportation Research Board,* 2369**,** 11–19.

Erlingsson, S., Rahman, S. & Salour, F. 2017. Characteristic of unbound granular materials and subgrades based on multi stage RLT testing. *Transportation Geotechnics,* 13**,** 28-42.

Erri 1999a. D 214 / RP 9 - Rail bridges for Speeds > 200 km/h. Annex E: Data for train types considered in studies, Final Report. European Rail Research Institute. Utrecht, Netherlands.

Erri 1999b. D 230.1 / RP1 - Embankment structure transition, Bridge ends. European Rail Research Institute. Utrecht, Netherlands.

Erri 1999c. D 230.1 / RP2 - Description of Phase II work, Bridge ends. European Rail Research Institute. Utrecht, Netherlands.

Erri 1999d. D 230.1 / RP3 - State of the art report. Embankment structure transition, Bridge ends. European Rail Research Institute. Utrecht, Netherlands.

Esveld, C. 2001. *Modern Railway Track,* MRT-Productions.

Esveld, C. & Markine, V. 2006. Assessment of high-speed slab track design. *European Railway Review,* 12**,** 55-62.

European_Rail_Research_Institute 1999. Bridge ends-embankment structure transition, state of art report. Utrecht, The Netherlands: European Rail Research Institute.

Faria, R. 1994. *Avaliação do Comportamento Sísmico de Barragens de Betão através de um Modelo de Dano Contínuo.* PhD Thesis, Faculty of Engineering of University of Porto, Porto.

Fernández Ruiz, J., Alves Costa, P., Calçada, R., Medina Rodríguez, L. E. & Colaço, A. 2017. Study of ground vibrations induced by railway traffic in a 3D FEM model formulated in the time domain: experimental validation. *Structure and Infrastructure Engineering,* 13**,** 652-664.

Ferreira, P. 2010. *Modelling and prediction of the dynamic behaviour of railway infrastructures at very high speeds.* PhD Thesis, Instituto Superior Técnico, Lisboa, Portugal.

Ferreira, P. A. & López-Pita, A. 2013. Numerical modeling of high-speed train/track system to assess track vibrations and settlement prediction. *Journal of Transportation Engineering,* 139**,** 330-337.

Fib 2006. *Precast Concrete Railway Track Systems,* Bulletin 37, FIB, September 2006.

Ford, R. 1995. Differential Ballast Settlement, and Consequent Undulations in Track, Caused by Vehicle-Track Interaction. *Vehicle System Dynamics,* 24**,** 222-233.

Fortunato, E. 2005. *Renovação de plataformas ferroviárias. Estudos relativos à capacidade de carga.* PhD Thesis, Faculty of Engineering of the University of Porto, Porto.

Fra 2007. Bridge Approaches and Track Stiffness, RR07-12. U. S. Department of Transportation. Washington, USA.

Fredlund, D. G., Began, A. T. & Wong, P. K. 1977. Relation between Resilient Modulus and Stress Conditions for Cohesive Subgrade Soils. *Transport Research Record: Journal of the Transportation Research Board,* 62**,** 73-81.

Fredlund, D. G., Bergan, A. T. & Sauer, E. K. 1975. Deformation Characterization of Subgrade Soils for Highways and Runways in Northern Environments. 12**,** 213-223.

Fröhling, R. D. 1997. *Deterioration of railway track due to dynamic vehicle loading and spatially varying track stiffness.* PhD thesis, University of Pretoria. Pretoria.

Fröhling, R. D., Scheffel, H. & Ebersöhn, W. 1996. The vertical dynamic response of a rail vehicle caused by track stiffness variations along the track. *Vehicle System Dynamics,* 25**,** 175-187.

Gallage, C., Dareeju, B. & Dhanasekar, M. State-of-the-art : track degradation at bridge transitions. Proceedings of the 4th international conference on structural engineering and construction management, 2013. 40–52.

Gallego Giner, I. & López Pita, A. 2009. Numerical simulation of embankment—structure transition design. *Proceedings of the Institution of Mechanical Engineers, Part F: Journal of Rail and Rapid Transit,* 223**,** 331-343.

Galvín, P. & Domínguez, J. 2009. Experimental and numerical analyses of vibrations induced by high-speed trains on the Córdoba-Málaga line. *Soil Dynamics and Earthquake Engineering,* 29**,** 641-657.

Galvín, P., Romero, A. & Domínguez, J. 2010. Fully three-dimensional analysis of high-speed train–track–soil-structure dynamic interaction. *Journal of Sound and Vibration,* 329**,** 5147-5163.

Garg, N. & Thompson, M. R. 1997. Triaxial characterization of Minnesota road research project granular materials. *Transp. Res. Rec,* 1577, Transportation Research Board, Washington, D.C., 27–36.

Gautier, J. L. 2006. Asphalt treated base material under ballast: an innovative experiment on the east european high speed track. *Workshop Track for high-speed railways, FEUP.* Porto, Portugal.

Gautier, P.-E. 2015. Slab track: Review of existing systems and optimization potentials including very high speed. *Construction and Building Materials,* 92**,** 9-15.

Gidel, G., Hornych, P., Chauvin, J.-J., Breysse, D. & Denis, A. 2001. A new approach for investigating the permanent deformation behaviour of unbound granular material using the repeated load triaxial apparatus. *Bulletin des Laboratoires des Pont et Chaussées,* 233**,** 5–21.

Goicoechea, J. N. Principios esenciales en el diseño de la infraestructura ferroviaria. Innnovaciones técnicas en la línea Madrid-Sevilla. Jornadas técnicas para alta velocidade, 2007 Córdoba, Espanha.

Gomes Correia, A. 2000. Influence of compaction conditions on resilient and permanent deformations of aggregates mixtures of granite. *Gomes Correia and Quibel (Editors), Compaction of soils and granular materials.* Paris: Presse Nationale des Ports et des Chaussées.

Gomes Correia, A. 2004. Evaluation of mechanical properties of unbound granular materials for pavements and rail tracks. *Gomes Correia and Loizos (Editors), Geotechnics in Pavement and Railway Design and Construction., MillPress.*

Gomes Correia, A. Innovations in design and construction of granular pavements and railways. *In:* ELLIS, E., YU, H.-S., MCDOWELL, G., DAWSON, A. & THOM, N., eds. Advances in Transportation Geotechnics - Proceedings of the 1st International Conference on Transportation Geotechnics, 2008 Nottingham, UK. CRC Press - Taylors & Francis Group, 3-13.

Gomes Correia, A., Anhdan, L. Q., Koseki, J. & Tatsuoka, F. 2001. Small strain stiffness under different isotropic and anisotropic stress conditions of two granular granite materials. *In:* TATSUOKA, F., SHIBUYA & KUWANO, eds. Advanced laboratory stress-strain testing of geomaterials, 2001. Balkema, Swets & Zeitlinger, 209-215.

Gomes Correia, A. & Cunha, J. 2014. Analysis of nonlinear soil modelling in the subgrade and rail track responses under HST. *Transportation Geotechnics,* 1**,** 147-156.

Gomes Correia, A., Hornych, P. & Akou, Y. 1999. Review of models and modelling of unbound granular materials *In:* CORREIA, A. G., ed. Proceedings of an International Workshop on Modelling and Advanced Testing for Unbound Granular Materials, 1999 Lisbon/21-22 January. A.A.Balkema/Rotterdam/Brookfield.

Gray, J. E. 1962. Characteristics of graded base course aggregates determined by triaxial tests. *Engrg. Res. Bull.* National Crushed Stone Association.

Grégoire, C. C., António G; De Bel, R; Dethy, B. 2011. Mechanical behavior of natural and recycled granular materials for roads. *Journal of Testing and Evaluation* 39.

Grossoni, I., Powrie, W., Zervos, A., Bezin, Y. & Le Pen, L. 2021. Modelling railway ballasted track settlement in vehicle-track interaction analysis. *Transportation Geotechnics,* 26**,** 100433.

Gu, F., Zhang, Y., Droddy, C. V., Luo, R. & Lytton, R. L. 2016. Development of a new mechanistic empirical rutting model for unbound granular material. *J. Mater. Civ,* 28.

Guo, L. 2013. *Experimental study on the static and cyclic behavior of saturated soft clay under complex stress path.* PhD Thesis, Zhenjiang Univ., Hangzhou, China (in Chinese).

Gupta, S. & Degrande, G. 2010. Modelling of continuous and discontinuous floating slab tracks in a tunnel using a periodic approach. *Journal of Sound and Vibration,* 329**,** 1101-1125.

Heath, D. L., Waters, J. M., Shenton, M. J. & Sparrow, R. W. 1972. Design of conventional rail track foundations. *Proceedings of the Institution of Civil Engineers,* 51**,** 251-267.

Hess, J. 2007. Rail expansion joints - the underestimated track work material? *Workshop Track-Bridge Interaction on High-Speed Railways.* Porto, Portugal.

Hettler, A. 1984. Bleibende Setzungen des Schotteroberbaus. . *ETR Eisenbahntechnische Rundschau 33,* 11**,** 847-853.

Hicks, R. G. 1970. *Factors influencing the resilient properties of granular materials.* PhD Thesis, University of California, Berkeley, Berkeley, Calif.

Hicks, R. G. & Monismith, C. L. 1971. Factors influencing the resilient properties of granular materials. *Highway Research Record,* 345**,** 15-31.

Hölscher, P. & Meijers, P. 2007. Literature study of knowledge and experience of transition zones. Technical report, GeoDelft.

Hornych, P. & Abd, A. E. 2004. Selection and evaluation of models for prediction of permanent deformations of unbound granular materials in road pavements. *Work Package 5, Performance-based specifications.* SAMARIS.

Hornych, P., Kazai, A. & Piau, J. M. 1998. Study of the resilient behaviour of unbound granular materials. *In:* NORDAL, R. S. & RAFSDAL, G., eds. Proceedings 5th Int. Conf. on the Bearing Capacity of Roads and Airfields, 1998. 1277–1287.

Hossain, M. & Kim, W. 2015. Estimation of Subgrade Resilient Modulus for Fine-Grained Soil from Unconfined Compression Test. *Transportation Research Record: Journal of the Transportation Research Board,* 2473**,** 126-135.

Hu, J., Bian, X., Xu, W. & Thompson, D. 2019. Investigation into the critical speed of ballastless track. *Transportation Geotechnics,* 18**,** 142-148.

Huang, H. & Brennecke, B. 2013. Track Stiffness Transition Zone Studied with Three-Dimensional Sandwich Track Model. 2374**,** 136-142.

Hujeux, J. C. 1985. Une loi de comportement pour le chargement cyclique des sols, Génie parassismique, . V. Davidovici (Editor), Génie Parasismique, 1985 Paris, France. Presse des Ponts et Chaussées, 316-331.

Hunt, H. E. M. 1996. Track settlement adjacent to bridge abutments. Paper presented at the Vehicle-Infrastructure Interaction IV, San Diego, CA. *Paper presented at the Vehicle-Infrastructure Interaction IV, San Diego, CA.*

Hunt, H. E. M. 1997. Settlement of railway track near bridge abutments. *Proceedings of the Institution of Civil Engineers: Transport,* 123**,** 68-73.

Huurman, M. 1997. *Permanent deformation in concrete block pavement.* PhD Thesis, Delft University of Technology, Netherlands.

Hwang, R. & Lysmer, J. 1981. Response of buried structures to travelling waves. *Journal of Geotechnical Engineering Division,* 107.

Hyde, A. F. L. 1974. *Repeated load triaxial testing of soils.* PhD thesis, University of Nottingham, Nottingham.

Indraratna, B., Babar Sajjad, M., Ngo, T., Gomes Correia, A. & Kelly, R. 2019. Improved performance of ballasted tracks at transition zones: A review of experimental and modelling approaches. *Transportation Geotechnics,* 21.

Indraratna, B., Ngo, N. T. & Rujikiatkamjorn, C. 2013. Deformation of coal fouled ballast stabilized with geogrid under cyclic load. *Journal of Geotechnical and Geoenvironmental Engineering,* 139**,** 1275-1289.

Indraratna, B. & Nimbalkar, S. 2013. Stress-strain degradation response of railway ballast stabilized with geosynthetics. *Journal of Geotechnical and Geoenvironmental Engineering,* 139**,** 684-700.

Indraratna, B. & Nimbalkar, S. 2016. Improved behaviour of railway track substructure using 2D (planar) and 3D (cellular) geo-inclusions. *CORE 2016 - Conference On Railway Excellence.* Melbourne, Australia.

Indraratna, B., Nimbalkar, S., Christie, D., Rujikiatkamjorn, C. & Vinod, J. 2010. Field assessment of the performance of a ballasted rail track with and without geosynthetics. *Journal of Geotechnical and Geoenvironmental Engineering,* 136**,** 907-917.

Indraratna, B., Nimbalkar, S. & Neville, T. 2014. Performance assessment of reinforced ballasted rail track. *Proceedings of the Institution of Civil Engineers - Ground Improvement,* 167**,** 24-34.

343

Indraratna, B., Salim, W. & Rujikiatkamjorn, C. 2011. *Advanced rail geotechnology: Ballasted track*, CRC Press/Balkema, Rotterdam, Netherlands.

Indraratna, B., Shahin, M. A. & Salim, W. 2007. Stabilising granular media and formation soil using geosynthetics with special reference to railway engineering. *Proceedings of the Institution of Civil Engineers - Ground Improvement,* 11**,** 27-44.

Insa, R., Salvador, P., Inarejos, J. & Medina, L. 2013. Analysis of the performance of under-sleeper pads in high-speed line transition zones. *Proceedings of the Institution of Civil Engineers - Transport,* 167**,** 63-77.

Ionescu, D. 2004. *Evaluation of the engineering behaviour of railway ballast.* PhD Thesis, University of Wollongong.

Iso14837-1 2005. Mechanical vibration - Ground-borne noise and vibration arising from rail systems - Part 1: General guidance.

Jiang, H. G., Bian, X. C., Xu, X., Chen, Y. M. & Jiang, J. Q. 2014. Full-scale model tests on dynamic performances of ballastless high-speed railways under moving train loads. *Yantu Gongcheng Xuebao/Chinese Journal of Geotechnical Engineering,* 36**,** 354-362.

Johnson, K. L. 1985. *Contact Mechanics,* Cambridge, Cambridge University Press.

Johnson, T. C., Berg, R. L. & Dimillio, A. 1986. Frost Action Predictive Techniques: an overview of research results. *Transportation Research Record***,** 147-161.

Jouve, P. & Elhannani, M. 1994. Application de modèles non linéaires au calcul des chaussées souples. *Bulletin des liaison Laboratoires des Pont et Chaussées,* 190**,** 39-55.

Jouve, P., Martinez, J., Paute, J. L. & Ragneau, E. Rational model for the flexible pavements deformations. Proceedings of the 6th International Conference on Structural Design of Asphalt pavements, 1987 Ann Arbor. 50-64.

Kallas, B. F. & Riley, J. 1967. Mechanical properties of asphalt pavement materials. *2nd Int. Conf. on Struct. Design of Asphalt Pavements.* University of Michigan.

Kamal, M. A., Dawson, A. R., Farouki, O. T., Hughes, D. a. B. & Sha'at, A. A. 1993. Field and laboratory evaluation of the mechanical behaviour of unbound granular materials in pavements. *Transp. Res. Rec.* Transportation Research Board, Washington D.C.

Karasahin, M. 1993. *Resilient behaviour of granular materials for analysis of highway pavements.* PhD Thesis, University of Nottingham.

Kennedy, J., Woodward, P. K., Medero, G. & Banimahd, M. 2013. Reducing railway track settlement using three-dimensional polyurethane polymer reinforcement of the ballast. *Construction and Building Materials,* 44**,** 615-625.

Khedr, S. 1985. Deformation characteristics of granular base course in flexible pavements. *Transportation Research Record,* 1043**,** 131-138.

Kim, M. & Sung, D. 2019. Experimental investigation on effects of track configurations on long-term behavior of ballasted track. *Journal of Structural Integrity and Maintenance,* 4**,** 76-85.

Kirwan, R. W., Farrell, E. R. & Maher, M. L. J. 1979. Repeated load parameters of a glacial till related to moisture content and density. *7th European Conf. on Soil Mech. and Found. Engrg., England.*

Knothe, K. & Wu, Y. 1998. Receptance behaviour of railway track and sub-grade. *Archive of Applied Mechanics,,* 68**,** 457-470.

Kolisoja, P. 1997. Factors affecting deformation properties of coarse grained granular materials. Proceedings of the Fourteenth International Conference on Soil Mechanics and Foundation Engineering, 1997 Hamburg 6.-12. September 1997.

Korkiala-Tanttu, L. A new material model for permanent deformations in pavements. Proc. of the Seventh Conference on Bearing Capacity of Roads and Airfields, 2005 Trondheim, Norway. 10.

Kouroussis, G., Van Parys, L., Conti, C. & Verlinden, O. 2014. Using three-dimensional finite element analysis in time domain to model railway-induced ground vibrations. *Advances in Engineering Software,* 70**,** 63-76.

Kouroussis, G., Verlinden, O. & Conti, C. 2011. Finite-Dynamic Model for Infinite Media: Corrected Solution of Viscous Boundary Efficiency. *Journal of Engineering Mechanics,* 137**,** 509-511.

Kozak, A. J. 1992. Track and structure characterization to improve freight train performance. *Report R-820.* Association of American Railroads, Colorado, USA.

Kuhlemeyer, R. & Lysmer, J. 1973. Finite Element Method Accuracy for Wave Propagation Problems. *Journal of the Soil Mechanics and Foundations Division,* 99**,** 421-427.

Lackenby, J. 2006. *Triaxial behaviour of ballast and the role of confining pressure under cyclic loading.* PhD Thesis, University of Wollongong.

Lane, H., Ekevid, T., Kettil, P., Ching, C. Y. & Wiberg, N.-E. 2007a. Vehicle-track-underground modeling of rail induced wave propagation. *Computers & Structures,* 85**,** 1215-1229.

Lee, W., Bohra, N. C., Altschaeffl, A. G. & White, T. D. 1997. Resilient Modulus of Cohesive Soils. *Journal of Geotechnical and Geoenvironmental Engineering,* 123**,** 131-136.

Lei, X. & Mao, L. 2004. Dynamic response analyses of vehicle and track coupled system on track transition of conventional high speed railway. *Journal of Sound and Vibration,* 271**,** 1133-1146.

Lei, X. & Zhang, B. 2010. Influence of track stiffness distribution on vehicle and track interactions in track transition. *Proceedings of the Institution of Mechanical Engineers, Part F: Journal of Rail and Rapid Transit,* 224**,** 592-604.

Lei, X. & Zhang, B. 2011. Analysis of dynamic behavior for slab track of high-speed railway based on vehicle and track elements. *Journal of Transportation Engineering,* 137**,** 227-240.

Lekarp, F. 1999. *Resilient and permanent deformation behavior of unbound aggregates under repeated loading.* PhD Thesis, The Royal Institute of Technology, KTH, Stockholm, Sweden.

Lekarp, F. & Dawson, A. 1998. Modelling permanent deformation behaviour of unbound granular materials. *Construction and Building Materials,* 12**,** 9-18.

Lekarp, F., Isacsson, U. & Dawson, A. 2000a. Permanent strain response of unbound aggregates. *Journal of Transportation Engineering,* 126**,** 76-83.

Lekarp, F., Isacsson, U. & Dawson, A. 2000b. State of the art. I: Resilient Response of unbound aggregates. *Journal of Transportation Engineering,* 126**,** 66-75.

Lentz, R. W. & Baladi, G. Y. Simplified procedure to characterize permanent strain in sand subjected to cyclic loading. Proceedings Int. Symposium on Soils Under Cyclic and Transient Loading, 1980 Swansea. 89-95.

Leykauf, G., Lechner, B. & Stahl, W. Optimisation of Track for High-Speed. Track for High-Speed Railways, 2006 Porto, Portugal.

Li, D. & Davis, D. 2005. Transition of railroad bridge approaches. *Journal of Geotechnical and Geoenvironmental Engineering,* 131**,** 1392-1398.

Li, D., Hyslip, J., Sussmann, T. & Chrismer, S. 2016. *Railway Geotechnics,* CRC Press - Taylor & Francis Group.

Li, D. & Selig, E. T. 1994. Resilient modulus for fine-grained subgrade soils. *Journal of Geotechnical Engineering,* 120**,** 939-957.

Li, D. & Selig, E. T. 1996. Cumulative plastic deformation for fine-grained subgrade soils. *Journal of Geotechnical and Geoenvironmental Engineering,* 122**,** 1006-1013.

Li, D. & Selig, E. T. 1998. Method for railroad track foundation design. I: Development. *Journal of Geotechnical and Geoenvironmental Engineering,* 124**,** 316-322.

Li, H. & Wu, G. 2020. Fatigue Evaluation of Steel Bridge Details Integrating Multi-Scale Dynamic Analysis of Coupled Train-Track-Bridge System and Fracture Mechanics. *Applied Sciences,* 10**,** 3261.

Li, M. X. D. & Berggren, E. G. 2010. A Study of the Effect of Global Track Stiffness and Its Variations on Track Performance: Simulation and Measurement. *Proceedings of the Institution of Mechanical Engineers, Part F: Journal of Rail and Rapid Transit,* 224**,** 375-382.

Li, W., Bian, X., Duan, X. & Tutumluer, E. 2018a. Full-Scale Model Testing on Ballasted High-Speed Railway: Dynamic Responses and Accumulated Settlements. *Transportation Research Record.*

Li, Y., Zhang, J., Wang, X., Mao, G. & Shi, X. 2018b. Effects of track-subgrade parameters on the dynamic stress response in subgrade of high-speed railway. *Zhongshan Daxue Xuebao/Acta Scientiarum Natralium Universitatis Sunyatseni,* 57**,** 56-62.

Li, Z. G. & Wu, T. X. Vehicle/Track Impact Due to Passing the Transition between a Floating Slab and Ballasted Track. In: Schulte-Werning B. et al. (eds) Noise and Vibration Mitigation for Rail Transportation Systems. Notes on Numerical Fluid Mechanics and Multidisciplinary Design, vol 99. Springer, Berlin, Heidelberg, 2008.

Liang, R. Y., Rababah, S. & Khasawneh, M. 2008. Predicting moisture-dependent resilient modulus of cohesive soils using soil suction concept. *Journal of Transportation Engineering,* 134**,** 34-40.

Lin, H. S., Liu, X. Y., Yan, H. & Ren, J. J. Long-term behavior and performance of ballastless track superstructure on China's Suining-Chongqing railway line. Proceedings of the ASME Joint Rail Conference 2010, JRC2010, 2010. 299-303.

Ling, X., Li, P., Zhang, F., Zhao, Y., Li, Y. & An, L. 2017. Permanent deformation characteristics of coarse grained subgrade soils under train-induced repeated load. *Advances in Materials Science and Engineering,* 2017 15.

Liu, S. & Wang, J. Application of shakedown theory in track substructure design. Proceedings of the Institution of Civil Engineers – Ground Improvement, 2019.

Liu, X., Zhao, P. & Dai, F. 2011. Advances in design theories of high-speed railway ballastless tracks. *Journal of Modern Transportation,* 19**,** 154-162.

Lopes, P. 2015. *Vibrações induzidas por tráfego ferroviário em túneis.* PhD Thesis, Faculdade de Engenharia da Universidade do Porto, Porto, Portugal.

Lopes, P., Alves Costa, P., Ferraz, M., Calçada, R. & Silva Cardoso, A. 2014. Numerical modeling of vibrations induced by railway traffic in tunnels: From the source to the nearby buildings. *Soil Dynamics and Earthquake Engineering,* Volumes 61–62**,** 269–285.

Lopes, P., Costa, P. A., Calçada, R. & Cardoso, A. S. 2013. Numerical modeling of vibrations induced in tunnels: A 2.5D FEM-PML approach. *Traffic induced Environmental Vibrations and Controls: Theory and Application.*

López-Pita, A., Teixeira, P. F., Casas-Esplugas, C. & Ubalde, L. 2006. Deterioration in geometric track quality on high speed lines: the experience of the Madrid-Seville high speed line (1992-2002). *Transportation Research Board 85th Annual Meeting.* Washington DC, United States.

Louay, N. M., Huang, B., Puppala, A. J. & Allen, A. 1999. Regression Model for Resilient Modulus of Subgrade Soils. *Transportation Research Record,* 1687**,** 47-54.

Lundqvist, A. & Dahlberg, T. 2005. Load impact on railway track due to unsupported sleepers. *Proceedings of the Institution of Mechanical Engineers, Part F: Journal of Rail and Rapid Transit,* 219**,** 67-77.

Lundqvist, A., Larsson, R. & Dahlberg, R. 2006. Influence of railway track stiffness variations on wheel/rail contact force. Workshop Track for high speed railways, Porto, Portugal.

Luomala, H. & Nurmikolu, A. Railway Track Stiffness Measurements at Bridge Transition Zones. Advances in Transportation Geotechnics II, 10-12 Sep 2012 Hokkaido University, Japan. 811-816.

Lysmer, J. & Kuhlemeyer, R. L. 1969. Finite Dynamic Model For Infinite Media. *Journal of the Engineering Mechanics Division,* 95**,** 859-878.

Lytton, R. L., Uzan, J., Fernando, E. G., Roque, R., Hiltunen, D. & Stoffels, S. M. 1993. Development and validation of performance prediction models and specifications for asphalt binders and paving mixes. Report SHRPA-357: TRB, National Research Council, Washington, D.C.

Madshus, C. & Kaynia, A. M. 2000. High-speed railway lines on soft ground: dynamic behaviour at critical train speed. *Journal of Sound and Vibration,* 231**,** 689-701.

Mahmoud, E., Papagiannakis, A. T. & Renteria, D. Discrete Element Analysis of Railway Ballast under Cycling Loading. Advances in Transportation Geotechnics 3. The 3rd International Conference on Transportation Geotechnics (ICTG 2016), 2016 Guimarães, Portugal. 1068–1076.

Mathworks. 2020. *Least-Squares (Model Fitting) Algorithms* [Online]. Available: https://www.mathworks.com/help/optim/ug/least-squares-model-fitting-algorithms.html [Accessed 2020].

Mayhew, H. C. 1983. Resilient properties of unbound road base under repeated triaxial loading. Lab. Rep. 1088, TRRL, Crowthorne, U.K.

Mezher, S. B., Connolly, D. P., Woodward, P. K., Laghrouche, O., Pombo, J. & Costa, P. A. 2016. Railway critical velocity - Analytical prediction and analysis. *Transportation Geotechnics,* 6**,** 84-96.

Mishra, D., Qian, Y., Huang, H. & Tutumluer, E. 2014. An integrated approach to dynamic analysis of railroad track transitions behavior. *Transportation Geotechnics,* 1**,** 188-200.

Momoya Y., Sekine E. & F., T. 2005. Deformation characteristics of railway roadbed and subgrade under moving-wheel load. *Soils Found.,* 45**,** 99-118.

Monismith, C. L., Ogawa, N. & Freeme, C. R. 1975. Permanent deformation characteristics of subgrade soils due to repeated loading. *Transportation Research Record,* 537**,** 1-17.

Monismith, C. L., Seed, H. B., Mitry, F. G. & Chan, C. K. 1967. Prediction of pavement deflections from laboratory tests. Proc., 2nd Int. Conf. Struct. Des. of Asphalt Pavements, 1967. 109–140.

Montenegro, P. 2015. *A methodology for the assessment of the train running safety on bridges.* PhD Thesis, Faculdade de Engenharia da Universidade do Porto, Porto, Portugal.

Moossazadeh, J. M. & Witczak, M. W. 1981. Prediction of Subgrade Moduli for Soil that Exhibits Nonlinear Behavior. *Transport Research Record: Journal of the Transportation Research Board,* No 810, Transportation Research Board of the National Academies**,** 9-17.

Muller, K. 2007. *Dreidimensionale dynamische Tunnel-Halbraum-Interaktion.* PhD Thesis, Technische Universitat Munchen, Munchen

Namura, A., Kohata, Y. & Miura, S. 2004. Effect of Sleeper Size on Ballasted Track Settlement. *Quarterly Report of Rtri,* 45**,** 156-161.

Namura, A. & Suzuki, T. 2007. Evaluation of Countermeasures against Differential Settlement at Track Transitions. *Quarterly Report of Rtri,* 48**,** 176-182.

Navaratnarajah, S., Indraratna, B. & Ngo, T. 2018. Influence of Under Sleeper Pads on Ballast Behavior Under Cyclic Loading: Experimental and Numerical Studies. *Journal of Geotechnical and Geoenvironmental Engineering,* 144**,** 04018068.

Neidhart, T. True-to-scale in situ tests determining dynamic performance of earthworks under high speed train loading. Proc., Geotechnics for Roads, Rail Tracks and Earth Structures, 2001 Rotterdam, Netherlands. 213–223.

Neves, S. 2016. *An efficient method for modelling the nonlinear train-bridge interaction.* PhD Thesis, Faculdade de Engenharia da Universidade do Porto, Porto, Portugal.

Ng, C. W. W., Zhou, C., Yuan, Q. & Xu, J. 2013. Resilient modulus of unsaturated subgrade soil: Experimental and theoretical investigations. *Canadian Geotechnical Journal,* 50**,** 223-232.

Nicks, J. 2009. *The bump at the end of the railway bridge.* PhD Thesis, Texas A&M University

Nielsen, J. C. O. 2008. High-frequency vertical wheel–rail contact forces—Validation of a prediction model by field testing. *Wear,* 265**,** 1465-1471.

Nielsen, J. C. O., Berggren, E. G., Hammar, A., Jansson, F. & Bolmsvik, R. 2018. Degradation of railway track geometry – Correlation between track stiffness gradient and differential settlement. *Proceedings of the Institution of Mechanical Engineers, Part F: Journal of Rail and Rapid Transit.*

Nielsen, J. C. O. & Igeland, A. 1995. Vertical dynamic interaction between train and track. influence of wheel and track imperfections. *Journal of Sound and Vibration,* 187**,** 825-839.

Nielsen, J. C. O. & Li, X. 2018. Railway track geometry degradation due to differential settlement of ballast/subgrade – Numerical prediction by an iterative procedure. *Journal of Sound and Vibration,* 412**,** 441-456.

Nielsen, J. C. O., Lundén, R., Johansson, A. & Vernersson, T. 2003. Train-Track Interaction and Mechanisms of Irregular Wear on Wheel and Rail Surfaces. *Vehicle System Dynamics,* 40**,** 3-54.

Nimbalkar, S. & Indraratna, B. 2015. Implications of ballast degradation under cyclic loading. *12th Australia New Zealand Conference on Geomechanics (ANZ 2015): "The Changing Face of the Earth – Geomechanics & Human Influence".* New Zealand.

Nimbalkar, S., Punetha, P. & Kaewunruen, S. 2020. Performance Improvement of Ballasted Railway Tracks Using Geocells: Present State of the Art. *In:* SITHARAM, T. G., HEGDE, A. M. & KOLATHAYAR, S. (eds.) *Geocells: Advances and Applications.* Singapore: Springer Singapore.

Norman, C. 2004. *Measurement of railroad track modulus from a moving railcar.* Master thesis, University of Nebraska.

Np-En13450 2005. Agregados para Balastro de Via Férrea. Instituto Português da Qualidade.

Np-En134581-2 2009. Aplicações Ferroviárias. Via - Requisitos de desempenho para sistemas de fixação. Parte 2: sistemas de fixação para travessas de betão. EN13481, Instituto Português da Qualidade.

Ochoa De Olza Galé, A. 2007. Nuevas Tendencias en el Diseño de Vía. *Jornadas Técnicas: Ingeniería para Alta Velocidad, Veinte Años de Experiencia en España.* Córdoba.

Okabe, Z. 1961. Laboratory investigation of railroad ballasts. *Bulletin of the Permanent Way Society of Japan,* 4**,** 1-19.

Ooi, P. S. K., Archilla, A. R. & Sandefur, K. G. 2004. Resilient Modulus Models for Compacted Cohesive Soils. 1874**,** 115-124.

Ore 1970. Question D 71, Stresses in the Rails, the Ballast and the Formation Resulting from Traffic Loads. Report No. D71/RP1/E, Int. Union of Railways. Utrecht: ORE.

Orobio, A. & Zaniewski, J. P. 2011. Sampling-based sensitivity analysis of the mechanistic-empirical pavement design guide applied to material inputs. *J. of Trans. Res. Rec.,* 2226**,** 95-93.

Paixão, A. 2014. *Transition Zones in railway tracks - an experimental and numerical study on the structural behaviour.* PhD Thesis, Faculdade de Engenharia da Universidade do Porto, Porto, Portugal.

Paixão, A., Alves Ribeiro, C., Pinto, N., Fortunato, E. & Calçada, R. 2015. On the use of under sleeper pads in transition zones at railway underpasses: experimental field testing. *Structure and Infrastructure Engineering,* 11**,** 112-128.

Paixão, A., Fortunato, E. & Antunes, M. L. 2009. Emerging trends for high-speed rail track super structures - ballastless track as an alternative to the ballasted track *Bearing Capacity of Roads, Railways and Airfields.* University of Illinois at Urbana - Champaign, Champaign, Illinois, USA.

Paixão, A., Fortunato, E. & Calçada, R. 2013. Design and Construction of Backfills for Railway track Transition Zones. *Proceedings of the Institution of Mechanical Engineers, Part F: Journal of Rail and Rapid Transit,* 229 58-70.

Paixão, A., Fortunato, E. & Calçada, R. 2014. Transition zones to railway bridges: Track measurements and numerical modelling. *Engineering Structures,* 80**,** 435-443.

Paixão, A., Fortunato, E. & Calçada, R. 2016. A contribution for integrated analysis of railway track performance at transition zones and other discontinuities. *Construction and Building Materials,* 111**,** 699-709.

Paixão, A., Varandas, J. N., Fortunato, E. & Calçada, R. 2018. Numerical simulations to improve the use of under sleeper pads at transition zones to railway bridges. *Engineering Structures,* 164**,** 169-182.

Pappin, J. W. 1979. *Characteristics of a granular material for pavement analysis.* PhD Thesis, University de Nottingham.

Parreira, A. B. & Goncalves, R. F. 2000. The influence of moisture content and soil suction on the resilient modulus of a lateritic subgrade soil. *GeoEng – An international conference on geotechnical & geological engineering.* Melbourne, Australia.

Paute, J., Hornych, P. & Benaben, J. 1988. Comportement mecanique des graves non traitees. *Bull Liasion Laboratories Ponts Chaussées,* 156**,** 21-36.

Paute, J. L., Hornych, P. & Benaben, J. P. 1994. Comportement mécanique des graves non traitées. *Bulletin de Liaison des Laboratoires des Ponts et Chaussées,* 190**,** 27-38.

Pezo, R. F. 1993. A general method of reporting resilient modulus tests of soils—A pavement engineer's point of view. *72nd Annu. Meeting of the TRB.*

Pezo, R. F., Kim, D.-S., Stokoe, K. H. & Hudson, W. R. 1991. Aspects of a reliable resilient modulus testing system. *Transp. Res. Board Preprint, 70th Annual Meeting.* Washington, D.C., Jan.

Pinto, N., Ribeiro, C. A., Gabriel, J. & Calçada, R. 2015. Dynamic monitoring of railway track displacement using an optical system. 229**,** 280-290.

Popp, K., H., K. & Kaiser, I. 1999. Vehicle-Track Dynamics in the Mid-Frequency Range. *Vehicle System Dynamics,* 31**,** 423-464.

Popp, K., Knothe, K. & Pöpper, C. 2005. System dynamics and long-term behaviour of railway vehicles, track and subgrade: report on the DFG Priority Programme in Germany and subsequent research. *Vehicle System Dynamics,* 43**,** 458-538.

Porr. 2012. *Slab Track Austria - System ÖBB-PORR elastically supported slab* [Online]. Porr Bau GmbH. Available: http://www.slabtrackaustria.com/fileadmin/content/39_slabtrackaustria/04_download/image _brochure_slab_track_austria.pdf [Accessed 2016].

Puppala, A. J., Mohammad, L. N. & Allen, A. 1999. Permanent deformation characterization of subgrade soils from RLT test. *Journal of Materials in Civil Engineering,* 11**,** 274-282.

Puppala, A. J., Saride, S. & Chomtid, S. 2009. Experimental and modeling studies of permanent strains of subgrade soils. *Journal of Geotechnical and Geoenvironmental Engineering,* 135**,** 1379–1389.

Qian, J., Lin, H., Gu, X. & Xue, J. 2018. Dynamic shakedown limits for flexible pavement with cross-anisotropic materials. *Road Materials and Pavement Design***,** 1-21.

Qian, J., Shiyuan Li, Xiaoqiang Gu & Zhang, J. 2019a. A unified model for estimating the permanent deformation of sand under a large number of cyclic loads. *Ocean Engineering* 181 293‐302.

Qian, J., Wang, Y., Wang, J. & Huang, M. 2019b. The influence of traffic moving speed on shakedown limits of flexible pavements. *International Journal of Pavement Engineering,* 20**,** 233-244.

Quante, F. 2001. *Innovative Track Systems - Technical Construction, ProMain* [Online]. [Accessed].

Raad, L., Minassian, G. & Gartin, S. 1992. Characterization of saturated granular bases under repeated loads. *Transp. Res. Rec.* Transportation Research Board, Washington D.C.

Rahim, A. M. & George, K. P. 2005. Models to estimate subgrade resilient modulus for pavement design. *International Journal of Pavement Engineering,* 6**,** 89–96.

Rahman, M., Islam, K. M. & Gassman, S. 2019. Estimation of Resilient Modulus for Coarse-Grained Subgrade Soils from Quick Shear Tests for Mechanistic-Empirical Pavement Designs. *Materials,* 3**,** 48.

Rahman, M. M. & Gassman, S. L. 2019. Permanent deformation characteristics of coarse grained subgrade soils using repeated load triaxial tests. *In:* MEEHAN, C. L., KUMAR, S., PANDO, M. A. & COE, J. T. (eds.) *Geo-Congress 2019.* Philadelphia, Pennsylvania.

Rahman, M. S. & Erlingsson, S. 2015. A model for predicting permanent deformation of unbound granular materials. *Road Materials and Pavement Design,* 16**,** 653-673.

Ramos, A., Gomes Correia, A., Indraratna, B., Ngo, T., Calçada, R. & Costa, P. A. 2020. Mechanistic-empirical permanent deformation models: Laboratory testing, modelling and ranking. *Transportation Geotechnics,* 23**,** 100326.

Ramos, A. L., Correia, A. G., Calçada, R. & Costa, P. A. 2018. Influence of permanent deformations of substructure on ballasted and ballastless tracks performance. Proceedings of 7th Transport Research Arena TRA 2018, April 16-19, 2018 Vienna, Austria. Zenodo.

Raymond, G. P. 1978. Design for Railroad Ballast and Subgrade Support. *Journal of the Geotechnical Engineering Division, ASCE,* 104**,** 45-60.

Raymond, G. P., Gaskin, P. N. & Svec, O. 1975. Selection and performance of railroad ballast. *Railroad track mechanics and technology, Kerr, R., ed., Princeton, NJ, 369–385.*

Read, D. & Li, D. 2006. Design of track transitions. TCRP Research Results Digest.

Real, T., Zamorano, C., Hernández, C., García, J. A. & Real, J. I. 2016. Static and dynamic behavior of transitions between different railway track typologies. *KSCE Journal of Civil Engineering,* 20**,** 1356-1364.

Rheda-System 2011. Rheda 2000. Ballastless Track System. Rail One, Germany.

Riessberger, K. 2008. Ballasted Track for High Speed Operation. *Railway Technical Review, Special (March 2008)***,** 55–60.

Robertson, I., Masson, C., Sedran, T., Barresi, F., Caillau, J., Keseljevic, C. & Vanzenberg, J. M. 2015. Advantages of a new ballastless trackform. *Construction and Building Materials,* 92**,** 16–22.

Robnett, Q. L. & Thompson, M. R. 1976. Effect of lime treatment on the resilient behavior of fine-grained soils. *Transp. Res. Rec.,* 560**,** 11-20.

Sadri, M., Lu, T., Zoeteman, A. & Steenbergen, M. Railway track design & degradation. *In:* DIMITROVOVÁ, Z., ed. MATEC Web of Conferences, 2018 Lisbon, Portugal.

Sadri, M. & Steenbergen, M. 2018. Effects of railway track design on the expected degradation: Parametric study on energy dissipation. *Journal of Sound and Vibration,* 419**,** 281-301.

Sainz-Aja, J., Pombo, J., Tholken, D., Carrascal, I., Polanco, J., Ferreño, D., Casado, J., Diego, S., Perez, A., Filho, J. E. A., Esen, A., Cebasek, T. M., Laghrouche, O. & Woodward, P. 2020. Dynamic calibration of slab track models for railway applications using full-scale testing. *Computers and Structures,* 228.

Salour, F. & Erlingsson, S. 2015a. Permanent deformation characteristics of silty sand subgrades from multistage RLT tests. *International Journal of Pavement Engineering,* 18**,** 236-246.

Salour, F. & Erlingsson, S. 2015b. Resilient modulus modelling of unsaturated subgrade soils: laboratory investigation of silty sand subgrade. *Road Materials and Pavement Design,* 16**,** 553–568.

Salour, F. & Erlingsson, S. Characterization of permanent deformation of silty sand subgrades from multistage RLT tests. The 3rd International Conference on Transportation Geotechnics (ICTG 2016), 2016 Guimarães, Portugal. 300–307.

Santos, N. 2013. *Vibrações Induzidas por Tráfego na Via e na Envolvente de Linhas Ferroviárias: Modelação Numérica 3D e Validação Experimental.* PhD thesis, Faculdade de Engenharia da Universidade do Porto, Porto, Portugal.

Sañudo, R., Cerrada, M., Alonso, B. & Dell'olio, L. 2017. Analysis of the influence of support positions in transition zones. A numerical analysis. *Construction and Building Materials,* 145**,** 207-217.

Sañudo, R., Dell'olio, L., Casado, J. A. & Diego, S. 2016a. Track transition in railways: A review. Construction and Building Materials. *Construction and Building Materials,* 112**,** 140–157.

Sañudo, R., Miranda, M., Markine, V. & DelĺOlio, L. 2016b. The Influence of Train Running Direction and Track Supports Position on the Behaviour of Transition Zones. *Transportation Research Procedia,* 18**,** 281-288.

Sas, W., Głuchowski, A., Gabrys, K., Soból, E. & Szymański, A. 2017. Resilient Modulus Characterization of Compacted Cohesive Subgrade Soil. *Applied Sciences,* 7.

Sato, Y. Optimization of track maintenance work on ballasted track. Proceedings of the World Congress on Railway Research (WCRR'97), 1997 Florence, Italy.

Sauer, E. K. & Monismith, C. L. 1968. Influence of soil suction on behavior of a glacial till subjected to repeated loading. *Hwy. Res. Rec., 215, 8-23.*

Sawangsuriya, A., Edil, T. B. & Benson, C. H. 2009. Effect of suction on resilient modulus of compacted fine-grained subgrade soils. *Transportation Research Record: Journal of the Transportation Research Board,* 2101**,** 82-87.

Sayeed, M. A. & Shahin, M. A. Investigation into Impact of Train Speed for Behavior of Ballasted Railway Track Foundations. Advances in Transportation Geotechnics 3. The 3rd International Conference on Transportation Geotechnics (ICTG 2016), 2016a Guimarães, Portugal. 1152–1159.

Sayeed, M. A. & Shahin, M. A. 2016b. Three-dimensional numerical modelling of ballasted railway track foundation for high-speed trains with special reference to critical speed. *Transportation Geotechnics,* 6**,** 55-65.

Sayeed, M. A. & Shahin, M. A. 2017. Design of ballasted railway track foundations using numerical modelling. Part I: Development. *Canadian Geotechnical Journal,* 55**,** 353-368.

Schooleman, R. B. 1996. *Overgang kunstwerk-aardebaan voor de hoge-snelheidslijn.* Master thesis., Delft University of Technology. Delft, The Netherlands.

Seara, I. & Gomes Correia, A. 2008. Zonas de transição de vias-férreas. A importância de uma solução geoestrutural. *XI Congresso Nacional de Geotecnia.* Coimbra. Portugal.

Seara, I. & Gomes Correia, A. 2010. Performance assessment solutions for transition zones. Embankment-bridge railways trough numerical simulation 3D. *Semana de Engenharia 2010.* Guimarães, 11 a 15 de Outubro.

Seed, H. B., Chan, C. K. & Lee, C. E. 1962. Resilience characteristics of subgrade soils and their relation to fatigue failures in asphalt pavement. Proc. First Int: Conf. on Struct. Design of Asphah Pavements, 1962 University of Michigan, Ann Arbor.

Seed, H. B., Mitry, F. G., Monismith, C. L. & Chan, C. K. 1967. Prediction of flexible pavement deflections from laboratory repeated load tests. *NCHRP Report* National Cooperative Highway Research Program.

Selig, E. T. & Waters, J. M. 1994. *Track Geotechnology and Substructure Management,* Thomas Telford Services Ltd., London.

Shackel, B. 1973. The derivation of complex stress-strain relations. *Proc. 8th Int. Conf. on Soil Mech. and Found. Engrg., Moscow,* 353-359.

Shahraki, M., Warnakulasooriya, C. & Witt, K.-J. 2015. Numerical Study of Transition Zone Between Ballasted and Ballastless Railway Track. *Transportation Geotechnics,* 3**,** 58–67.

Shahraki, M. & Witt, K.-J. 2015. 3D Modeling of Transition Zone between Ballasted and Ballastless High-Speed Railway Track. *Journal of Traffic and Transportation Engineering* 3**,** 234-240.

Shan, Y., Albers, B. & A., S. S. 2013. Influence of different transition zones on the dynamic response of track–subgrade systems. *Computers and Geotechnics,* 48**,** 21-28.

Shan, Y., Shu, Y. & Zhou, S. 2017. Finite-infinite element coupled analysis on the influence of material parameters on the dynamic properties of transition zones. *Construction and Building Materials,* 148**,** 548-558.

Sharpe, P. 2002. *Innovative design of transition zones.*

Sheng, X., Jones, C. J. C. & Petyt, M. 1999. Ground vibration generated by a load moving along a railway track. *Journal of Sound and Vibration,* 228**,** 129-156.

Sheng, X., Jones, C. J. C. & Thompson, D. J. 2006. Prediction of ground vibration from trains using the wavenumber finite and boundary element methods. *Journal of Sound and Vibration,* 293**,** 575-586.

Shenton, M. J. 1978. Deformation of Railway Ballast under Repeated Loading Condition. *In:* KERR, A. D. (ed.). Railroad Track Mechanics and Technology: Proceeding of a Symposium 21st-23rd April 1978, Princeton University.

Shenton, M. J. 1984. Ballast Deformation and Track Deterioration. *Track Technology. London: Thomas Telford Ltd.*

Shi, J., Chan, A. H. & Burrow, M. P. N. Influence of unsupported sleepers on the dynamic response of a heavy haul railway embankment. Proceedings of the Institution of Mechanical Engineers, Part F: Journal of Rail and Rapid Transit. , 2013b. 657-667.

Shifley, L. H., Jr. & Monismith, C. L. 1968. Test road to determine the influence of subgrade characteristics on the transient deflections of asphalt concrete pavements. *Report No. TE 68-5, Office of Res. Services.* Univ. of California, Berkeley, Aug.

Shin, E., Kim, D. & Das, B. 2002. Geogrid-reinforced railroad bed settlement due to cyclic load. *Geotechnical and Geological Engineering,* 20**,** 261-271.

Smekal, A. Transition structures of railway bridges. World Congress on Railway Research, 1997 Florence, Italy.

Sol-Sánchez, M., Moreno-Navarro, F. & Rubio-Gámez, M. C. 2015. The use of elastic elements in railway tracks: A state of the art review. *Construction and Building Materials,* 75**,** 293-305.

Sonneville. 2009. *Low Vibration Track (LVT): Overall Presentation (Doc No: DPD038.GN)* [Online]. Available: https://www.sonneville.com/documents/1-LVTO-verallPresentation-2009.pdf [Accessed].

Sousa, C. 2012. *Analysis of Cyclic and Long-Term Effects in Continuous Precast Railway Bridge Decks.* PhD Thesis, Faculdade de Engenharia da Universidade do Porto, Porto, Portugal.

Stewart, H. E. & Selig, E. T. 1984. Correlation of Concrete Tie Track Performance in Revenue Service and at the Facility for Accelerated Service Testing. Prediction and Evaluation of Track Settlement. Washington DC: U.S. Department of Transportation Federal Railroad Administration.

Suiker, A. 2002. *The mechanical behaviour of ballasted railway tracks.* PhD Thesis, Delft University of Technology, Netherlands.

Sun, Y. Q. & Dahnasekar, M. 2002. A dynamic model for the vertical interaction of the rail track and wagon system. *International Journal of Solids and Structures,* 39**,** 1337-1359.

Sussmann, T., Ebersöhn, W. & Selig, E. T. 2001. Fundamental Nonlinear Track Load-Deflection Behavior for Condition Evaluation. *Transportation Research Record,* 1742**,** 61-67.

Sweere, G. T. H. 1990. *Unbound granular bases for roads.* PhD Thesis, Delft University of Technology, Netherlands.

Sykora, D. W. 1987. Creation of a data base of seismic shear wave velocities for correlation analysis. *Geotech. Lab. Miscellaneous Paper GL-87-26, U.S. Army Eng.*

Tam, W. A. & Brown, S. F. 1988. Use of the falling weight deflectometer for in situ evaluation of granular materials in pavements. Proc., 14th ARRB Conf., 1988. 155–163.

Tang, Y., Xiao, S. & Yang, Q. 2019. Numerical study of dynamic stress developed in the high speed rail foundation under train loads. *Soil Dynamics and Earthquake Engineering,* 123**,** 36-47.

Tanimoto, K. & Nishi, M. 1970. On resilience characteristics of some soils under repeated loading. *Soils Found.,* 10**,** 75-92.

Tarifa, M., Zhang, X., Ruiz, G. & Poveda, E. 2015. Full-scale fatigue tests of precast reinforced concrete slabs for railway tracks. *Engineering Structures,* 100**,** 610-621.

Tarmac. 2015. *Delivering Innovation: slab track solutions of UK high speed rail* [Online]. Tarmac/Max-Bögl. Available: http://tarmac-maxboegl.com/wp-content/uploads/2016/04/Tarmac-Max-Bogl-JV-Slab-Track-Brochure.pdf [Accessed 2021].

Tatsuoka, F. & Gomes Correia, A. 2018. Importance of controlling the degree of saturation in soil compaction linked to soil structure design. *Transportation Geotechnics,* 17, 3-23.

Tatsuoka, F., Ishihara, M., Uchimura, T. & Gomes Correia, A. 1999. Non-linear resilient behaviour of unbound granular materials by the cross-anisotropic hypo-quasi-elasticity model. *In:* GOMES CORREIA, A., ed. Unbound Granular Materials - Laboratory Testing, In-situ Testing and Modelling, 1999 Lisbon/21-22 January. A. A. Balkema/Rotterdam/Brookfield, 197-204.

Tayabji, S. & Thompson, M. 1977. Considerations in the analysis of conventional railway track support system. 103, 279-292.

Thom, N. 1988. *Design of road foundations* PhD thesis.

Thom, N. H. & Brown, S. F. The effect of grading and density on the mechanical properties of a crushed dolomitic limestone. Proceedings, 14th ARRB Conference, 1988. 94-100.

Thom, N. H. & Oakley, J. Predicting Differential Settlement in a Railway Trackbed. Railway Foundations. 2006 Birmingham, UK.

Thompson, M. & Robnett, Q. 1976. Resilient properties of subgrade soils. Report No. FHWA-IL-UI-160: Federal Highway Administration, Washington DC.

Titi, H. H., Elias, M. B. & Helwany, S. Determination of Typical Resilient Modulus Values for Selected Soils in Wisconsin. 2006.

Trackelast. *Slab Track Mats* [Online]. http://www.trackelast.com/slab-track-mats.html. [Accessed 2021].

Tseng, K. H. & Lytton, R. L. 1989. Prediction of permanent deformation in flexible pavements materials, implication of aggregates in the design, construction, and performance of flexible pavements. *ASTM STP 1016, ASTM, West Conshohocken, PA,* 154–172.

Uic 1994. UIC Code 719 R. Earthworks and track-bed layers for railway lines. International Union of Railways, Paris, France.

Uic 2002. Feasibility Study Ballastless Track. UIC Infrastructure Commission - Civil Engineering Support Group.

Uic 2005. Code 518 OR: Testing and Approval of Railway Vehicles from the Point of View of Their Dynamic Behaviour : Safety, Track Fatigue, Ride Quality.

Uic 2008. UIC Code 719 R. Earthworks and Track Bed for Railway Lines. International Union of Railways.

Uic. 2015. *High Speed Rail Brochure - 2015* [Online]. http://www.uic.org/IMG/pdf/high_speed_brochure.pdf. [Accessed 2017].

Uic. 2018. *Harmonised methodology for infrastructure lifetime assessment* [Online]. https://uic.org/projects/harmonised-methodology-for-infrastructure-lifetime-assessment. [Accessed].

Ullidtz, P. 1993. Mathematical model of pavement performance under moving wheel load. *J. of Trans. Res. Rec., Washington, D.C.,* 1384, 94-99.

Uzan, J. 1985. Characterization of Granular Material. *Transportation Research Record No. 1022, Transportation Research Board, Washington DC, 52-59.*

Uzan, J. 1999. Permanent deformation of a granular base material. *Transp. Res. Rec.,* 1673, 89–94.

Vale, C. 2010. *Influência da qualidade dos sistemas ferroviários no comportamento dinâmico e no planeamento da manutenção preventiva de vias de alta velocidade.* PhD Thesis, Faculdade de Engenharia da Universidade do Porto.

Van Dalen, K. N. & Metrikine, A. V. 2008. Transition radiation of elastic waves at the interface of two elastic half-planes. *Journal of Sound and Vibration,* 310, 702-717.

Van Dalen, K. N., Tsouvalas, A., Metrikine, A. V. & Hoving, J. S. 2015. Transition radiation excited by a surface load that moves over the interface of two elastic layers. *International Journal of Solids and Structures,* 73-74**,** 99-112.

Varandas, J. N., Hölscher, P. & Silva, M. A. 2013. Settlement of ballasted track under traffic loading: Application to transition zones. *Proceedings of the Institution of Mechanical Engineering, Part F: Journal of Rail and Rapid Transit.*

Varandas, J. N., Hölscher, P. & Silva, M. a. G. A Settlement Model for Ballast at Transition Zones. *In:* TOPPING, B. H. V., ADAM, J. M., PALLARÉS, F. J., BRU, R. & ROMERO, M. L., eds. Proceedings of the Tenth International Conference on Computational Structures Technology, 2010 Valencia-Spain. Civil-Comp Press, Stirlingshire, Scotland.

Varandas, J. N., Hölscher, P. & Silva, M. a. G. 2011. Dynamic behaviour of railway tracks on transitions zones. *Computers & Structures,* 89**,** 1468-1479.

Varandas, J. N., Hölscher, P. & Silva, M. a. G. 2016. Three-dimensional track-ballast interaction model for the study of a culvert transition. *Soil Dynamics and Earthquake Engineering,* 89**,** 116-127.

Vermeer, P. A. A five-constant model unifying well-established concepts. Proc., Int. Workshop on Constitutive Relations for Soils, 1982. A.A. Balkema, Rotterdam, Netherlands, 175–197.

Vuong, B. 1992. Influence of density and moisture content on dynamic stress-strain behaviour of a low plasticity crushed rock. *Rd. and Transp. Res.,* 1**,** 88-100.

Wair, B. R., Dejong, J. T. & Shantz, T. 2012. Guidelines for Estimation of Shear Wave Velocity Profiles. University of California, Department of Transportation, PEER - Pacific Earthquake Engineering Research Center.

Wang, H. & Markine, V. 2018a. Modelling of the long-term behaviour of transition zones: Prediction of track settlement. *Engineering Structures,* 156**,** 294-304.

Wang, H. & Markine, V. 2019. Dynamic behaviour of the track in transitions zones considering the differential settlement. *Journal of Sound and Vibration,* 459**,** 114863.

Wang, H., Markine, V. & Liu, X. 2017a. Experimental analysis of railway track settlement in transition zones. *Proceedings of the Institution of Mechanical Engineering, Part F: Journal of Rail and Rapid Transit,* 232**,** 1774–1789.

Wang, H. & Markine, V. L. 2018b. Methodology for the comprehensive analysis of railway transition zones. *Computers and Geotechnics,* 99**,** 64-79.

Wang, H., Markine, V. L., Shevtsov, I. Y. & Dollevoet, R. 2015. *Analysis of the Dynamic Behaviour of a Railway Track in Transition Zones With Differential Settlement.*

Wang, H., Silvast, M., Markine, V. L. & Wiljanen, B. 2017b. Analysis of the Dynamic Wheel Loads in Railway Transition Zones Considering the Moisture Condition of the Ballast and Subballast. *Applied Sciences,* 7**,** 1208.

Wang, J. & Yu, H. 2013. Residual stresses and shakedown in cohesive-frictional half-space under moving surface loads. *Geomech Geoeng* 8**,** 1–14.

Wei, X., Wang, G. & Wu, R. 2017. Prediction of traffic loading–induced settlement of low-embankment road on soft subsoil. *International Journal of Geomechanics,* 17.

Werkmeister, S. 2003. *Permanent deformation behavior of unbound granular materials.* PhD Thesis, University of Technology, Dresden, Germany.

Werkmeister, S., Dawson, A. & Wellner, F. 2005. Permanent deformation behaviour of granular materials. *Road Materials and Pavement Design,* 6**,** 31–51.

Werkmeister, S., Numrich, R. & Wellner, F. The development of a permanent deformation design model for unbound granular materials with the shakedown-concept. Proc. of the 6th International Conference on the Bearing Capacity of Roads and Airfields, 2002 Lisbon, Portugal. 1081–1096.

White, W., Lee, I. K. & Valliappan, S. 1977. A unified boundary for finite dynamic models. *Journal of the Engineering Mechanics Division,* 103**,** 949-964.

Witczak, M. W., Andrei, D. & Houston, W. N. 2000. Resilient Modulus as Function of Soil Moisture - Summary of Predictive Models. *Development of the 2002 Guide for the Development of New and Rehabilitated Pavement Structures, NCHRP 1-37 A, Inter Team Technical Report (Seasonal 1)*. Arizona State University, Tempe, Arizona.

Wolff, H. & Visser, A. T. Incorporating elasto-plasticity in granular layer pavement design. Proceedings of the Institution of Civil Engineers-Transport, 1994. 259–272.

Woodward, P. K., El Kacimi, A., Laghrouche, O., Medero, G. & Banimahd, M. 2012. Application of polyurethane geocomposites to help maintain track geometry for high-speed ballasted railway tracks. *Journal of Zhejiang University SCIENCE A,* 13**,** 836-849.

Wriggers, P. 2002. *Computational Contact Mechanics*, Wiley.

Wu, T. X. & Thompson, D. 1999b. A double Timoshenko beam model for vertical vibration analysis of railway track at high frequencies. *Journal of Sound and Vibration,* 224**,** 329-348.

Wu, T. X. & Thompson, D. J. 2001. A Hybrid Model for Wheel/Track Dynamic Interaction and Noise Generation due to Wheel Flats. . ISVR Technical Memorandum No. 859: University of Southampton - Institute of Sound and Vibration Research.

Xiao, J., Juang, C., Wei, K. & Xu, S. 2014. Effects of principal stress rotation on the cumulative deformation of normally consolidated soft clay under subway traffic loading. *Journal of Geotechnical and Geoenvironmental Engineering,* 140.

Xiao, Y., Tutumluer, E. & Mishra, D. 2015. Performance evaluation of unbound aggregate permanent deformation models for different aggregate physical properties. *Transport Research Record: Journal of the Transportation Research Board,* 2525**,** 20-30.

Yang, S.-R. & Huang, W.-H. 2007. Permanent deformation and critical stress of cohesive soil under repeated loading. *Transport Research Record: Journal of the Transportation Research Board,* 2016**,** 23-30.

Yang, S.-R., Huang, W.-H. & Liao, C.-C. 2008. Correlation between resilient modulus and plastic deformation for cohesive subgrade soil under repeated loading. *Transport Research Record, Transportation Research Board,* 2053.

Yang, S. R., Huang, W. H. & Tai, Y. T. 2005. Variation of resilient modulus with soil suction for compacted subgrade soils. *Transportation Research Record: Journal of the Transportation Research Board,* 1913**,** 99-106.

Yang, Y. & Hung, H. 2001. A 2.5D finite/infinite element approach for modelling visco-elastic body subjected to moving loads *International Journal for Numerical Methods in Engineering* 51**,** 1317-1336.

Yau, A. & Von Quintus, H. 2004. Predicting Elastic Response Characteristics of Unbound Materials and Soils. *Transportation Research Record,* 1874**,** 47-56.

Yesufa, G. Y. & Hoffa, I. 2015. Finite element modelling for prediction of permanent strains in fine-grained subgrade soils. *Road Materials and Pavement Design,* 16**,** 392-404.

Yu, Z., Connolly, D. P., Woodward, P. K. & Laghrouche, O. 2019. Settlement behaviour of hybrid asphalt-ballast railway tracks. *Construction and Building Materials,* 208**,** 808-817.

Zbiciak, A., Kraśkiewicz, C., Oleksiewicz, W., Płudowska, M. & Lipko, C. 2017. Mechanical modelling and application of vibroacoustic isolators in railway tracks. *MATEC Web of Conferences,* 117**,** 00090.

Zhai, W. M. & True, H. 2000. Vehicle-track dynamics on a ramp and on the bridge: Simulation and measurements. *Vehicle System Dynamics,* 33**,** 604-615.

Zhai, W. M., Wang, K. Y. & Lin, J. H. 2004. Modelling and experiment of railway ballast vibrations. *Journal of Sound and Vibration,* 270**,** 673-683.

Zhang, J., Peng, J., Zheng, J., Dai, L. & Yao, Y. 2019a. Prediction of Resilient Modulus of Compacted Cohesive Soils in South China. 19, 04019068.

Zhang, S., Xiao, X., Wen, Z. & Jin, X. 2008. Effect of unsupported sleepers on wheel/rail normal load. *Soil Dynamics and Earthquake Engineering,* 28**,** 662-673.

Zhang, S., Zhang, W. & Jin, X. 2007. Dynamics of high speed wheel/rail system and its modelling. *Chinese Science Bulletin,* 52**,** 1566-1575.

Zhang, X., Zhao, C., Zhai, W., Shi, C. & Feng, Y. 2019b. Investigation of track settlement and ballast degradation in the high-speed railway using a full-scale laboratory test. *Proceedings of the Institution of Mechanical Engineers, Part F: Journal of Rail and Rapid Transit,* 233**,** 869-881.

Zhu, J. Y., Thompson, D. J. & Jones, C. J. C. 2011. On the effect of unsupported sleepers on the dynamic behavior of a railway track. *Vehicle System Dynamics: International Journal of Vehicle Mechanics and Mobility,* 49**,** 1389–1408.

Zuada Coelho, B., Priest, J. & Hölscher, P. 2017. Dynamic behaviour of transition zones in soft soils during regular train traffic. *Proceedings of the Institution of Mechanical Engineers, Part F: Journal of Rail and Rapid Transit,* 232**,** 645-662.

Annex

An extensive list of the permanent deformation and resilient models based on laboratory tests is presented in this Annex.

Although these tables are constructed in a uniform manner, especially the nomenclature of the variables and the parameters and characteristics of the materials, the authors still maintained the original symbols and nomenclature describe in the original paper.

Some models were developed using certain SI units, and where possible, these units are described in the column "*variables and empirical constants*".

Regarding the resilient modulus' tables, Rahim and George (2005) defined w_c as actual moisture content, w_c as optimum moisture content (which is equal to W_{opt}) and w_{cr} as the relation between the actual moisture content and the optimum moisture content. In this analysis, the fines are measured through the *passing sieve #200* or through the *percentage of fines*. Furthermore, the *maximum dry unit weight* is also defined as *maximum dry density*. The constants such as A, B, C, or k_i are defined as fitting, regression, material and model parameters according to the original formulation defined by the author. The symbols p_a and p_0 are defined as atmospheric stress/pressure and reference stress and it is different from p_u which means unite pressure. Regarding the stress variables, the symbol θ is defined as bulk stress ou sum of principal stresses, and the deviator stress can be represented by the symbols q, q_r and σ_d. The symbol q is different from q_m which represents the mean value of the deviator stress.

The permanent deformation is an adimensional parameter that can also be designated as permanent strain or plastic strain and its nomenclature varies, as mentioned above. The plastic/permanent deformation is defined as not recoverable. The materials that are part of the pavements and railway structures accumulate some amount of permanent deformation due to the traffic cyclic load. The stress parameters (induced by the cyclic loads) are one of the main inputs of these models. The inclusion of this parameter in the permanent deformation model varies as well as the nomenclature. Indeed, there are models dependent on the p and q (mean and deviatoric) stresses or on the octahedral stresses, for example.

In the permanent deformation tables, the deviator stress is represented by q_d, q, or σ_d, the variable for the atmospheric pressure/reference stress is represented by σ_{atm}, p_0, p_a, or p_{ref}, while the equation models were developed under different conditions, so permanent deformation is represented in the following

357

tables by the nomenclatures: ε_p, $\varepsilon_{p1,N}$, ε_z^p, ε_{qr}(axial residual strain), ε_1^p, $\varepsilon_p(N)$, $\varepsilon_1^p(N)$. The constants of the models used to fit the model to the available data are represented by different letters and symbols which are defined as material parameters, model constants, and model parameters and soil parameters, as listed in the permanent deformation tables.

Table A.1 - Models that describe resilient modulus of fine-grained soils - clays

UIC	ASTM classification	Author's model	Equation model	Variables and Empirical Constants	Parameters and characteristics	Observations
QS0*	CH (no information about the particle size curve) High plasticity	Ng et al. (2013)	$$M_r = k_1 p_a \left(\frac{\theta_{net}}{p_a}\right)^{k_2} \left(\frac{\tau_{oct}}{p_a} + 1\right)^{k_3} \left(\frac{\psi_m}{\theta_{net}} + 1\right)^{k_4}$$	- θ_{net} is the net bulk stress ($\theta_{net}=\theta$-$3u_a$); - τ_{oct} is the octahedral shear stress; - ψ_m is the matric suction; - p_a is the atmospheric stress; - k_i are the material parameters.	- W_L=61%; - W_P=25%; - IP=36%; - G_s=2.69.	- The model is similar to Cary and Zapata (2011) model; - The last term related to the suction parameter is normalized with the net bulk stress instead of the atmospheric pressure; - The model does not consider the effect of the pore-water pressure under saturated conditions.
QS0*	CH (no information about the particle size curve); High plasticity	Ng et al. (2013)	$$M_r = k_1 p_a \left(\frac{\theta_{net}}{p_a}\right)^{k_2} \left(\frac{\tau_{oct}}{p_a} + 1\right)^{k_3} \left(\frac{\psi_m}{\theta_{net}} + 1\right)^{k_4}$$	- θ_{net} is the net bulk stress ($\theta_{net}=\theta$-$3u_a$); - τ_{oct} is the octahedral shear stress; - ψ_m is the matric suction; - p_a is the atmospheric stress; - k_i are the material parameters.	- W_L=71%; - W_P=23%; - IP=48%; - G_s=2.73.	- The model is similar to Cary and Zapata (2011) model; - The last term related to the suction parameter is normalized with the net bulk stress instead of the atmospheric pressure; - The model does not consider the effect of the pore-water pressure under saturated conditions.
QS0	CL High plasticity	Sawangsuriya et al. (2009)	$$M_r = k_1 p_a \left(\frac{\theta - 3k_4}{p_a}\right)^{k_2} \left(\frac{\tau_{oct}}{p_a} + k_5\right)^{k_3}$$ $$MR_{opt} = \frac{M_{rs}}{M_{rs;opt}} = c + d \log \psi_m$$	- MR_{opt} is the modulus ratio; - M_{rs} is the modulus at certain suction (or moisture) - $M_{rs,opt}$ is the modulus at optimum moisture content; - c and d are model parameters; - p_a is the atmospheric pressure (101 kPa); - k_i are fitting parameters.	- W_L=85%; - IP=52%; - G_s=2.75; - Sand content=3.1%; - Silt content=21.2%; - Clay content=75.2%; - Fines content=96.4%; - W_{opt}=27.5%; - Maximum dry unit weight=14.4 kN/m³.	- Model developed based on four tested fine-grained soils; - This model demands significant regression parameters and several combinations of parametric values to fit laboratory tests; - The test specimens were initially saturated and then subjected to desorption until the matric suction was 154 or 350 kPa. - All the test soils were prepared at OPT water content and at a dry density corresponding to 98% or

						103% relative compaction for a standard Proctor.
QS0-QS1	CL Medium plasticity	Drumm and Pierce (1990)	$E_r = \dfrac{a' + b'\sigma_d}{\sigma_d} \, for \, \sigma_d > 0$	- a' and b' are material parameters: $a' = 318.2 + 0.337(q_u) + 0.73(\% \, clay) + 2.26(PI) - 0.915(\gamma) - 2.19(S) - 0.304(\% \, finer \, \#200)$ $b' = 2.10 + 0.00039(1/a) + 0.104(q_u) + 0.09(LL) - 0.10(\% \, finer \, \#200)$	- W_L=42.1%; - W_P=22.0%; - IP=20.1%; - G_s=2.76; - Clay content=36%; - Passing sieve #200=93%; - Maximum dry density=15.20 kN/m³.	- The hyperbola predicts excessive values of E_r when σ_d is close to zero.
QS1	CL Low plasticity	Drumm and Pierce (1990)	$E_r = \dfrac{a' + b'\sigma_d}{\sigma_d} \, for \, \sigma_d > 0$	- a' and b' are material parameters: $a' = 318.2 + 0.337(q_u) + 0.73(\% \, clay) + 2.26(PI) - 0.915(\gamma) - 2.19(S) - 0.304(\% \, finer \, \#200)$ $b' = 2.10 + 0.00039(1/a) + 0.104(q_u) + 0.09(LL) - 0.10(\% \, finer \, \#200)$	- W_L=30.5%; - W_P=22.1%; - IP=8.4%; - G_s=2.66; - Clay content=17.0%; - Passing sieve #200=95.0%; - Maximum dry density=16.28 kN/m³.	- The hyperbola predicts excessive values of E_r when σ_d is close to zero.
QS1	CL Medium plasticity	Drumm and Pierce (1990)	$E_r = \dfrac{a' + b'\sigma_d}{\sigma_d} \, for \, \sigma_d > 0$	- a' and b' are material parameters: $a' = 318.2 + 0.337(q_u) + 0.73(\% \, cl + 2.26(PI) - 0.915(\gamma) - 2.19(S) - 0.304(\% \, finer \, \#200)$ $b' = 2.10 + 0.00039(1/a) + 0.104(q_u) + 0.09(LL) - 0.10(\% \, finer \, \#200)$	- W_L=38.8%; - W_P=23.3%; - IP=15.5%; - G_s=2.65; - Clay content=18.0%; - Passing sieve #200=100.0%; - Maximum dry density=15.98 kN/m³.	- The hyperbola predicts excessive values of E_r when σ_d is close to zero.

QS1	CL Low plasticity	Drumm and Pierce (1990)	$E_r = \dfrac{a' + b'\sigma_d}{\sigma_d} \, for \, \sigma_d > 0$	- a' and b' are material parameters: $a' = 318.2 + 0.337(q_u) + 0.73(\% cl$ $+ 2.26(PI) - 0.915(\gamma) - 2.19(S)$ $- 0.304(\% \, finer \, \#200)$ $b' = 2.10 + 0.00039(1/a) +$ $0.104(q_u) + 0.09(LL)\text{-}0.10(\%$ finer #200)	- W_L=29.5%; - W_P=20.1%; - IP=9.4%; - G_s=2.67; - Clay content=16.0%; - Passing sieve #200=78.0%; - Maximum dry density=17.16 kN/m³.	- The hyperbola predicts excessive values of E_r when σ_d is close to zero.
QS1	CL Low plasticity	Drumm and Pierce (1990)	$E_r = \dfrac{a' + b'\sigma_d}{\sigma_d} \, for \, \sigma_d > 0$	- a' and b' are material parameters: $a' = 318.2 + 0.337(q_u)$ $+ 0.73(\% \, clay) + 2.26(PI)$ $- 0.915(\gamma) - 2.19(S)$ $- 0.304(\% \, finer \, \#200)$ $b' = 2.10 + 0.00039(1/a) +$ $0.104(q_u) + 0.09(LL)\text{-}0.10(\% \, finer$ #200)	- W_L=28.5%; - W_P=19.2%; - IP=9.3%; - G_s=2.73; - Clay content=20.0%; - Passing sieve #200=73.0%; - Maximum dry density=17.36 kN/m³.	- The hyperbola predicts excessive values of E_r when σ_d is close to zero.
QS1	CL Low plasticity	Sawangsuriya et al. (2009)	$M_r = k_1 p_a \left(\dfrac{\theta - 3k_4}{p_a}\right)^{k_2} \left(\dfrac{\tau_{oct}}{p_a} + k_5\right)^{k_3}$ $MR_{opt} = \dfrac{M_{rs}}{M_{rs;opt}} = c + d \log \psi_m$	- MR_{opt} is the modulus ratio; - M_{rs} is the modulus at certain suction (or moisture) - $M_{rs,opt}$ is the modulus at optimum moisture content; - c and d are model parameters; - p_a is the atmospheric pressure (101 kPa); - k_i are fitting parameters.	- W_L=26.0%; - IP=9.0%; - G_s=2.66; - Sand content=36.3%; - Silt content=45.3%; - Clay content=14.5%; - Percent fines=59.7%; - W_{opt}=16.0%; - Maximum dry unit weight=17.70 kN/m³.	- Model developed based on four tested fine-grained soils; - This model demands significate regression parameters and several combinations of parametric values to fit laboratory tests; - The test specimens were initially saturated and then subjected to desorption until the matric suction was 154 or 350 kPa. - All the test soils were prepared at OPT water content and at a dry density corresponding to 98% or 103% relative compaction for a standard Proctor.

QS1	CL Low plasticity	Liang et al. (2008)	$M_r = k_1 p_a \left(\dfrac{\theta + \chi\psi_m}{p_a}\right)^{k_2} \left(\dfrac{\tau_{oct}}{p_a} + 1\right)^{k_3}$	- θ is the bulk stress; - τ_{oct} is the octahedral shear stress; - χ is the Bishop's effective stress parameter; - ψ_m is the matric suction; - k_i are the material parameters.	- W_L=30.8%; - W_P=18.4%; - IP=12.3%; - Passing sieve #200=68.8%; - W_{opt}=16.5%; - Maximum dry density=17.70 kN/m³.	- The model takes into account, explicitly, the effect of the confining and octahedral shear stress; - It is used for a large range of unbound materials; - The effect of the matric suction is included in the effective stress; - The model is similar to the model developed by Uzan (1985)
≤QS1 (based on AASHTO classification)	-	Rahim and George (2005)	$M_r = k_1 P_a \left(1 + \dfrac{\sigma_d}{1+\sigma_c}\right)^{k_2}$	- M_r is the resilient modulus (MPa); - σ_d is the deviator stress (kPa); - σ_c is the confining pressure (kPa); - P_a is the atmospheric pressure (kPa); - k_1 and k_2 are model parameters.	- γ_d=16.92 kN/m³; - γ_{dr}=0.97; - w_{cr}=1.48; - w_c=20.7%; - Optimum w_c=14.0%; - Maximum dry density=17.4 kN/m³; - Passing sieve #200=89%.	- k_1 is dependent on γ_d, LL and w_c - k_2 is dependent on γ_d, LL, w_{cr} and #200, where γ_{dr} and w_{cr} are the density and moisture ratio, respectively;
≤QS1 (based on AASHTO classification)	-	Rahim and George (2005)	$M_r = k_1 P_a \left(1 + \dfrac{\sigma_d}{1+\sigma_c}\right)^{k_2}$	- M_r is the resilient modulus (MPa); - σ_d is the deviator stress (kPa); - σ_c is the confining pressure (kPa); - P_a is the atmospheric pressure (kPa); - k_1 and k_2 are model parameters.	- γ_d=19.87 kN/m³; - γ_{dr}=1.10; - w_{cr}=0.82; - w_c=11.5%; - Optimum w_c=14.0%; - Maximum dry density=18.4 kN/m³; - Passing sieve #200=44%;	- k_1 is dependent on γ_d, LL and w_c - k_2 is dependent on γ_d, LL, w_{cr} and #200, where γ_{dr} and w_{cr} are the density and moisture ratio, respectively;
QS1	CL-ML Low plasticity	Liang et al. (2008)	$M_r = k_1 p_a \left(\dfrac{\theta + \chi\psi_m}{p_a}\right)^{k_2} \left(\dfrac{\tau_{oct}}{p_a} + 1\right)^{k_3}$	- θ is the bulk stress; - τ_{oct} is the octahedral shear stress; - χ is the Bishop's effective stress parameter; - ψ_m is the matric suction; - k_i are the material parameters.	- W_L=27.8%; - W_P=19.8%; - IP=8%; - Passing sieve #200=56.3%; - W_{opt}=14.2%; - Maximum dry density=17.75 kN/m³.	- The model takes into account, explicitly, the effect of the confining and octahedral shear stress; - It is used for a large range of unbound materials; - The effect of the matric suction is included in the effective stress; - The model is similar to the model developed by Uzan (1985).

| QS1** | CL (no information about the particle size curve) Low to medium plasticity | Ng et al. (2013) | $$M_r = k_1 p_a \left(\frac{\theta_{net}}{p_a}\right)^{k_2} \left(\frac{\tau_{oct}}{p_a} + 1\right)^{k_3} \left(\frac{\psi_m}{\theta_{net}} + 1\right)^{k_4}$$ | - θ_{net} is the net bulk stress (θ_{net}=θ-3u$_a$);
- τ_{oct} is the octahedral shear stress;
- ψ_m is the matric suction;
- p_a is the atmospheric stress;
- k_i are the material parameters. | - W_L=37%;
- W_P=18%;
- IP=19%;
- G_s=2.69. | - The model is similar to Cary and Zapata (2011) model;
- The last term related to the suction parameter is normalized with the net bulk stress instead of the atmospheric pressure;
- The model does not consider the effect of the pore-water pressure under saturated conditions. |

*Classification based on the plasticity index and AASHTO classification (A-7-5 → >35% passing the 0.075 mm sieve).

** Classification based on the plasticity index and AASHTO classification (A-7-6 → >35% passing the 0.075 mm sieve).

Table A.2 - Models that describe resilient modulus of fine-grained soils – silts

UIC	ASTM classification	Author's model	Equation model	Variables and Empirical Constants	Parameters and characteristics	Observations
QS0	MH (no information about the particle size curve) High plasticity	Yang et al. (2005)	$M_r = k_1 p_a (\sigma_d + \chi \psi_m)^{k_2}$	- χ is the Bishop's effective stress parameters (it is function of the degree of saturation of the soil); - ψ_m is the matric suction; - k_i are the materials parameters;	- W_L=54.0%; - IP=20%; - G_s=2.71; - W_{opt}=18%; - Maximum dry density=17.26 kN/m³.	- This model does not take into account the effect of confining stress; - The model can be applied to a large range of moisture content; - The model is dependent on only two material parameters.
QS0	MH High plasticity	Drumm and Pierce (1990)	$E_r = \dfrac{a' + b'\sigma_d}{\sigma_d} \, for \, \sigma_d > 0$	- a' and b' are material parameters: $a' = 318.2 + 0.337(q_u) + 0.73(\% \, clay) + 2.26(PI) - 0.915(\gamma) - 2.19(S) - 0.304(\% \, finer \, \#200)$ $b' = 2.10 + 0.00039(1/a) + 0.104(q_u) + 0.09(LL)$-0.10(% finer #200)	- W_L=68.5%; - W_P=39.2%; - IP=29.3%; - G_s=2.71; - Clay content=28.7%; - Passing sieve #200=80.0%; - Maximum dry density=12.55 kN/m³.	- The hyperbola predicts excessive values of E_r when σ_d is close to zero
QS0	MH High plasticity	Drumm and Pierce (1990)	$E_r = \dfrac{a' + b'\sigma_d}{\sigma_d} \, for \, \sigma_d > 0$	- a' and b' are material parameters: $a' = 318.2 + 0.337(q_u) + 0.73(\% \, clay) + 2.26(PI) - 0.915(\gamma) - 2.19(S) - 0.304(\% \, finer \, \#200)$ $b' = 2.10 + 0.00039(1/a) + 0.104(q_u) + 0.09(LL)$-0.10(% finer #200)	- W_L=69.5%; - W_P=42.6%; - IP=26.9%; - G_s=2.73; - Clay content=55.0%; - Passing sieve #200=80.0%; - Maximum dry density=13.83 kN/m³.	- The hyperbola predicts excessive values of E_r when σ_d is close to zero
QS0-QS1	MH (no information about the particle size curve)	Yang et al. (2005)	$M_r = k_1 p_a (\sigma_d + \chi \psi_m)^{k_2}$	- χ is the Bishop's effective stress parameters (it is function of the degree of saturation of the soil); - ψ_m is the matric suction; - k_i are the materials parameters;	- G_s=2.67; - W_L=50.0%; - IP=23%; - W_{opt}=17%; - Maximum dry density=17.65 kN/m³.	- This model does not take into account the effect of confining stress; - The model can be applied to a large range of moisture content; - The model is dependent on only two material parameters.

	Medium to high plasticity					
QS1	ML Low plasticity	Sawangsuriya et al. (2009)	$M_r = k_1 p_a \left(\dfrac{\theta - 3k_4}{p_a}\right)^{k_2} \left(\dfrac{\tau_{oct}}{p_a} + k_5\right)^{k_3}$ $MR_{opt} = \dfrac{M_{rs}}{M_{rs;opt}} = c + d \log \psi_m$	- MR_{opt} is the modulus ratio; - M_{rs} is the modulus at certain suction (or moisture) - $M_{rs,opt}$ is the modulus at optimum moisture content; - c and d are model parameters; - p_a is the atmospheric pressure (101 kPa); - k_i are fitting parameters.	- W_L=28.0%; - IP=11.0%; - G_s=2.69; - Sand content=11.9%; - Silt content=82.4%; - Clay content=5.7%; - Fines content=88.1%; - W_{opt}=13.5%; - Maximum dry unit weight=17.9 kN/m³.	- Model developed based on four tested fine-grained soils; - This model demands significate regression parameters and several combinations of parametric values to fit laboratory tests; - The test specimens were initially saturated and then subjected to desorption until the matric suction was 154 or 350 kPa. - All the test soils were prepared at OPT water content and at a dry density corresponding to 98% or 103% relative compaction for a standard Proctor.
QS1 (low plasticity) ML		Sawangsuriya et al. (2009)	$M_r = k_1 p_a \left(\dfrac{\theta - 3k_4}{p_a}\right)^{k_2} \left(\dfrac{\tau_{oct}}{p_a} + k_5\right)^{k_3}$ $MR_{opt} = \dfrac{M_{rs}}{M_{rs;opt}} = c + d \log \psi_m$	- MR_{opt} is the modulus ratio; - M_{rs} is the modulus at certain suction (or moisture) - $M_{rs,opt}$ is the modulus at optimum moisture content; - c and d are model parameters; - p_a is the atmospheric pressure (101 kPa); - k_i are fitting parameters.	- W_L=42.0%; - IP=24.0%; - G_s=2.69; - Sand content =8.9%; - Silt content=63.8%; - Clay content=27.3%; - Fines content=91.1%; - W_{opt}=22.0%; - Maximum dry unit weight=15.8 kN/m³.	- Model developed based on four tested fine-grained soils; - This model demands significate regression parameters and several combinations of parametric values to fit laboratory tests; - The test specimens were initially saturated and then subjected to desorption until the matric suction was 154 or 350 kPa. - All the test soils were prepared at OPT water content and at a dry density corresponding to 98% or 103% relative compaction for a standard Proctor.

QS1	ML Medium plasticity	Ng et al. (2013)	$M_r = k_1 p_a \left(\frac{\theta_{net}}{p_a}\right)^{k_2} \left(\frac{\tau_{oct}}{p_a} + 1\right)^{k_3} \left(\frac{\psi_m}{\theta_{net}} + 1\right)^{k_4}$	- θ_{net} is the net bulk stress ($\theta_{net}=\theta$-3u_a); - τ_{oct} is the octahedral shear stress; - ψ_m is the matric suction; - p_a is the atmospheric stress; - k_i are the material parameters.	- W_L=43%;W_P=29%; - IP=14%; - G_s=2.73; - Sand content=24%; - Silt content=72%; - Clay content=4%; - C_u=4.55; C_c=0.61; - W_{opt}=16.3%; - Maximum dry density=17.26 kN/m³.	- The model is similar to Cary and Zapata (2011) model; - The last term related to the suction parameter is normalized with the net bulk stress instead of the atmospheric pressure; - The model does not consider the effect of the pore-water pressure under saturated conditions.
QS1	ML Low plasticity	Drumm and Pierce (1990)	$E_r = \frac{a' + b'\sigma_d}{\sigma_d} \ for \ \sigma_d > 0$	- a' and b' are material parameters: $a' = 318.2 + 0.337(q_u) + 0.73(\% \ clay) + 2.26(PI) - 0.915(\gamma) - 2.19(S) - 0.304(\% \ finer \ \#200)$ $b' = 2.10 + 0.00039(1/a) + 0.104(q_u) + 0.09(LL)$-0.10(% finer #200)	- W_L=36.2%; - W_P=34.1%; - IP=2.1%; - G_s=2.66; - Clay content=18.0%; - Passing sieve #200=80.0%; - Maximum dry density=13.14 kN/m³.	- The hyperbola predicts excessive values of E_r when σ_d is close to zero
QS1	ML Low plasticity	Drumm and Pierce (1990)	$E_r = \frac{a' + b'\sigma_d}{\sigma_d} \ for \ \sigma_d > 0$	- a' and b' are material parameters: $a' = 318.2 + 0.337(q_u) + 0.73(\% \ clay) + 2.26(PI) - 0.915(\gamma) - 2.19(S) - 0.304(\% \ finer \ \#200)$ $b' = 2.10 + 0.00039(1/a) + 0.104(q_u) + 0.09(LL)$-0.10(% finer #200)	- W_L=37.1%; - W_P=27.0%; - IP=10.0%; - G_s=2.67; - Clay content=35.0%; - Passing sieve #200=68.0%; - Maximum dry density=14.91 kN/m³.	- The hyperbola predicts excessive values of E_r when σ_d is close to zero
QS1	ML Medium plasticity	Parreira and Goncalves (2000)	$M_r = k_1 p_a \sigma_d^{k_2} \psi_m^{k_3}$	- σ_d is the deviator stress; - ψ_m is the matric suction; - k_i are the regression parameters.	- W_L=46.4%; - W_P=28.8%; - IP=17.6%; - G_s=2.66; - Clay content=38%;	- The model does not take into account the effect of confining stress; - It is only valid for a limited range of moisture content; - When the soils get saturated and matric suction is equal to zero (high moisture

					- Passing sieve #200=52%; - W_{opt}=19.5%; - Maximum dry density=16.28 kN/m³.	content) the resilient modulus is close to zero; - Low moisture content values lead to high (unrealistic) resilient modulus; - The suction was determined through the paper filter method.

Table A.3 - Models that describe resilient modulus of granular soils – sands

UIC	ASTM classification	Author's model	Equation model	Variables and Empirical Constants	Parameters and characteristics	Observations
QS1	SM-CL Low plasticity	Drumm and Pierce (1990)	$E_r = \dfrac{a' + b'\sigma_d}{\sigma_d} \, for \, \sigma_d > 0$	- a' and b' are material parameters: $a' = 318.2 + 0.337(q_u) + 0.73(\% \, clay) + 2.26(PI) - 0.915(\gamma) - 2.19(S) - 0.304(\% \, finer \, \#200)$ $b' = 2.10 + 0.00039(1/a) + 0.104(q_u) + 0.09(LL)\text{-}0.10(\% \, finer \, \#200)$	- W_L=21.0%; - W_P=14.1%; - IP=6.9%; - G_s=2.65; - Clay content=16.0%; - Passing sieve #200=36.0%; - Maximum dry density=18.04 kN/m³.	- The hyperbola predicts excessive values of E_r when σ_d is close to zero
QS1	SM Low plasticity	Drumm and Pierce (1990)	$E_r = \dfrac{a' + b'\sigma_d}{\sigma_d} \, for \, \sigma_d > 0$	- a' and b' are material parameters: $a' = 318.2 + 0.337(q_u) + 0.73(\% \, clay) + 2.26(PI) - 0.915(\gamma) - 2.19(S) - 0.304(\% \, finer \, \#200)$ $b' = 2.10 + 0.00039(1/a) + 0.104(q_u) + 0.09(LL)\text{-}0.10(\% \, finer \, \#200)$	- W_L=20.7%; - W_P=19.0%; - IP=1.7%; - G_s=2.60; - Clay content=17.0%; - Passing sieve #200=20.0%; - Maximum dry density=17.55 kN/m³.	- The hyperbola predicts excessive values of E_r when σ_d is close to zero
QS1	SC (the fines are classified as CL) Low plasticity	Cary and Zapata (2011)	$M_r = k_1 p_a \left(\dfrac{\theta_{net} - 3\Delta u_{w-sat}}{p_a}\right)^{k_2} \left(\dfrac{\tau_{oct}}{p_a} + 1\right)^{k_3} \left(\dfrac{\psi_m - \Lambda\psi_m}{p_a} + 1\right)^{k_4}$	- θ_{net} is the net bulk stress (θ_{net}=θ-3u$_a$); - $\Delta u_{w\text{-}sat}$ is the pore-water pressure build-up in a saturated condition (ψ_m=0); - $\Delta\psi_m$ is the relative change in matric suction with respect to the initial matric suction in an unsaturated condition ($\Delta u_{w\text{-}sat}$=0)	- W_L=22%; - W_P=18%; - IP=5% - G_s=2.71; - Passing sieve #200=47%; - W_{opt}=12.1%; - Maximum dry density =18.73 kN/m³.	- The model is based on the Universal model with an additional term that includes the matric suction effects into the resilient modulus
QS1	SC (clayed sand) Low plasticity	Shackel (1973)	$M_r = k \dfrac{\sigma_{oct}^n}{\tau_{oct}^m}$	- σ_{oct} and τ_{oct} are the octahedral normal and shear stresses, respectively.	- W_L=26%; - W_P=17.6%; - IP=8.4%;	- This model is difficult to apply (Li and Selig, 1994).

					- 60% sand and 40% kaolinite by weight.	
QS2	SP Poor-graded sand	Karasahin (1993)	$M_r = A\left(\frac{p_m}{p_u}\right)^B\left(\frac{p_u}{p}\right)^C$	- q_m is the mean value of deviator stress; - p_m is the mean value of mean normal stress - p is the mean normal stress - p_u – unite pressure (1 kPa) - A, B and C are constants.	- G_s=2.64; - C_o≈2.5; - C_z≈1.5.	- This model is based on the triaxial tests carried out in six aggregates; - The model is based on laboratory triaxial testing (constant and variable confining pressure) (Lekarp et al., 2000b).
QS2	SP Poor-graded sand	Karasahin (1993)	$M_r = A\left(\frac{p_m}{p_u}\right)^B\left(\frac{p_u}{p}\right)^C$	- q_m is the mean value of deviator stress; - p_m is the mean value of mean normal stress - p is the mean normal stress - p_u – unite pressure (1 kPa) - A, B and C are constants.	- G_s=2.64; - C_o≈2.0; - C_z≈1.04.	- This model is based on the triaxial tests carried out in six aggregates; - The model is based on laboratory triaxial testing (constant and variable confining pressure) (Lekarp et al., 2000b).
QS3	SP Poor-graded sand	Karasahin (1993)	$M_r = A\left(\frac{p_m}{p_u}\right)^B\left(\frac{p_u}{p}\right)^C$	- q_m is the mean value of deviator stress; - p_m is the mean value of mean normal stress - p is the mean normal stress - p_u – unite pressure (1 kPa) - A, B and C are constants.	- G_s=2.61; - Aggregate abrasion value=1.9; - C_o≈28; - C_z≈0.54.	- This model is based on the triaxial tests carried out in six aggregates; - The model is based on laboratory triaxial testing (constant and variable confining pressure) (Lekarp et al., 2000b).
QS3	SP Poor-graded sand	Karasahin (1993)	$M_r = A\left(\frac{p_m}{p_u}\right)^B\left(\frac{p_u}{p}\right)^C$	- q_m is the mean value of deviator stress; - p_m is the mean value of mean normal stress - p is the mean normal stress - p_u – unite pressure (1 kPa) - A, B and C are constants.	- G_s=2.24; - W_{opt}= 8-12%; - Permeability index=0.0002 m/s; - C_o≈30; - C_z≈0.5.	- This model is based on the triaxial tests carried out in six aggregates. - The model is based on laboratory triaxial testing (constant and variable confining pressure) (Lekarp et al., 2000b).
QS3	SW Well-graded sand	Kolisoja (1997)	$M_r = A(n_{max} - n)p_0\left(\frac{\theta}{p_0}\right)^{0.5}$ $M_r = B(n_{max} - n)p_0\left(\frac{\theta}{p_0}\right)^{0.7}\left(\frac{q}{p_0}\right)^{-0.2}$	- θ is the sum of principal stresses; - p_o is the reference stress, 100 kPa; - n is the porosity of the material;	- C_o≈5.9; - C_z≈1.2.	- This model is based on laboratory triaxial testing (constant confining pressure) (Lekarp et al., 2000b); - The model is based on tests carried out in several types of coarse-grained

				- n_o is the theoretical maximum value of porosity when $M_r=0$ - A is a material parameter.		- granular materials typically used in unbound layers of road and railroad pavements; - The density was incorporated in the model by the porosity parameter; - Materials classified as natural gravels; - The study also includes crushed gravel and crushed rock.
QS3	SW Well-graded sand	Kolisoja (1997)	$$M_r = A(n_{max}-n)p_0\left(\frac{\theta}{p_0}\right)^{0.5}$$ $$M_r = B(n_{max}-n)p_0\left(\frac{\theta}{p_0}\right)^{0.7}\left(\frac{q}{p_0}\right)^{-0.2}$$	- θ is the sum of principal stresses; - p_o is the reference stress, 100 kPa; - n is the porosity of the material; - n_o is the theoretical maximum value of porosity when $M_r=0$ - A is a material parameter.	- $C_a\approx16$; - $C_c\approx1.0$.	- This model is based on laboratory triaxial testing (constant confining pressure) (Lekarp et al., 2000b); - The model is based on tests carried out in several types of coarse-grained granular materials typically used in unbound layers of road and railroad pavements; - The density was incorporated in the model by the porosity parameter; - Materials classified as natural gravels; - The study also includes crushed gravel and crushed rock.
QS3	SW Well-graded sand	Kolisoja (1997)	$$M_r = A(n_{max}-n)p_0\left(\frac{\theta}{p_0}\right)^{0.5}$$ $$M_r = B(n_{max}-n)p_0\left(\frac{\theta}{p_0}\right)^{0.7}\left(\frac{q}{p_0}\right)^{-0.2}$$	- θ is the sum of principal stresses; - p_o is the reference stress, 100 kPa; - n is the porosity of the material; - n_o is the theoretical maximum value of porosity when $M_r=0$ - A is a material parameter.	- $C_a\approx50$; - $C_c\approx1.0$.	- This model is based on laboratory triaxial testing (constant confining pressure) (Lekarp et al., 2000b); - The model is based on tests carried out in several types of coarse-grained granular materials typically used in unbound layers of road and railroad pavements; - The density was incorporated in the model by the porosity parameter; - Materials classified as natural gravels; - The study also includes crushed gravel and crushed rock.

QS3	SW Well-graded sand	Gomes Correia et al. (2001)	$E_v = C\sigma'_v{}^m$	- C is a parameter that depends on the mineralogy of the particles, shape of the grains, particle size curve (in the case of granular materials. In the case of the cohesive materials, it also depends on the percentage of fines and Atterberg limits.	- D_{50}=3.5 mm; - G_s=2.71; - C_u=28; - $C_c \approx 1.0$.	- The vertical Young's modulus is independent of the lateral stress.

Table A.4 - Models that describe resilient modulus of granular soils – gravels

UIC	ASTM classification	Author's model	Equation model	Variables and Empirical Constants	Parameters and characteristics	Observations
QS2	GP-GM	Cary and Zapata (2011)	$M_r = k_1 p_a \left(\dfrac{\theta_{net} - 3\Delta u_{w-sat}}{p_a} + 1\right)^{k_2} \left(\dfrac{\tau_{oct}}{p_a} + 1\right)^{k_3} \left(\dfrac{\psi_m - \Lambda \psi_m}{p_a} + 1\right)^{k_4}$	- θ_{net} is the net bulk stress ($\theta_{net}=\theta-3u_a$); - $\Delta u_{w\text{-}sat}$ is the pore-water pressure build-up in a saturated condition ($\psi_m=0$); - $\Delta\psi_m$ is the relative change in matric suction with respect to the initial matric suction in an unsaturated condition ($\Delta u_{w\text{-}sat}=0$)	- IP=NP; - G_s=2.71; - Passing sieve #200=7%; - W_{opt}=7.2%; - Maximum dry density =22.16 kN/m³.	- The model is based on the Universal model with an additional term that includes the matric suction effects into the resilient modulus
QS2	GP Poor-graded gravel	Karasahin (1993)	$M_r = A \left(\dfrac{p_m}{p_u}\right)^B \left(\dfrac{p_u}{p}\right)^C$	- q_m is the mean value of deviator stress; - p_m is the mean value of mean normal stress - p is the mean normal stress (1 kPa) - p_u – unite pressure (1 kPa) - A, B and C are constants.	- G_s=2.69; - C_u≈5.3; - C_c≈4.7.	- This model is based on the triaxial tests carried out in six aggregates; - The model is based on laboratory triaxial testing (constant and variable confining pressure) (Lekarp et al., 2000b).
QS3	GW Well-graded gravel	Karasahin (1993)	$M_r = A \left(\dfrac{p_m}{p_u}\right)^B \left(\dfrac{p_u}{p}\right)^C$	- q_m is the mean value of deviator stress; - p_m is the mean value of mean normal stress - p mean normal stress - p_u – unite pressure (1 kPa) - A, B and C are constants.	- G_s=2.69; - Aggregate abrasion value=5.1; - C_u≈61; - C_c≈2.11.	- This model is based on the triaxial tests carried out in six aggregates; - The model is based on laboratory triaxial testing (constant and variable confining pressure) (Lekarp et al., 2000b).
QS2-QS3	GP Poor-graded gravel	Gomes Correia et al. (2001)	$E_v = C \sigma'_v{}^m$	- C is a parameter that depends on the mineralogy of the particles, shape of the grains, particle size curve (in the case of the granular materials)	- D_{50}=8.5 mm; - G_s=2.71; - C_u=53; - C_c≈4.5.	- The vertical Young's modulus is independent of the lateral stress; - The parameter C, in the case of the cohesive materials, also depends on the percentage of fines and Atterberg limits.
≥QS2	-	Rahim and George (2005)	$M_r = k_1 P_a \left(1 + \dfrac{\theta}{1 + \sigma_d}\right)^{k_2}$	- M_r is the resilient modulus (MPa); - σ_d is the deviator stress (kPa);	- γ_{dr}=16.07 kN/m³; - γ_{dr}=1.02; - w_c=16.3%;	- k_1 is dependent on γ_{dr}, w_{cr}, #200 and C_u, where γ_{dr} and w_{cr} are the density and moisture ratio, respectively;

(based on AASHTO classification)				- θ is the bulk stress (kPa) - P_a is the atmospheric pressure (kPa); - k_1 and k_2 are model parameters.	- w_{cr}=1.05; - Optimum w_c=15.5%; - Maximum dry density=15.7 kN/m³; - Passing sieve #200=11%.	- k_2 is dependent on γ_{dr}, w_{cr}, #200 and C_u
≥QS2 (based on AASHTO classification)	-	Rahim and George (2005)	$M_r = k_1 P_a \left(1 + \dfrac{\sigma_d}{1 + \sigma_c}\right)^{k_2}$	- M_r is the resilient modulus (MPa); - σ_d is the deviator stress (kPa); - θ is the bulk stress (kPa) - P_a is the atmospheric pressure (kPa); - k_1 and k_2 are model parameters.	- γ_d=18.04 kN/m³; - γ_{dr}=1.10; - w_{cr}=1.15; - w_c=17.32%; - Optimum w_c=15.0%; - Maximum dry density=16.7 kN/m³; - Passing sieve #200=34%.	- k_1 is dependent on γ_{dr}, w_{cr}, #200 and C_u, where γ_{dr} and w_{cr} are the density and moisture ratio, respectively; - k_2 is dependent on γ_{dr}, w_{cr}, #200 and C_u

Table A.5 – Other resilient models

UIC	ASTM classification	Author's model	Equation model	Variables and Empirical Constants	Parameters and characteristics	Observations
-	-	Monismith et al. (1967) Dunlap 1963	$M_r = k_1(\sigma_3)^{k_2}$	- σ_3 is the confining pressure; - k_1 and k_2 are material constants.	-	- This model is based on the resilient modulus and *Poisson*'s ratio; - Model-based on laboratory triaxial testing (constant confining pressure) (Lekarp et al., 2000b).
-	-	Seed et al. (1967) Brown and Pell (1967) Hicks and Monismith (1971)	$M_r = k_1(\theta)^{k_2}$	- θ is the bulk stress (sum of the principal stresses σ_1, σ_2 and σ_3); - ki are the regression parameters.	-	- Commonly known as the K-θ model; Hyperbolic relationship; - This model assumes a constant *Poisson*'s ratio. However, several studies show that this parameter varies with the applied stress; - The effect of stress on the resilient modulus is only considered by the bulk stress (sum of the principal stresses); - It is a simplified version of the Universal Model; - This model is based on laboratory triaxial testing (constant confining pressure) (Lekarp et al., 2000b); - The model fits well in the case of tests with constant confining pressure and shows poor results in the case of variable confining pressure (Gomes Correia et al., 1999).
-	-	Thompson and Robnett (1976)	$M_r = K_1 + K_2\sigma_d$, when $\sigma_d < \sigma_{di}$ $M_r = K_3 + K_4\sigma_d$, when $\sigma_d > \sigma_{di}$	- K_1, K_2, K_3 and K_4 are model parameters dependent upon soil type and its physical state	-	- This is a bi-linear model.

				(normally, K_2 and K_4 are negative); - σ_d is the deviator stress at which the slope of M_r versus σ_d changes.		
-	-	Fredlund et al. (1977)	$\log M_r = c_{ld} - m_{ld}(\sigma_1 - \sigma_3)$	- c_{ld} and m_{ld} are functions of matrix suction; - σ_1 and σ_3 are the major and minor principal stresses.	-	- The model wasn't fully validated with laboratory data; - This model is characterized as a semilog model;
-	-	Boyce (1980)	$$\varepsilon_v = \frac{1}{K_1}p^n\left[1 - \beta\left(\frac{q}{p}\right)^2\right]$$ $$\varepsilon_s = \frac{1}{3G_1}p^n\left(\frac{q}{p}\right)$$ $$K = \frac{p}{\varepsilon_v}$$ $$G = 3.\frac{q}{\varepsilon_q}$$	- p is the mean normal stress; - q is the deviator stress; - ε_{vr} is the recoverable volumetric strain and ε_{sr} is the shear strain; - K is the bulk modulus; - G is the shear modulus.	-	- Model using shear-volumetric approach; - This is a non-linear elastic model that takes into account the effect of the stress path and it is expressed in terms of the bulk and shear modulus, that are stress-dependent; - The model is elastic and follows the application of the theorem of reciprocity; - The shear and volumetric components of stress and strain are treated separately; - The granular materials show an inelastic response and this elastic model can lead to inaccurate predictions; - The model is based on variable confining pressure; - Sweere (1990) used this model but keep the relationship between shear and volumetric strains with stresses independent from each other.

- (no information about the materials)	- (no information about the materials)	Moossazadeh and Witczak (1981)	$M_r = k_1 (\sigma_d)^{k_2}$	- k_1 and k_2 are constants dependent on the material; - σ_d is the deviator stress;	-	- The model is characterized by a power model; - A modified elastic layered computer program was made to determine equivalent subgrade modulus values; multiple regression techniques were used to determine predictive equations for the equivalent subgrade modulus. - This model was widely used by other authors and good results were obtained (in agreement with test results).
- (no information about the materials)	- (no information about the materials)	Uzan (1985)	$M_r = k_1 p_0 \left(\frac{\theta}{p_0}\right)^{k_2} \left(\frac{q}{p_0}\right)^{k_3}$ or $M_r = k_1 p_0 \left(\frac{\theta}{p_0}\right)^{k_2} \left(\frac{\tau_{oct}}{p_0}\right)^{k_3}$	- θ is the bulk stress (sum of the principal stresses σ_1, σ_2 and σ_3); - τ_{oct} is the octahedral shear stress ; - p_0 is the atmospheric pressure; - k_i are the material parameters.	-	- The model shows good results in the case of pre-failure stresses. However, in the case of stresses that go beyond the static failure, the predictions are poor; - This model is suitable for a large range of materials: from fine-grained soils to coarse-granular materials; - This model is based on laboratory triaxial testing (constant confining pressure) (Lekarp et al., 2000b).
-	-	Brown and Pappin (1985)	$\varepsilon_v = \delta \left[\left(\frac{p}{A}\right)^B \left[1 - C \left(\frac{q}{p}\right)^2\right]\right]$ $\varepsilon_s = D\delta \left[\frac{q}{p+E}\right]\left[\frac{\sqrt{p_r^2 + q_r^2}}{p_m}\right]^F$	- p is the mean normal stress; - q is the deviator stress; - A, B, C, D and E are material constants.	-	- Model using shear-volumetric approach; - Two materials were considered: well-graded crushed limestone and uniformly graded limestone; - This model is also known as the contour model and take into account effective mean and deviatoric stresses and stress path dependency;

376

						- This model predicts the shear strain (considering the length of the stress path corresponding to the load cycle); - The material parameters in the two parts of the contour model are independent of each other. In fact, independent material parameters mean that the model is inelastic (unlike the Boyce model).
-	-	Johnson et al. (1986)	$M_r = k_1 \left(\dfrac{J_2}{\tau_{oct}} \right)^{k_2}$	- k_1 and k_2 are constants; - J_2 is the second stress invariant; - τ_{oct} is the octahedral shear stress.	-	- Model-based on laboratory triaxial testing (constant confining pressure) (Lekarp et al., 2000b).
-	-	Tam and Brown (1988)	$M_r = k_1 \left(\dfrac{p}{q} \right)^{k_2}$	- k_1 is a material constant; - p is the mean normal stress; - q is the deviator stress;	-	- Model-based on laboratory triaxial testing (constant confining pressure) (Lekarp et al., 2000b).
-	-	Thom (1988)	$\varepsilon_v = A(\delta \ln p)^B (\delta p)^C$ $\qquad - D \left[\delta \left(ln \dfrac{\sigma_1}{\sigma_3} \right)^2 \right]^E$ $\varepsilon_s = E \left[\delta \left(ln \dfrac{\sigma_1}{\sigma_3} \right)^2 \right]^F \left(\delta_T + \dfrac{1}{3} \delta S \right)$	- σ_1 and σ_3 are the major and minor principal stresses - T and S are 2D stress invariants.	-	- Model developed for prediction of the results of triaxial and hollow cylinder tests; - The model separates the volumetric and shear components as the Boyce's and contour models; - Karasahin (1993) verified the model but found it very difficult to obtain the material parameters by nonlinear regression analysis;
-	-	Elliot and Lourdesnathan (1989)	$M_r = k_1 \dfrac{\theta^{k_2}}{10^{A1}}$	- θ is the bulk stress (sum of the principal stresses σ_1, σ_2 and σ_3); - k_1 is a constant parameter; - $A_1 = mR_f$, m=regression coefficient determined from	-	- K-θ model that includes a failure term (the impact is insignificant until the failure is approached; - The failure deviator stress is determined based on the confining

-	-	Developed by Mayhew (1983) and re-written by Brown and Selig (1991)	$$\varepsilon_v = \frac{1}{K_1}p^A\left[1 - C\left(\frac{q}{p}\right)^2\right]$$ $$\varepsilon_s = \frac{1}{3G_1}p^B\left(\frac{q}{p}\right)$$	laboratory data and R is the stress/strength ratio (deviator stress divided by the failure deviator stress).		pressure and the static triaxial shear stress; - This model is based on laboratory triaxial testing (constant confining pressure) (Lekarp et al., 2000b).
-	-	Developed by Mayhew (1983) and re-written by Brown and Selig (1991)	$$\varepsilon_v = \frac{1}{K_1}p^A\left[1 - C\left(\frac{q}{p}\right)^2\right]$$ $$\varepsilon_s = \frac{1}{3G_1}p^B\left(\frac{q}{p}\right)$$	- p is the mean normal stress; - q is the deviator stress; - ε_v is the recoverable volumetric strain and ε_{sr} is the shear strain; - K is the bulk modulus; - G is the shear stress.	-	- Model similar to the contour model; - The author plot the shear and volumetric strains in the p-q space; - The author concludes that the stress path length (included in the contour model) had little impact on the shear strain response. The model removes the stress path dependence and the equations of the contour model turn into the inelastic modified version of the Boyce model.
-	-	Elhannani (1991)	$$\varepsilon_v = p_0^{1-B}p^B\left[\frac{1}{A} - \frac{(1-B)}{6C}\left(\frac{q}{p}\right)^2 - \frac{B}{D}\left(\frac{q}{p}\right)\right]$$ $$\varepsilon_s = p_0^{1-B}p^B\left[\frac{1}{3C}\left(\frac{q}{p}\right) - \frac{1}{D}\right]$$	- -	- Model-based on Boyce's model; the author introduced the concept of anisotropy.	-
		Pezo (1993) Garg and Thompson (1997)	$$M_r = N_1 q^{N_2}(\sigma_3)^{N_3}$$	- σ_3 is the confining pressure; - q is the deviator stress.	-	- Model-based on laboratory triaxial testing (constant confining pressure) (Lekarp et al., 2000b)
-	-	Li and Selig (1994)	$$R_{m1} = 0.98 - 0.28(w - w_{opt}) + 0.029(w - w_{opt})^2 -$$	- R_{m1}=M_r/M_{ropt} for the case of constant dry density; M_r is the resilient modulus at moisture content w(%) and the same dry density as M_{ropt}; M_{ropt} is the	-	- This model includes the soil's physical state by two quantities: moisture content and dry density that are related to the soil-compaction curve.

				resilient modulus at the maximum dry density and optimum moisture content w_{opt}(%) for any compaction effort.	- The results are based on repeated load triaxial test results on fine-grained soils from literature (Seed et al. (1962); Sauer and Monismith (1968); Culley (1971); Robnett and Thompson (1976); Fredlund et al. (1977); Edil and Moran (1979); Kirwan et al. (1979); Elfino and Davidson (1989)); - The power-law model was selected for the representation of the relationship between resilient modulus and deviator stress;
-	-	Li and Selig (1994)	$R_{m2} = 0.96 - 0.18(w - w_{opt}) + 0.0067(w - w_{opt})^2$	- R_{m2}=M$_r$/M$_{r,opt}$ for constant compaction effort; M$_r$ is the resilient modulus at moisture (%) and the same compaction effort as M$_{r(opt)}$;	- This model includes the soil's physical state by two quantities: moisture content and dry density that are related to the soil-compaction curve. - The results are based on repeated load triaxial test results on fine-grained soils from literature (Seed et al. (1962); Kallas and Riley (1967); Shifley and Monismith (1968); Tanimoto and Nishi (1970); Edris and Lytton (1976); Fredlund et al. (1977); Kirwan et al. (1979); Pezo et al. (1991) - The power-law model was selected for the representation of the relationship between resilient modulus and deviator stress.

-	-	Hornych et al. (1998)	$$\varepsilon_v = \frac{p^{*A}}{p_0^{A-1}}\left[\frac{\gamma+2}{3K_1} + \frac{A-1}{18G_1}(\gamma + 2)\left(\frac{q^*}{p^*}\right)^2 + \frac{\gamma-1}{3G_1}\left(\frac{q^*}{p^*}\right)\right]$$ $$\varepsilon_s = \frac{2}{3}\frac{p^{*A}}{p_0^{A-1}}\left[\frac{\gamma-1}{3K_1} + \frac{A-1}{18G_1}(\gamma - 1)\left(\frac{q^*}{p^*}\right)^2 + \frac{2\gamma+1}{6G_1}\left(\frac{q^*}{p^*}\right)\right]$$	- $p^* = \frac{\gamma G_1 + 2\sigma_3}{3}$; $q^* = \gamma\sigma_1 - \sigma_3$ - γ is the coefficient of anisotropy; - The parameter γ means that the material is isotropic (when $\gamma=1$) and the material behaves more anisotropically as γ deviates further from $\gamma=1$; when $\gamma<1\rightarrow$ material is stiffer vertically than horizontally;	-	- This model is based on Boyce's model and is also known as the anisotropic Boyce model.
-	-	Tatsuoka et al. (1999)	$$E_V = \frac{\partial\sigma_v}{\partial\varepsilon_v} = (E_v)_0 \cdot \left(\frac{\sigma_v}{\sigma_0}\right)^{nv} \cdot F(e)/F(e_0)$$ $$E_h = \frac{\partial\sigma_h}{\partial\varepsilon_h} = (E_h)_0 \cdot \left(\frac{\sigma_h}{\sigma_0}\right)^{nv} \cdot F(e)/F(e_0)$$ $\frac{E_V}{E_h} = \frac{(E_v)_0}{(E_h)_0} \cdot R^n = aR^n$ (when powers nv and nh are the same and equal to n)	- the power n represents the stress-dependency of the quasi-elastic vertical Young's modulus E_v and E_h; - a quantifies the inherent anisotropy; - $R = \frac{\sigma_h}{\sigma_v}$ and quantifies the stress-induced anisotropy at the isotropic stress states; - E_{v0} is the reference vertical stress - Fe is the void ratio function;	-	- Cross-anisotropic-hypo-quasi-elasticity model; - This model depends on four material constants (E_{v0}, v_v, n and a); - The model can predict non-linear and anisotropic resilient stress-strain properties for general stress paths under general stress conditions.
-	-	Witczak et al. (2000)	$$M_r = 10^A k_1 p_a \left(\frac{\theta}{p_a}\right)^{k_2} \left(\frac{\tau_{oct}}{p_a} + 1\right)^{k_3}$$	- $A = a + \frac{b-a}{1+\exp\left(\beta + k_s(S - S_{opt})\right)}$; - S is the degree of saturation and S_{opt} is the saturation at OPT conditions; - θ is the bulk stress; - τ_{oct} is the octahedral shear; - p_a = atmospheric pressure;	-	- The first term of the expression represents the environment related to the contribution of changes in moisture content.

				- k_1, k_2, k_3, a, b and k_s are fitting parameters - β=ln(-b/a).		
-	-	ARA Inc. ERES Division (2004)	$$log\,\frac{M_r}{M_{ropt}} = a + \frac{b-a}{1 + \exp\left(\ln(-b/a) + k_m(S - S_{opt})\right)}$$	- M_r/M_{ropt} is the resilient modulus ratio, where M_r is the resilient modulus at optimum moisture content; - a is the minimum of log(M$_r$/M$_{ropt}$); - b is the maximum of log(M$_r$/M$_{ropt}$); - k_m is a regression parameter; - (S-S_{opt}) is the variation in the degree of saturation.	-	- This model can be used in the case of fine-grained and coarse-grained materials (the difference is expressed in terms of the parameters a, b and k$_m$); - The constants of the model are determined based on RLT testing data; - The model does not combine the effects of the stress state and the moisture content; - The model estimated the change of the resilient modulus at a certain moisture content and at a certain known stress state; - Based on an intensive literature review study, it was developed (selected) a model that analytically predicts changes in modulus due to changes in moisture
-	-	Dawson and Gomes Correia (1993)	$$E_r = 49200 + 950p'_0 - 370q_r - 2400w_p$$	- p'_0 is the initial mean normal effective stress (in kPa); - q_r is the repeated deviator stress (in kPa); - w_p is the plastic limit in %.	-	- This is an analysis based on repeated load triaxial testing carried out on recompacted soils.

Table A.6 - Summaries of permanent deformation models for fine-grained soils – clays

UIC	ASTM classification	Author's model	Equation model	Variables and Empirical Constants	Parameters and characteristics	Observations
-	-	Monismith et al. (1975)	$\varepsilon^p = AN^b$	- ε_p is the plastic deformation (%); - N is the number of load cycles; - A and b are two parameters that represent the influence of other factors.	-	- This model has a limited practical used since there are other factors, besides N, that can influence the permanent deformation; - b is an independent parameter on the deviatoric stress; - The coefficient A corresponds to the plastic deformation after the first cyclic load.
-	-	Chai and Miura (2002)	$\varepsilon^p = a\left(\dfrac{q_d}{q_f}\right)^m \left(1+\dfrac{q_s}{q_f}\right)^n N^b$	- q_s is the initial static deviatoric stress; - n=constant.	-	- This model includes the effects of initial static stress, the magnitude and number of applied loads associated with the passage of the vehicle, and the properties of the subsoil in terms of compression and strength.
-	-	Yesufa and Hoffa (2015)*	$\varepsilon_{p1,N} = N^{m(1-(\sigma_d/q_s))}\varepsilon_{p1,0}$	- $\varepsilon_{p1,N}$ is the axial permanent deformation for the cyclic load N; - $\varepsilon_{p1,0}$ is the cumulative axial permanent deformation after the first cyclic load; - σ_z is the deviatoric stress induced by the passage of the vehicle; - q_s is the static stress measured on the soil; - m is a constant determined to fit the laboratory test results.	-	- The parameters of these materials were found through triaxial tests: the static deviatoric stress comes from the difference between the axial and confining stress in failure; - $\varepsilon_{p1,0}$ is from the equivalent static load in the first cyclic load (based on the plasticity theory).
-	-	Cai et al. (2015)	$\varepsilon_z^p = \alpha_1 N^{\alpha_2}\left(\dfrac{\sigma_{oct}}{\sigma_{atm}}\right)^{\alpha_3}\left(\dfrac{\tau_{oct}}{\sigma_{atm}}\right)^{\alpha_4}$ $\left(\sqrt{1+4\eta^2}\right)^{\alpha_5}$	- $\alpha_1, \alpha_2, \alpha_3, \alpha_4$ and α_5 are constants of the model and determined through laboratory tests; - σ_{oct} and τ_{oct} are the normal and shear octahedral stresses, respectively; - σ_{atm} is the reference stress;	-	- This model is based on a series of tests using the hollow cylinder apparatus. The characteristics of the permanent deformation of a sand were then studied in drained conditions by considering different confining stress levels, ratio of the cyclic vertical stress and ratio of the cyclic torsional stress;

				η is the cyclic torsional stress ratio.		The model was developed to include the rotation of principal stresses.
QS0 High plasticity	CH Fat clay	Li and Selig (1996)	$\varepsilon^p = a\left(\dfrac{q_d}{q_f}\right)^m N^b$	- q_d is the traffic-load-induced dynamic deviator stress; - q_f is the static failure deviator stress of soil; - a, b and m are soil parameters and are related to the plasticity index of the subsoil.	- a=0.64; - b=0.10; - m=1.7.	
QS0 Heavy clay	CH Fat Clay	Puppala et al. (1999)	$\log \varepsilon^p$ $= \log A + \alpha \log N + \beta \, log\left(\dfrac{\sigma_{oct}}{\sigma_{atm}}\right)$	- A, β and α are soil parameters; - σ_{oct} and τ_{oct} are the octahedral normal and shear stresses, respectively.	- W_L=93%; - W_P=29%; - I_P=64% (high plasticity); - Sand content=0%; - Silt content=5%; - Clay content=95%.	The model was tested based on triaxial tests; During this study, materials such as well graded sand, silty clay and clay were considered.
QS0 W_L=60% High plasticity	(without enough data to carry out the ASTM classification)	Wei et al. (2017) – based on Guo (2013) - (Wenzhou structural clay)	$\varepsilon_{q,r} = AN^b;$ $A = \varepsilon_{q,r} = \alpha K_q K_T K_\alpha K_\sigma$	- $\varepsilon_{q,r}$ is the axial residual strain; - A is the residual strain generated in the first cycle; - b is a material parameter determining the cumulating rate of the residual strain with loading cycles and is equal to the gradient of the residual strain curve in the $\ln \varepsilon_{q,r}$ – $\ln N$ coordinate; - K_q and K_T are functions to reflect the effect of wheel load-induced stress; - K_α and K_σ are functions to reflect the effect of initial static stress state and dynamic stress combinations.	- W_n=60-62%; - G_s=2.71; S_t=5.9; - M (critical stress ratio) = 1.31.	This model is based on the power function developed by Monismith et al. (1975); Parameter A depends on the initial stress state and the imposed dynamic stress on non-remoulded Wenzhou clay samples (Guo, 2013). The samples were collected from a depth of 6-7 m; The parameters are based on the work by Xiao et al. (2014) who carried out a series of tests based on the hollow cylinder apparatus.
QS1 (low plasticity)	CL Lean clay	Hyde (1974)	$\varepsilon_1^p = a\dfrac{q}{\sigma_3}$	- a is a constant; - σ_3 is the confining stress; - q is deviator stress.	- W_L=32%; - W_P=18%; - I_P=14%: - G_s=2.74.	The tests included a constant and a variable confining stress; During the analysis, the behaviour of the marl was studied; The author states that these results would be the same if medium confining stress was applied.

383

QS1 Low to medium plasticity	CL Lean clay	Li and Selig (1996)	$\varepsilon^p = a\left(\dfrac{q_d}{q_f}\right)^m N^b$	- q_d is the traffic-load-induced dynamic deviator stress; - q_f is the static failure deviator stress of soil; - a, b and m are soil parameters and are related to the plasticity index of the subsoil.	- a=0.84; - b=0.13; - m=2.0.	
QS1 Silty clay	CL Lean clay	Puppala et al. (1999)	$\log \varepsilon^p = \log A + \alpha \log N + \beta \, log\left(\dfrac{\sigma_{oct}}{\sigma_{atm}}\right)$	- A, β and α are soil parameters; - σ_{oct} and τ_{oct} are the octahedral normal and shear stresses, respectively.	- W_L=44%; - W_p=15%; - I_p=29% (medium plasticity); - Sand content=10%; - Silt content=70%; - Clay content=20%.	- The model was tested based on triaxial tests; - During this study, well-graded sand, silty clay and clay were tested.
QS1 Silty clay	CL Lean clay	Puppala et al. (2009)	$\varepsilon^p = \alpha_1 N^{\alpha_2}\left(\dfrac{\sigma_{oct}}{P_{ref}}\right)^{\alpha_3}\left(\dfrac{\tau_{oct}}{P_{ref}}\right)^{\alpha_4}$	- $\alpha_1, \alpha_2, \alpha_3$ and α_4 are the model constants determined from laboratory tests; - σ_{oct} and τ_{oct} are the octahedral normal and shear stresses, respectively; - P_{ref} is the reference stress.	- W_L=28.19%; - I_p=12.55% (low plasticity); - G_s=2.63; - Passing #200 =80%; - Maximum dry unit weight = 17.10 kN/m³; - W_{opt}=17.11%; - c=60 kPa; - ϕ=18°.	- The model is based on 10,000 cycles; - It includes the effects of mean and shear stresses; - The model was tested based on the cyclic triaxial tests; - The permanent deformation of clay, silt and sand were measured from samples of compacted soil with different water content.
QS1 Silty clayed sand	CL Lean Clay	Puppala et al. (2009)	$\varepsilon^p = \alpha_1 N^{\alpha_2}\left(\dfrac{\sigma_{oct}}{P_{ref}}\right)^{\alpha_3}\left(\dfrac{\tau_{oct}}{P_{ref}}\right)^{\alpha_4}$	- $\alpha_1, \alpha_2, \alpha_3$ and α_4 are the model constants determined from laboratory tests; - σ_{oct} and τ_{oct} are the octahedral normal and shear stresses, respectively; - P_{ref} is the reference stress.	- W_L=16.70%; - I_p=7.50% (low plasticity); - G_s=2.70; - Passing #200=38%; - Maximum dry unit weight =16.9 kN/m³; - W_{opt}=19.3%; - c=103 kPa,; - ϕ=35°.	- The model is based on 10,000 cycles; - It includes the effects of the mean and shear stresses; - The model was tested based on the cyclic triaxial tests; - The permanent deformations of clay, silt and sand were measured from samples of c soil compacted with different water contents.
QS1	CL Lean clay	Wei et al. (2017) – based on Xiao et al. (2014) - Clay (Shanghai	$\varepsilon_{q,r} = AN^b$; $A = \varepsilon_{q,r} = \alpha K_q K_T K_\alpha K_\sigma$	- $\varepsilon_{q,r}$ is the axial residual strain; - A is the residual strain generated in the first cycle; - b is a material parameter determining the cumulating rate of the residual strain with loading cycles and is equal to the gradient of the residual strain	- I_p=21.8%; - I_L= 1.35 (medium plasticity); - G_s=2.74; - W_n=51.8%; - e_o=1.402; - M (critical stress ratio) = 1.28.	- The model is based on the power function developed by Monismith et al. (1975); - Parameter A depends on the initial stress state and the imposed dynamic stress on samples of non-remoulded Wenzhou clay (Guo, 2013). The samples were collected from a depth of 6-7 m;

| | | structural soft clay) | | curve in the ln $\varepsilon_{q,r}$ – ln N coordinate;
- K_q and K_T are functions to reflect the effect of wheel load-induced stress;
- K_α and K_σ are functions to reflect the effect of initial static stress state and dynamic stress combinations. | | - The parameters were determined based on the work by Xiao et al. (2014) who performed a series of tests based on the hollow cylinder apparatus. |

Table A.7 - Summarises of permanent deformation models for fine-grained soils – silts

UIC	ASTM classification	Author's model	Equation model	Variables and Empirical Constants	Parameters and characteristics	Observations
QS1 Low to medium plasticity	ML Silt	Li and Selig (1996)	$\varepsilon^p = a\left(\dfrac{q_d}{q_f}\right)^m N^b$	- q_d is the traffic-load-induced dynamic deviator stress; - q_f is the static failure deviator stress of soil; - a, b and m are soil parameters and are related to the plasticity index of the subsoil.	- a=1.2; - b=0.18; - m=2.4.	
QS1	ML-CL Silt - Lean clay	Chen et al. (2014)	$\varepsilon_1^p(N)$ $= \varepsilon_1^{p0}[1$ $- e^{-BN}]\left(\dfrac{\sqrt{p_{am}^2 + q_{am}^2}}{p_a}\right)^a \cdot$ $\dfrac{1}{m\left(1 + \dfrac{p_{ini}}{p_{am}}\right) + \dfrac{s}{p_{am}} - \dfrac{(q_{ini} + q_{am})}{p_{am}}}$	- $\varepsilon_1^p(N)$ is the strain settlement; - ε_1^{p0}, B, a, s and m are material parameters; - p_a=100 kPa; - p_{ini} and q_{ini} are the mean and deviator stress in the initial state of the layer; - p_{am} and q_{am} are the amplitude of mean stress and deviator stress for train loadings, respectively; - s is the intersection of the *Mohr-Coulomb yielding criterion* in the q axle in the *p-q* space; - m is the slope of the yielding criterion.	- W_L=35 %; - W_P =24 %; - I_P =11 % (low to medium plasticity); - G_s=2.67; - C_u=2.51;C_c=1.32; - Maximum dry density =15.89 kN/m³; - Hydraulic permeability = 5.3×10⁷ m/s; - c'=11.7 kPa; - φ'=16.4°.	The model is based on Gidel's model (Gidel et al., 2001); This model takes into account the direct influence of the initial stress state.

Table A.8 - Permanent deformation models for granular soils (sands)

UIC	ASTM classification	Author's model	Equation model	Variables and Empirical Constants	Parameters and characteristics	Observations
-	-	MEPDG model (ARA Inc. ERES Division, 2004)	$\varepsilon_p = \beta_s \left(\dfrac{\varepsilon_0}{\varepsilon_r} \right) e^{-(\rho/N)^\beta} \varepsilon_v$	- β_s is the global calibration coefficient; - ε_r is the resilient strain imposed in the laboratory test; - ε_v is the average vertical resilient strain (in the base layer of the flexible pavements, for example).	-	- This model considers the effect of the stress on permanent deformation by linearly projecting the plastic deformation obtained from the laboratory tests through vertical strains. This projection is an assumption without any experimental or mechanical justification; it is, therefore, inaccurate due to the nonlinear effect that stress has on the permanent deformation of unbound granular materials - UGM (Gu et al., 2016).
-	-	Korkiala-Tanttu (2005)	$\varepsilon_p(N) = CN^b \dfrac{R}{A - R}$	- C is a parameter dependent on the stress and also compaction degree and water content; - b is a parameter dependent on the stress level, ratio of failure, compaction degree and water content; - A corresponds to the maximum value of the ratio (the author suggests a value close to 1.05); - $R = \dfrac{q}{q_f}$, q is the deviatoric stress and q_f corresponds to the failure deviatoric stress;	-	- This model is based on Sweere's model (Sweere, 1990). - It uses the deviatoric stress ratio to capture the nonlinear effect of the stress state. However, plastic deformation is infinity when the load cycles go to infinity, so the model cannot demonstrate the hardening and softening behavior of UGM.
-	-	Chow et al. (2014)	$\varepsilon^p = AN^B \sigma_d^C \left(\dfrac{\tau_f}{\tau_{max}} \right)^D$	- σ_d is the deviatoric shear stress; - τ_f is the shear stress; - τ_{max} is the shear strength; - A, B, C and D are the regression coefficients.	-	- The model includes the power functions of deviatoric shear stress and the shear strength ratio; - The author developed 16 types of materials with one confining pressure (=34.5 kPa) and three deviatoric stresses. The RLT tests show that this model has higher R^2 values but when the number of load cycles (N) goes to infinity, the accumulated plastic deformation also goes to infinity at one

						confining pressure. Moreover, the deviatoric shear stress term affects the shear ratio in the model and both parameters represent the softening behavior of the material without including the hardening phenomenon.
-	-	Xiao et al. (2015)	$\varepsilon_p = a\left(\dfrac{\theta}{p_0}\right)^b \left(\dfrac{\tau_f}{\tau_{máx}}\right)^c N^d$ $\cdot EXP\Big[e$ $\cdot (S - S_{opt}) + f$ $\cdot wPI + g \cdot wPI$ $\cdot \dfrac{\tau_f}{\tau_{max}} + h \cdot (S$ $- S_{opt}) \cdot \dfrac{\theta}{p_0}\Big]$	- θ is the sum of the principal stresses; - $\tau_t/\tau_{máx}$ is the ratio related to the shear stress; - S corresponds to the saturation level; - S_{opt} corresponds to the optimum saturation level; - wPI corresponds to a weighted plasticity index; - a, b, c, d, e, f, g and h are the parameters determined based on regression analysis.	-	- Triaxial cyclic tests took place on the limestone, dolomite and gravel samples (materials used in base, sub-base and subgrade layers treated in Illinois); - The cohesion and friction angle were determined for three confining stresses.
QS1 Silty sand with high fines content	SM Silty sand	Rahman and Erlingsson (2015) and Salour and Erlingsson (2016)	$\varepsilon_p(N) = \alpha N^{bS_f} S_f$ $S_f = \dfrac{\left(\dfrac{q}{p_a}\right)}{\left(\dfrac{p}{p_a}\right)^\alpha}$	- q is deviatoric stress; - p is mean stress; - p_a atmospheric pressure; - a, b and α are the regression parameters.	- $C_u \approx 28$; $C_c \approx 0.54$; - $G_s = 2.68$; - Fines content=42.2%; - Maximum dry density =19.6 kN/m³; - W_{opt}=10.1%.	- The triaxial tests were carried out by considering the constant confining stress; - They considered high stress levels and reduced stress levels.
QS1 Silty sand with high fines content	SM Silty sand	Rahman and Erlingsson (2015) and Salour and Erlingsson (2016)	$\varepsilon_p(N) = \alpha N^{bS_f} S_f$ $S_f = \dfrac{\left(\dfrac{q}{p_a}\right)}{\left(\dfrac{p}{p_a}\right)^\alpha}$	- q is deviatoric stress; - p is mean stress; - p_a atmospheric pressure; - a, b and α are the regression parameters.	- $C_u \approx 33$; $C_c \approx 0.75$; - $G_s = 2.67$; - Fines content=27.4%; - Maximum dry density =20.3 kN/m³; - W_{opt}=7.6%.	
QS2	SP Poorly graded sand	Huurman (1997)	$\varepsilon_1^p(N) = A\left[\left(\dfrac{N}{1000}\right)^B\right] + C$ $\cdot (e^{D\frac{N}{1000}} - 1)$	A, B, C, D are parameters function of stress level and stress ratio (σ_1/σ_{1f}).	- C_u=1.69; C_c=1.39; - Maximum dry Density = 16.68 kN/m³; - W_{opt}=12.5%; - c=4.08 kPa; ϕ=43.9°.	

QS2	SP Poorly graded sand	Huurman (1997)	$\varepsilon_1^p(N) = A\left[\left(\dfrac{N}{1000}\right)^B\right] + C \cdot (e^{D\frac{N}{1000}} - 1)$	A, B, C, D are parameters function of stress level and stress ratio (σ_1/σ_{1f}).	- C_u=1.69; C_c=0.998; - Maximum dry Density = 16.73 kN/m³; - W_{opt}=13.0%; - c=6.76 kPa; ϕ=43.0°.	
QS2	SP Poorly graded sand	Huurman (1997)	$\varepsilon_1^p(N) = A\left[\left(\dfrac{N}{1000}\right)^B\right] + C \cdot (e^{D\frac{N}{1000}} - 1)$	A, B, C, D are parameters function of stress level and stress ratio (σ_1/σ_{1f}).	- C_u=1.88; C_c=1.04; - Maximum dry Density = 16.56 kN/m³ - W_{opt}=14.0%; - c=6.34 kPa; ϕ=41.8°.	
QS2	SP Poorly graded sand	Huurman (1997)	$\varepsilon_1^p(N) = A\left[\left(\dfrac{N}{1000}\right)^B\right] + C \cdot (e^{D\frac{N}{1000}} - 1)$	A, B, C, D are parameters function of stress level and stress ratio (σ_1/σ_{1f}).	- C_u=2.10; C_c=1.05; - Maximum dry Density = 16.90 kN/m³; - W_{opt}=12.5%; - c=5.60 kPa; ϕ=48.2°.	Cyclic triaxial tests took place on the sands used in the base layers; The samples were subjected to a confining stress equal to 12 kPa (corresponds to a depth equal to 0.60m); During the test, a million cycles were applied (frequency equal to 5 Hz).
QS2	SP Poorly graded sand	Huurman (1997)	$\varepsilon_1^p(N) = A\left[\left(\dfrac{N}{1000}\right)^B\right] + C \cdot (e^{D\frac{N}{1000}} - 1)$	A, B, C, D are parameters function of stress level and stress ratio (σ_1/σ_{1f}).	- C_u=1.70; C_c=1.10; - Maximum dry Density = 15.61 kN/m³; - W_{opt}=14.50%. - c=7.19 kPa; ϕ=42.8°;	
QS2	SP Poorly graded sand	Huurman (1997)	$\varepsilon_1^p(N) = A\left[\left(\dfrac{N}{1000}\right)^B\right] + C \cdot (e^{D\frac{N}{1000}} - 1)$	A, B, C, D are parameters function of stress level and stress ratio (σ_1/σ_{1f}).	- C_u=2.35; C_c=1.14; - Maximum dry Density = 16.16 kN/m³; - W_{opt}=14.5%; - c=7.99 kPa; - ϕ=39.7°.	
QS2	SP Poorly graded sand	Huurman (1997)	$\varepsilon_1^p(N) = A\left[\left(\dfrac{N}{1000}\right)^B\right] + C \cdot (e^{D\frac{N}{1000}} - 1)$	A, B, C, D are parameters function of stress level and stress ratio (σ_1/σ_{1f}).	- C_u=3.76; C_c=1.37; - Maximum dry Density = 16.16 kN/m³; - W_{opt}=13.5%; - c=7.48 kPa; - ϕ=42.9°.	
QS2	SP Poorly graded sand	Sweere (1990)	$log\left(\varepsilon_1^p(N)\right) = a + b\, log\,(N)$	a, b – material parameters for each stress level, separate permanent strain parameters a and b need to be determined from the results of the cyclic load triaxial test.	Density = 16.79 kN/m³; - C_u =1.68; - C_c =1.10.	- Application of 10^6 cyclic loads during the triaxial cyclic tests; - The samples consisted of granular materials used in the base layers, and sands; - The *UGM* samples were subjected to triaxial cyclic tests.

				**Sweeres's formula is valid for granular materials (Gidel et al., 2001).		
QS2 Sa (>0.063 to 2)	SP Poorly graded sand	Puppala et al. (2009)	$\varepsilon^p = \alpha_1 N^{\alpha_2}\left(\dfrac{\sigma_{oct}}{P_{ref}}\right)^{\alpha_3}\left(\dfrac{\tau_{oct}}{P_{ref}}\right)^{\alpha_4}$	$\alpha_1, \alpha_2, \alpha_3$ and α_4 are the model constants determined from laboratory tests; σ_{oct} and τ_{oct} are the octahedral normal and shear stresses, respectively; P_{ref} is the reference stress.	- W_L=26.40%; - G_s=2.71%; - Passing #200=0.70%; - C_u= 1.79; C_c=0.89; - Maximum dry unit weight =15.70 kN/m³; - W_{opt}=13.70%; - c=20 kPa; - ϕ=42°.	- The model is based on 10,000 cycles, and includes the effects of mean and shear stresses; - The model was tested based on the cyclic triaxial tests; - The permanent deformation of clay, silt and sand were measured using the soil samples compacted with different water content.
QS2 Gravelly sand (SaGr)	SP Sand poorly graded	Chen et al. (2014)	$\varepsilon_1^p(N)$ $= \varepsilon_1^{p0}[1$ $- e^{-BN}]\left(\dfrac{\sqrt{p_{am}^2 + q_{am}^2}}{p_a}\right)^a \cdot$ $\dfrac{1}{m\left(1 + \dfrac{p_{ini}}{p_{am}}\right) + \dfrac{s}{p_{am}} - \dfrac{(q_{ini} + q_{am})}{p_{am}}}$	$\varepsilon_1^p(N)$ is the strain settlement; ε_1^{p0}, B, a, s and m are material parameters; p_a=100 kPa; p_{ini} and q_{ini} are the mean and deviator stress in the initial state of the layer; p_{am} and q_{am} are the amplitude of mean stress and deviator stress for train loadings, respectively.	- G_s=2.66; - C_u=4.8; C_c=0.62; - Maximum dry density =20.69 kN/m³; - Minimum dry density =15.89 kN/m³; - Hydraulic permeability = 3.2×10⁻⁵m/s; - c'=0 kPa; - ϕ'=33°.	- The model is based on Gidel's model (Gidel et al., 2001); - It is considered the direct influence of the initial stress state.
QS2 Sa (>0.063 to 2) Fine sand	SP Poorly graded sand	Cai et al. (2015)	$\varepsilon_z^p = \alpha_1 N^{\alpha_2}\left(\dfrac{\sigma_{oct}}{\sigma_{atm}}\right)^{\alpha_3}\left(\dfrac{\tau_{oct}}{\sigma_{atm}}\right)^{\alpha_4}$ $\left(\sqrt{1 + 4\eta^2}\right)^{\alpha_5}$	$\alpha_1, \alpha_2, \alpha_3, \alpha_4$ and α_5 are constants of the model and determined through laboratory tests; σ_{oct} and τ_{oct} are the normal and shear octahedral stresses, respectively; σ_{atm} is the reference stress η is the cyclic torsional stress ratio.	- G_s=2.70; - $C_u \approx$1.63; - $C_c \approx$0.89; - D_{50}=0.17 mm; - e_{max}=1.142; e_{min}=0.628.	- The model is based on a series of tests using the hollow cylinder apparatus. The permanent deformation of a sand was studied in drained conditions by considering different levels of confining stress, and the ratios of cyclic vertical stress and cyclic torsional stress; - This model was developed to incorporate the rotation of principal stresses.
QS2	SP Poorly-graded sand	Lekarp and Dawson (1998)	$\dfrac{\varepsilon_1^p(N_{ref})}{(L/p_0)} = a \cdot \left(\dfrac{q}{p}\right)_{max}^b$	a and b: N_{ref}; $L = \sqrt{q^2 + p^2}$; $p_0 = 100$ kPa (reference mean stress).	- Dry density=14.91 kN/cm³; - $C_u \approx$1.5; - $C_c \approx$1.0.	Triaxial cyclic tests and hollow cylinder tests were carried out on limestone, sand and gravel.
QS2	SP Poorly-graded sand	Qian et al. (2019a)	$\varepsilon_N^{acc} = (\alpha_1\Delta\gamma + \alpha_2) + (\alpha_3\Delta\gamma + \alpha_4)ln\dfrac{N}{100}$	ε_N^{acc} is the Nth vertical accumulative strain in percentage;	- G_s=2.54; - $C_u \approx$1.65; - $C_c \approx$1.00;	Drained cyclic triaxial tests with different levels of initial mean effective stress (p), relative density (D), initial static

				- N is the number of loading cycles - $\Delta\gamma$ is the calculated shear strain amplitude in percentage - $\alpha_1 - \alpha_4$ are model parameters	- D_{50}=0.16 mm; - e_{max}≈0.931; - e_{min}=0.611.	stress ratio (n_s) and cyclic stress ratio were performed on saturated Toyoura sand. Indeed, the effects of cyclic stress ratio and initial mean effective stress on the permanent deformation; The estimated permanent strains show a good agreement with the measured data. The deviation between the estimation and the measurement is less than 20%.
QS3	SP Poorly graded sand	Hyde (1974)	$\varepsilon_1^p = a\,\dfrac{q}{\sigma_3}$	- a is a constant; - σ_3 is the confining stress; - q is deviator stress.	- G_s=2.72; - C_u≈16; - C_c≈0.69; - Maximum dry density=21.76 kN/m³; - W_{opt}=7.5±0.5%;	The tests were carried out under a constant and variable confining stress; During the analysis, the behaviour of the marl was studied; The author states that the results would be the same if medium confining stress was applied.
QS3	SP Poorly-graded sand	Lekarp and Dawson (1998)	$\dfrac{\varepsilon_1^p(N_{ref})}{(L/p_0)} = a\cdot\left(\dfrac{q}{p}\right)^b_{max}$	- a and b; - N_{ref}; - $L = \sqrt{q^2 + p^2}$; - $p_0 = 100$ kPa (reference mean stress).	- Dry density=20.10 kN/m³; - C_u≈32; - C_c≈0.2.	Triaxial cyclic tests and hollow cylinder tests were carried out on limestone, sand and gravel.
QS3 Sa(>0.063 to 2)	SW Well-graded sand	Puppala et al. (1999)	$\log\varepsilon^p = \log A + \alpha\log N$ $+ \beta\,log\left(\dfrac{\sigma_{oct}}{\sigma_{atm}}\right)$	- A, β and α are soil parameters; - σ_{oct} and τ_{oct} are the octahedral normal and shear stresses, respectively.	- % sand =100.	The model was tested based on triaxial tests; During his study, well-graded sand, silty clay and clay were considered.
QS3	SW Well-graded sand	Huurman (1997)	$\varepsilon_1^p(N) = A\left[\left(\dfrac{N}{1000}\right)^B\right] + C$ $\cdot\left(e^{D\frac{N}{1000}} - 1\right)$	- A, B, C, D are parameters function of stress level and stress ratio ($\sigma_1/\sigma_{1,f}$)	- C_u=10.5; C_c=1.25; - Maximum dry Density = 17.21 kN/m³; - W_{opt}=10.5%; - c=8.68 kPa; - ϕ=50.2°.	Cyclic triaxial tests were carried out on the sands used in the base layers; The samples were subjected to a confining stress equal to 12 kPa (corresponds to a depth equal to 0.60m); During the test, a million cycles were applied (frequency equal to 5 Hz).

391

Table A.9 - Permanent deformation model for granular soils (gravels and sandy gravels)

UIC	ASTM classification	Author's model	Equation model	Variables and Empirical Constants	Parameters and characteristics	Observations
QS2 Sandy gravel (GrSa) $C_u \approx 200$; $C_c \approx 0.8$	GP-GM/GC Poorly-graded sandy gravel (no information about the fines)	Rahman and Erlingsson (2015)	$\varepsilon_p(N) = \alpha N^{bS_f} S_f$ $$S_f = \frac{\left(\frac{q}{p_a}\right)}{\left(\frac{p}{p_a}\right)^\alpha}$$	- q is deviatoric stress; - p is mean stress; - p_a atmospheric pressure; - a, b and α are the regression parameters.	- G_s=2.54; - Maximum dry density =21.67 kN/m³; - Fines Content = 10.2%; - W_{opt} =6%.	
QS2 Sandy gravel (GrSa) $C_u \approx 73$; $C_c \approx 1.5$	GW-GM/GC Well-graded sandy gravel (no information about the fines)	Rahman and Erlingsson (2015)	$\varepsilon_p(N) = \alpha N^{bS_f} S_f$ $$S_f = \frac{\left(\frac{q}{p_a}\right)}{\left(\frac{p}{p_a}\right)^\alpha}$$	- q is deviatoric stress; - p is mean stress; - p_a atmospheric pressure; - a, b and α are the regression parameters.	- G_s=2.68; - Fines Content = 8.6%; - Maximum dry density = 23.05 kN/m³; - W_{opt} =6.9%.	The triaxial tests took place by considering constant confining stress; The tests considered high stress levels and reduced stress levels.
QS2 Sandy gravel (GrSa) $C_u \approx 98$; $C_c \approx 2.8$	GW-GM/GC Well-graded sandy gravel (no information about the fines)	Rahman and Erlingsson (2015)	$\varepsilon_p(N) = \alpha N^{bS_f} S_f$ $$S_f = \frac{\left(\frac{q}{p_a}\right)}{\left(\frac{p}{p_a}\right)^\alpha}$$	- q is deviatoric stress; - p is mean stress; - p_a atmospheric pressure; - a, b and α are the regression parameters.	- G_s=2.64; - Fines Content = 6.5%; - Maximum dry density = 22.16 kN/m³; - W_{opt} =6 %.	
QS2 Sandy gravel (GrSa) $C_u \approx 117$; $C_c \approx 2.2$	GW-GM/GC Well-graded sandy gravel (no information about the fines)	Rahman and Erlingsson (2015)	$\varepsilon_p(N) = \alpha N^{bS_f} S_f$ $$S_f = \frac{\left(\frac{q}{p_a}\right)}{\left(\frac{p}{p_a}\right)^\alpha}$$	- q is deviatoric stress; - p is mean stress; - p_a atmospheric pressure; - a, b and α are the regression parameters.	- G_s=2.64; - Fines Content = 12%; - Maximum dry density =21.77 kN/m³; - W_{opt} =6.5 %.	
QS2-QS3 (average to good soils) Classification based on the LA and MDE results.	-	Gidel et al. (2001)	$\varepsilon_p(N) = \varepsilon^0 \left[1 - \left(\frac{N}{100}\right)^{-B}\right]$ $\times \left(\frac{L_{máx}}{p_a}\right)^u \left(m + \frac{s}{p_{max}} - \frac{q_{max}}{p_{max}}\right)^{-1}$	- ε^0, B and u are material parameters - p_{max} and q_{max} are the maxima applied hydrostatic stress and the deviator stress, respectively. - s is the intercept of the Mohr-Coulomb failure line in the p-q space - m is the slope of this failure line - p_a correspond to the reference stress (100 kPa).	0/20 mm (limestone unbound granular material); LA=22; MDE=15; p_{aSPO}=2450 kg/m³; W_{SPO}=4.4%; Fines content=10%; D=160 mm; H=320 mm.	- This model is based on cyclic triaxial tests on two samples where the particles had different dimensions: hard limestone (0/20 mm) and microgranite (0/10 mm); - The tests included several load levels (40) at almost 20,000 cycles.

				- The value $L_{máx}$ is calculated considering the following expression: - - $L_{máx} = \sqrt{p_{max}^2 + q_{max}^2}$		
QS2-QS3 (average to good soils) Classification of the subgrade (based on the LA and MDE results):	-	Gidel et al. (2001)	$\varepsilon_p\left(N\right) = \varepsilon^0\left[1 - \left(\dfrac{N}{100}\right)^{-B}\right]$ $\times \left(\dfrac{L_{máx}}{p_a}\right)^u \left(m + \dfrac{s}{p_{max}} - \dfrac{q_{max}}{p_{max}}\right)^{-1}$	- ε^o, B and u are material parameters - p_{max} and q_{max} are the maxima applied hydrostatic stress and the deviator stress, respectively. - s is the intercept of the Mohr-Coulomb failure line in the p-q space - m is the slope of this failure line - p_a correspond to the reference stress (100 kPa). - The value $L_{máx}$ is calculated considering the following expression: - $L_{máx} = \sqrt{p_{max}^2 + q_{max}^2}$	0/10 mm (granular material obtained from microgranite); LA=20; MDE=13; p_{dSPO}=2200 kg/m³; W_{SPO}=6.3% Fines content=7.8%; D=76.2 mm.	
QS2 – QS3 Sandy gravel (GrSa)	GW Well-graded gravel	Ling et al. (2017)	$\varepsilon_{acc}(N) = f_{ampl}f_n f_p f_N$	- f_{ampl} describes the range intensity of PD with the increase of the cyclic stress amplitude; - f_r represents the influence of the initial mean stress; - f_r represents the influence of the initial stress ratio; - f_N characterizes the trend of the variation's deformation with the number of cyclic loads.	C_u≈60; C_c≈1.3; Sand content=40%; Gravel content =60%;	The study focused on granular materials.
QS3	GP Poorly-graded gravel	Lekarp and Dawson (1998)	$\dfrac{\varepsilon_1^p\left(N_{ref}\right)}{(L/p_0)} = a \cdot \left(\dfrac{q}{p}\right)^b_{max}$	- a and b; - N_{ref}; - $L = \sqrt{q^2 + p^2}$; - $p_0 = 100$ kPa (reference mean stress).	Dry density=21.18 kN/m³; C_u≈92; C_c≈6.4.	Triaxial cyclic tests and hollow cylinder tests took place on limestone, sand and gravel.
QS3 Sandy gravel (GrSa)	GP Poorly-graded sandy gravel	Rahman and Erlingsson (2015)	$\varepsilon_p(N) = \alpha N^{bS_f} S_f$	- q is deviatoric stress; - p is mean stress; - p_a atmospheric pressure;	G_s=2.49; Fines Content (<0.075 mm) = 3.8%;	The triaxial tests considered constant confining stress;

393

$C_u \approx 26$; $C_c \approx 0.9$			$S_f = \dfrac{\left(\dfrac{q}{p_a}\right)}{\left(\dfrac{p}{p_a}\right)^\alpha}$	- a, b and α are the regression parameters.	W_{opt} =7.5%; Maximum dry density = 20.89 kN/m³.	The tests also considered high stress levels and reduced stress levels.
QS3 Sandy gravel (GrSa) $C_u \approx 35$; $C_c \approx 4.6$	GP Poorly-graded sandy gravel	Rahman and Erlingsson (2015)	$\varepsilon_p(N) = \alpha N^{bS_f} S_f$ $S_f = \dfrac{\left(\dfrac{q}{p_a}\right)}{\left(\dfrac{p}{p_a}\right)^\alpha}$	- q is deviatoric stress; - p is mean stress; - p_a atmospheric pressure; - a, b and α are the regression parameters.	Fines Content (<0.075 mm) = 1.4%; W_{opt} =5%; Gs=2.61; Maximum dry density = 21.18 kN/m³.	
QS3	GW Well-graded Gravel	Lekarp and Dawson (1998)	$\dfrac{\varepsilon_1^p(N_{ref})}{(L/p_0)} = a \cdot \left(\dfrac{q}{p}\right)_{max}^b$	- a and b; - N_{ref}; - $L = \sqrt{q^2 + p^2}$; - $p_0 = 100$ kPa (reference mean stress);	Dry density=20.50 kN/m³; Cu≈75; Cc≈1.3.	Triaxial cyclic tests and hollow cylinder tests took place on limestone, sand and gravel.
QS3	GW Well-graded Gravel	Lekarp and Dawson (1998)	$\dfrac{\varepsilon_1^p(N_{ref})}{(L/p_0)} = a \cdot \left(\dfrac{q}{p}\right)_{max}^b$	- a and b; - N_{ref}; - $L = \sqrt{q^2 + p^2}$; - $p_0 = 100$ kPa (reference mean stress).	Dry density=22.16 kN/m³; Cu≈55; Cc≈1.3.	
QS3 Sandy gravel (GrSa) $C_u \approx 16$; $C_c \approx 1.6$	GW Well-graded sandy gravel	Rahman and Erlingsson (2015)	$\varepsilon_p(N) = \alpha N^{bS_f} S_f$ $S_f = \dfrac{\left(\dfrac{q}{p_a}\right)}{\left(\dfrac{p}{p_a}\right)^\alpha}$	- q is deviatoric stress; - p is mean stress; - p_a atmospheric pressure; - a, b and α are the regression parameters.	G_s=2.64; Fines Content= 2.4%; Maximum dry density = 20.59 kN/m³; W_{opt} =5.5 %.	The triaxial tests considered constant confining stress; The tests also considered high stress levels and reduced stress levels.
QS3 Sandy gravel (GrSa) $C_u \approx 20$; $C_c \approx 1.5$	GW Well-graded sandy gravel	Rahman and Erlingsson (2015)	$\varepsilon_p(N) = \alpha N^{bS_f} S_f$ $S_f = \dfrac{\left(\dfrac{q}{p_a}\right)}{\left(\dfrac{p}{p_a}\right)^\alpha}$	- q is deviatoric stress; - p is mean stress; - p_a atmospheric pressure; - a, b and α are the regression parameters.	G_s=2.63; Fines Content= 2.2%; Maximum dry density =20.35 kN/m³; W_{opt} =5.5 %.	
QS3	GW Well-graded Grave (granite aggregate)	Gu et al. (2016)	$\varepsilon^p = \varepsilon_0 e^{-\left(\frac{\rho}{N}\right)} \left(\sqrt{J_2}\right)^m (\alpha I_1 + K)^n$ $\alpha = \dfrac{2\sin\varnothing}{\sqrt{3}(3 - \sin\varnothing)}$ $K = \dfrac{c \cdot 6\cos\varnothing}{\sqrt{3}(3 - \sin\varnothing)}$	- J_2 is the second invariant of the deviatoric stress tensor; - I_1 is the first invariant of the stress tensor; - c and ϕ are the cohesion and friction angle, respectively; - ε_0, ρ, β, m and n are model coefficients.	γ_d=2.162 kg/m³; ω= 6.7%; PI=4; LL=25; ϕ=51.3°; c=20.2 kPa; $C_u \approx 25$; $C_c \approx 2.8$.	This model used the shear strength ratio and stress terms in the Drucker-Prager model to construct a stress-dependent model; The stress term $\sqrt{J_2}$ represents the softening effects that deviatoric shear stress has on the material, and a larger

394

| QS3 | GW Well-graded Gravel (limestone conglomerate aggregate) | Gu et al. (2016) | $\varepsilon^p = \varepsilon_0 e^{-\left(\frac{\rho}{N}\right)} \left(\sqrt{J_2}\right)^m (\alpha I_1 + K)^n$

 $\alpha = \dfrac{2\sin\emptyset}{\sqrt{3}(3 - \sin\emptyset)}$

 $K = \dfrac{c \cdot 6\cos\emptyset}{\sqrt{3}(3 - \sin\emptyset)}$ | - J_2 is the second invariant of the deviatoric stress tensor;
 - I_1 is the first invariant of the stress tensor;
 - c and ϕ are the cohesion and friction angle, respectively;
 - ε_0, ρ, β, m and n are model coefficients. | - γ_d=1.934 kg/m³;
 - ω= 13.5%;
 - PI=non-plastic; LL=not applicable;
 - ϕ=54.9°; c=66.2 kPa;
 - C_u≈45; C_c≈1.25. | value yields larger permanent deformation;
 - The power m is always positive and the term $\alpha I_1 + K$ indicates the hardening/strengthening effect that hydrostatic stress has on UGM; it is highly affected by the strength parameter (cohesion and friction angle);
 - A higher value of $\alpha I_1 + K$ leads to smaller plastic deformation. The power n is always a negative number. The authors carried out a compressive strength test to determine the cohesion, the friction angle, and also α and K by plotting the diagram $\sqrt{J_2} - I_1$and Repeated Load Triaxial Tests (N=10,000 cycles). |